Convective Heat Transfer with and without Film Cooling in High Temperature, Fuel Rich and Lean Environments

DISSERTATION

Nathan J. Greiner, Captain, USAF

AFIT-ENY-DS-14-S-28

DEPARTMENT OF THE AIR FORCE
AIR UNIVERSITY

AIR FORCE INSTITUTE OF TECHNOLOGY

Wright-Patterson Air Force Base, Ohio

AFIT-ENY-DS-14-S-28

CONVECTIVE HEAT TRANSFER WITH AND WITHOUT FILM COOLING IN HIGH TEMPERATURE, FUEL RICH AND LEAN ENVIRONMENTS

DISSERTATION

Presented to the Faculty
Graduate School of Engineering and Management
Air Force Institute of Technology
Air University
Air Education and Training Command
in Partial Fulfillment of the Requirements for the
Degree of Doctor of Philosophy

Nathan J. Greiner, BS, MS
Captain, USAF

September 2014

DISTRIBUTION STATEMENT A. APPROVED FOR PUBLIC RELEASE;
DISTRIBUTION UNLIMITED.

AFIT-ENY-DS-14-S-28

CONVECTIVE HEAT TRANSFER WITH AND WITHOUT FILM COOLING IN HIGH TEMPERATURE, FUEL RICH AND LEAN ENVIRONMENTS

Nathan J. Greiner, BS, MS
Captain, USAF

Approved:

Marc D Polanka
Marc D. Polanka, PhD (Chairman)

25 AUG 2014
Date

Maj James L. Rutledge, PhD (Member)

26 Aug 2014
Date

Paul I. King, PhD (Member)

24 Aug 14
Date

Kevin C. Gross, PhD (Member)

25-Aug-2014
Date

David L. Blunck, PhD (Member)

8/18/14
Date

Accepted:

Adedeji Badiru
ADEDEJI B. BADIRU, PhD
Dean, Graduate School of Engineering
and Management

29 Aug 2014
Date

AFIT-ENY-DS-14-S-28

Abstract

Modern turbine engines require high turbine inlet temperatures and pressures to maximize thermal efficiency. Increasing the turbine inlet temperature drives higher heat loads on the turbine surfaces. In addition, increasing pressure ratio increases the turbine coolant temperature such that the ability to remove heat decreases. As a result, highly effective external film cooling is required to reduce the heat transfer to turbine surfaces. Testing of film cooling on engine hardware at engine temperatures and pressures can be exceedingly difficult and expensive. Thus, modern studies of film cooling are often performed at near ambient conditions. However, these studies are missing an important aspect in their characterization of film cooling effectiveness. Namely, they do not model effect of thermal property variations that occur within the boundary and film cooling layers at engine conditions. Also, turbine surfaces can experience significant radiative heat transfer that is not trivial to estimate analytically.

The present research first computationally examines the effect of large temperature variations on a turbulent boundary layer. Subsequently, a method to model the effect of large temperature variations within a turbulent boundary layer in an environment coupled with significant radiative heat transfer is proposed and experimentally validated. Next, a method to scale turbine cooling from ambient to engine conditions via non-dimensional matching is developed computationally and the experimentally validated at combustion temperatures.

Increasing engine efficiency and thrust to weight ratio demands have driven increased combustor fuel-air ratios. Increased fuel-air ratios increase the possibility of unburned fuel species entering the turbine. Alternatively, advanced ultra-compact combustor designs have been proposed to decrease combustor length, increase thrust, or generate power for directed energy weapons. However, the ultra-compact combustor design requires a film cooled vane within the combustor. In both these environments, the unburned fuel in the core flow encounters the oxidizer rich film cooling stream, combusts, and can locally heat the turbine surface rather than the intended cooling of the surface. Accordingly, a method to quantify film cooling performance in a fuel rich environment is prescribed. Finally, a method to film cool in a fuel rich environment is experimentally demonstrated.

AFIT-ENY-DS-14-S-28

To My Wife and Children

Acknowledgements

There are many who, through their help and support, have made this dissertation possible. Dr. Marc Polanka has lent his time and expertise to forming the direction of my research and has spent countless hours helping to decipher the experimental and computational results. His tireless support has had a tremendous impact on developing me as both an engineer and an officer.

I also thank Maj James Rutledge, Dr. Paul King, Dr. Kevin Gross, and Dr. David Blunck for serving on my committee. Their diverse backgrounds and areas of expertise have strengthened this document immeasurably. I especially thank Maj James Rutledge for the copious hours he spent with me discussing this research. Many parts of this work are a direct result of those discussions.

I thank Lt Jacob Robertson for his essential leadership in designing and assembling the experimental facility. He and I spent many hours learning to operate the facility and fine-tuning the experiment. Andrew Shewhart was also instrumental in making improvements to the heat transfer diagnostics and in operating the facility to gather the experimental measurements presented in this document.

The staff of the Air Force Research Lab Combustion and Fuels Branches gave extraordinary support in assembling, operating, and maintaining the experimental facility. In addition, they afforded me abundant patience as I learned much from their extensive experiences. Dr. Scott Stouffer gave many hours of indispensable assistance in operating the facility and diagnosing issues. Also, Richard Zehring and Mike Arstingstall played pivotal roles in assembling the facility and daily operations. Their immense skill and expertise were invaluable and enabled the experimental studies. Harold Day voluntarily donated his time and worked over the winter break to allow us to continue testing. Jerry Grieselhuber acquired parts for the facility and Mark Laber assembled the plumbing. Their efforts allowed the combustion temperature

testing of this research. I also thank Jack Yoder for his help in coordinating test article fabrication and Steve Pennington for his role in machining test articles.

From the Department of Defense Supercomputing Resource Center, I thank Hugh Thornburg for his assistance in assembling computational domains for grid convergence studies and for providing indispensable guidance on executing the computational studies. From the Air Force Institute of Technology, I thank David Doak for his persistent help in resolving issues with both the computational hardware and software.

To my wife, I give my sincerest gratitude. She has sacrificed much over the past three years. She has been my inspiration, my encouragement, and my strength. Without her, I could not have finished this challenging and demanding program.

To my children, I give my sincerest apologies. Your father is an engineer and you are stuck with him!

Nathan J. Greiner

Table of Contents

Page

List of Figures

Figure Page

Figure Page

Figure Page

Figure Page

Figure Page

Figure Page

List of Tables

Table Page

Nomenclature

Symbols

a	Speed of sound (m/s)
A	Arrhenius pre-exponential factor or cross-sectional area (m^2)
(A/F)	Air to fuel ratio by mass
c_f	Coefficient of friction, $\tau_w/0.5\rho u_\infty^2$
c_p	Specific heat at constant pressure (J/kg K)
c_v	Specific heat at constant volume (J/kg K)
D	Film cooling hole diameter (m)
D_h	Hydraulic diameter, $4A/P$ (m)
Da	Damköhler number, $\tau_{\mathrm{flow}}/\tau_{\mathrm{chem}}$
DR	Density ratio, ρ_c/ρ_∞
E	Arrhenius exponential factor
F	Force (N)
g	Centripetal acceleration as a multiple of earth's gravity
G	Mass flux ($\mathrm{kg/m^2\,s}$)
h	Convective heat transfer coefficient ($\mathrm{W/m^2\,K}$)
i	Enthalpy (J/kg) or Radiation intensity ($\mathrm{W/m^2\,sr}$)
I	Momentum ratio, $\rho_c u_c^2/\rho_\infty u_\infty^2$
k	Thermal conductivity (W/m K) or turbulent kinetic energy ($\mathrm{m^2/s^2}$)
$k^{('/'')}$	Forward/reverse reaction rate coefficient
l_0	Integral length scale (m)
$\dot{m}$	Mass flow rate (kg/s)
M	chemical symbol abbreviation or Mass flux (blowing) ratio, $\rho_c u_c/\rho_\infty u_\infty$
Ma	Mach number u_∞/a
n	Number of samples

N	Number of reactant or product species in a reaction
Nu_L	Nusselt number with length scale L, hL/k
p	Pressure (Pa)
P	Distance around perimeter (m) or rate of production
$\mathrm{PF}_{\mathrm{pattern}}$	Pattern factor, $(T_{t,\mathrm{exit,max}} - T_{t,4})/(T_{t,4} - T_{t,3})$
$\mathrm{PF}_{\mathrm{profile}}$	Profile factor, $((\overline{T_{t,\mathrm{exit}}})_{\mathrm{max}} - T_{t,4})/(T_{t,4} - T_{t,3})$
Pr	Prandtl number, $\mu c_p/(k)$
q	Heat addition or rejection per unit mass (W/kg)
q''	Heat flux (W/m^2)
$\Delta q''_f$	Non-reacting net heat flux reduction, $1 - q''_f/q''_0$
$\Delta q''_r$	Reacting net heat flux reduction, $1 - q''_f/q''_0$
$\nabla q''_r$	Degradation of net heat flux reduction , $\Delta q''_f - \Delta q''_r$
r	Recovery factor
Re_L	Reynolds number with length scale L, $\rho u_\infty L/\mu$
R_u	Universal gas constant (J/mol K)
s	Specific entropy (J/kg K)
S	Speed (m/s) or Sutherland's Law coefficient (K)
St	Stanton Number, $h/\rho u_\infty c_p$
ST	Specific thrust, $F_p/\dot{m}_a$
t	Time (s)
T	Temperature (K)
$\hat{T}$	Temperature after Kirchhoff transformation (K)
T_0	Sutherland's Law coefficient (K)
TSFC	Thrust specific fuel consumption, $\dot{m}_{\mathrm{fuel}}/F_p$
Tu	Turbulence intensity, $u'_{\mathrm{rms}}/u_\infty$
u	Streamwise Velocity (m/s)

$\overline{u}$	Time averaged, steady component of u
u'	Unsteady component of u
u_τ	Friction velocity, $\sqrt{\tau_w/\rho}$ (m/s)
v	Wall normal velocity (m/s)
V	Magnitude of the velocity vector (m/s)
$\dot{V}$	Volumetric flow rate (L/min)
VR	Velocity ratio, u_c/u_∞
w	Work per unit mass (W/kg)
x	Streamwise direction or distance from the leading edge (m)
X	Linearization parameter
y	Wall normal direction or distance (m)
Y	Linearization parameter
z	Spanwise direction or distance (m)

Subscripts

0	Without film cooling or initial
1	Engine inlet
2	Low pressure compressor inlet
2.5	High pressure compressor inlet
3	Compressor exit, regenerator inlet or combustor inlet if no regenerator install
3.5	Regenerator exit (if installed), combustor inlet
4	Combustor exit, high pressure turbine inlet
4.5	Low pressure turbine inlet
5	Low pressure turbine exit
act	Actual
ad	Adiabatic flame

app	Apparent from measurements and linearized convective heat transfer
aw	Adiabatic wall
b	Blade or block material
c	Coolant
chem	Characteristic of the chemistry
cond	Conductive heat transfer
conv	Convective heat transfer
corr	Corrected
CP	Constant properties evaluated in the freestream
d	Difference between total and recovery
e	Film cooling hole exit
est	Estimated quantity
exit	Exit of the system control volume
f	With film cooling or final
fit	Parameter determined by linear regression
flow	Characteristic of the flow
fuel	Fuel
g	Radiation from participating gas
i	Incident radiation or internal of turbine wall or index notation
in	Into the system control volume
inlet	Inlet of the system control volume
j	Counter for the jth species in the reaction equation
L	Laminar flame or arbitrary length scale (m)
LCP	Locally constant properties
max	Maximum
min	Minimum

net	Net, difference between output and input
o	Radiation leaving a surface
out	Out of the system control volume
p	Propulsive or entrance of the film cooling plenum
r	Recovery or counter for the rth reaction equation
rad	Radiative heat transfer
ref	Reference
rms	Root mean square
R	Reference temperature for evaluating flow properties
std	Standard temperature (294 K) and pressure (1 atm)
stoic	Stoichiometric
t	Total
$trip$	Turbulent trip step
w	Wall
x	Streamwise direction
y	Wall normal direction
z	Spanwise direction
∞	Freestream

Superscripts

b	Arrhenius rate exponent
E	Arrhenius rate exponent
n	Empirical exponent
m	Empirical exponent
β	Empirical exponent
$+$	Wall coordinates (properties evaluated at the wall)

$*$	Modified wall coordinates (properties evaluated locally)
$('/'')$	Forward/reverse reaction direction
$\overline{(...)}$	Averaged quantity

Greek Letters

α	Damping coefficient or film cooling injection angle (downstream $= 0°$)
α_w	Total absorptivity of optically gray wall
β_1	Inlet angle
β_2	Outlet angle
γ	Ratio of specific heats, c_p/c_v
δ	Thickness or height (m)
$\delta(...)$	Uncertainty
δ_1	Displacement thickness (m)
δ_2	Momentum thickness (m)
δ_3	Variable property viscous sublayer length scale (m)
δ_{99}	Velocity boundary layer thickness (m)
Δ	Difference in spatial locations
ϵ	Regenerator efficiency, $q_{\text{regen,act}}/q_{\text{regen,max}}$, or turbulent dissipation rate
ϵ_w	Total emissivity of optically gray wall
ε	Small change in wall temperature (K)
η	Adiabatic effectiveness, $(T_r - T_{\text{aw}})/(T_r - T_{c,e})$
η_p	Propulsive efficiency, $w_{\text{p}}/q_{\text{in}}$
η_{th}	Thermal efficiency, $w_{\text{net}}/q_{\text{in}}$
θ	Non-dimensional temperature, $(T - T_{c,e})/(T_r - T_{c,e})$
θ_w	Non-dimensional wall temperature, $(T_w - T_{c,e})/(T_r - T_{c,e})$
λ	Regression parameter

μ	Dynamic viscosity (kg/m s)
μ_0	Sutherland's Law coefficient (kg/m s)
μ_t	Turbulent viscosity (kg/m s)
ν	Kinematic viscosity (m^2/s) or stoichiometric coefficient
π_c	Pressure ratio, p_3/p_2
ρ	Density (kg/m^3)
σ	Standard deviation or Heat flux augmentation, $1 - q''_r/q''_f$
σ_0	Stefan–Boltzmann constant ($5.670 \times 10^{-8}\,\mathrm{W/m^2\,K^4}$)
τ	Characteristic time (s)
τ_w	Wall shear stress (Pa)
χ_k	Volumetric fraction of specie k
ϕ	Overall effectiveness, $(T_r - T_w)/(T_r - T_{c,i})$
Φ	Equivalence ratio, $(A/F)_{\mathrm{stoic}}/(A/F)$
ω	Vorticity

Abbreviations

AFIT	Air Force Institute of Technology
AFRL	Air Force Research Laboratory
CEA	Chemical Equilibrium with Applications
CFD	Computational Fluid Dynamics
Co-flow	Film cooling hole with a downstream injection angle
CRVP	Counter Rotating Vortex Pair
CT	Constant Temperature
DNS	Direct Numerical Simulation
ID	Inner Diameter
IR	Infrared

ISAT	In-Situ Adaptive Tabulation
ITB	Inter-Turbine Burner
L^2-Norm	Root sum squared of regression residuals
NCT	Near-Constant Temperature
NGV	Nozzle Guide Vane
NHFR	Net Heat Flux Reduction
OD	Outer Diameter
OGV	Outlet Guide Vane
Opposed-flow	Film cooling hole with an upstream injection angle
RANS	Reynolds Averaged Navier-Stokes
RNG	Re-Normalization Group
SIMPLE	Semi-Implicit Method for Pressure-Linked Equations
SLPM	Standard Liters per Minute
S/N	Serial Number
SST	Shear-Stress Transport
TB	Turbine Burner
Temp	Temperature
UCC	Ultra-Compact Combustor
UHC	Unburned Hydrocarbon
WSR	Well-Stirred Reactor

CONVECTIVE HEAT TRANSFER WITH AND WITHOUT FILM COOLING IN HIGH TEMPERATURE, FUEL RICH AND LEAN ENVIRONMENTS

I. Introduction

Designers of modern aviation gas turbine engines strive to maximize turbine engine efficiency and thrust to weight ratio. To achieve the former, modern gas turbine engines run at high pressure ratios and turbine inlet temperatures. However, the turbine inlet temperature far exceeds the turbine material melting temperature. Thus, effective cooling of turbines is required to maximize the allowable turbine inlet temperature while maintaining turbine durability.

1.1 High Temperature Heat Transfer

Effective cooling of turbines requires accurate methods for measuring heat transfer at high temperatures. A turbine environment is subject to large temperature gradients due to the high core flow temperatures and much lower temperatures of the cooled turbine surfaces. As a result, large temperature and, thus, fluid property variations are present in the boundary layer above the turbine surface. However, variable properties within a boundary layer due to large core flow to surface temperature differences is not a well understood topic.

An additional consequence of the extreme turbine environment is that radiative heat transfer can play a significant role in the total heat transfer. This is especially true on the leading edge of the first stage of turbine vanes. These vanes are located in the flow path directly aft of the combustor. Thus, they have a view of the highly radiative combustion environment. In addition, radiation between surfaces of dissimilar temperature also plays a significant role in turbine heat transfer.

Radiation between gray surfaces is a relatively well understood topic for simple geometries. However, analytically quantifying radiative heat transfer in a complex environment like a turbine is non-trivial. Moreover, radiative heat transfer through and from participating media like combusting flows adds a significant and potentially impractical level of complication to analytic or computational modeling.

In a turbine environment, convective and radiative heat transfer are coupled components of the total conductive heat transfer to the turbine surface. Since effective cooling of a turbine requires accurate heat transfer measurements and predictions, the present research will address coupled radiative and variable property convective heat transfer. Specifically, Chapter V of this research will develop and experimentally validate a method to isolate and quantify the convective and radiative heat transfer components. Ultimately, these techniques will enable a more accurate assessment of turbine cooling.

1.2 Non-Reacting Film Cooling

Turbine inlet temperatures have long exceeded the melting temperature of viable turbine blade materials. Modern military gas turbine engines achieve turbine inlet temperatures well over 1800 K [8]. Early designs cooled the turbine by running air bled from the compressor through the turbine surfaces and out the trailing edge. Since then, the turbine inlet temperature has outgrown the ability of internal cooling alone. Since the 1970s, film cooling has been a crucial component of turbine cooling. Film cooling is a method of bleeding air from the compressor and ejecting it from the turbine surface. This forms a layer of cool air between the blade material and the hot core flow exiting the combustor. The result is a decreased heat load to the turbine surface and a corresponding decrease in wall temperature.

Since turbine coolant is air bled from the compressor, an additional consequence of increasing pressure ratio is also increasing the temperature of the the coolant. As a result, the coolant's potential to remove heat is reduced. Thus, the margin for error in the cooling configuration is reduced and effective cooling designs and heat transfer predictions are required to maintain turbine durability.

Though turbine film cooling is applied at high temperatures and pressures, experiments to quantify film cooling performance are often performed at near ambient conditions. Moreover, experiments are often performed using a nearly adiabatic surface such that the film cooling scheme's ability to reduce the driving temperature can be quantified. However, turbines are far from adiabatic. Thus, despite the effective cooling required in modern turbine engines, experiments of film cooling often do not model the true physics of engine conditions. Moreover, little is known on how film cooling performance measured at near ambient conditions can be scaled to engine conditions. Chapter VI will address these gaps by developing and experimentally validating a method to scale film cooling performance from near ambient conditions to engine conditions.

1.3 Reacting Film Cooling

Since its inception, film cooling has developed into a mature and effective method for cooling turbines. However, the higher fuel to air ratios employed to increase turbine inlet temperature have developed a new problem: an increasing probability of unburned, energetic species exiting the combustor and entering the turbine section. This probability is driven even higher by the desire to minimize combustor length to increase the thrust to weight ratio. As shown in Fig. 1.1, these species can combine with the oxygen rich film cooling layer in the turbine section. The result is secondary reaction of combustion gases occurring within the turbine section near the turbine

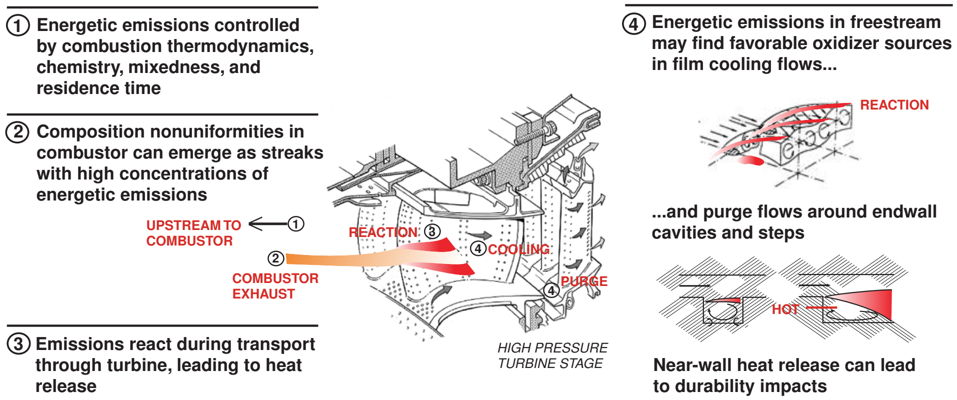

Figure 1.1: Mechanism of secondary heat release in turbine cooling [38]

surfaces rather than in the combustor. This not only neutralizes the intended objective of film cooling to decrease heat transfer to turbine surfaces, it increases the temperature adjacent to the blade and increases the heat transfer to the surface.

Another occurrence of this problem revolves around an effort to increase the thrust to weight ratio: the Ultra-Compact Combustor (UCCs). In conventional combustors, the flow exiting the final stage of compressor rotors is straightened by an Outlet Guide Vane (OGV). Then, the portion of this flow that is not bled off for coolant is routed into the combustor where fuel is added and burned as the flow travels axially as seen in Fig. 1.2. At the exit of the combustor, the flow is turned to the appropriate angle for the first stage turbine rotor in the Nozzle Guide Vane (NGV).

Alternatively, the UCC concept proposes routing a portion of the air exiting the compressor to a cavity which runs circumferentially around the axial core flow as also seen in Fig. 1.2. There, fuel is injected and burned at a fuel to air ratio above stoichiometric. Next, the reacting combustor flow exits the cavity and mixes with the core flow where it burns at a lean fuel to air ratio before entering the turbine section. This concept proposes integrating the OGV and NGV into a single vane which resides under the circumferential cavity. In doing so, the UCC is expected to be significantly shorter than a traditional axial combustor as depicted in the cutaway comparison of

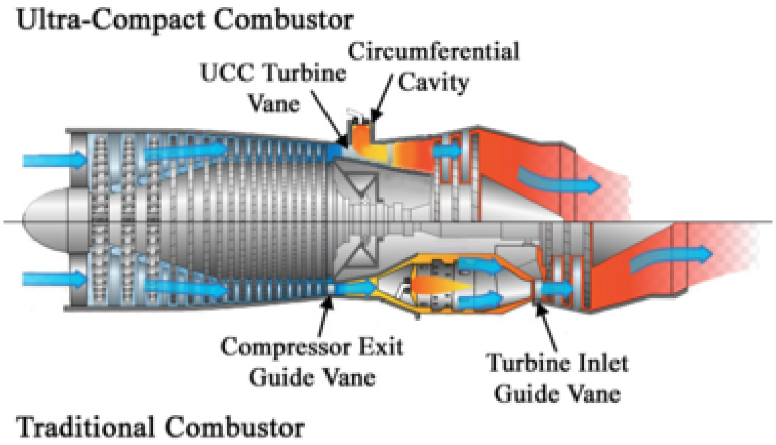

Figure 1.2: Cutaway comparison of traditional combustor vs. UCC [9]

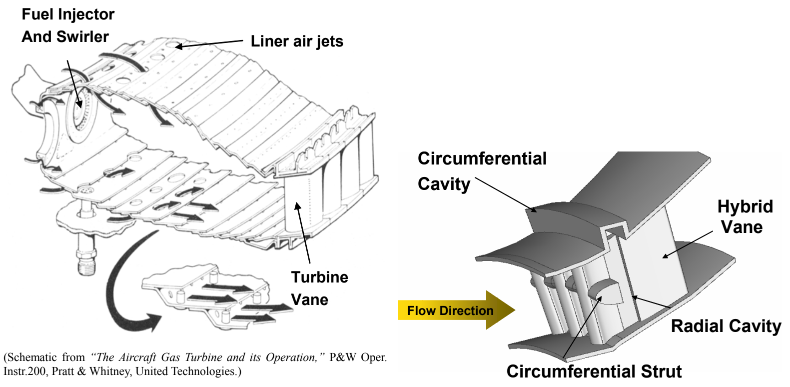

(Schematic from *“The Aircraft Gas Turbine and its Operation,”* P&W Oper. Instr.200, Pratt & Whitney, United Technologies.)

Figure 1.3: Conventional axial combustor (left) and Ultra-Compact Combustor (right); adapted from Zelina et al. [72]

Fig. 1.2.

Traditional axial combustors cool the combustor liner with slot cooling as seen in Fig. 1.3. This scheme is intended to create a smooth sheet of coolant which mixes minimally with the fuel rich combustor flows to mitigate the potential for fuel and oxidizer rich coolant to burn adjacent to the combustor wall. The UCC, however, operates at a fuel rich condition in the circumferential cavity. The result is a high temperature, fuel rich flow exiting the UCC cavity and flowing over the integrated OGV and NGV hybrid vane seen in Fig. 1.3.

As with combustor and turbine surfaces, the high temperatures incident on the vane drive the requirement to film cool the vane. However, mixing of the fuel rich combustor cavity flow and oxidizer rich film cooling flow makes localized burning near the surface a certainty in the hybrid vane film cooling layers. This presents a significant challenge to cooling the vane and enabling the UCC concept.

Overall, film cooling in a fuel rich environment has applications in current turbine engines where incomplete combustion occurs as well as in advanced combustor designs. However, unlike non-reacting film cooling, reacting film cooling is a relatively new subject. Accordingly, relatively little literature exists on the subject. Thus, Chapter VII of the present research will examine film cooling in a fuel rich environment. First, a methodology to measure film cooling performance in a fuel rich environment will be developed. Second, a method to film cool in a fuel rich environment will be experimentally demonstrated. Ultimately, this cooling method will form the basis for future schemes to film cool fuel rich applications such as the UCC.

1.4 Summary of Research Objectives

This chapter opened by presenting some of the challenges of quantifying heat transfer in a high temperature environment. Next, the disconnect between near ambient experiments of film cooling and film cooling at engine temperatures was discussed. Finally, applications for film cooling in a fuel rich environment were presented. Each of these discussions identified knowledge gaps in the present literature and objectives for the present research which are summarized here:

1. Develop a method to measure the convective and radiative heat transfer components in a high temperature environment with large freestream to wall temperature differences

2. Determine a methodology that enables scaling of non-reacting film cooling performance from near ambient conditions to engine conditions

3. Determine a methodology to evaluate film cooling performance in a fuel rich, reacting environment
4. Determine the film cooling scheme characteristics which are effective at cooling a flat plate in a fuel rich, reacting environment

To lay the foundation for the present research, Chapter II will discuss the existing literature relevant to these research objectives. Next, Chapters III and IV will detail the experimental and computational tools, respectively, that will be utilized to satisfy the objectives. Chapter V will first address Objective 1 using computational tools to develop an understanding of how variable properties effect convective heat transfer. Subsequently, Chapter V will use experimental data to examine variable property convective heat transfer in an environment with a significant radiative heat transfer component. Chapter VI will study scaling of film cooling performance both computationally and experimentally to satisfy Objective 2. Finally, Chapter VII will present experimental measurements of film cooling in a fuel rich environment to satisfy Objectives 3 and 4.

II. Background

Considerable research has taken place leading up to the current study. This chapter will review the relevant background nomenclature as well as the relevant literature. First, the fundamentals of convective heat transfer will be presented. Then an overview of the history and current state of turbine cooling will be discussed followed by techniques for measuring turbine cooling performance. Next, the fundamentals of hydrocarbon combustion and gas turbine engine cycles will be presented. Then, the background of the UCC and film cooling in a fuel rich environment will be presented. Last, computational modeling techniques will be presented with a focus on which techniques are most applicable to the current research program.

2.1 Convective Heat Transfer

Modeling the flow physics of practical applications can often be complex. For wall bounded flow, characteristics such as temperature, boundary layer structure, fluid material, etc. can have a significant impact on the heat flux, q'', into or out of the wall. A simplified approach commonly used linearizes q'' as

$$q'' = h(T_{\text{ref}} - T_w) \tag{2.1}$$

where T_w is the temperature of the wall, T_{ref} is an appropriately selected reference temperature and h is the convective heat transfer coefficient. The latter term, h, conveniently wraps the effects of fluid properties and flow conditions on the heat flux into a single term.

2.1.1 Constant Property Flows.

For a non-zero q'', $T_{\text{ref}} \neq T_w$. This presents the issue of what temperature is appropriate for evaluating properties when quantifying h. However, many cases have T_{ref} and T_w differences sufficiently small such that the differences in properties at each temperature is negligible. In this special case, T_{ref} is generally selected as the appropriate temperature at which to evaluate flow properties.

For most simple low speed, external flows, the appropriate T_{ref} is the freestream temperature, T_∞, such that

$$q''_0 = h_0(T_\infty - T_w) \tag{2.2}$$

where the 0 subscript denotes a value without film cooling. Within a boundary layer, flow transitions from the freestream velocity, u_∞, far from the wall to zero at the wall. So, for high speed flows, the appropriate T_{ref} must account for temperature increases within the boundary layer due to stagnation and viscous heating. The appropriate T_{ref} for high speed flows without film cooling is the recovery temperature

$$T_r = T_\infty + r\frac{u_\infty^2}{2c_p} \tag{2.3}$$

where r is a recovery factor. It is defined as [68]

$$r = \frac{T_r - T_\infty}{T_t - T_\infty} \tag{2.4}$$

where T_t is the total temperature (Eq. 2.3 with $r = 1$). For laminar flows, r is the square root of Prandtl number, $r = \sqrt{\text{Pr}}$ [29]. For turbulent flows, it becomes a more complicated function of the flow characteristics as discussed by White [68]. Thus, adjusting Eq. 2.1 to the case of a turbine wall with no film cooling gives

$$q_0'' = h_0(T_r - T_w) \tag{2.5}$$

For flows with large differences between T_r and T_w, the properties can have significant variations within the boundary layer which invalidate Eq. 2.5. This effect was investigated as an objective of this research program and will be further addressed in Chapter V.

The simplest convective heat transfer case is flow over a flat plate. These cases generally assume the plate has a sharp edge such that the momentum and thermal boundary layers begin growing at the leading edge of the plate. Downstream locations on the flat plate are then denoted by the distance from the leading edge, x.

Growth of a laminar or turbulent boundary layer as well as at what distance it transitions to turbulent are well characterized by the Reynolds number

$$\mathrm{Re}_x = \frac{\rho u_\infty x}{\mu} \tag{2.6}$$

However, transition is a complicated process creating modeling difficulties for locations downstream of the onset of transition. For some cases it is convenient to assume the boundary layer is tripped at the leading edge such that the boundary layer is turbulent from $x = 0$. In such a case, Re_x well characterizes growth of the turbulent boundary layer.

The vast majority of a turbulent boundary layer is dominated by momentum driven mixing. However, very close to the bounding wall, the turbulent mixing is dampened by the no-slip surface and viscosity dominates the flow. As a result, the flow very close to the wall is characteristic of a Couette flow. Thus, for a constant property flow the shear stress is constant with vertical distance (y) in this near wall, Couette flow region.

Since all turbulent boundary layers share this characteristic, the conditions at the fluid-wall interface are traditionally utilized to non-dimensionalize the entire boundary layer. The non-dimensionalized quantities, known as wall coordinates, are defined by

$$y^+ = \frac{y u_\tau}{\nu_w} \tag{2.7}$$

$$u^+ = \frac{u}{u_\tau} \tag{2.8}$$

$$T^+ = \frac{(T_w - T) u_\tau}{q''/\rho_w c_{p,w}} \tag{2.9}$$

In the above equations, the friction velocity (u_τ) is a velocity characteristic of momentum being dissipated by the shear stress at the wall such that

$$u_\tau = \sqrt{\tau_w/\rho_w} \tag{2.10}$$

Since the coordinates defined above were derived from the conditions in the Couette flow region, it is seen that

$$u^+ = y^+,\ 0 \leq y^+ \leq 5 \tag{2.11}$$

$$T^+ = \mathrm{Pr}\, y^+,\ 0 \leq y^+ \leq 5 \tag{2.12}$$

where $y^+ = 5$ is generally accepted to be the termination of the Couette flow region. This region is also known as the viscous sublayer as seen in Fig. 2.1(a).

Models exist for the other regions of the boundary layer in Fig. 2.1(a), but the Van Driest mixing length theory [29] has been shown to model a constant property turbulent boundary layer from the wall up to the wake region. The wake region defines the outer edge of the boundary layer where the boundary layer transitions to the freestream conditions. Though the freestream conditions (and, thus, the wake region)

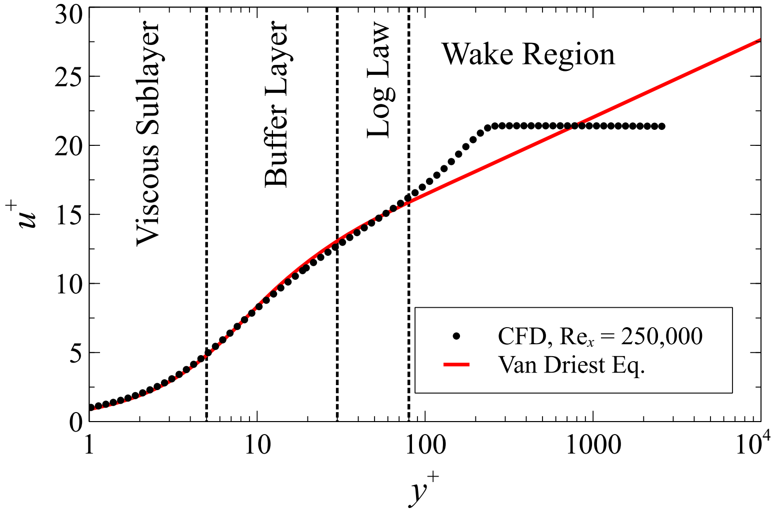

(a) Defined regions of turbulent boundary layer

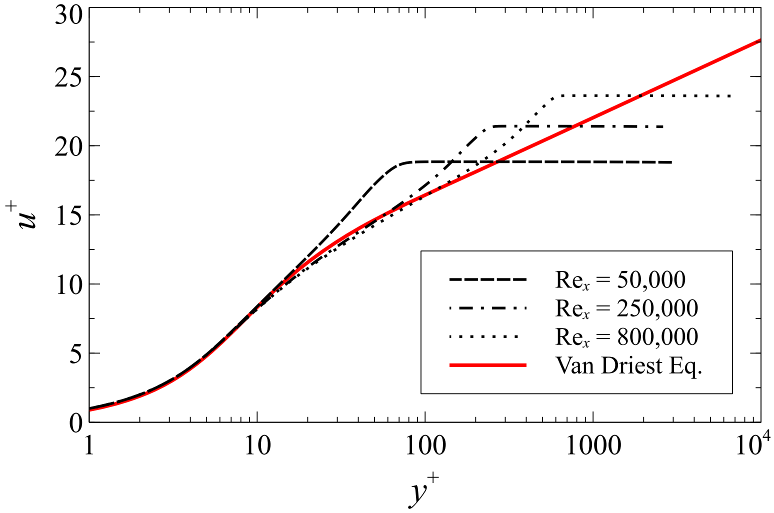

(b) Development of boundary layer with Re_x

Figure 2.1: Turbulent boundary layer in wall coordinates

can differ from flow to flow, the region modeled by Van Driest's mixing length [29] is constant for all constant property, zero-pressure-gradient, fully turbulent boundary layers with no wall suction or blowing at arbitrary Reynolds number. However, the y^+ where the wake region occurs depends heavily on Reynolds number as shown in Fig. 2.1(b).

It should be noted that the wall coordinate definitions presented above indicate that the properties should be evaluated at the wall. However, the development of wall coordinates assumed constant properties within the boundary layer. Thus, the question of where to evaluate the properties was irrelevant. It was assumed in the presentation of the wall coordinates above that, since wall coordinates are intended to non-dimensionalize by conditions near the wall, the properties should be evaluated at the wall. Section 5.4.3 will examine this assumption in the context of a boundary layer with large property variations.

Convective heat transfer differs from conduction by having bulk motion of the heat transfer medium. Therefore convective heat transfer is the result of coupled momentum and thermal boundary layers. Thus, the wall shear stress τ_w is the momentum analogy to h and is generally non-dimensionalized by the coefficient of friction defined as

$$c_f = \frac{\tau_w}{\frac{1}{2}\rho_\infty u_\infty} \tag{2.13}$$

Similarly, h can be non-dimensionalized by the Nusselt number

$$\mathrm{Nu}_L = \frac{hL}{k} \tag{2.14}$$

where L is a characteristic length and k is the conductivity of the fluid.

For a laminar flow along a flat plate, an exact solution for c_f as a function of Re_x

has been developed and is given by [29]

$$c_f = 0.664\mathrm{Re}_x^{-1/2} \tag{2.15}$$

For turbulent flows under the same flat plate conditions, c_f is defined as For a turbulent flow under the same conditions, c_f is given as [68]

$$c_f = 0.027\mathrm{Re}_x^{-1/7} \tag{2.16}$$

Since the τ_w and h of laminar and turbulent boundary layers are defined by similar transport phenomena, they can be related by the Reynolds Analogy [29]

$$\mathrm{St} = (c_f/2) \times \mathrm{Pr}^{-2/3} \tag{2.17}$$

where

$$\mathrm{St} = \frac{\mathrm{Nu}_x}{\mathrm{Pr}\,\mathrm{Re}_x} = \frac{h}{\rho_\infty u_\infty c_{p,\infty}} \tag{2.18}$$

Alternatively, for turbulent flows only, Kays et al. [29] derived St from correlations for the turbulent wall coordinates u^+ and T^+ in the log and wake regions of the boundary layer. Their derivation leads to

$$\mathrm{St} = \frac{c_f/2}{\sqrt{c_f/2}(13.2\mathrm{Pr} - 9.25) + 0.85} \tag{2.19}$$

However, they discuss that for $0.5 < \mathrm{Pr} < 1.0$ and $5 \times 10^5 < \mathrm{Re}_x < 5 \times 10^6$, Eq. 2.18 gives satisfactory results.

The above correlations were founded on the assumption of constant properties within the boundary layer. However, when large temperature variations exist in the boundary layer, property variations also become large and these correlations break down. The following section will discuss existing methods to model variable property flows.

2.1.2 Variable Property Flows.

For high speed flows, viscous heating results in large temperature variations in the boundary layer. Eckert [15] proposed utilizing constant property solutions (e.g. Eqs. 2.15–2.17) by evaluating the fluid properties at a reference temperature given as

$$T_R = T_t + 0.5(T_w - T_\infty) + 0.22(T_r - T_\infty) \tag{2.20}$$

For flows with large variations in c_p, Eckert [15] prescribed evaluating the properties at a reference enthalpy given by

$$i_R = i_t + 0.5(i_w - i_\infty) + 0.22(i_r - i_\infty) \tag{2.21}$$

When considering sufficiently low speed flow, Eq. 2.20 can be simplified by assuming $T_t \approx T_r \approx T_\infty$ such that the low speed reference temperature is defined as

$$T_R = 0.5(T_w + T_\infty) \tag{2.22}$$

Similarly, for flows with large variations in c_p, Eq. 2.21 can be simplified such that the low speed reference enthalpy is defined as

$$i_R = 0.5(i_w + i_\infty) \tag{2.23}$$

However, the preponderance of Eckert's [15] data are at high Mach numbers with T_w/T_∞ near one. Eckert [15] included a single case at $T_\infty = 1.8T_w$ and a high Mach number around seven and noted that the accuracy of his method suffered somewhat at this condition. However, he stated that this could be attributed to larger experimental uncertainties at $T_\infty = 1.8T_w$. He further states that he had no data to validate his method at high temperatures or large temperature differences and cautions that his method is tentative for these conditions.

The effect of variable properties on a variety of flow regimes is discussed by Kays et al. [29]. They propose that, for gaseous flows, the ratio of the variable property to constant property coefficients of friction and Stanton number are given as

$$\frac{c_f}{c_{f,\mathrm{CP}}} = \frac{\tau_w}{\tau_{w,\mathrm{CP}}} = \left(\frac{T_w}{T_\infty}\right)^m \tag{2.24}$$

$$\frac{\mathrm{St}}{\mathrm{St}_{\mathrm{CP}}} = \frac{h}{h_{\mathrm{CP}}} = \left(\frac{T_w}{T_\infty}\right)^n \tag{2.25}$$

In these equations, the CP subscript denotes the constant property solution with all properties evaluated in the freestream. Additionally, m and n are empirical parameters for a given flow regime. For all the non-dimensional parameters in Eqs. 2.24 and 2.25 (c_f, $c_{f,\mathrm{CP}}$, St, and $\mathrm{St}_{\mathrm{CP}}$), the thermodynamic properties are evaluated in the freestream.

Kays et al. [29] employed a finite difference code with a mixing length model for simulating turbulence to calculate m and n. For a constant Re_x, they recommend using $m = -0.47$ and $n = -0.39$ for fully developed turbulent external gas flows where $T_w/T_\infty < 1$. They assert these values are valid for $T_w/T_\infty = 0.75$ and explain that m and n can be expected to decrease somewhat with increasing T_w/T_∞.

2.2 Radiative Heat Transfer

Radiative heat transfer is a phenomena by which heat can be exchanged between two sources in the absence of media connecting the two sources. In a turbine environment, radiative heat transfer can play a significant role in the total heat transfer.

This is especially true of the first stage of vanes which have a direct view of the highly radiative combustor environment.

Howell et al. [26] explain that the total radiative heat flux to or from a surface (q''_{rad}) can be described as the difference of the radiation from the surface ($q''_{\text{rad},o}$) and incident on the surface from external sources ($q''_{\text{rad},i}$). Thus, the total radiation can be written as

$$q''_{\text{rad}} = q''_{\text{rad},o} - q''_{\text{rad},i} \tag{2.26}$$

Many surfaces are optically gray such that their emissivity and absorptivity are equal ($\epsilon_w = \alpha_w$). Since an opaque gray surface will reflect a portion of $q''_{\text{rad},i}$ according to $1 - \epsilon_w$, Eq. 2.26 can be rewritten as

$$q''_{\text{rad}} = \epsilon_w \sigma_0 T_w^4 - \epsilon_w q''_{\text{rad},i} \tag{2.27}$$

While this seems like a convenient formula, accurate quantification of $q''_{\text{rad},i}$ can be exceedingly difficult. Ignoring participating media, $q''_{\text{rad},i}$ is a function of the geometry, emissivities, and temperatures of surrounding surfaces as well as the component of heat flux emitted from the surface of interest reflected from the surroundings back to the surface of interest. For cases where participating media play a significant role, the level of complication can often become prohibitive.

2.3 Turbine Film Cooling

Early gas turbine engines of the 1940s and 1950s achieved turbine inlet temperatures around $T_4 = 815\,\text{K}$ [11]. At these temperatures, the turbine required little to no cooling to maintain integrity and durability. As T_4 increased in subsequent designs, so did the requirement to cool the turbine materials to prevent oxidation at around 1450 K and melting at around 1550 K [40]. The first implementations of

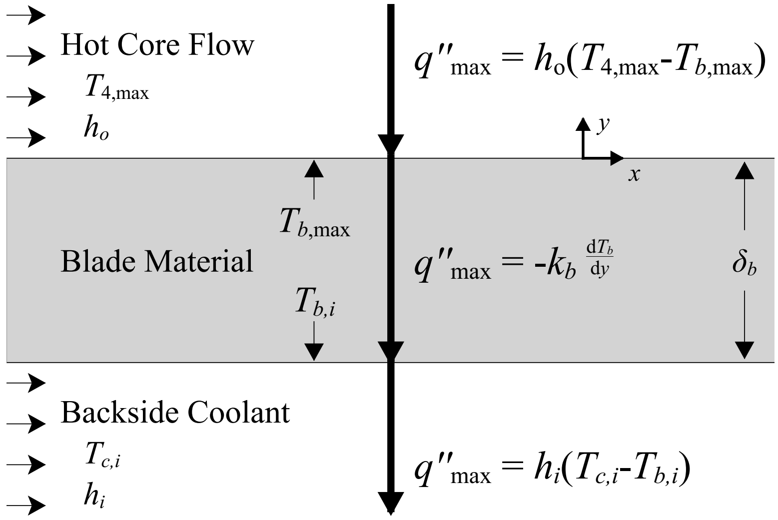

Figure 2.2: One dimensional heat transfer problem to find $T_{4,\max}$

turbine cooling bled relatively cool flow from the compressor, routed it around the combustor, through a path within the vanes and blades, and expelled it into the core flow at the trailing edge.

The capability of such a backside cooling scheme is limited by the maximum temperature for the blade material ($T_{b,\max}$) and the ability to extract heat from the blade backside. The maximum turbine inlet temperature allowed by a backside cooling scheme can be solved by a heat flux balance through the blade material. The maximum allowable heat flux through the blade wall is given when $T_{b,\max}$ occurs on the hot side of the blade such that

$$q''_{\max} = k_b \frac{T_{b,\max} - T_{b,i}}{\delta_b} \tag{2.28}$$

where k_b is the blade conductivity, $T_{b,i}$ is the internal blade temperature, and δ_b is the blade wall thickness. Assuming a priori knowledge of convective coefficient between the blade wall and the internal coolant (h_i), the one dimensional heat transfer problem given in Fig. 2.2 can be solved to find $T_{4,\max}$.

Using a similar analysis, Esgar [17] showed that small increases in $T_{b,\max}$ or small decreases in $T_{c,i}$ can result in drastic increases in $T_{4,\text{max}}$. Unfortunately, material temperature limit increases lag behind engine designs with increasing T_4 as shown in Fig. 2.3. Additionally, Fig. 2.4 depicts a trend toward increasing operating pressure ratio which also drives an increase in $T_{c,i}$ since it is bled from the back stages of the compressor. The only other option to increase backside cooling effectiveness would be to increase h_i. Many backside cooling designs do this by adding turbulators, trips, obstacles, etc. to the backside to increase mixing, but these designs can only increase h_i a finite amount. The other option to increase h_i is to increase the mass flow rate of backside cooling air to the blade. However, Esgar [17] demonstrated that the coolant requirement for backside cooling increases exponentially with T_4 while the coolant requirements for full coverage film cooling increases nearly linearly with T_4. Thus, to accommodate modern T_4 designs, the practical method to maintain blade temperatures below $T_{b,\text{max}}$ is to decrease heat flux from the hot core flow to the blade by means of film cooling.

In an effort to reduce q'', various configurations of discrete film cooling holes are machined into the blade surface. The result, depicted in Fig. 2.5 is that air bled from the compressor is used as backside cooling and then is ejected from turbine surface to form a layer of cool air between the turbine surfaces and the hot core flow. For the case of a film cooled surface, the heat flux is linearized by modifying Eq. 2.5 to

$$q''_f = h_f(T_{\text{aw}} - T_w) \tag{2.29}$$

where h_f is the convective heat transfer coefficient with film cooling. Film cooling is known to increase mixing which causes $h_f > h_0$. For example, experimental work of Smith et al. [60] found h_f was 21% larger than h_0. If this were all film cooling accomplished, Eq. 2.29 shows it would serve to increase q'' rather than decrease it. Thus, it is the goal of film cooling to decrease T_{aw} sufficiently to outweigh the increase

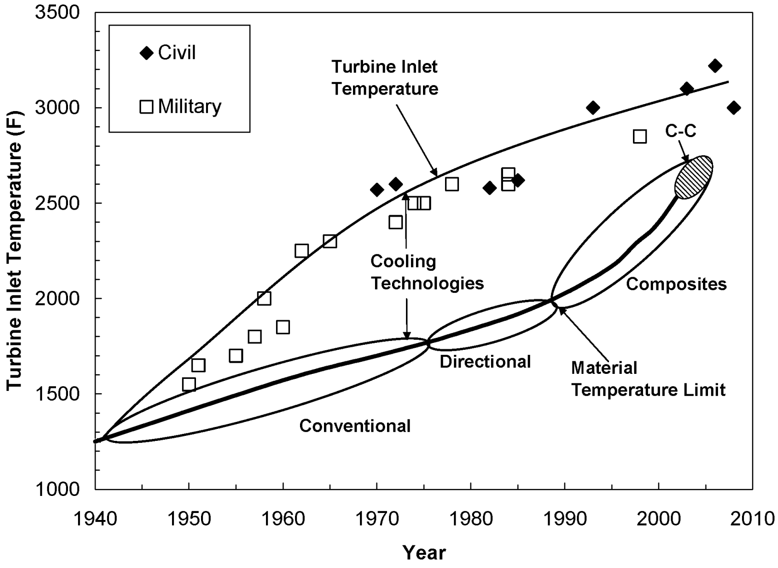

Figure 2.3: Advances in turbine inlet temperature and material limitations [6]

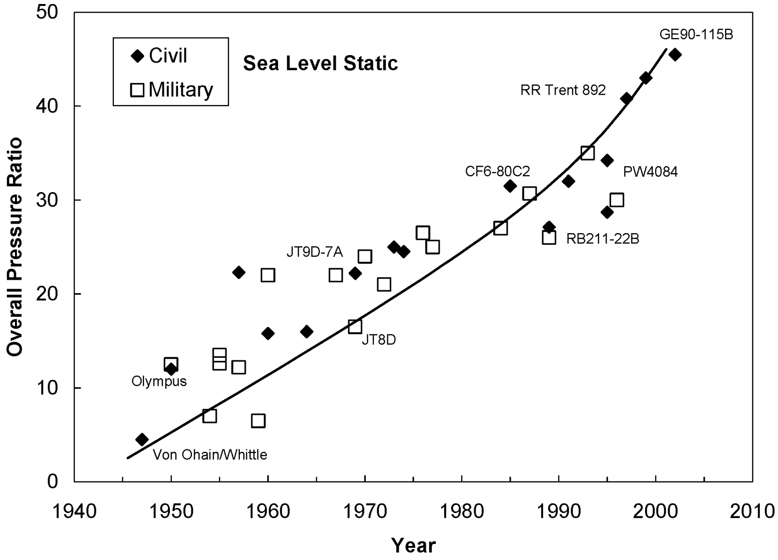

Figure 2.4: Advances in overall pressure ratio [6]

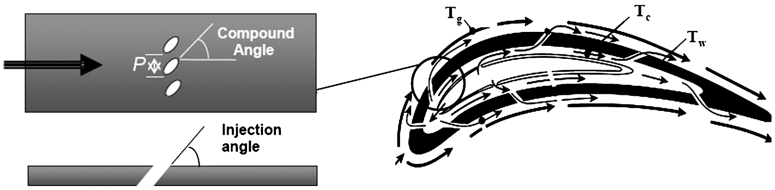

Figure 2.5: Schematic of typical film cooling configuration (right) and injection angles (left) [19]

in h to decrease q'' and keep the wall temperatures below $T_w = T_{b,\max}$.

A similar method to decrease q_0'' is transpiration cooling. This involves using a porous medium for the blade material such that cooling flow would flow evenly through the blade wall. It would be particularly advantageous for two reasons. First, heat transfer to the coolant as it passes through the porous medium would become a dominant mode of cooling. Second, due to the large ejection area, the coolant leaving the porous medium would have extremely low momentum compared to film cooling at the same mass flow rate. As a result, the coolant would remain attached to the surface and form an idealized film cooling layer. However Esgar [17] asserts there are no transpiration materials which can viably be used in a turbine environment. He explains that possible materials would oxidize under the extreme heat causing large blockages on the blade surface negating the benefits of transpiration scheme. Consequently, modern designs have steered away from transpiration cooling in favor of film cooling.

2.3.1 Film Cooling Effectiveness Parameters.

Given reducing T_{aw} is the main objective of film cooling, reporting profiles of T_{aw} is central to much of the film cooling literature. To generalize the value of T_{aw}, it is non-dimensionalized to adiabatic effectiveness given by

$$\eta = \frac{T_r - T_{\text{aw}}}{T_r - T_{c,e}} \tag{2.30}$$

where $T_{c,e}$ is the temperature of the coolant at the exit of the cooling hole where it meets the core flow. Some challenges exist in acquiring an accurate measurement of η. For one, measurement of $T_{c,e}$ is difficult without disrupting the cooling flow and biasing the data. Second, measurement of T_{aw} is challenging as many experiments never achieve a perfectly adiabatic wall condition. Some experiments use a low conductivity wall such that the heat flux to the wall is small. They then apply a rudimentary conduction correction to estimate T_{aw}. Since the heat flux is small, the error in the correction is generally small such that the correction error has little impact on T_{aw}. Other experiments extrapolate T_{aw} from heat flux measurements at two or more wall temperatures. In the case of high temperature tests characteristic of turbine engines, the true T_{aw} is well above the melting temperature of most viable materials. So, measuring T_{aw} directly becomes impossible for experiments using such materials. Ceramics are capable of withstanding the high T_{aw} condition but crack after repeated heating and cooling cycles. Thus, ceramics not viable in most cases.

Though film cooling is a dominate method used to cool turbine blades, it is not the only mode of cooling. Before being ejected to the blade surface, the coolant passes through channels within the blade and flow through the film cooling holes. These processes are the other modes of turbine cooling. By examining the effect of both film cooling and blade internal cooling, another effectiveness parameter can be defined by non-dimensionalizing T_w. The accepted non-dimensionalization, overall effectiveness, is given by

$$\phi = \frac{T_r - T_w}{T_r - T_{c,i}} \tag{2.31}$$

This is often a useful parameter as maintaining $T_w < T_{b,\text{max}}$ is what the turbine structure requires to maintain integrity.

In summary, η is very useful when optimizing film cooling schemes. It offers a measure of how well a scheme is cooling any given location on a wall. A value of one represents an optimal cooling condition while zero denotes the scheme has no effect on that location. Likewise, ϕ gives an analogous measure on the entire cooling scheme including internal and external cooling.

As discussed, reducing heat flux to the turbine walls is central to keeping $T_w < T_{b,\max}$. Thus, quantifying the the Net Heat Flux Reduction (NHFR) achieved by a film cooling scheme becomes important. NHFR can be calculated by the following:

$$\Delta q''_f = 1 - \frac{q''_f}{q''_0} \tag{2.32}$$

where q''_f and q''_0 denote heat flux to the wall with and without film cooling, respectively. By combining Eqs. 2.5, 2.29, 2.30, and 2.31, Eq. 2.32 can also be expressed as

$$\Delta q''_f = 1 - \frac{h_f(T_{\mathrm{aw}} - T_w)}{h_0(T_r - T_w)} = 1 - \frac{h_f}{h_0}\left[1 - \frac{\eta}{1-\theta_w}\right] \tag{2.33}$$

where θ_w is the non-dimensional wall temperature given by

$$\theta_w = \frac{T_w - T_{c,e}}{T_\infty - T_{c,e}} \tag{2.34}$$

This is often a useful parameter for cases where heat flux can be measured but the adiabatic wall temperature cannot. However, this parameter offers the specific challenge of requiring heat flux measurements with and without film cooling while maintaining the same T_w. Therefore, meeting this condition can require a method to independently control the wall temperature.

2.3.2 Cooling Characterization Parameters.

Many studies have been done to parametrize film cooling with non-dimensional characterizations of the cooling flow. The most common flow descriptions are density ratio, velocity ratio, mass flux or blowing ratio, and momentum ratio. Each of these parameters provide specific information about the flow and allow results from multiple experiments to be compared and scaled to practical applications.

Gas turbine engines are characterized by high freestream to coolant temperature differences. Given both the freestream and coolant originate from the compressor exit, they are at nearly the same pressure with the coolant pressure slightly higher to allow for coolant ejection. Thus, a large density gradient near a factor of two can exist between the freestream and coolant. Some studies [2, 5, 10, 28, 70] attempt to model engine conditions by matching the density ratio given by

$$\mathrm{DR} = \frac{\rho_c}{\rho_\infty} \tag{2.35}$$

where ρ is density and the c and ∞ denote evaluation in the coolant and freestream, respectively. Like measuring η, this parameter, too, requires the challenging measurement of coolant temperature exiting the hole. Since the coolant temperature within the blade is much easier to measure, Esgar [17] analytically estimated the temperature rise through the cooling passages. He calculated that, for $T_{c,i} = 811\,\mathrm{K}$ and an exterior blade temperature of $T_{b,\max} = 1255\,\mathrm{K}$, the coolant temperature increased $250\,\mathrm{K}$ through the passage from inside the blade passages to its exit into the freestream. For a freestream temperature of $T_\infty = 1700\,\mathrm{K}$, this effectively lowers the density ratio from 2.1 to 1.6.

Film cooling flows are often injected at a velocity different than the freestream velocity. Consequently, a shear layer forms which is scaled by the velocity ratio given as

$$\mathrm{VR} = \frac{u_c}{u_\infty} \tag{2.36}$$

The mass flux ratio or blowing ratio is defined as

$$M = \frac{\rho_c u_c}{\rho_\infty u_\infty} = \frac{A_\infty}{A_c}\frac{\dot{m}_c}{\dot{m}_\infty} \tag{2.37}$$

As shown in Eq. 2.37, M is directly proportional to the mass flow rate of coolant, $\dot{m}_c$, and inversely proportional to the mass flow rate in the freestream, $\dot{m}_\infty$ where A_c and A_∞ are the areas through which the coolant and freestream flow, respectively. Thus, unlike the other characterization parameters, quantifying M requires only knowledge of mass flow rates and no knowledge of temperatures or velocities. Since many experiments are controlled on a mass flow basis, M is a very convenient parameter and tends to dominate the literature.

Thole et al. [63] showed that penetration depth of the coolant into the freestream and subsequent separation from the wall is scaled by the momentum ratio given as

$$I = \frac{\rho_c u_c^2}{\rho_\infty u_\infty^2} \tag{2.38}$$

Accordingly, the η profile following a row of cylindrical holes is well scaled by I in the near hole region as confirmed by Baldauf et al. [5]. This is due to the near hole region's extreme sensitivity to separation. Similarly, they confirmed that η in the in the far downstream region is well parameterized by M.

Given the discussion above, increasing DR will result in a higher M for a constant I. As a result, a larger mass flow of coolant will be achievable without inducing flow separation. Thus, Kakade et al. [28] demonstrated that increasing DR while keeping I constant increased η.

Turbulence in the freestream also has a marked effect on film cooling. To achieve rapid, efficient reactions, the combustor is designed to maximize mixing. Thus, the flow exiting the combustor is highly turbulent. Turbulent flows are, by definition, unsteady due to time varying properties and velocities caused by eddies. This time transient nature of properties and velocities can be modeled by a Reynold's decomposition which breaks the transient term into a time averaged value and a time dependent value. For example, velocity in the streamwise direction can be decomposed by

$$u(t) = \bar{u} + u'(t) \tag{2.39}$$

where $\bar{u}$ is the time averaged component and $u'(t)$ is the fluctuating time dependent component. Then, u'_{rms} is defined such that

$$u'_{\mathrm{rms}} = \sqrt{\overline{(u')^2}} \tag{2.40}$$

The level of turbulence in the freestream is characterized by the freestream turbulence intensity

$$\mathrm{Tu} = \frac{u'_{\mathrm{rms}}}{u_\infty} \tag{2.41}$$

Bogard and Thole [8] report a nominal turbulence intensity of 20% exiting the combustor. For cylindrical hole configurations, Harrington et al.[21], Kakade et al. [28], and Baldauf et al. [5] demonstrated that adiabatic effectiveness increased with increased freestream turbulence for all blowing ratios. However, only a small increase was seen for small blowing ratios and a significant increase was seen for large blowing ratios. They concluded that, for separated jets, high levels of mainstream turbulence can increase the jet dispersion by transporting detached back coolant to the surface.

2.3.3 Effect of Film Cooling Geometry.

Since the inception of film cooling, researchers have instigated methods to maximize film cooling effectiveness and minimize the required coolant mass flow. While the above flow characterization parameters have clear effects on effectiveness, the parameters themselves are irrelevant without defining a cooling hole geometry. Despite the copious number of studies on a wide variety of film cooling geometries over the last few decades, this continues to be an active area of research. This section will review selected film cooling geometries and their relative benefits and disadvantages.

2.3.3.1 Cylindrical Holes.

Early film cooling designs ejected coolant through cylindrical holes in the blade surface. Cylindrical holes are relatively easy to machine in turbine surfaces at a low cost. However, computational fluid dynamics studies have revealed some significant disadvantages in the flow physics downstream of cylindrical injection sites. As a result, cylindrical holes are often a baseline case to which other designs are compared.

A major consideration in film cooling designs is the lateral pitch or spacing of coolant holes. Baldauf et al. [5] found that that a small spacing increases cooling coverage but also increases the mass flow per unit span. Therefore, the largest spacing that can still meet the cooling requirements is preferred to minimize the required coolant mass flow. Generally, the spacing distance is reported as a distance relative to the diameter of the cooling hole. A typical spacing is three hole diameters, D, but spacings up to eight diameters have be used [8].

As discussed in Section 2.3.2, the coolant extracts heat from the wall within the cooling passage and can experience significant temperature rises. The computational conjugate heat transfer results of Oguntade et al. [47] found that the heat transfer within the coolant passage dominated the overall heat transfer for small hole diameters. Similarly, Andrews [2] showed that, for the same mass flow rate, a large spacing increases h and decreases ϕ compared to a small spacing. He attributes this effect to lower exit velocities and better coolant attachment at small spacings. Though increased velocities in the coolant passages increase the heat extraction within the

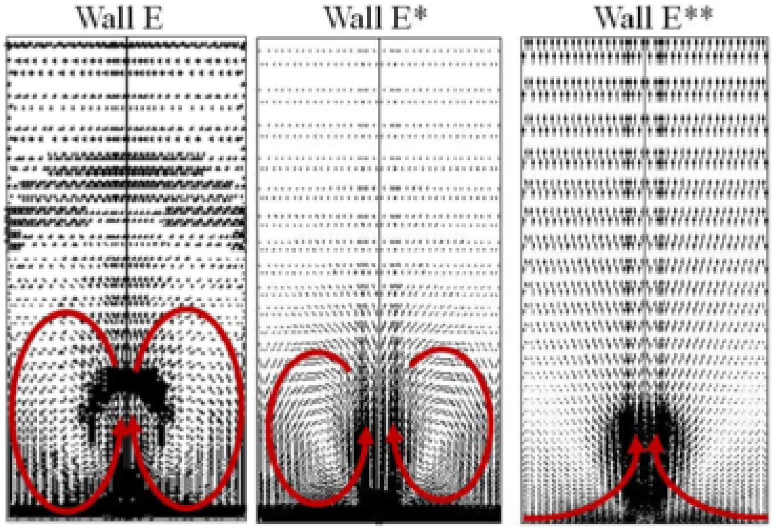

Figure 2.6: Formation of CRVPs around normal and co-flow film cooling jets and prevention of CRVPs for opposed-flow jet: E - Normal, E* - Co-flow, E - Opposed-flow [48]**

passages, it is outweighed by the disadvantages of large exit velocities. Thus, he advocates for small spacing designs to minimize the heat transfer coefficient and maximize accumulation of coolant near the wall.

The angles at which the coolant is injected are important design considerations. As seen in Fig. 2.5, compound angle measures the jet angle off axial and injection angle, α, measures the jet angle off the surface. Baldauf et al. [5] showed that low injection angles maximize jet attachment and adiabatic effectiveness. However, manufacturing limitations generally constrain α to greater than 30°.

Oguntade et al. [48] examined the effect of injecting coolant at three angles through cylindrical holes. They considered normal to the flow ($\alpha = 90°$), in the downstream (co-flow) direction with $\alpha = 30°$, and in the upstream (opposed-flow) direction with $\alpha = 160°$. Their results confirmed that the normal and co-flow configurations create a counter rotating vortex pair (CRVP) similar to the vortex pair that would shed from a cylinder in crossflow at high Reynolds numbers. Figure 2.6 shows that the CRVPs resulting from normal and co-flow configurations have the undesired effect of

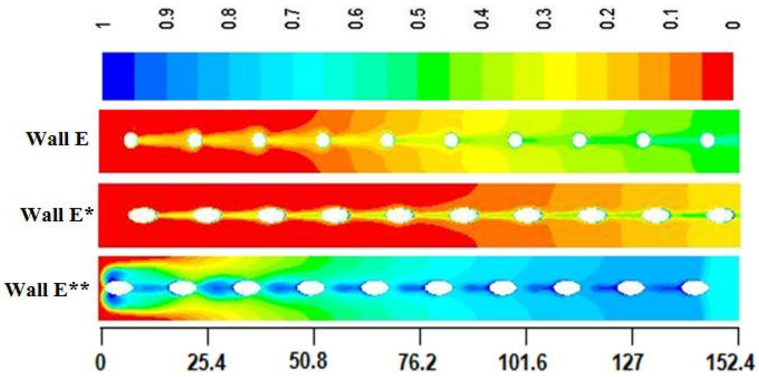

Figure 2.7: Contours of η for cylindrical holes at various angles: E - Normal, E* - Co-flow, E - Opposed-flow [48]**

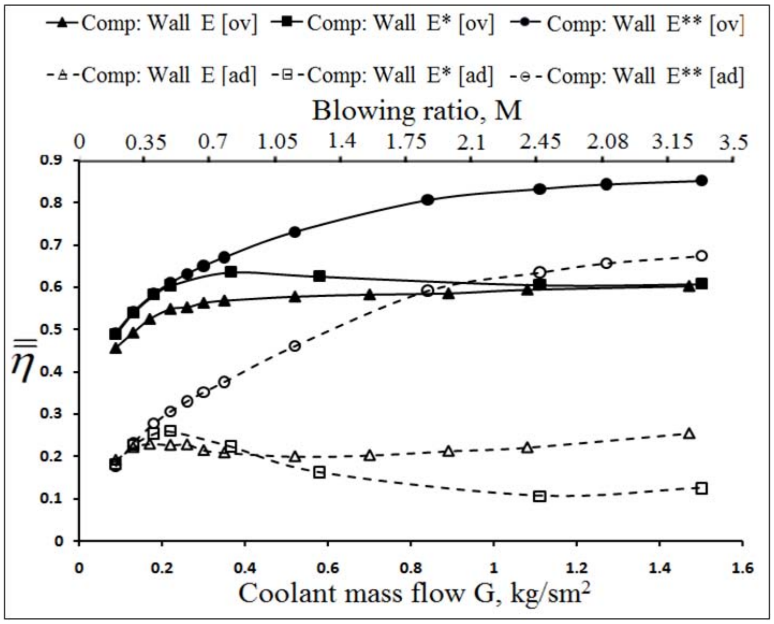

Figure 2.8: Effect of mass flow rate on η and ϕ for cylindrical holes at various angles: E - Normal, E* - Co-flow, E - Opposed-flow; [ad] = η [ov] = ϕ [48]**

sweeping hot core flow toward the wall. Conversely, Oguntade et al. [48] found that the opposed-flow configuration prevents the formation of the CRVP. Figure 2.6 shows the opposed-flow configuration creating a stagnation point upstream of the coolant hole which tends to sweep fluid near the wall into the freestream rather than hot freestream fluid toward the wall. Furthermore, the stagnation point created by the opposed-flow configuration causes a lateral spreading of the coolant while keeping the coolant near the wall.

Figure 2.7 shows the normal and co-flow configurations are severely undermined by the CRVP in the wake of the jet and by the lack of coolant spreading. On the other hand, the opposed-flow configuration displays significantly better adiabatic effectiveness profiles with clearly superior jet spreading and attachment characteristics. Figure 2.8 shows that increasing the mass flow rate through the normal and co-flow configurations causes separation and a decrease in the average η and ϕ. The opposed-flow case, however, displays an increasing η and ϕ with mass flow rate. Additionally, Oguntade et al. [48] calculated that the pressure loss across the opposed-flow configuration was on par with that of the co-flow configuration. Both well outperformed the normal hole configuration after four rows of upstream cooling by up to a factor of two.

2.3.3.2 Fan-Shaped Holes.

Co-flow and normal cylindrical holes are notorious for poor jet spreading and jet separation for $I > 0.8$ [63]. Fan-shaped holes aim to improve on these deficiencies by diffusing the flow before ejecting coolant onto the blade surface. The diffusing is accomplished by machining a cylindrical hole with a 10° layback in the axial and spanwise directions like that seen in Fig. 2.9. Colban [12] experimentally compared the performance of the cylindrical and shaped hole geometries on a turbine endwall.

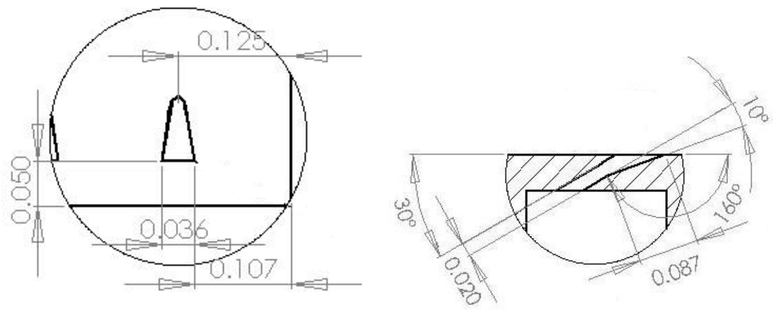

(a) Top view (b) Side view cutaway

Figure 2.9: Drawing of typical shaped hole [18]

His results indicated that, for low turbulence intensities, the shaped hole geometry increased η an average of 75% over the cylindrical geometry. The computational study of Lin et al. [36] suggested that the superior performance of shaped holes is due to their ability to reduce the effect of CRVPs by maintaining a well attached flow. Despite the clear benefits of shaped holes, they are difficult and expensive to machine compared to the cylindrical geometry. Thus, their use must be justified by their relative benefits over cheaper geometries.

2.3.3.3 Slot.

A major challenge to discrete film cooling is in achieving a well distributed coolant layer to protect the entire blade surface. Configurations which cool one area very well but others very poorly will result in large wall temperature gradients. These gradients cause thermal stresses which will seriously degrade the blade durability. Slot cooling is often considered to be the optimal configuration for achieving a laterally uniform, 2-D layer of coolant. Additionally, Hartnett et al. [23] showed that slot injection is not prone to separation due to the large ejection area and low exit velocity. His results showed injecting at an angle of 30 deg maintained the mass, momentum, and energy introduced through the slot close to the wall.

The second and possibly most significant benefit of slot cooling follows from its laterally continuous nature. Unlike cylindrical jets which result in shedding CRVPs, slot cooling is essentially a two dimensional process which does not allow for three dimensional structures like CRVPs. Thus, slot cooling creates an ideal film cooling case with even lateral distribution of well attached coolant that is not hindered by CRVPs sweeping hot freestream flow toward the wall.

Though the slot geometry achieves an excellent cooling effectiveness profile, it suffers from two major flaws. First, the slot geometry results in a large jet area. This large area results in a proportionally large mass flow for a given pressure drop through the channel. Second, the slot geometry lacks the structural integrity required for practical turbine applications. In general these flaws prevent the implementation of slots in modern gas turbine engines.

2.3.3.4 Trench.

The trench geometry attempts to reap the benefits of slot cooling while mitigating its fundamental flaws. The geometry consists of discrete, angled cylindrical holes embedded in a trench such that a portion of the flow exiting the holes impacts the trench wall. Bunker [10] theorized that the downstream trench edge acts as a blockage to the coolant which spreads the coolant spanwise within the trench before ejecting onto the surface as seen in Fig. 2.10. He also suggests that the vorticies created by the blockage may help to counteract the vorticies resulting from typical discrete film cooling jets in cross flow. If this is the case, it would help prevent the sweeping of hot core flow toward the wall.

Bunker [10] measured only small increases in adiabatic effectiveness with increasing blowing ratio from $M = 1$ to 4. His results suggest that the diffusing process within the trench results in a well attached coolant flow that is not sensitive to blowing ratio. Further, he proposes that the trench configuration protects the jet exit from

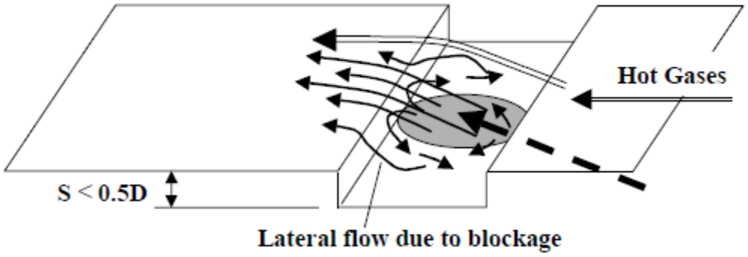

Figure 2.10: Mechanism of trench spreading cooling laterally [10]

immediate intrusion or interaction with the hot gases. Bunker [10] also studied the effect of trench width on cooling effectiveness. His data showed that the trench design is optimized when the width is as small as possible to maximize lateral spreading.

Compared to conventional configurations, Bunker [10] and Harrison et al. [22] showed that the trench configuration produced a 50-75% improvement in η in the near hole region of $x/D < 40$. Thus, the trench design provides a relatively inexpensive method to either improve cooling effectiveness or decrease the required mass flow of coolant. Furthermore, it shows promise for flattening the lateral adiabatic effectiveness profile.

Waye and Bogard [67] studied the effect of trench width and leading and trailing edge conditions on performance of trenches one half diameter deep. They varied the configurations by a rectangular insert, triangular insert, or no insert at the upstream and downstream lips of the trench as seen in Fig. 2.11. They found that configurations with the rectangular insert downstream of the hole gave laterally averaged adiabatic effectivenesses, $\bar{\eta}$, 50% higher near the hole and 20% higher farther downstream. Of these configurations, the configuration with the rectangular insert both upstream and downstream of the hole outperformed the other configurations with the rectangular insert downstream only by 10%. This corroborates the theory of Bunker [10] that trench widths as small as possible are optimal. Furthermore, their results showed that the configurations with downstream rectangular inserts were insensitive to separation

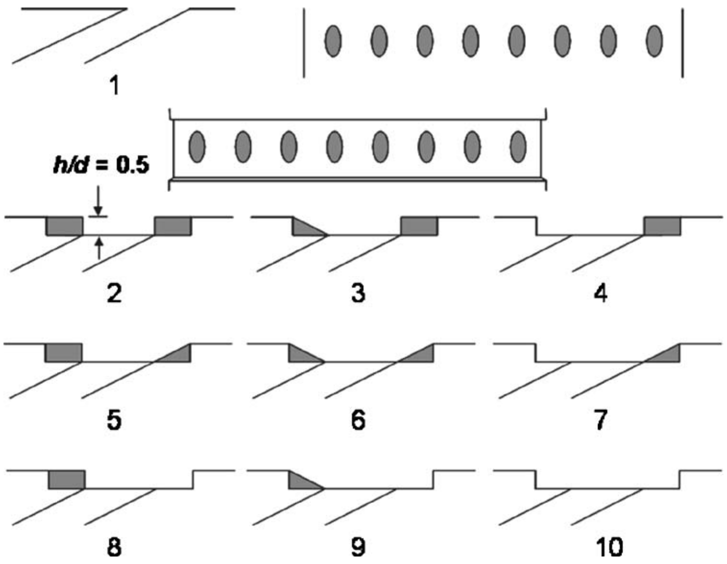

Figure 2.11: Trench leading and trailing edge conditions examined by Waye and Bogard [67]

at higher blowing ratios unlike the other configurations. Finally, Waye and Bogard [67] measured a 5-10% increase in $\bar{\eta}$ for every 0.1 increase in M from $M = 0.3$ to 1.0. Above $M = 1.0$, $\bar{\eta}$ plateaued and saw little increase with M.

Lu et al. [37] examined the effect of trench width and depth on trench performance. They found an optimal trench depth of $0.75D$ and width of $3D$. This width is in contrast the results of Bunker [10] and Waye and Bogard [67] which suggested the optimal width was as small as possible ($2D$ for $\alpha = 30°$ holes). However, neither Bunker [10] nor Waye and Bogard [67] examined the effect of trench depth. For their experiments, they held the depth constant at $0.43D$ and $0.5D$, respectively. In fact, for a trench with a depth of $0.5D$, the results of Lu et al. [37] are consistent with the two previous studies. At this shallow depth, the narrow trench outperforms the wide trench. Therefore, the optimal trench depth of $0.75D$ and width of $3D$ found by Lu et al. [37] could still be experimentally consistent.

Lu et al. [37] also showed that shaped holes produced a $\Delta q''_f$ at least 20% greater than all trench configurations considered for $M \leq 1.5$. However, they pointed out that shaped holes are significantly more expensive to manufacture. Additionally, thermal barrier coatings are often applied to blade surfaces to minimize heat flux to the wall. Therefore, trench configurations can be implemented by machining the holes into the blade material and masking off the desired trench geometry. Then, by applying the coating to the entire blade and removing the masking, the trench would be for with the thermal barrier coating forming the upstream and downstream steps. This further increases the utility of the trench configuration as a potentially cost effective method for replacing shaped holes.

2.3.4 Low Temperature Film Cooling Measurement Methods.

Once known, η and h_f can be very useful parameters for evaluating a film cooling scheme. However, measurement of these values proposes certain challenges. Methods have been developed to quantify these parameters at low temperatures, but high temperatures characteristic of a turbine section present further challenges and limitations.

Han et al. [20] described some of the early methods to measure η and h_f using steady state heat transfer experiments. To quantify T_{aw}, a test rig was designed to have a well insulated wall such that its thermal conductivity was near zero. Then, an ambient temperature mainstream was flowed over the wall and heated or cooled coolant was flowed through a film cooling configuration in the wall. Finally, temperature measurements were taken downstream of the coolant injection. Since the wall was well insulated, the heat flux was nearly zero. Therefore, a rudimentary conductive heat transfer correction can be applied to quantify T_{aw} within a small uncertainty. Then, T_{aw} could be non-dimensionalized by Eq. 2.30 to quantify η. After measuring T_{aw}, the wall would be heated or cooled by heat generation or rejection schemes embedded in the wall. Then, the heat flux to or from the wall and the wall temperature would be measured. Finally, these measurements and the T_{aw} measured in the previous experiment would be inserted in Eq. 2.29 to calculate h_f. With T_{aw} and h_f known, η and $\Delta q''_f$ could then be quantified.

Popp et al. [53] developed a method to measure performance parameters using a quasi-steady technique. They showed that, for no film cooling present, Eq. 2.5 can be rearranged to

$$q''_0 = h_0(T_t - T_w) - h_0 \cdot T_d \tag{2.42}$$

where T_d is the difference between the total temperature and the recovery temperature given by

$$T_d = T_t - T_r = (1 - r)\frac{u_\infty^2}{2c_p} \tag{2.43}$$

Their experiment varied T_t and measured the quasi-steady response of T_w and q''_0 over the duration of the experiment. Then, by applying a linear regression of Eq. 2.42 to the measurements, h_0 and T_d were quantified.

Popp et al. [53] extended their method to a film cooled case by rearranging Eq. 2.29 to

$$\frac{q''_f}{T_r - T_{c,e}} = h_f \frac{T_r - T_w}{T_r - T_{c,e}} - h_f \cdot \eta \tag{2.44}$$

Then, by an analogous regression process, h_f and η were quantified. This technique's utilization of Eq. 2.44 requires a priori knowledge of T_r. Popp et al. [53] recommend using the T_d measured by the no film cooling method to determine T_r. Thus, h_f and η can be quantified by two transient experiments: one with no film cooling followed by one with film cooling.

Vedula and Metzger [65] presented a method for measuring h_f and η with a high spatial resolution. They painted liquid crystals on the surface to measure T_w over time with a high spatial resolution. Then, by making a change in the freestream and modeling the wall as a semi-infinite solid [44], h_c and η distributions were calculated from a conduction analysis of the transient response. This method's use of liquid crystals give it the distinct advantage of being able to determine the profiles of h_c and η rather than being limited to spatially discrete measurements at thermocouple locations. Subsequently, Ekkad et al. [16] extended the method of Vedula and Metzger [65] by using infrared (IR) imaging rather than liquid crystals.

2.4 Hydrocarbon Combustion

Many aspects of combustion like emissions, flame speed, and adiabatic flame temperature are well characterized by the equivalence ratio, Φ [64]. The equivalence ratio is defined by

$$\Phi = (A/F)_{\text{stoic}}/(A/F) \tag{2.45}$$

where (A/F) is the ratio of air to fuel in the mixture by mass. The subscript 'stoic' denotes the stoichiometric balance of air and fuel by mass to completely react the fuel with no air or fuel left over. Modern fuels used in gas turbine engines are complex and difficult to model.

The staple fuel for many aeronautical applications is JP-8. However, JP-8 is a complex mixture of many different fuels leading to difficulty in modeling its combustion chemistry. To reduce computational expense, JP-8 is often approximated by propane (C_3H_8) which has similar emissions characteristics.

2.4.1 Combustion Modeling.

The combustion process for any hydrocarbon involves numerous molecular species and reaction paths. For methane (CH_4), a relatively simple hydrocarbon, Turns [64] identifies 279 reactions. However, the combustion of hydrocarbons can be approximated by an ideal reaction equation known as complete combustion. This equation is obtained by selecting the reaction products that will result in minimum stored chemical energy (maximum heat release). For propane, complete combustion is given by

$$C_3H_8 + 5(O_2 + 3.76N_2) \rightarrow 3CO_2 + 4H_2O + 18.8N_2 \tag{2.46}$$

While this is an extremely compact and convenient model, it does not replicate the true combustion process or equilibrium products. For closed, adiabatic systems, the mixture of complete reaction products is determined by maximizing the product mixture entropy. For closed, isothermal systems, the mixture of complete reaction products is given by minimizing Gibbs free energy. Thus, rather than the simple reaction model given by Eq. 2.46, true combustion is modeled by hundreds of reaction paths among numerous intermediate and stable product species.

The individual reaction paths are known as elementary reactions. Each elementary reaction represents a single step in the reaction process. For example, O_2 molecules must be split into O atoms before reacting, so it's elementary reaction is given as

$$O_2 \underset{k''}{\overset{k'}{\rightleftarrows}} 2O \tag{2.47}$$

where the reaction rate coefficients k' and k'' govern the rate at which the reaction occurs in the right and left directions, respectively. The rate coefficients can be calculated from the Arrhenius form

$$k^{('/'')} = A^{('/'')} T^{b^{('/'')}} e^{-E^{('/'')}/R_u T} \tag{2.48}$$

where $A^{('/'')}$, $b^{('/'')}$, and $E^{('/'')}$ are empirical coefficients for a specific reactions in the right ($'$) and left ($''$) directions available in the literature [64]. With this definition, the system of combustion reactions can be defined generally as

$$\sum_{j=1}^{N'} \nu'_{jr} M'_j \underset{k''_r}{\overset{k'_r}{\rightleftarrows}} \sum_{j=1}^{N''} \nu''_{jr} M''_j \tag{2.49}$$

where r denotes the rth reaction of the system, j denotes the jth species, $M^{('/'')}$ is the species' symbolic abbreviation (e.g. C_3H_8), $v^{('/'')}$ are the stoichiometric coefficients. By modeling each elementary reaction with Eq. 2.49, the combustion process can be numerically advanced through time to model both transient and steady state combustion. Such models create a much more accurate and detailed picture of the combustion process and products than the simplified approach illustrated by Eq. 2.46.

2.4.2 Flame Characterization.

One important quantity for any combustion system is the adiabatic flame temperature, T_{ad}. This is the temperature that would result from combusting a given mixture in a closed system with no heat loss from the system. To calculate T_{ad}, one must first calculate the enthalpy of the initial, unreacted mixture, i'. Since the system is assumed to be adiabatic and closed, the enthalpy will remain constant over the combustion process such that $i'' = i'$. It is only the mixture of species which change in an adiabatic combustion process. So, with a priori knowledge of the final mixture of product species, T_{ad} is the temperature where the sum of the product species' enthalpies at T_{ad} such that

$$i''(T_{\mathrm{ad}}) = i' \tag{2.50}$$

In most cases, the specific mixture of product species is unknown. The simplest method to predict the products is to assume complete combustion products like the example for propane in Eq. 2.46. Another method is to numerically model the combustion process from initiation to steady state via Eq. 2.49. Then, by assuming the temperature is constant through each sufficiently small time step, an updated temperature can be solved at the end of each time step until a steady state solution is reached. The steady state temperature would then be T_{ad}. For turbomachinery specifically, this value describes the ideal $T_{4,\text{ad}}$. Comparing this to the actual T_4 then gives an accurate assessment on the efficiency of the combustor and the amount of heat lost through the combustor.

While the adiabatic flame temperature, T_{ad}, is instrumental to describing the flame steady state, the Damköhler number (Da) defines the interaction of the combustion and the turbulence processes. It is defined as

$$\text{Da} = \frac{\tau_{\text{flow}}}{\tau_{\text{chem}}} = \frac{l_0/u'_{\text{rms}}}{\delta_L/S_L} \tag{2.51}$$

where τ_{flow} and τ_{chem} are characteristic flow and chemical times, respectively. The δ_L and S_L terms defining τ_{chem} are the thickness and speed of a flame in a premixed laminar flow, respectively. The integral length scale, l_0, is the length characteristic of the largest eddies in the flow.

Ultimately, Da is a comparison of the relative importance of turbulent heat and mass transfer via eddies and the chemical combustion process. For large Da, turbulent processes are significant and can increase the rate of reactions as well as influence the structure of the flame. Lukachko et al. [38] discussed that, for reactions within a film cooling layer, increasing Da resulted in reactions completing in a shorter axial distance due to increased mixing. Thus, Da is of great importance to characterizing reactions within a film cooling layer. Lukachko et al. [38] estimated that, for current era engines, Da based on a typical blade row is 10-500 for ignition and 1-25 for reactions. Reactions within the film cooling layer will be discussed further in Section 2.7.

2.4.3 The Well-Stirred Reactor.

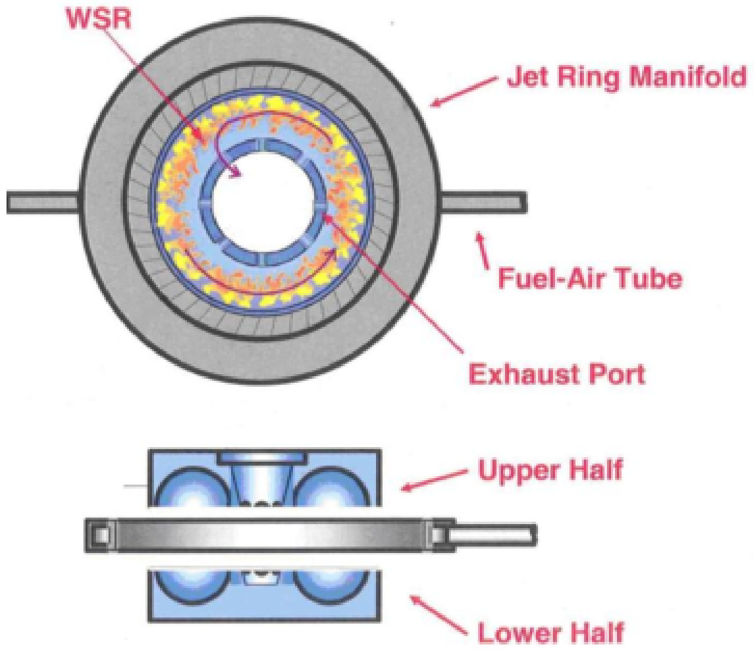

Figure 2.12: Diagram of a well-stirred reactor [62]

Experimental facilities that seek to recreate turbine conditions require an upstream reactor to simulate the gas conditions exiting a realistic combustor. Zelina and Ballal [71] presented the Well-Stirred Reactor (WSR) as a method to reproduce realistic combustor exit conditions. Unlike typical axial combustors, the WSR design injects premixed air and fuel in the outer diameter (OD) of a toroid as depicted in Fig. 2.12. The flow is injected at an angle such that it swirls around the toroid as it burns to create a well mixed and stable flame. Finally, the hot combustion products exit the toroid via a gap in the ID of the WSR and flows into a test channel selected by the experimenter.

This method of burning gave the WSR excellent performance characteristics. In testing Zelina and Ballal [71] showed the WSR could produce a combustion efficiency above 99% over a wide range of Φ and reactor loading. Additionally, their WSR was capable of peak loading almost two times higher than the preceding spherical WSR design.

2.4.4 High-g Combustion.

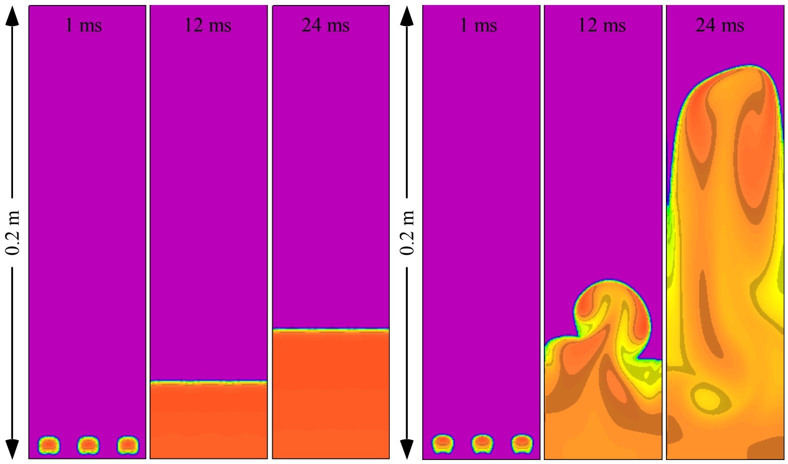

(a) 10g (b) 500g

Figure 2.13: Effect of downward g-loading on flame propagation [72]

Lewis [34] studied the effect of g-loading on combustion. He found that, at a sufficiently high centrifugal acceleration, flame speeds increased drastically. This effect was attributed to hot, less dense reaction products being forced toward smaller radii while cool, more dense unreacted species were forced toward larger radii. This buoyancy effect, shown in Fig. 2.13, results in a bubble of hot reaction products being transported through the unreacted mixture resulting in a significantly increased flame speed known as the bubble velocity.

This is very similar to the ability of turbulence to increase burning rates by promoting mixing. Lewis [34] found that the bubble transport dominated the flame speed for accelerations over 500g and caused flame extinction for accelerations over 3500. This is why Fig. 2.13(a) shows no indication of bubble transport while Fig. 2.13(b) clearly displays the bubble transport phenomenon. He concluded that the actual flame speed will be the greatest of the laminar, turbulent, and bubble flame speeds.

Thus, to take advantage of high-g combustion, a system must utilize angular accelerations high enough for bubble transport to dominate while avoiding accelerations high enough to extinguish the flame.

2.5 Cycle Analysis

The combustor and turbine are only part of the gas turbine engine system. Thus, to evaluate the system, the system as a whole must be analyzed. Cycle analysis takes a broad thermodynamic view of the application's process of extracting work or heat to quantify process efficiency.

2.5.1 Brayton Cycle.

Neglecting changes in potential energy, thermodynamic cycles can be modeled by [11]

$$(q_{\text{in}} - q_{\text{out}}) + (w_{\text{in}} - w_{\text{out}}) = (i_{\text{exit}} - i_{\text{inlet}}) + \frac{V_{\text{exit}}^2 - V_{\text{inlet}}^2}{2} \tag{2.52}$$

where q is heat addition (in) or rejection (out) per unit mass, w is work per unit mass, i is enthalpy per unit mass, and V is the magnitude of the velocity vector.

The Brayton cycle which governs gas turbine engines, is designed to compress air, add heat by combustion at a constant pressure, extract work in the turbine, and exhaust it to the atmosphere. Since the cycle requires mass to cross the engine's control volume, it is considered to be an open cycle. The first three steps trace to Eq. 2.52 as w_{in}, q_{in}, and w_{out}, respectively. The fourth an final process, exhaust, expels the gas at the end of the cycle with a higher enthalpy and velocity than the gas entering the compressor at the beginning of the cycle such that the right hand side of Eq. 2.52 is non-zero.

Since heat addition or rejection are defined as heat entering or leaving the working fluid, respectively, the adiabatic, open system Brayton cycle model has $q_{\text{out}} = 0$.

Alternatively, closed systems where no mass crosses the control volume have the right hand side of Eq. 2.52 summing to zero and have $q_{\text{out}} \neq 0$. The open system Brayton cycle can be modeled as a closed system by lumping the right hand side of Eq. 2.52 into the q_{out} term such that

$$q_{\text{out}} = (i_{\text{inlet}} - i_{\text{exit}}) + \frac{V_{\text{inlet}}^2 - V_{\text{exit}}^2}{2} \tag{2.53}$$

and rearranging Eq. 2.52 gives the net work from the the cycle

$$w_{\text{net}} = w_{\text{out}} - w_{\text{in}} = q_{\text{in}} - q_{\text{out}} \tag{2.54}$$

Using the closed system model, the ideal Brayton cycle is given by 4 reversible processes taking the working fluid through from one engine stage to another [11]. Typically, gas turbine engine stages are numbered as 2: compressor inlet; 3: combustor inlet; 4: turbine inlet; 5: turbine exit. Thus, the four processes of the closed system Brayton cycle are depicted in Fig. 2.14 to be 2-3: isentropic compression in the compressor; 3-4: constant-pressure heat addition in the combustor; 4-5: isentropic expansion in the turbine; 5-2: constant-pressure heat rejection by rejecting exhaust to the atmosphere.

The thermal efficiency of the closed system Brayton cycle is given as the usable work (w_{net}) over the input power (q_{in}) [11]:

$$\eta_{\text{th}} = \frac{w_{\text{net}}}{q_{\text{in}}} = 1 - \frac{q_{\text{out}}}{q_{\text{in}}} = 1 - \frac{\int_{T_2}^{T_5} c_p(T)dT}{\int_{T_3}^{T_4} c_p(T)dT} \tag{2.55}$$

By assuming c_p is constant throughout the cycle, Eq. 2.55 can be approximated by

$$\eta_{\text{th}} \approx 1 - \frac{c_p(T_5 - T_2)}{c_p(T_4 - T_3)} = 1 - \frac{T_2(T_5/T_2 - 1)}{T_3(T_4/T_3 - 1)} \tag{2.56}$$

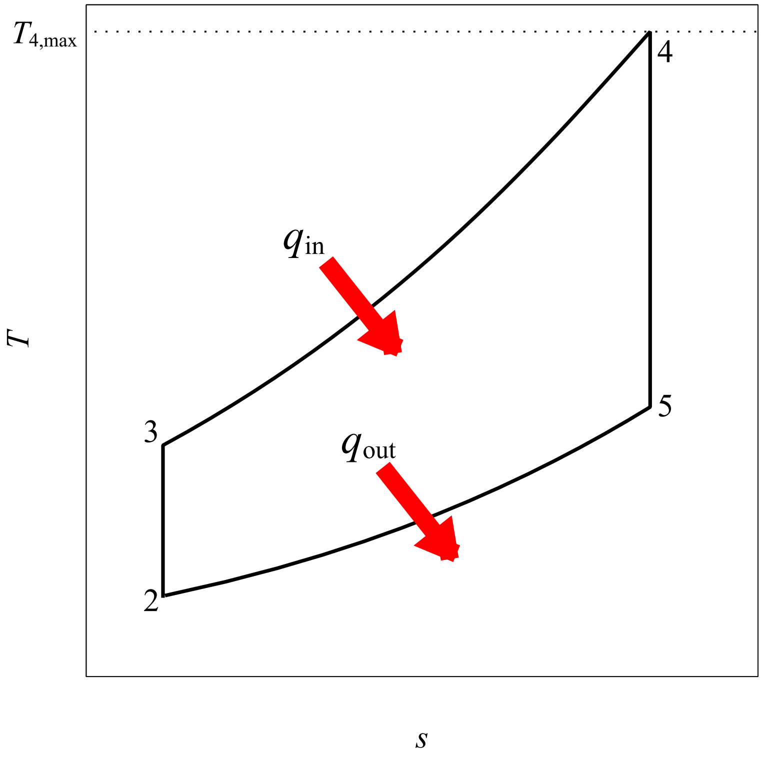

Figure 2.14: Typical Brayton cycle diagram with engine station numbers

The flow through the compressor and turbine are modeled as isentropic, so $p_3 = p_4$ and $p_5 = p_2$, and the compression and expansion are polytropic processes such that

$$\frac{T_3}{T_2} = \left(\frac{p_3}{p_2}\right)^{(\gamma-1)/\gamma} = \left(\frac{p_4}{p_5}\right)^{(\gamma-1)/\gamma} = \frac{T_4}{T_5} \tag{2.57}$$

Thus, $T_5/T_2 = T_4/T_3$, and the thermal efficiency can be simplified to

$$\eta_{\text{th}} = 1 - \frac{1}{\pi_c^{(\gamma-1)/\gamma}} \tag{2.58}$$

where the pressure ratio $\pi_c = p_3/p_2$. Therefore, thermal efficiency increases with pressure ratio.

As discussed in Section 2.3, turbine inlet temperature (T_4) is limited by the ability to cool the turbine to a maximum inlet temperature of $T_{4,\max}$. Despite the clear benefit of increasing the pressure ratio, it is limited by two factors. First, increasing the π_c increases T_3 which in turn increases T_4 for the same q_{in} through the combustor. Second, increasing π_c requires a larger w_{in} to drive the compressor. To meet the increased w_{in} requirements, q_{in} must also increase resulting in increased T_4. Thus, increasing π_c has a two-fold effect driving increased T_4. The result is a π_c limited by $T_{4,\text{max}}$ which places a limit the thermal efficiency.

2.5.2 Improvements to the Brayton Cycle.

Since the first successful implementation in the 1930s, gas turbine engines have made incredible advances. Early designs of the 1940s and 1950s achieved a turbine inlet temperature, T_4, of approximately 815 K and thermal efficiencies of about 17% [11]. The low efficiency was largely due to compressor and turbine inefficiencies along with a low T_4 to maintain turbine integrity. With continuing improvements of materials and cooling techniques, modern engines achieve turbine inlet temperatures exceeding 1700 K and thermal efficiencies of approximately 40% [11]. The increases in efficiency were, to a great extent, made possible by computer-aided design to minimize aerodynamic losses. Unfortunately, increasing T_4 leads to two problems. First, increasing T_4 increases bleed air requirements for turbine cooling. This decreases the airflow in the combustor without decreasing the q_{in} required to drive the compressor which further increases T_4. Second, higher combustion temperatures result in increased NO_x production leading to ozone production at ground levels and smog [11].

Çengel and Boles [11] described that significant improvements can be realized by implementing intercooling, regeneration, and reheating to the classic Brayton cycle. Intercooling is the process of cooling the flow between compressor stages. Regeneration is the processes of extracting heat from the flow exiting the turbine and injecting the heat into the flow exiting the compressor before it enters the combustor. This process of regeneration is practical only when the turbine exit temperature is higher than the compressor exit temperature. Otherwise, the opposite effect will be achieved resulting in a cooled compressor exit and a heated turbine exit. Reheating is the process of increasing the temperature either within the turbine or between the high and low pressure turbine stages. Çengel and Boles [11] assert that intercooling nearly doubled the thermal efficiency of early engines. However, in the aircraft engine industry, cost savings of the the improvements are outweighed by the cost of higher development and implementation costs as well as weight.

2.5.2.1 Regeneration.

Regenerators are compared to ideal regenerators by regenerator effectiveness defined as

$$\epsilon = \frac{q_{\text{regen,act}}}{q_{\text{regen,max}}} = \frac{i_{3.5} - i_3}{i_5 - i_3} \tag{2.59}$$

where the subscript 3.5 denotes the station just after the regenerator and just before the combustor. Çengel and Boles [11] state that the effectiveness of most practical regenerators is $\epsilon = 0.85$. Regenerators will cause a larger pressure drop, so their benefit must be balanced with fuel savings. They derived the thermal efficiency of an ideal Brayton cycle with regeneration to be

$$\eta_{\text{th}} = 1 - \frac{T_2}{T_4}\pi_c^{(\gamma-1)/\gamma} \tag{2.60}$$

2.5.2.2 Reheating.

As discussed, the performance of gas turbine engines is limited by $T_{4,\text{max}}$. However, the fluid temperature drops considerably as work is extracted in the turbine. Sirignano et al. [59] proposed taking advantage of this fact by adding a heat addition process

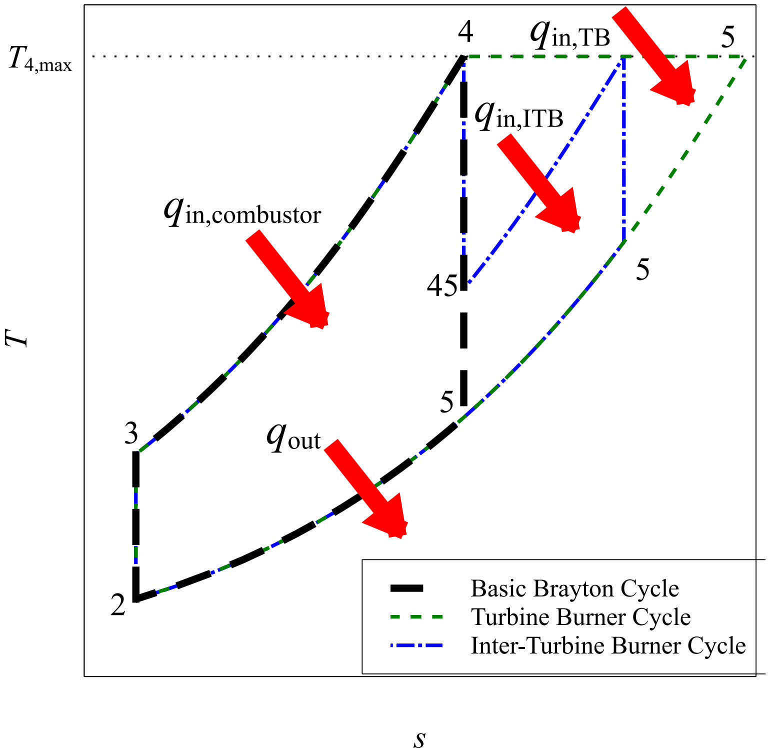

Figure 2.15: Effect of turbine burning and inter-turbine burning processes on the Brayton cycle

such that the stagnation temperature remains constant through the turbine section as seen in Fig. 2.15. By maintaining a temperature of $T_{4,\max}$ through the turbine, they calculated significant thermodynamic benefits.

Their constant temperature (CT) expansion concept was designed to augment thrust, net work, or both upon user request similar to the modern usage of an afterburner to augment thrust. Sirignano et al. [59] analyzed the thermodynamics of four cases: 1) no afterburner or turbine-burner; 2) afterburner and no turbine-burner; 3) turbine-burner and no afterburner; 4) afterburner and turbine-burner; all in addition to a conventional, axial combustor. For the turbine burning cases, enough fuel was added to maintain the stagnation temperature through the turbine. For the afterburner cases, enough fuel was added to bring the temperature to 1900 K followed by expansion through the nozzle.

Sirignano et al. [59] focused their results on the effect of turbine burning on specific thrust (ST) and thrust specific fuel consumption (TSFC). ST is defined as

$$\mathrm{ST} = \frac{F_p}{\dot{m}_{\mathrm{air}}} \tag{2.61}$$

where F_p is the propulsive force or thrust and $\dot{m}_{\mathrm{air}}$ is the mass flow rate of air through the system. TSFC is defined by

$$\mathrm{TSFC} = \frac{\dot{m}_{\mathrm{fuel}}}{F_p} \tag{2.62}$$

where $\dot{m}_{\mathrm{fuel}}$ is the sum of the rates of fuel mass addition in the combustor, turbine, and afterburner. They calculated that the afterburner and turbine burner case produces more ST at a lower TSFC for all Mach numbers and pressure ratios considered. For a Mach number of $\mathrm{Ma} = 1$ and $\pi_c = 20$, they found a 1.5% increase in ST with a 5% decrease in TSFC. For $\mathrm{Ma} = 3$ and $\pi_c = 20$, they found a 13% increase in ST with a 14% decrease in TSFC.

Sirignano et al. [59] admitted burning in the turbine would result in a lower thermal efficiency compared to conventional combustors due to the decreased pressure in the turbine section. So, rather than eliminating the conventional combustor in favor of a turbine-burner, they suggested that turbine-burning could replace the afterburner as a thrust or net work augmenter. They calculated that this would save on weight and length as well as decrease TSFC by up to 17%. They also calculated that this benefit decreased ST by 10-15% for the same engine cross section with an afterburner. Sirignano et al. [59] concluded that burning in the turbine can decrease the weight and volume of an aircraft for a fixed range or increase the range with the same quantity fuel. Additionally, extra work extracted from a turbine-burner could be used to power equipment on board military aircraft such as directed energy weapons. Sirignano et al. [59] also hypothesized that the decreasing temperatures within the turbine could result in a reduction in NO_x production.

Sirignano et al. [59] pointed out several challenges to turbine burning. First, they discussed that the exothermic reactions, significant viscous dissipation (due to high speed flow), and favorable pressure gradients will result in a non-monotonic velocity profile variation within the boundary layer. This could cause instabilities and vortical structures in the turbine passage resulting in increased mixing and possibly making cooling the turbine more difficult. Furthermore, they estimated a 10^5g, 10^4g, and 10^5g acceleration in the azimuthal, radial and axial directions, respectively, due to expansion and turning within the turbine. Such accelerations can provide challenges to flame stability and increase the risk of flame extinction. They also suggested that the widely varying velocity profiles could cause very different residence times along different flow paths which could also cause flame instabilities and possibly flame extinction.

A major barrier to turbine burning is the inability of turbines to cope with energetic species in the freestream. This topic will be discussed more in Section 2.7. Thus CT expansion is impractical for current turbine designs. Another practical option is the near-constant temperature (NCT) expansion. The NCT design implements a second stage of combustion between the high and low pressure turbines in the inter-turbine duct. The cycle resulting from this inter-turbine burning is in Fig. 2.15. However, the small axial space in the inter-turbine duct precludes the use of an axial combustor without a significant increase in engine length. Section 2.6 will present a combustor design which may meet the tight axial length requirements of NCT expansion.

2.5.2.3 Reheating with Regeneration.

Sirignano et al. [59] discussed that, due to the much higher temperatures exiting a turbine burner, coupling it with heat regeneration, as depicted in Fig. 2.16, dramatically increases the specific power and thermal efficiency. They calculated that adding a reheating process like turbine burning without a regeneration process will increase specific power but will decrease the thermal efficiency compared to a conventional system. However, their results seen in Fig. 2.17 revealed that adding a regeneration process will maintain the specific power and increase the thermal efficiency compared to a conventional system both with and without regeneration.

Modern airborne gas turbine engines do not employ regeneration due to its increase in weight, complexity, and implementation costs. Even so, with the clear benefits of reheating with regeneration, future designs may find turbine-burning increases the benefits of regeneration sufficiently to justify its implementation. Ground based gas turbine engines, which were approximately 17% of the gas turbine market in 2002-2011 [6], could much more readily employ regeneration and reap the benefits of turbine-burning.

2.5.3 Propulsion Cycle.

The propulsion cycle is defined by examining the inputs and outputs from the engine. From this view, there is no work in or out across the engine control volume such that $w_{\text{in}} = 0$ and $w_{\text{out}} = 0$. Thus, Eq. 2.52 can be modified and the velocities can be rearranged such that

$$q_{\text{in}} - q_{\text{out}} = (i_{\text{exit}} - i_{\text{inlet}}) + (V_{\text{exit}} - V_{\text{inlet}})V_{\text{inlet}} + \frac{(V_{\text{exit}} - V_{\text{inlet}})^2}{2} \tag{2.63}$$

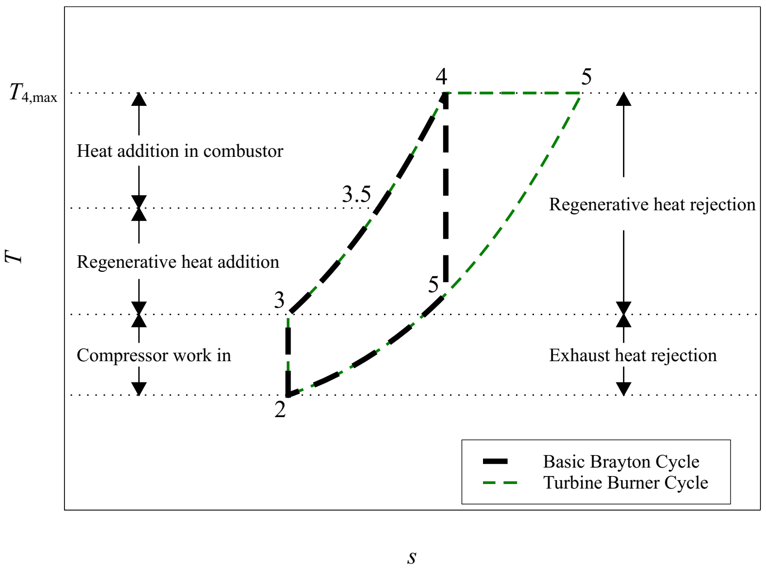

Figure 2.16: Brayton cycle with reheating and regeneration processes

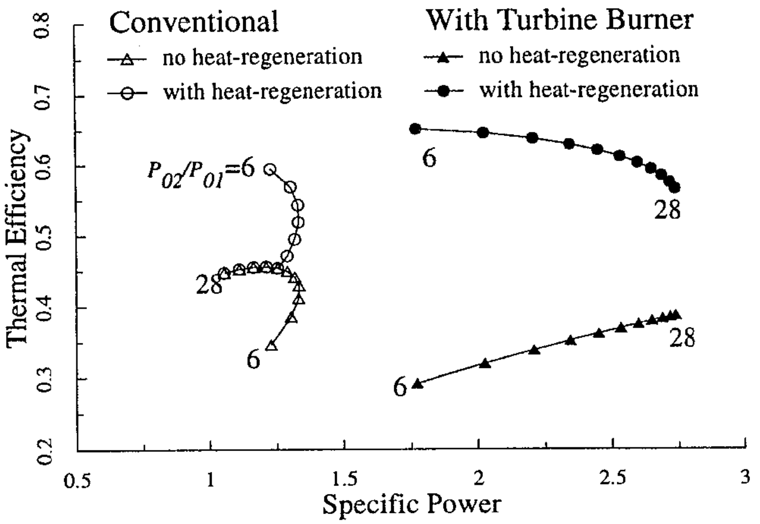

Figure 2.17: Benefits of Reheating and Regeneration to the Brayton Cycle ($\pi_c = P_{02}/P_{01}$ for this figure only) [59]

The middle term in the right hand side of 2.63 multiplied by the mass flow rate is defined as the aircraft propulsive power. While it does not meet the definition of work into or out of the system, this term can be viewed as the propulsive work per unit mass

$$w_p = (V_{\text{exit}} - V_{\text{inlet}})V_{\text{inlet}} \tag{2.64}$$

Therefore, the propulsive efficiency can be defined as the work extracted over the input energy

$$\eta_p = \frac{w_p}{q_{\text{in}}} \tag{2.65}$$

As a result, the inefficiencies in the propulsion process are defined as the remaining terms: heat loss through the engine walls, increased enthalpy at the engine exit, and kinetic energy from which no propulsive work is derived.

As discussed above, thermal inefficiency in the Brayton cycle is due to an increased velocity and enthalpy at the turbine exit compared to the compressor inlet. However, the propulsive cycle requires a difference in inlet and exit velocities. Additionally, it uses enthalpy exhausted from the turbine to further increase the exit velocity in the nozzle. Therefore, thermal efficiency and thrust output are in direct conflict.

In fact, the wasted kinetic energy increases with the square of the exit velocity as given by the final term in Eq. 2.63. However, since Eq. 2.63 is on a per mass basis, increasing the mass flow rate increases kinetic energy loss linearly. Therefore, it is more efficient to increase thrust by increasing the mass flow rate rather than the exit velocity.

To take advantage of this concept, some modern gas turbine engines employ a large fan before the inlet to the high pressure compressor. The fan is driven independently of the high pressure compressor and turbine by a low pressure turbine following the high pressure turbine. Some of flow exiting the fan is then routed into the high pressure compressor to extract work via the Brayton cycle. The remainder of the flow is routed around the high pressure section and the low pressure turbine and exhausted through the nozzle purely for thrust. The ratio of the around and through flow rates is known as the bypass ratio. Though increasing the bypass ratio increases the propulsive efficiency at a given thrust, it is currently limited by the structural integrity required for a larger fan and ability to extract work in the low pressure turbine to drive the fan. The turbine and inter-turbine burning techniques discussed in Section 2.5.2.2 would enable large amounts of work to be extracted by the low pressure turbine to drive an ultra-high bypass ratio and increase propulsive efficiency.

2.5.4 Combustor Exit Temperature Profile Characterization.

Ideal turbine operation assumes a constant temperature profile at each axial location. Then, each radial location would experiences the same temperature drop across the stage. Thus, conventional combustors seek to have an exit temperature profile as close to constant as possible. This also leads to more predictable cooling requirements and smaller temperature gradients on the blade surface. Ultimately, a constant profile maximizes work output potential as well as helps to maximize blade life. Pattern factor ($\mathrm{PF}_{\mathrm{pattern}}$) is one metric used to determine closeness of a temperature profile to constant. It is defined by

$$\mathrm{PF}_{\mathrm{pattern}} = \frac{T_{t,\mathrm{exit,max}} - T_{t,4}}{T_{t,4} - T_{t,3}} \tag{2.66}$$

where $T_{t,e,\mathrm{max}}$ is the maximum total temperature at the exit of the combustor. Thermodynamically, the ideal pattern factor is $\mathrm{PF}_{\mathrm{pattern}} = 0$. However, from a cooling standpoint, $\mathrm{PF}_{\mathrm{pattern}} = 0$ would result in higher temperatures near the walls resulting in excess heating to the walls. In general, cooling combustor walls and imperfect mixing in the combustor are expected to increase $\mathrm{PF}_{\mathrm{pattern}}$. A similar metric is the profile factor given as

$$\mathrm{PF}_{\mathrm{profile}} = \frac{(\overline{T_{t,\mathrm{exit}}})_{\mathrm{max}} - T_{t,4}}{T_{t,4} - T_{t,3}} \tag{2.67}$$

where $(\overline{T_{t,\mathrm{exit}}})_{\mathrm{max}}$ is the maximum circumferentially averaged temperature at the combustor exit.

2.6 Ultra-Compact Combustor

Designers of future gas turbine engines seek to minimize engine length to reduce manufacturing costs, reduce engine weight, and increase the thrust to weight ratio. Additionally, designers seek to maximize thermal efficiency by maximizing T_4 while meeting increasingly strict NO_x emissions standards. However, Zelina and Ballal [71] found NO_x emissions increase with both residence time and temperature. Thus, these requirements are in direct conflict as increased combustion temperatures increase N_2 dissociation driving up NO_x production. One method to meet all these requirements simultaneously is to minimize the combustor length. The shorter residence times in the combustor that result from decreased length reduce NO_x emissions. However, shorter residence times can increase the concentration of CO and unburned hydrocarbons (UHCs) entering the turbine [72]. Since burning in the turbine is less than desirable in current designs, new combustion methods must be developed to meet the increasingly aggressive engine requirements. One design showing promise in satisfying future requirements is the high-g Ultra-Compact Combustor (UCC) presented by Zelina et al. [72]. It proposes burning circumferentially rather than axially to take advantage of high-g combustion (Section 2.4.4) while burning in a small axial distance.

Typical axial combustors require axial flow with no swirl. Thus, the flow exiting the compressor is straightened in the outlet guide vane (OGV), flows axially in the combustor, and is turned once again in the nozzle guide vane (NGV) to achieve the

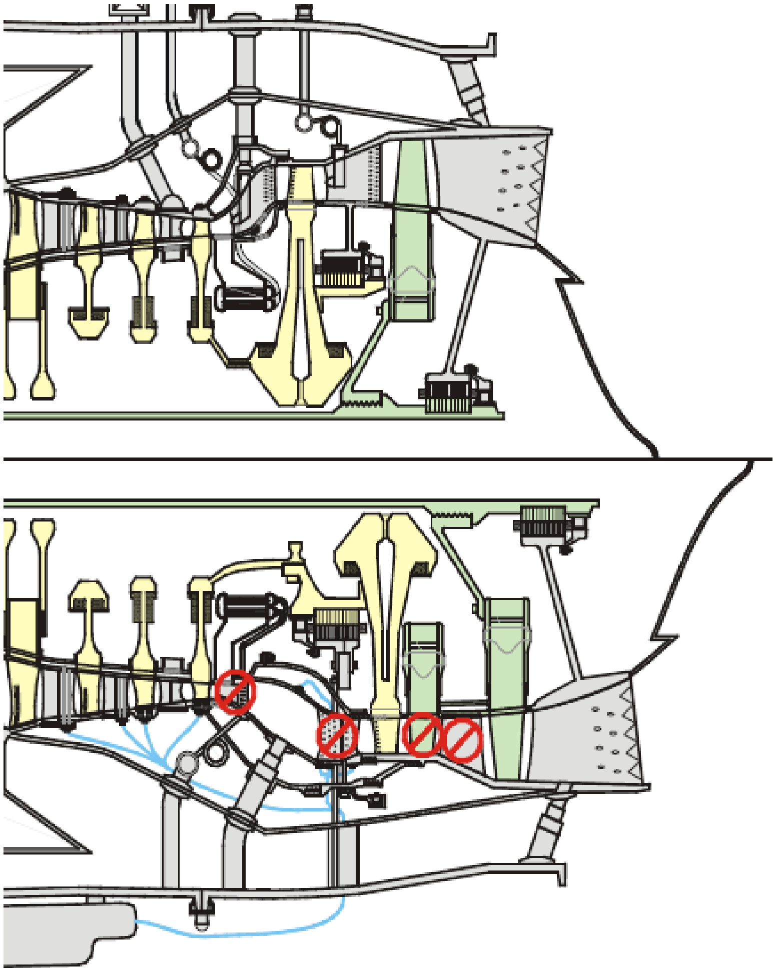

Figure 2.18: Detailed hot section cutaway comparison of conventional and UCC with an ITB configurations with proposed vane elimination [72]

desired angle entering the turbine. The UCC concept, however, has no requirement for axial flow since the design itself hinges on swirl within the UCC cavity. Thus, the UCC concept proposes eliminating the OGV and NGV by merging them into a single hybrid vane positioned directly under the UCC cavity as seen in Fig. 2.18. The curvature of the hybrid vane would be designed such that the inlet angle is the same as the OGV inlet angle and the outlet angle is the same as the NGV outlet angle as depicted in Fig. 2.19. Furthermore, Zelina et al. [72] suggests machining geometry into this vane to assist in extraction of the UCC cavity products into the freestream.

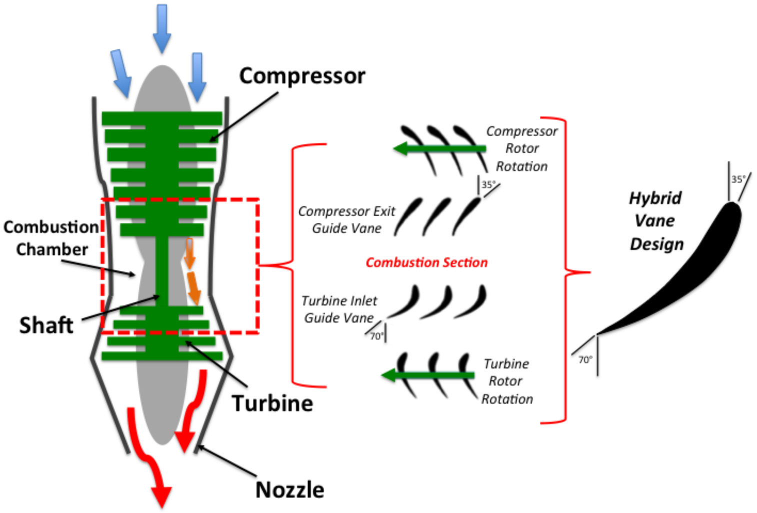

Figure 2.19: Hybrid vane design to accomodate compressor exit and turbine inlet angles [27]

Zelina et al. [72] built a small scale UCC as a proof of the UCC concept. During initial testing, they measured that, like the WSR discussed in Section 2.4.3, the UCC was capable of combustion efficiencies over 99% for a wide operating range with flame lengths half that of axial combustors. Further, they found the combustor was capable of heat release rates twice that of conventional combustors as well as capable stable efficient operation at combustor loadings 2-3 times that of conventional combustors.

Bohan [9] studied the effects of vane solidity on the interaction of the fluid in the circumferential cavity and the core flow by varying the number of vanes around the annulus. He developed computational domains for a typical NGV vane (inlet angle $\beta_1 = 0°$, outlet angle of $\beta_2 = 70°$) featuring 20-, 30-, 45-, and 60-vanes around the annulus. For the hybrid vane design ($\beta_1 = 54°$, outlet angle of $\beta_2 = 70°$), he created domains with 20- and 30-vanes. Finally, he created a 0-vane domain using the 30-hybrid vane domain with the vanes removed. His results indicated that increasing the number of vanes increases the pressure loss over the vane and combustor section. This reduction in pressure helped extract fluid from the circumferential cavity. However,

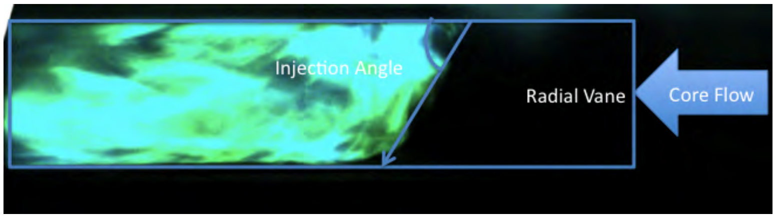

Figure 2.20: Injection angle from UCC cavity to core cavity [32]

vane counts above 20 decreased the mass flow rate in the cavity indicating that the reduction in pressure was dominated by the flow path blockage. Bohan [9] claims traditional can-type combustors currently have average pressure drops of 6%. His results estimated a total pressure drop of 5.45% and 9.39% for high pressure engine conditions and atmospheric rig conditions, respectively.

LeBay [32] studied flow migration from the UCC cavity to the core flow. His experiments used optical techniques to gather a detailed understanding of the UCC flow/core flow interface. Rather than constructing a full annulus rig, his experiments used a sectional rig which models one sixth of the full annulus tested by Zelina et al. [72]. Since the UCC is designed to have cool, unreacted products remain at the OD until combusting, LeBay [32] pointed out that his rig was limited since the UCC flow which did not migrate to the core flow was exhausted rather than recirculated.

High speed video taken by LeBay [32] found that the flow exiting the UCC traveled across the core channel at a linear injection angled as seen in Fig. 2.20. By varying UCC g-loading LeBay [32] found that flow migration scaled close to linearly with g-loading. However, the injection angle was independent of g-loading. He found that the injection angle changed with both UCC/core velocity and mass flux ratios. Since this correlation of injection angle with velocity ratio was found for a constant UCC/core mass flux ratio, it is currently hypothesized that, similar to film cooling jets, it is the UCC/core momentum ratio (the product of the velocity and mass flux ratios) which truly scales the injection angle. The full annulus UCC CFD study of

Bohan [9] corroborated the linear injection angle found by the LeBay [32] sectional rig.

LeBay [32] tested the effect of vane height and UCC/core mass flux ratio on flow migration from the UCC cavity. He found that for mass flux ratios below 0.1, the flow did not span the core cavity and produced poor temperature distribution at the combustor exit. Conversely, a large mass flux ratio exceeding 0.3 caused the UCC flow to span the core cavity, impact the ID endwall and roll back up to impact the OD endwall. This produced significant heating on the endwalls providing significant cooling challenges. An optimal mass flux ratio was found between these two extremes which produced reasonable temperature distribution while avoiding significant endwall heating. LeBay [32] found that the optimal UCC/core mass flux ratio was 0.2 regardless of vane height. He concluded that increased vane height decreased core velocities which increased the UCC/core velocity ratio. Thus, the injection angle would also increase such that the ideal mass flux ratio was invariant with vane height.

Keeping the mass flux ratio constant, Bohan [9] studied the effect of the number of hybrid vanes around a 317.5 mm ID on mass extraction. His computational results showed that if the distance between the vanes were too small, the high velocity fluid exiting the UCC cavity would roll up the vane surface and could re-enter the cavity or block downstream mass extraction as well as heat the OD endwall. Bohan [9] concluded that 20-hybrid vanes around the annulus was sufficient to extract UCC cavity flow while avoiding the negative effects of flow rolling back up the vane surface.

The radial vane cavity seen in Fig. 2.21(b) was implemented by Zelina et al. [72] to assist in UCC cavity mass extraction. However, the results of LeBay [32] showed that the injection angle was independent of the radial vane cavity angle. Parks [49] worked to desensitize the UCC flow migration to operating conditions. He sought

(a) Blank vane

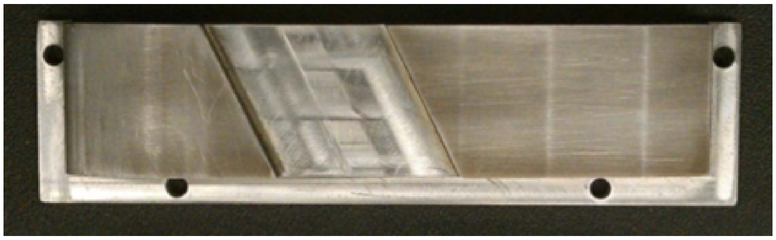

(b) Radial vane cavity design of Zelina et al. [72]

(c) Tiger claw design of Parks [49]

Figure 2.21: Hybrid vane design concepts; core flow from left to right, UCC flow from top to bottom [49]

to prevent excessive ID and OD endwall heating while maintaining an acceptable $\mathrm{PF}_{\mathrm{pattern}}$ at the combustor exit.

To accomplish these objectives, Parks [49] designed and implemented the tiger claw vane design seen in Fig. 2.21(c). He showed his design successfully desensitized the flow migration for UCC/core mass flux ratios of 0.2 and 0.3 but were not met at 0.1. However, this desensitization came at the cost of decreased mixing and combustor efficiency. He hypothesized that this was due to eliminating UCC flow impingement on the ID endwall. Even so, the tiger claw design was found to produce an emissions profile which was more uniformly distributed than the radial vane cavity.

The computational UCC model of Johnson [27] indicated that the tiger claw design of Parks [49] resulted in a pressure drop of 10.2% at atmospheric rig conditions and a $\mathrm{PF}_{\mathrm{profile}}$ of 0.48. In contrast, the baseline blank vane case like that seen in Fig. 2.21(a) resulted in a pressure drop of 10.5% and a $\mathrm{PF}_{\mathrm{profile}}$ of 0.40.

2.7 Film Cooling in a Fuel Rich Environment

As presented in Section 2.3, due to high turbine inlet temperatures, film cooling must be applied to the turbine materials to maximize durability and maintain integrity. However, if energetic fuel species were present in the turbine, the species close to the turbine walls would mix with the oxygen rich film cooling source. There, the oxygen and energetic species would combust resulting in a locally increased T_{aw} and reversing the desired effect of film cooling. In fact, Kirk et al. [30] found secondary reactions can increase h by as much as a factor of two further increasing the heat flux to the wall. To avoid this two-fold effect on heat load to the turbine materials, traditional gas turbine engines employ combustors such that fuel is added, mixed, and completely reacted before entering the turbine section.

Since reactions within the film cooling layer are the collateral of other main processes, they are known as secondary reactions. The secondary reactions depicted in Fig. 2.22 show that slot cooling keeps the coolant and, hence, the flame near the wall. The normal cylindrical hole injection, however, has significant separation from the wall resulting in secondary reactions far from the wall but does little to cool the wall. Thus, for a single row of film cooling, the traditional film cooling tenants of maximizing jet attachment and lateral spreading can actually produce worst case results by keeping secondary reactions close to the wall.

Figure 2.22: Secondary reactions occurring within a film cooling layer: slot injection (left); normal cylindrical hole injection followed by normal holes embeded within a trench (right) [14]

2.7.1 Motivation.

Despite the design rule of completing combustion upstream of the turbine, the study of Lukachko et al. [38] showed that 10% of the fuel energy may be available for heat release within the turbine. They explained that, as mixedness decreases, flow from the combustor is more likely to emerge with streaks of energetic, unburned species. Their results showed that reactive streaks larger than 20% of span do not have time to fully mix in the combustor and may be a mode in which energetic emissions enter the turbine. As a result, Lukachko et al. [38] claim that oxidation of energetic emissions due to interactions with cooling air can be fairly common even in current era combustors. Therefore, learning to cool effectively in a fuel rich environment could help increase the robustness of current designs.

Constant Temperature (CT) expansion was described in Section 2.5.2.2 to have clear benefits for future engines. The main barrier to implementing a CT turbine is in cooling the turbine in a fuel rich environment. NCT expansion systems experience similar cooling challenges. The computational UCC studies of both Bohan [9] and Johnson [27] indicated high fuel concentrations and high temperatures are expected to impinge on the suction side of the hybrid vane just downstream of the leading edge. This can be clearly seen in Fig. 2.23. This presents significant challenges to cooling the vane passage. Thus, developing a scheme to cool blade materials in a fuel

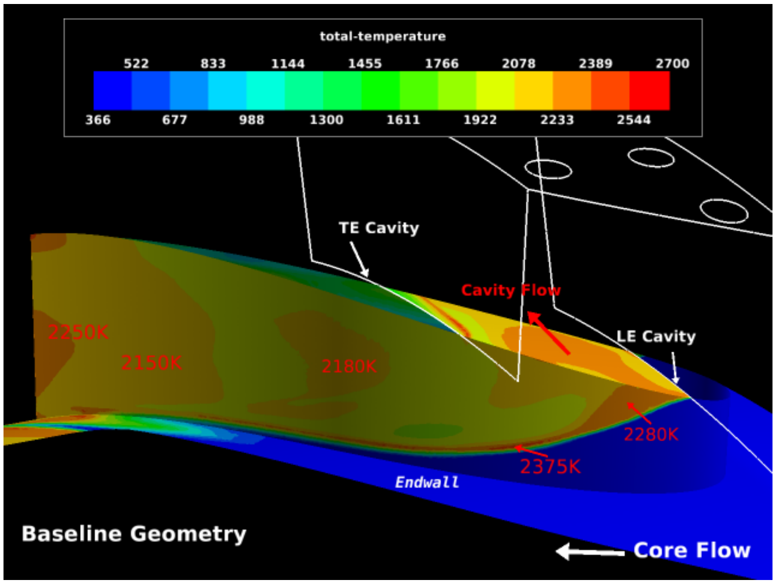

Figure 2.23: Adiabatic wall temperature profile on an uncooled hybrid vane [27]

rich environment could be essential to enabling advanced, next-generation engines.

2.7.2 Modeling Combustor Exit Conditions.

For typical turbine conditions, air-fuel mass ratios of 50 or above are typical. So it is reasonable to model combustion gases as air and to assume the mass flow rate of fuel is negligible. This also allows the assumption that mass flow rate is constant throughout the system [11]. However, when considering a fuel rich freestream, it is important to quantify the amount of untapped chemical energy is in the core flow. Some studies report the ratio of air to fuel mass flow rates in terms of Φ. For example, a flow entering the turbine with $\Phi = 1.1$ would correspond to the case of Lukachko et al. [38] with 10% of the initial chemical energy still available for release within the turbine.

Studies [30, 36] have demonstrated that for fuel rich conditions ($\Phi > 1.0$), secondary reactions can occur within a film cooling layer resulting in a negative η. In other words, adding film cooling increases the heat load to the blade rather than decreasing. Alternatively, for fuel lean cases ($\Phi < 1.0$), Polanka et al. [51] and Evans [18] found no indication of secondary combustion. The experimental results of Bohan [9] showed the largest heat flux augmentation for $\Phi = 1.3$.

Combustion products are numerous which presents a challenge to modeling complexity. A short list of some species participating in hydrocarbon combustion are CO, O, OH, O_2, unburned hydrocarbons (UHCs), H, and H_2. Rather than simply reporting Φ or measuring and modeling each species independently, Lukachko et al. [38] suggests modeling energetic species with a CO-equivalent concentration. The study of Kirk et al. [30] estimated a 20,000 ppm CO-equivalent case represents a combustor operating at $\Phi = 0.5$ at 85% efficiency or $\Phi = 1.0$ at 100% efficiency. Additionally, they calculated that a 60,000 ppm CO-equivalent case models either a 1-σ deviation in mixedness from a combustor at $\Phi = 1.0$ or 3-σ deviations from a modern combustor with $\Phi = 0.5$. Bohan [9] found that running the UCC cavity at $\Phi = 2.2$ and quenching to $\Phi = 0.42$ in the core flow resulted in a radial distribution of combustion completeness just downstream of the UCC cavity. While the OD and ID were found to have a CO-equivelent near zero while the middle had a CO-equivelent of approximately 59,500 ppm.

2.7.3 Flat Plate Research.

The idea that burning in the turbine could be occurring in current engines [38] and could have significant thermodynamic benefits [59] is still in its infancy. As a result, there are relatively few studies in the area compared to non-reacting film cooling. The few studies that have been done attempt to build the framework by focusing on the simplest flat plate cases.

An early computational study of Kirk et al. [30] and Milanes et al. [42] worked to parameterize secondary reactions using co-flow cylindrical holes and injection following a backward facing step, respectively. They concluded that the impact of secondary reactions are primarily a function of Da, heat release potential (CO-equivalent) and blowing ratio. The heat load to the wall increased with increased Da, CO-equivalent, and $M \leq 2.0$. For $M > 2.0$, the jet was sufficiently separated such that the secondary reactions took place away from the wall. The worst case examined by Kirk et al. [30] (highest Da and CO-equivalent) produced the highest heat flux augmentation of 30% over a cooling case with no secondary reactions. Their data also indicated that the peak wall temperature occurred off center at $z/D = \pm 1$ for the detached $M = 2.0$ jet and on centerline for the attached $M = 0.5$ jet.

The effect of secondary reactions in normal cylindrical, co-flow cylindrical, and shaped hole configurations was examined experimentally by Anderson et al. [1] and Polanka et al. [51] and computationally by Lin et al. [36]. To quantify the effect of secondary reactions for each geometry and M they first ejected N_2 from the holes and measured the heat flux to the wall downstream of the injection site. They then switched the coolant to air and measured the heat flux again. The first measurement approximated the heat flux resulting from an air cooled surface with no secondary reactions, q''_f. The second measurement represented the heat flux resulting from a film cooled surface with secondary reactions present, q''_r. Then, these two measurements were used to quantify the heat flux augmentation due to secondary reactions

$$\sigma = 1 - \frac{q''_r}{q''_f} \tag{2.68}$$

Anderson et al. [1], Polanka et al. [51], and Lin et al. [36] agreed that, for all three geometries, heat flux increased due to secondary reactions with increasing blowing ratios on the range of $0.5 \leq M \leq 2.0$. Anderson et al. [1] demonstrated that the heat flux augmentation was substantially higher for the angled holes than for the normal holes for $\Phi > 1.0$. For the same M, the normal holes separate from the airfoil surface

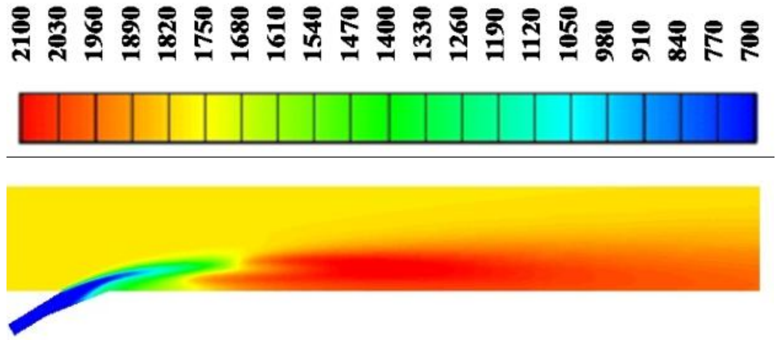

(a) Air Injection

(b) N_2 Injection

Figure 2.24: Effect of secondary reactions on mid-plane temperature (K) profile following shaped hole injection; $\Phi = 1.5$**,** $M = 2.0$ [**36**]

farther than the angled holes. This makes the reaction occur off the surface thus reducing the heat flux to the wall due to secondary reactions.

Evans [18] showed that, compared to normal and angled cylindrical holes, shaped holes result in the smallest convective heat transfer coefficient. However, the experimental and computational studies of Evans [18], Anderson et al. [1] and Polanka et al. [51] demonstrated that the augmentation following the shaped hole configuration was the greatest of the cases considered. This was because the coolant flow was maintained close to the surface and resulted in heat release due to reactions also occurring near the wall as seen in Fig. 2.24. The computational results of Polanka et al. [51] produced an increases in T_{aw} due to secondary combustion following shaped, angled, and normal holes of 350 K, 200 K, and 100 K, respectively.

While secondary reactions occurring off the surface may seem advantageous, it has two major disadvantages. First, the separated flow does not keep coolant near the wall to decrease T_{aw}. Second, Lin et al. [36] revealed that CRVPs following normal jets swept hot core flow toward the wall and allowed fuel to penetrate under the coolant jet and spread along the surface. Though the angled jet had less fuel near the wall, the shaped hole minimized the effect of CRVPs and had the largest region of low fuel concentration near the wall. They assert that the shaped configuration sweeps less fuel to the wall along with keeping the secondary combustion products attached to the surface. This two-fold effect is thought to explain the low concentrations of fuel near the wall.

Lin et al. [36] showed that higher blowing ratios increased jet separation which increased concentrations of fuel near the wall by sweeping fuel under the jet as seen in Fig. 2.25. While not necessarily detrimental to a single row of film cooling, the sweeping of fuel toward the wall creates a condition where each downstream cooling row encounters an equally fuel rich freestream. So, while a single row of shaped holes results in maximum heat flux augmentation, it also results in the lowest concentrations of fuel near the wall. Thus, when considering multiple rows in series, methods which maximize jet spreading and attachment may minimize heat flux augmentation in downstream rows.

The experiment of Bohan [9] studied the effect of two rows of film cooling in series with variable upstream and downstream geometries and blowing ratios. He found that for $\Phi = 1.5$, a slot at $M = 2.0$ followed by fan-shaped holes resulted $\sigma \approx 0$. He concluded that the slot provided sufficient oxygen to complete the near wall reactions. Furthermore, as discussed in Section 2.3.3.3, the slot geometry does not result in CRVPs which precludes the sweeping of more fuel toward the wall. The result was a completely reacted flow encountering the downstream fan-shaped holes resulting in negligible secondary reactions. His results showed a heat flux augmentation near zero for these conditions.

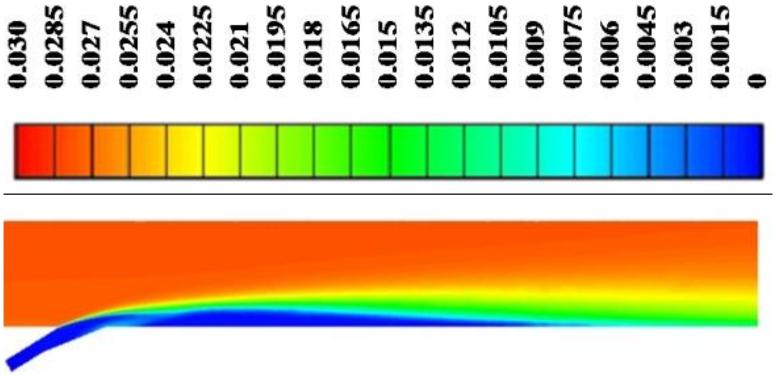

(a) Air Injection, $M = 1.0$

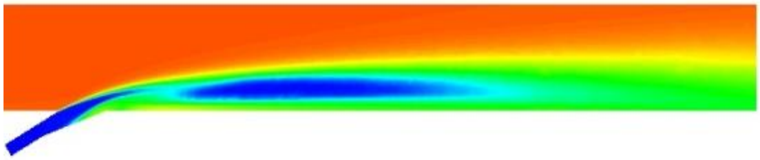

(b) Air Injection, $M = 2.0$

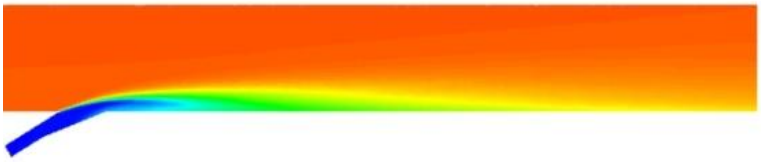

(c) N_2 Injection, $M = 1.0$

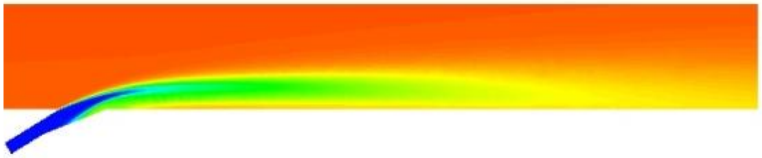

(d) N_2 Injection, $M = 2.0$

Figure 2.25: Effect of M on C_3H_8 mass fraction at the mid-plane for $\Phi = 1.5$ in the freestream following a shaped hole with and without secondary reactions (air and N_2, respectively) [36]

DeLallo [14] continued the research of Bohan [9] by experimenting with a blank plate, normal cylindrical holes, and slot configurations in the upstream row and trench, shaped, and ramp configurations in the downstream row. The latter ramp configuration was modeled after combustor liners where the coolant is injected with $\alpha = 0$ on from the vertical face of a backward facing step. DeLallo [14] showed that a slot followed by a low momentum ratio cooling configuration in the downstream row (e.g. trench or shaped hole geometries) resulted in a highly effective strategy for mitigating secondary reactions. These configurations resulted in augmentations close to zero (<2%).

His results indicated that the ramp configuration with no upstream cooling produced lower heat flux augmentation than trench configurations. He hypothesized this was because the ramp configuration causes reactions to take place off the wall while the other two result in reactions close to the wall. However, when preceded by a slot configuration, the ramp produces the largest heat flux augmentations.

Though slot cooling produces the lucrative results presented both here and in Section 2.3.3.3, its large cross-sectional area tends to make it structurally unsound. Section 2.3.3.4 described how the trench design of Bunker [10] could reproduce many of the benefits of slot cooling without its crippling disadvantages. Unfortunately, no studies employed a trench configuration in the upstream row.

The experimental work of Robertson [54] examined the effect of multiple closely spaced rows of cooling holes in a fuel rich environment. He hypothesized that, with a sufficient number of cooling hole rows, a layer of coolant would be developed such that reactions took place in a mixing layer between the coolant layer and freestream rather than incident on the wall. He tested configurations with one row, three rows and five rows of co-flow $\alpha = 30°$ cylindrical holes. The five row configuration was found to achieve his layer build-up objective.

As discussed in 2.3.3.1, Oguntade et al. [48] showed that opposed-flow $\alpha = 150°$ holes create a stagnation point resulting in excellent coolant attachment, spreading, as well as prevention of CRVPs. In an attempt to take advantage of these benefits, Robertson [54] reversed the first two upstream rows of cylindrical holes to be opposed flow $\alpha = 150°$ holes. He found that this configuration resulted in increased σ over the entirely co-flow five row configuration. However, he showed that the two row opposed-flow configuration resulted in the shortest flame length following the first row of injection. Thus, this configuration had the unique ability of causing rapid consumption of fuel. It is currently hypothesized that the benefits of the opposed-flow holes were severely compromised by the downstream co-flow injection sites before useful measurements could be taken. Unfortunately no study has been performed using multiple rows of purely opposed-flow holes in a fuel rich environment.

2.7.4 Cooling a UCC Hybrid Vane.

As discussed in Section 2.7.1, high temperatures and concentrations of energetic species are expected to impinge on the hybrid vane suction surface. The computational work of Johnson [27] took a first cut at cooling the UCC hybrid vane. He fitted the vane geometry of Bohan [9] with two geometries of film cooling to study the effect of each independently.

Johnson [27] investigated both a normal hole and a contoured trench cooling scheme on an adiabatic hybrid vane. His computational results showed his cooling configurations increased $\mathrm{PF}_{\mathrm{profile}}$ from the baseline (uncooled) value of 0.40 to 0.72 and increased $\mathrm{PF}_{\mathrm{pattern}}$ from the baseline value of 0.71 to 0.77-0.79. Despite the poorer temperature distributions, his cooling configuration decreased the total pressure loss from the baseline value of 10.5% to 9.1-9.3% for blowing ratios of 1.0, 1.5, and 2.0.

As discussed by Horlock and Lakshminarayana [25], secondary flow occurs when

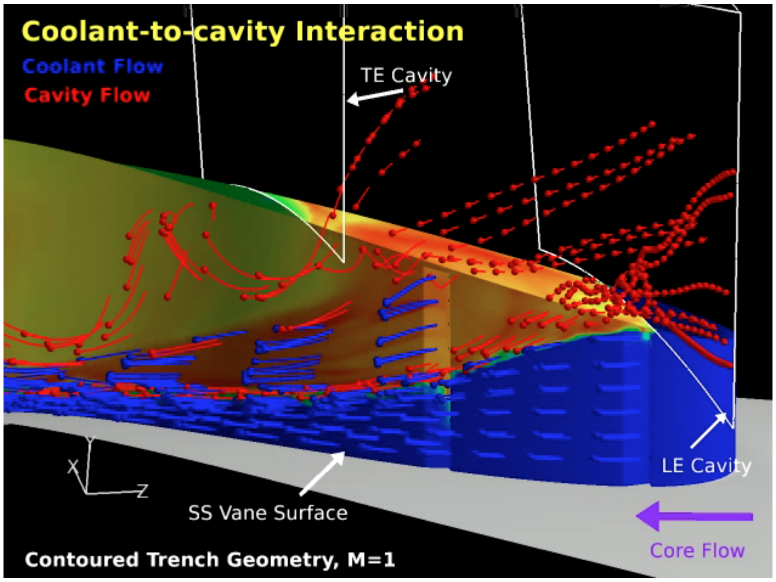

Figure 2.26: Interaction of hybrid vane film cooling flow and UCC cavity flow [27]

flow with streamwise vorticity, like that found in a boundary layer, is deflected in a spanwise direction. As such, secondary flow is produced when flow entering the turbine is initially sheared by the endwalls and, at the leading edge of a blade row, is deflected. Then, a passage vortex will shed down the pressure and suction sides of the blade. In addition to the passage vortex, Bohan [9] and Johnson [27] found a vortex sheds from the point where the UCC cavity flow exits the cavity and impinges on the hybrid blade as seen in Fig. 2.26.

Wurm et al. [70] showed that swirled flow can block film cooling layer penetration in some locations. Their results suggest it can take up to two rows of cooling holes to recover. In addition, results of Marosky et al. [39] revealed that a swirling core flow produces a suction effect which entrains coolant from the wall and into the core flow. This entrainment can lead to strong fluctuations of coolant concentration and performance on the wall. The hybrid vane cooling configuration of Johnson [27] was seen to suffer just this problem. Coolant near the wall was entrained by the passage vorticies away from the wall. This effect was especially strong near the UCC cavity where the vortex from the cavity entrained coolant into the mainstream as seen in Fig. 2.26.

Bohan [9] found that flow exiting the cavity had enough momentum to span the hybrid vane passage and impinge on the ID wall. This resulted in extreme temperatures on the ID wall. To mitigate this effect, he proposed placing a divider plate slightly elevated off the ID endwall to help cool the ID. Bohan [9] showed that this divider plate kept the ID endwall cool while trapping the vane leading edge vortex under the plate as seen in Fig. 2.27. The plate also caused a vortex to form from the cavity fluid impacting and rolling up the vane suction side.

Beyond the thermal management benefits of the divider plate proposed by Bohan [9], it also resulted in a 2% and 1% reduction in static and total pressure loss to 9.6% and 8.3%, respectively. This could be attributed to superior management of secondary flows. Despite the enticing thermal and pressure drop improvements, they come at the cost of $\mathrm{PF}_{\mathrm{pattern}}$ increased from 0.34 to 0.44.

An additional method to prevent excessive ID endwall heating is the tiger claw design of Parks [49]. Johnson [27] showed that the tiger claw design routes the cavity flow in the streamwise direction rather than allowing it to impact the ID endwall before being redirected downstream as seen in Fig. 2.28. This causes the fuel rich vortex to remain off the suction side surface and maintains a pocket of cool air near the surface until farther downstream. However, Johnson [27] reported a $\mathrm{PF}_{\mathrm{pattern}}$ of 0.85, a significant increase from the divider plate design of Bohan [9]. Even so, the tiger claw design shows promise in increasing control of the flow migrating from the UCC cavity. With some optimization, it is anticipated that significant improvements can be made on the temperature profile downstream of the tiger claw design.

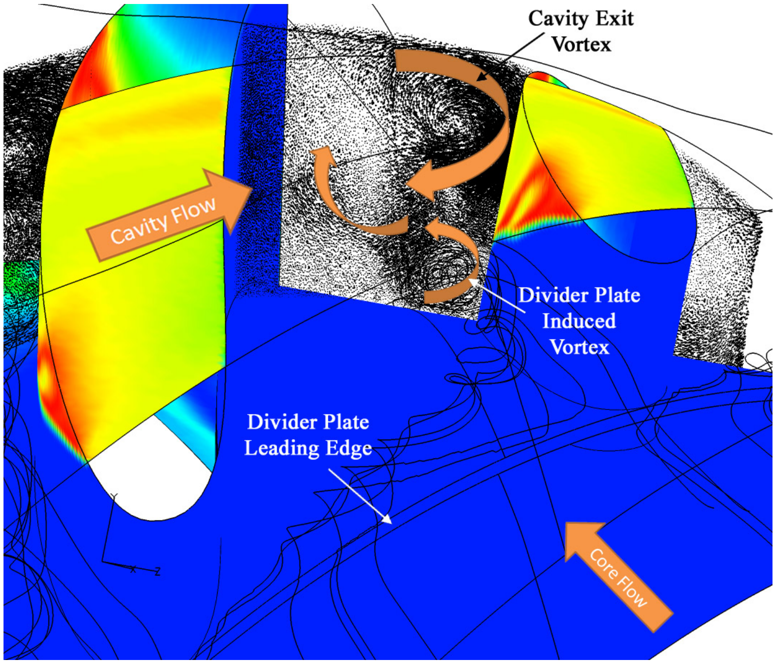

Figure 2.27: Interaction of divider plate vortex with UCC cavity vortex [9]

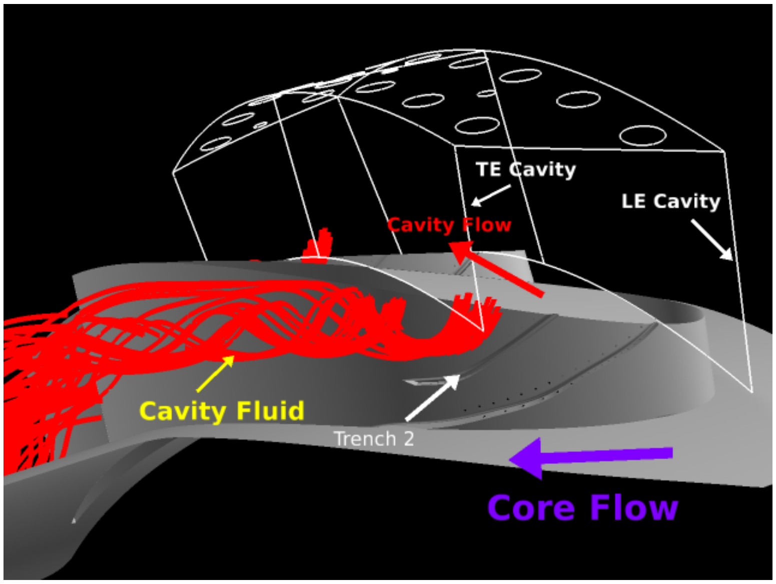

Figure 2.28: Interaction of tiger claw design [49] with UCC cavity vortex [27]

2.8 Computational Modeling

Detailed modeling of practical flows is extremely complex. The additional expense of modeling reacting flows adds significantly more complexity. The CFD studies discussed in this chapter employ a number of turbulence and chemistry models to simulate their flows. This section will review the models and the relative benefits and disadvantages of each.

2.8.1 Turbulence Modeling.

CFD simulations are accomplished by discretizing the flow domain into small volumes. Then, the equations governing the flow are applied to each of these small volumes. Then, by solving the governing equations in each of these volumes, the compilation of all the volumes produces an estimation of the flow physics and properties throughout the flow domain.

Turbulent flows involve eddies ranging from relatively large to extremely small. To accurately capture the smallest eddies, the domain must be discretized into many volumes on the order of the smallest eddies. Such a technique is known as a Direct Numerical Simulation (DNS). Unfortunately, DNS simulations are so computationally expensive that modeling all but the simplest cases takes an impractical amount of time. Therefore, it is critical to discretize the domain into larger volumes which cannot capture the smallest eddies. Then, from experimental knowledge of turbulent flows, the effect of the small eddies within the larger volumes can be calculated using models.

Many of the modern models modify the governing equations by the Reynolds decomposition as exemplified by Eq. 2.40. Then, by temporally averaging the governing equations, all time fluctuating quantities are eliminated except for one which acts like a turbulent shear stress. This is termed the Reynolds stress and the temporally averaged governing equations are known as the Reynolds Averaged Navier-Stokes (RANS) equations [7]. All RANS models seek to add additional equations to solve for the Reynolds stress. Once the Reynolds stress is known, the governing equations are closed and can be solved to simulate the flow.

Two dominant RANS models are the k-ϵ model of Launder and Spalding [31] and the k-ω model of Wilcox [69]. The former is generally best far from bounding walls while the latter better models near wall boundary layer flows. To take advantage of each model's specialization, the RANS k-ω Shear-Stress Transport (SST) turbulence model utilizes the standard k-ω model in the near wall region and gradually changes to the k-ϵ model with distance from the wall. Thus, the RANS k-ω SST turbulence model is generally well suited for both near-wall and far-field regions. The flat plate investigations of Polanka et al. [51] and Lin et al. [36] concluded that the RANS k-ω SST model was well suited to model film cooling in a fuel rich environment.

To model secondary flows in the vane passage, Bohan [9] implemented a RANS Re-Normalization Group (RNG) k-ϵ model for its ability to handle stagnation flows and conditions with streamline curvature. However, Johnson [27] showed that the SST k-ω model better captured the film cooling physics than the RNG k-ϵ model. Thus, Johnson [27] used the SST k-ω model to simulate the UCC with coolant flows.

2.8.2 Chemistry Modeling.

Propane is a good low level model for modern fuels like JP-8. Thus, it is the fuel used for this research program. The work of Polanka et al. [51] and Lin et al. [36] implemented a two-step combustion model for propane given by

$$\mathrm{C_3H_8 + 3.5O_2 \rightleftarrows 3CO + 4H_2O} \tag{2.69}$$

$$\mathrm{CO + O_2 \rightleftarrows 2CO_2} \tag{2.70}$$

Then, the reactions were integrated through time via the Arrhenius rate equation (Eq. 2.49). To increase computational efficiency, the In-Situ Adaptive Tabulation (ISAT) algorithm used by Lin et al. [36] will be implemented to pre-calculate the numeric integration for certain ranges of conditions and stored in a table. Then, the result of the numeric integral with initial conditions inside given bounds can be looked up rather than calculated. To model turbulence-chemistry interactions, Polanka et al. [51] and Lin et al. [36] utilized the eddy-dissipation concept (EDC) approach which assumes chemical reactions are controlled by turbulence.

Bohan [9] implemented two chemistry models. The first was a 5-species model which assumed a one step reaction of propane to complete combustion given by Eq. 2.46. The second was a 12-species model which had numerous reaction paths. The 12-species model yielded a much more detailed understanding of the chemistry and flow but was significantly more computationally expensive. On the other hand, the the 5-species model was much less computationally expensive and produced a reasonable approximation of the more detailed 12-species model. As a balance of these two models, Johnson [27] implemented the 5-species, two step model given by Eqs. 2.69 and 2.70. Since the reaction given by Eq. 2.70 is the dominant source of heat release, the two step model balances computational expense with capturing the important reaction paths.

2.9 Chapter Summary and Research Outline

The present research is concerned with satisfying the research objectives outlined in Section 1.4. This chapter outlined the relevant literature to both motivate the research objectives as well as to set the stage for the research that will be presented in the remainder of this document. Specifically, Chapters III and IV will discuss the experimental and computational tools, respectively, that will be used to address the research objectives. Then, Chapter V will computationally and experimentally examine convective and radiative heat transfer in the absence of film cooling to satisfy Objective 1. Next, Chapter VI study non-reacting film cooling computationally and experimentally to address 2. Last, Chapter VII experimentally examine film cooling in a fuel rich environment to satisfy Objectives 3 and 4.

III. Experimental Method

To satisfy the research objectives outlined in Section 1.4, the present research relied on a combination of experimental and computational studies. These tools were utilized to understand how variable properties effect flow on a flat plate with and without film cooling as well as film cooling with and without secondary reactions. This chapter will provide an overview of the facility seen in Fig. 3.1 used to gather the experimental data while the following chapter will describe the computational method. A more detailed description of the experimental facility can be found in Appendix A.

3.1 Facility Overview

The facility used in the present work was the Air Force Research Laboratory Combustion Branch's Lab 153 in Building 490 on Wright Patterson Air Force Base. Several previous studies have used the present facility to study reacting film cooling including Evans [18], Anderson et al. [1], Polanka et al. [51], Bohan [9], DeLallo [14], Robertson [54], and Shewhart [57]. Similar to these studies, the present work selected this facility for its combustion capabilities, its ability to support high tem-

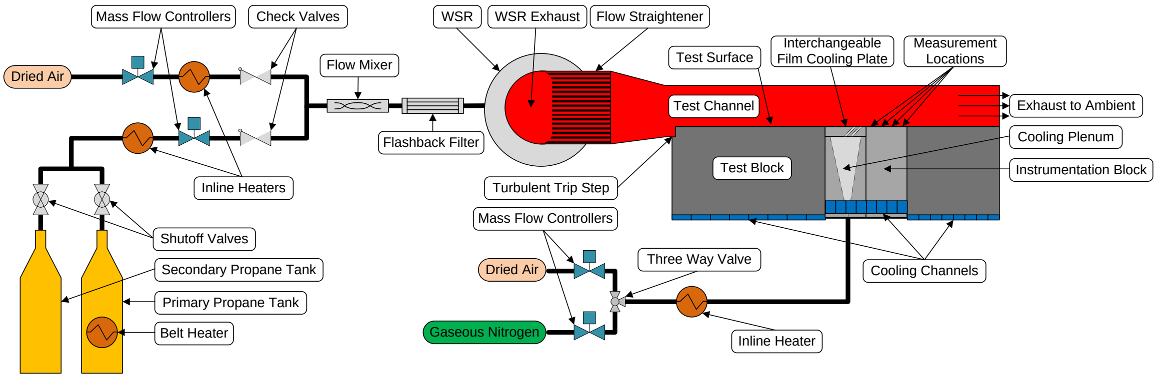

Figure 3.1: Diagram of experimental facility

perature heat transfer experiments, as well as its ability to support a large number of simultaneous thermocouple measurements.

A diagram of the facility is seen in Fig. 3.1. The facility housed a reactor which was capable of creating a high temperature flow ranging from fuel lean to fuel rich. A flat plate test rig was placed downstream of this reactor such that the high temperature reactor exhaust would flow over the flat plate and vent to ambient. The flat plate was fitted with backside cooling paths which, with varying coolant fluids and flow rates, was capable of varying the wall temperature. The flat plate was fitted with a film cooling plenum capable of accepting modular test coupons of selected film cooling schemes. Downstream of the cooling plenum was an instrumentation block capable of measuring the surface temperature and conductive heat flux.

3.2 Mass Flow Controllers

As seen in Fig. 3.1, the facility used mass flow controllers to provide air, nitrogen, and gaseous propane to the test rig. These controllers were used to supply the combustion process which created a hot core flow. In addition, they supplied the film cooling plenum to create various film cooling scenarios. This section will give an overview of the mass flow controller's operation and calibration while the following two sections will discuss how the flows resulting from these controllers were used.

The mass flow controllers operated on a 4-20 mA control and feedback loop. In this system, the operator requests a flow rate via the control panel seen in Fig. 3.2. Then, the control interface converts the desired flow rate to a current between 4 and 20 mA where 4 mA requests zero flow and 20 mA requests maximum flow from the controller. The maximum flow of each controller is also listed in Fig. 3.2. The controller continuously measures the flow rate through the controller by the mechanism described in detail in Section A.1.1. Then, given an input from the control interface,

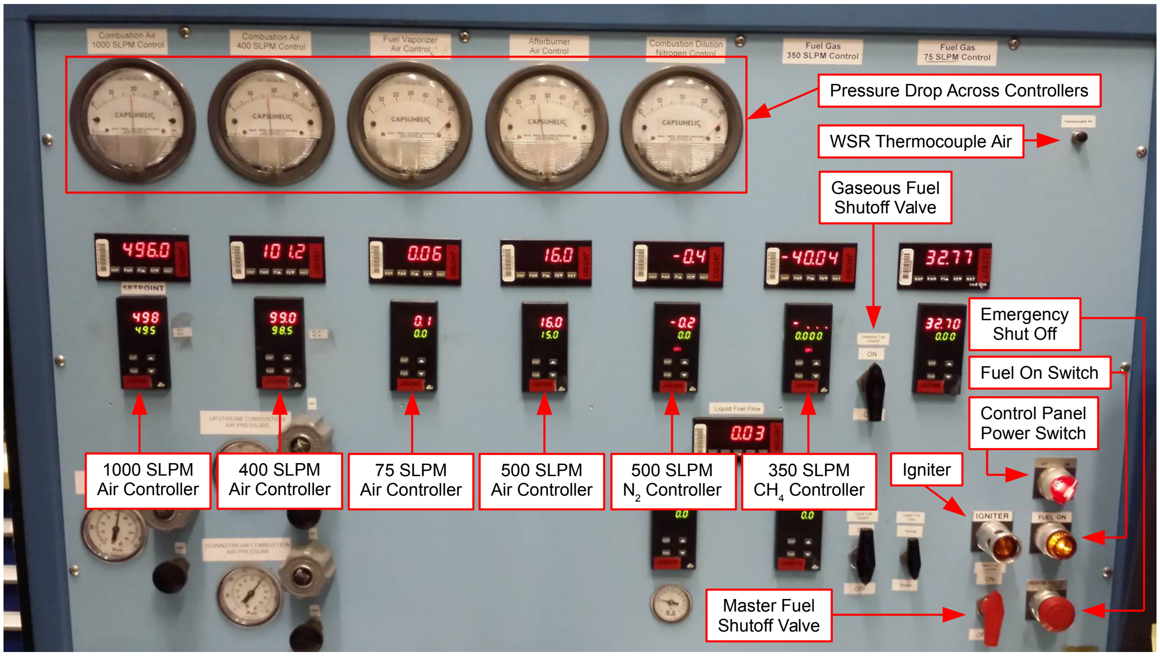

Figure 3.2: Control panel used in experimental facility

the controller throttles a solenoid valve until the desired flow rate is achieved. Finally, the controller outputs a feedback signal on the same 4-20 mA scale which is read and displayed on the control interface and recorded in the data acquisition system.

To ensure the controller is accurately measuring the flow rate, a calibration of each controller was accomplished. These calibrations involved first requesting various flow rates from each controller. Then, the achieved flow rates were measured using the sonic nozzle, dry flow meter, and Gilibrator methods detailed in Section A.1.2. Next, the signal from the controller's feedback loop was also recorded. Finally, a calibration curve was created by a linear regression of the measured flow rates as a function of the feedback signal. The resulting linear function allowed the data acquisition system to read the 4-20 mA feedback signal from the mass flow controller and convert it to the actual mass flow through the controller. Table A.1 provides the uncertainties of each controller's calibration which were all within 4.2%. The following two sections will discuss the applications of the flows resulting from these controllers.

3.3 Well Stirred Reactor

The present research required a hot core flow which was fuel rich for most experimental conditions and fuel lean for the remaining conditions. To create these conditions, a toroidal Well Stirred Reactor (WSR) with a volume of 250mL burned a mixture of air and propane at the desired equivalence ratio (Φ) to generate a high temperature flow. The WSR was similar to the design presented by Zelina and Ballal [71] and discussed in Section 2.4.3 with an important distinction. The WSR of Zelina and Ballal [71] was uncooled and made entirely of alumina (Al_2O_3) ceramic. Unfortunately, after continued use of the ceramic WSR and many heating and cooling cycles, the reactor would crack and erode.

Unlike the ceramic WSR, the present WSR seen in Fig. 3.1 was constructed of Inconel® with a thermal barrier coating applied to the interior of the toroid. To keep the reactor materials sufficiently cool, channels were machined into the exterior of the reactor. These channels were then supplied with water to actively remove heat from the material.

Similar to the ceramic WSR of Zelina and Ballal [71], the present WSR injected the fuel and air mixture with a high degree of swirl. Primarily, this created a uniformly and completely burned flow at the exit of the WSR. Second, the g-loading imparted by swirl increased the combustion stability such that burning propane at Φ between 0.7 and 1.4 were achievable. This range of Φ enabled the present scope of work.

The fuel and air delivery system included several safety features to prevent a flame front from propagating backwards through the plumbing. First, the fuel and air were injected into the combustion chamber at a high sonic velocity through small diameter holes to extinguish any flames propagating backward through the injection holes. Second, after the fuel and air mixed but before they entered the WSR, the fuel-air mixture passed through a long, fine honeycomb mesh to extinguish any flames propagating outside the WSR. Last, before the fuel and air were mixed, check valves were placed on the fuel and air delivery lines. This prevented any fuel from flowing into the air lines or the reverse.

This section provided an overview of the WSR's design and safety features. A more detailed description of WSR's design and plumbing are presented in Section A.2. The following section will describe the test channel which utilizes the output of the WSR.

3.4 Test Channel

As seen in Fig. 3.1, the hot exhaust from the WSR was routed through a flow straightener to remove the swirl component, through a transition section, through the test section, and exhausted to ambient. This section will give an overview of these components of the test rig. A more detailed discussion is presented in Section A.3.2.

3.4.1 Transition Section.

As discussed in Section 3.3, the WSR results a highly swirled flow exiting the reactor. Thus, the ceramic flow straightener seen in Fig. 3.3 was installed to remove this swirl component. Next, the ceramic transition section also seen in Fig. 3.3 was used to modify the flow cross-section from circular at the WSR exit to nearly rectangular cross-section at the test section inlet.

To help insulate the flow passing through the transition section, an additional ceramic sleeve was placed around the transition section. Finally, to provide structural integrity and support for mounting the test section, a metal sleeve was placed around the entire ceramic transition as seen at the bottom left of Fig. 3.4. Despite the structural support, the extreme heating and cooling cycle of each test day caused the brittle ceramic flow straightener and transition section to crack and deteriorate

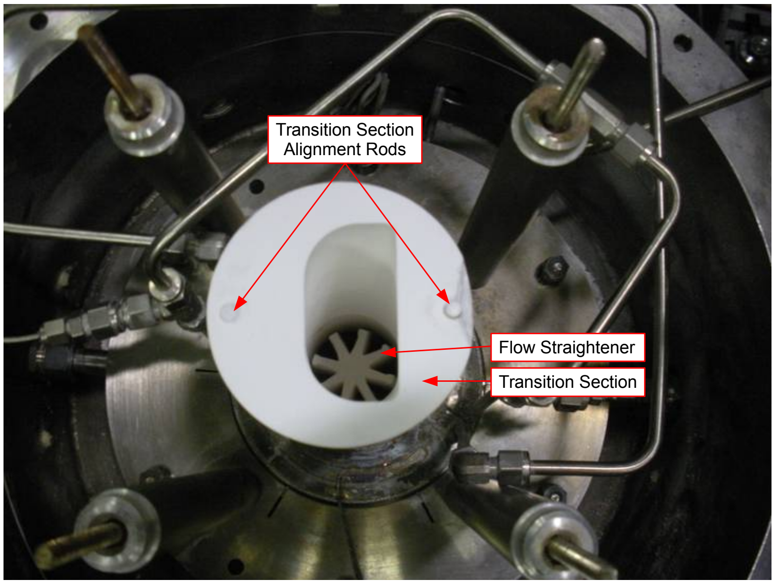

Figure 3.3: Transition section adjusting flow cross-section from WSR exit to test section entrance

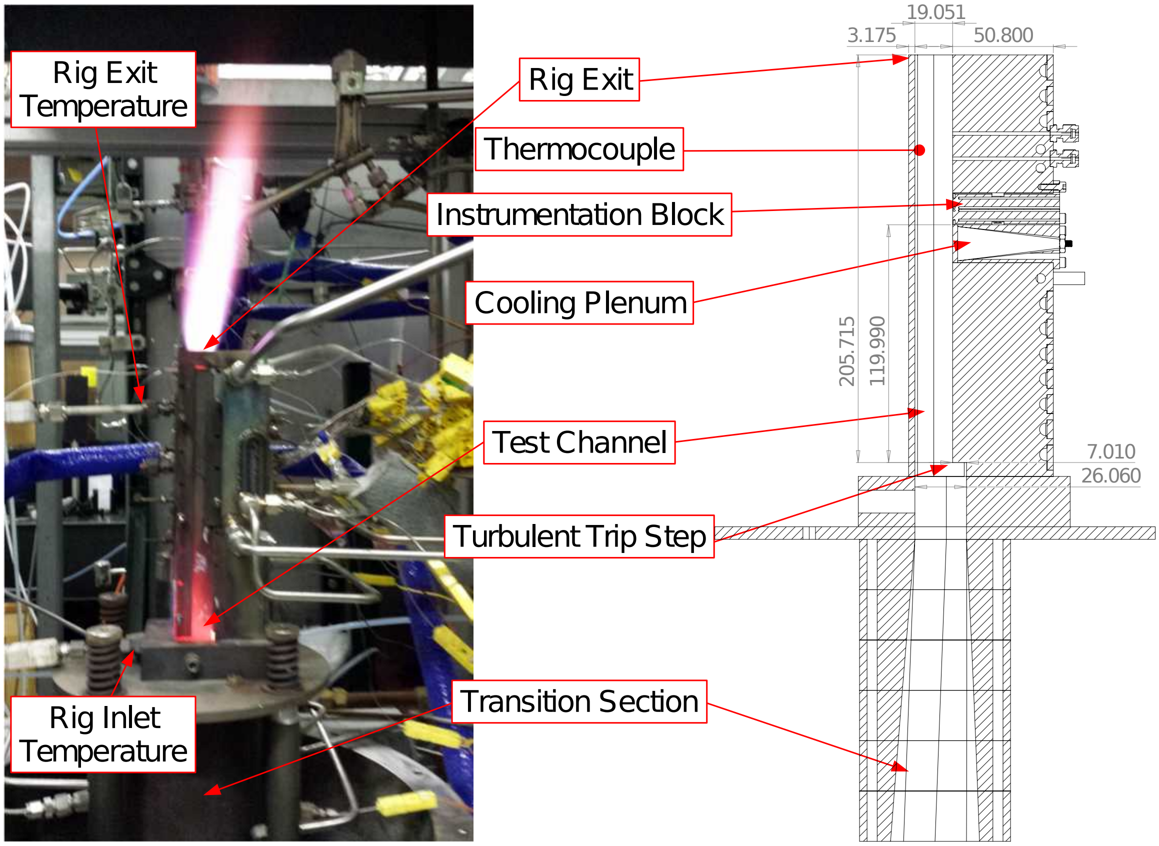

Figure 3.4: Comparison of rig hardware (left) to cutaway drawing of transition section and test channel (right); flow from WSR (bottom) to rig exit (top); dimensions in mm

over many test days. Each test cycle required heating the ceramics from near room temperature to around 1400 K, holding for up to 10 hours followed by cooling back to room temperature at the completion of the test day. However, despite the cracking, the ceramics were seen to be sufficiently durable to support 6-8 weeks of testing before the cracking became sufficiently severe to require replacing.

3.4.2 Test Section.

After exiting the transition section, Fig. 3.1 shows that the hot flow from the WSR entered the test section. To ensure the flow within the test section was fully turbulent, a forward facing step was placed at the test section's inlet. At the nominal test conditions, the analysis of Section A.3.2 indicated that a step 3.2 mm or more in height would be sufficient to ensure a fully turbulent flow. Thus, to provide sufficient margin, the 7 mm step seen in Fig. 3.4 was implemented.

The walls bounding the test section were modular to support solid Hastelloy X [24] walls or windows. This modularity enabled various testing configurations to meet a wide variety of test objectives. Namely, quartz windows enabled visual spectrum images or laser diagnostics of reacting film cooling layers. Additionally, a sapphire window could be installed to take infrared images of the film cooled surface.

The majority of the present work implemented Hastelloy X [24] walls with no windows. The cross-section of the all metal wall configuration is seen in Fig. 3.5(a) with dimensions. The cross-sectional area and hydraulic diameter of this configuration were $A = 871\,\mathrm{mm}^2$ and $D_h = 27.2\,\mathrm{mm}$, respectively.

It will be seen in Section 5.3 that radiative heat transfer played a significant role in the total heat transfer to the test surface. Subsequently, a method to measure the radiative heat transfer was proposed. To substantiate the proposed method, a thermocouple was mounted to the surface of the wall opposite the instrumentation

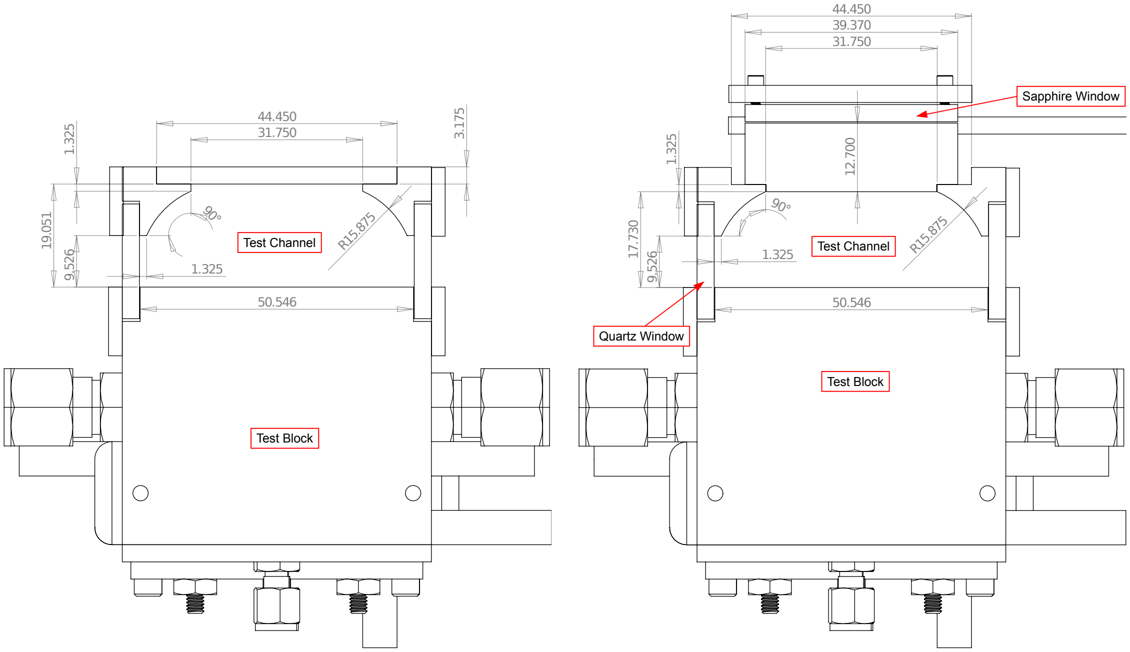

(a) Without windows (b) With windows

Figure 3.5: Dimensions of test channel cross section in mm

block as seen in Fig. 3.4. Then, the measured temperature along with known radiative properties of Hastelloy X [24] allowed for a simplified estimation of the radiative heat transfer to the test surface. This estimation was then compared to the measured radiative heat transfer to provide evidence for the method's validity.

To demonstrate the generality of the radiative heat transfer measurement method, a second cross-sectional configuration with windows was examined. This configuration replaced one side wall with a quartz window and replaced the wall opposite from the test block with a thicker wall as seen in Fig. 3.5(b). A sapphire window was integrated into this thicker wall to support the parallel study of Shewhart [57] which employed infrared imaging of the film cooled surface.

Comparing dimensions of the cross-section with windows (Fig. 3.5(b)) to that without windows (Fig. 3.5(a)) reveals a slight difference in their cross-sectional geometry. Specifically, the wall opposite from the test block on the configuration with windows has a small tab which extends into the flow area. This difference resulted in

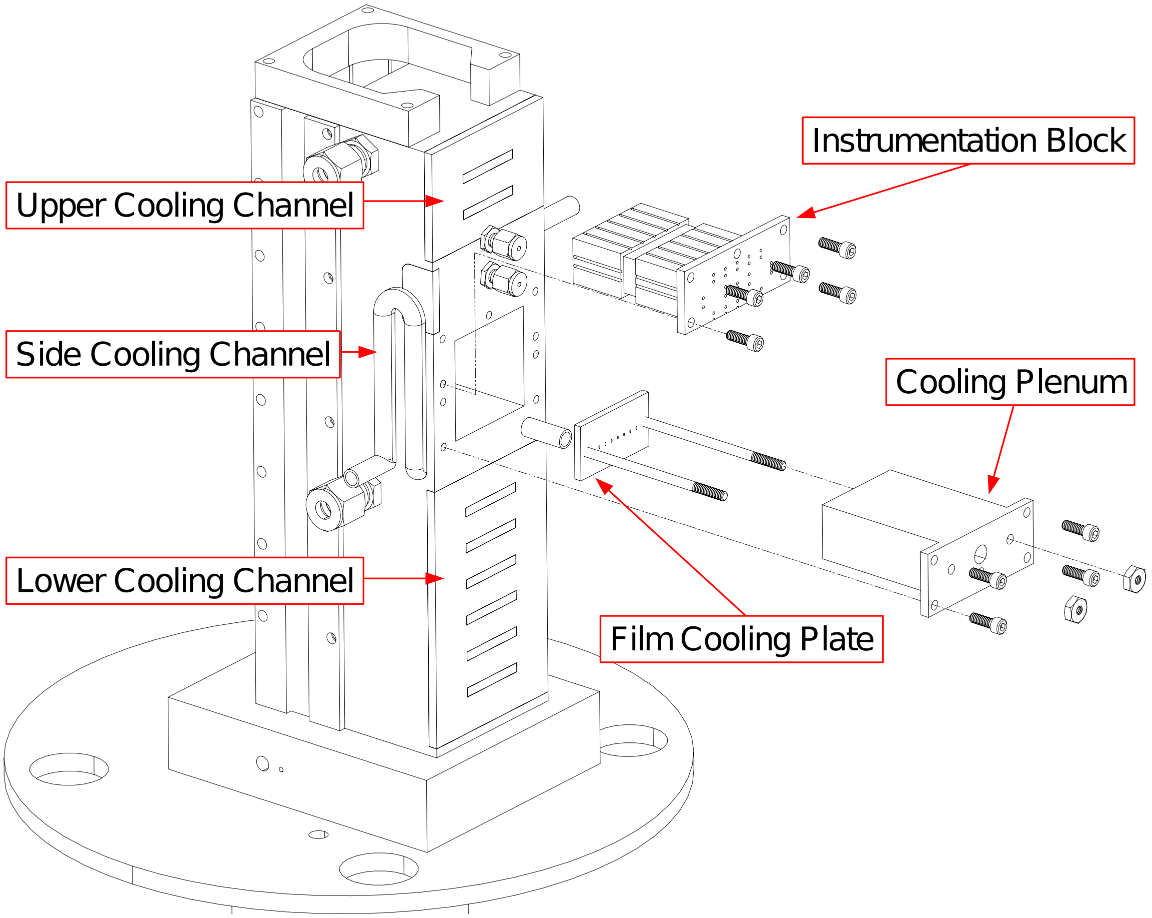

Figure 3.6: Drawing of rig cooling channels and test insert assembly with hardware

the slightly different flow dimensions of $A = 828\,\mathrm{mm}^2$ and $D_h = 26.4\,\mathrm{mm}$.

As shown in Fig. 3.1 two inserts were placed in the test block. The purpose of these inserts was to provide modularity to the rig and allow for flexible cooling configurations and measurements. The upstream insert seen in Fig. 3.6 was a cooling plenum which was configured to accept interchangeable film cooling plates. The insert downstream of the cooling plenum seen in Fig. 3.6 enabled surface temperature and heat flux measurements following the film cooling injection. The next two sections will discuss the two inserts in more detail.

3.4.3 Film Cooling Plenum.

The film cooling plenum was designed to accept interchangeable film cooling plates as seen in Fig. 3.7 such that the effect of film cooling geometry could be studied. Seven cooling configurations were studied in the present research. Four of the coupons were single row configurations of cylindrical holes, shaped holes, cylindrical holes embedded in a trench, and rows of slots. The remaining three were five row configurations of cylindrical holes, cylindrical holes embedded in trenches and a slot. A five row shaped hole configuration was not tested due to the manufacturing time, difficulty and expense required. The relative benefits and drawbacks of each of the four hole geometries were discussed in Section 2.3.3. However, for convenience, a summary of this section is provided here.

Cylindrical holes are the cheapest to manufacture of all the configurations but have poor jet attachment, poor lateral spreading, and create intense counter rotating vortex pairs (CRVPs). These CRVPs tend to sweep hot freestream flow toward the wall and lift coolant off the wall. Shaped holes are cylindrical holes which diffuse the flow at the hole exit. This diffusion vastly improves the jet attachment and lateral spreading as well as decreases the strength and effect of the CRVPs. Despite their excellent performance, shaped holes are very expensive to manufacture.

The trench configuration is similar to the shaped hole geometry in that it diffuses the flow. However, the shaped hole configuration diffuses using a lateral and streamwise diffusion while the trench configuration diffuses into a lateral trench before ejecting into the core flow. Trenches have been shown to decrease separation and increase lateral coolant spreading. Unlike the shaped holes, trenches are less expensive to manufacture. However, the study of Lu et al. [37] indicated that the shaped holes outperformed the trenches.

Finally, slot configurations create a 2-D sheet of coolant to maximize lateral

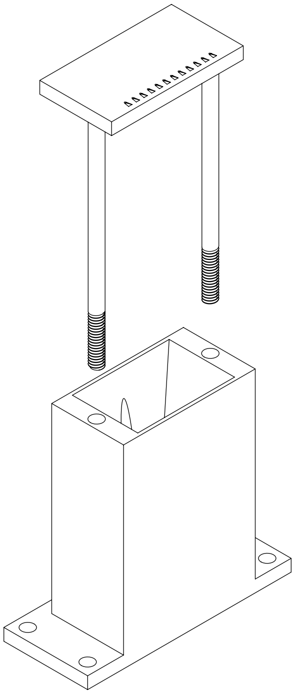

Figure 3.7: Cooling plenum and interchangeable film cooling plate

spreading, minimize jet separation, and eliminate the presence of CRVPs. These characteristics make slots the ideal film cooling geometry. However, they remove structural integrity from the turbine material such that they cannot be used in practical applications.

The drawings and full dimensions of these configurations are given in Figs. 3.8–3.14. To help visualize the cooling configurations, isometric views are also included in Figs. A.13–A.19. These figures show that all configurations featured a characteristic opening of $D = 0.51$mm with the holes angled at 30° off the test surface.

Both the single and five row configurations had a spanwise hole pitch spacing of $4D$. The five row configurations also feature a $4D$ streamwise pitch spacing. In the case of the five row cylindrical and trench configurations, the holes were offset in each row such that the centerline of the holes in the even rows was centered half way between two holes in the odd rows. The following section will discuss the technique for measuring heat transfer following the film cooling injection.

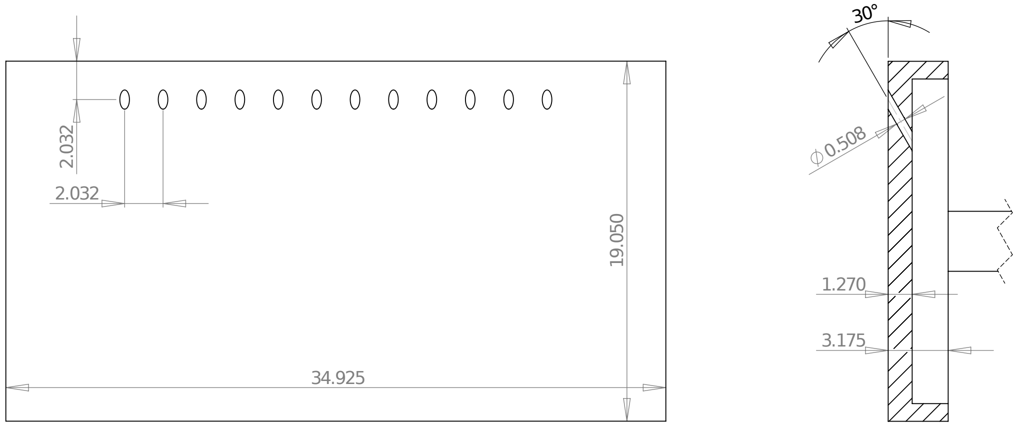

(a) Front view

(b) Cutaway side view

Figure 3.8: Drawing of one row of cylindrical hole test coupon; freestream flow from bottom to top; dimensions in mm

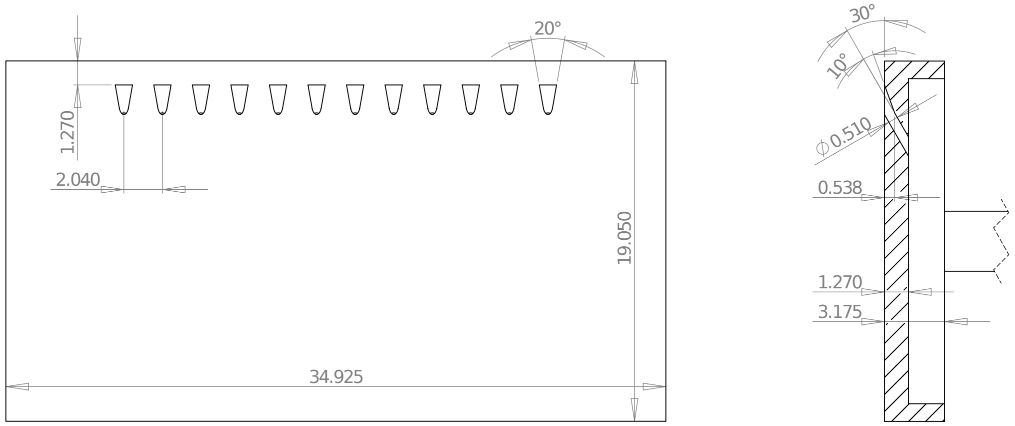

(a) Front view

(b) Cutaway side view

Figure 3.9: Drawing of one row of shaped hole test coupon; freestream flow from bottom to top; dimensions in mm

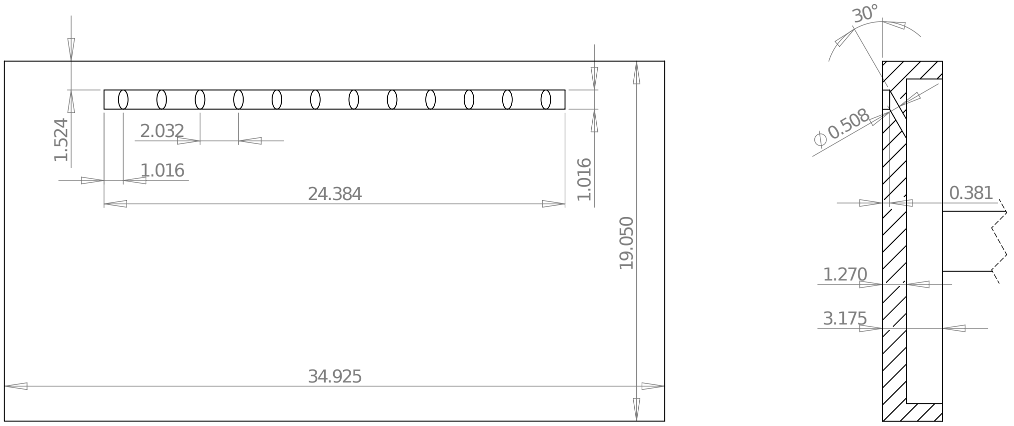

(a) Front view

(b) Cutaway side view

Figure 3.10: Drawing of one trench row test coupon; freestream flow from bottom to top; dimensions in mm

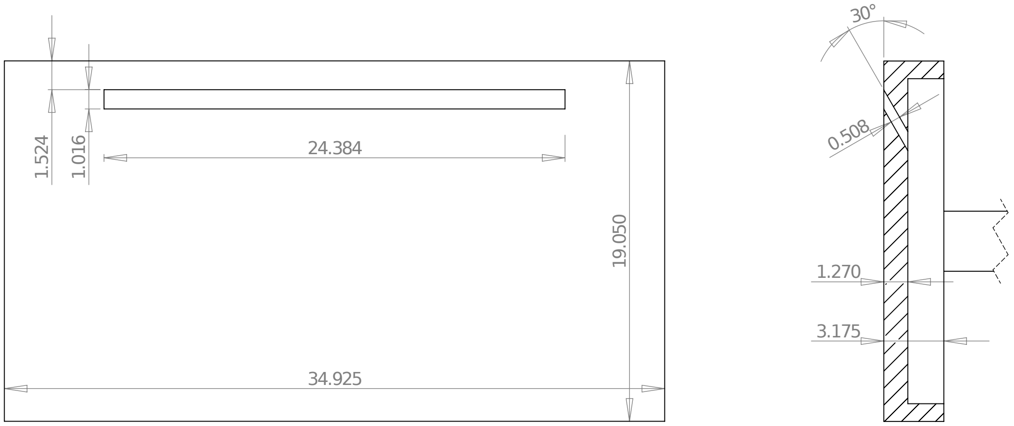

(a) Front view

(b) Cutaway side view

Figure 3.11: Drawing of one slot row test coupon; freestream flow from bottom to top; dimensions in mm

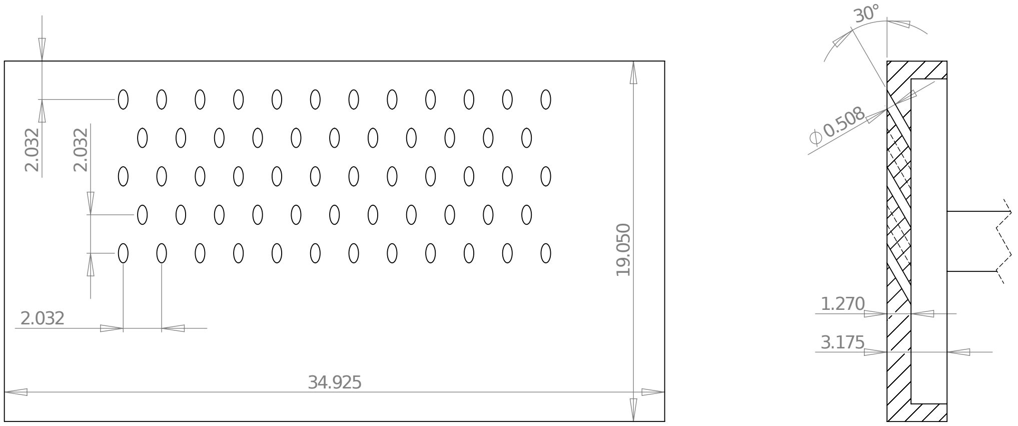

(a) Front view

(b) Cutaway side view

Figure 3.12: Drawing of five row of cylindrical hole test coupon; freestream flow from bottom to top; dimensions in mm

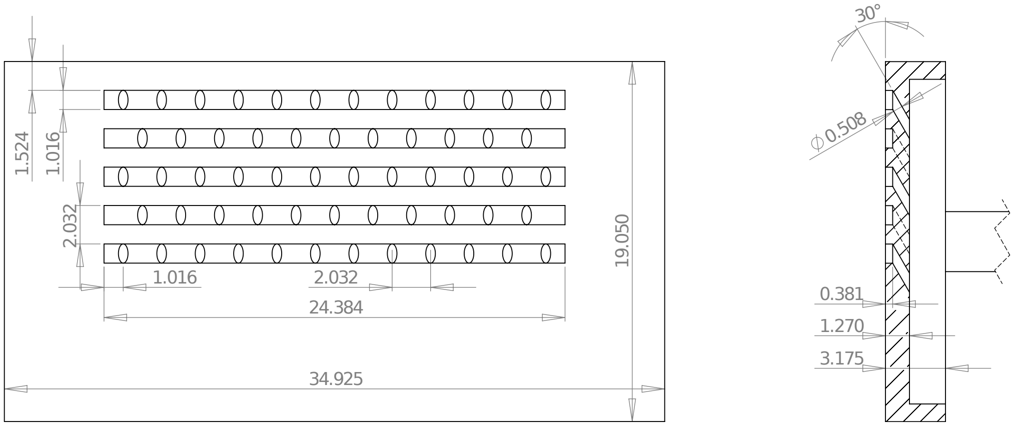

(a) Front view

(b) Cutaway side view

Figure 3.13: Drawing of five trench row test coupon; freestream flow from bottom to top; dimensions in mm

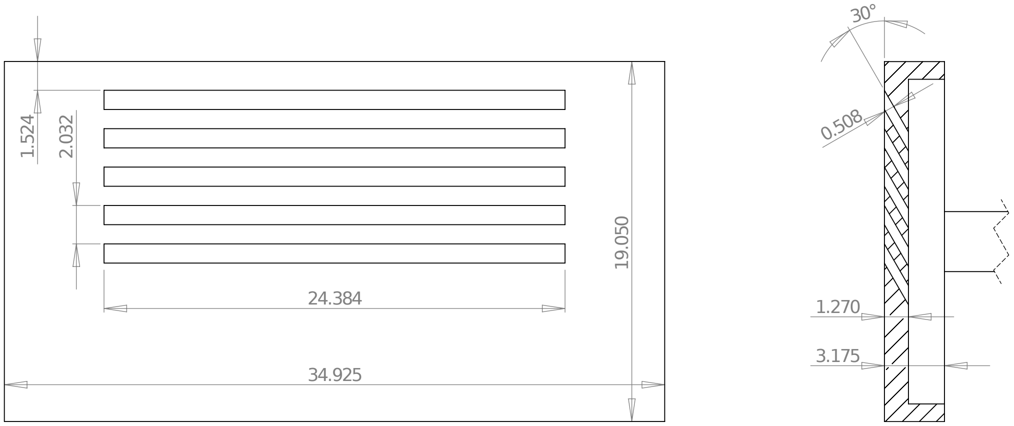

(a) Front view

(b) Cutaway side view

Figure 3.14: Drawing of five slot row test coupon; freestream flow from bottom to top; dimensions in mm

3.4.4 Instrumentation Block.

Figure 3.6 shows that downstream of the cooling plenum was an instrumentation block. This block enabled measuring the surface temperature (T_w) and conductive heat flux into the surface (q''_{cond}) at 16 spatial locations downstream of the film cooling injection site. The 16 locations were placed in four streamwise rows located at x/D locations of approximately 9, 16, 22, and 28 measured from the end of the most downstream row of film cooling holes. The full dimensions of the instrumentation block are given in Fig. 3.15 and the x/D and z/D measurement locations are summarized in Table A.2.

To drive heat transfer through the instrumentation block, cooling channels were applied to the back and side of the test rig seen in Fig. 3.6. These cooling channels served two purposes. First, they ensured that conduction near the surface of the instrumentation block in the wall normal direction (y) was the dominant component. This enabled the assumption of one-dimensional (1-D) heat conduction through the block. This assumption was subsequently verified by both the computational and experimental analyses found in Section A.5.1.

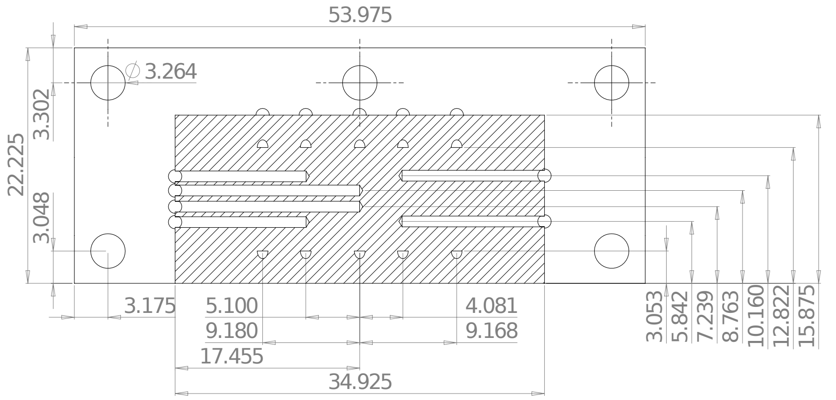

(a) Top view

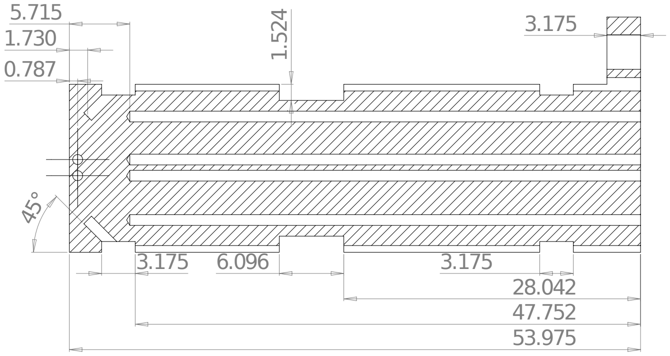

(b) Side view

Figure 3.15: Drawing of instrumentation block; freestream flow from bottom to top; dimensions in mm

Second,the cooling channels provided a method for varying T_w while keeping nearly constant freestream conditions in the test section. This was accomplished by changing the amount of backside cooling by varying flow rates of water and nitrogen in the cooling channels. In this way, surface temperatures on the range of $700\,\mathrm{K} < T_w < 1000\,\mathrm{K}$ were achieved.

The T_w and q''_{cond} into the block were calculated at each location via two thermocouples embedded at two known depths in the wall normal direction. These measurements were then used as boundary conditions to solve the non-linear differential equation governing the heat conduction given by

$$\frac{\mathrm{d}}{\mathrm{d}y}\left[k_b(T)\frac{\mathrm{d}T}{\mathrm{d}y}\right] = 0 \tag{3.1}$$

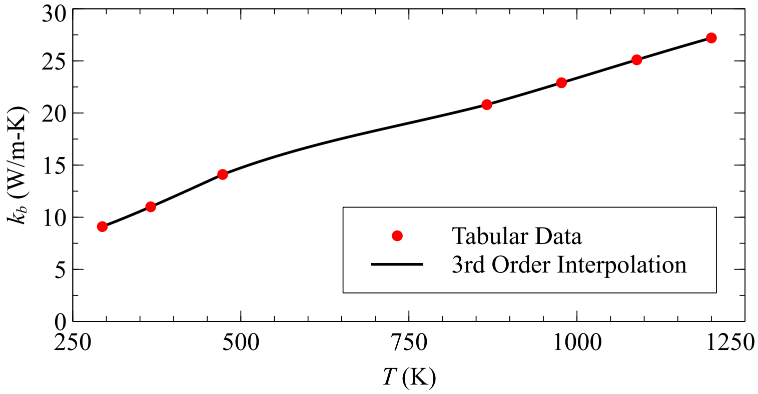

Figure 3.16: Interpolation of instrumentation block conductivity data reported by Haynes International [24]

where $k_b(T)$ is the conductivity of the instrumentation block as a function of temperature. Since the block was constructed of Hastelloy X [24], a continuous function of k_b with respect to temperature was developed by a third order interpolation of the conductivity data provided by the manufacturer [24]. A plot of this function along with the manufacturer's data are provided in Fig. 3.16.

The process to solve the non-linear differential equation given by Eq. 3.1, is derived in Section A.5.2, but was computationally expensive. Fortunately, the analysis of Section A.5.2 revealed that the differential equation could be linearized by assuming the material thermal conductivity was a constant value evaluated at the average of the embedded temperature measurements with a negligible loss in accuracy. This linearized form allowed approximation of T_w by a linear extrapolation of the measurements, such that

$$T_w = -\frac{T_2 - T_1}{y_2 - y_1}(y_1) + T_1 \tag{3.2}$$

where T_1 and T_2 are measured at known depths y_1 and y_2. Additionally, q''_{cond} can be approximated by

$$q''_{\text{cond}} = -k_b \frac{T_2 - T_1}{y_2 - y_1} \tag{3.3}$$

The following section will discuss the uncertainty in these and other measurements.

3.5 Uncertainty

The uncertainty in the experimental measurements were calculated by the method of Moffat [43]. The derivations and full details of the calculations are presented in Section A.6. Table 3.1 summarizes the experimental uncertainties calculated in Section A.6.

Table 3.1: Summary of the experimental uncertainties calculated in Section A.6

	Uncertainty (±)	
Description	**Low Temp**	**High Temp**
T_w (K)	1.4	0.58
T_∞ (K)	5.8	7.4
T_w/T_∞ (%)	0.42	0.41
q''_{cond}(%)	2.48	3.70
q''_{rad}(%)	2.02	8.07
$q''_{\text{rad},i}$ (%)	1.37	1.37
q''_{conv}(%)	2.98	3.98
h_{CP}(%)	10.5	10.5
h (%)	2.84	4.05
h/h_{CP} (%)	11.2	10.8
θ_w (-)	0.072	0.053
$\Delta q''_f$(-)	0.0176	0.0249
$\Delta q''_r$(-)	0.0176	0.0249
σ (-)	0.0176	0.0249
$\nabla q''_r$ (-)	0.0249	0.0352

Section A.6.4 found that the uncertainty in q''_{cond} was exceedingly high (up to 29.2%) due to the uncertainty in the temperature measurements and measured thermocouple depths. To reduce the uncertainty, the statistical correction procedure presented in Section A.6.5 was implemented. This procedure first assumed that the heat flux to the instrumentation block was uniform due to the small size of the block's hot side surface. Then, using the q''_{cond} measured at the 16 locations as a statistical sample, the average q''_{cond} was determined. Finally, the thermocouple depths were corrected to conform each location to the average q''_{cond}. After correction, the uncertainty in q''_{cond} were reduced to the values summarized in Table 3.1.

3.6 Core Flow Temperature Measurement

Some of the calculations in the present work hinged on knowledge of the core flow temperature, T_∞. To measure T_∞, the freestream was interrogated with an OMEGA® B-Type thermocouple at $x/D = 106$. This corresponded to $78D$ downstream of the last row of heat transfer measurements such that the thermocouple would not interfere with the film cooling measurements. However, the presence of a film cooling upstream of the T_∞ could have resulted in biased measurements. Since both film cooled and non-film cooled (i.e. $M = 0$) measurements were taken in parallel, T_∞ was measured only during the no cooling cases and averaged to give $\overline{T_\infty}$. Amongst the T_∞ measured during the no cooling cases, it was found that they varied only 18 K from $\overline{T_\infty}$ with a 95% confidence interval. This deviation was only 3% of the smallest driving temperature ($\overline{T_\infty} - T_w$) observed in testing. Thus, using $\overline{T_\infty}$ was deemed sufficient.

3.7 Emissions Measurements

Much of the present research examined the effect of a fuel rich core flow on film cooling performance. Thus, maintaining a consistent core flow composition was critical. To verify that the composition remained sufficiently constant through the testing campaign, emissions measurements were taken at the exit of the test channel as discussed in Section A.7. The measured emissions were also validated by the Chemical Equilibrium with Applications (CEA) [41] code. The core flow temperature, pressure, and combustion equivalence ratio (Φ) were input to the code to calculate the expected composition of the flow. Comparing the measurements to the calculations revealed an agreement within an absolute volumetric percentage difference of 0.2%

throughout the testing campaign.

3.8 Summary

The present work relied on both experiments and computations to satisfy the research objectives outlined in Section 1.4. This chapter gave an overview of the experimental facility used in the present work. It presented details on the mass flow controllers, the well stirred reactor used to create the hot core flow, and the test channel. In addition, the chapter gave an overview of the measurement techniques and uncertainties. A more detailed description of the facility along with supporting analyses is included in Appendix A. The following chapter will describe the method by which the computational component of the present work was accomplished.

IV. Computational Method

Objectives 1 and 2 of the present work are concerned with developing methodologies for use in a high temperature convective environment without and with film cooling, respectively. Experiments are an essential component to developing theory and validating models. However, experiments at combustion temperatures present many challenges. First, high temperature facilities can be expensive to construct and operate. Second, the high temperature environment limits the diagnostic techniques and instrumentation available to the experimentalist. Also, high temperature environments can have a significant contribution of radiative heat transfer which can obscure measurements of convective heat transfer.

Unlike experiments, Computational Fluid Dynamics (CFD) simulations provide a venue for specifying desired conditions to study individual phenomena. However, CFD relies on experimentally validated models to ensure the simulations accurately capture real-world physics. Despite its dependence on experimental validation, judicious application of CFD allows for a detailed study of flow features such as boundary layers. In addition, CFD permits detailed parametric studies to be accomplished relatively quickly and inexpensively.

For these reasons, the present work employed CFD to carry out parametric studies of convective heat transfer without and with film cooling in support of Objectives 1 and 2 of the present research, respectively. These studies will be presented in Chapters V and VI, respectively. Subsequently, each chapter will provide experimental validation using measurements in the facility described in Chapter III.

Each of the two computational studies utilized a different computational domain. The first study employed a 2-D, flat plate, zero-pressure-gradient domain to study the effect of variable properties within a boundary layer in support of Objective 1. The second study examined a flat plate with a single row of fan shaped film cooling holes to develop a methodology to scale film cooling performance in support of Objective 2. The remainder of this chapter will describe the technique used to solve the flow fields followed by the details of the two computational domains.

4.1 Solver Details

The simulations of the present work were computed using the FLUENT$^{\circledR}$ 14.5 [3] finite volume, pressure based, steady state solver. Pressure-velocity coupling was modeled by the Semi-Implicit Method for Pressure-Linked Equations (SIMPLE) algorithm [7]. A steady implicit Euler scheme was used for temporal discretization. A second-order upwind differencing scheme was used for all spatial discretization except pressure which used a second-order scheme.

As discussed in Section 2.8.1, creating a computational domain which resolves down to the smallest length scales of turbulence is extremely computationally expensive. Thus, most modern CFD simulations utilize significantly less fine domains and use Reynolds Averaged Navier-Stokes (RANS) models to imitate the effect of the smaller turbulent length scales on the flow solution.

The k-ω Shear Stress Transport (SST) RANS model was selected to model turbulence in the present work. This model was chosen based on the its superior ability to model the entire turbulent boundary layer from the wall through the wake region, as discussed by Blazek [7]. The k-ω SST's fidelity within the boundary layer will be essential to the study of variable properties within the boundary and film cooling layers in Chapters V and VI, respectively. The following two sections will discuss the computational domains utilized in Chapters V and VI, respectively.

4.2 2-D Flat Plate

Section 2.1.2 asserted that wall bounded flows with large freestream to wall temperature differences have large property variations within the boundary layer such that linear constant property theory no longer applies. Subsequently, two methods to account for variable property effects were presented: the reference method of Eckert [15] (Eqs. 2.20 and 2.21) and the temperature ratio method of Kays et al. [29] (Eqs. 2.24 and 2.25).

However, very little research has been done to validate these two methods in a low speed, turbulent boundary layer. As discussed in Section 2.1.2, the work of Eckert [15] was aimed at variable properties due to high speed flows and viscous heating. Alternatively, the method of Kays et al. [29] requires knowledge of the empirical exponents m and n. Kays et al. [29] proposed a value for both m and n, but these values were calculated using a finite difference code, mixing length turbulence modeling, and at a single temperature ratio of $T_w/T_\infty = 0.75$. However, there have been many advancements in CFD since the computations of Kays et al. [29].

Part of Objective 1 of the present research is to determine an appropriate method to account for variable properties within a boundary layer. Section 5.1 will address this aspect by comparing the methods of Eckert [15] and Kays et al. [29] to CFD results gathered using the modern computational modeling techniques described in Section 4.1. The next section will present the details of the computational domain employed in the study of Section 5.1.

4.2.1 Domain Details.

To demonstrate the ability of the reference and temperature ratio methods to nondimensionalize variable properties regardless of freestream temperature, three cases were examined with $T_\infty = 1600\,\mathrm{K}$, $1000\,\mathrm{K}$, and $300\,\mathrm{K}$. For each of these T_∞, several

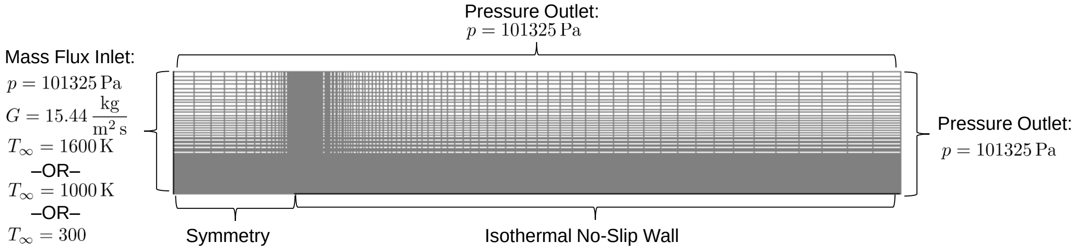

Figure 4.1: Grid and boundary conditions for 2-D flat plate computational domain

sub-cases were calculated with different isothermal wall temperatures (T_w/T_∞) to cover a large range of temperature ratios (T_w/T_∞) between zero and one. The shear stress and heat flux were then extracted at discrete Re_x for each case. These were then compared to reference and temperature ratio method predictions of τ_w and h to validate their ability to predict variable property effects.

To study variable property effects in the most basic wall bounded flow regime, a two-dimensional zero pressure gradient flat plate was simulated. The structured grid was assembled in POINTWISE® 17.1R2 [50] and the boundary conditions shown in Fig. 4.1 were applied. The isothermal no-slip wall was 1 m in length and was discretized with 400 nodes. The symmetry boundary condition upstream of the wall modeled a uniform flow encountering a sharp edge flat plate. It was 0.2 m in length and was resolved by 100 nodes. The mass flux inlet and the right pressure outlet face were each 0.2 m and were each discretized with 400 nodes.

To capture the turbulent boundary layer, the grid used an initial node spacing of $1 \times 10^{-6}\,\mathrm{m}$ off the wall and leading edge of the plate. The cell size then uses the POINTWISE® [50] tanh growth function to increase the cell size in both the wall normal and streamwise directions. This initial spacing and growth function resulted in a well resolved turbulent boundary layer as seen in Fig. 4.2. Only the $T_\infty = 300\,\mathrm{K}$ condition is shown in Fig. 4.2 as it was found to have the smallest and, thus, the least resolved viscous sublayer. The figure also displays that the grid resolves down

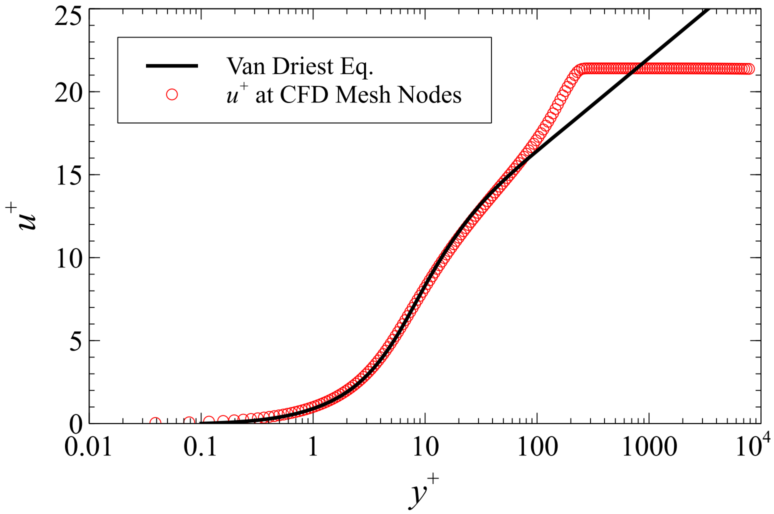

Figure 4.2: Resolution of the turbulent boundary layer in wall coordinates; $T_\infty = 300\,\mathbf{K}$, $T_w/T_\infty = 1$, $\mathbf{Re}_x = 250,000$

to distances from the surface in wall coordinates (see Section 2.1.1) below $y^+ = 0.1$. This resulted in a well resolved viscous sublayer.

To model the thermodynamic and transport properties of air, continuous functions of tabular data [29] were used. Specifically, the Ideal Gas Law was used to model density (ρ) and curve fits of tabular data [29] were used to model specific heat (c_p), thermal conductivity (k), viscosity (μ) [68]. The exact functions and coefficients used as well as plots comparing the property functions to the tabular data [29] are included in Appendix B.

4.2.2 Grid Convergence.

Three methods were used to verify grid convergence. First, the profiles of the coefficient of friction (c_f) and Nusselt number (Nu_x) along the surface of the flat plate were compared to empirical correlations given in Section 2.1.1 as seen in Fig. 4.3. Each of the three T_∞ cases were seen to produce the same c_f and Nu_x profiles with Re_x, thus Fig. 4.3 is presented without regard to T_∞.

Due to the initial laminar region seen in Fig. 4.3, the hydrodynamic and thermal

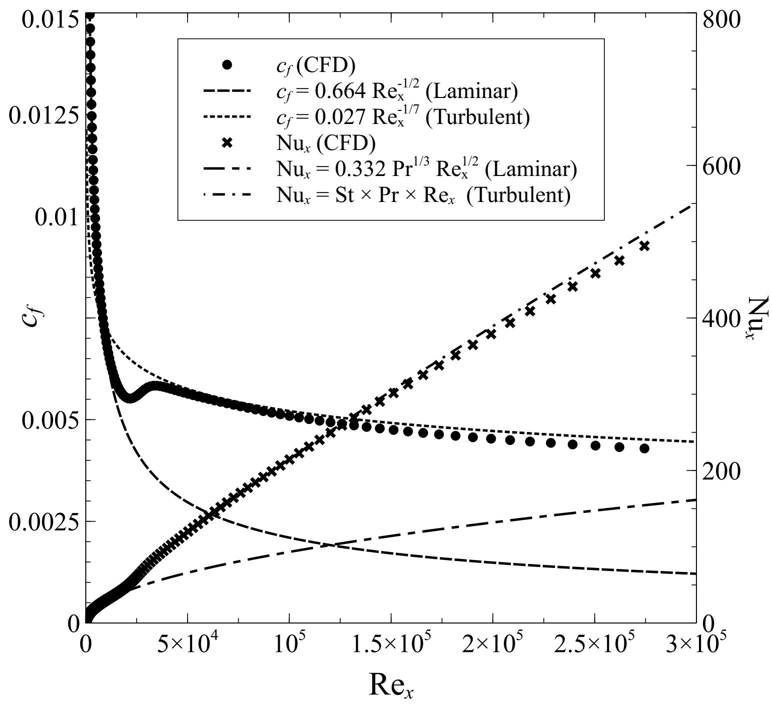

Figure 4.3: Comparison of c_f and Nu_x along a flat plate calculated via CFD to analytical correlations

boundary layers did not grow as fully turbulent layers from $x = 0$. This nuance will be discussed later in this section. As a result of the initial laminar region, Fig. 4.3 shows the CFD calculations under-predicting the turbulent c_f correlation by up to 5% and under-predicting the turbulent Nu_x correlation by up to 4%. Despite the small quantitative difference, the c_f and Nu_x CFD calculations are seen to follow the qualitative trends of the flat plate correlations. Thus, this reasonable agreement gave the first evidence of grid convergence and that turbulence was appropriately modeled.

The second grid convergence method compared the present grid to grids of higher and lower resolution to verify the solution was invariant with grid resolution. The grid refinement was implemented by doubling or halving the number of nodes on each face for the high and low resolution grids, respectively. Subsequently, the solution was calculated using the freestream conditions in Fig. 4.1. Two temperature ratios of $T_w/T_\infty = 1.0$ and 0.4 were considered. In doing so, six cases were calculated for each grid resolution. The cases were permutations of $T_\infty = 1600\,\mathrm{K}$, $1000\,\mathrm{K}$, and $300\,\mathrm{K}$ each with cases of $T_w/T_\infty = 1.0$ and 0.4. For each of the six cases, the shear stress and heat flux along the wall calculated using the three grid resolutions were compared. In all cases and at all locations along the flat pate, the heat flux and shear stress changed by less than 0.4% between the two grid resolutions. This small difference gave further evidence of sufficient grid convergence.

Finally, the velocity boundary layer was extracted at various Re_x for the $T_\infty = 1600\,\mathrm{K}$, $1000\,\mathrm{K}$, and $300\,\mathrm{K}$ freestream conditions with $T_w/T_\infty = 1.0$. Figure 4.4(a) compares boundary layers of the low, standard, and high resolution grids in wall coordinates. The invariability of the boundary layer with grid resolution gives further evidence of grid convergence. In addition, Fig. 4.4(b) shows that the velocity profile at a constant Re_x was identical for each $T_\infty = 1600\,\mathrm{K}$, $1000\,\mathrm{K}$, and $300\,\mathrm{K}$ case. Given the independence of the boundary layer on T_∞, Fig. 4.5 presents the development of the boundary layer with Re_x without regard to T_∞. This figure indicates that the boundary layer agrees with the constant property Van Driest mixing length theory till the wake region of the boundary layer discussed in Section 2.1.1.

The velocity profiles were seen to agree well with constant property turbulent boundary layer theory. Figure 4.5 compares the velocity profiles extracted from the CFD results to the Van Driest mixing length equation [29] for turbulent boundary layer from the viscous sublayer through the log-law region (see Section 2.1.1). The profiles were seen to adhere well to this curve up to the wake region which blends the turbulent boundary layer into the freestream condition. The wake region is visualized by the hooks in the data at large y^+ seen in Fig. 4.5.

Grid convergence was also examined at T_w/T_∞ of 0.1 and 0.2 at $\mathrm{Re}_x = 50,000$ and 250,000. However, The low temperature ratios and resulting variable properties of these cases resulted in boundary layers with different characteristics than those seen

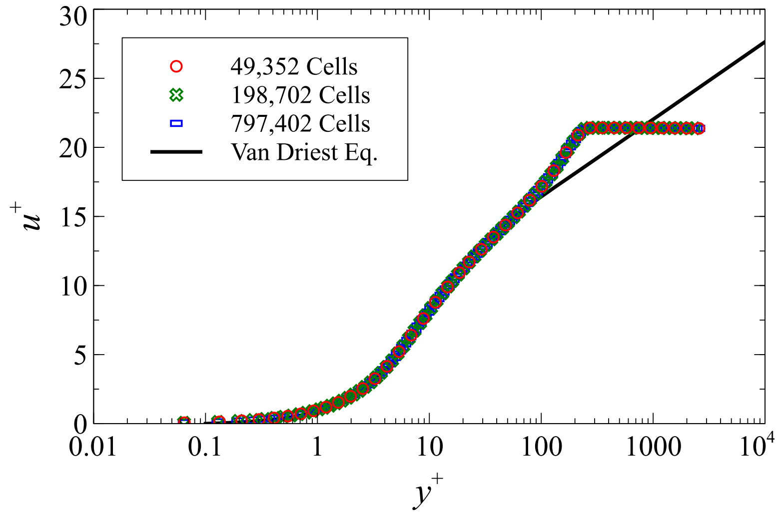

(a) Grid convergence of momentum boundary layer; $T_\infty = 1600\,\mathrm{K}$

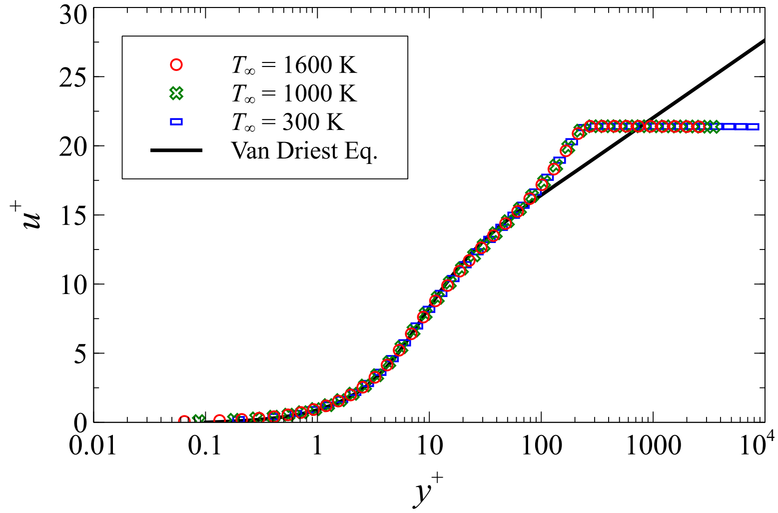

(b) Various T_∞, 198,702 cell grid

Figure 4.4: Agreement of momentum boundary layers of various cases; $T_w/T_\infty = 1.0$**,** $\mathbf{Re}_x = 250,000$

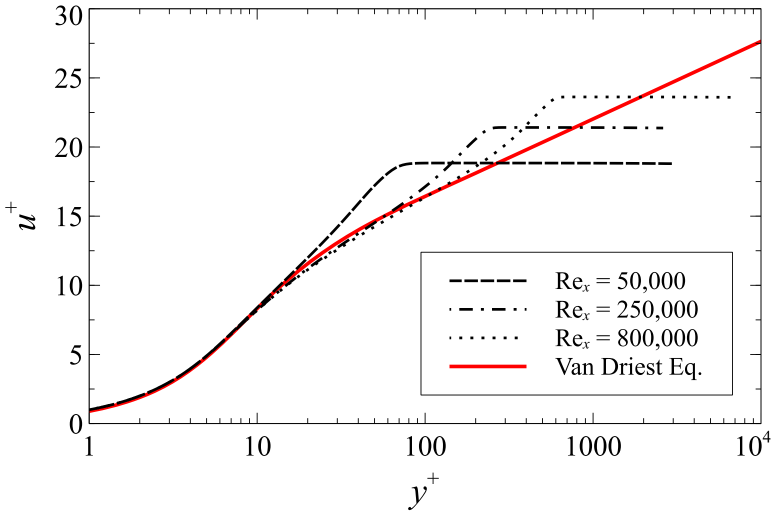

Figure 4.5: Streamwise development of the turbulent boundary layer calculated in CFD in wall coordinates

in the constant property boundary layers. Thus, discussion of the boundary layers with $T_w/T_\infty < 1$ are not presented in this section. Rather, they will be presented in Section 5.4 which specifically addresses how the boundary layer varies with T_w/T_∞. Though the results are not included in this section, it was seen that all three grid resolutions produced identical boundary layer profiles at all T_w/T_∞ for any of three T_∞ cases. Thus, the consistency of the boundary layers between T_∞ conditions and grid resolutions as well as the agreement with constant property turbulent boundary layer theory provided the final evidence of sufficient grid convergence.

4.2.3 Transition from Laminar to Turbulent.

Comparison of the CFD results and correlations in Section 4.2.2 revealed a region around $\text{Re}_x = 2.5 \times 10^4$ where the flow transitioned from laminar to fully turbulent. According to the FLUENT® documentation [3], the k-ω SST model includes a damping coefficient which limits the ω production in low-Reynolds number regions such as stagnation points. FLUENT® [3] calculates the production of ω by

$$P_\omega = \alpha \frac{\omega}{k} P_k \tag{4.1}$$

where α is a damping coefficient defined by

$$\alpha = \frac{1/9 + [\mu_t/\mu]/2.95}{1 + [\mu_t/\mu]/2.95} \tag{4.2}$$

In a Reynolds averaged sense, the effect of turbulence appears as an increase to the effective viscosity at a given location in the flow field. Thus, μ_t is a measure of this effective increase in viscosity calculated by [3]

$$\mu_t = \frac{\rho k}{\omega} \tag{4.3}$$

From Eq. 4.2 it is seen that, as μ_t/μ goes to infinity, α goes to one. Thus, the damping coefficient resulted in a laminar flow at the leading edge of the flat plate where μ_t/μ was small, a transitional flow as μ_t/μ grew and the effect of the damping coefficient faded, followed by fully turbulent flow when μ_t/μ was sufficiently large.

Rumsey and Spalart [55] documented the effect of inlet freestream turbulence intensity (Tu, Eq. 2.41) and viscosity ratio (μ_t/μ) on the transition region. They found that increasing either of these boundary conditions moved the transition location toward the leading edge of the plate. However, for reasonable inlet turbulence levels, the selection of Tu and μ_t/μ had a negligible effect on the fully turbulent results downstream.

They performed a similar study of how Tu and μ_t/μ affected the transition to turbulence. Several cases comparing different levels of Tu at constant μ_t/μ are plotted in Fig. 4.6. Congruent with the finding of Rumsey and Spalart [55], the difference

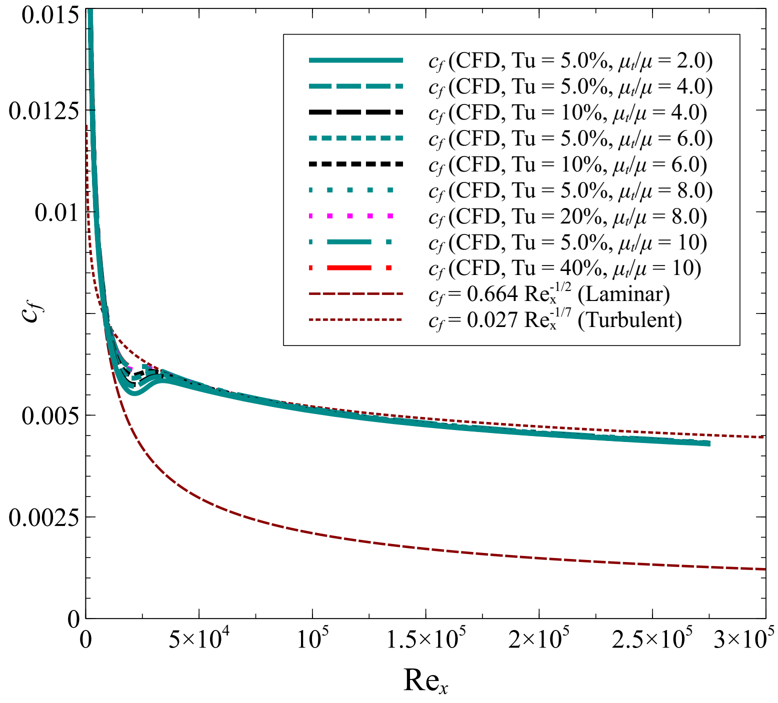

(a) Full range of Re$_x$and c_f

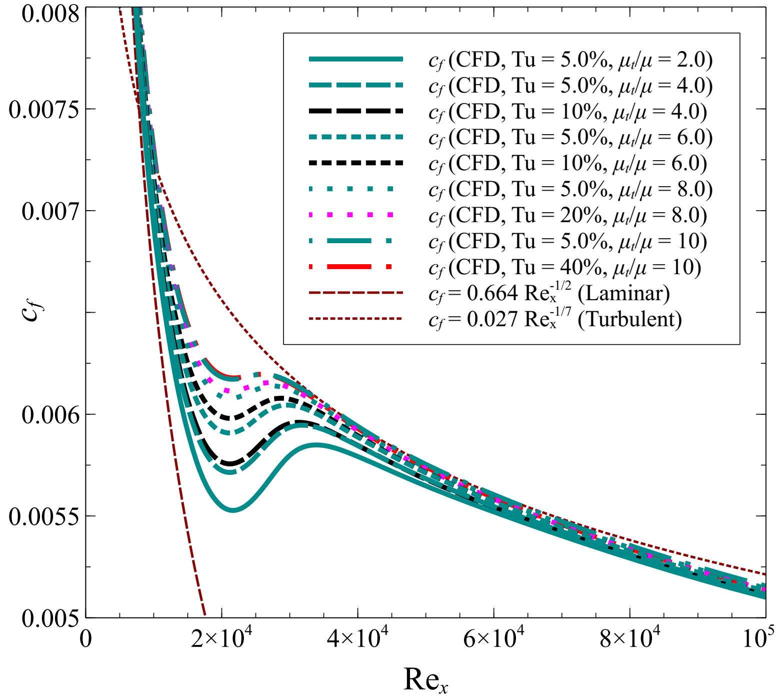

(b) Scale zoomed to transition region

Figure 4.6: Effect of viscosity ratio (μ_t/μ) and turbulence intensity (Tu) on coefficient of friction (c_f)

between these cases after the transition region was found to be negligible. It was seen that Tu had a small effect on the transition region compared to μ_t/μ. In fact, for $\mu_t/\mu = 10$, Tu was found to have a negligible effect on the transition region.

Since the inlet turbulence specifications of Tu and μ_t/μ were found to have a negligible effect on the results after the transition region, the lowest values examined in Fig. 4.6 were selected. Namely, values of $Tu = 5.0\%$ and $\mu_t/\mu = 2.0$ were chosen for the computational study. Overall, these turbulence specifications, the computational domain discussed in Section 4.2.1, and the boundary conditions displayed in Fig. 4.1 were utilized to gather the computational data in Chapter V in support of Objective 1 of the present research. The following section will discuss the method used to gather the computational data in Chapter VI.

4.3 Flat Plate with Shaped Hole Film Cooling

Due to the high cost and difficulty of studying film cooling at engine conditions, film cooling experiments are often performed at near ambient conditions. However, little research has been done on scaling film cooling performance measured in a laboratory to an engine condition. Objective 2 of the present research addresses this knowledge gap. To develop an understanding of the physics which govern scaling of film cooling performance, Section 6.1 examines film cooling computationally. This allowed for studying the effect of various parameters on scaling film cooling performance in the absence of experimental difficulties and confounding factors like radiative heat transfer. Next, Section 6.2 applies the understanding gained computationally to an experimental study of film cooling at combustion temperatures. The present section discusses the computational method applied in Section 6.1 to study scaling of film cooling performance.

4.3.1 Domain Details.

As discussed in Section 2.7.3, Lin et al. [36] studied film cooling from normal cylindrical, co-flow cylindrical, and shaped hole geometries. Their study focused on modeling the experimental measurements of non-reacting and reacting film cooling of Polanka et al. [51]. These experimental measurements were taken using the test rig developed by Evans [18].

The work of Lin et al. [36] examined normal cylindrical holes, angled co-flow cylindrical holes, and shaped holes. Since shaped holes are a common film cooling geometry, the previously used and validated shaped hole grid of Lin et al. [36] was selected for the computational examination of film cooling to satisfy Objective 2 of the present research.

The selected computational domain is shown in Fig. 4.7 along with the boundary conditions. Figure 4.8 shows the inlet and outlet geometry of the shaped hole configuration. The experiments of Polanka et al. [51] incorporated a single row of ten shaped holes. However, the corresponding computational model of Lin et al. [36] only included a single shaped hole. Then, symmetry boundary conditions were applied to the faces on the left and the right of the hole as seen in Fig. 4.7. The symmetry boundary conditions established spanwise periodicity such that an infinite row of shaped holes was modeled with a spanwise pitch of $z/D = 7.5$.

Following the measurements of Polanka et al. [51], Lin et al. [36] applied freestream and coolant inlet conditions of $T_\infty = 1829\,\mathrm{K}$, $u_\infty = 49.4\,\mathrm{m/s}$, $\mathrm{Tu}_\infty = 10\%$, $T_c = 625\,\mathrm{K}$, $u_c = 16.0\,\mathrm{m/s}$, and $\mathrm{Tu}_c = 1\%$ for a blowing ratio of $M = 0.946$. In addition, they applied two corrections to the turbulence model provided by FLUENT® [3]: the low-Reynolds number correction and the compressibility correction. To verify that these boundary conditions and turbulence models produced physically reasonable results, they were compared to flat plate correlations for c_f.

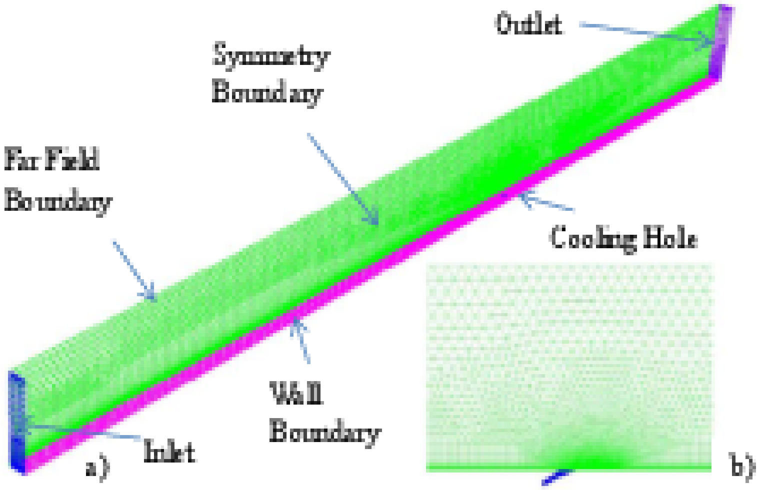

Figure 4.7: a) Computational Domain with boundary conditions [36] b) Resolution of grid near the cooling hole [36]

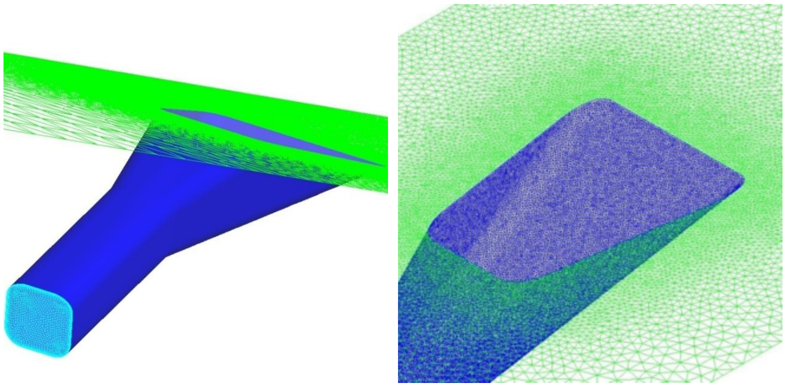

(a) Grid for the cooling hole inlet (b) Grid for the cooling hole outlet

Figure 4.8: Grid for shaped coolant hole [36]

First, the boundary conditions were changed slightly such that $M = 0$ and $u_c = 0$. This produced the results in Fig. 4.9(a) labeled as "CFD w/ turbulence corrections, $u_\infty = 49\,\mathrm{m}/s$". Here it is seen that c_f diverges significantly from constant property flat plate theory for $\mathrm{Re}_x > 1 \times 10^4$. A disturbance in the c_f data is also observed around $\mathrm{Re}_x = 2.5 \times 10^4$ where the film cooling hole is located.

Next, the boundary layer just upstream of the cooling hole at $x/D = -15$ was examined and is plotted in Fig. 4.9(b). This figure shows that for $y^+ < 10$, the data conforms to the analytical Van Driest mixing length theory curve. However, for $y^+ > 10$, the data are seen to fall below the theoretical curve. Referring to the discussion of turbulent boundary layers given in Section 2.1.1, it is expected that the data will conform to the Van Driest mixing length curve from the wall ($y^+ = 0$) until the wake region where the data should form a hook which overshoots the Van Driest mixing length curve. Thus, it was observed that using the turbulence model corrections creates a boundary layer which does not reflect turbulent boundary layer theory.

To correct this deviation from theory, the turbulence corrections were removed from the simulation while keeping the same freestream boundary conditions. This resulted in the curve in Fig. 4.9(a) labeled "CFD w/o turbulence corrections, $u_\infty = 49\,\mathrm{m/s}$". Here it is seen that the CFD results agree well with the turbulent flat plate correlation. Again, a slight deviation from the turbulent correlation was observed at $\mathrm{Re}_x = 2.5 \times 10^4$ corresponding to the film cooling hole.

Examining the boundary layer at $x/D = -15$ in Fig. 4.9(b) for these settings reveals that the data begins to deviate from the Van Driest mixing length curve around $y^+ = 10$. This is a y^+ which is so low that the log law region indicative of a fully turbulent boundary layer was absent completely. Moreover, these conditions produced $\mathrm{Re}_x = 24,000$ at $x/D = -15$. It was seen in Fig. 4.3 that, at this Re_x,

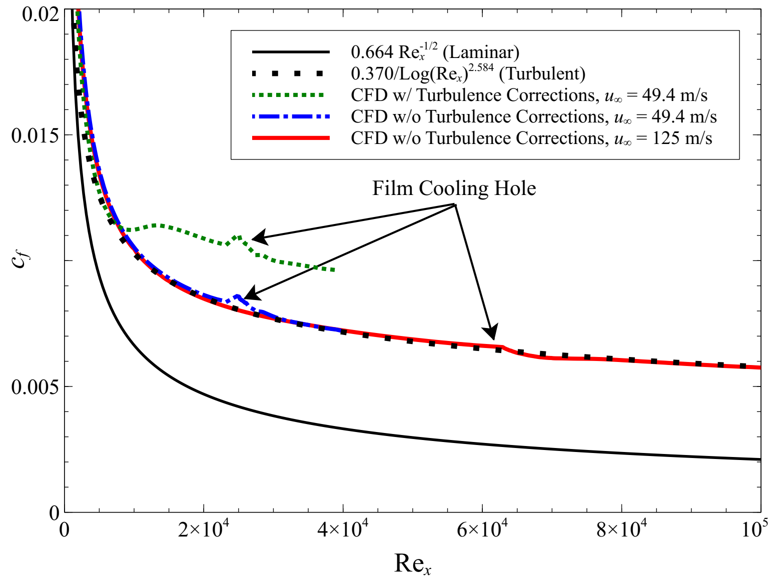

(a) Development of c_f with Re$_x$

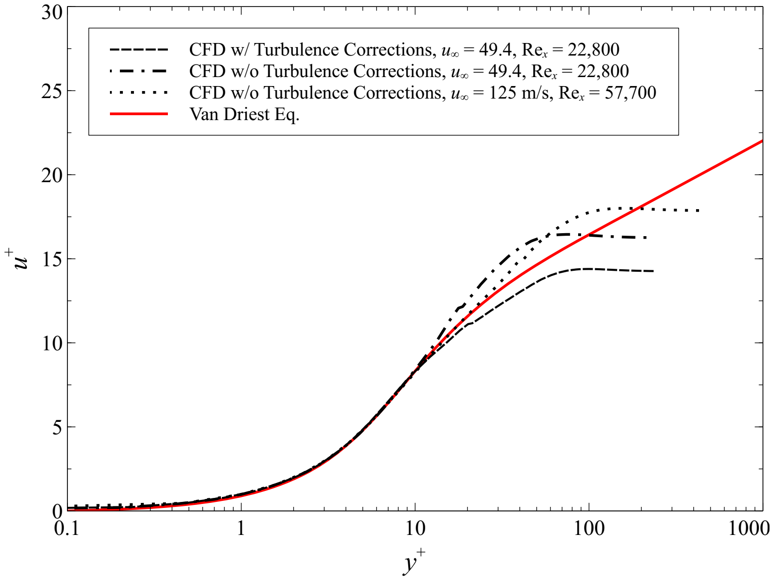

(b) Boundary layer at $x/D = -15$ in wall coordinates

Figure 4.9: Comparison of turbulence model corrections and freestream velocities

the k-ω SST turbulence model predicted flow transition from laminar to turbulent. Thus, it was determined that the Reynolds number must be increased to induce a fully turbulent boundary layer upstream of the cooling hole.

To create a fully turbulent boundary layer, the present work used different boundary conditions than Lin et al. [36]. Namely, the nominal freestream boundary conditions were changed to $T_\infty = 1829\,\mathrm{K}$, $u_\infty = 125\,\mathrm{m/s}$, and $\mathrm{Tu}_\infty = 10\%$. These conditions resulted in $\mathrm{Re}_x = 60,700$ at $x/D = -15$ and $\mathrm{Ma} = 0.151$. Thus, the increased u_∞ increased Re_x to a value which was found to be fully turbulent on the 2-D flat plate grid, as seen in Fig. 4.3. In addition, the increase in u_∞ was small enough to maintain a Ma in the incompressible regime. Similarly, for cases with film cooling, the nominal coolant conditions were $T_c = 625\,\mathrm{K}$, $u_c = 42.8\,\mathrm{m/s}$, and $\mathrm{Tu}_c = 1\%$ resulting in blowing ratio of $M = 1.00$.

Similar to above, a case was examined using these freestream conditions but with $M = 0$ such that $u_c = 0$. The development of c_f with Re_x is seen in Fig. 4.9(a) to agree with the flat plate correlation. Moreover, the boundary layer in Fig. 4.9(b) is seen to conform to the Van Driest mixing length theory up to a y^+ of approximately 30 where it transitions to the wake region.

When modeling turbulent boundary layers using the k-ω SST model, it is necessary to resolve the boundary layer through the viscous sublayer down to a y^+ on the order of one. Since Lin et al. [36] designed this grid for a freestream velocity less than half the selected velocity of $u_\infty = 125\mathrm{m/s}$, it was essential to examine the resolution of the boundary layer. Figure 4.10 displays that the boundary layer is sufficiently resolved including including the viscous sublayer which is resolved to $y^+ < 1$.

Though the Mach number of the Lin et al. [36] model was low ($\mathrm{Ma} = 0.086$), viscous terms were included in the energy equation for fidelity. Similarly, the Mach number of the present work was low ($\mathrm{Ma} = 0.15$). However, the present model did

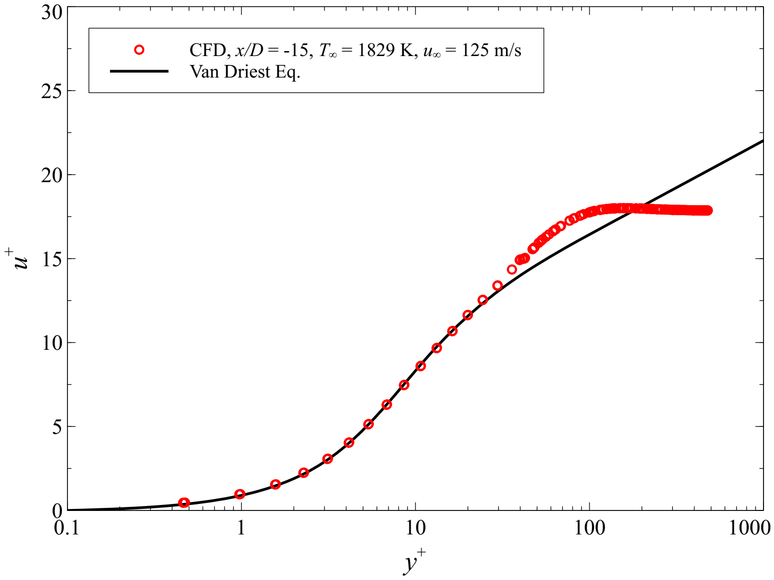

Figure 4.10: Resolution of the turbulent boundary layer in wall coordinates at $x/D = -15$ upstream of shaped hole

not include viscous terms in the energy equation. Since the Mach number was low, the effect of viscous heating was inconsequential with Brinkman numbers given by

$$\mathrm{Br} = \frac{\mu u_\infty^2}{k(T_\infty - T_w)} \tag{4.4}$$

below 0.02 for most cases. Even so, as T_w approached T_∞, by definition the Brinkman number increases to infinity such that viscous heating plays a significant role. As a result, including viscous terms in the energy equation causes the wall not to be adiabatic when $T_w = T_\infty$. However, the calculation of h as well as implementation of the temperature ratio method of Kays et al. [29] require precise knowledge of T_{aw}. Thus, viscous terms were not included in the present work such that $T_{\text{aw}} = T_\infty$.

Similar to the computational method described in Section 4.2.1, most of the film cooling cases used the real properties of air defined by the functions given in Appendix B. However, some cases used fictitious fluid properties to create desired flow scenarios. The details of the simulations which used modified properties will be presented in

Section 6.1.1.

4.3.2 Grid Convergence.

Analogous to the 2-D flat plate discussed in Section 4.2.2, grid convergence was shown by three methods. First, the c_f and Nu_x profiles along the centerline of the domain were compared to empirical flat plate correlations as seen in Fig. 4.11 for the nominal freestream conditions discussed above. As with Fig. 4.9, a disturbance in the data was observed around $\mathrm{Re}_x = 65,000$ due to the presence of the of the film cooling hole. However, before this disturbance, Fig. 4.11 shows good agreement between the c_f and Nu_x data and turbulent flat plate correlations. This agreement with experimental correlations gives evidence of grid convergence.

Second, grids of higher and lower resolution were developed to give further evidence of grid convergence. The present domain was meshed with 10.4 million cells. The higher and lower resolution grids were meshed with 20.5 and 6.7 million cells, respectively.

The computational studies of Sections 6.1.1 and 6.1.2 will examine the scalability of adiabatic effectiveness (η) and net heat flux reduction ($\Delta q_f''$) from temperatures near ambient to engine temperatures. Thus, the grid convergence study calculated spatially averaged $\overline{\overline{\eta}}$ and $\overline{\overline{\Delta q_f''}}$ for each grid resolution at a high and low temperature to display grid independence. These spatial averages of these parameters were taken from $-12 < x/D < 43$ and across the domain's span.

The high temperature condition utilized the boundary conditions outlined above. The low temperature condition featured $T_\infty = 292\,\mathrm{K}$ and $T_c = 100\,\mathrm{K}$ while u_∞ and u_c were adjusted to match the Reynolds number of the coolant and maintain $M = 1.00$. The exact details of both the high temperature and low temperature cases are presented in Table 6.2 under the headings of Baseline and Case 8, respectively. To

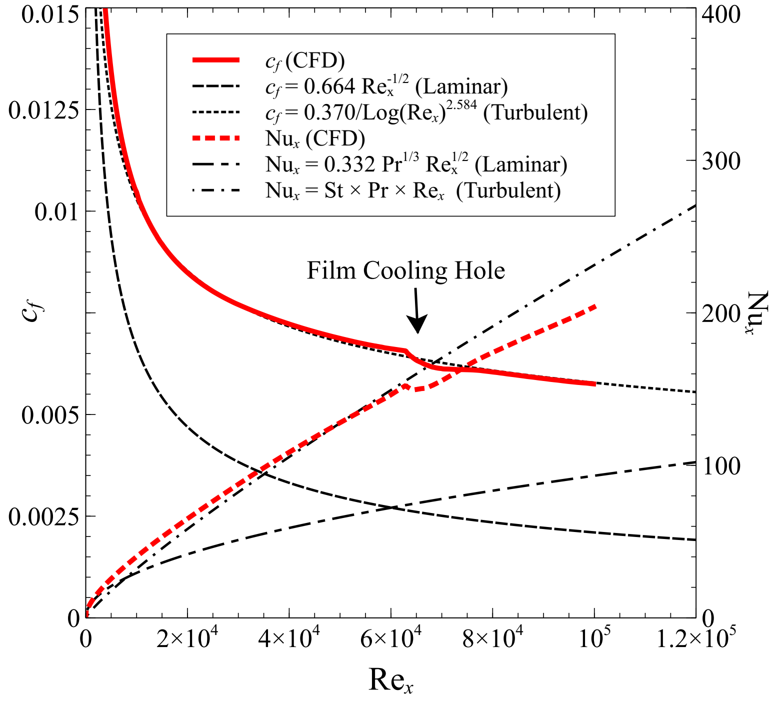

Figure 4.11: Comparison of c_f and Nu_x along centerline of shaped hole grid calculated via CFD to analytical correlations

calculate $\overline{\overline{\eta}}$, the wall was set to an adiabatic boundary condition. Then, the resulting spatially averaged $\overline{\overline{T_w}} = \overline{\overline{T_{\mathrm{aw}}}}$ was non-dimensionalized to $\overline{\overline{\eta}}$ by Eq. 2.30.

To calculate $\overline{\overline{\Delta q''_f}}$, the wall was set to a non-dimensional wall temperature of $\theta_w = 0.4$ where θ_w is defined by Eq. 2.34. Then, the spatially averaged heat flux for cases with $M = 1$ and $M = 0$ ($\overline{\overline{q''_f}}$ and $\overline{\overline{q''_0}}$, respectively) were calculated. Finally, $\overline{\overline{\Delta q''_f}}$ was calculated by comparing these heat fluxes via Eq. 2.32.

The results of this process are given in Table 4.1. Significant differences were seen between the 6.7 and 10.4 million cell grids. However, the 10.4 and 20.5 million cell grids were found to be in good agreement. Specifically, the $\overline{\overline{\eta}}$ and $\overline{\overline{\Delta q''_f}}$ results were seen to agree to within 0.006 for all cases. This indicated that the 10.4 million cell grid was sufficiently converged to produce grid independent results.

Last, the boundary layer profile was examined $15D$ upstream of the cooling hole and compared to turbulent boundary layer theory. This was previously presented

Table 4.1: Grid convergence results for single row of shaped holes grid

Number of Cells	6.7×10^6	10.4×10^6	20.5×10^6
$\overline{\overline{\eta}}$: High Temperature	0.171	0.094	0.088
$\overline{\overline{\eta}}$: Low Temperature	0.172	0.091	0.097
$\overline{\overline{\Delta q''_f}}$: High Temperature	0.326	0.212	0.218
$\overline{\overline{\Delta q''_f}}$: Low Temperature	0.337	0.227	0.231

in Fig. 4.9(b) while determining the appropriate turbulence model corrections and freestream conditions. In this figure, it was seen that the present 10.4 million cell grid and freestream conditions conformed to the expected boundary layer profile. Thus, this in conjunction with the agreement with flat plate c_f and Nu_x correlations along with the grid independent solution provided sufficient evidence of grid convergence.

4.4 Summary

This chapter presented the computational methods that will be used in Chapters V and VI in support of Objectives 1 and 2 of the present research. The details of the domain geometries and boundary conditions were presented. Subsequently, each computational domain was examined to show sufficient grid convergence. The following two chapters will utilize the computational domains presented in this chapter to develop theory that will be applied in experiments of each respective chapter.

V. Scaling Convective Heat Transfer: Without Film Cooling

Flow environments with high freestream temperatures and much lower surface temperatures are central to the operation of a gas turbine engine hot section. Classical literature approaches the aerodynamics and heat transfer of a moving fluid by assuming the flow has constant thermodynamic and transport properties. The assumption of constant properties becomes invalid in environments such as a turbine due to large temperature and, thus, property variations within the boundary layer. Accordingly, classical constant property methods break down in the hot turbine environment.

In addition to variable property convective heat transfer, hot environments like a turbine can also have significant radiative heat transfer. This is especially true on the leading edge of the first stage turbine vane which has a direct view of the combustor. However, radiative heat transfer can be exceedingly difficult to calculate analytically in practical environments like a combustor or a turbine. It can be equally as difficult to create an experimental facility which matches the radiative heat transfer of end item hardware. As such, radiation measured in an experiment typically cannot be scaled to end item hardware, unlike convective heat transfer. Thus, it is critical to quantify the radiative component of the total heat transfer in an experiment such that the convective component can be property measured and scaled to end item hardware.

Variable property convective heat transfer is not a well understood phenomena. Accordingly, total heat transfer of variable property flows in an environment with a significant radiative heat transfer component has not been addressed in the literature. Addressing this gap is the crux of Objective 1 of the present research which is restated here: Develop a method to measure the convective and radiative heat transfer components in a high temperature environment with large freestream to wall temperature differences.

To satisfy Objective 1 of the present research, this chapter will first present computational data to develop an understanding of variable property effects in the absence of radiation. This data will then be used to validate two existing analytical variable property methods. Second, this chapter will apply these two analytical methods to quantify the effect of variable properties on conventional constant property methods.

Next, this chapter will present experimental measurements in an environment with variable property convective heat transfer coupled with radiative heat transfer. The variable property method of Kays et al. [29], which was validated computationally in Section 5.1.2, will be utilized to propose a method to individually quantify the convective and radiative components of the total heat transfer. This method will be used to satisfy Objective 1.

To gain a better understanding of variable property effects, the computational data presented at the beginning of this chapter will be used to visualize how the boundary layer changes due to variable properties. The knowledge gained in this examination will then be used to propose a new method to account for variable property effects. Finally, the new method will be compared to an existing model validated at the beginning of this chapter to determine which is more appropriate for use in the present work.

5.1 Validation of Existing Variable Property Methods

Section 4.2 discussed in detail the computational model implemented to analyze variable property effects. In summary, the present analysis employed a 2-D flat plate zero-pressure-gradient grid with forced convection across the surface to create a fully turbulent boundary layer. Three inlet freestream temperatures of $T_\infty = 1600\,\mathrm{K}$, $1000\,\mathrm{K}$, and $300\,\mathrm{K}$ were examined to display how variable property affects a variety of flow conditions. Then, for each T_∞, multiple cases were computed by setting isothermal temperature on the flat plate surface (T_w) such that a range of temperature ratios (T_w/T_∞) could be examined.

This section will first compare the computational data to the reference method of Eckert [15] to verify that the results are consistent with an existing variable property method. Next, the computational data will be examined in the context of the temperature ratio method of Kays et al. [29]. From this examination, recommendations for the empirical coefficients necessitated by the temperature ratio method of Kays et al. [29] will be presented.

5.1.1 Comparison with the Method of Eckert.

As discussed in Section 2.1.2, Eckert [15] proposed accounting for variable property effects by evaluating the properties in correlations for wall shear (τ_w) and the convective heat transfer coefficient (h) at a reference temperature. His method was developed for high speed flows and proposed evaluating the reference temperature (T_R) by Eq. 2.20. However, for low speed flows Eq. 2.20 can be simplified to the average of T_∞ and T_w as seen in Eq. 2.22. Alternatively, for flows with large variations in c_p, he suggested evaluating properties at a reference enthalpy. For low speed flows, the formula for the reference enthalpy (i_R) simplifies to the average of the enthalpies evaluated in the freestream (i_∞) and at the wall (i_w) as seen in Eq. 2.23. Eckert [15] demonstrated that his method could accurately account for variable properties due to viscous heating in a turbulent boundary layer with a supersonic freestream. However, he had no data to validate his model against variable properties caused by large freestream to wall temperature differences in a low Mach number boundary layer.

The present study was primarily interested in developing theory for the high temperature, low speed, flat plate experiments that will be presented later in this chapter as well as in Chapters VI and VII. Therefore, only cases where $T_w < T_\infty$ and Ma $<< 1.0$ were considered in the present computational study. Unlike the high speed environment where the reference method of Eckert [15] is well validated, variable properties are a result of a large $T_\infty - T_w$ rather than viscous heating within the boundary layer. Thus, both the high speed flows studied by Eckert [15] and the low speed flows considered in the present work share the characteristic of a significantly hotter flow adjacent to a colder surface. This similarity provides evidence that the low speed form of the reference method of Eckert [15] can be applied to low speed flows with large $T_\infty - T_w$, despite the lack of experimental validation.

Three freestream conditions were selected for study to compare the reference method of Eckert [15] and the CFD model over a large range of freestream conditions. The selected conditions are given in Table 5.1. For each freestream condition, several CFD solutions were computed. Each case was computed with a different T_w boundary condition while all other boundary conditions were held constant. In doing so, the CFD results produced predictions for how τ_w and h changed with temperature ratio (T_w/T_∞) to reflect the temperature ratio method of Kays et al. [29]. Similarly, τ_w and h were calculated via both the reference temperature and reference enthalpy methods of Eckert [15] over the range $0 < T_w < T_\infty$ and compared to the CFD results.

Table 5.1: Freestream conditions of computational cases

Case	$G_\infty \left(\frac{\text{kg}}{\text{m}^2\,\text{s}}\right)$	T_∞ (K)	$u_\infty \left(\frac{\text{m}}{\text{s}}\right)$	Ma
1	15.44	1600	70.0	0.090
2	15.44	1000	43.8	0.071
3	15.44	300	13.1	0.038

As seen in Fig. 4.3, the constant property CFD results did not perfectly match the constant property, zero-pressure-gradient flat plate correlations for c_f and Nu_x. Thus, since the reference method of Eckert [15] utilizes the flat plate correlations to calculate τ_w and h, comparing the τ_w and h computed via CFD directly to that calculated by the reference method produced a bias in the comparison. To remove this bias, τ_w and h were non-dimensionalized by a ratio with their constant property values of $\tau_{w,\mathrm{CP}}$ and h_{CP}.

These constant property values are the τ_w and h that would be measured when $T_w = T_\infty$ such that $\tau_w/\tau_{w,\mathrm{CP}} = h/h_{\mathrm{CP}} = 1$ when $T_w/T_\infty = 1$. However, since $h = q''/(T_\infty - T_w)$, it can only be measured when $T_w \neq T_\infty$. Thus, to quantify h_{CP}, values of h were calculated at $T_w/T_\infty = 0.9$ and 0.8 and linearly extrapolated to $T_w/T_\infty = 1$.

The results of the above process are presented in Figs. 5.1 and 5.2. Examining these figures reveals that the reference temperature and reference enthalpy methods of Eckert [15] tend to diverge from each other as T_w/T_∞ decreases for each T_∞ case. The divergence is small for the $T_\infty = 300\,\mathrm{K}$ case but grows significantly as T_∞ increases to the $1000\,\mathrm{K}$ and $1600\,\mathrm{K}$ cases.

This effect is expected due to the difference in the methods' definitions. By using the definition of enthalpy, the low speed reference enthalpy given by Eq. 2.23 can be expanded to

$$i_R = \int_{T_{\mathrm{ref}}}^{T_R} c_p(T)\mathrm{d}T + i_{\mathrm{ref}} = 0.5\left(\int_{T_{\mathrm{ref}}}^{T_\infty} c_p(T)\mathrm{d}T + \int_{T_{\mathrm{ref}}}^{T_w} c_p(T)\mathrm{d}T\right) + i_{\mathrm{ref}} \tag{5.1}$$

where i_{ref} is the enthalpy at T_{ref}. For T_w near T_∞, c_p will be relatively constant between T_w and T_∞. Thus, for T_w near T_∞, Eq. 5.1 can be solved for T_R and reduced back to the reference temperature method's equation for T_R. However, for T_w much lower than T_∞, c_p can not be assumed to be constant between T_w and T_∞ resulting in the divergence between the reference temperature and enthalpy methods seen in Figs. 5.1 and 5.2.

Figure 5.1 displays that the CFD prediction of $\tau_w/\tau_{w,\mathrm{CP}}$ agrees similarly well with

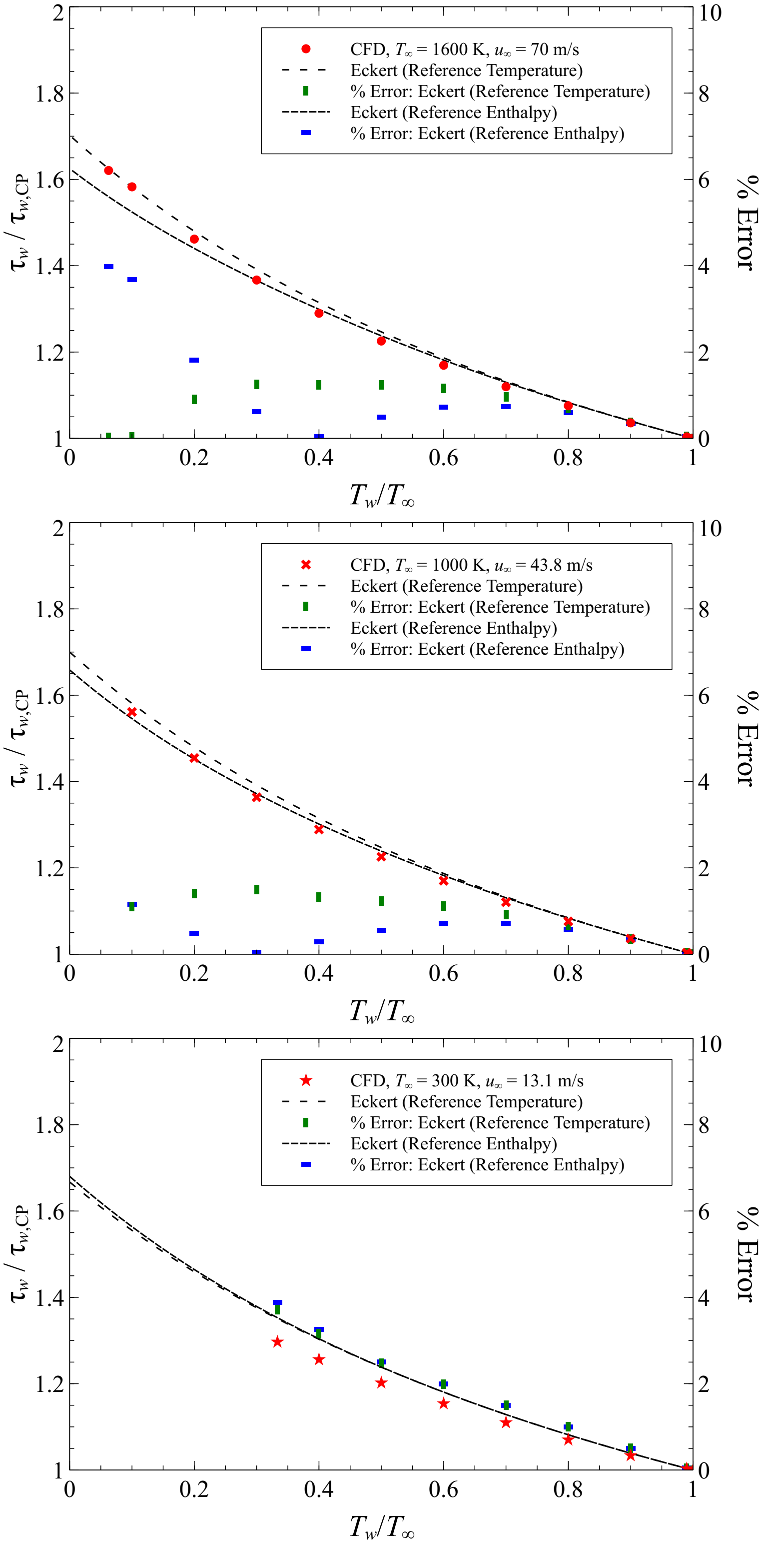

Figure 5.1: Comparison of wall shear stress (τ) ratio computed using CFD to the reference methods of Eckert [15]

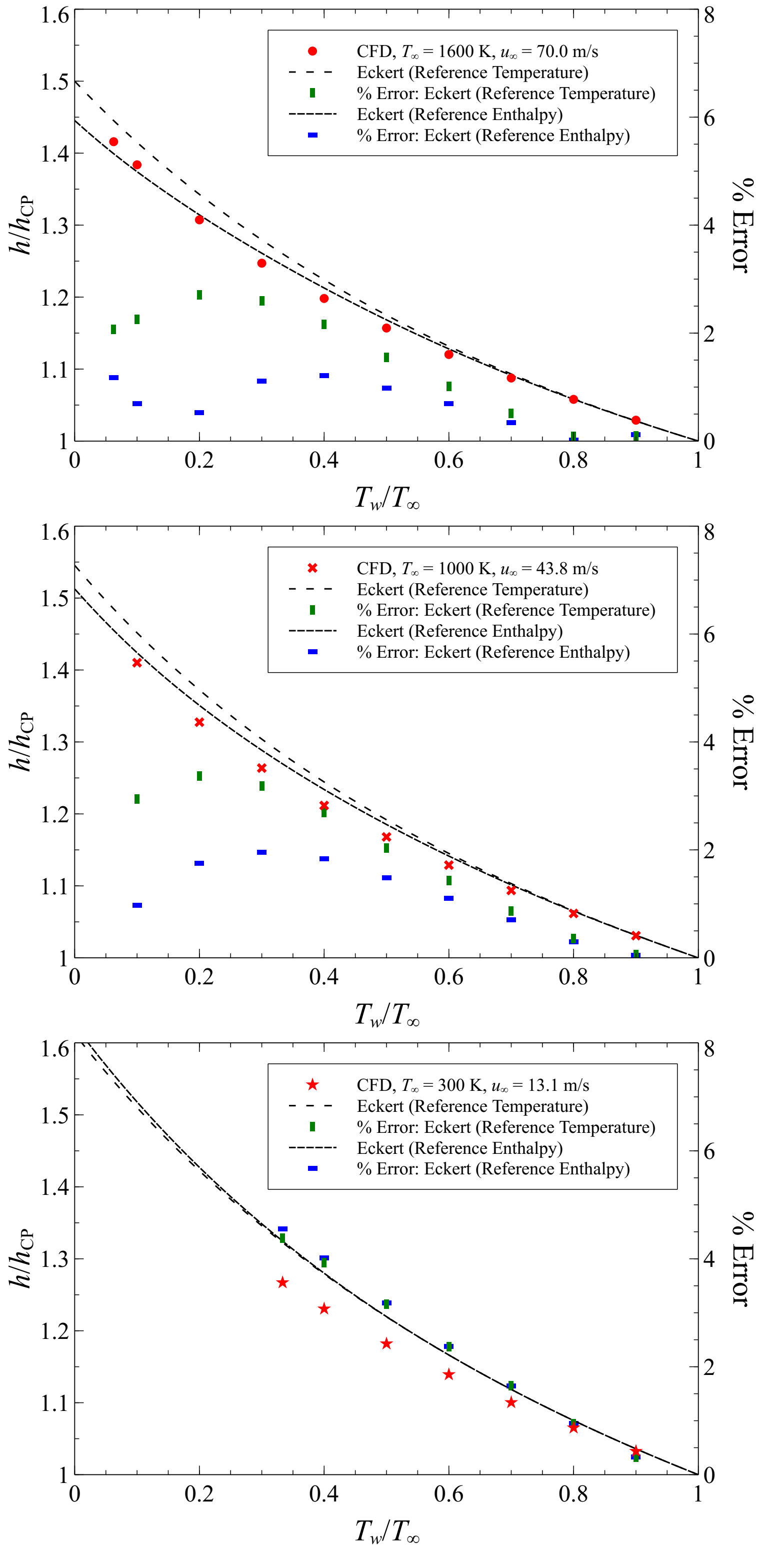

Figure 5.2: Comparison of convective heat transfer coefficient (h) ratio computed using CFD to the reference methods of Eckert [15]

both the reference temperature and reference enthalpy methods of Eckert [15] for the $T_\infty = 1000\,\mathrm{K}$ and $300\,\mathrm{K}$ cases. The same applies to the $T_\infty = 1600\,\mathrm{K}$ case for $T_w/T_\infty \geq 0.2$. However, the CFD data for the $T_\infty = 1600\,\mathrm{K}$ case is seen to agree best with the reference temperature method for $T_w/T_\infty < 0.2$. The nearly equal or better agreement of the reference temperature method compared to the reference enthalpy method seems to indicate that c_p variation within the boundary layer does not have a marked effect on the wall shear stress.

Similarly, Fig. 5.2 shows that the CFD prediction of h/h_{CP} agrees equally with the reference temperature and reference enthalpy methods of Eckert [15] for the $T_\infty = 300\,\mathrm{K}$ case. This was due to the minimal c_p variation within the boundary layer of this case and subsequent near equality of the reference temperature and reference enthalpy methods. However, the reference enthalpy method is seen to outperform the reference temperature method at all T_w/T_∞ for the $T_\infty = 1600\,\mathrm{K}$ and $1000\,\mathrm{K}$ cases. As was shown with Eq. 5.1, these cases can have large c_p variations within the boundary layer such that the reference temperature and enthalpy methods diverge with decreasing T_w/T_∞. Thus, the better agreement of the h/h_{CP} CFD data with the reference enthalpy method restates the critical role c_p (in concert with ρ, μ, and k) plays in convective heat transfer.

Admittedly both Figs. 5.1 and 5.2 show that the $T_\infty = 300\,\mathrm{K}$ case has a decidedly worse agreement with the reference methods of Eckert [15] compared to the $T_\infty = 1600\,\mathrm{K}$ and $1000\,\mathrm{K}$ cases. Consulting the plots of air's properties shown in Appendix B reveals two crucial effects. The first is that the $T_\infty = 300\,\mathrm{K}$ case resides on the asymptotic region of ρ as a function of T. This resulted in large increases in density with decreasing T_w/T_∞ compared to the $T_\infty = 1600\,\mathrm{K}$ and $1000\,\mathrm{K}$ cases. Similarly, c_p changes from decreasing to increasing with T near $T = 300\,\mathrm{K}$. This in conjunction with the variations of μ and k with T cause a significant increase in Pr for temperatures decreasing below $T = 300\,\mathrm{K}$. This increase and the inherent link of Pr to the thermal boundary layer directly correlates to the inaccuracy of the reference methods of Eckert [15] seen in the $T_\infty = 300\,\mathrm{K}$ case.

Given the findings above, three recommendations can be made. First, Fig. 5.1 suggests that the temperature dependence of c_p has little effect on τ_w. Thus, the reference temperature method of Eckert [15] is more appropriate to account for the effect of variable properties on τ_w. Second, Fig. 5.2 demonstrated that the temperature dependence of c_p has a significant effect on h. Thus, the reference enthalpy method is more appropriate to account for the effect of variable properties on h. Both the reference temperature method and the reference enthalpy method for estimating the variable property τ_w and h, respectively, were found to be within 2% of the CFD data for the $T_\infty = 1600\,\mathrm{K}$ and $1000\,\mathrm{K}$ cases at all $T_w/T_\infty < 1.0$.

Last, little difference was seen between the reference temperature and reference enthalpy methods of Eckert [15] in the $T_\infty = 300\,\mathrm{K}$ case. However, the methods of Eckert [15] were found to differ from the $T_\infty = 300\,\mathrm{K}$ CFD results by up to 5%. Though this agreement is worse than the $T_\infty = 1600\,\mathrm{K}$ and $1000\,\mathrm{K}$ cases, it is still within tolerance for most engineering applications.

This section compared CFD and the reference method of Eckert [15] in low speed regime with variable properties driven by a large $T_\infty - T_w$. No experimental validation was available from previous work in this regime. However, the agreement of the two very different methods (CFD and the reference method) provides corroborating evidence that the physics of variable properties within a boundary layer were accurately modeled. In the next section, the reasonably validated CFD model was used to expand the generality of the temperature ratio method proposed by Kays et al. [29].

5.1.2 Comparison with the Method of Kays et al.

In addition to the variable property methods of Eckert [15], Section 2.1.2 presented the variable property method of Kays et al. [29]. Their temperature ratio method proposes modeling variable properties by a ratio of temperatures raised to an empirical coefficient as given in Eqs. 2.24 and 2.25 for τ and h, respectively. Though this method seems convenient, little research has been done on turbulent, external, gaseous boundary layers to determine the appropriate empirical powers of m and n for use in Eqs. 2.24 and 2.25, respectively. The present section explores the temperature ratio method in the context of the CFD data which was corroborated by the reference method of Eckert [15] in the previous section.

Several curves of the temperature ratio method with various m and n are plotted on Fig. 5.3 along with the CFD data from the previous section. As seen in this figure, no single value of m or n best fit the entire range of T_w/T_∞. In their proposal of the temperature ratio method, Kays et al. [29] used their finite difference CFD code with a mixing-length turbulence model at a single temperature ratio of $T_w/T_\infty = 0.75$. They observed empirical powers of $m = -0.47$ and $n = -0.39$. The curves with these powers are compared to the CFD data calculated with the more recent finite volume CFD code with the k-ω SST turbulence model in Fig. 5.3. This figure suggests that assuming $m = -0.47$ and $n = -0.39$ as proposed by Kays et al. [29] is accurate to within 5% for $0.75 < T_w/T_\infty < 1$.

To increase the agreement with the CFD data over a larger range of T_w/T_∞, new values of $m = -0.28$ and $n = -0.20$ are proposed. Figures 5.4(a) and 5.5(a) show that assuming $m = -0.28$ and $n = -0.20$ proved to be good general use values in predicting $\tau_w/\tau_{w,\mathrm{CP}}$ and h/h_{CP}, respectively. These values were accurate to within 3% for $0.3 \leq T_w/T_\infty \leq 1$ for all three T_∞ cases. Since many turbine environments have a maximum T_∞ on the order of 2000 K and T_w on the order of 1000 K, the $m = -0.28$

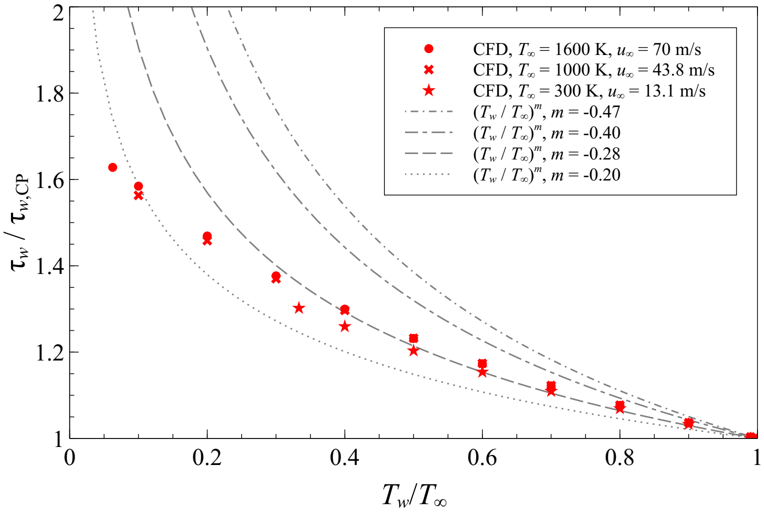

(a) Shear Stress Ratio

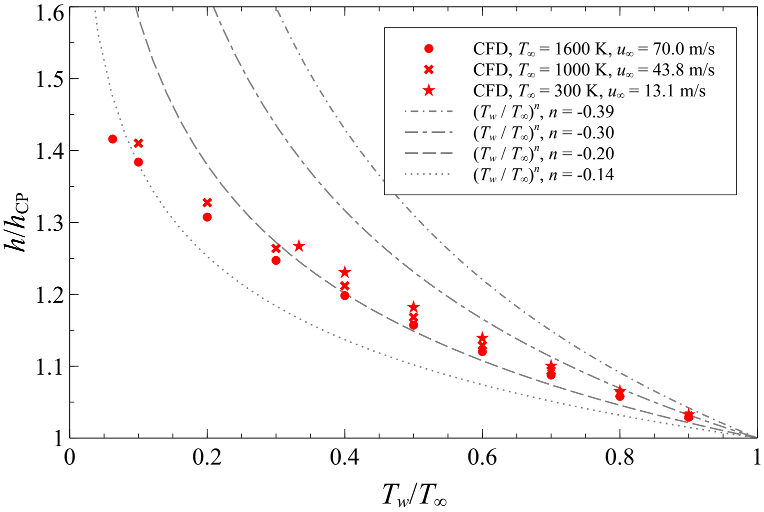

(b) Convective heat transfer coefficient ratio

Figure 5.3: Comparison of shear stress (τ) and convective heat transfer coefficient (h) ratio computed using CFD to the temperature ratio method method of Kays et al. [29]

and $n = -0.20$ values are expected to meet most practical applications.

Contrary to assuming uniform values of m and n, Kays et al. [29] explained that m and n decrease somewhat with increasing temperature ratio. Examining Fig. 5.3(a) shows that $m = -0.40$ fits the $\tau_w/\tau_{w,\mathrm{CP}}$ data best for T_w/T_∞ near one while $m = -0.20$ fits best for T_w/T_∞ near zero. To take advantage of this fact, m can be made a function of temperature ratio by assuming $m = -0.40$ when $T_w/T_\infty = 1$, $m = -0.20$ when $T_w/T_\infty = 0.0625$, and linearly interpolating m for $0.0625 < T_w/T_\infty < 1$ such that

$$m = -(0.187 + 0.213T_w/T_\infty) \tag{5.2}$$

The resulting curve is plotted in Fig. 5.4(b). In this figure, the temperature ratio method is seen to predict the $\tau_w/\tau_{w,\mathrm{CP}}$ calculated via CFD to within 2% for $0.2 \leq T_w/T_\infty \leq 1.0$.

Similarly, examining Fig. 5.3 reveals that $n = -0.30$ fits the h/h_{CP} data best for temperature ratios near one while $n = -0.14$ fits best for temperature ratios near zero. Again, n can be made a function of temperature ratio by assuming $n = -0.30$ when $T_w/T_\infty = 1$, $n = -0.14$ when $T_w/T_\infty = 0.0625$, and linearly interpolating n for $0.0625 < T_w/T_\infty < 1$ such that

$$n = -(0.129 + 0.171T_w/T_\infty) \tag{5.3}$$

The resulting curve is plotted in Fig. 5.5(b). This figure shows that the temperature ratio method predicts the h/h_{CP} calculated via CFD with different accuracies for each T_∞ case considered. Certainly Eq. 5.3 could be optimized for each T_∞ case, but the case of greatest interest to the turbine environment is the hottest case of $T_\infty = 1600\,\mathrm{K}$. Additionally, the accuracy of the n optimized to the $T_\infty = 1600\,\mathrm{K}$ condition is well within engineering accuracy tolerances for the $T_\infty = 1000\,\mathrm{K}$ and

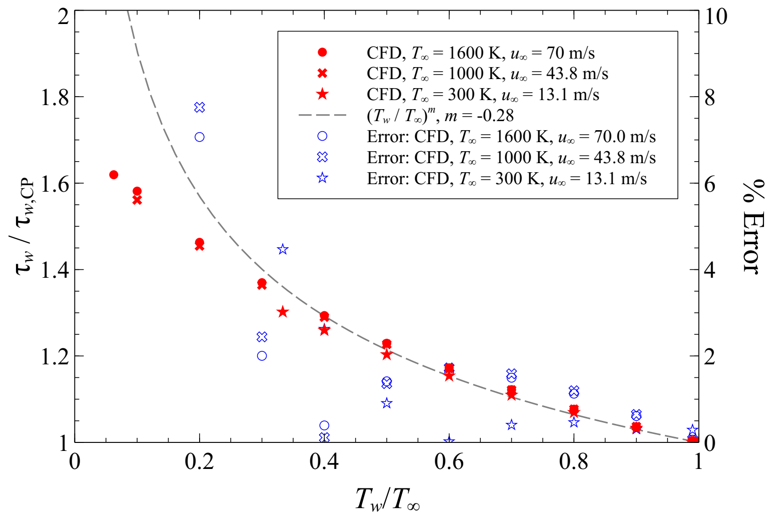

(a) Uniform $m = -0.28$

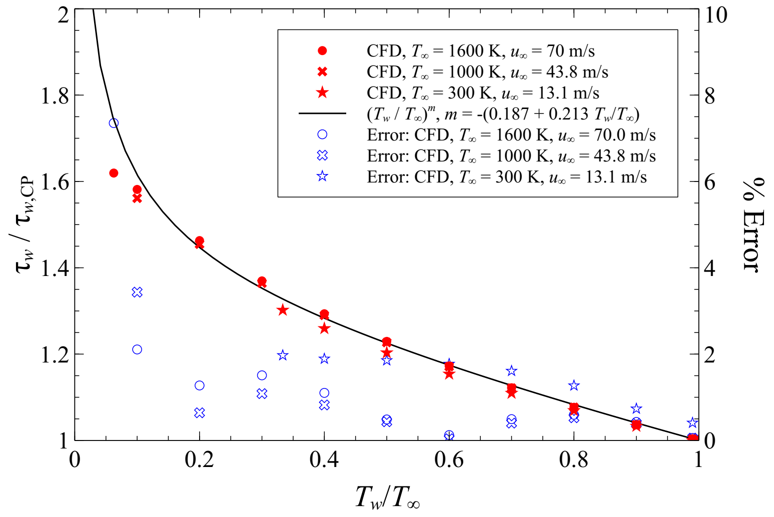

(b) Blended $m = -(0.187 + 0.213 T_w/T_\infty)$

Figure 5.4: Accuracy of the temperature ratio method of Kays et al. [29] with two selected emperical coefficients (m) to predict the shear stress (τ) ratio computed using CFD

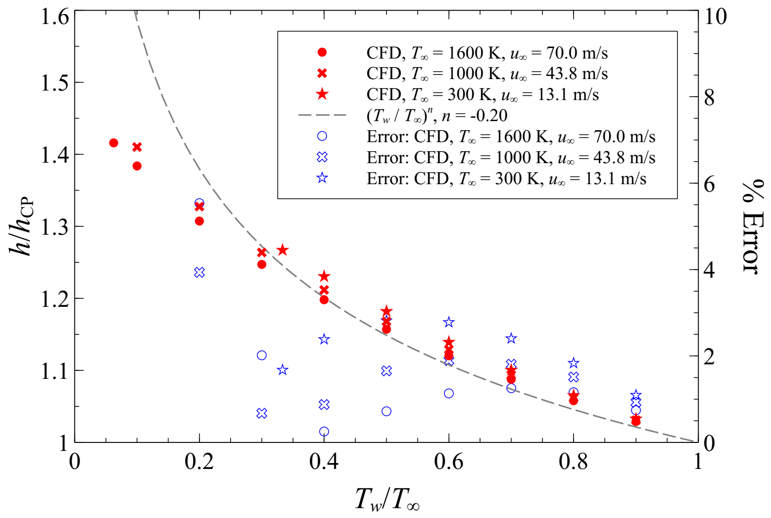

(a) Uniform $n = -0.20$

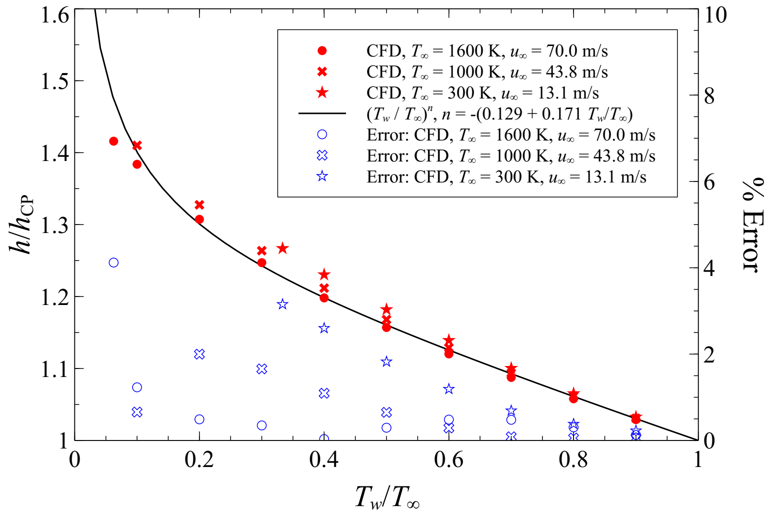

(b) Blended $n = -(0.129 + 0.171T_w/T_\infty)$

Figure 5.5: Accuracy of the temperature ratio method of Kays et al. [29] with two selected emperical coefficients (n) to predict the convective heat transfer coefficient (h) ratio computed using CFD

300 K cases. Specifically, the method was found to be accurate to within 1% for $T_\infty = 1600\,\mathrm{K}$ over the range of $0.2 \leq T_w/T_\infty \leq 1.0$, 2% for $T_\infty = 1000\,\mathrm{K}$ over the range of $0.1 \leq T_w/T_\infty \leq 1.0$, and 4% for $T_\infty = 300\,\mathrm{K}$ over the range of $0.33 \leq T_w/T_\infty \leq 1.0$.

5.1.3 Section Summary.

This section computationally validated the reference methods of Eckert [15] and the temperature ratio method of Kays et al. [29]. The reference methods of Eckert [15] are both intuitive and accurate compared to the CFD data. However, his methods are inextricably tied to a priori correlations for τ_w and h. Alternatively, the temperature ratio method of Kays et al. [29] simply proposes that τ_w and h vary from their constant property values by a ratio of characteristic temperatures to an empirical power. Therefore, judicious application of the temperature ratio method allows the prediction of τ_w and h at arbitrary T_w/T_∞ from measurements of their constant property values or conversely. This unique advantage of the temperature ratio method over the reference temperature method will be applied in Section 5.3 to assist in the quantification of an unknown radiative heat flux to a surface to satisfy Objective 1 of the present research. The following section will analyze these variable property methods to show the effect of variable properties on conventional constant property measurement techniques.

5.2 Analysis of Variable Property Methods

Many heat transfer experiments are performed at near ambient conditions with small T_∞ and T_w differences. As a result, the fluid properties within the boundary layer are essentially constant. However, when considering high temperature environments with much lower surface temperatures like that in a turbine, large property variations are present within the boundary layer. Therefore, constant property methods can no longer be applied. Eckert [15] and Kays et al. [29] each proposed a method to account for variable property effects in such an environment. Namely, they proposed the reference and temperature ratio methods, respectively.

Section 5.1 computationally validated the methods of Eckert [15] and Kays et al. [29]. The present section will employ these methods to calculate h as a function of T_w to quantify the effect of variable properties on conventional constant property measurement techniques. This study will demonstrate why accounting for variable properties is essential in high temperature environments like a turbine and Objective 1 of the present work. Finally, a technique will be proposed to predict adiabatic conditions from non-adiabatic measurements using an inversion of the temperature ratio method of Kays et al. [29].

5.2.1 Analytical Method.

The present analysis employed the reference temperature method of Eckert [15] and the temperature ratio method of Kays et al. [29] to calculate h as a function of T_w. Both laminar and fully turbulent flows were examined using the Reynolds Analogy (Eq. 2.17) and the flat plate c_f correlations defined by Eqs. 2.15 and 2.16, respectively. The correlations were evaluated using the real properties of air via the functions developed for the computational study of Section 5.1 and detailed in Appendix B. Next, $h(T_w)$ was inserted into Eq. 2.1 with $T_{\text{ref}} = T_\infty$ to define q'' as a function of T_w. Finally, the method applied conventional constant property methods to the q'' curve and determined the effect of variable properties on the method's ability to measure T_{aw} and h.

Over a small range of temperatures, fluid properties are constant within a small percentage. Thus, over the same small range of temperatures h is also constant. This concept will be central to the following analysis and thus is denoted as locally

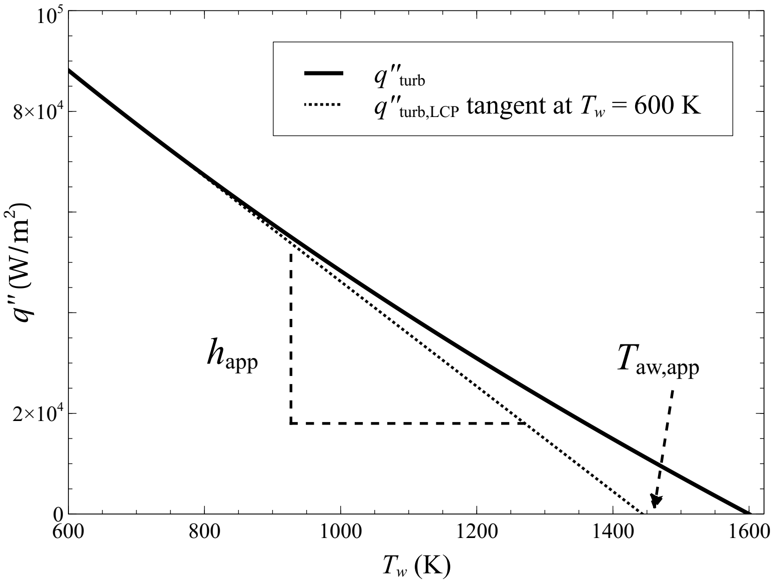

Figure 5.6: Example extrapolation of a locally constant property (LCP) technique

constant properties (LCP). In this definition, local refers to a sufficiently small range of temperatures above and below a given T_w such that property variation is negligible.

In a low temperature, constant property method, one would be searching for the h and T_{aw} over a relatively small temperature range. Such a method yields an approximation for the apparent convective coefficient h_{app} assuming constant properties as shown graphically in Fig. 5.6. In terms of Eq. 2.1, this is written as

$$h_{\text{app}}(T_w) = -\frac{\mathrm{d}q''(T_w)}{\mathrm{d}T_w} \tag{5.4}$$

where T_w is the wall temperature at which h_{app} is measured. Next, assuming h_{app} is valid for all T_w (i.e. assuming a constant property flow) heat flux can be written in point slope form as

$$q''|_{T_{\text{aw,app}}} - q''|_{T_w} = -h_{\text{app}} \cdot (T_{\text{aw,app}} - T_w) \tag{5.5}$$

Therefore, the apparent adiabatic wall temperature can be found by inserting its definition ($q(T_{\mathrm{aw}}) = 0$) into Eq. 5.5. Rearranging gives the apparent adiabatic wall temperature written as

$$T_{\mathrm{aw,app}}\big|_{T_w} = q''\big|_{T_w} / h_{\mathrm{app}} + T_w \tag{5.6}$$

and seen graphically in Fig. 5.6. The following section will apply these definitions to show the effect of variable properties on constant property measurement techniques.

5.2.2 Analytical Results.

The flow condition inputs to the analytical method were chosen to parallel the computational work of Section 5.1. Specifically, the analysis modeled air with a velocity of $u_\infty = 70\,\mathrm{m/s}$ at distances of $x = 0.15\,\mathrm{m}$ and $0.9\,\mathrm{m}$ from the sharp leading edge of a flat plate. At these conditions, the flow is expected to be fully turbulent. However, to study the sensitivity of both laminar and turbulent flows to property variations within the boundary layer, the laminar case was included and evaluated at $x = 0.15\,\mathrm{m}$.

5.2.2.1 Small Temperature Differences: Reference Temperature Method.

To analytically evaluate the validity of low temperature, constant property methods, low wall and freestream temperature differences were given as inputs to the reference temperature method. Specifically, a freestream temperature of $T_\infty = 323\,\mathrm{K}$ and a wall temperature in the range of $273\,\mathrm{K} < T_w < T_\infty$ were assumed to mirror the experiment of Popp et al. [53]. Applying the analytical method described above produces the results seen in Fig. 5.7(a).

In the laminar case, h is seen to be nearly constant, varying less than 0.5% over the range of wall temperatures. This results in a nearly linear variation of heat flux with wall temperature. In the turbulent case, h is seen to vary approximately 6%

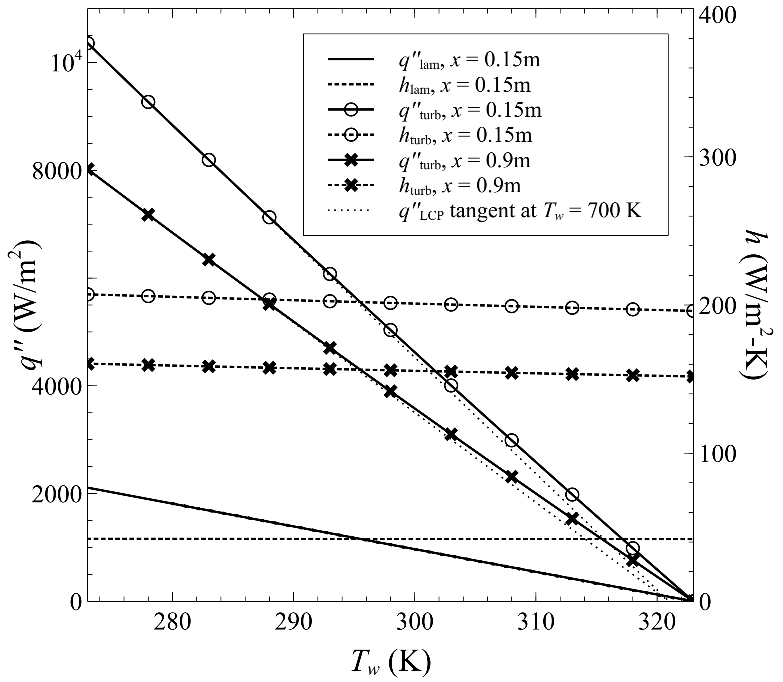

(a) Convective heat transfer coefficients and heat fluxes calculated from turbulent and laminar correlations

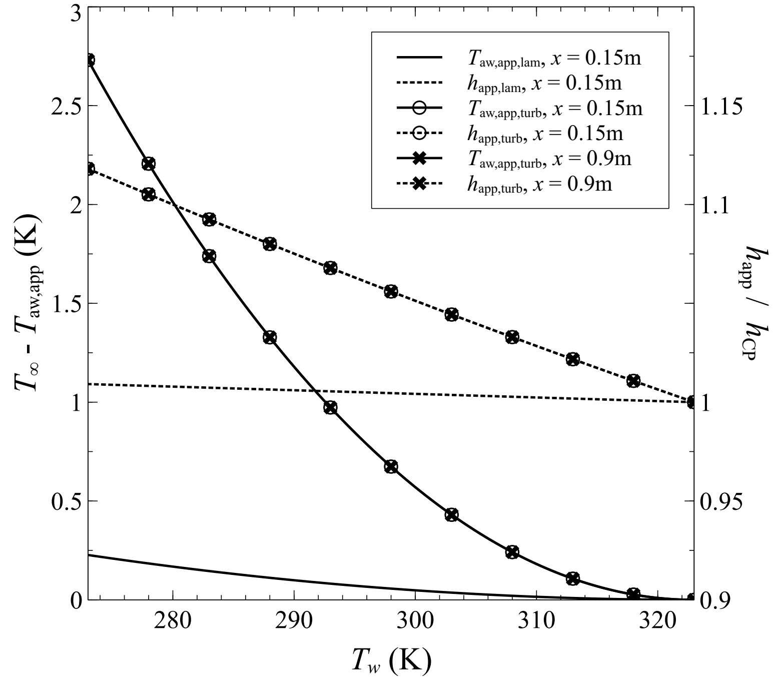

(b) Apparent h (based on slope of q'' at T_w) and apparent T_{aw} (abscissa-intercept of line tangent to q'' at T_w)

Figure 5.7: Reference temperature method for small $T_\infty - T_w$: $T_\infty = 323$K, $u_\infty = 70$m/s

over the range of wall temperatures for both x distances. This produces a slight non-linearity in the heat flux predictions.

For the low range of T_w considered, the laminar LCP line is indistinguishable from the variable property curve. The deviation of the turbulent LCP line from its variable property curve is slightly noticeable near its abscissa-intercept. This indicates only slight property variations within the boundary layer over the T_w range considered.

The apparent h and T_{aw} resulting from applying Eqs. 5.4 and 5.6 to the data of Fig. 5.7(a) are shown in Fig. 5.7(b). For the laminar case, the data in Table 5.2 shows h_{app} is nearly equal to h_{CP} (i.e. h when $T_R = T_w = T_\infty = 323\,\mathrm{K}$). The result is a $T_{\mathrm{aw,app}}$ which has only small variations ($< 0.25\,\mathrm{K}$) over the range of T_w. The turbulent case, however, is more sensitive to variations in T_w. Interestingly, the turbulent $h_{\mathrm{app}}/h_{\mathrm{CP}}$ and $T_\infty - T_{\mathrm{aw,app}}$ curves are seen to be independent of x. As summarized in Table 5.2, the turbulent h_{app} was seen to deviate up to 11.8% from h_{CP} over the range of T_w. This variation caused a larger variation in the $T_{\mathrm{aw,app}}$ than its laminar counterpart. However, the error is contained to within 2.7 K.

5.2.2.2 Large Temperature Differences: Reference Enthalpy Method.

To study the effect of large temperature differences on constant property methods, a freestream temperature of $T_\infty = 1600\,\mathrm{K}$ and a wall temperatures in the range of $600\,\mathrm{K} < T_w < T_\infty$ were assumed. As discussed in Section 5.1.1, the large variations in c_p of the $T_\infty = 1600\,\mathrm{K}$ condition warrants use of the reference enthalpy method instead of the reference temperature method. Therefore, the reference enthalpy method was used to produce the results in Fig. 5.8(a). For the laminar case, h was seen to be fairly constant, varying from h_{CP} by $< 1\%$ over the range of T_w. The turbulent case, however, was much more sensitive to wall temperature variations. For the turbulent curves at both x locations, h was seen to deviate as much as 22% from its h_{CP}

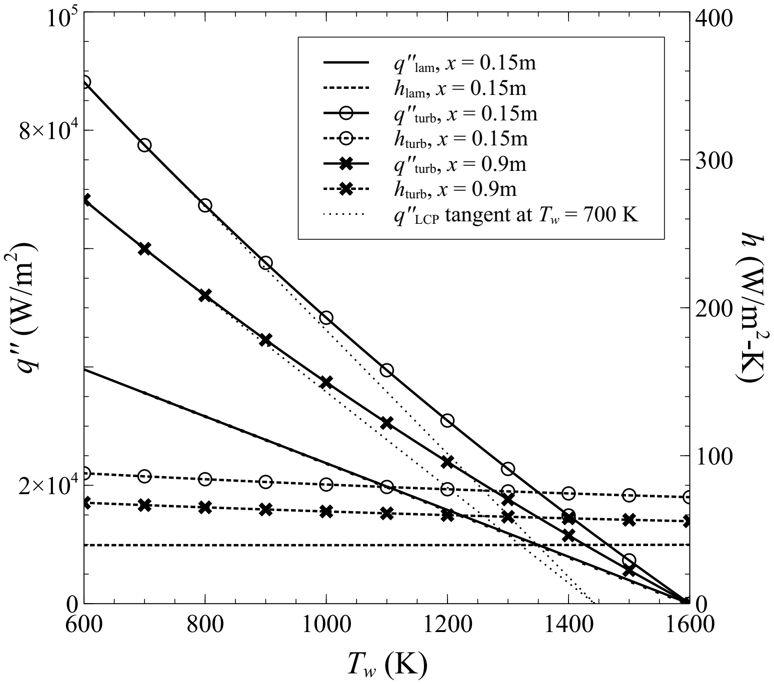

(a) Convective heat transfer coefficients and heat fluxes calculated from turbulent and laminar correlations

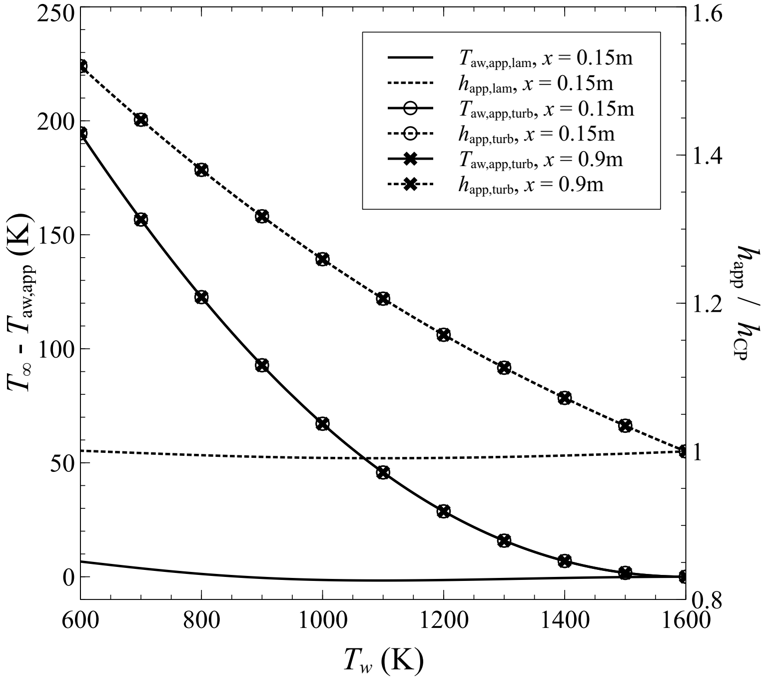

(b) Apparent h (based on slope of q'' at T_w) and apparent T_{aw} (abscissa-intercept of line tangent to q'' at T_w)

Figure 5.8: Reference enthalpy method for large $T_\infty - T_w$: $T_\infty = 1600$K, $u_\infty = 70$m/s

companion where all properties were evaluated in the freestream.

Comparing the laminar q'' curve to an LCP tangent line in Fig. 5.8(a) reveals that the LCP line deviates only slightly, indicating a relatively constant $h_{\mathrm{app}}(T_w)$. However, the turbulent LCP line is seen to deviate significantly from its q'' curve. This indicates a significant variation in h_{app} over the range of T_w.

Figure 5.8(b) shows the apparent convective coefficients and adiabatic wall temperatures which result from applying Eqs. 5.4 and 5.6, respectively, to the data of Fig. 5.8(a). Figure 5.8(b) serves to quantify the variation in the turbulent h_{app} and $T_{\mathrm{aw,app}}$ seen qualitatively in Fig. 5.8(a). Once again, the laminar case was seen to have little temperature dependence. The turbulent case, however, was seen to have significant variations with temperature. Interestingly, as with the low temperature case, $h_{\mathrm{app}}/h_{\mathrm{CP}}$ and $T_\infty - T_{\mathrm{aw,app}}$ were seen to be independent of distance along the plate. As given in Table 5.2, the turbulent h_{app} was seen to vary 52.0% from its h_{CP}. Furthermore, $T_{\mathrm{aw,app}}$ was seen to have up to a 194 K error from its true value of $T_{\mathrm{aw}} = T_\infty = 1600\,\mathrm{K}$.

5.2.2.3 Large Temperature Differences: Temperature Ratio Method.

As an alternative to the reference enthalpy method presented above, the temperature ratio method (Eq. 2.25) was applied in an analogous fashion with identical freestream conditions and wall temperature range. As suggested by Kays et al. [29], the laminar case assumed $n = 0.0$. Based on the computational results of Section 5.1.2, the turbulent n was assumed to be a function of temperature as given by Eq. 5.3. This analysis produced the convective heat transfer coefficients and heat fluxes given in Fig. 5.9(a) as a function of wall temperature.

In the laminar case, h_{app} was found to be exactly constant with a perfectly linear q'' due to the assumed empirical exponent of $n = 0.0$. For both the laminar and turbulent

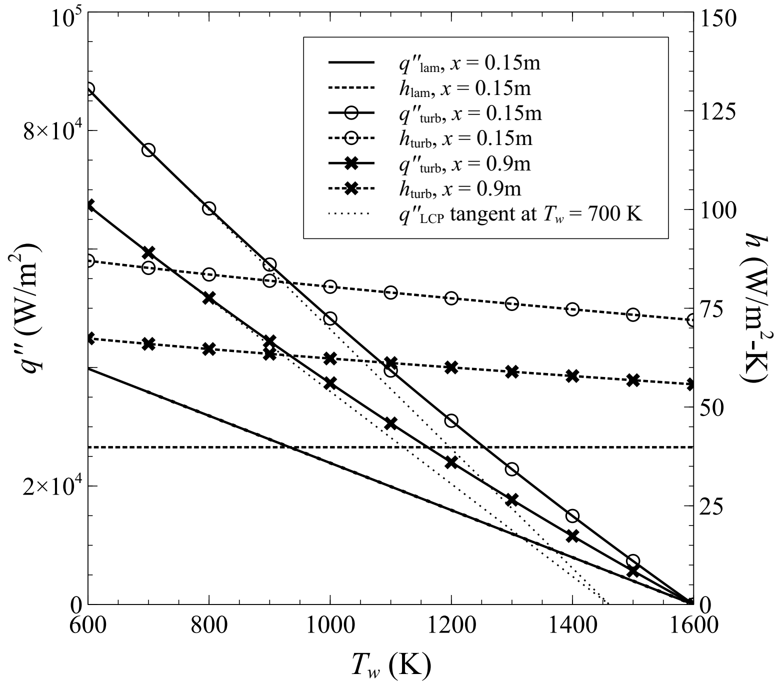

(a) Convective heat transfer coefficients and heat fluxes calculated from turbulent and laminar correlations

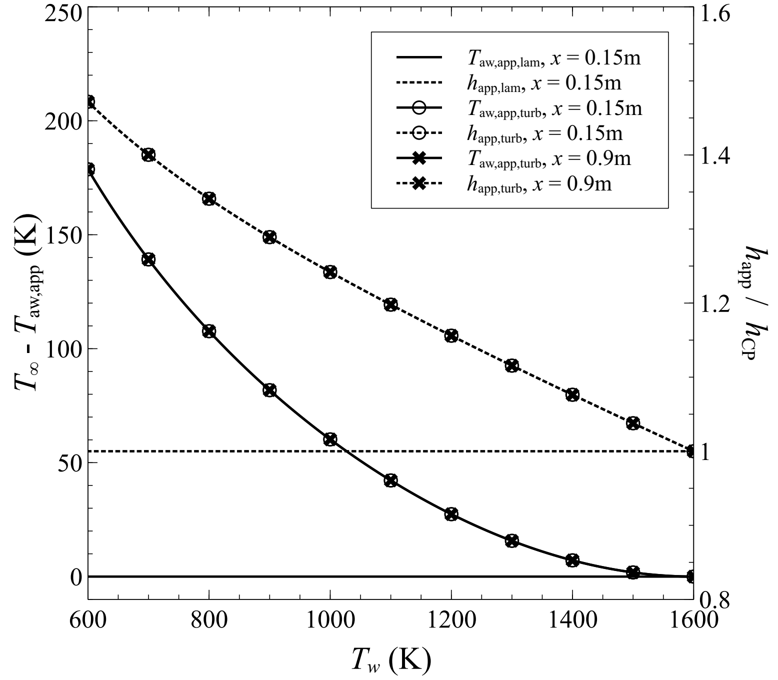

(b) Apparent h (based on slope of q'' at T_w) and apparent T_{aw} (abscissa-intercept of line tangent to q'' at T_w)

Figure 5.9: Temperature ratio method for large $T_\infty - T_w$: $T_\infty = 1600$K, $u_\infty = 70$m/s

Table 5.2: Summary of analytical results: maximum deviation of $T_{\mathrm{aw,app}}$ from T_{aw} calculated as $\Delta T_{\mathrm{aw,max}} = (T_{\mathrm{aw,app}} - T_{\mathrm{aw}})_{\mathrm{max}}$ and maximum deviation of h_{app} from h_{CP}

Flow	Method	T_∞	$T_{w,\mathrm{min}}$	$\Delta T_{\mathrm{aw,max}}$	$\left\lvert\left[\frac{h_{\mathrm{app}}}{h_{\mathrm{CP}}}\right] - 1\right\rvert_{\mathrm{max}}$
Lam	Ref	323 K	273 K	0.2 K	0.9%
	Ref	1600 K	600 K	6.7 K	0.9%
	Ratio	1600 K	600 K	0 K	0%
Turb	Ref	323 K	273 K	2.7 K	11.8%
	Ref	1600 K	600 K	194 K	52.0%
	Ratio	1600 K	600 K	179 K	47.2%

cases, the curves were found to be in good agreement with the reference enthalpy curves. Once again, the turbulent LCP tangent line was seen to deviate significantly from the turbulent q'' curve indicating significant effects of variable properties.

Next, the $q''(T_w)$ functions plotted in Fig. 5.9(a) were differentiated and extrapolated according to Eqs. 5.4 and 5.6 to calculate h_{app} and $T_{\mathrm{aw,app}}$, respectively, to produce the data in Fig. 5.9(b). As with the reference enthalpy method, the turbulent h_{app} and $T_{\mathrm{aw,app}}$ curves were found to be independent of x. Using the temperature ratio method, h_{app} and $T_{\mathrm{aw,app}}$ were seen to deviate 47.2% and 179 K from their constant property values, respectively.

The temperature ratio results were in good agreement with the reference enthalpy method. Thus, combined with the computational evidence, they served to ratify the effect of variable property flows on h_{app} measurements and $T_{\mathrm{aw,app}}$ extrapolations. Interestingly, both methods indicated that laminar flows are insensitive to property variations within the boundary layer. Finally, both methods suggested that the percent deviation of h_{app} from h_{CP} and $T_{\mathrm{aw}} - T_{\mathrm{aw,app}}$ are independent of distance along the flat plate, x.

5.2.3 Inverse Application.

The reference method of Eckert [15] is relatively easy to evaluate and, as seen in Fig. 5.2, produced accurate estimations of h/h_{CP} over a wide range of T_w/T_∞. However, it does not provide an explicit equation for how h/h_{CP} varies with T_w/T_∞. Alternatively, the temperature ratio method gives h as explicit function of T_w/T_∞. Furthermore, when n is allowed to vary with T_w/T_∞ according to Eq. 5.3, Section 5.1 showed that the temperature ratio method is also slightly more accurate.

For low temperature experiments, an unknown T_{aw} can be measured by using a wall with low thermal conductivity such that q'' into the wall is near zero. Then, the measured wall temperature is near T_{aw} and a rudimentary correction for wall conduction can be applied to acquire an accurate estimation of T_{aw}. However, for many practical applications (like that found in a modern turbine engine), T_{aw} is sufficiently high such that no viable material would survive at temperatures near T_{aw}. This makes direct measurement of an unknown T_{aw} near combustion temperatures impractical. Low temperature methods have also used extrapolation techniques to measure T_{aw} by assuming constant properties. However, as shown above, such techniques are not accurate for high $T_\infty - T_w$ environments where properties vary significantly within the boundary layer.

Using the temperature ratio method's explicit form of h as a function of T_w/T_∞ with a priori knowledge of n presents a new practicable method to determine adiabatic conditions from non-adiabatic measurements. The first step is taking heat flux measurements at constant freestream conditions over $T_w - \varepsilon < T_w < T_w + \varepsilon$ where ε is sufficiently small to maintain approximately constant properties. Second, calculate a q''_{LCP} line akin to those found in Figs. 5.7(a), 5.8(a), and 5.9(a) by a linear fit of the T_w and q'' measurements. From this q''_{LCP} line, $T_{\text{aw,app}}$ can be calculated. Then, by assuming a constant n (e.g. -0.20) and combining Eqs. 2.1 with $T_{\text{ref}} = T_\infty$, 2.25, 5.4,

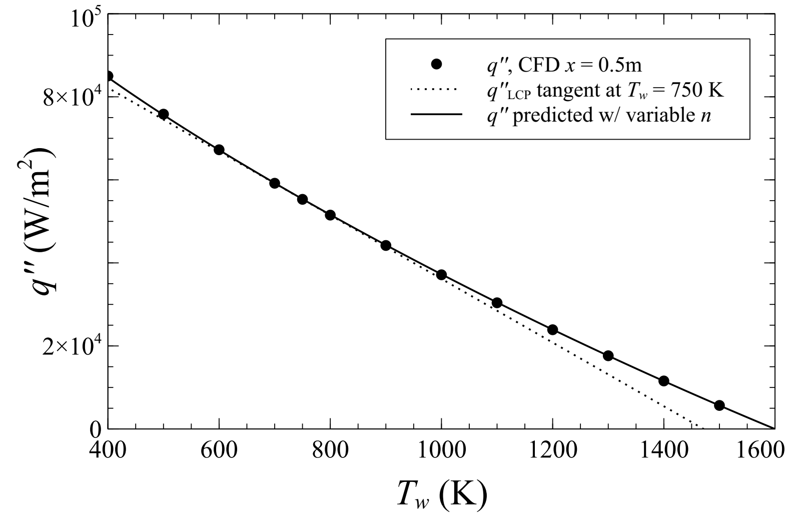

Figure 5.10: Effect of temperature ratio on the ratio of variable to constant property convective heat transfer coefficients; $T_\infty = 1600$K, $u_\infty =$ 70m/s

and 5.6, T_{aw} can be solved for explicitly as

$$T_{\text{aw}} = \frac{T_w(nT_w - (1+n)T_{\text{aw,app}})}{(n-1)T_w - nT_{\text{aw,app}}} \tag{5.7}$$

Similarly, h_{CP} can be calculated by

$$h_{\text{CP}} = \left(\frac{q''|_{T_w}}{T_{\text{aw}} - T_w}\right)\left(\frac{T_w}{T_{\text{aw}}}\right)^{-n} \tag{5.8}$$

For improved accuracy, a temperature dependent n (e.g. Eq. 5.3) can also be used. In such a case, the values of T_{aw} and h_{CP} can be determined by simultaneous numerical solving of Eqs. 2.1 with $T_{\text{ref}} = T_\infty$, 2.25, 5.3, 5.4, and 5.6 for T_{aw} and h_{CP}.

To display the utility of this process, it was applied to the numerical results of Section 5.1. Figure 5.10 shows heat flux calculated in CFD as a function of wall temperature. From the CFD results, this curve was calculated to have $T_{\text{aw}} = 1600\,\text{K}$ and $h_{\text{CP}} = 55.6\,\text{W/m}^2\,\text{K}$. Three data points were set to have T_w in the immediate vicinity of 750 K at 700 K, 750 K, and 800 K. To follow the process outlined above, a

q_{LCP} line was fitted through these points. This line was found to have $T_{\mathrm{aw,app}} = 1471\,\mathrm{K}$ and $h_{\mathrm{app}} = 76.7\,\mathrm{W/m^2\,K}$. From this line and assuming constant $n = -0.20$, Eqs. 5.7 and 5.8 with $n = -0.20$ predicted $T_{\mathrm{aw}} = 1643\,\mathrm{K}$ and $h_{\mathrm{CP}} = 52.9\,\mathrm{W/m^2\,K}$, respectively. These represent errors of $(T_{\mathrm{aw}} - T_{\mathrm{aw,predict}})/(T_{\mathrm{aw}} - T_w) = 5.1\%$ and $h_{\mathrm{CP,predict}}/h_{\mathrm{CP}} - 1 = 4.8\%$, respectively. Alternatively, using the variable n defined in Eq. 5.3 and solving numerically predicts $T_{\mathrm{aw}} = 1592\,\mathrm{K}$ (a 0.9% error) and $h_{\mathrm{CP}} = 56.1\ \mathrm{W/m^2\,K}$ (a 0.9% error), respectively.

5.2.4 Section Summary.

This section applied the variable property methods presented in Section 5.1 to determine the effect of variable properties on constant property measurement techniques. The present section confirmed that assuming constant properties can be validly employed over small temperature ranges to determine a linearized convective heat transfer coefficient and driving temperature. However, over large temperature ranges, the constant property assumption breaks down due to property variation within the boundary layer. Thus, the apparent adiabatic wall temperature that might be predicted by constant property convective heat transfer theory may be significantly different than the true temperature at which there is no heat flux. This conclusion motivates Objective 1 of the present work, as understanding how variable property effects will be critical to making accurate heat transfer measurements in the experimental portion of this research.

The analysis presented in this section becomes more relevant when the driving temperature is unknown. Section 5.2.3 proposed a new method to measure the adiabatic wall temperature and variable property heat transfer coefficient where the adiabatic wall temperature is too high to be measured directly. Using experimental measurements, the following section will extend this method to quantify radiative heat transfer in addition to the variable property convective heat transfer. Ultimately, the method proposed in the following section will be used to satisfy Objective 1 of the present research.

5.3 Experimental Validation

Section 5.1 used CFD to validate the variable property methods of Eckert [15] and Kays et al. [29]. Next, Section 5.2 applied these variable property methods to delineate the importance of accounting for variable properties in a high temperature flow. This section presents experimental data which was collected in the facility described in Chapter III. The data will be used to experimentally validate the temperature ratio method of Kays et al. [29] as well as propose a method to quantify radiative heat transfer. This method will subsequently satisfy Objective 1 of the present research.

5.3.1 Method to Account for Variable Properties and Radiation.

As discussed in Section 3.4.4, the test surface was actively cooled by backside coolant channels. However, the remaining surfaces bounding the test channel were not actively cooled. Thus, the uncooled surfaces were significantly hotter than the test surface. It will be seen that this temperature difference drove a significant radiative heat transfer component compared to the convective component.

Section 3.4.4 discussed that the current facility used an instrumentation block to measure conductive heat flux to the test surface. The instrumentation block was located just downstream of a film cooling plenum. This plenum was discussed in Section 3.4.3 and supports mounting of modular film cooling hole configurations. Though the data presented in this section was not film cooled, the single row of shaped holes configuration discussed in Section 3.4.3 was mounted to the plenum because a blank plate was not available. However, no coolant was supplied to the plenum.

The conductive heat transfer measured by the instrumentation block is a sum of the convective and radiative components such that

$$q''_{\text{cond}} = q''_{\text{conv}} - q''_{\text{rad}} \tag{5.9}$$

The sign convention in Eq. 5.9 follows the sign conventions generally accepted in the literature: convective heat flux to the wall and radiative heat flux from the wall are considered positive. Section 2.2 discussed that the total radiative heat transfer to a surface is the sum of the components incident on the surface from outside sources ($q''_{\text{rad},i}$) and leaving the surface. Subsequently, Eq. 2.27 was derived to represent the total q''_{rad} to or from a grey body surface. Thus, using the variable property method of Kays et al. [29] to model variable property convective heat flux and Eq. 2.27 to model the total radiative heat flux, Eq. 5.9 can be expanded to

$$q''_{\text{cond}} = h_{\text{CP}} \left(\frac{T_w}{T_\infty} \right)^n (T_\infty - T_w) - (\epsilon_w \sigma_0 T_w^4 - \epsilon_w q''_{\text{rad},i}) \tag{5.10}$$

In Eq. 5.10, q''_{cond}, T_w, and T_∞ were measured as described in Chapter 5.2. In addition, the computational results of Section 5.1.2 indicated that n could be could be modeled by Eq. 5.3 for the turbulent flat plate flow of the present facility. Finally, the rig total hemispherical emissivity was assumed to be $\epsilon_w = 0.85$ based on the measurements of Wade [66] for highly oxidized Hastelloy X [24].

Thus, the only unknowns which remain in Eq. 5.10 are h_{CP} and $q''_{\text{rad},i}$. To take advantage of the presence of only two unknowns, Eq. 5.10 can be rearranged by letting

$$X = -\frac{1}{\epsilon_w} \left(\frac{T_w}{T_\infty} \right)^n (T_\infty - T_w) \tag{5.11}$$

$$Y = -\left(\frac{q''_{\text{cond}}}{\epsilon_w} + \sigma_0 T_w^4\right) \tag{5.12}$$

such that

$$Y = h_{\text{CP}} \cdot X + q''_{\text{rad},i} \tag{5.13}$$

From this form, it is clear that measurements of Y at several X would allow a linear regression to quantify the unknowns of h_{CP} and $q''_{\text{rad},i}$. Finally, the calculated h_{CP} and $q''_{\text{rad},i}$ can be used to quantify the convective and radiative components of the total conductive heat flux, respectively.

Radiative heat transfer is a complex phenomenon depending on many factors including temperature, material, and geometry. Therefore, it is exceedingly difficult to match radiation between test facilities or between an experiment and end item hardware. Thus, the radiative component measured in a laboratory environment may be of little use outside the particular experiment.

Convective heat transfer, however, is readily scalable through parameters such as the Nusselt and Stanton numbers. In addition, Section 5.1.2 showed computationally that variable property effects scale relatively well via the h/h_{CP} parameter. Therefore, to take advantage of this, Eq. 5.10 can be non-dimensionalized by rearranging such that

$$\frac{h}{h_{\text{CP}}} = \left(\frac{T_w}{T_\infty}\right)^n = \frac{q''_{\text{cond}} + (\epsilon_w \sigma_0 T_w^4 - \epsilon_w q''_{\text{rad},i})}{h_{\text{CP}}(T_\infty - T_w)} \tag{5.14}$$

This form will enable a demonstration of this methods ability to non-dimensionalize the convective heat transfer for three freestream temperatures, velocities, and radiative heat transfer conditions presented in the following section.

5.3.2 Experimental Results.

This investigation focused on the three freestream conditions provided in Table 5.3. Each case featured a different combustion equivalence ratio (Φ). This variation

Table 5.3: Freestream conditions of experimental cases

Case	Φ	T_∞ (K)	u_∞ $\left(\frac{\mathrm{m}}{\mathrm{s}}\right)$	Ma	$q''_{\mathrm{rad},i,\mathrm{est}}$ $\left(\frac{\mathrm{W}}{\mathrm{m}^2}\right)$
1	0.71	1345	71.0	0.10	80,100
2	0.985	1460	60.5	0.08	95,900
3	1.3	1410	59.4	0.08	88,000

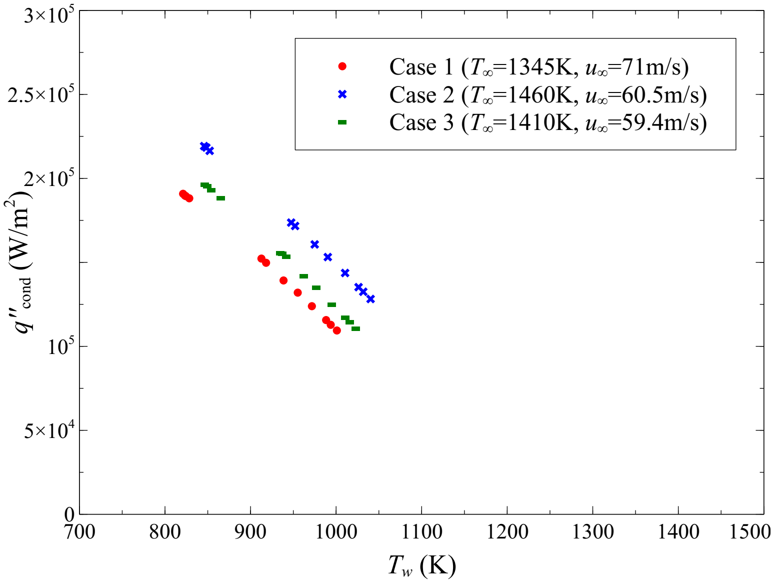

Figure 5.11: Conductive heat flux ($q''_{\mathrm{cond}} = q''_{\mathrm{conv}} - q''_{\mathrm{rad}}$) for each experimental cases in Table 6.3

in Φ resulted in a different T_∞ as well as a different freestream composition for each case. It will be seen that the different freestream compositions resulted in different radiative properties which affected the total radiative heat transfer to the test surface.

For the three cases considered, the measurements of T_w and q''_{cond} are shown in Fig. 5.11. The computational study of Section 5.1 predicted that variable properties will cause q''_{conv} as a function of T_w to have a concave upward curvature. However, the data in Fig. 5.11 seem to have a slightly concave downward curvature.

Due to the high temperature environment, both variable properties and radiative heat transfer were expected to play significant roles. The combination of these two effects was hypothesized to cause the downward curvature. To show this, three models of varying fidelity were fitted to the data. The following results will show the ability of each of these models to capture the physics of the data.

5.3.2.1 Constant Property Model Assuming Negligible Radiation.

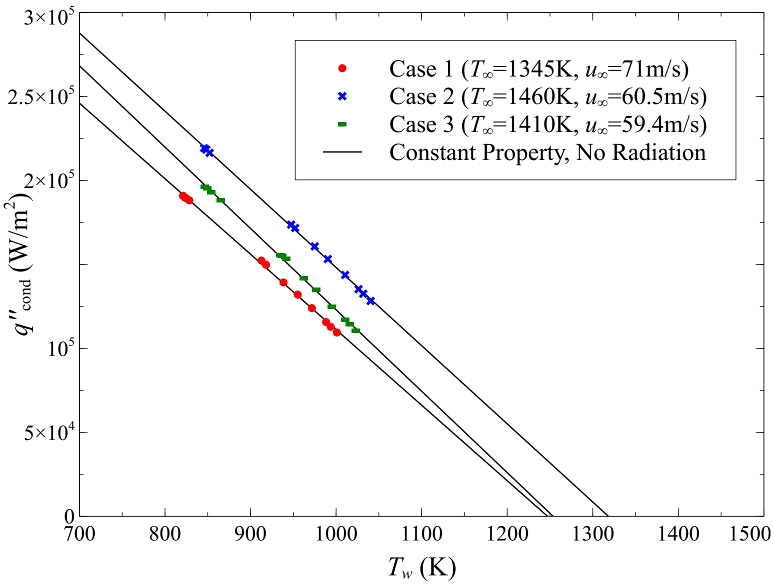

Figure 5.12: Conductive heat flux with fitted function assuming constant property flow and negligible radiation

The first model was the conventional constant property method given by Eq. 2.1 assuming $T_{\mathrm{ref}} = T_{\mathrm{aw}}$ and $q''_{\mathrm{rad}} = 0$ (i.e. $q''_{\mathrm{cond}} = q''_{\mathrm{conv}}$). A linear regression of the data was used to solve for T_{aw} and h. This technique would be typical of a low temperature experimental method like that of Popp et al. [53].

The result of this constant property method is seen in Fig. 5.12. Upon first examination, it seems that the constant property method produces a sufficient model for the data. However, examining the fitted coefficients given in Table 5.4 the T_{aw} predicted by these models (i.e. T_w where the model crosses the abscissa in Fig. 5.12) are far to low. Specifically, the T_{aw} predicted for Cases 1, 2, and 3 were 98 K, 142 K, and 156 K lower than the expected value of T_∞, respectively. This indicates that a constant property method which neglects radiation does not sufficiently capture the physics of the data.

Table 5.4: Fitted quantities for the convective models in Section 5.3.2.1 (Model 1) and 5.3.2.2 (Model 2) for each case in Table 5.3

Case	Fitted Quantity	Model 1	Model 2
1	$T_{\text{aw,fit}}$ (K)	1247	1345
	$h_{\text{CP,fit}}$ (W/m^2 K)	449	317
2	$T_{\text{aw,fit}}$ (K)	1318	1460
	$h_{\text{CP,fit}}$ (W/m^2 K)	465	304
3	$T_{\text{aw,fit}}$ (K)	1254	1410
	$h_{\text{CP,fit}}$ (W/m^2 K)	484	297

5.3.2.2 Variable Property Model Assuming Negligible Radiation.

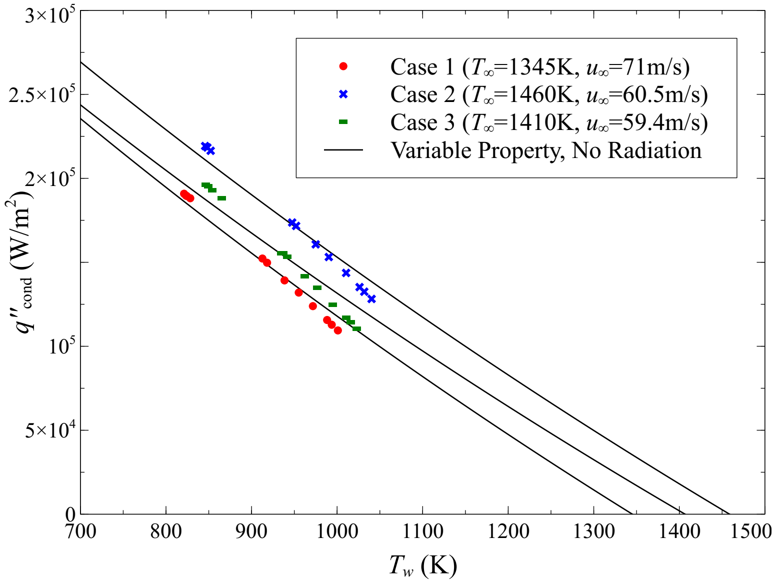

Figure 5.13: Conductive heat flux with fitted function assuming variable property flow and negligible radiation

The second method again assumed $q''_{\text{rad}} = 0$ but accounted for variable properties in h via the temperature ratio method of Kays et al. [29] defined by Eq. 2.25. Following the results of Section 5.1.2, the empirical coefficient n required by their method was assumed to be defined by Eq. 5.3. Next, T_{aw} was forced to equal the measured T_∞. Finally, a linear curve fit was used to determine h_{CP}.

The results of these process are given in Fig. 5.13 and the fitted values for h_{CP} are given in Table 5.4. Unlike the previous model where T_{aw} was a fitted quantity, forcing

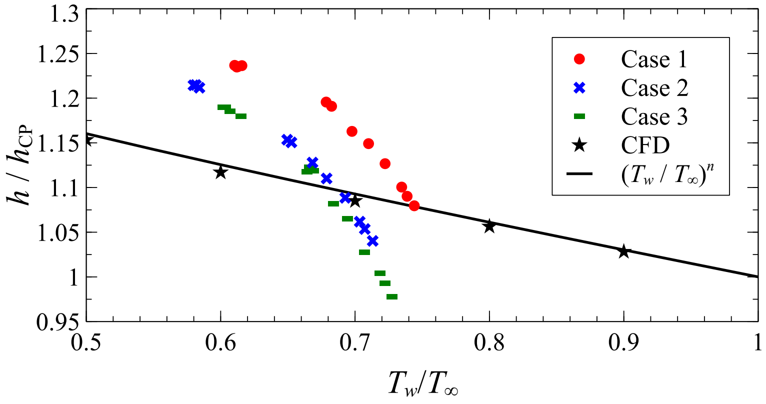

Figure 5.14: Measured convective heat transfer coefficient (h) ratio without accounting for radiation compared to CFD

$T_{\mathrm{aw}} = T_\infty$ in this model was seen to produce a worse fit of the data. Specifically, the model predicts concave upward curvature consistent with the variable property theory defining the model. However, as discussed above, the data seem to have a slightly downward curvature.

The difference in curvature is accentuated by comparing the h/h_{CP} predicted by this method compared to the computational results of Section 5.1 as seen in Fig. 5.14. This figure prominently displays the disagreement between the CFD prediction of h/h_{CP} and the h/h_{CP} measured by this model. In addition, the CFD suggests that the h/h_{CP} of various conditions should collapse to a single curve. However, the data of each case was not seen to collapse. Thus, this indicates that accounting for variable properties while neglecting to model radiation does not sufficiently capture the physics of the data.

5.3.2.3 Variable Property Model Assuming Significant Radiation.

The final model accounted for both variable properties in h as well as radiation via Eq. 5.10. The effect of assuming various n on this model will be explored in the following section. For the present examination, n was assumed to follow Eq. 5.3. Next, a linear regression of the data was used to determine h_{CP} and $q_{\mathrm{rad},i}$ as described

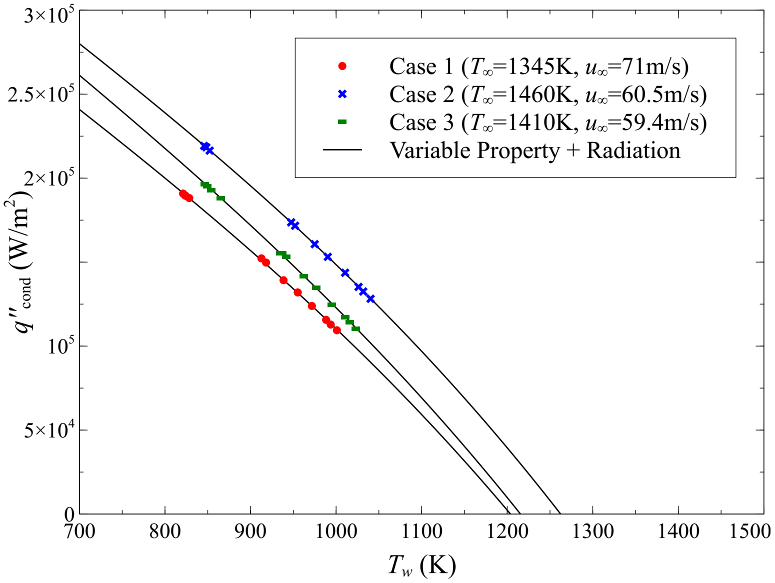

Figure 5.15: Conductive heat flux with fitted function assuming variable property flow and significant radiation

above. The results of this process are given in Fig. 5.15 and a summary of the fitted quantities is presented in Table 5.5.

Unlike the previous two models, this final model is seen in Fig. 5.15 to capture the downward curvature. Interestingly, the figure indicates that each of Cases 1, 2, and 3 is adiabatic at a T_w 141 K, 197 K, and 193 K lower than T_∞, respectively. This observation is the result of an important distinction. To enable the linear curve fit, the convective adiabatic wall temperature was forced to be the measured T_∞ such that $q''_{\text{conv}} = 0$ when $T_w = T_\infty$. However, the summation of the q''_{conv} and the net q''_{rad}via Eq. 5.9, made the surface conductively adiabatic ($q''_{\text{cond}} = 0$) at a much lower temperature than than T_∞.

5.3.2.4 Effect of Changing Temperature Ratio Exponent.

The curve fits in Fig. 5.15 accounted for variable properties using the method of Kays et al. [29] with the empirical exponent (n) developed in Section 5.1 and defined by Eq. 5.3. However, n was developed using only computational data. Thus, the

Table 5.5: Results of fitting Eq. 5.10 to the experimental no-cooling data and comparison of fitted and estimated incoming radiative component for each case in Table 5.3

n	Fitted Quantity	Case 1	Case 2	Case 3
0.00	$h_{\text{CP,fit}}$ (W/m^2 K)	306	305	328
	$q''_{\text{rad},i,\text{fit}} \cdot 10^{-4}$ (W/m^2)	6.20	6.67	4.41
	$q''_{\text{rad},i,\text{fit}}$ % Error	-22.6	-30.4	-49.8
	L^2-Norm$\cdot 10^3$ (W/m^2 K)	10.1	4.43	11.0
-0.14	$h_{\text{CP,fit}}$ (W/m^2 K)	270	266	289
	$q''_{\text{rad},i,\text{fit}} \cdot 10^{-4}$ (W/m^2)	7.20	8.01	5.63
	$q''_{\text{rad},i,\text{fit}}$ % Error	-10.2	-16.5	-36.0
	L^2-Norm$\cdot 10^3$ (W/m^2 K)	15.5	4.43	15.0
-0.20	$h_{\text{CP,fit}}$ (W/m^2 K)	257	251	274
	$q''_{\text{rad},i,\text{fit}} \cdot 10^{-4}$ (W/m^2)	7.59	8.52	6.10
	$q''_{\text{rad},i,\text{fit}}$ % Error	-5.33	-11.2	-30.6
	L^2-Norm$\cdot 10^3$ (W/m^2 K)	18.3	5.98	17.3
-0.30	$h_{\text{CP,fit}}$ (W/m^2 K)	236	228	251
	$q''_{\text{rad},i,\text{fit}} \cdot 10^{-4}$ (W/m^2)	8.19	9.59	6.83
	$q''_{\text{rad},i,\text{fit}}$ % Error (%)	2.21	-2.89	-22.3
	L^2-Norm$\cdot 10^3$ (W/m^2 K)	23.5	9.64	21.6
-0.39	$h_{\text{CP,fit}}$ (W/m^2 K)	219	210	232
	$q''_{\text{rad},i,\text{fit}} \cdot 10^{-4}$ (W/m^2)	8.69	9.97	7.44
	$q''_{\text{rad},i,\text{fit}}$ % Error	8.47	3.91	-15.4
	L^2-Norm$\cdot 10^3$ (W/m^2 K)	28.7	13.7	26.1
Eq. 5.3	$h_{\text{CP,fit}}$ (W/m^2 K)	253	248	270
	$q''_{\text{rad},i,\text{fit}} \cdot 10^{-4}$ (W/m^2)	7.57	8.43	6.06
	$q''_{\text{rad},i,\text{fit}}$ % Error	-5.5	-12.1	-31.1
	L^2-Norm$\cdot 10^3$ (W/m^2 K)	17.4	5.03	16.5

effect of changing n on the h/h_{CP} results of fitting Eq. 5.10 to the data was examined to help validate Eq. 5.3 for n.

The h/h_{CP} data in Fig. 5.16 were calculated by assuming an n, fitting the model discussed above, and non-dimensionalizing the results according to Eq. 5.14 for each of the three cases. Six different n were chosen for this fitting process to produce the $h_{\text{CP,fit}}$ and $q''_{\text{rad},i,\text{fit}}$ found in Table 5.5. Figure 5.16 displays that Eq. 5.14 can successfully non-dimensionalize the measurements from the various cases. This is indicated by their collapse to a single curve. However, it is seen that each n collapses

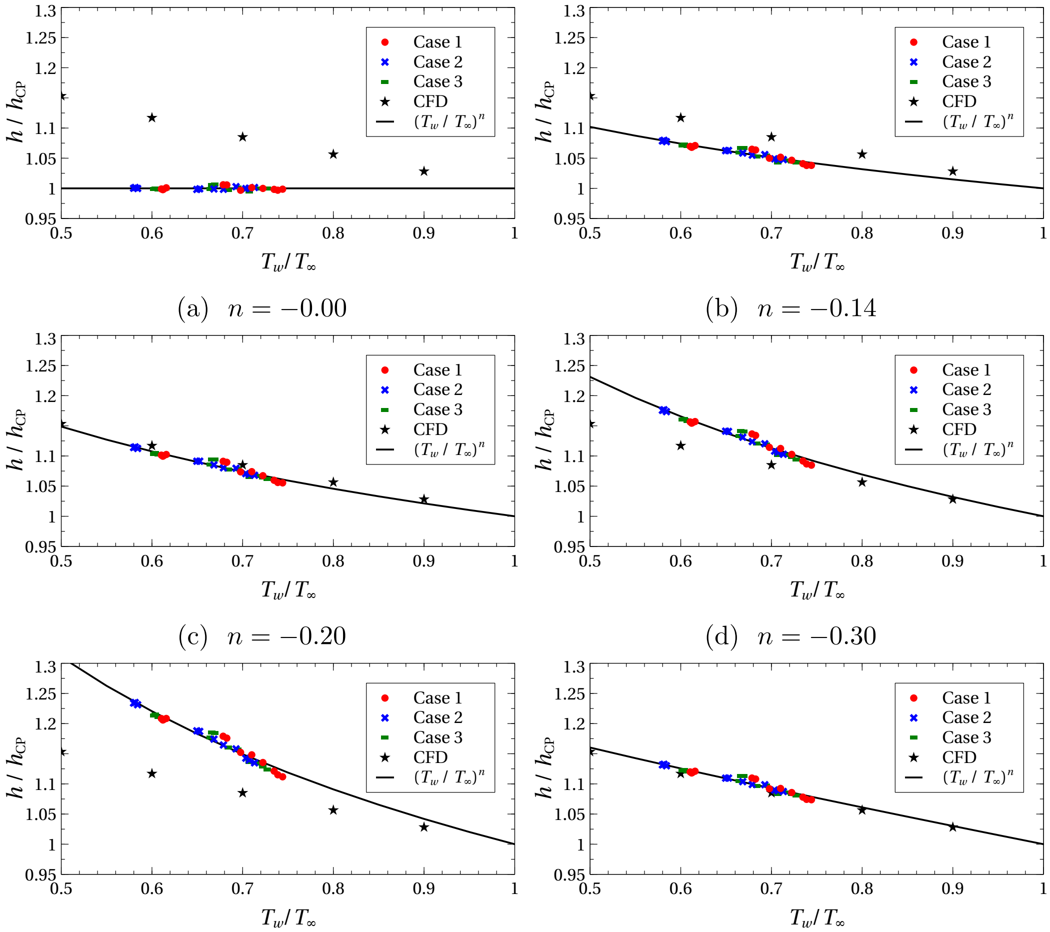

(a) $n = -0.00$

(b) $n = -0.14$

(c) $n = -0.20$

(d) $n = -0.30$

(e) $n = -0.39$

(f) $n = -(0.129 + 0.171T_w/T_\infty)$

Figure 5.16: Non-dimensionalized ratio of convective heat transfer coefficient with a radiation correction for various n applied to the temperature ratio method of Kays et al. [29]

the data, so this figure alone cannot be used to propose an appropriate n. Rather, it shows that accounting for radiation is critical in quantifying and non-dimensionalizing the convective heat transfer.

To assist in determining an appropriate n, the $q''_{\text{rad},i,\text{fit}}$ calculated for each case and selection of n was compared to an estimated incident radiation, $q''_{\text{rad},i,\text{est}}$. Since all the surfaces bounding the test channel for this study were constructed of Hastelloy X [24], the radiation from the surrounding surfaces to the test surface could be approximated as gray body radiation with an emissivity of $\epsilon_s = 0.85$ such that

$$q''_{\text{rad},i,\text{est}} = \epsilon_s \sigma_0 T_s^4 \tag{5.15}$$

The temperature of the surroundings (T_s) was measured by mounting an OMEGA® K-type thermocouple to the wall opposite of the test surface. The estimated value for each case is given in Table 5.3.

Finally, the measured value of $q''_{\text{rad},i}$ was compared to the estimation in the form of an error: $= q''_{\text{rad},i,\text{fit}}/q''_{\text{rad},i,\text{est}} - 1$ given as $q''_{\text{rad},i,\text{fit}}$ % Error in Table 5.5. It should be noted that Eq. 5.15 does not account for radiation reflected back to the emitting surface or participating media. Thus, these errors are a rough estimation intended only to give the $q''_{\text{rad},i}$ fitted from the data credibility. Therefore, the errors cannot conclusively be used to recommend a value for n. However, they will be used as evidence to suggest an n.

Interestingly, the difference in error between Case 1 and Case 2 is approximately 6% for each n in Table 5.5. Similarly, the difference in error between Case 1 and Case 3 is approximately 25% for each n in Table 5.5. As shown in Table 5.3, the equivalence ratio (Φ) increases for each case from a minimum of $\Phi = 0.71$ in Case 1 to a maximum of $\Phi = 1.3$ in Case 3. Turns [64] explains that combustion emissions are a strong function of Φ. Furthermore, as Φ increases above one, non-diatomic molecules (e.g. CO_2, H_2O, hydrocarbons, etc.) remain in the freestream which make stronger contributions to radiation emission and absorption. Thus, as Φ increases, the effect of participating media is expected to also increase. It is hypothesized that the nearly constant difference in $q''_{\text{rad},i}$ error from case to case is indicative of the effect of the increase in participating media with Φ. Moreover, it was seen that increasing Φ resulted in a $q''_{\text{rad},i,\text{fit}}/q''_{\text{rad},i,\text{est}} - 1$ which was more negative. However, it was expected that, since the participating media was at a higher temperature than the channel

Table 5.6: Temperature and gas composition (volumetric fraction) inputs to RadCal [45]

Case	Φ	T_∞	CH_4	H_2O	CO_2	CO	N_2	O_2
1	0.71	1345	0.0	0.11	0.084	1.3×10^{-7}	0.75	0.057
2	0.985	1460	0.0	0.15	0.11	5.6×10^{-6}	0.73	0.0029
3	1.3	1410	0.0	0.14	0.080	0.060	0.67	0.0

surfaces, that the participating media would increase $q''_{\mathrm{rad},i}$.

The National Institute of Standards and Technology has developed a code to better understand the effect of participating media on radiative heat transfer. The code, known is as RADCAL [45], allows the user to study radiation through a combustion product medium containing CO_2, H_2O, CH_4, CO, N_2, O_2, and soot. Moreover, the code allows specification of an arbitrary, non-uniform spatial distribution of both fluid temperature and composition. This feature is especially relevant to post-processing CFD simulations of combustion to analyze radiative heat transfer in the flow solution.

For the present work, RADCAL [45] was employed to better understand the effect of participating media on the radiative environment. First, the CEA [41] code discussed in Section 3.7 was used to calculate the expected species distributions for each experimental case. The resulting species distribution is given in Table 5.6. These inputs were assumed to be uniform within the test channel to simplify the RADCAL [45] analysis. As discussed in Section 3.7, the volumetric fractions of CO_2, CO, and O_2 calculated by CEA [41] were found to be within an absolute difference of 0.2% compared to those measured at the exit of the test channel.

Using the inputs in Table 5.6, RADCAL [45] was used to calculate the spectral radiation intensity from the freestream gas and the spectral transmissivity of the gas for wavelengths between $1\,\mu$m and $200\,\mu$m. This was accomplished for path lengths ranging from the shortest possible path in the test channel (0.019 m) to the longest (0.133 m). Then, net radiation intensity from the gas (i_g) by integrating the spectral radiation intensity over the wavelength range of $1\,\mu$m and $200\,\mu$m for each path length considered. Next, the radiation intensity from the gray body of the surrounding surface (i_s) was calculated by integrating Planck's distribution [26] evaluated at the measured surrounding wall temperature multiplied by ϵ_s multiplied by the spectral transmissivity calculated by RADCAL [45] over the wavelength range of $1\,\mu$m and $200\,\mu$m for each path length considered.

The intensities resulting from these processes along with their sum (the total intensity, i_t) are plotted in Fig. 5.17(a). In this figure, it is seen that RADCAL [45] predicts an increase in radiation intensity with the path length. An increased path length translates to an increase of participating media. Thus, this result indicates that, as expected, radiation intensity (and, thus, the heat flux) increased with increasing participating media.

Interestingly, by normalizing the intensity contributions of the gas and surroundings by the total intensity, Fig. 5.17(b) shows that the intensities of the three cases collapse to a common curve within ± 0.025. Thus, despite differences in chemical composition and temperature, the relative contribution of the participating media and the surrounding surface to the radiation intensity incident on the test surface is nearly equal for each case. This is hypothesized to occur due to the tendency of media with a high emissivity to have a low transmissivity and media with a low emissivity to have a high transmissivity.

Since Case 1 featured a $\Phi = 0.71$, Fig. 5.17(b) showed that it was least affected by participating media. Specifically, minimal role of participating media in Case 1 suggests that $q''_{\mathrm{rad},i,\mathrm{est}}$ and $q''_{\mathrm{rad},i,\mathrm{fit}}$ should be close. The values of n which produce the best agreement between $q''_{\mathrm{rad},i,\mathrm{est}}$ and $q''_{\mathrm{rad},i,\mathrm{fit}}$ for Case 1 are seen in Table 5.5 to be $n = -0.20$, -0.30, and Eq. 5.3. Thus, the $q''_{\mathrm{rad},i}$ resulting from each of these n suggests that these values are most appropriate to capture variable property effects in n. To better delineate amongst these n, the goodness of the fit of the data to the

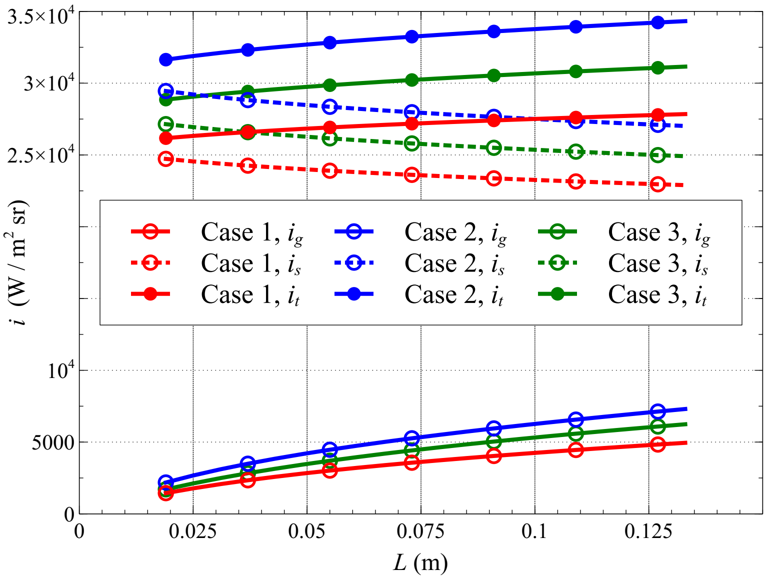

(a) Dimensional

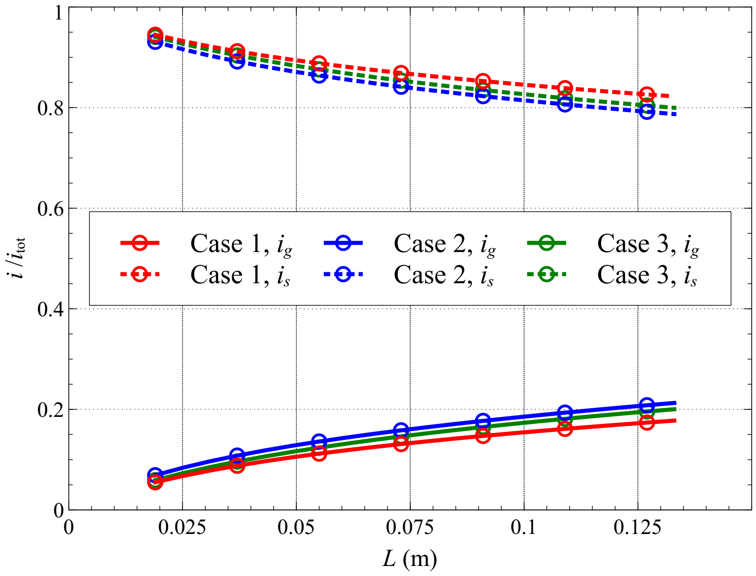

(b) Normalized by I_{tot}

Figure 5.17: Radiation intensity from the gas (g), from surroundings through the gas (s), and total (t) incident on test surface as a function of distance from surrounding surface to test surface (L) as calculated by RADCAL [45] with inputs listed in Table 5.6

analytical h/h_{CP} curve was examined.

Figure 5.16 and the L^2-norms (root sum squared of the fit residuals) in Table 5.5 allow an examination of how well the data agree with the h/h_{CP} curves of each n. While assuming $n = -0.30$ and -0.39 (Figs. 5.16(d) and 5.16(e), respectively) results in little error between the data and the curves, careful inspection of the figures reveals some concave down curvature to the data which was not removed by the correction process. Additionally, these are found to have significantly higher L^2-norms than the other n cases. This indicates that, for the temperature ratio range presented in the data, the values of $n = -0.30$ and -0.39 do not accurately account for variable property effects. This conclusion is supported by the computational work of Section 5.1.2.

For $n = -0.14$, -0.20, and Eq. 5.3 (Figs. 5.16(b), 5.16(c), and 5.16(f), respectively), reveal a good fit of the data to the analytical curve. This is reflected in their similarly small L^2-norms. Though each of these n result in different $q''_{\text{rad},i}$ and h/h_{CP}, they are each within 5% of each other. Therefore, since this is within the uncertainty of the facility listed in Table 3.1, an objective recommendation among these three n is impossible using only the present data.

Finally, assuming $n = 0.00$ allowed an evaluation of accounting for radiative heat transfer but assuming a constant property flow (i.e. no variation of h with T_w/T_∞). The data of each case are seen to seen in Fig. 5.16(a) to conform well to the analytical curve. In addition, the $n = 0.00$ case is seen in Table 5.5 to have produced the best L^2-norm of all the n. However, $q''_{\text{rad},i,\text{fit}}$ was found to be 22.6% lower than $q''_{\text{rad},i,\text{est}}$ for Case 1. As discussed above, Case 1 is expected to have a small contribution of participating media such that $q''_{\text{rad},i,\text{est}}$ and $q''_{\text{rad},i,\text{fit}}$ should be close. Thus, the observed difference of 22.6% seems exceedingly high and is well outside the experimental uncertainty of the facility listed in Table 3.1.

For each n studied above, the data were seen to collapse to a single curve. Some n produced better L^2-norms while others produced more reasonable $q''_{\text{rad},i,\text{fit}}$. However, neither factor could be used to make a conclusive statement on which n was most appropriate. Even so, the good agreement of $q''_{\text{rad},i,\text{est}}$ and $q''_{\text{rad},i,\text{fit}}$ as well as the relatively low L^2-norm for Case 1 combined with the computational evidence presented in Section 5.1.2 allowed the remainder of the present work to use the variable n defined by Eq. 5.3. Moreover, this equation for n remains as the recommended function for variable properties in a turbulent, gaseous, zero-pressure-gradient flow over a flat plate.

5.3.2.5 Independent Convective and Radiative Components.

Using n defined by Eq. 5.3, the individual contributions of convective and radiative heat transfer of the total conductive heat transfer could be quantified as seen in Fig. 5.18. Figure 5.18(a) shows that, after removing the radiative component, the convective component takes on the concave upward curvature that is expected from Section 5.2. Figure 5.18(b) displays the heat flux components normalized by the conductive component. This figure shows the clear contribution of radiation to the total conductive heat flux with a q''_{rad} component of up to 25% of q''_{cond}.

5.3.3 Section Summary.

Overall, this section showed that radiative heat transfer must be accounted for in a high temperature environment. In fact, Fig. 5.18(b) showed that radiative heat transfer made up as much as 25% of the total conductive heat transfer to the test surface. Subsequently, a method to account for variable properties and radiative heat transfer was proposed (Eq. 5.10) to satisfy Objective 1 of the present research. It was seen that, after accounting for radiation, the convective component could be

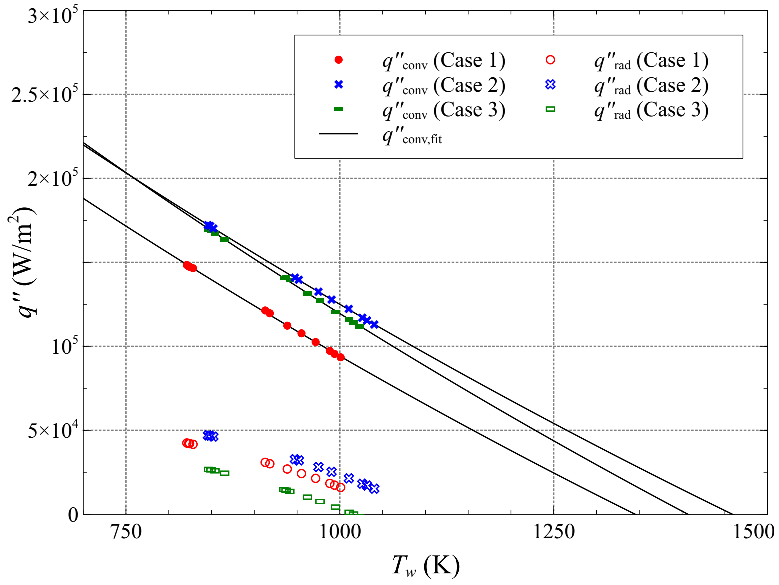

(a) Dimensional

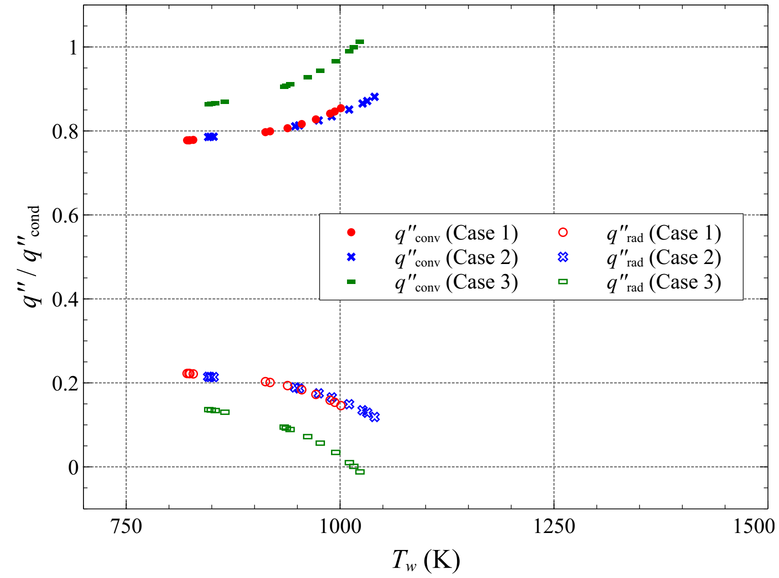

(b) Normalized by q''_{cond}

Figure 5.18: Contribution of convective and radiative heat transfer to the total heat transfer

non-dimensionalized by the temperature ratio method of Kays et al. [29].

The computational work of Section 5.1.2 indicated that the temperature ratio method enabled scaling variable properties. Thus, the ability of the present method to non-dimensionalized three different conditions to the temperature ratio method via Eq. 5.14 is significant for two reasons. First, it allows the convective and radiative components of heat flux to be decoupled and quantified individually. Second, it allows the measured convective component to be scaled to applications outside the test facility. As discussed, it can be exceedingly difficult to match or scale radiative heat transfer. Thus, quantifying the radiative component may not be useful outside of it enabling quantification of the convective component.

Though this section has displayed the utility of temperature ratio method of Kays et al. [29], the method required an n exponent which did not have a firm footing in underlying physics. To better understand the physics of variable properties, the following section will return to the computational study of Section 5.1. Then, how the boundary layer varies with temperature ratio will be examined. Subsequently, a new method to account for variable properties will be proposed and compared with the temperature ratio method of Kays et al. [29].

5.4 Variation of the Boundary Layer with Temperature Ratio

This chapter began by computationally validating the existing variable property methods of Eckert [15] and Kays et al. [29] methods in Section 5.1. Section 5.1.2 focused on the temperature ratio method of Kays et al. [29] which assumes the convective heat transfer coefficient (h) varies with a temperature ratio (T_w/T_∞) raised to an empirical exponent (n) according to Eq. 2.25. It was found that, rather than assuming a single value for n, assuming n was a linear function of T_w/T_∞ according to Eq. 5.3 made the temperature ratio method accurate over a broad range of T_w/T_∞.

Subsequently, Section 5.3 experimentally validated that the temperature ratio method could non-dimensionalize the convective heat transfer of different freestream conditions to a single temperature ratio curve with n defined by Eq. 5.3. This demonstration was used to satisfy Objective 1 of the present research.

Though the temperature ratio method of Kays et al. [29] was seen to be effective, allowing n to vary with T_w/T_∞ was not derived from fundamentals. Rather, it was a function which allowed a simplified model to conform to the computational data. Thus, the method lacks a footing in understanding of the underlying physics.

To better understand the physics, this section will examine how the boundary layer changes with T_w/T_∞. This will help augment Objective 1 by gaining a better understating of how variable properties effect the boundary layer. The following section will build upon the knowledge gained in this section using a semi-empirical approach to develop an alternative variable property method. Finally, the next section will present a comparison of the new variable property method and the method of Kays et al. [29] to suggest which is a more practical method for the present research.

5.4.1 Non-dimensionalized by Boundary Conditions.

To gain an intuitive view of how the boundary layer changes with T_w/T_∞, the velocity and temperature profiles were non-dimensionalized by their boundary conditions. It will be shown in Section 5.4.5 that the velocity boundary layer thickness (δ_{99}) changes negligibly with T_w/T_∞. However, to ensure readily comparable results $\delta_{99,\mathrm{CP}}$ (δ_{99} when $T_w/T_\infty = 1$) was selected as the appropriate quantity to non-dimensionalize y in the present examination of the boundary layer.

Figure 5.19 shows the result of this selection of non-dimensionalization for each T_∞ considered at two T_w/T_∞. Interestingly, the three T_∞ cases at each T_w/T_∞ exhibit excellent agreement in both the non-dimensional momentum and thermal boundary

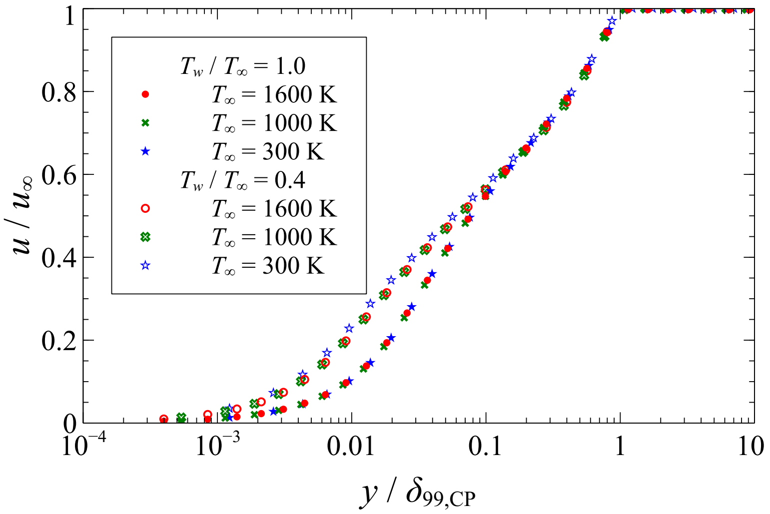

(a) Momentum boundary layer

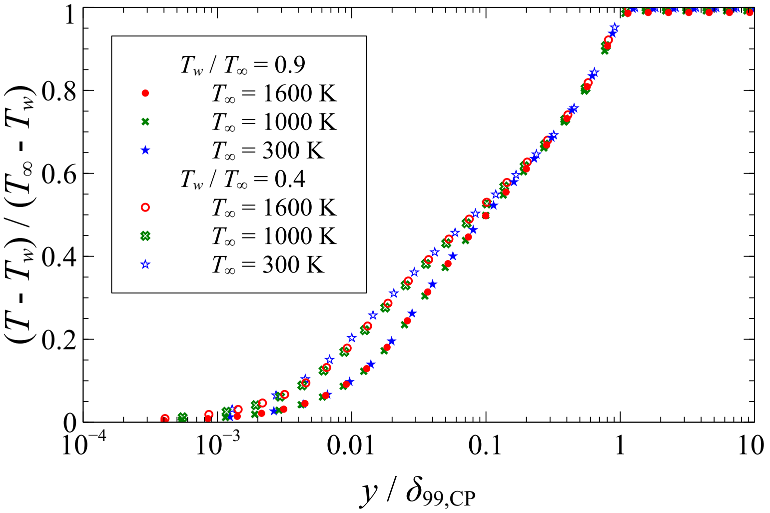

(b) Thermal boundary layer

Figure 5.19: Variation in the momentum and thermal boundary layers with temperature ratio (T_w/T_∞) and T_∞; Re$_x = 250,000$

layers. Due to this excellent agreement, it was assumed that the non-dimensional $T_\infty = 1600\,\mathrm{K}$ case could sufficiently represent the non-dimensional boundary layers of the other two cases at all applicable T_w/T_∞. Thus, Fig. 5.20 shows only the $T_\infty = 1600\,\mathrm{K}$ case but with a higher resolution of T_w/T_∞.

Figure 5.20 indicates increasing temperature and velocity gradients near the wall with decreasing T_w/T_∞. This mirrors the results of Section 5.1.2 which found τ_w and h both increase with decreasing T_w/T_∞. Interestingly, the curves for each T_w/T_∞ begin to diverge around $y/\delta_{99,\mathrm{CP}} = 0.1$ and smaller.

Pope [52] explained that the region of the boundary layer with $y/\delta_{99,\mathrm{CP}} < 0.1$ is determined by the friction velocity u_τ (Eq. 2.10) and y^+ (Eq. 2.7) independent of u_∞ and δ_{99}. Thus, the divergence seen for $y/\delta_{99,\mathrm{CP}} < 0.1$ is due to the transition from a momentum dominated flow near the freestream to the viscosity dominated flow near the wall. Specifically, the momentum dominated flow is less sensitive to property changes as it is controlled mainly by the Reynolds stresses rather than shear caused by molecular viscosity.

The following section will validate the discussion of Pope [52] by taking an alternative view of the boundary layer. This will be accomplished by non-dimensionalizing with conditions near the wall using wall coordinates. It will be seen that, in line with Pope [52], wall coordinates collapse the boundary layers to a single curve in the near the wall region.

5.4.2 Non-dimensionalized by Wall Coordinates.

Unlike the previous section, this section will non-dimensionalize the boundary layer using wall coordinates. As discussed in Section 2.1.1, wall coordinates use conditions at the fluid-wall interface to non-dimensionalize the boundary layer. The momentum and thermal boundary layers calculated for $T_\infty = 1600\,\mathrm{K}$ at several T_w/T_∞

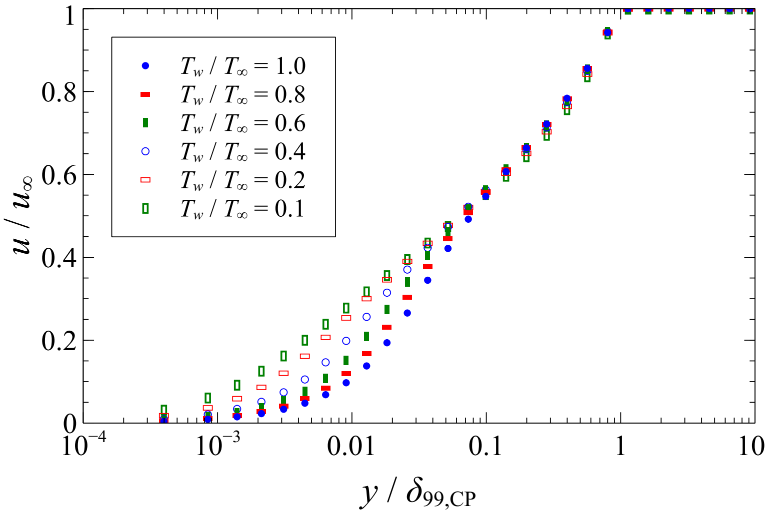

(a) Momentum boundary layer

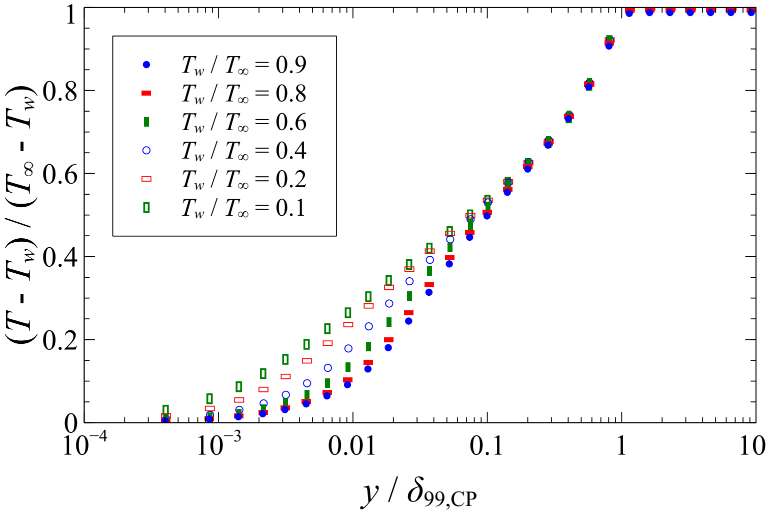

(b) Thermal boundary layer

Figure 5.20: Variation in the momentum and thermal boundary layers with temperature ratio (T_w/T_∞); $T_\infty = 1600\,\mathbf{K}$, $\mathbf{Re}_x = 250,000$

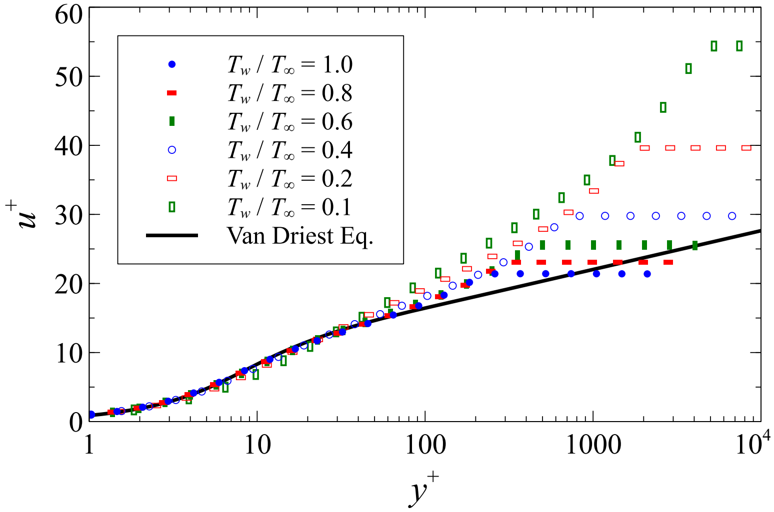

(a) Momentum boundary layer

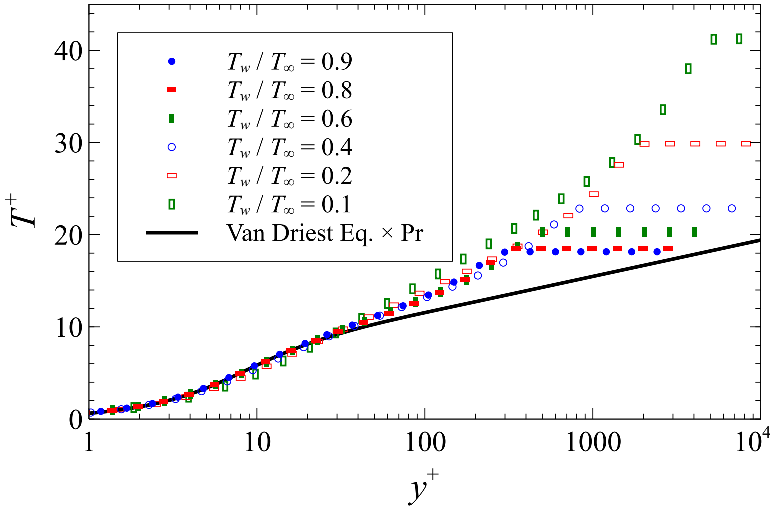

(b) Thermal boundary layer

Figure 5.21: Variation of the momentum and thermal boundary layers with temperature ratio (T_w/T_∞) in traditional wall coordinates; T_∞ = $1600\,\mathbf{K}$, $\mathbf{Re}_x = 250,000$

are plotted in Fig. 5.21 in wall coordinates. Similar to Fig. 5.19(a), the y^+-u^+ profiles seen in Fig. 5.21(a) are only plotted for the $T_\infty = 1600\,\mathrm{K}$ case due to the nearly identical profiles of the other two cases. Alternatively, small but significant differences were seen amongst the y^+-T^+ profiles of each T_∞ case at a given T_w/T_∞. However, Section 5.4.3 will show that introducing a subtle modification to the traditional wall coordinates results in excellent agreement amongst all the temperature profiles. Therefore, at present, only the $T_\infty = 1600\,\mathrm{K}$ case will be discussed as it represents the qualitative trends of the other T_∞ cases.

As discussed, the previous section used freestream conditions to non-dimensionalize the boundary layer. In doing so, it was seen that the u and T profiles of each T_w/T_∞ case considered collapsed to a single curve for $0.1 < y/\delta_{99,\mathrm{CP}}$. In contrast, the present section uses wall coordinates to non-dimensionalize the u and T profiles by characteristics of the boundary layer at the wall. Accordingly, examining Fig. 5.21 reveals that the y^+-u^+ and y^+-T^+ profiles of all the T_w/T_∞ cases plotted adhere to the constant property Van Driest mixing length equation for $y^+ < 50$. Alternatively, the y^+-u^+ and y^+-T^+ profiles were seen to diverge for $y^+ > 50$. Interestingly, Pope [52] defines $y^+ < 50$ as the viscous wall region where viscosity makes a significant contribution to the shear stress. Since the u^+ wall coordinate non-dimensionalizes u using the shear at the wall, it makes sense that the wall coordinate non-dimensionalization is only effective in the $y^+ < 50$ viscous wall region.

Though differences between the y^+-u^+ and y^+-T^+ profiles at each T_w/T_∞ can be identified for $y^+ > 50$, they tend to be small for the cases with $T_w/T_\infty \geq 0.4$ and for y^+ between 50 and the wake region. Alternatively, the wake region is seen to extend to higher u^+ with decreased T_w/T_∞.

Figure 5.21 indicates that the profiles with $T_w/T_\infty < 0.4$ begin to deviate significantly from the constant property curves for $y^+ > 30$. Interestingly, it was asserted in

Section 5.1.2 that letting $m = -0.28$ and $n = -0.20$ in the temperature ratio method of Kays et al. [29] accurately captured variable property effects for $0.3 \leq T_w/T_\infty \leq 1$. Connecting these two results suggests that the ability to use a single value for m and n on $0.3 \leq T_w/T_\infty \leq 1$ is due to the minimal deviation of the y^+-u^+ and y^+-T^+ profiles from the constant property theory.

In addition to the deviation amongst the data for $y^+ > 50$, the y^+ location of the wake region is also seen to shift to a larger y^+ with decreasing T_w/T_∞. This is due to the increased τ_w with decreasing T_w/T_∞. Consulting Eq. 2.7 reveals that increasing τ_w results in an increased y^+ at a constant y. The following section will further examine the divergence for $y^+ > 50$. Subsequently, a subtle modification to the wall coordinate non-dimensionalization will be proposed to increase the agreement amongst the data at arbitrary T_w/T_∞ for $y^+ > 50$.

5.4.3 Non-Dimensionalized by Modified Wall Coordinates.

As discussed in Section 2.1.1, wall coordinates (Eqs. 2.7-2.9) were developed assuming the properties within the boundary layer were constant. As such, turbulent boundary layer theory does not explicitly state where in the boundary layer the the non-dimensionalizing properties should be evaluated. Thus, since wall coordinates are intended to non-dimensionalize by conditions near the wall, it was assumed that traditional wall coordinates require evaluation of properties at the wall. Despite this understanding of traditional wall coordinates, it was seen in the previous section that the y^+-u^+ and y^+-T^+ profiles of $T_w/T_\infty < 1$ cases could vary significantly from the constant property y^+-u^+ and y^+-T^+ profiles.

By rearranging the definition of u_τ given in Eq. 2.10, it is seen that

$$\tau_w = \rho_w u_\tau^2 \tag{5.16}$$

From this equation it is seen that the physical meaning of u_τ is a velocity characteristic of the momentum being dissipated at the wall. Subsequently, for a constant property flow, the definition of u^+ can be rearranged to give

$$u^+ = \sqrt{\frac{\rho_w u^2}{\tau_w}} \tag{5.17}$$

From this form, it is seen that u^+ has physical meaning as square root of the ratio of momentum in the x-direction at a given y^+ to momentum being dissipated at the wall.

By embracing these physical definitions of u_τ and u^+ it is seen that letting $u_\tau = \sqrt{\tau_w/\rho_w}$ no longer gives the square root of the ratio of momentum present at a given y^+ to momentum being dissipated at the wall. This is due to the variability of ρ within the boundary layer. A direct consequence of this observation is the asymptotic deviation of the wake region with decreasing T_w/T_∞ seen in Fig. 5.20.

To rectify the deficiencies of traditional constant property wall coordinates, the following modified wall coordinates are proposed:

$$y^* = \frac{y u_\tau^*}{\nu} \tag{5.18}$$

$$u^* = \frac{u}{u_\tau^*} \tag{5.19}$$

$$T^* = \frac{(T_w - T) u_\tau^*}{q''/\rho c_p} \tag{5.20}$$

where

$$u_\tau^* = \sqrt{\tau_w/\rho} \tag{5.21}$$

The subtle difference of these modified wall coordinates is that they prescribe evaluation of the properties locally rather than at the wall. Additionally, it is seen from these equations that the modified wall coordinates equal the traditional wall coordinates in a constant property flow.

Figure 5.22 shows the result of applying the modified wall coordinates presented above to the u and T profiles calculated via CFD and discussed in the previous sections. The y^*-u^* and y^*-T^* profiles seen in Fig. 5.22 are presented without regard to T_∞ because the profiles were indistinguishable amongst the three T_∞ at a given Re_x and T_w/T_∞.

Similarly, the previous section presented that the y^+-u^+ profiles were nearly identical T_∞ at a given Re_x and T_w/T_∞. However, small but significant differences were seen in the y^+-T^+ profiles like that seen in Fig. 5.23(a). Interestingly, converting from traditional wall coordinates to the modified wall coordinates presented above is seen in Fig. 5.23(b) to collapse the T profiles to a single curve.

Comparing Figs. 5.21 and 5.22 shows that the modified wall coordinates cause the momentum and thermal profiles to collapse toward the non-dimensional constant property momentum and thermal profile, respectively. However, clear deviations in the y^*-u^* and y^*-T^* profiles from their constant property profiles can be seen in Fig. 5.22. The next section will discuss this nuance and explain why the qualitative trends are physically reasonable.

5.4.4 Apparent Wall Suction.

Upon first examination of Fig. 5.22, it seems the modified wall coordinates proposed in the previous section are useful but do not perfectly collapse the data to a single non-dimensional curve. However, the continuous decrease in u^* with T_w/T_∞ for $y^* > 10$ is analogous to another flow regime: the turbulent boundary layer with wall suction.

Due to wall shear extracting momentum from a wall bounded flow, a zero-pressure-

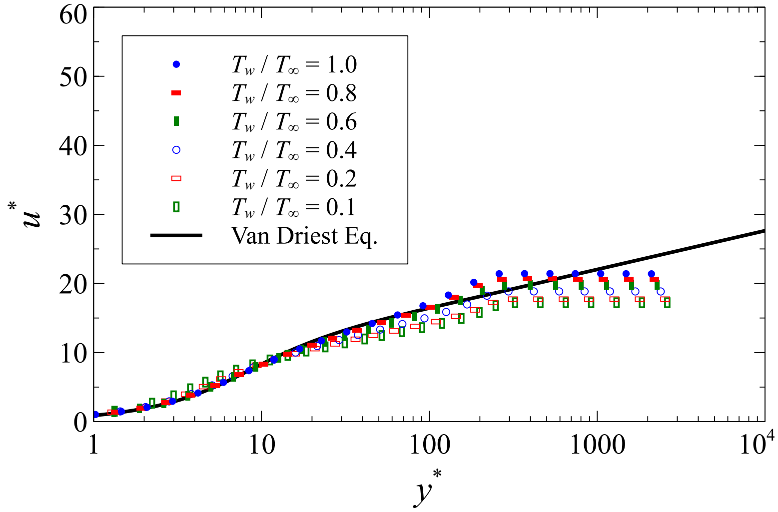

(a) Momentum boundary layer

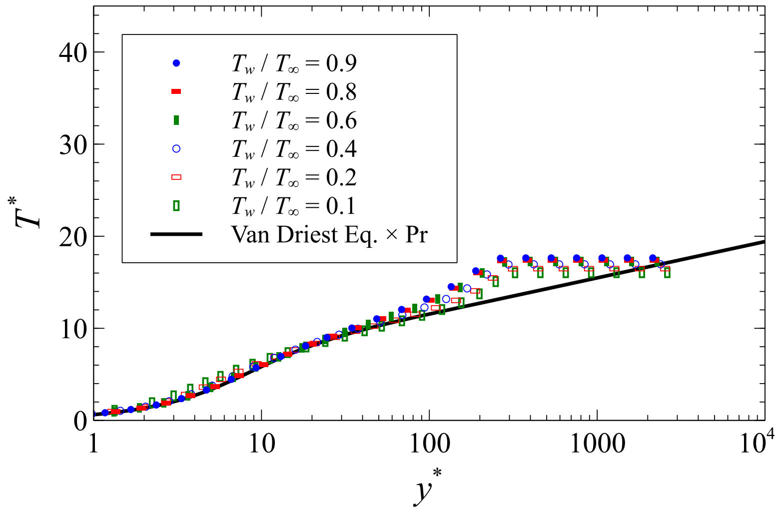

(b) Thermal boundary layer

Figure 5.22: Variation of the momentum and thermal boundary layers with temperature ratio (T_w/T_∞) in modified wall coordinates; $T_\infty = 1600\,\mathbf{K}$, $\mathbf{Re}_x = 250,000$

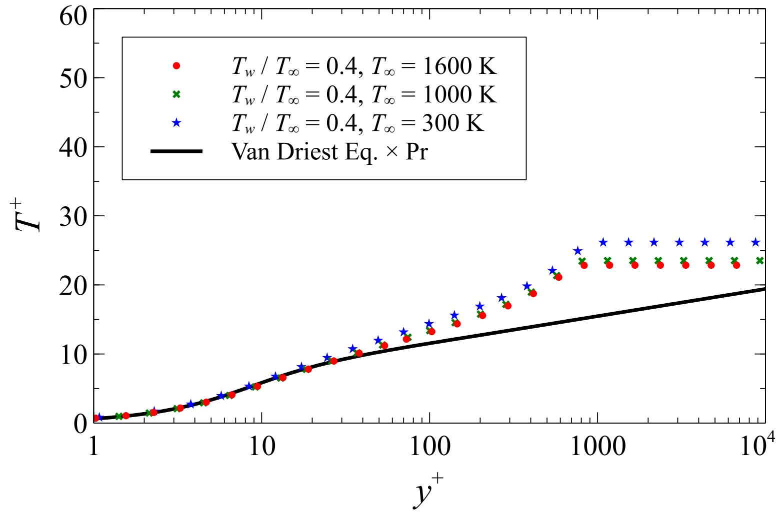

(a) Traditional Wall Coordinates

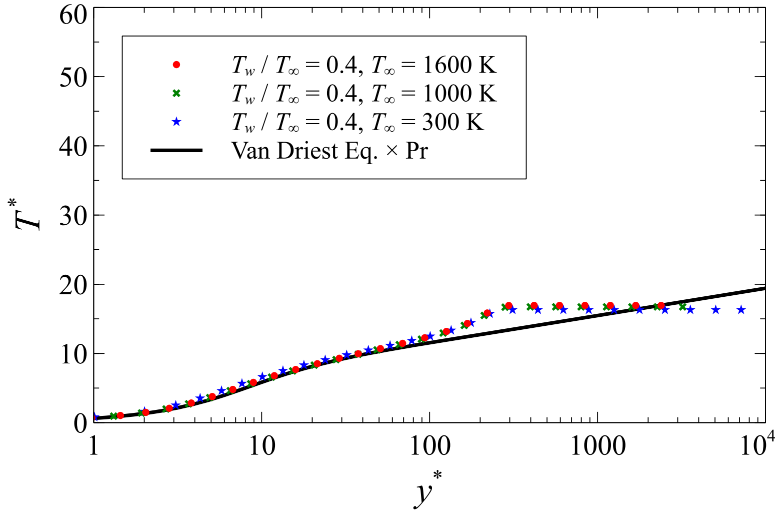

(b) Modified Wall Coordinates

Figure 5.23: Variation of the thermal boundary layer with T_∞ at $T_w/T_\infty = 0.4$ in traditional and modified wall coordinates; Re$_x = 250,000$

gradient boundary layer will constantly decelerate with distance from the leading edge. Thus, to satisfy continuity, the boundary layer velocity profile will have a vertical component away from the wall. Wall suction will effectively reduce the magnitude of this vertical component or, for sufficiently large wall suction, reverse the vertical component.

Simpson [58] utilized a porous surface to apply suction to a constant property turbulent boundary layer. His measurements indicated that wall suction cases u^+ to decrease for $y^+ > 10$. An analogous process occurs in the present simulations. Due to the wall's constant cooling of the boundary layer, all locations within the boundary layer are cooling and becoming more dense with distance from the leading edge. Thus, continuity dictates that, from a Lagrangian view, the particles in the $y^+ > 10$ region would see suction in the direction of the wall.

Figure 5.24 visualizes the effect of cooling and contracting on the wall normal component. From this figure it is clear that near the wall has a wall normal component of mass flux that increases with T_w/T_∞. This is attributable to the increasing shear at the wall with decreasing T_w/T_∞ as discussed in Sections 5.1.1 and 5.1.2. The increase in shear causes a larger streamwise decelerating velocity gradient resulting in an increased upward mass flux to satisfy continuity.

Alternatively, further from the wall the normal component was seen to decrease with T_w/T_∞. As discussed above, this is a direct result of the cooling and contracting of the boundary layer. The decreasing temperature in the streamwise direction and subsequent increasing density reduces the vertical component of mass flux to satisfy continuity. The effects of increased wall normal mass flux due to increased wall shear and decreased wall normal mass flux due to increasing density are present throughout the boundary layer. However, the individual effects become dominant near the wall and further from the wall, respectively, as seen in Fig. 5.24.

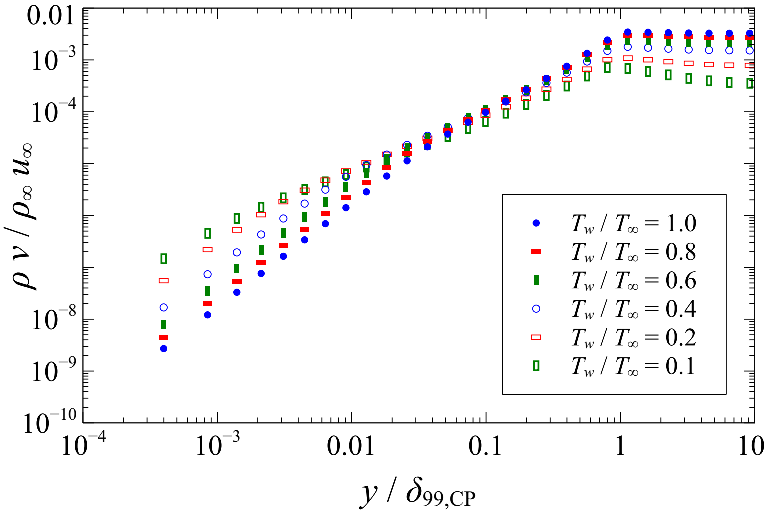

(a) Distance from wall (y) normalized by freestream condition

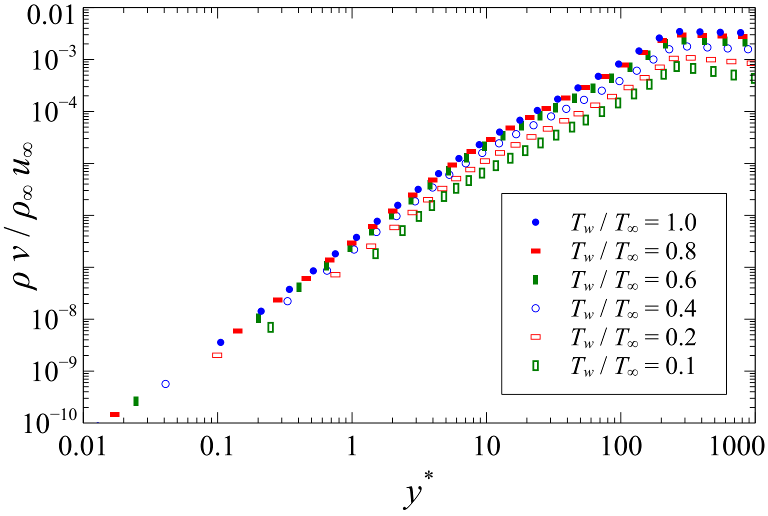

(b) Distance from wall (y) normalized by modified wall coordinates

Figure 5.24: Variation of wall normal mass flux (ρv) with temperture ratio (T_w/T_∞); $T_\infty = 1600\,\mathrm{K}$, $\mathrm{Re}_x = 250,000$

Figure 5.24(b) takes an alternate view of the vertical component by normalizing y using the modified wall coordinate, y^* (Eq. 5.18). The figure shows that at any given y^*, the vertical component decreases with decreasing T_w/T_∞. In addition, the amount that the vertical component decreases from the constant property ($T_w/T_\infty = 1$) vertical component decreases with y^*. This observation is in line with the results of Fig. 5.22 where the apparent suction is stronger at large y^* and decreases to an indistinguishable effect at $y^* < 10$.

Ultimately, the cooling and contracting of the boundary layer resulted in trends identical to those seen in Simpson's [58] boundary layer measurements with wall suction. The analogy to his data is that decreasing T_w/T_∞ results in increased cooling and contracting of the boundary layer. Thus, decreasing T_w/T_∞ produced an effect identical to increased wall suction. Namely, the u^* of the present computations decreased for $y^* > 10$ with decreasing T_w/T_∞. The following section will explore the effect of the increased degree of contracting of the boundary layer and increased shear stress with decreasing T_w/T_∞ on the boundary layer's characteristic thicknesses.

5.4.5 Boundary Layer Thickness.

Examining the boundary layer's characteristic thicknesses assists in further understanding of effects of increased shear and density. Specifically, Fig. 5.25 shows how the velocity boundary layer thickness (δ_{99}), displacement thickness (δ_1), and momentum thickness (δ_2) change with T_w/T_∞. As expected, the increase in boundary layer density with T_w/T_∞ was seen to decrease δ_1. Similarly, the increase in wall shear stress with T_w/T_∞ was seen to increase δ_2.

Last, δ_{99} was seen to be an extremely weak function of T_w/T_∞. Only the $T_\infty = 300\,\mathrm{K}$ was seen to have a δ_{99} that decreases slightly with T_w/T_∞. This seems to indicate that δ_{99} is mainly a function of the turbulent mixing of the boundary layer

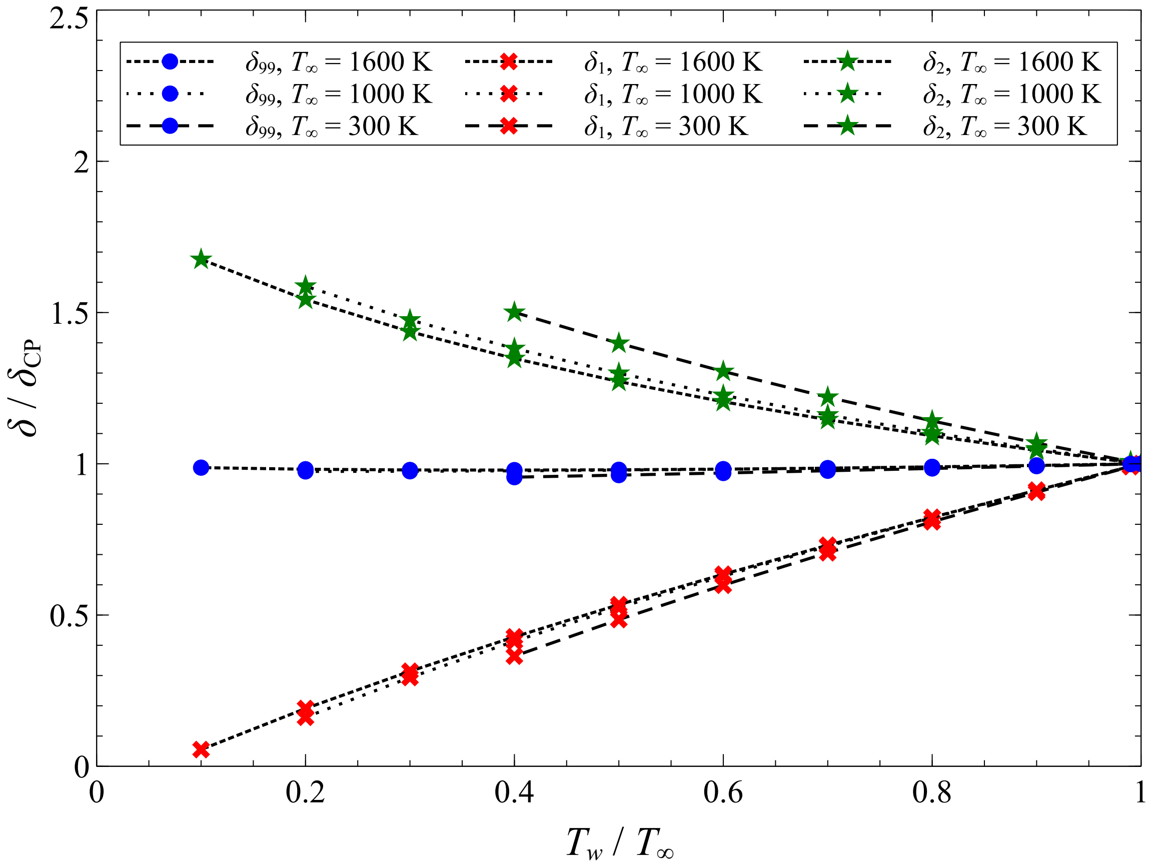

Figure 5.25: Variation of the velocity boundary layer thickness (δ_{99}), displacement thickness (δ_1), and momentum thickness (δ_2) with temperature ratio (T_w/T_∞)

and not of the thermodynamic or diffusion properties of air.

It was seen in Section 5.1.1 that the reference method of Eckert [15] accurately predicted $\tau_w/\tau_{w,\mathrm{CP}}$ and h/h_{CP} for the $T_\infty = 1600\,\mathrm{K}$ and $1000\,\mathrm{K}$ cases across all T_w/T_∞ examined. However, his method was seen to be less accurate for the $T_\infty = 300\,\mathrm{K}$ case. Similar to this result, the δ_{99}, δ_1, and δ_2 of the $T_\infty = 1600\,\mathrm{K}$ and $1000\,\mathrm{K}$ cases are seen in Fig. 5.25 to follow a common curve. Alternatively, the $T_\infty = 300\,\mathrm{K}$ case is seen to diverge from the curves of the other two T_∞ cases. Granted, the deviation in δ_{99} is small, but visible. This is another testimony to the different nature of the $T_\infty = 300\,\mathrm{K}$ case likely caused by the different trends of the fluid properties at very low temperatures. Even so, the following section will use the knowledge gained in this section to derive a model which captures the variable property effects of all three T_∞ cases considered.

5.5 Novel Variable Property Method

The majority of this chapter was spent validating the existing variable property method of Kays et al. [29] to satisfy Objective 1 of the present research. In doing so, a deeper fundamental understanding of how variable properties effect a boundary layer was gained. This section will take advantage of the knowledge gained thus far to develop an alternative variable property method to assist in augmenting Objective 1 of the present research. Finally, this section will compare the newly developed variable property model to the temperature ratio method of Kays et al. [29].

It should be noted that the following process was examined at several Re_x. It was found that the results were a very weak function of Re_x. Thus, the below figures were created using the data at $\mathrm{Re}_x = 250,000$ but are representative of the results at all fully turbulent Re_x in the following development.

5.5.1 Development.

It was shown in Section 5.4.2 that regardless of T_∞ or T_w/T_∞, all cases considered collapsed to the analytical u^+ and T^+ curves in the viscous sublayer. To take advantage of this observation, consider how the turbulent boundary layer is defined. Adjacent to the wall, there is a viscous sublayer in which molecular viscosity dominates over momentum. Farther from the wall is a region where turbulent mixing and inertia dominate over molecular viscosity. Between these two regions is a transition from viscosity dominated to momentum dominated. The range of distances off the wall (y) of these zones are defined by balancing the relative effects of momentum and viscosity. Namely, they are defined by a characteristic Reynolds number, y^+.

Now, rather than using y^+ as the characteristic Reynolds number, consider

$$\mathrm{Re}_y = \frac{\rho u y}{\mu} \tag{5.22}$$

where ρ, u, and μ are evaluated at y. Next, consider a Re_y value that is small enough to meet two conditions. First, that it resides within the viscous sublayer. Second, that the temperature at Re_y is close enough to T_w such that the properties at the location can be approximated as equal to the properties at the wall. A location satisfying these conditions will be referred to as being a distance of $y = \delta_3$ from the wall with a corresponding Reynolds number of Re_{δ_3}. An infinite number of δ_3 exist near the wall. In addition, this definition requires a precise criterion for what constitutes properties that are approximately equal to those at the wall. To avoid this conundrum, a limit as Re_{δ_3} goes to zero will be used to ensure that the properties at δ_3 are, by definition, those at the wall.

Since δ_3 is defined to be within the viscous sublayer and the properties between the wall and δ_3 are constant, the velocity gradient is also constant such that

$$u(\delta_3) = \delta_3 \frac{\mathrm{d}u}{\mathrm{d}y} = \delta_3 \frac{\tau_w}{\mu_w} \tag{5.23}$$

Thus, the Reynolds number can be rewritten as

$$\mathrm{Re}_{\delta_3} = \frac{\rho_w u(\delta_3)\delta_3}{\mu_w} = \frac{\rho_w \tau_w \delta_3^2}{\mu_w^2} \tag{5.24}$$

Next, the constant property boundary layer and the variable property boundary layer at an arbitrary T_w/T_∞ can be compared at a constant Reynolds number such that

$\mathrm{Re}_{\delta_{3,\mathrm{CP}}} = \mathrm{Re}_{\delta_3}$. Then, by taking a limit,

$$\lim_{\mathrm{Re}_{\delta_3} \to 0} \frac{\mathrm{Re}_{\delta_3}}{\mathrm{Re}_{\delta_{3,\mathrm{CP}}}} = \frac{\rho_w \tau_w \delta_3^2 / \mu_w^2}{\rho_\infty \tau_{w,\mathrm{CP}} \delta_{3,\mathrm{CP}}^2 / \mu_\infty^2} = 1 \tag{5.25}$$

Finally, solving for τ/τ_{CP} gives

$$\frac{\tau_w}{\tau_{w,\mathrm{CP}}} = \left(\frac{\mu_w}{\mu_\infty}\right)^2 \left(\frac{\rho_w}{\rho_\infty}\right)^{-1} \left(\frac{\delta_3}{\delta_{3,\mathrm{CP}}}\right)^{-2} \tag{5.26}$$

However, Eq. 5.26 requires knowledge of $\delta_3/\delta_{3,\mathrm{CP}}$. To attempt to parameterize $\delta_3/\delta_{3,\mathrm{CP}}$, first $\delta_3/\delta_{3,\mathrm{CP}}$ was quantified for each computational case considered. This was accomplished by solving Eq. 5.26 with the properties known at the boundary conditions and the shear stresses calculated by the simulation. Next, it was assumed that $\delta_3/\delta_{3,\mathrm{CP}}$ was a function of viscosity and density such that

$$\frac{\delta_3}{\delta_{3,\mathrm{CP}}} = \left(\frac{T_w}{T_\infty}\right)^{\beta_1} \left(\frac{\mu_w}{\mu_\infty}\right)^{\beta_2} \tag{5.27}$$

where β_1 and β_2 are empirical powers to fit the data. It should be noted that the pressure was constant through out the computational domain and amongst cases. Therefore $T_w/T_\infty = \rho_\infty/\rho_w$, and they will be used interchangeably in the present analysis.

Attempting to optimize β_1 and β_2 simultaneously could yield several sets of β_1 and β_2 which each model the data equally well. Thus, to ensure the uniqueness of β_1 and β_2, a simplification of Eq. 5.27 was introduced. This simplification involved examining Sutherland's law. The law is a reasonably accurate function for μ at moderate temperatures and is defined by White [68] as

$$\mu(T) = \mu_0 \left(\frac{T}{T_0}\right)^{3/2} \frac{T_0 + S}{T + S} \tag{5.28}$$

where, for air, $\mu_0 = 1.72 \times 10^{-5}\,\mathrm{Pa \cdot s}$, $T_0 = 273.11\,\mathrm{K}$, and $S = 110.56\,\mathrm{K}$. Using Eq. 5.28, the ratio of μ_w/μ_∞ can be written as

$$\frac{\mu_w}{\mu_\infty} = \left(\frac{T_w}{T_\infty}\right)^{3/2} \frac{T_\infty + S}{T_w + S} \tag{5.29}$$

From this equation, it is seen that for T_w and T_∞ much greater than S,

$$\frac{\mu_w}{\mu_\infty} \approx \left(\frac{T_w}{T_\infty}\right)^{1/2} \tag{5.30}$$

Using this observation allows simplification of Eq. 5.27 when T_∞ and T_w are large such that

$$\frac{\delta_3}{\delta_{3,\mathrm{CP}}} \approx \left(\frac{T_w}{T_\infty}\right)^{\beta_3} \tag{5.31}$$

where $\beta_3 = \beta_1 + \beta_2/2$. This form effectively reduced the number of optimization parameters to one such that β_3 could be determined uniquely.

It was found that allowing $\beta_3 = 5/4$ such that

$$\beta_1 = 5/4 - \beta_2/2 \tag{5.32}$$

tended to match the large T_∞ and T_w data well as seen in Fig. 5.26(a). Specifically, Eqs. 5.31 and 5.32 were seen to predict the $\delta_3/\delta_{3,\mathrm{CP}}$ of the $T_\infty = 1600\,\mathrm{K}$ and $1000\,\mathrm{K}$ cases within 2% for $0.5 < (T_w/T_\infty)^{5/4} < 1.0$. Outside this range and for the $T_\infty = 300\,\mathrm{K}$ case, T_∞, T_w, or both T_∞ and T_w did not sufficiently large to allow simplification of μ_w/μ_∞ from Eq. 5.29 to 5.30. Accordingly, Eqs. 5.31 and 5.32 produced a poor prediction of the $\delta_3/\delta_{3,\mathrm{CP}}$ data.

Next, the simplified function of Eq. 5.31 was be extended to low T_∞ and T_w. Since β_1 was defined as a function of β_2 by Eq. 5.32, β_2 was the only parameter which remained to be determined. This was accomplished by adjusting β_2 to allow

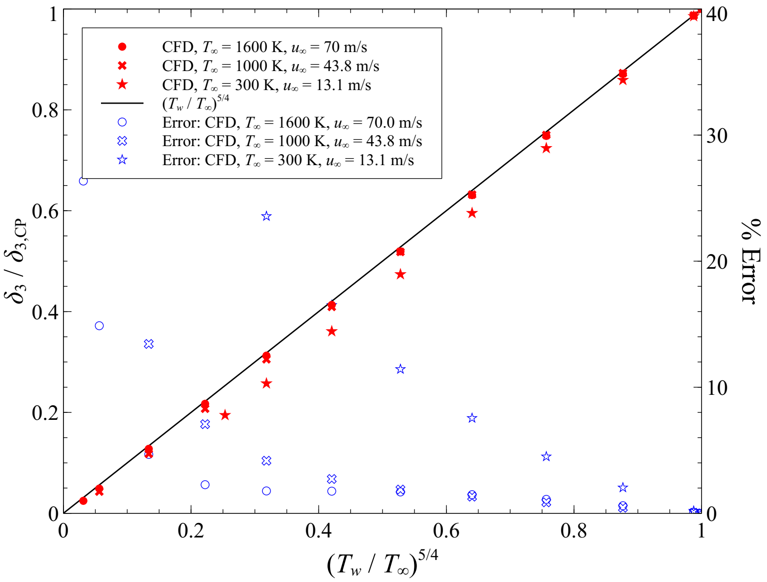

(a) Simplified viscosity ratio, Eq. 5.31

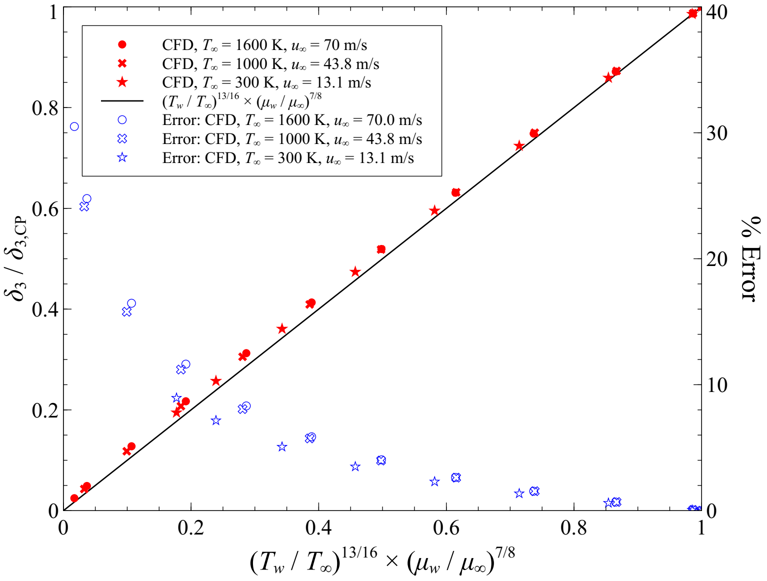

(b) Not simplified, Eq. 5.27

Figure 5.26: Linearization of $\delta_3/\delta_{3,\mathrm{CP}}$

Eq. 5.27 to more accurately predict the $\delta_3/\delta_{3,\mathrm{CP}}$ across all cases considered. This process found that $\beta_1 = 13/16$ and $\beta_2 = 7/8$ most accurately predicted the data across the three freestream conditions considered as seen in Fig. 5.26(b). The errors are seen to rise asymptotically as $\delta_3/\delta_{3,\mathrm{CP}}$ goes to zero. Nevertheless, the errors of each case are seen to follow a somewhat consistent curve amongst the three T_∞ cases.

Combining the β_1 and β_2 derived above with Eqs. 5.26 and 5.27 asserts that

$$\frac{\tau_w}{\tau_{w,\mathrm{CP}}} = \left(\frac{T_w}{T_\infty}\right)^{-5/8} \left(\frac{\mu_w}{\mu_\infty}\right)^{1/4} \tag{5.33}$$

The shear stress data are plotted using this function in Fig. 5.27(a). This figure shows that the data deviates significantly from the expected curve. However, the plot shows that each case was non-dimensionalized to a single, though unknown, curve.

Next, Eq. 5.33 was transformed using Prandtl number to examine this method's ability to capture the variation of h/h_{CP} with T_w/T_∞. Since the above derivation has focused on a region of the boundary layer very close to the wall, the role of Prandtl number on the viscous sublayer was used in the transformation. Specifically, Eqs. 2.11 and 2.12 define the viscous sublayer in wall coordinates as $u^+ = y^+$ and $T^+ = \mathrm{Pr}\, y^+$, respectively. Thus, Prandtl number was used to transform Eq. 5.33 in an analogous fashion such that

$$\frac{h}{h_{\mathrm{CP}}} = \frac{\tau_w}{\tau_{w,\mathrm{CP}}} \left(\frac{\mathrm{Pr}_w}{\mathrm{Pr}_\infty}\right) = \left(\frac{T_w}{T_\infty}\right)^{-5/8} \left(\frac{\mu_w}{\mu_\infty}\right)^{1/4} \left(\frac{\mathrm{Pr}_w}{\mathrm{Pr}_\infty}\right) \tag{5.34}$$

The result of applying this equation is seen in Fig. 5.27(b). Again, significant deviations were seen from the expected analytical curve, but the cases are seen to cling to a common, though unknown, curve.

The collapsing of the three cases to common $\tau_w/\tau_{w,\mathrm{CP}}$ and h/h_{CP} curves indicates that the β_1 and β_2 powers derived above capture some of the physics present in the

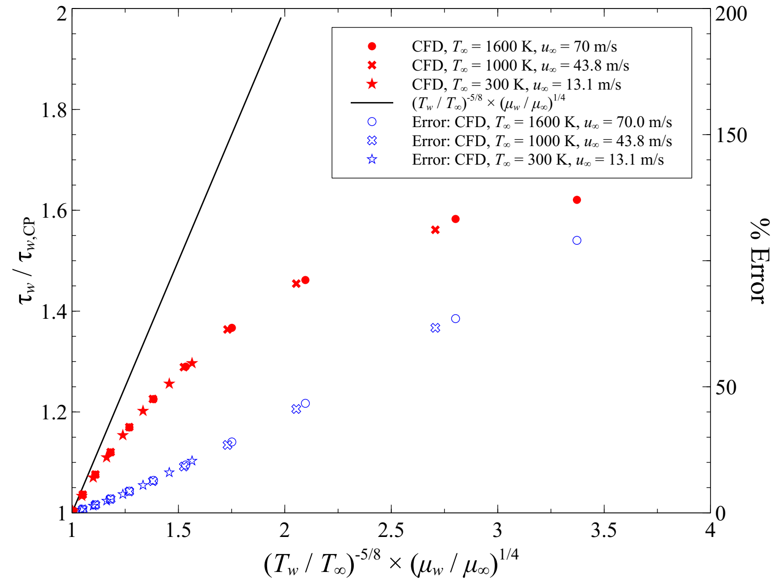

(a) Wall shear stress

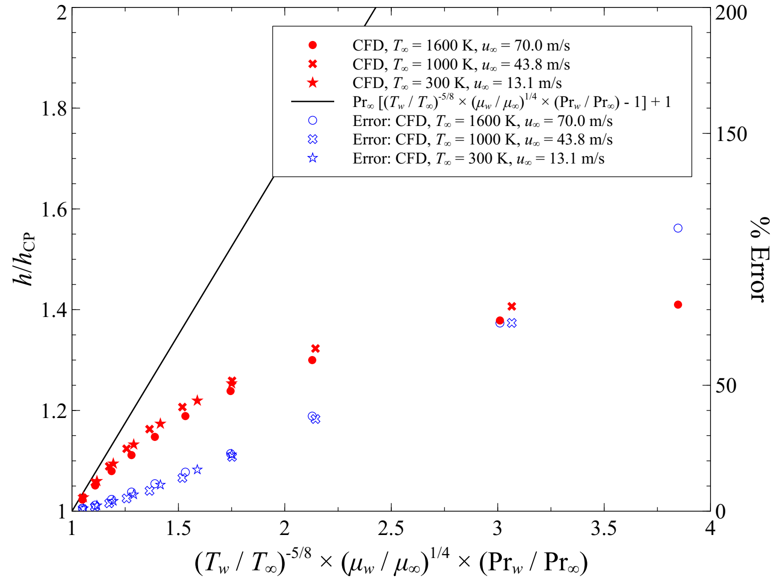

(b) Convective heat transfer coefficient

Figure 5.27: Linearization of variable property effects on wall shear stress (τ_w) and convective heat transfer coefficient (h)

data. Thus, to build upon the success Eqs. 5.33 and 5.34 were adjusted to better fit the data. Specifically, in each case the function plotted on the abscissa axis was inverted to produce the data in Fig. 5.28. Though this process does not stem directly from the derivations above, the figure displays the data of each case falling into a linear trend.

It was found that the linearized trend of the shear stress data in Fig. 5.28(a) was best modeled by

$$\frac{\tau_w}{\tau_{w,\mathrm{CP}}} = 0.82\left[1 - \left(\frac{T_w}{T_\infty}\right)^{5/8}\left(\frac{\mu_w}{\mu_\infty}\right)^{-1/4}\right] + 1 \tag{5.35}$$

It was seen that the $\tau_w/\tau_{w,\mathrm{CP}}$ data deviates from Eq. 5.35 somewhat for $(T_w/T_\infty)^{5/8}(\mu_w/\mu_\infty)^{-1/4} < 0.6$. However, the error of these data points are contained to less than 4%. Moreover, they correspond to temperature ratios of $T_w/T_\infty < 0.4$, which is likely a range which is irrelevant to most engineering applications. Alternatively, for $(T_w/T_\infty)^{5/8}(\mu_w/\mu_\infty)^{-1/4} > 0.6$ ($T_w/T_\infty > 0.4$), Eq. 5.35 was seen to model the $\tau_w/\tau_{w,\mathrm{CP}}$ data to within 1%. Most importantly, the error compared to Eq. 5.35 was seen to follow a nearly identical trend for all T_∞ cases considered. This is in direct contrast to the methods of Eckert [15] and Kays et al. [29] which were seen in Section 5.1 to produce different trends in error for each T_∞ case examined.

Similarly, it was found that the linearized trend of the heat transfer coefficient ratio data in Fig. 5.28(b) was best captured by

$$\frac{h}{h_{\mathrm{CP}}} = 0.82\mathrm{Pr}_\infty\left[1 - \left(\frac{T_w}{T_\infty}\right)^{5/8}\left(\frac{\mu_w}{\mu_\infty}\right)^{-1/4}\left(\frac{\mathrm{Pr}_w}{\mathrm{Pr}_\infty}\right)^{-1}\right] + 1 \tag{5.36}$$

Again, this model for the h/h_{CP} trends was developed by using the $\tau_w/\tau_{w,\mathrm{CP}}$ model (Eq. 5.35) and adding a Prandtl number factor. Unlike the $\tau_w/\tau_{w,\mathrm{CP}}$ data in Fig. 5.28(a), the h/h_{CP} data are seen in Fig. 5.28(b) to cling to Eq. 5.36 within 2% over

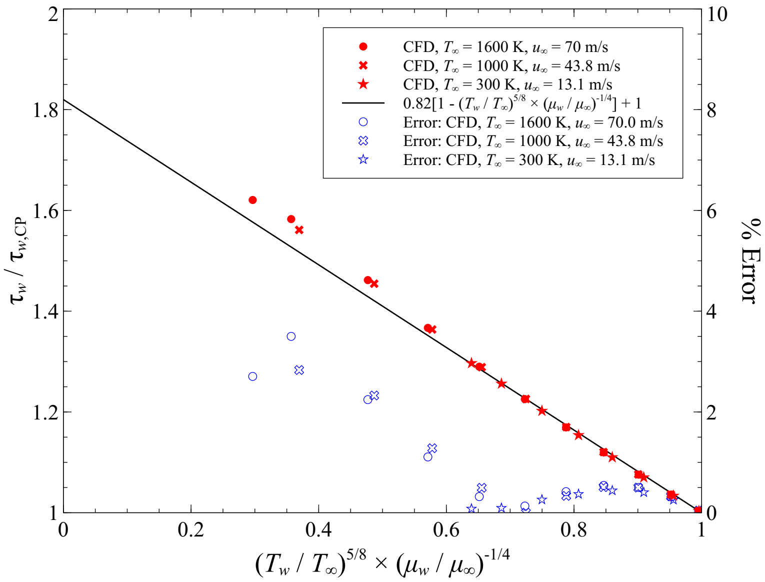

(a) Wall shear stress

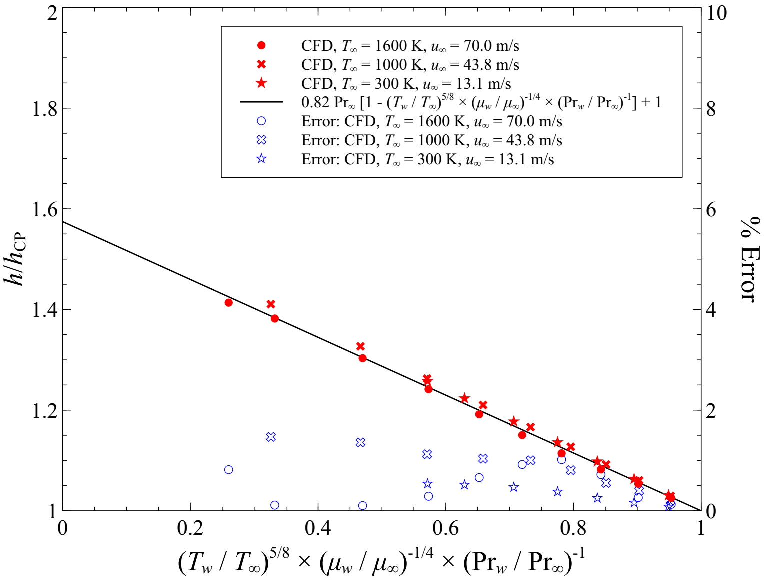

(b) Convective heat transfer coefficient

Figure 5.28: Adjusted linearization of variable property effects on wall shear stress (τ_w) and convective heat transfer coefficient (h)

the whole range. It should be noted that, since Eq. 5.36 includes a Pr_∞ factor in the slope, each T_∞ case has a slightly different analytical curve. For simplicity, Fig. 5.28(a) only shows the $T_\infty = 1600\,\mathrm{K}$ curve, but the error of each T_∞ case was calculated using their respective evaluations of Eq. 5.36.

5.5.2 Comparison with the Method of Kays et al.

Section 5.1.2 used computational data to validate the variable property method of Kays et al. [29]. The computational data were used to determine appropriate empirical coefficients of m and n to account for variable properties in τ_w and h via Eqs. 2.24 and 2.25, respectively. It was seen that no single values of m and n was ideal over the entire range of $0 < T_w/T_\infty < 1$. Rather, it was seen that the entire range considered could be modeled by allowing m and n to vary with T_w/T_∞ according to Eqs. 5.2 and 5.3, respectively. However, these functions were derived by fitting to the computational data rather than from a physics based derivation.

To better understand the physics of variable properties, Section 5.4 examined how the boundary layer varied with T_w/T_∞. The knowledge gained from this examination was then used in the previous section to develop a new method to account for the effect of variable properties. The semi-empirical approach resulted in models for $\tau_w/\tau_{w,\mathrm{CP}}$ and h/h_{CP} given by Eqs. 5.35 and 5.36, respectively.

These models were seen to collapse the computational data of three cases with $T_\infty = 1600\,\mathrm{K}$, $1000\,\mathrm{K}$ and $300\,\mathrm{K}$, as seen in Fig. 5.28. This is an accomplishment which was not previously realized by the variable property methods of Eckert [15] (Figs. 5.1 and 5.2) and Kays et al. [29] (Figs. 5.4 and 5.5). However, compared to the method of Kays et al. [29], the variable property method derived in the previous section requires evaluation of viscosity as well as Prandtl number, in the case of h/h_{CP}.

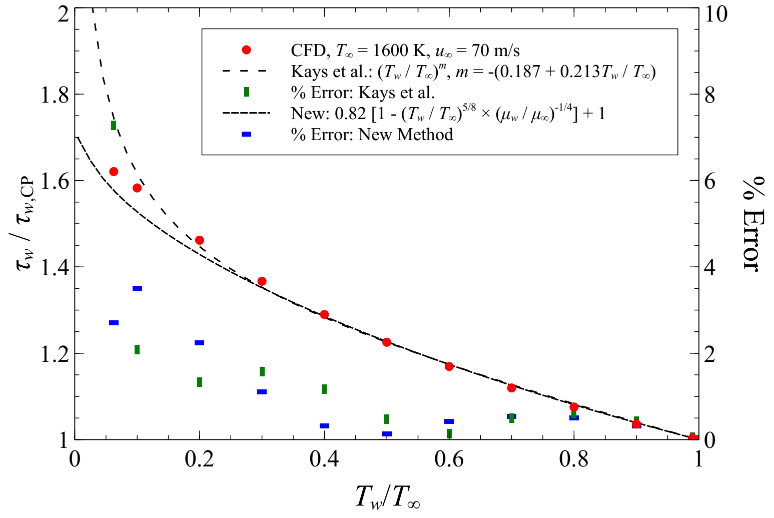

(a) Wall shear stress

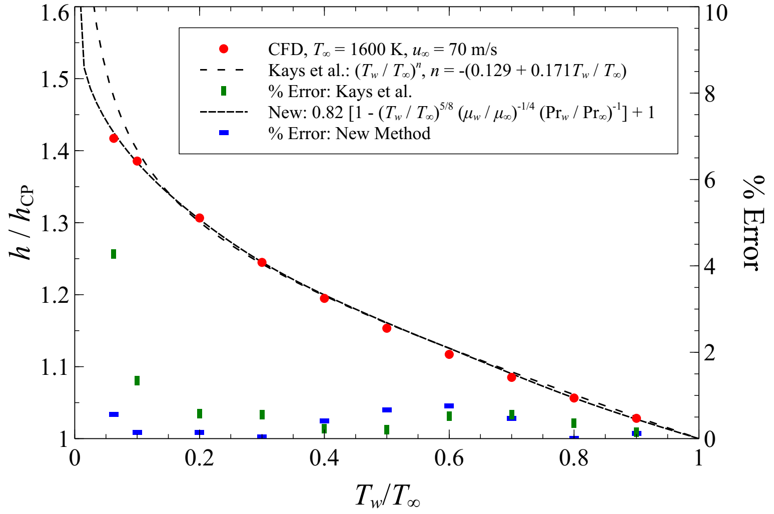

(b) Convective heat transfer coefficient

Figure 5.29: Comparison of the temperature ratio method of Kays et al. [29] and the method developed in Section 5.5.1

These additional evaluations add complexity to the model which must be justified. Thus, both models are plotted on Fig. 5.29 to compare their accuracy. Since the experimental portion of the present work is mainly concerned with high T_∞, only the $T_\infty = 1600\,\mathrm{K}$ computational data were examined. The figure shows that both the method of Kays et al. [29] and the method developed in the previous section have errors of less that 2% over $0.3 < T_w/T_\infty < 1$ for $\tau_w/\tau_{w,\mathrm{CP}}$ and over $0.1 < T_w/T_\infty < 1$ for h/h_{CP}.

These ranges cover the most practical applications including the experimental portion of the present research. Thus, since the method derived in the previous section does not increase accuracy, its additional complexity was deemed unnecessary for the present work. Moreover, the method was derived using computational data alone and required a leap in the derivation's logic to correct the major divergence from the data seen in Fig. 5.27. Alternatively, the temperature ratio method of Kays et al. [29] has been used and experimentally validated in other flow regimes. Thus, the established and significantly simpler method of Kays et al. [29] coupled with Eq. 5.10 will be used to quantify variable property convective heat transfer and radiative heat transfer in the following chapters in accordance with Objective 1 of the present work.

5.6 Chapter Summary

The focus of this chapter was on satisfying Objective 1 of the present research: to develop a method to measure the convective and radiative heat transfer components in a high temperature environment. The chapter began by addressing the convective component of this objective. Since convective heat transfer at high temperatures can have large differences between the freestream and wall temperature, large property variations can exist within the boundary layer.

Section 5.1 studied two existing methods to account for the effect of variable properties on both wall shear and convective heat transfer coefficient: the reference method of Eckert [15] and the temperature ratio method of Kays et al. [29]. However, neither of these methods have extensive validation for the the low speed, gaseous, turbulent flows of the present work. Thus, computations covering a variety of freestream conditions and wall to freestream ratios ranging from 0.0625 to one were used to computationally validate the existing variable property methods in a turbulent regime. Subsequently, an empirical exponent for the method of Kays et al. [29] which varied with temperature ratio was shown computationally to accurately capture variable property effects for temperature ratios less than one.

Next, Section 5.2 applied the methods of Eckert [15] and Kays et al. [29] to quantify the effect of variable properties on conventional constant property measurement techniques. It was seen that constant property methods can successfully be applied in environments with small freestream to wall temperature differences. However, when the temperature differences became large, constant property techniques were seen to vastly under-predict the adiabatic wall temperature and over-predict the convective heat transfer coefficient. Subsequently, a method to predict the adiabatic wall temperature and constant property convective heat transfer coefficient from non-adiabatic measurements was proposed.

Section 5.3 applied the temperature ratio method of Kays et al. [29] experimentally to an environment where both variable properties and radiative heat transfer played significant roles. A new technique was proposed to couple the method of Kays et al. [29] with radiative heat transfer theory to quantify the individual contribution of convective heat transfer and radiative heat transfer to the total heat transfer conducted into the test surface. The technique was then validated such that Objective 1 was satisfied.

Though the method of Kays et al. [29] was seen to be effective both computationally and experimentally, it required an exponent which was not rooted in underlying physics. Thus, to gain a better physical understanding of the effect of variable properties, a detailed analysis of the boundary layers from the computations of Section 5.1 was presented in Section 5.4. Next, Section 5.5 used the knowledge gained in Section 5.4 to develop a new method to account for variable properties using a semi-empirical approach. Finally, the new method was compared to the method of Kays et al. [29]. It was seen that, for the conditions relevant to the present work, no increase in accuracy was gained by using the new method. Thus, it was deemed that the much simpler model of Kays et al. [29] was most appropriate for use in the remainder of the present work.

Overall, this chapter developed a method to satisfy Objective 1 of this research. The resulting method to quantify convective and radiative heat transfer will be used in the following chapters. Specifically, Chapters VI and VII will use this technique to remove the ambient radiative heat transfer from measurements of non-reacting and reacting film cooling layers, respectively.

VI. Scaling Convective Heat Transfer: Film Cooling

Chapter V presented a method to account for variable property convective heat transfer and radiative heat transfer to satisfy Objective 1 of the present research. The current chapter will build on the knowledge gained in Chapter V and examine film cooling in a high temperature environment. Both computational and experimental studies will be presented with the ultimate intent of satisfying Objective 2 of the present research: Determine a methodology that enables scaling of non-reacting film cooling performance from near ambient conditions to engine conditions.

As discussed in the Chapter IV, experiments at combustion temperatures come with certain challenges like radiative heat transfer and limited flow diagnostic tools. Alternatively, Computational Fluid Dynamics (CFD) provides a unique venue for studying flows under carefully controlled scenarios. Moreover, CFD enables detailed examinations of the flow features. Thus, to develop the underlying theory to satisfy Objective 2 this chapter will first examine film cooling computationally. This examination will be used to suggest an appropriate, scalable parameter to quantify film cooling.

Though CFD provides distinct capabilities, it is inextricably linked to experimental validation. Thus, the latter portion of this chapter will be dedicated to experimental validation of the computational conclusions. However, the validation will be limited due to relatively small range of experimental factors which could be controlled in the present experimental facility. Thus, to augment the experimental validation, the qualitative trends of film cooling performance amongst various film cooling geometries and configurations will be examined. It will be shown that the performance trends observed in low temperature experiments scale accordingly to a combustion temperature experiment.

6.1 Computational Results

To establish the scalability of cooling performance in support of Objective 2, this section will utilize the shaped hole computational domain discussed in Section 4.3. In order, the parameters that will be studied are adiabatic effectiveness (η), Net Heat Flux Reduction (NHFR or $\Delta q''_f$), the ratio of film cooled to non-film cooled convective heat transfer coefficient (h_f/h_0), and, finally, the scalability of h_f via the temperature ratio method of Kays et al. [29]. For these studies, first, the computed performance of the film cooling scheme at a baseline engine temperature of 1829 K will be presented. Next, the performance of the cooling scheme at a condition near ambient with various schemes of non-dimensional matching will be examined. Finally, the high and low temperature results will be compared to determine the ability of the non-dimensional matching scheme to scale the film cooling performance from ambient to engine temperatures.

6.1.1 Scaling Adiabatic Film Effectiveness.

Several low temperature cases were developed to test the effect of matching select baseline flow parameters on matching the high engine temperature baseline cooling performance. A summary of the intent of each case is give in Table 6.1. To augment this summary, the full list of freestream and coolant conditions for both the high temperature baseline and the low temperature cases is provided in Table 6.2. It should be noted that, since the momentum equation for a boundary layer with wall blowing has a direct dependence on M, all cases will match the M of the high temperature case they are attempting to model.

To successfully model engine condition film cooling in a low temperature experiment, convective heat transfer theory [29] suggests that the relevant non-dimensional parameters must be matched. Specifically, these parameters include the Reynolds

Table 6.1: Short description of the intent of each low temperature experiment case presented in Table 6.2

Case	Description of case
BASE	Baseline high temperature case to be matched
1	Low temperature + Match M and Re_∞
2	Low temperature + Match M and Re_c
3	Low temp + Match M & DR but not Re_∞ or Re_c
4	Case 3 + Match all ratios via coolant properties
5	Case 4 + Match Re via fluid properties but not Pr
6	Case 4 + Match Re_∞ & Re_c via mass fluxes
7	Case 3 + Match Re_∞ via mass fluxes
8	Case 3 + Match Re_c via mass fluxes
9	Basline + $\rho_c u_c$ reduced by factor of 0.5
10	Case 7 + $\rho_c u_c$ reduced by factor of 0.5
11	Case 8 + $\rho_c u_c$ reduced by factor of 0.5
12	Basline + $\rho_c u_c$ increased by factor of 3
13	Case 7 + $\rho_c u_c$ increased by factor of 3
14	Case 8 + $\rho_c u_c$ increased by factor of 3

number of both the coolant hole (Re_c) and freestream (Re_∞), Prandtl number of the coolant (Pr_c) and freestream (Pr_∞). In addition, parameterization of film cooling [8] suggests that blowing ratio (M) and momentum ratio (I) must also be matched. Unfortunately, the nature of property variations with temperature requires one or more of these parameters to go unmatched.

Unlike laboratory experiments, CFD provides a venue for arbitrarily specifying properties such that any non-dimensional matching to an engine condition can be achieved. As seen in Table 6.2, Cases 3-5 modified the properties of the coolant to achieve various non-dimensional matchings which will be discussed more in Section 6.1.1.3. In addition to the coolant properties, Case 5 also modified the dynamic viscosity of the freestream.

In these cases, the properties' functions of temperature were modified from the real properties of air to a linear interpolation between the desired freestream property at T_∞ and the desired coolant property at T_c. This method forced the desired properties

Table 6.2: Full details of inlet conditions; † = matched to baseline, ‡ = approximately matched to baseline, * = artificially modified property

Property	BASE	Case 1	Case 2	Case 3	Case 4	Case 5	Case 6	Case 7	Case 8
T_c (K)	625	273	273	100	100	100	100	100	100
T_∞ (K)	1829	323	323	292	292	292	292	292	292
ρ_c (m^3/kg)	0.564	1.29	1.29	3.53	3.53	3.53	3.53	3.53	3.53
ρ_∞ (m^3/kg)	0.193	1.09	1.09	1.21	1.21	1.21	1.21	1.21	1.21
DR	2.92	1.18	1.18	**2.92** †	**2.92** †	**2.92** †	**2.92** †	**2.92** †	**2.92** †
$c_{p,c} \times 10^{-3}$ (J/kg K)	1.06	1.01 ‡	1.01 ‡	1.03 ‡	*0.828* *	*0.828* *	*0.828* *	1.03 ‡	1.03 ‡
$c_{p,\infty} \times 10^{-3}$ (J/kg K)	1.29	1.01	1.01	1.01	1.01	1.01	1.01	1.01	1.01
$c_{p,c}/c_{p,\infty}$	0.822	0.998	0.998	1.03	**0.822** †*	**0.822** †*	**0.822** †*	1.03	1.03
$k_c \times 10^3$ (W/m K)	47.0	24.0	24.0	9.17	*10.6* *	*10.6* *	*10.6* *	9.17	9.17
$k_\infty \times 10^3$ (W/m K)	113	27.8	27.8	25.5	25.5	25.5	25.5	25.5	25.5
k_c/k_∞	0.417	0.866	0.866	0.359	***0.417*** †*	***0.417*** †*	***0.417*** †*	0.359	0.359
$\mu_c \times 10^6$ (kg/m s)	31.1	17.2	17.2	7.10	*9.20* *	***31.1*** †*	*9.20* *	7.10	7.10
$\mu_\infty \times 10^6$ (kg/m s)	61.4	19.6	19.6	18.1	18.1	***61.4*** †*	18.1	18.1	18.1
μ_c/μ_∞	0.507	0.878	0.878	0.392	***0.507*** †*	***0.507*** †*	***0.507*** †*	0.392	0.392
Pr_c	0.699	0.719 ‡	0.719 ‡	0.799 ‡	*0.715** ‡	*2.42**	*0.715** ‡	0.799 ‡	0.799 ‡
Pr_∞	0.699	0.711 ‡	0.711 ‡	0.716 ‡	0.716 ‡	*2.42**	0.716 ‡	0.716 ‡	0.716 ‡
$\mathrm{Pr}_c\,/\,\mathrm{Pr}_\infty$	1.00	1.01 ‡	1.01 ‡	1.12 ‡	***1.00*** †*	***1.00*** †*	***1.00*** †*	1.12 ‡	1.12 ‡
u_c (m/s)	42.8	5.95	10.3	6.83	6.83	6.83	2.02	2.02	1.56
Ma_c	0.086	0.0180	0.0311	0.0344	0.0344	0.0344	0.0102	0.0102	0.00786
u_∞ (m/s)	125	7.05	12.2	20.0	20.0	20.0	5.91	5.91	4.56
Ma_∞	0.151	0.0195	0.0338	0.0582	0.0582	0.0582	0.0172	0.0172	0.0133
VR	0.342	0.845	0.845	**0.342** †	**0.342** †	**0.342** †	**0.342** †	**0.342** †	**0.342** †
$\rho_c u_c$ (kg/m^2 s)	24.1	7.70	13.3	**24.1** †	**24.1** †	**24.1** †	7.13	7.13	5.51
$\rho_\infty u_\infty$ (kg/m^2 s)	24.1	7.70	13.3	**24.1** †	**24.1** †	**24.1** †	7.13	7.13	5.51
M	1.00	**1.00** †	**1.00** †	**1.00** †	**1.00** †	**1.00** †	**1.00** †	**1.00** †	**1.00** †
$\rho_c u_c^2$ (kg/m s^2)	1030	45.8	137	165	165	165	14.4	14.4	8.59
$\rho_\infty u_\infty^2$ (kg/m s^2)	3020	54.2	162	482	482	482	42.1	42.1	25.1
I	0.342	0.845	0.845	**0.342** †	**0.342** †	**0.342** †	**0.342** †	**0.342** †	**0.342** †
Re_c	395	228	**395** †	1730	*1330**	***395*** †*	***395*** †*	512	**395** †
$\mathrm{Re}_\infty \cdot 10^{-4}$	6.07	**6.07** †	10.5	20.5	20.5	***6.07*** †*	**6.07** †	**6.07** †	4.69
$\mathrm{Re}_c/\mathrm{Re}_\infty \cdot 10^3$	6.51	3.76	3.76	0.843	***6.51*** †*	***6.51*** †*	***6.51*** †*	8.43	8.43

in the freestream and coolant while maintaining a smooth function for properties at temperatures between T_∞ and T_c. The remainder of this section will be dedicated to discussing the results of each computational case.

To quantify and visualize the ability of each case to match the high temperature baseline, the results of the current computational investigation are presented in several figures. The following will discuss the intent of each of these figures. Then, each case will be discussed in the context of its respective figures. Finally, a recommendation on what non-dimensional matching is required to scale η from a laboratory to an engine condition will be proposed.

Figure 6.1 presents a comparison of centerline η for the high temperature baseline to each case considered while Fig. 6.2 presents a similar comparison for spanwise averaged adiabatic effectiveness, $\overline{\eta}$. Next, Fig. 6.3 helps to visualize the coolant-freestream interaction with a view on the wall-normal centerline plane (mid-plane) of non-dimensional temperature given as

$$\theta = \frac{T - T_{c,e}}{T_\infty - T_{c,e}} \tag{6.1}$$

Figure 6.5 shows the spatial distribution of η on the wall following the injection site. To accent the differences between each case, Figs. 6.4 and 6.6 offer profiles of the over- or under-prediction of θ on the mid-plane and η on the wall, respectively, for each case compared to the baseline. This comparison is accomplished by subtracting the baseline θ or η contour from the θ or η contour of each case.

Finally, Fig. 6.7 shows the wall-normal contour of θ for each case at $x/D = 2.5$ with overlaid vectors of in-plane velocity. To ensure the vectors were comparable amongst the various cases, the magnitude of the vectors were proportional to the magnitude of the in-plane velocity normalized by the freestream velocity of the respective case. Similar to a cylinder in crossflow, when the freestream encounters the discrete coolant jet it can be seen shedding a counter rotating vortex pair (CRVP) as a shear layer forms between the freestream and coolant as shown computationally by Oguntade [48]. CRVPs are detrimental to film cooling performance because they sweep hot freestream gases toward the wall and separate the coolant from the wall. Figure 6.7 highlights the relative effect of CRVPs on each case.

6.1.1.1 Matching M and Re: Cases 1 and 2.

The first two cases studied both matched the M of the high temperature baseline case at a lower DR near one, as is often the case in the literature. The difference between the two cases was that in Case 1 the freestream Reynolds number (Re_∞) was

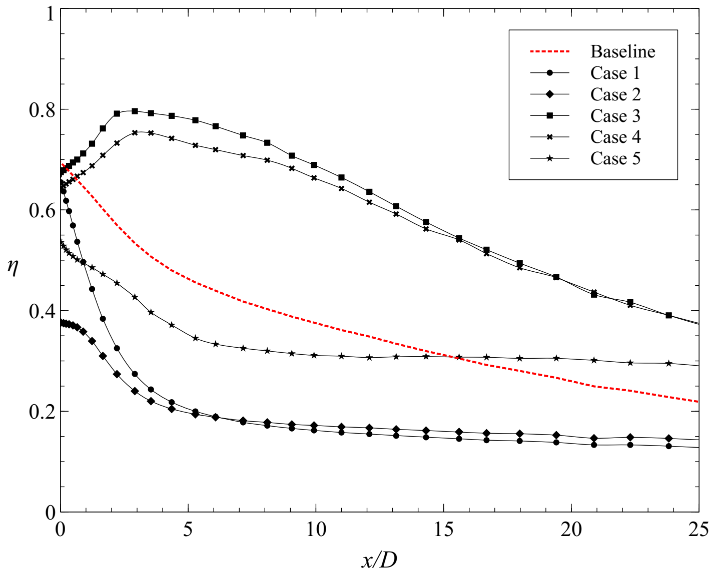

(a) Low Temperature Cases 1-5

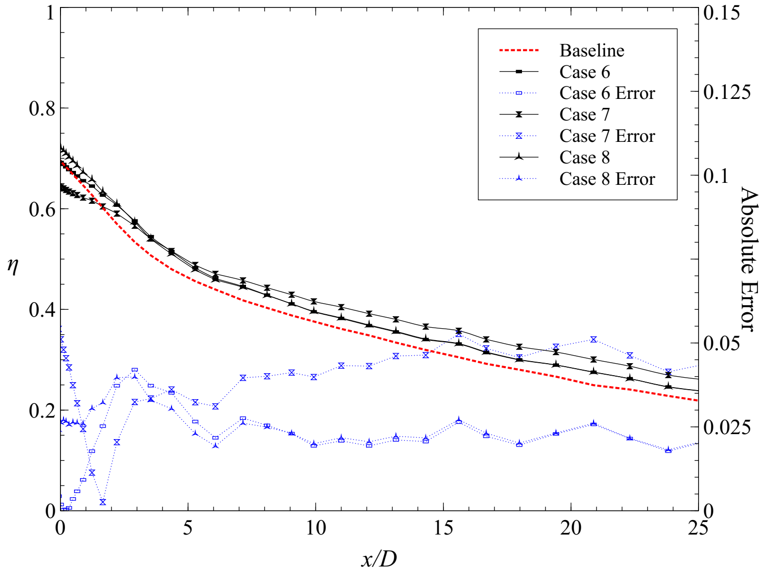

(b) Low Temperature Cases 6-8

Figure 6.1: Comparison of centerline adiabatic effectiveness (η); Baseline and Cases 1-8, $M = 1$

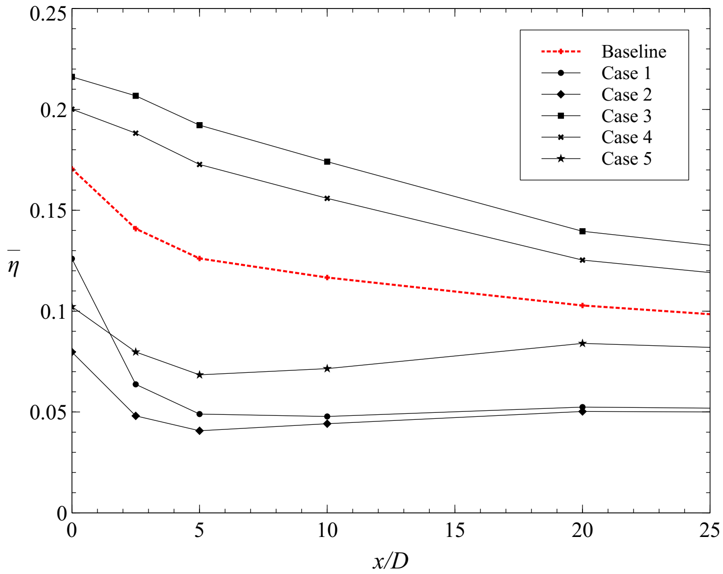

(a) Low Temperature Cases 1-5

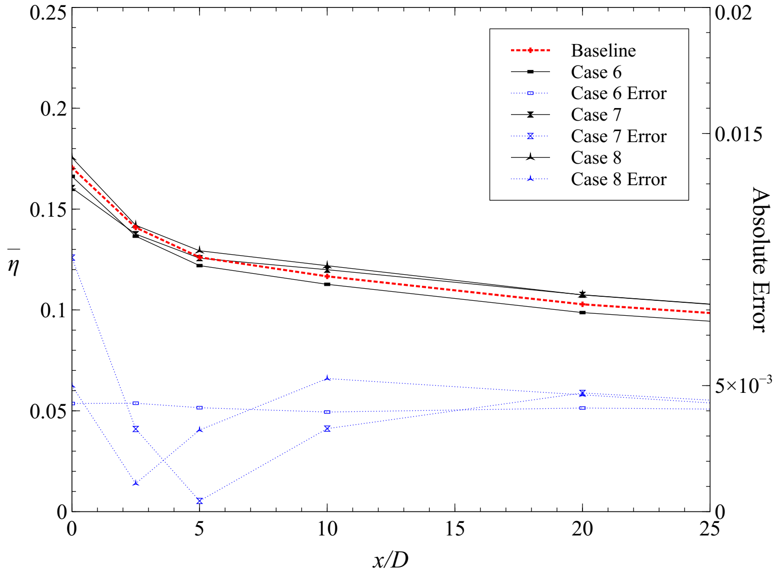

(b) Low Temperature Cases 6-8

Figure 6.2: Comparison of spanwise averaged adiabatic effectiveness ($\overline{\eta}$); Baseline and Cases 1-8, $M = 1$

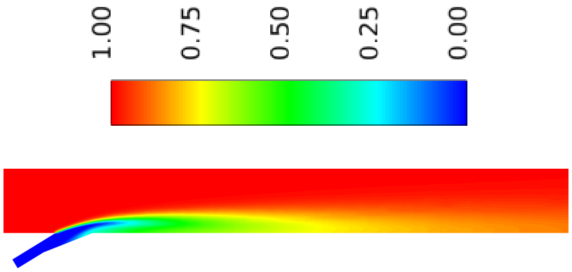

(a) High Temperature Baseline

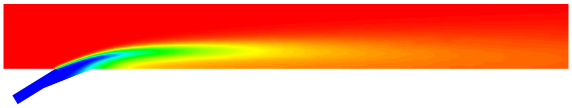

(b) Low Temperature Case 1

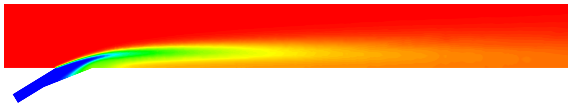

(c) Low Temperature Case 2

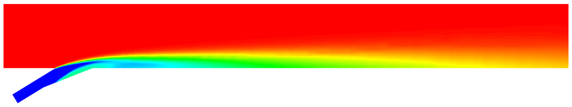

(d) Low Temperature Case 3

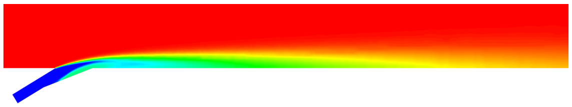

(e) Low Temperature Case 4

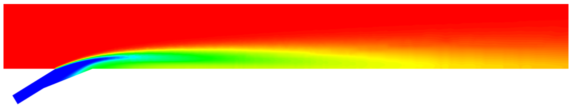

(f) Low Temperature Case 5

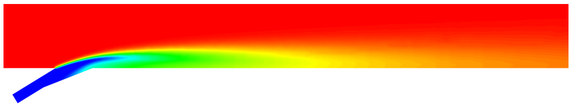

(g) Low Temperature Case 6

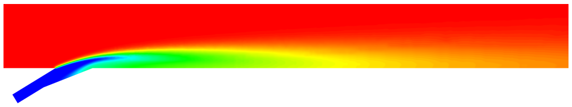

(h) Low Temperature Case 7

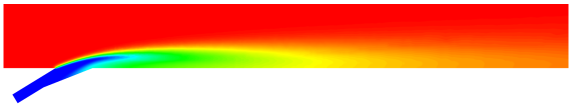

(i) Low Temperature Case 8

Figure 6.3: Mid-plane profile of non-dimensional temperature (θ); Baseline and Cases 1-8

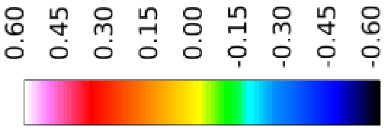

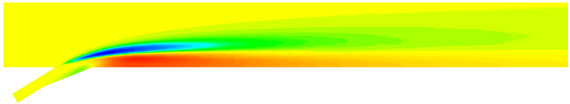

(a) Low Temperature Case 1

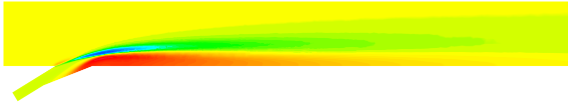

(b) Low Temperature Case 2

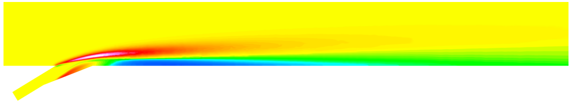

(c) Low Temperature Case 3

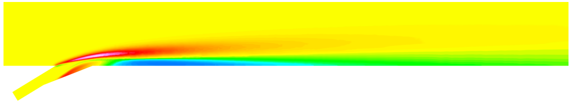

(d) Low Temperature Case 4

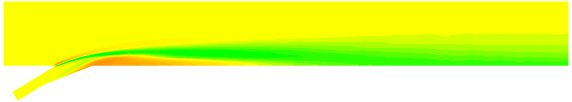

(e) Low Temperature Case 5

(f) Low Temperature Case 6

(g) Low Temperature Case 7

(h) Low Temperature Case 8

Figure 6.4: Difference between mid-plane profiles of non-dimensional temperature ($\theta_{\text{Case}} - \theta_{\text{Baseline}}$); Cases 1-8

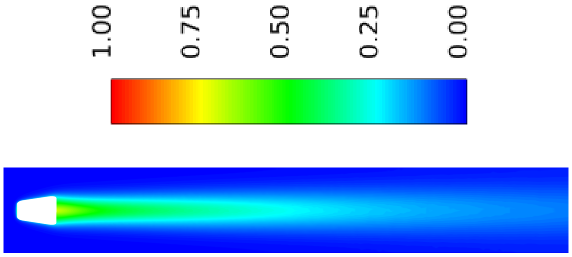

(a) High Temperature Baseline

(b) Low Temperature Case 1

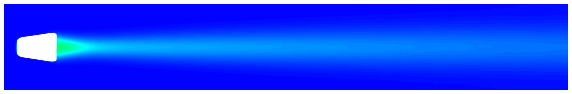

(c) Low Temperature Case 2

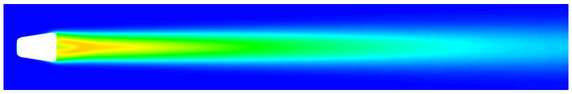

(d) Low Temperature Case 3

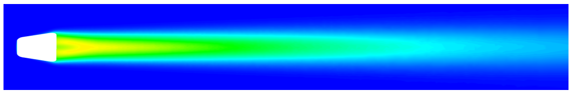

(e) Low Temperature Case 4

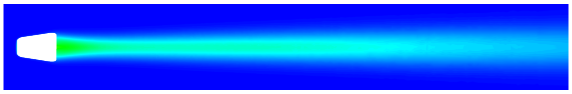

(f) Low Temperature Case 5

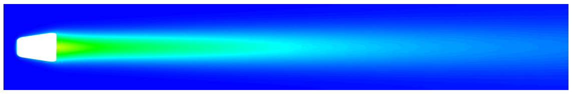

(g) Low Temperature Case 6

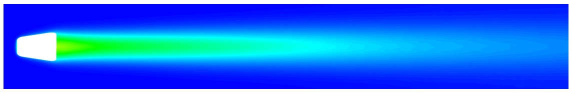

(h) Low Temperature Case 7

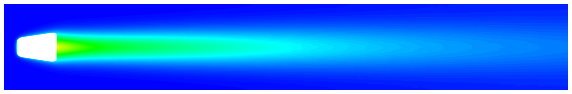

(i) Low Temperature Case 8

Figure 6.5: Contours of adiabatic effectiveness (η); Baseline and Cases 1-8

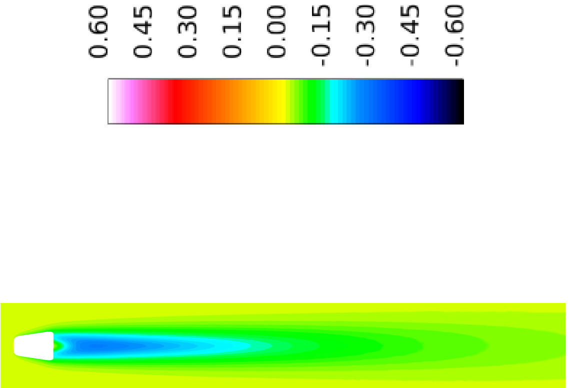

(a) Low Temperature Case 1

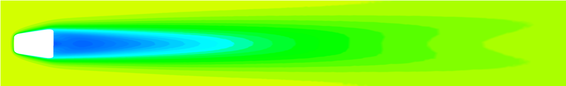

(b) Low Temperature Case 2

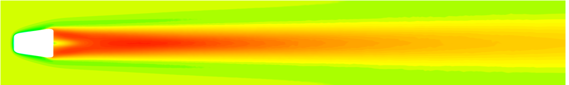

(c) Low Temperature Case 3

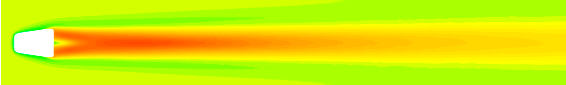

(d) Low Temperature Case 4

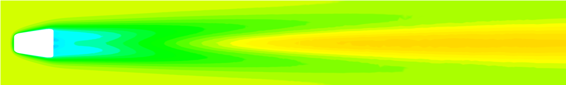

(e) Low Temperature Case 5

(f) Low Temperature Case 6

(g) Low Temperature Case 7

(h) Low Temperature Case 8

Figure 6.6: Difference between contours of adiabatic effectiveness ($\eta_{\text{Case}} - \eta_{\text{Baseline}}$); Cases 6-8

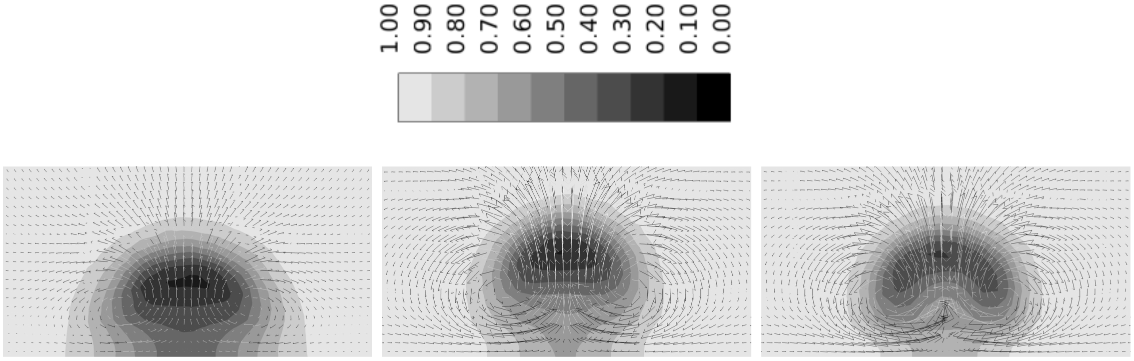

(a) High Temperature Baseline (b) Low Temperature Case 1 (c) Low Temperature Case 2

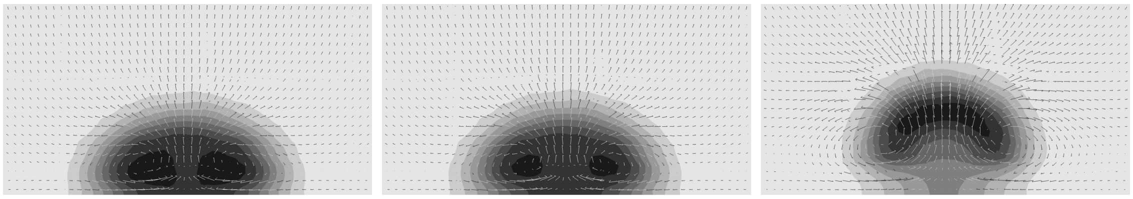

(d) Low Temperature Case 3 (e) Low Temperature Case 4 (f) Low Temperature Case 5

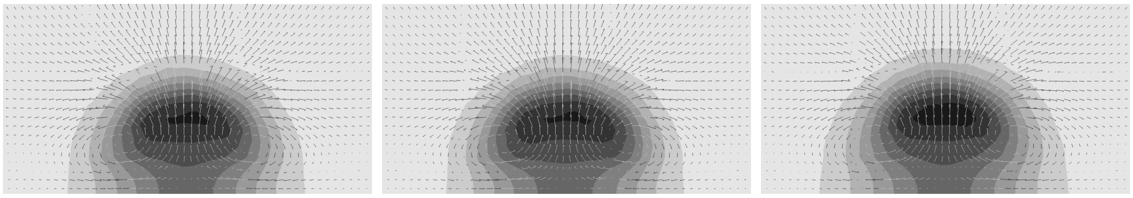

(g) Low Temperature Case 6 (h) Low Temperature Case 7 (i) Low Temperature Case 8

Figure 6.7: Contours of non-dimensional temperature (θ) with overlaid velocity vectors showing CRVPs at $x/D = 2.5$; Basline and Cases 1-8

matched while in Case 2 the coolant Reynolds number (Re_c) was matched. Many studies present the experiment's Re_∞, but it is rarely studied as an independent parameter. Moreover, Re_c is rarely presented or studied as an independent parameter. Other than the present work, the only known study of Re_c is that of Rutledge and Polanka [56].

Despite the nearly exclusive attention M receives in many studies, Fig. 6.1(a) shows that matching M and either Re_∞ or Re_c (Cases 1 or 2, respectively) results in severe under-prediction of centerline η. Similarly, Fig. 6.1(b) shows that the spanwise adiabatic effectiveness ($\overline{\eta}$) also suffers from a large under-prediction. The source of this under-prediction is seen in Figs. 6.4(a) and 6.4(b) to be increased separation of

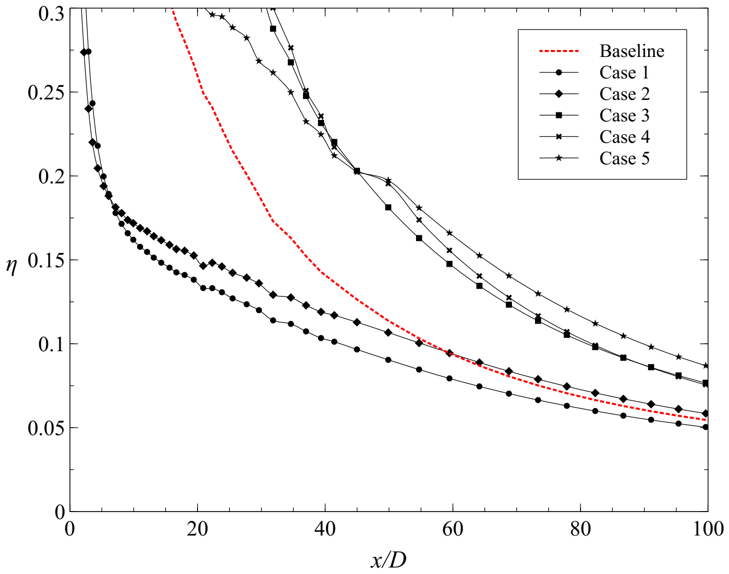

Figure 6.8: Comparison of centerline adiabatic effectiveness (η); Baseline and Cases 1-5, large x/D, $M = 1$

the coolant from the surface.

The separation of the jet from the surface is a direct consequence of testing with a DR near one. Examining Cases 1 and 2 in Table 6.2 reveals that matching M while maintaining density ratio lower than the high temperature baseline results in an increased momentum flux ratio (I). Table 6.2 also indicates that Case 2 has a larger I than Case 1 which causes the larger jet separation and stronger CRVPs seen in 6.7(c). In comparison, the lower I of the high temperature baseline case results in the weak CRVPs seen in Fig. 6.7(a) compared to Cases 1 and 2. Figures 6.7(b) and 6.7(c) display CRVPs downstream of the Case 1 and 2 coolant injections, respectively. These figures give a clear depiction of the jet separation. The effect of this separation translates to the under-prediction in η seen in Figs. 6.6(a) and 6.6(b).

Alternatively, Fig. 6.8 shows that for large x/D Cases 1 and 2 converge to the high temperature solution. This observation is in agreement with the conclusion of Baldauf et al. [5] that I scales η in the near hole region, while M scales η in the far down stream region. Thus, the results of this section suggest that matching DR which, combined with matching M, results in matching I, is necessary to scale η from low temperatures to engine temperatures.

6.1.1.2 Matching DR and *M*: Case 3.

Since DR is known to play an important role in film cooling performance, Case 3 considers the effect of matching M and DR (and, hence, VR and I) but not matching Re_∞ or Re_c. Rather than matching Reynolds numbers, Table 6.2 displays that this case matches the mass fluxes of the freestream ($\rho_\infty u_\infty$) and coolant ($\rho_c u_c$), respectively. The result was a factor of 3.38 and 4.38 increase in Re_∞ and Re_c over the high temperature baseline case, respectively.

Liess [35] studied the effect of freestream displacement thickness on film cooling performance. He found that a freestream flow with a smaller displacement thickness had more momentum near the wall and tended to keep the coolant jet more attached to the wall. As a result, η increased with decreasing displacement thickness. White [68] explained that the displacement thickness on a flat plate can be accurately modeled by

$$\delta_1 = \frac{0.16x}{\mathrm{Re}_x^{1/7}} \tag{6.2}$$

Referring to Table 6.2, it is seen that Case 3 has an $\mathrm{Re}_x = \mathrm{Re}_\infty$ which is 3.4 times larger than the high temperature baseline. Accordingly, since all cases share a common x at the hole location, Case 3 has a δ_1 which is 16% smaller than the high temperature baseline. Consistent with the results of Liess [35], the reduced displacement thickness is seen in Fig. 6.6(c) to increase η significantly. Specifically, Fig. 6.1(a) indicates a increase in centerline η of up to 0.35 and Fig. 6.2(a) indicates an increase in $\overline{\eta}$ of up to 0.05.

An additional consequence of the increased amount of freestream momentum near the wall due to the decreased displacement thickness is an increased degree of freestream and jet mixing near the hole. The vectors near the wall in Fig. 6.7(d) show hot core flow being swept under the coolant jet from the sides. Then, on the centerline of the jet where the two CRVPs meet, the hot flow is seen to be swept back up into the freestream. This circuit of swirling freestream flow is what causes the warm streak in the center of the jet and the two pockets of cooler air on either side of the hot streak seen in Fig. 6.7(d). In comparison, the baseline case is seen to have less fluid being swept under the coolant jet. This difference indicates an increased strength and intensity of CRVPs in Case 3 over the baseline case due to the reduced displacement thickness.

In summary for Case 3, the effect of the reduced displacement thickness was seen to be two fold. First, it resulted in stronger CRVPs which reduced η on centerline and very close to the hole. Second, it caused the flow to stay better attached downstream which subsequently increased η for all but very close to the injection site.

6.1.1.3 Modifying Fluid Properties to Match Flow and Property Ratios: Cases 4, 5, and 6.

As it is common in film cooling literature to describe the flow as a ratio of the respective coolant and freestream parameters (e.g. DR, M, etc.), Case 4 examines the effect of matching the coolant to freestream ratios of all the parameters in Table 6.2 (i.e. ratios of coolant to freestream for all properties and all flow parameters like I and Re). However, the variation of air's properties with temperature prevents matching all these ratios. Thus, the properties of the coolant were modified to meet the parameter matching requirements of Case 4 as discussed in Section 6.1.1. Despite this manipulation, the results display the same qualitative characteristics as Case 3. Namely, Fig. 6.1(a) indicates that Case 4 has a large improvement in centerline η over the baseline with the exception of very close to the hole. Similarly, Fig. 6.2(a) shows that Case 4 has a significant increase in $\overline{\eta}$ compared to the baseline.

The clear disagreement of Case 4 with the baseline indicates that film cooling is not non-dimensionalized simply by ratios of the parameters presented in this study. Instead the results of Cases 1 and 2 imply a dependence on, at a minimum, the absolute values, rather than ratios, of Re_∞ and Re_c along with the typical film cooling parameters of DR and M (and, hence, VR and I).

In light of this, Case 5 matched all the conditions of Case 4 except μ_∞ and μ_c. These were adjusted such that Re_∞ and Re_c matched the high temperature baseline case. However, modifying μ with constant c_p and k mandates a change in Pr. Table 6.2 shows that Pr_∞ and Pr_c change from near 0.7 to 2.42. Such high Prandtl numbers are implicative of a liquid freestream and coolant rather than gas.

The inextricable dependence of film cooling heat transfer on the Prandtl number is visualized by Figs. 6.4(e) and 6.6(e). Though the Reynolds numbers are matched in this case, failing to match the Prandtl numbers is seen in these figures to produce a poor match to the high temperature baseline case. This result restates the importance of Pr as the inherent link between the momentum and energy equations.

The effect of not matching Pr on the thermal field is further visualized in Fig. 6.7(f). In this figure it is seen that the θ contour of Case 5 is quite different than the baseline case's contour seen in Fig. 6.7(a). Alternatively, Case 5 matched DR, M, Re_∞, and Re_c. Thus, the hydrodynamic flow field of Case 5 should be nearly identical to the baseline. Again examining Fig. 6.7(f) reveals that, though the θ profile is different, the CRVPs of Case 5 are seen to be very similar to those of the baseline seen in Fig. 6.7(a).

The severe shortcomings of Case 5 were remedied by taking a different tact. For Case 6, the conditions of Case 4 are used with the exception of the freestream and coolant mass fluxes which were modified to match the absolute values of Re_∞ and Re_c

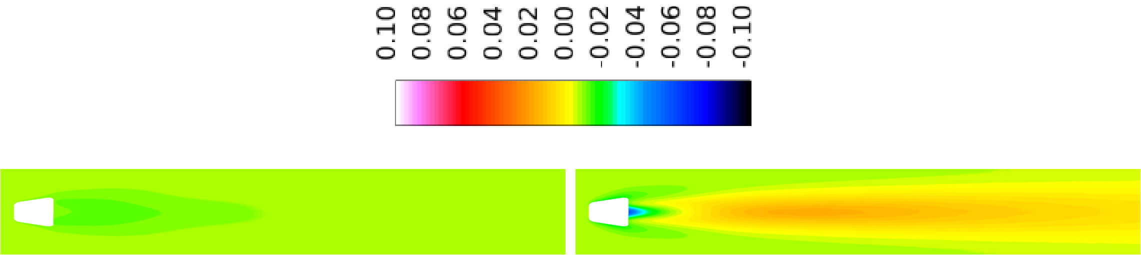

(a) Low Temperature Case 6

(b) Low Temperature Case 7

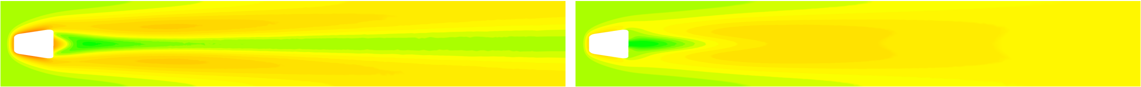

(c) Low Temperature Case 8

(d) Average of Cases 7 and 8

Figure 6.9: Difference between contours of adiabatic effectiveness ($\eta_{\text{Case}} - \eta_{\text{Baseline}}$); Cases 6-8, zoomed scale

of the high temperature baseline. By this method, the ratios of all parameters are matched, the absolute values of Re_∞ and Re_c are matched, and the Prandtl numbers are approximately matched by virtue of Pr remaining near 0.7 for gases. Figure 6.6(f) shows that matching the baseline case in this manor produces agreement with the baseline that far outperforms its predecessors.

To better visualize the Case 6 η profile, Fig. 6.9(a) displays Fig. 6.6(f) with a zoomed scale. The figure shows that Case 6 produces a nearly exact match (within 0.01) to the baseline η profile. This result reflects classical knowledge that scaling heat transfer requires matching the Reynolds numbers and Prandtl numbers. Similarly, the result reflects existing film cooling knowledge which states that DR and M must also be matched to scale η.

6.1.1.4 Matching DR, *M*, and Re with Real Properties: Cases 7 and 8.

Despite the promising results of Case 6, they require unrealistic fluid properties which are not achievable in a laboratory setting. For a flat plate experiment, a test case could be designed to adjust x such that both Re_∞ and Re_c are matched to other flat plate experiments. However, the flat plate experiment comes at the price of an inability to match the curvature of the practical turbine engine case it was designed to model. Alternatively, choosing to test film cooling on a representative turbine vane or blade geometry comes at the cost of fixed length scales (e.g. x and D). Thus, recognizing that

$$\frac{\mathrm{Re}_c}{\mathrm{Re}_\infty} = M\frac{\mu_\infty D}{\mu_c x} \tag{6.3}$$

reveals that, for fixed x and D, attempting to match DR, M, Re_∞, and Re_c in a low temperature experiment is impossible because matching DR and μ_∞/μ_c are mutually exclusive. Thus, the question of which parameters should be matched has yet to be answered. Since the previous cases have shown that matching DR and M as well as maintaining a Prandtl number representative of air are required, the remaining unknown is whether to match Re_∞ or Re_c.

Cases 7 and 8 examine this trade-off by using the conditions of Case 3 (real properties of air and matching DR and M) while also matching Re_∞ and Re_c in each case, respectively, by adjusting the freestream and coolant mass fluxes appropriately. As shown in Fig. 6.1(b), matching Re_∞ (Case 7) tends not to match centerline η as well as matching Re_c (Case 8). However, examining $\overline{\eta}$ in Fig. 6.2(b) shows an opposite trend: matching Re_∞ (Case 7) is seen to produce a slightly improved accuracy over matching Re_c, though matching Re_c is still in excellent agreement.

Interestingly, by comparing Figs. 6.9(b) and 6.9(c), it is seen that Case 7 generally over-predicts η in locations where Case 8 under-predicts η. The converse is also seen to be true. To take advantage of this observation, Fig. 6.9(d) shows the result of averaging the η profiles of Cases 7 and 8 and comparing them to the baseline case.

Though the near-hole region is still seen to be slightly under-predicted, a nearly exact match is seen to result over the rest of the profile. Admittedly, the increase gained by this process is small when compared to Case 8 and may not be worth the cost requiring two experiments to average the Re_∞ and Re_c matched profiles when simply matching Re_c may suffice. However, it will be seen that this averaging process may pay dividends in the case of a well attached coolant jet.

6.1.1.5 Matching M=0.5 and M=3: Cases 9-14.

The above results have used an $M = 1$ condition to provide evidence that a low temperature film cooling experiment can non-dimensionally match a high temperature film cooling condition. The following discussion will present results at low and high M to show that the recommendations developed at $M = 1$ still apply. The cases to be examined are given as Cases 9-14 in Table 6.1. Specifically, Case 9 utilized the baseline conditions but halved the coolant mass flow resulting in a blowing ratio of $M = 0.5$. Cases 10 and 11 then matched the Re_∞ and Re_c of Case 9, respectively, along with DR and M. Additionally, Case 12 tripled the coolant mass flow rate for a blowing ratio of $M = 3$. Cases 13 and 14 then matched the Re_∞ and Re_c of Case 12 along with DR and M. The mid-plane θ contours in 6.11 indicate that for $M = 0.5$ the coolant is well attached while for $M = 3$ the coolant jet is severely detached from the surface.

Since both $M = 1$ and $M = 0.5$ conditions result in a well attached jet, similar conclusions can be drawn. By examining Figs. 6.14(a) and 6.14(b), it is seen that matching Re_c (Case 10) produces a superior η profile prediction over matching Re_∞ (Case 11). The main draw back of Case 11 is the large over-prediction of η following the injection site. Again, the averaging of Cases 10 and 11 is seen in Fig. 6.14(c) to improve the match with the high temperature profile (Case 9), though the improvement is small compared to Case 10 (Re_c matched).

Alternatively, the $M = 3$ condition (Case 12) is unlike the previous high temperature $M = 1$ (baseline) and $M = 0.5$ (Case 9) conditions in that the jet is severely

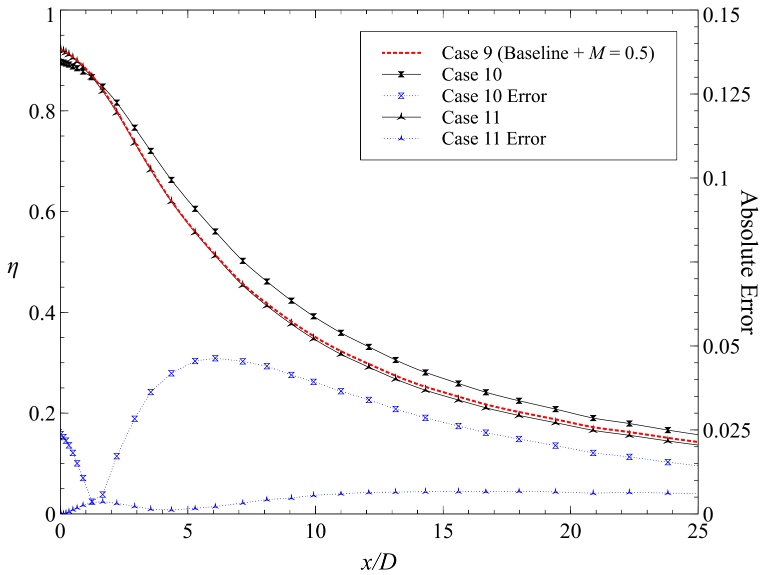

(a) Centerline η

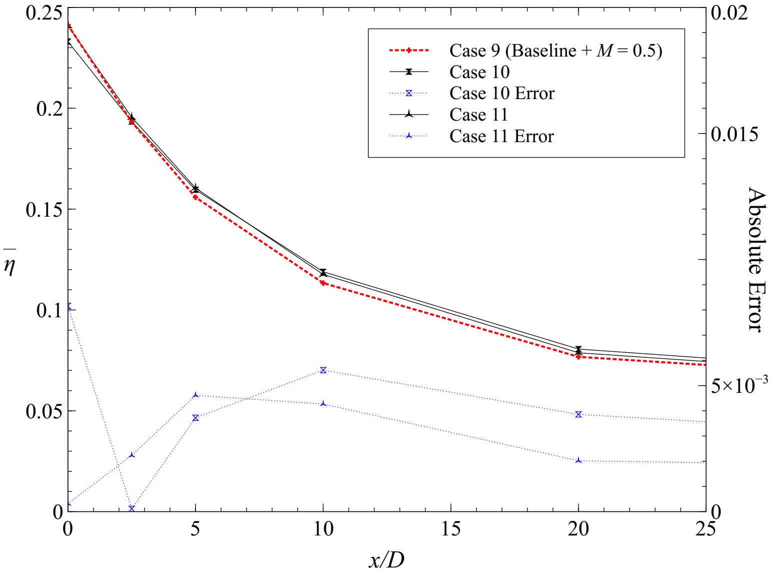

(b) Spanwise Averaged η ($\overline{\eta}$)

Figure 6.10: Comparison of adiabatic effectiveness (η); Cases 9-11, $M = 0.5$

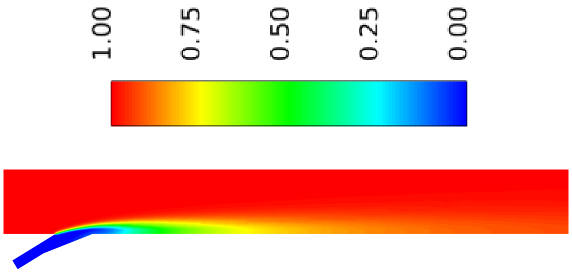

(a) High Temperature Case 9

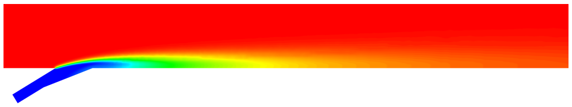

(b) Low Temperature Case 10

(c) Low Temperature Case 11

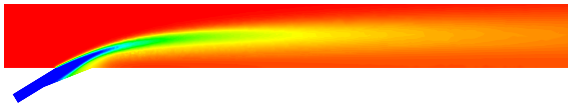

(d) High Temperature Case 12

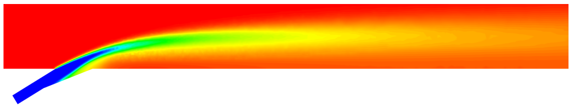

(e) Low Temperature Case 13

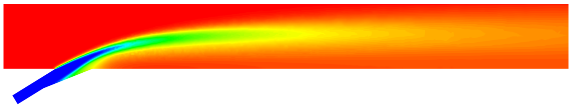

(f) Low Temperature Case 14

Figure 6.11: Mid-plane profile of non-dimensional temperature (θ); Cases 10, 11, 13, and 14

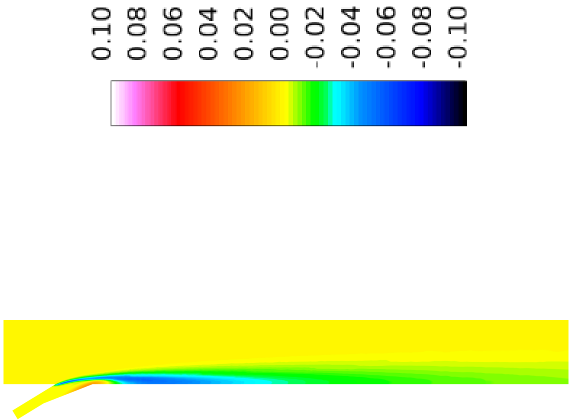

(a) Low Temperature Case 10

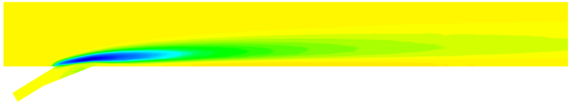

(b) Low Temperature Case 11

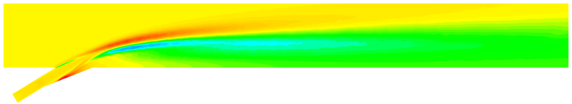

(c) Low Temperature Case 13

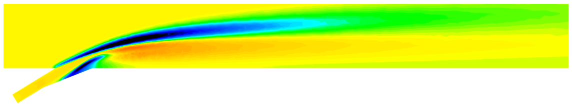

(d) Low Temperature Case 14

Figure 6.12: Difference between mid-plane profiles of non-dimensional temperature ($\theta_{\text{Case 10,11/13,14}} - \theta_{\text{Case 9/12}}$); Cases 10, 11, 13, 14

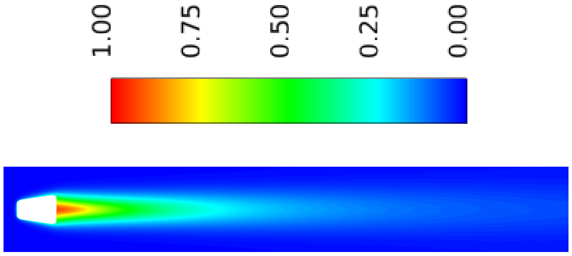

(a) High Temperature Case 9

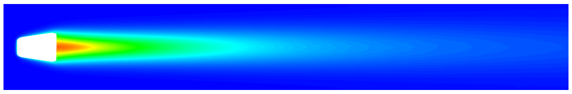

(b) Low Temperature Case 10

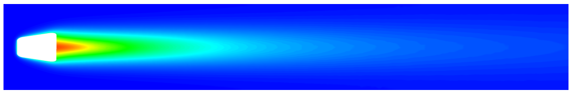

(c) Low Temperature Case 11

(d) High Temperature Case 12

(e) Low Temperature Case 13

(f) Low Temperature Case 14

Figure 6.13: Contours of adiabatic effectiveness (η); Cases 9-14

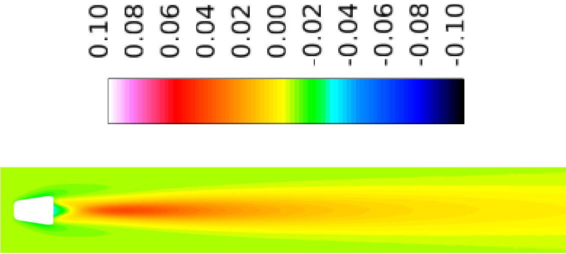

(a) Low Temperature Case 10

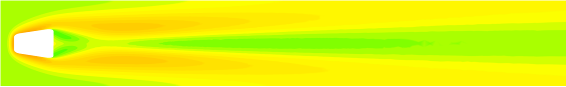

(b) Low Temperature Case 11

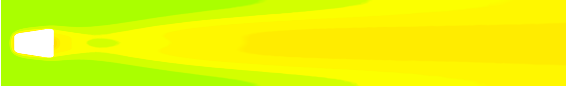

(c) Average of Cases 10 and 11

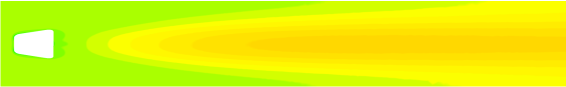

(d) Low Temperature Case 13

(e) Low Temperature Case 14

(f) Average of Cases 13 and 14

Figure 6.14: Difference between contours of adiabatic effectiveness ($\eta_{\textbf{Case 10,11/13,14}} - \eta_{\textbf{Case 9/12}}$); Cases 10, 11, 13, 14

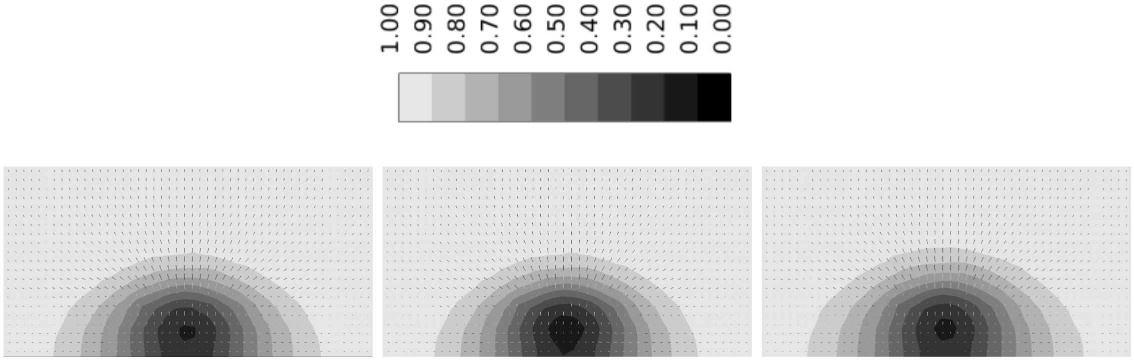

(a) High Temperature Case 9 (b) Low Temperature Case 10 (c) Low Temperature Case 11

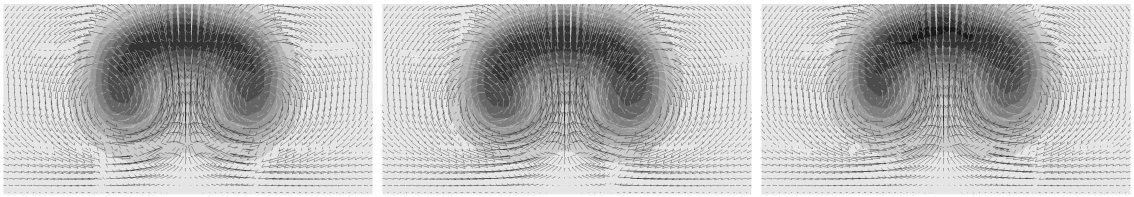

(d) High Temperature Case 12 (e) Low Temperature Case 13 (f) Low Temperature Case 14

Figure 6.15: Contours of non-dimensional temperature (θ) with overlaied velocity vectors showing CRVPs at $x/D = 2.5$; Cases 9-14; Cases 12-14 Vectors Scaled Down by Factor of Three

separated. Here, both matching Re_∞ (Case 13) and matching Re_c (Case 14) are seen in Figs. 6.14(d) and 6.14(e) to produce similar accuracies with a slight advantage given to Case 14. Here it is seen that averaging the Case 13 and 14 η profiles decreases accuracy close to the hole.

By examining results of the $M = 3$ case along side the $M = 1$ and $M = 0.5$ cases, it is seen that, in general, matching Re_c at the expense of matching Re_∞ produced an η profile which most accurately matched its respective high temperature η profile. This is in direct contrast with film cooling literature which generally focuses on Re_∞ with no attention given to Re_c. Additionally, it was found that slight gains in η profile accuracy could be gained by averaging the Re_∞ matched and Re_c matched η profiles of a well attached jet. However, for a detached jet, averaging the profiles was seen to decrease the match of the resulting η profile to its respective high temperature η profile.

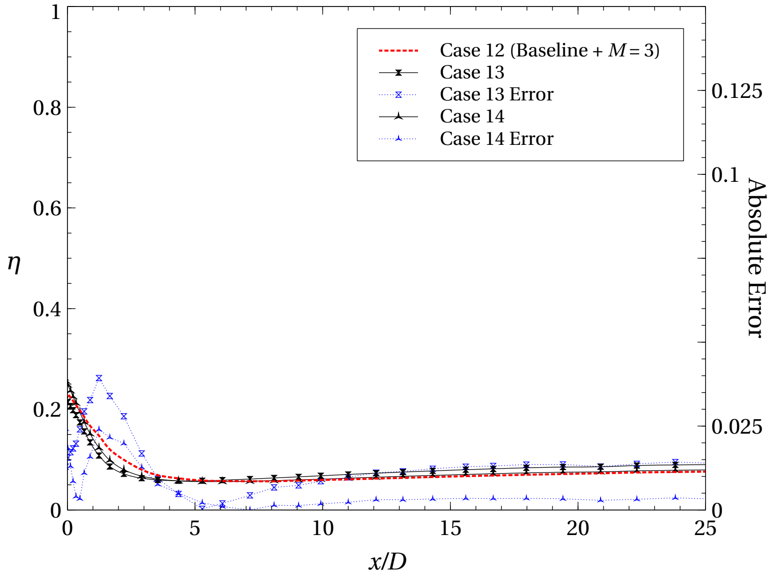

(a) Full scale

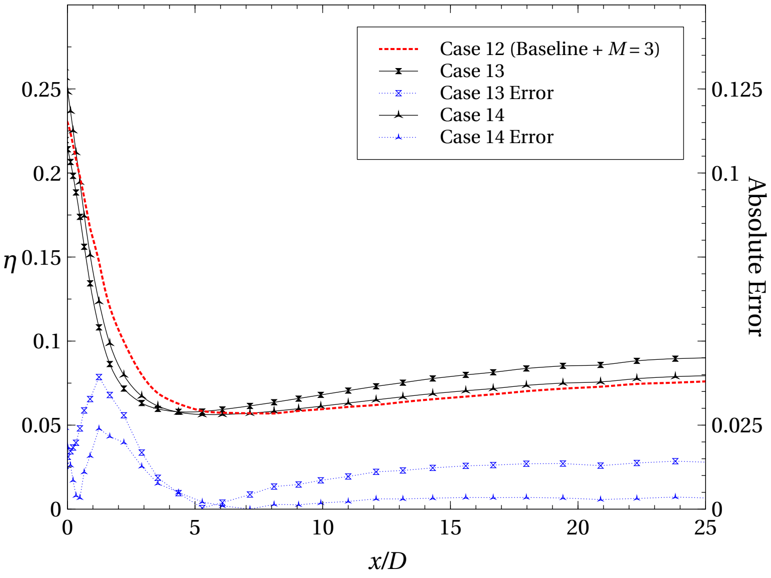

(b) Zoomed scale

Figure 6.16: Comparison of centerline adiabatic effectiveness (η); Cases 12-14, $M = 3$

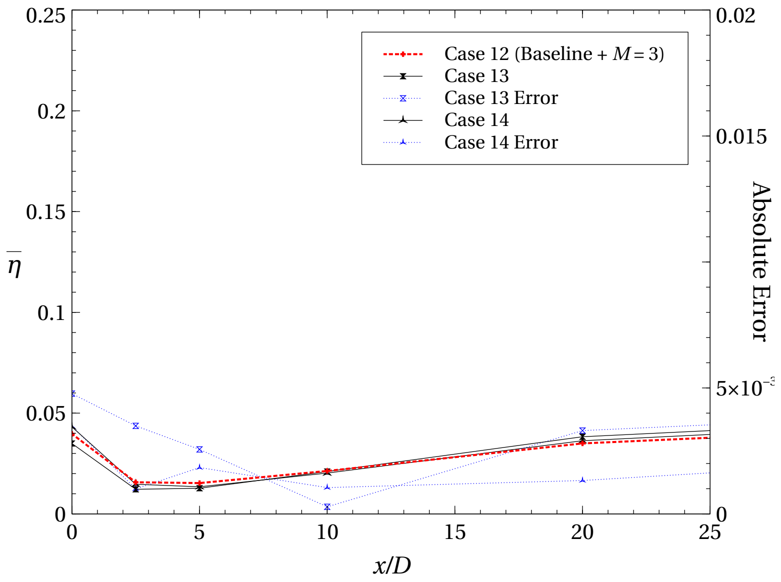

(a) Full scale

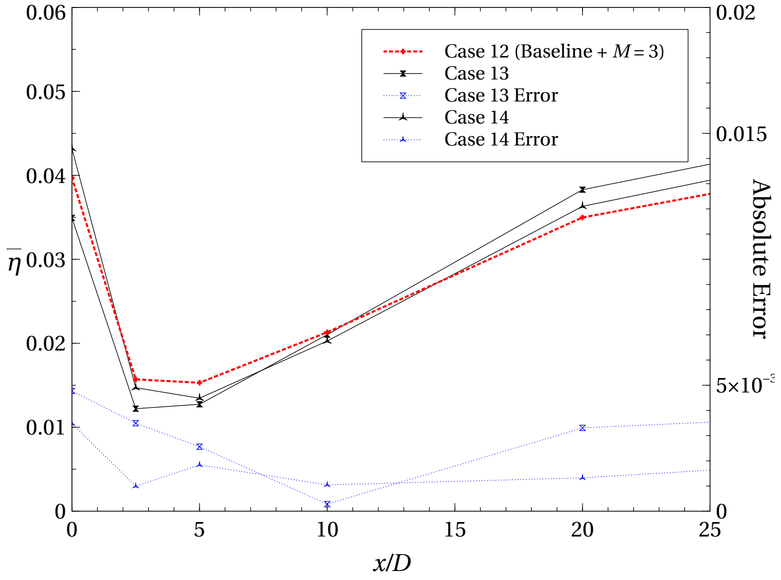

(b) Zoomed scale

Figure 6.17: Comparison of spanwise averaged adiabatic effectiveness ($\overline{\eta}$); Cases 12-14, $M = 3$

6.1.1.6 Matching Engine Conditions.

The computational results of this section gave evidence that, by matching the appropriate parameters, the η profile measured in a low temperature experiment using air closely matches the η profile that would be measured in a high temperature experiment using air. However, attempting to scale low temperature experiments using air to engine conditions produces the quandary that the core flow passing through the turbine is no longer air. Rather, the flow entering the turbine consists of the combustion products which have properties different than air at the same temperature.

Fortunately, the nature of gaseous properties is such that the balance of properties results in a nearly constant Prandlt number near 0.7. As was shown in the above case studies, scaling of η is not sensitive to matching individual properties or property ratios but on matching non-dimensional parameters including the Prandtl number. Thus, though the individual properties of the combustion products may differ significantly from the individual properties of air at the same temperature, the Prandtl numbers remain comparable and the η measured at a low temperature using air can be scaled to turbine flows of combustion products. Similarly, gaseous properties other than density (ρ) are not strong functions of pressure. Thus, by accounting for density differences between an atmospheric and engine condition with a matched Reynolds number, the scaling methodology of this section should remain true when scaling to engine pressures as well as temperatures.

6.1.1.7 Comparison of Wall Boundary Conditions.

The above computational results calculated η by specifying an adiabatic boundary condition on the film cooled surface. Such a procedure is common in the literature. However, modeling the surface as adiabatic creates a condition which is non-physical in practical applications of film cooling. Namely, film cooled surfaces are non-adiabatic due to their cooling schemes.

Very close to a film cooling hole, the coolant adjacent to the surface can be colder than the film cooled surface. As a result, regions near the hole can experience net heat flux out of the surface. Farther downstream, the film cooling layer will have heated to a temperature higher than the surface resulting in a net heat flux to the film cooled surface. In addition, a non-adiabatic surface will develop a thermal boundary layer upstream of the cooling injection. Logically, this is expected to have an impact on the observed T_{aw} compared to an adiabatic boundary condition with no thermal boundary layer.

Since η is a non-dimesionalization of T_{aw}, it follows that quantification of η is dependent on the boundary condition used. This section will examine two aspects of this nuance. First, the η calculated using an isothermal boundary condition will be compared to that calculated using an adiabatic condition. Second, the η scaling methodology developed using the adiabatic results will be applied to the isothermal results. Objective 1 of the present research focuses on scaling film cooling performance to engine conditions. Thus, this first study will verify that the scaling methodology developed using an adiabatic condition still applies to the more realistic case of an isothermal surface.

To accomplish these two tasks, the computational domain presented in Section 4.3 and utilized in the adiabatic study above was used. However, rather than assuming an adiabatic boundary condition wall, this section applied an isothermal wall temperature T_w boundary condition. Using the isothermal condition, profiles of heat flux on the film cooled surface (q''_f) were calculated at numerous T_w. The selected T_w were between T_c and T_∞ such that q''_f would switch from into the wall to out of the wall at some $T_c < T_w < T_\infty$. Then, the T_w and q''_f data were interpolated to determine T_{aw} at select spatial locations.

Section 6.1.1 concluded that the η calculated using an adiabatic boundary condition could be scaled from ambient to engine temperatures by matching DR, M, Pr_∞, Pr_c, and either Re_∞ or Re_c. To determine if this methodology can also scale the η calculated using an isothermal boundary condition, the same matching scheme was applied to the isothermal methodology described above. Specifically, the high temperature baseline described in Table 6.2 was computed with several isothermal conditions. Similarly, the low temperature Cases 7 and 8 were computed at several isothermal conditions. These cases each non-dimensionally matched the DR, M, Pr_∞, and Pr_c of the high temperature baseline case. In addition to these parameters, the two cases matched the baseline case along with Re_∞ or Re_c, respectively.

The resulting centerline η and $\overline{\eta}$ calculated using the isothermal boundary conditions is compared to that calculated using the adiabatic boundary condition in Figs. 6.18 and 6.19. Figure 6.18 focuses on the near hole region and indicates that both centerline η and $\overline{\eta}$ are significantly higher when calculated using the isothermal methodology. This is due to the thermal boundary layer that develops on the isothermal surface before reaching the film cooling injection site. The result is that, rather than the film cooling jet encountering a cross-stream that is uniformly at T_∞, it encounters a cross-stream which has been cooled by the preceding wall. This causes the cooling jet to be heated less and produce an improved η profile.

Alternatively, Fig. 6.19 shows that far downstream the isothermal and adiabatic methodologies converge to a common centerline η and $\overline{\eta}$. This is due to the reduced cooling effectiveness at the far downstream locations. Specifically, the η calculated with both the adiabatic and isothermal methodologies can be expected to approach zero as x/D approaches infinity. Thus, the convergence seen in Fig. 6.19 is as expected.

Though the adiabatic and isothermal conditions produced different quantitative

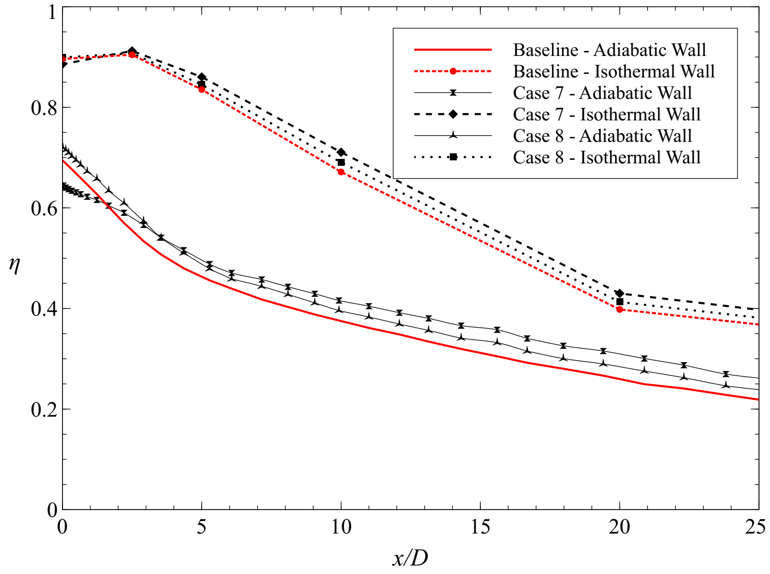

(a) Centerline adiabatic effectiveness η

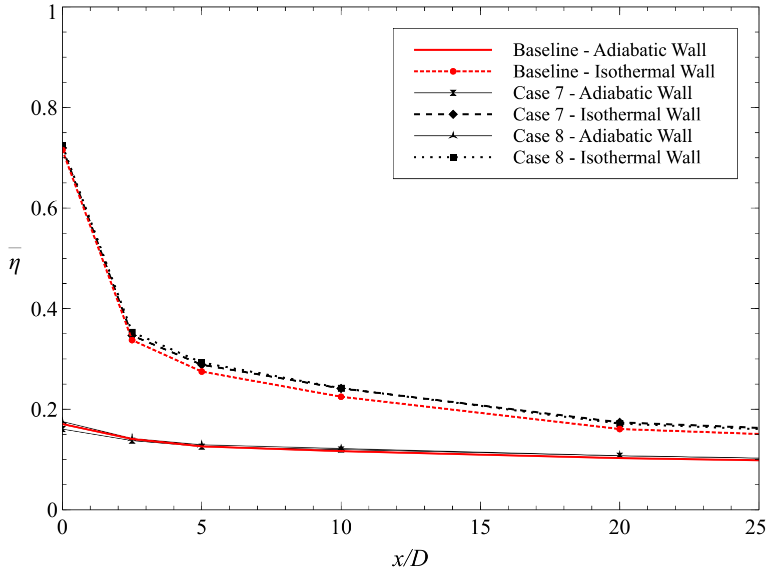

(b) Spanwise averaged adiabatic effectiveness $\overline{\eta}$

Figure 6.18: Comparison of adiabatic effectiveness (η) calculated using an adiabatic vs. isothermal wall boundary condition close to the injection site

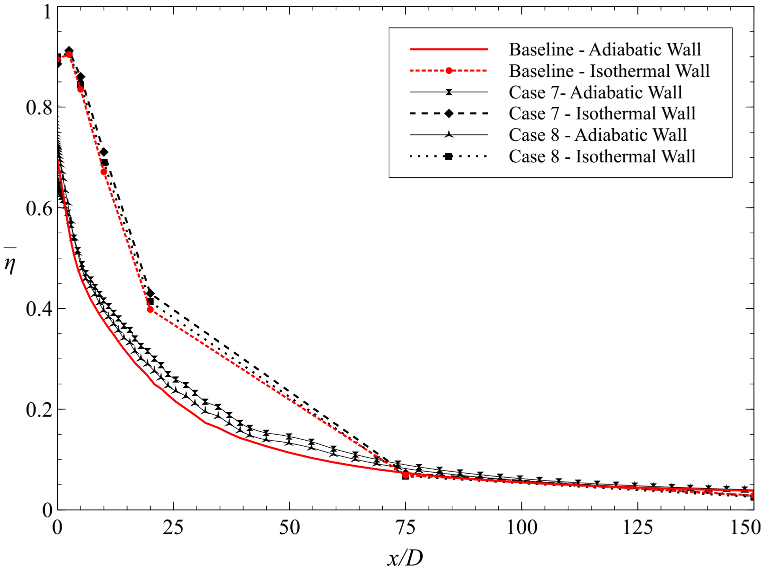

(a) Centerline adiabatic effectiveness η

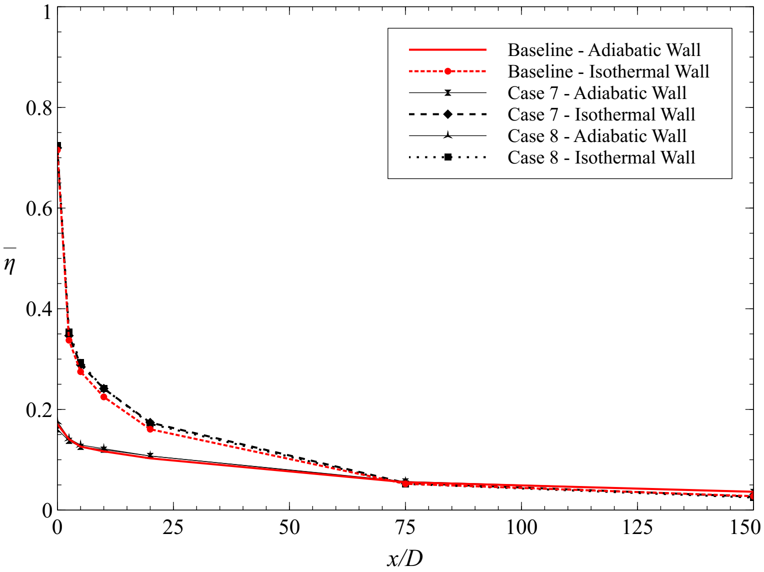

(b) Spanwise averaged adiabatic effectiveness $\overline{\eta}$

Figure 6.19: Comparison of adiabatic effectiveness (η) calculated using an adiabatic vs. isothermal wall boundary condition far from the injection site

results, they produced similar qualitative results. Specifically, the low temperature isothermal boundary condition results match well with the isothermal high temperature baseline. This observation indicates that the η scaling methodology developed using an adiabatic wall boundary condition above can scale the η calculated using an isothermal boundary condition. Moreover, Fig. 6.18(a) shows that both the adiabatic and isothermal studies indicated that Case 8 (Re_c matched) better matched the high temperature centerline η than Case 7 (Re_∞ matched). Similarly, the $\overline{\eta}$ seen in Fig. 6.18(b) show that both Cases 7 and 8 produce equally accurate predictions of the high temperature baseline for both the adiabatic and isothermal boundary conditions.

6.1.1.8 Summary of Scaling Adiabatic Effectiveness.

The literature commonly quantifies a film cooling scheme's performance by its ability to reduce the driving adiabatic wall temperature T_{aw}. This section showed that adiabatic effectiveness (η, the non-dimensionalization of T_{aw}) can be scaled from a laboratory condition to an engine condition by appropriate non-dimensional matching. Namely, matching of DR, M, Pr_∞, Pr_c, and either Re_∞ or Re_c are required to scale η. Contrary to the common focus of the literature on Re_∞, this section indicated that matching Re_c produced a superior scalability of η. Finally, this section showed that the η calculated using an adiabatic wall boundary condition was significantly lower than the η calculated using an isothermal boundary condition. This was due to the thermal boundary layer developed on the isothermal boundary condition.

6.1.2 Scaling Net Heat Flux Reduction.

The adiabatic effectiveness parameter studied in the previous sections is an important aspect of film cooling performance. However it does not fully define the scheme's ability to reduce the heat flux to the surface. The ratio of convective heat transfer coefficient with and without film cooling (h_f/h_0) is also present in the formulation for Net Heat Flux Reduction (NHFR or $\Delta q''_f$) as seen in Eq. 2.33. The final term in Eq. 2.33 is the non-dimensional wall temperature (θ_w). However, θ_w is a parameter which, by its definition, is scalable. Similar to the previous sections, this section will explore the scalability of NHFR from a near ambient temperature experiment to an engine condition.

6.1.2.1 Methodology.

To determine the scalability of NHFR, the computational domain utilized in the previous section and detailed in Section 4.3 will be used. All boundary conditions remained identical to the previous section with the exception of the wall's thermal condition. The previous section used both adiabatic and isothermal boundary conditions for the film cooled surface. This section implemented the isothermal thermal boundary condition to compute the heat flux to the surface with and without film cooling (q''_f and q''_0, respectively).

This calculation procedure was used to calculate the q''_f and q''_0 profiles following a single row of shaped holes at θ_w from 0.0 to 0.9 in increments of 0.1. The heat flux profiles were calculated for blowing ratios of $M = 0$ and 1. For each θ_w, the $M = 0$ and 1 heat flux profiles were compared according to Eq. 2.33 to generate profiles of NHFR. It should be noted that he q''_f data examined presently is identical to the data used in Section 6.1.1.7 which studied η measured using an isothermal boundary condition.

The results of Section 6.1.1.7 indicated that η could be scaled from a near ambient condition to an engine condition by non-dimensional matching. Namely, matching density ratio (DR), blowing ratio (M), Pr_∞, Pr_c, and either Re_∞ or Re_c produced a good agreement in η profiles between a condition near ambient and an engine condition. Following this conclusion, the purpose of this section is to determine if the same set of conditions can be utilized to scale NHFR. Specifically, Cases 7 and 8, as outlined in Table 6.2, will be analyzed and compared to the Baseline case. Each of these cases represent low temperature conditions that match the engine case where Re_∞ is matched in Case 7 and Re_c was matched in Case 8.

To visualize the NHFR profiles, contour plots similar to those found in Section 6.1.1 were created. However, creating a profiles for each of the three flow conditions at each of the ten θ_w considered would have made comparing the cases difficult. Thus, rather than showing the NHFR profiles at each θ_w, a single value of 0.4 was selected to reflect a common technique used in the literature to quantify NHFR.

The technique entails first experimentally measuring or computing η and h_f/h_0. Generally these are quantified on adiabatic and slightly heated or cooled walls, respectively. Next, an assumed overall effectiveness of $\phi = 0.6$ is adopted. This value is commonly accepted to reflect the the coolant temperature (T_c), freestream temperature (T_∞), and maximum wall temperature ($T_{w,\max}$) of modern engine technology and has been used by researchers such as Lu et al. [37]. By comparing Eqs. 2.31 and 2.34, it is seen that $\theta_w = 1 - \phi$ for the case of $T_{c,e} = T_{c,i}$. Therefore, assuming $\phi = 0.6$ combined with measured η and h_f/h_0 allows quantification of NHFR via Eq. 2.33 at a ϕ characteristic of an engine. To reflect this technique from the literature, the value of $\theta_w = 1 - \phi = 0.4$ was selected for closer examination.

To visualize the NHFR profiles, Fig. 6.20 displays contours of NHFR for the three flow conditions at $\theta_w = 0.4$. Similar to Section 6.1.1, it is difficult to compare and contrast the NHFR profiles in Fig. 6.20. Thus, to make the differences more apparent, Fig. 6.21 shows a difference between the NHFR contours of the respective low temperature conditions and the high temperature baseline they were designed to non-dimensionally match. Again, an average of the Re_∞ and Re_c matched cases was calculated and compared to the high temperature baseline case to visualize its potential benefits.

Since it would be difficult to compare and dissect the 30 NHFR profiles calculated, plots of centerline NHFR ($\Delta q''_f$) and spanwise averaged NHFR ($\overline{\Delta q''_f}$) were generated. To assist in parameterizing NHFR, the data were plotted with two different abscissa axes: θ_w at a constant x/D and x/D at a constant θ_w. These plots are presented in Figs. 6.22 and 6.24, respectively.

6.1.2.2 Net Heat Flux Reduction Results.

In line with the qualitative results of Section 6.1.1, Fig.6.21(a) shows matching Re_∞ (Case 7) under-predicts NHFR near the hole on centerline. Alternatively, Fig.6.21(b) shows that matching Re_c (Case 8) over-predicts NHFR near the hole on centerline. Thus, the averaging of these two cases, as shown in Fig. 6.21(c), increased the accuracy of NHFR on centerline near the hole from an error of up to 0.12 down to near zero. However, its benefits are limited to this area alone. Near the hole but outboard from centerline, errors of up to 0.09 were observed.

Also in agreement with the results of Section 6.1.1, matching Re_c was found to produce a superior prediction of NHFR over matching Re_∞. Matching Re_c is seen in Fig. 6.21(b) to predict NHFR to within 0.05 at all spatial locations excluding very near the hole where the prediction is within 0.09. Alternatively, matching Re_∞ was found to predict NHFR to within ± 0.15 near the hole and within 0.1 farther downstream.

Examining Fig. 6.22 indicates that, for a constant $x/D = 5$, 10 and 20, matching Re_∞ produced a slightly superior prediction of centerline $\Delta q''_f$ and spanwise $\overline{\Delta q''_f}$ for $0.5 < \theta_w$. In contrast, matching Re_c tended to be slightly more accurate for $\theta_w < 0.5$. Despite their slight differences, both cases produced similarly good predictions of

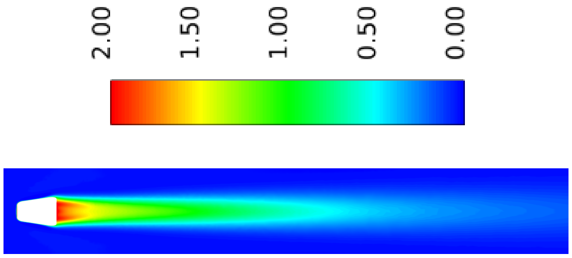

(a) High Temperature Baseline

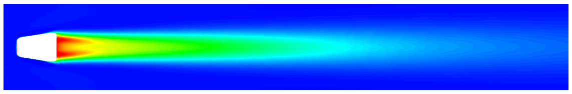

(b) Low Temperature Case 7 (Re_x matched)

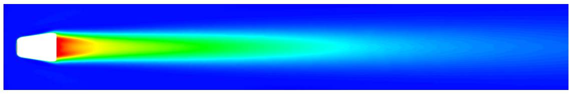

(c) Low Temperature Case 8 (Re_D matched)

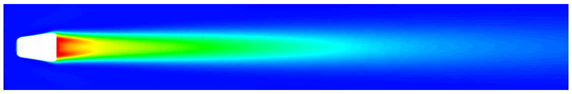

(d) Average of Cases 7 and 8

Figure 6.20: Contours of NHFR ($\Delta q''_f$) at $\theta_w = 0.4$ comparing high and non-dimensionally matched low temperature cases detailed in Table 6.2

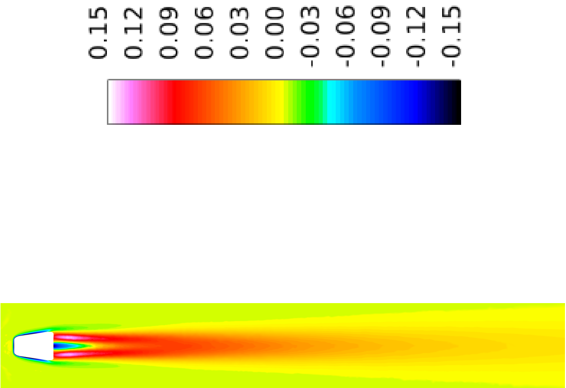

(a) Low Temperature Case 7 (Re_x matched)

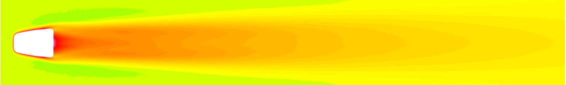

(b) Low Temperature Case 8 (Re_D matched)

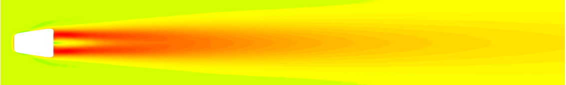

(c) Average of Cases 7 and 8

Figure 6.21: Contours of difference between low temperature and high temperature baseline NHFR ($\Delta q''_f$) from Fig.6.20 at $\theta_w = 0.4$

$\Delta q''_f$. Interestingly, since, by definition, q''_0 goes to zero as θ_w goes to one, $\Delta q''_f$ will asymptotically approach infinity as θ_w goes to one. Thus, small differences in the cases are amplified as θ_w goes to one. This resulted in the low temperature predictions to diverge somewhat from the high temperature baseline as θ_w goes to one.

To give further insight into the data, Fig. 6.24 plots centerline and spanwise averaged $\Delta q''_f$ as a function of x/D at constant values of θ_w. This figure is seen to reflect the trend of worsening agreement between the high and low temperature cases with increasing θ_w. Interestingly, Fig. 6.24 shows that the agreement or disagreement of the high and low temperature cases on $\overline{\Delta q''_f}$ is relatively constant over $2.5 < x/D < 20$. However, as expected, Fig. 6.23 shows that the high and low temperature predictions of $\Delta q''_f$ converge to zero as x/D goes to infinity.

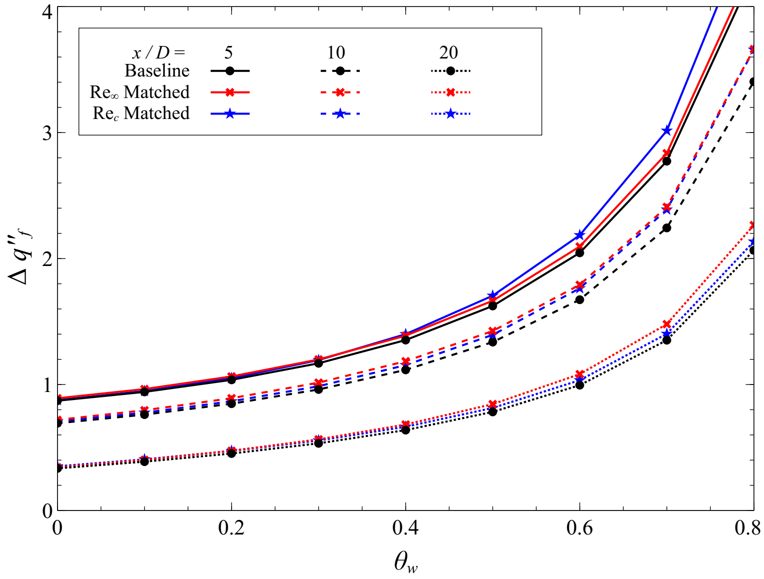

(a) Centerline NHFR ($\Delta q''_f$)

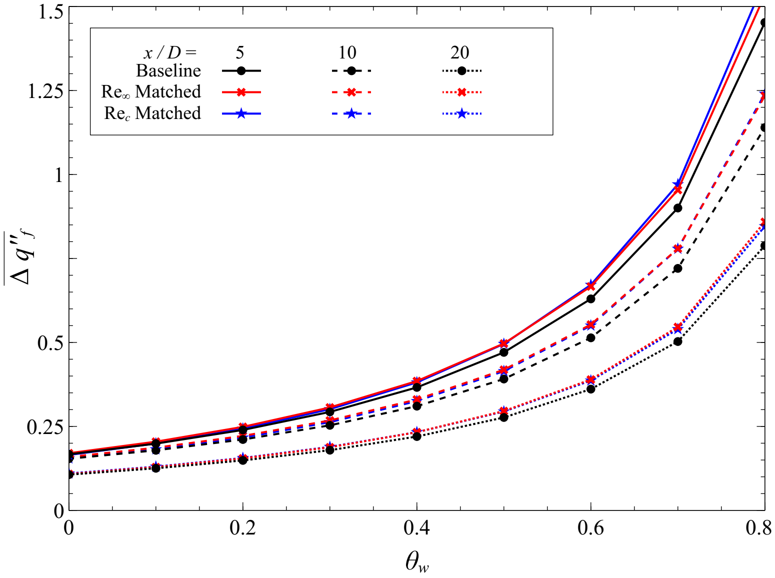

(b) Spanwise averaged NHFR ($\overline{\Delta q''_f}$)

Figure 6.22: Scalability of $\Delta q''_f$ vs. θ_w for select x/D

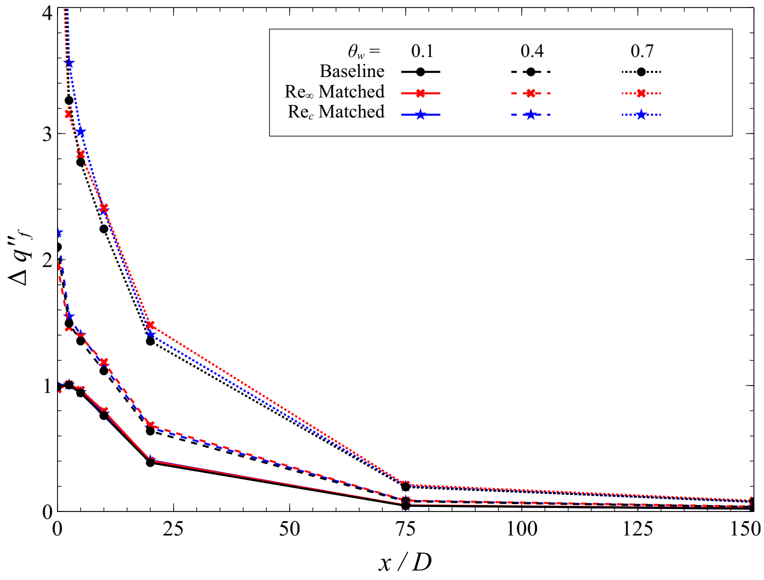

(a) Centerline NHFR ($\Delta q''_f$)

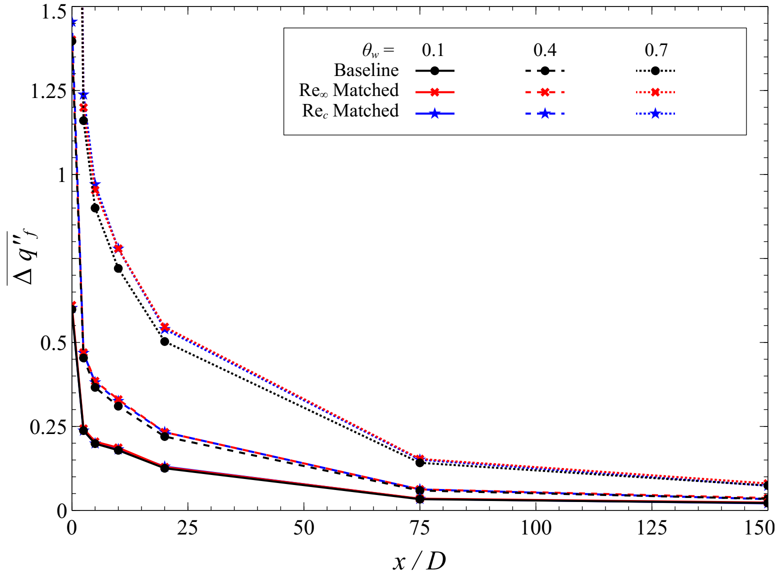

(b) Spanwise averaged NHFR ($\overline{\Delta q''_f}$)

Figure 6.23: Scalability of $\Delta q''_f$ vs. x/D for select θ_w and large x/D

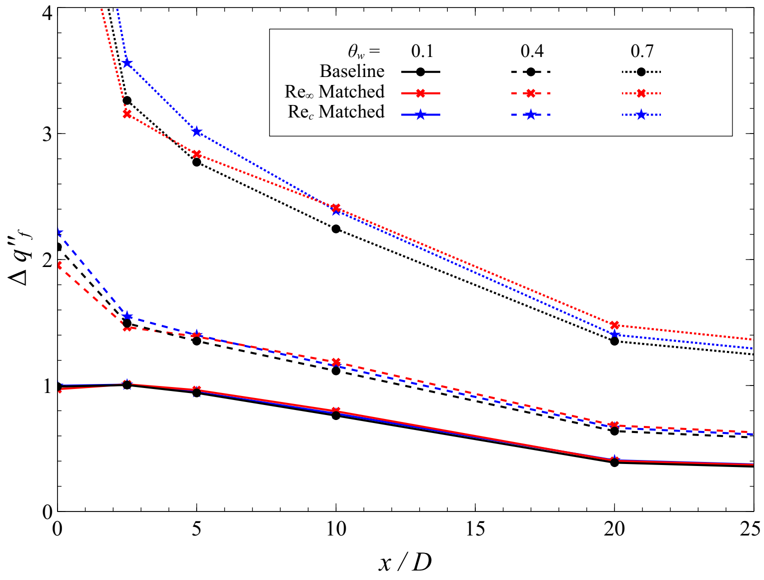

(a) Centerline NHFR $(\Delta q''_f)$

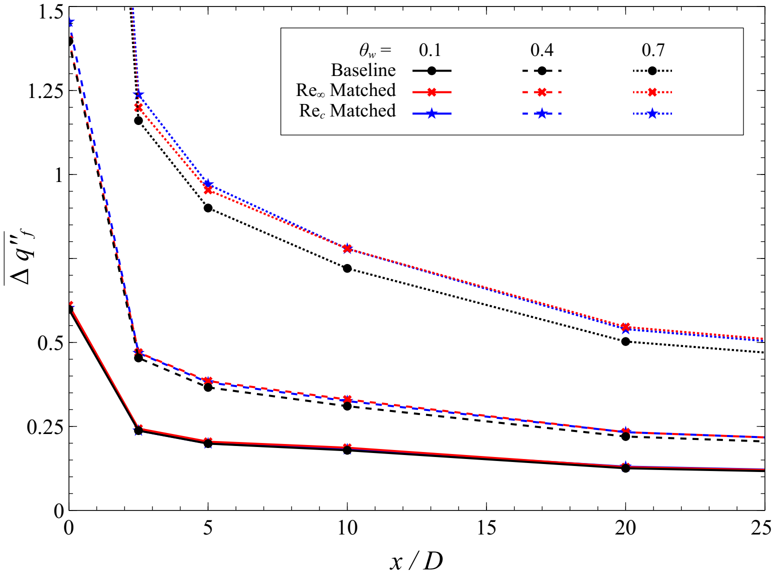

(b) Spanwise averaged NHFR $(\overline{\Delta q''_f})$

Figure 6.24: Scalability of $\Delta q''_f$ vs. x/D for select θ_w

6.1.2.3 Summary of Scaling Net Heat Flux Reduction.

This section first computed net heat flux reduction ($\Delta q_f''$) at numerous isothermal non-dimensional wall temperature conditions (θ_w). This was accomplished at the high temperature condition as well as the Re_∞ (Case 7) and Re_c (Case 8) matched conditions of Table 6.2. Figure 6.21 compared the high and low temperature contours of $\Delta q_f''$ and showed that, similar to Section 6.1.1, matching Re_c produced a $\Delta q_f''$ profile which matched the $\Delta q_f''$ profile on a point-by-point basis more accurately than matching Re_∞. Despite this distinction, Figs. 6.22(b) and 6.24(b) indicated that the Re_∞ and Re_c matched cases produced spanwise averaged NHFR values which were indistinguishable at all θ_w and $x/D > 5$. However, very close to the hole for $x/D < 5$, subtle differences were observed.

Section 6.1.1.7 showed computationally that the adiabatic effectiveness (η) measured by an isothermal method could be scaled from near ambient temperatures to engine temperatures. Examining the definition of $\Delta q_f''$ (Eq. 2.33) reveals that the scalability of η combined with the scalability of $\Delta q_f''$ implicitly states that the ratio of the film cooled to non-film cooled convective heat transfer coefficient (h_f/h_0) can also be scaled. This scalability is contingent on a matched θ_w between the high and low temperature cases. The following section will examine the scalability of h_f/h_0 in more detail. Later in this chapter, Section 6.2 will experimentally validate the scalability of NHFR to satisfy Objective 2 of the present research. Subsequently, NHFR will be employed to experimentally compare various cooling schemes' performance measured in a high temperature environment.

6.1.3 Scaling Convective Heat Transfer Ratio.

Objective 2 of the present research is directed towards determining an appropriate parameter to scale film cooling performance. Previously, Sections 6.1.1 and 6.1.2 ad-

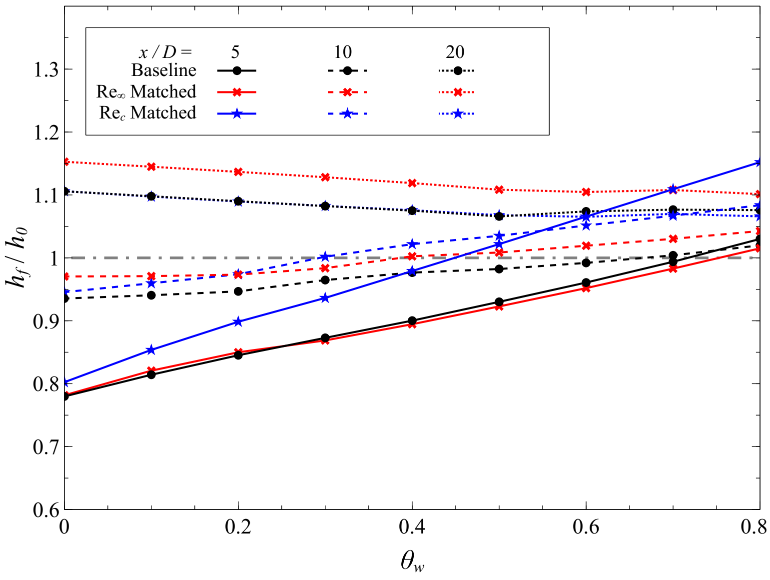

Figure 6.25: Scalability of centerline h_f/h_0 as a function of non-dimensional wall temperature (θ_w)

dressed the scalability of the adiabatic effectiveness (η) and Net Heat Flux Reduction (NHFR or $\Delta q_f''$) film cooling performance parameters, respectively. This section will examine the scalability of another important parameter: the ratio of the film cooled to non-film cool convective heat transfer coefficients (h_f/h_0).

From its definition in Eq. 2.33, NHFR is a function of non-dimensional wall temperature (θ_w), adiabatic effectiveness (η), and h_f/h_0. Therefore, by knowing any three of NHFR, θ_w, η, and h_f/h_0 are scalable would prove that the fourth is also scalable. As discussed, it was previously shown that NHFR and η are scalable. In addition, θ_w, according to Eq. 2.34, is scalable by definition. Therefore, by association, h_f/h_0 should also be a scalable parameter.

To substantiate this logic, Figs. 6.25 and 6.26 show the centerline h_f/h_0 extracted from the NHFR study of Section 6.1.2. Specifically, the NHFR study examined scaling NHFR from non-dimensionally matched low temperature conditions to a high temperature baseline condition. The conditions of the high temperature baseline, an the Re_∞ (Case 7) and Re_c (Case 8) matched cases are given in Table 6.2.

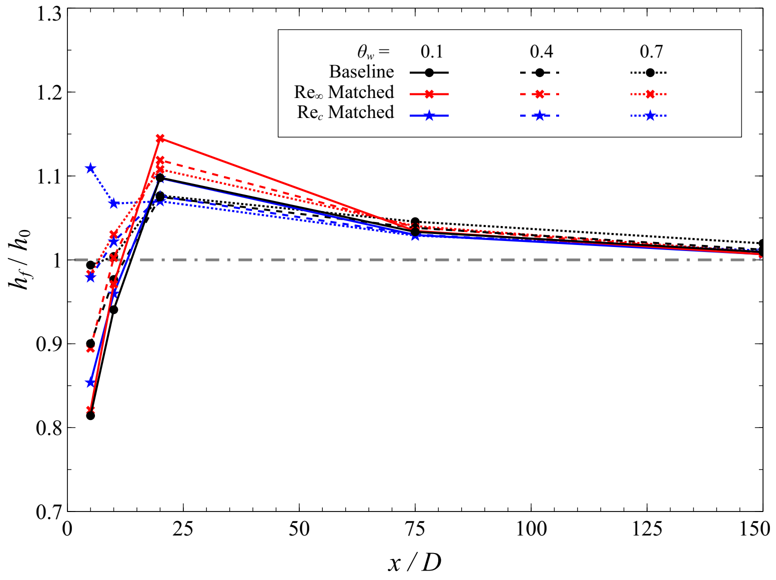

Figure 6.26: Scalability of centerline h_f/h_0 as a function of downstream distance (x/D)

Figure 6.25 indicates that close to the hole at $x/D = 5$, the centerline h_f/h_0 of the Re_c matched condition diverges from the high temperature baseline with increasing θ_w. Alternatively, at $x/D = 5$ the centerline h_f/h_0 of the Re_∞ matched condition agrees well with the high temperature baseline. However, examining farther downstream at $x/D = 20$, a nearly opposite trend was observed. Here, the Re_c matched condition is seen to have a nearly exact match to the high temperature baseline while the Re_∞ case is approximately 5% higher than the baseline at all $\theta_w$considered. Since h_f/h_0 is an integral part of NHFR, these trends are reflected in the NHFR results of Fig. 6.22.

Figure 6.26 displays h_f/h_0 as a function of x/D at $\theta_w = 0.1$, 0.4, and 0.7. This plot indicates that close to the hole, at $x/D = 5$, all but the $\theta_w = 0.7$, Re_∞ matched case had an $h_f/h_0 < 1$. This could be attributed to several factors. First, different properties near the wall due to the lower film cooled temperature could result in $h_f < h_0$. Second, the lower velocity of the coolant compared to the freestream could result in reduced convection. Third, since the $M = 1$ jet was seen to be well attached in Fig. 6.3(a), minimal mixing of the coolant and freestream could result in lower levels of turbulence at $x/D = 5$.

The peak level of h_f/h_0 was observed at $x/D = 25$ as seen in Fig. 6.26. For each case plotted, the peak was in the range of $1.06 < h_f/h_0 < 1.15$. In addition, the Re_∞ matched case was found to have the highest h_f/h_0. Though the h_f/h_0 at $x/D = 25$ is a somewhat larger spread amongst the cases, by $x/D = 75$, each case was observed to collapse to h_f/h_0 of approximately 1.05. Finally, as x/D increased, h_f/h_0 was seen to tend toward one.

In general, this section's study showed that centerline h_f/h_0 can be scaled from a near ambient temperature condition to an engine temperature with appropriate non-dimensional matching. Namely, as with Sections 6.1.1 and 6.1.2, non-dimensionally matching DR, M, Pr_∞, Pr_c, and either Re_∞or Re_c. However, the Re_∞ matched case was observed to produce nearly identical h_f/h_0 as the high temperature baseline near the hole at $x/D = 5$. Alternatively, the Re_c matched case diverged from the high temperature baseline with increasing θ_w. Farther from the hole at $x/D = 20$, the Re_c matched case was found to produce a nearly identical h_f/h_0 as the high temperature baseline while the Re_∞ case produced a h_f/h_0 5% higher. By $x/D = 75$, the h_f/h_0 of all the cases considered were found to collapse to $h_f/h_0 \approx 1.05$ and decay toward one with increasing x/D.

Section 5.1.2 presented the temperature ratio method of Kays et al. [29] which modeled variable property effects in h_0. Though this method was found to be effective both computationally and experimentally in Sections 5.1.2 and 5.3, respectively, it is unknown whether the temperature ratio method can be employed to model h_f. The following section will examine the h_f data of the present section to determine if variable property effects on h_f can be sufficiently captured by the temperature ratio method.

6.1.4 Measurement of Film Cooling Performance.

Objective 2 of the present research is focused on identifying a scalable parameter for film cooling performance. Sections 6.1.1–6.1.3 computationally examined the scalability of the common performance parameters of adiabatic effectiveness (η), Net Heat Flux Reduction (NHFR or $\Delta q''_f$), and the ratio of convective heat transfer coefficients with and without film cooling (h_f/h_0). The present section will consider techniques to measure these parameters in a high temperature environment. The result of this examination will be a down-select of these parameters to only one which can practicably be implemented at engine temperatures in support of Objective 2.

The definition for $\Delta q''_f$ given by Eq. 2.33 states that $\Delta q''_f$ is a unique function of h_0, h_f, η, and the non-dimensional wall temperature θ_w (Eq. 2.34). Often, film cooling experiments are performed at room temperatures such that $h_0$and $h_f$are invariant with changes in wall temperature (T_w and, hence, θ_w). However, as shown in Chapter V, large variations of temperature in the boundary layer results in large property variation such that h_0 is no longer constant with T_w.

In Section 5.1.2, the temperature ratio method of Kays et al. [29] (Eq. 2.25) was shown to accurately predict the effect of variable properties on h_0 over large temperature ranges. Subsequently, Section 5.2.3 presented a method to quantify an unknown freestream temperature (T_∞) and constant property h_0 ($h_{\mathrm{CP},0}$) using measurements at T_w far below T_∞. Since experiments at combustion temperatures have T_∞ higher than the melting temperature of viable materials, this method enabled the quantification of adiabatic conditions from non-adiabatic measurements.

Section 6.1.3, examined the effect of varying T_w on h_f/h_0. However, thus far no examination of the effect of varying T_w on h_f has been presented. Therefore, it is unknown whether the temperature ratio method of Kays et al. [29] can sufficiently model the effect of varying T_w on h_f. However, if the temperature ratio method sufficed for h_f, it would enable an analogous method to quantify the adiabatic wall temperature (T_{aw} and, hence, η) and constant property h_f ($h_{\text{CP},f}$). Moreover, if h_f could be modeled by the temperature ratio method of Kays et al. [29], Eq. 2.33 for NHFR could be modified to

$$\Delta q_f'' = 1 - \frac{h_f}{h_0}\left[1 - \frac{\eta}{1-\theta_w}\right] = 1 - \frac{h_{\text{CP},f}\left(\frac{T_w}{T_{\text{aw}}}\right)^{n_f}}{h_{\text{CP},0}\left(\frac{T_w}{T_\infty}\right)^{n_0}}\left[1 - \frac{\eta}{1-\theta_w}\right] \tag{6.4}$$

In this equation, the exponents are assigned subscripts to denote the film cooling or no film cooling exponent (f and 0 respectively) to acknowledge that the film cooling case could require a different exponent than the no film cooling case. Equation 6.4 introduces the new terms of T_w/T_{aw} and T_w/T_∞. The following will show that two film cooling conditions with appropriate non-dimensional matching will have the same T_w/T_{aw} and T_w/T_∞ at a common θ_w.

It was shown in Section 6.1.1 that non-dimensionally matched low and high temperature cases would produce the same η profiles. One of the non-dimensional parameters which required matching to match η was the density ratio (DR). From the definition of η in Eq. 2.30 evaluated at low speeds ($T_r = T_\infty$), it is seen that, for an ideal gas,

$$\eta = \frac{T_\infty - T_{\text{aw}}}{T_\infty - T_{c,e}} = \frac{1 - T_{\text{aw}}/T_\infty}{1 - \text{DR}^{-1}} \tag{6.5}$$

Therefore, since both η and DR are constant between the two cases, T_{aw}/T_∞ must then also be constant. Applying an analogous process to θ_w given by Eq. 2.34, it is seen that,

$$\theta_w = \frac{T_w - T_{c,e}}{T_\infty - T_{c,e}} = \frac{T_w/T_\infty - \text{DR}^{-1}}{1 - \text{DR}^{-1}} \tag{6.6}$$

Again, since DR is held constant, Eq. 6.6 indicates that T_w/T_∞ is a function of θ_w

alone. By combining Eqs. 6.5 and 6.6 it is found that

$$\frac{T_w/T_\infty}{T_{\text{aw}}/T_\infty} = \frac{T_w}{T_{\text{aw}}} \tag{6.7}$$

Thus, since T_{aw}/T_∞ is constant and T_w/T_∞ is a function of θ_w alone, then T_w/T_{aw} must also be a function of θ_w alone.

Chapter V examined two existing variable property methods and proposed a new method in support of Objective 1 of the present research. Though each method had its advantages, the above analysis indicates that temperature ratios are central to discussion of film cooling. Thus, the temperature ratio method of Kays et al. [29] seems to be well suited to the analysis of film cooling performance. However, the missing component is the empirical exponent, n_f, which has yet to be examined.

Section 5.1.2 proposed that n_0 best modeled the computational data by assuming it varied linearly with T_w/T_∞ according to Eq. 5.3. To reflect the analysis of Section 5.1.2, Fig. 6.27 took the q''_f data from the NHFR study of Section 6.1.2 and plots $h_f/h_{\text{CP},f}$ as a function of T_w/T_{aw} at four x/D. The q''_f data were computed at several T_w both above and below T_{aw} such that T_{aw} could be quantified interpolating the q''_f data to determine the T_w where $q''_f = 0$. Next, h_f was quantified by $q''_f/(T_{\text{aw}} - T_w)$ at all $T_w/T_{\text{aw}} < 0.95$ to avoid singularities and numerical error amplification. Finally, $h_{\text{CP},f}$ was quantified by using the two h_f with T_w/T_{aw} closest to one and extrapolating the h_f trend to $T_w/T_{\text{aw}} = 1$.

Upstream of the film cooling hole at $x/D = -15$, the $h_f/h_{\text{CP},f}$ data of the high temperature baseline and the low temperature Re matched cases were found to follow the $h_0/h_{\text{CP},0}$, as seen in Fig. 6.27. Specifically, analogous to the function for n_0 with T_w/T_∞ defined by Eq. 5.3, the film cooled data were found to follow the T_w/T_{aw} raised

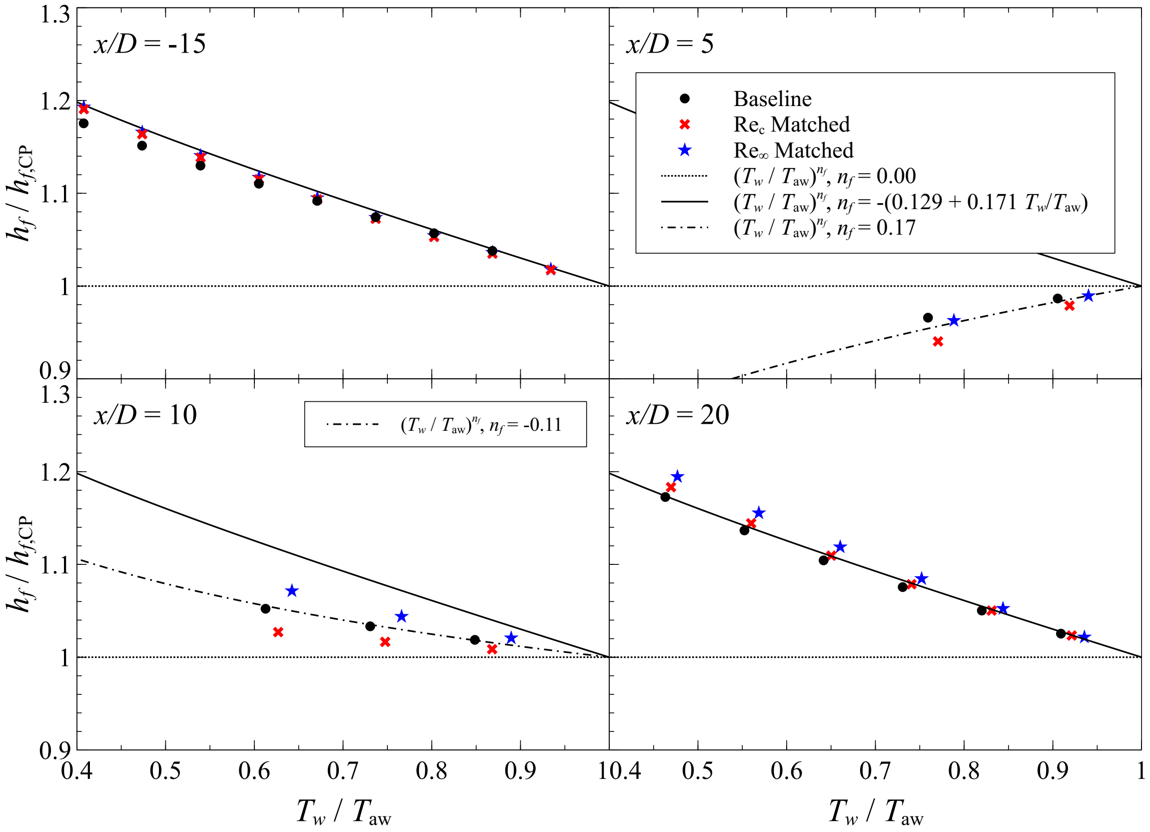

Figure 6.27: Variation of the film cooled convective heat transfer coefficient ratio ($h_f/h_{f,\mathrm{CP}}$) with temperature ratio ($T_w/T_{\mathbf{aw}}$)

to a n_f exponent defined by

$$n_f = -(0.129 + 0.171 T_w/T_{\mathrm{aw}}) \tag{6.8}$$

After the film cooling injection at $x/D = 5$ and 10, the $h_f/h_{\mathrm{CP},f}$ data were observed to deviate from this curve. However, by $x/D = 20$, the $h_f/h_{\mathrm{CP},f}$ data were found to return to the temperature ratio curve with n_f defined by Eq. 6.8. At both $x/D = -15$ and 20, the $h_f/h_{\mathrm{CP},f}$ data were observed to agree with the curve with n_f defined by Eq. 6.8 within 3% for both the high and low temperature cases.

It was observed in Section 5.2 that variable properties have a negligible effect on laminar boundary layers such that $n_0 = 0$ in the temperature ratio method. For turbulent flow, n_0 was observed to be negative to model the data's increasing $h_0/h_{\mathrm{CP},0}$ trend with decreasing T_w/T_∞. Though the transition region was not examined, it is expected that transitional flows will feature n_0 between $n_0 = 0$ and the fully turbulent, negative n_0. However, at $x/D = 5$ the $h_f/h_{\mathrm{CP},f}$ data are seen to decrease with decreasing T_w/T_{aw} such that n_f is positive. This is uncharacteristic of laminar and turbulent flows and is unique to the film cooled data close to the hole. However, the $h_f/h_{\mathrm{CP},f}$ of both the high and low temperature cases were seen to follow the temperature ratio curve with $n_f = 0.17$ to within 2%. At $x/D = 10$, Fig. 6.27 indicates that $h_f/h_{\mathrm{CP},f}$ increases with decreasing T_w/T_∞ such that n_f is negative. Though clear quantitative differences existed amongst the $h_f/h_{\mathrm{CP},f}$ data of the three cases, they were observed to follow the temperature ratio curve with $n_f = -0.11$ to within 3%.

In summary, it was seen in Section 5.1.2 that variation of $h_0/h_{\mathrm{CP},0}$ with T_w/T_∞ at any turbulent Re_x could be modeled by the temperature ratio method of Kays et al. [29] with n_0 defined by Eq. 5.3. In the present analysis, it was observed that $h_f/h_{\mathrm{CP},f}$ could also be modeled using the temperature ratio method of Kays et al. [29]. However, it was found that accurate modeling required an empirical exponent, n_f, which changed with x/D. In fact, n_f at $x/D = 5$ was positive. This did not align well with the $h_0/h_{\mathrm{CP},0}$ data which required $n_0 = 0.0$ for laminar flows and negative n_0 for turbulent flows.

Values for n_f were determined at each x/D which modeled the $h_f/h_{\mathrm{CP},f}$ to within 3%. However, it is likely that these n_f are not general to any film cooling flow. Changing parameters such as M or film cooling geometry are expected to change the optimal n_f at each x/D. Thus, the temperature ratio method is not recommended for modeling effect of varying T_w on h_f.

In a high temperature environment such as a turbine, T_{aw} can be higher than the melting temperature of viable materials. Thus, unlike low temperature experiments, direct measurement of the adiabatic conditions of $h_{\mathrm{CP},f}$ and T_{aw} can be impractical. It Section 5.2.3, it was seen that $h_{\mathrm{CP},0}$ and an unknown T_∞ could be quantified in a no-film cooling environment from non-adiabatic conditions by inverse application of the temperature ratio method of Kays et al. [29]. However, since the present analysis indicated that the temperature ratio method could not be generally applied to film cooling, it cannot be used to quantify $h_{\mathrm{CP},f}$ and T_{aw} from non-adiabatic measurements.

As a direct result, η cannot be quantified in a high temperature environment where adiabatic conditions are unattainable. In addition, until a model for h_f with θ_w is developed, measurements of $\Delta q''_f$ over a given range of θ_w cannot be used to predict $\Delta q''_f$ outside the θ_w range. Moreover, since a general mode for h_f/h_0 could not be found, measurement of η alone does not provide enough information to determine how much the film cooling scheme will reduce heat flux to the surface. Thus, the computational evidence suggests that $\Delta q''_f$ is the most appropriate parameter to scale film cooling performance and, with experimental validation, satisfies Objective 2 of the present research.

6.1.5 Section Summary.

This section examined scaling film cooling performance from near ambient experiments to engine conditions computationally in support of Objective 2 of the present research. Section 6.1.1 showed that adiabatic effectiveness (η) can be scaled by non-dimensionally matching the engine condition's density ratio (DR), blowing ratio (M), freestream Prandtl number (Pr_∞), coolant Prandtl number (Pr_c), and either the freestream or coolant Reynolds number (Re_∞ and Re_c, respectively). Next, Section 6.1.2 showed that Net Heat Flux Reduction (NHFR or $\Delta q''_f$) can be scaled by the same non-dimensional matching and also matching the non-dimensional wall temperature

(θ_w).

Section 6.1.3 indicated that the ratio of the film cooled to non-film cooled convective heat transfer coefficients (h_f/h_0) embedded within the definition of NHFR could also be scaled by the same methodology as NHFR. Chapter V showed that the temperature ratio method of Kays et al. [29] could model the variation of h_0 with θ_w. Similarly, Section 6.1.4 examined whether the temperature ratio method could also model variation in h_f with θ_w. It was found that the temperature ratio method could model h_f, but required an empirical exponent (n_f) which varied with distance from the hole (x/D) and could not be generally defined for an arbitrary film cooling scenario. As a result, since it is impractical to establish adiabatic conditions at high temperatures, it was determined that η could neither be measured nor applied to determine film cooling performance in a high temperature environment.

Thus, the computational studies of this section indicated that $\Delta q''_f$ was the best parameter to quantify and scale film cooling performance from near ambient temperature experiments to engine conditions in satisfaction of Objective 2. The scaling technique was found to consist of non-dimensionally matching the DR, M, Pr_∞, Pr_c, and Re_∞ or Re_c over a range of θ_w in a low temperature experiment. Then, since it would be difficult to match an engine θ_w exactly, the predicted NHFR in the engine conditions could be quantified by interpolating the low temperature NHFR measurements at the θ_w observed in the engine. Alternatively, when θ_w is unknown, the function for NHFR with θ_w could be an input to a heat transfer analysis to balance the internal and external cooling schemes and determine θ_w. The following section will examine NHFR experimentally and present a limited validation of the NHFR scaling methodology to fully satisfy Objective 2 of the present research.

6.2 Experimental Results

The former part of this chapter was dedicated to developing computational evidence of a methodology to scale film cooling performance from near ambient conditions to engine conditions in support of Objective 2 of the present research. It was found that Net Heat Flux Reduction (NHFR or $\Delta q''_f$) was the best parameter to quantify film cooling performance. In addition, the computational results suggested that, for $x/D > 5$, NHFR could be scaled by non-dimensionally matching the density ratio (DR), blowing ratio (M), freestream Prandtl number (Pr_∞), coolant Prandtl number (Pr_c), the coolant Reynolds number (Re_c), and the non-dimensional wall temperature (θ_w).

The present section will apply the theory developed above to experimental measurements of non-reacting film cooling gathered in the experimental facility described in Chapter III. First, the film cooling geometries and experimental conditions will be presented. Next, since Section 5.3 showed that the present facility has a significant radiative heat transfer component, a method to isolate the convective portion of the heat flux following the film cooling injection will be presented. This, in conjunction with heat flux measurements without film cooling, will enable quantification of NHFR. Subsequently, it will be shown that the scaling method developed computationally in the previous section can be employed to scale NHFR between two conditions with appropriate non-dimensional matching. Last, the NHFR downstream of several film cooling schemes will be compared to demonstrate that their relative performance compared to other schemes found at near ambient temperature hold true at combustion temperatures. Ultimately, this section will provide experimental validation of the theory developed in Section 6.1 to fully satisfy Objective 2 of this research.

6.2.1 Film Cooling Geometries.

Several film cooling schemes were selected for this experimental study. Four geometrical categories were examined: 1) cylindrical holes, 2) fan shaped holes, 3) cylindrical holes embedded within a trench, and 4) slots. Each of these geometries were studied in a single row configuration to display the individual row performance without considering the effect of superposition of sequential rows of holes. Then, all but the fan shaped hole geometry were examined in a five sequential row configuration to study the effect of a build-up of coolant. The five row shaped hole configuration was not included due to the time, cost, and difficulty associated with fabricating the test coupon.

Detailed dimensions of these configurations are included in Section 3.4.3 and the relative benefits and drawbacks of each configuration are discussed in Section 2.3.3. The characteristic hole opening dimension (slot height or hole diameter) was $D =$ 0.508mm. The pitch spacing of the holes was $4D$ and, for the five row configurations, the row spacing was also $4D$. In the five row configurations except the slot, the holes in each row were offset such that each hole's centerline was halfway between the centerlines of the adjacent holes in the rows fore and aft where applicable.

6.2.2 Experimental Test Conditions.

Similar to the experimental study of no film cooling presented in Section 5.3, three freestream conditions were examined as seen in Table 6.3. Given that the ultimate objective of this research was film cooling in a fuel rich environment, the majority of the experimental work was accomplished at a fuel rich condition with an equivalence ratio of $\Phi = 1.3$. To produce a non-reacting film cooling layer at this $\Phi > 1.0$ condition, N_2 was used as coolant. However, the single row of fan shaped holes configuration was also examined at equivalence ratios of $\Phi = 0.71$ and 0.985 to vary the freestream temperature (T_∞) and validate the scalability of NHFR. Previously, Evans [18] showed that using air coolant with a $\Phi < 1.0$ freestream condition produced film cooling layer which was not effected by reactions. Thus, for the present $\Phi < 1.0$ cases used air for the film coolant.

As discussed, appropriate non-dimensional matching is required to scale NHFR. Fortunately, Pr_∞ and Pr_c will be sufficiently matched due to the nature of gaseous property variations. Additionally, M and Re_c can be matched by judicious selection of freestream and coolant mass flow rates. However, the present test facility does not allow for precise control of the freestream or coolant temperatures which much be measured to quantify DR and θ_w.

To calculate DR, first the method outlined in Section 3.6 was used to measure T_∞. Since the freestream was composed of combustion products, the measured T_∞ was used as an input to the Chemical Equilibrium with Applications (CEA) [41] discussed in Section 3.7 which, assuming atmospheric pressure, calculated the composition and ρ_∞. Direct measurement of the coolant exit temperature ($T_{c,e}$) was impractical due to the high temperatures and a lack of instrumentation access. Thus, a method to approximate the coolant temperature will be presented in Section 6.2.2.2. Finally, ρ_c was calculated via the ideal gas law and DR for each case was quantified and listed in Table 6.3.

6.2.2.1 Quantification of Net Heat Flux Reduction.

As discussed in Section 2.3.1, an important requirement of NHFR is that both the heat flux without film cooling (q''_0) and with film cooling (q''_f) must be quantified at the same T_w. This requirement was satisfied in the CFD study of Section 6.1.2 by specifying identical T_w boundary conditions. However, the experimental facility did not allow for direct specification of T_w. Rather, T_w was implicitly determined by

Table 6.3: Non-reacting film cooling experimental conditions; * = Temperature from similar cases, direct measurement not available, † = Window test channel configuration (Fig.3.5(b))

#	Geometry	Rows	Φ	M	Coolant	$\overline{T_\infty}$ (K)	$\overline{T_{c,e}}$ (K)	DR	Ma_∞	Ma_c	$\mathrm{Re}_\infty \cdot 10^{-4}$	Re_c	Pr_∞	Pr_c
1	Cylindrical	1	1.3	1	N_2	1477	701	2.11	0.09	0.06	3.18	232	0.707	0.720
2	Shaped	1	1.3	1	N_2	1488	721	2.06	0.09	0.06	3.17	232	0.707	0.722
3	Shaped	1	0.985	1	Air	1603	755	2.12	0.09	0.06	2.92	218	0.740	0.703
4	Shaped	1	0.71	1	Air	1430	715	2.00	0.11	0.07	4.04	283	0.751	0.702
5	Shaped	1	0.71	0.8	Air	1436	711	2.02	0.11	0.06	4.03	226	0.750	0.702
6	Trench	1	1.3	1	N_2	1472	707	2.08	0.09	0.06	3.19	234	0.707	0.721
7	Slot	1	1.3	1	N_2	1489	730	2.04	0.09	0.01	3.17	43.2	0.707	0.723
8	Cylindrical	5	1.3	1	N_2	1486	672*	2.21	0.09	0.06	317	2.43	0.707	0.718
9 †	Cylindrical	5	1.3	1	N_2	1478	687*	2.15	0.09	0.06	3.18	239	0.707	0.719
10	Trench	5	1.3	1	N_2	1494	663	2.25	0.09	0.06	3.16	245	0.707	0.717
11	Slot	5	1.3	1	N_2	1498	672*	2.23	0.09	0.01	3.15	43.9	0.707	0.718

the balance of the heat flux to the test surface and the test block's backside cooling condition.

Thus, quantification of NHFR required two steps. First, the conductive heat fluxes measured with and without film cooling were corrected for radiation to isolate the convective components of q''_0 and q''_f, respectively. The process to correct the non-film cooled measurements for radiation utilized the method presented in Section 5.3. Alternatively, the method to correct the film cooled measurements for radiation will be presented in Section 6.2.3.

Conveniently, a secondary result of the process to account for radiation in the non-film cooled measurements is a formula for q''_0 as a function of T_w. Thus, though q''_0 and q''_f were not measured at identical T_w, q''_0 could be approximated at the T_w of the q''_f measurement via the convective portion of Eq. 5.10. Finally, the q''_f directly measured at T_w and the q''_0 approximated at T_w were used to calculated NHFR. Since the heat flux measurements were at locations distributed along the span at four x/D locations (see Table A.2), all the experimental results are presented as spanwise averaged NHFR given by

$$\overline{\Delta q''_f} = 1 - \frac{\overline{q''_f}}{\overline{q''_0}} \tag{6.9}$$

where $\overline{q''_f}$ and $\overline{q''_0}$ are spanwise averaged values and $\overline{q''_0}$ is evaluated at the spanwise averaged T_w for the film cooled condition.

6.2.2.2 Approximation of Coolant Temperature.

To properly non-dimensionalize the T_w measurements to θ_w, a method to approximate the coolant temperature at the exit of the film cooling hole ($T_{c,e}$) was required. As discussed in Section 3.4.4, the experimental test rig featured backside cooling channels. By providing various flow rates of water or nitrogen to the channels, the experiments varied T_w and q'' to the surface. As a result, each backside cooling con-

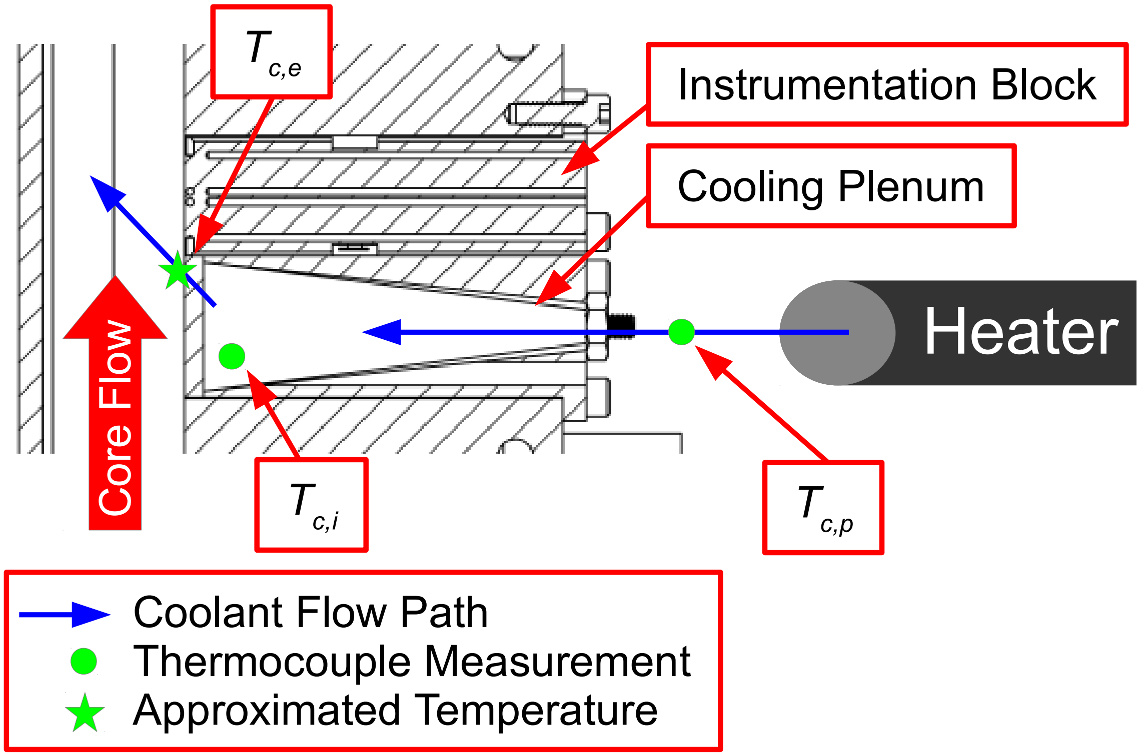

Figure 6.28: Locations of thermocouples used in $T_{c,e}$ approximation

dition caused a different spatial distribution of test block temperature such that the amount of heat picked up by the coolant within the plenum would vary. This section will develop a method to approximate $T_{c,e}$ at both the highest and lowest T_w condition for each test configuration. The high and low T_w approximations were used to estimate the maximum and minimum $T_{c,e}$ for each cooling configuration.

The temperature of the coolant within the plenum before it entered the film cooling hole ($T_{c,i}$) was measured at the location seen in Fig. 6.28. Since the geometry of the film cooling holes and the mass flow rate of coolant are known, it would be possible to estimate $T_{c,e}$ if the temperature of the cooling hole walls were known. However, the present research could not measure the metal temperature and, thus, a different method was required.

The present work employed a quasi-steady state method to approximate $T_{c,e}$. In addition to measuring $T_{c,i}$, the method entailed measuring the coolant temperature as it entered the film cooling plenum ($T_{c,p}$) at the location seen in Fig. 6.28. A heater was located upstream of the film cooling inlet as described in Section A.4.1 to heat the coolant entering the film cooling plenum. Due to the low flow rates of coolant, the heater could not be used to heat the coolant directly. Doing so resulted in large oscillations in coolant temperature due to large response times.

To avoid these oscillations, a separate process air with a mass flow rate which was nominally 100 times that of the coolant was heated instead. This effectively reduced the oscillations by significantly decreasing the response time of the control system. Next, the heated process air was routed through the outer diameter of a concentric tube assembly. Then, the coolant was routed through the inner tube of the assembly in the opposite direction to form a counterflow, concentric tube heat exchanger which heated the coolant.

The desired result of this process was to change $T_{c,p}$ and record the response of $T_{c,i}$. To do so, first, constant flow rates of process air and coolant were established with the heater initially off and at room temperature. Then, the heater of the process air was ramped from an unheated condition to a setting of 700 K. Subsequently, the process air would be heated which, in turn, would heat the coolant in the counterflow concentric tube heat exchanger such that $T_{c,p}$ would increase. Though the process air was heated to 700 K, the high driving temperatures and low flow rates of coolant resulted in steady state temperatures at the entrance of the plenum ($T_{c,p}$) which were up to 250 K lower. After the heater was engaged, the transient of $T_{c,p}$ and $T_{c,i}$ were recorded over time. Overall, from beginning to the heated steady state of $T_{c,p}$ and $T_{c,i}$, this process required approximately 20 minutes.

The quasi-steady state assumption of this method involved two assumptions. The first was that heating the coolant had a small effect on the distribution of temperatures on the plenum walls. The second was that, for any given time during the transient, $T_{c,i}$ was in equilibrium with the $T_{c,p}$ input.

To validate the first of these assumptions, the conclusions of Section A.5.1 were used. This section showed that the instrumentation block experienced nearly 1-D heat transfer in the wall normal direction despite being next to the cooling plenum as seen in Fig. 6.28. This indicated that the heat transfer to the plenum walls from the coolant is small compared to the heat flux in the wall normal direction from the hot core flow. Therefore, the temperature profile within the block was dominated by the hot core flow and the backside cooling scheme. As a result, changing $T_{c,p}$ had a small effect on the plenum wall temperatures such that the first quasi-steady assumption was sufficiently validated.

The second quasi-steady state assumption was validated by considering the time scales of the flow and $T_{c,p}$ heating processes. First, based on the mass flow rate of coolant and the area of the plenum at the exit, the residence time of the coolant in the plenum was on the order of 0.3 second. In comparison, the $T_{c,p}$ heating process took nominally 1200 seconds. Thus, since the coolant was assumed to have a small effect on the temperature of the plenum walls, $T_{c,i}$ was expected to reach equilibrium with changes in $T_{c,p}$ within a timescale on the order of 4000 times faster than changes in $T_{c,p}$. Thus, the second and final assumption to substantiate the quasi-steady method was validated. As a result, at any given time, $T_{c,i}$ was in quasi-steady state with $T_{c,p}$.

As $T_{c,p}$ heated, $T_{c,i}$ increased. However, there should exist a $T_{c,p}$ high enough such that larger $T_{c,p}$ would not increase $T_{c,i}$. This would occur due to the coolant being in an adiabatic condition with the cooling plenum near the $T_{c,i}$ measurement location seen in Fig. 6.28. Thus, when the coolant temperature entered the film cooling holes, it would be the same temperature as the metal and would not pick up or reject any heat such that $T_{c,i,\mathrm{aw}} = T_{c,e,\mathrm{aw}}$ where $T_{c,e}$ is the coolant temperature at the exit of the film cooling hole as seen in Fig. 6.28. In addition, $T_{c,e,\mathrm{aw}}$ represents the $T_{c,e}$ at this adiabatic condition.

Conceptually, this describes an asymptotic increase of $T_{c,i}$ to $T_{c,e,\mathrm{aw}}$ with increasing $T_{c,p}$. Therefore, a general asymptotic equation was adopted given by

$$T_{c,i} = (T_{c,e,\mathrm{aw}} - T_{c,i,0})\left(1 - e^{\lambda(T_{c,p} - T_{c,p,0})}\right) + T_{c,i,0} \tag{6.10}$$

where $T_{c,p,0}$ and $T_{c,i,0}$ are the coolant temperatures at the plenum inlet and film cooling hole inlets, respectively, with no upstream heating. Additionally, λ is an empirical fitting coefficient. It can be shown that the precise selection of the exponent base (in this case e) is irrelevant as it can be absorbed into the λ exponent.

Two examples representative of the $T_{c,i}$ response for the 1-row and 5-row configurations along with the fitted functions are given in Fig. 6.29(a). As seen in this figure, $T_{c,i}$ appears to approach an asymptote as $T_{c,p}$ is increased. The main result of fitting Eq. 6.10 to the $T_{c,i}$ temperature response is the temperature of the coolant given an adiabatic condition ($T_{c,e,\mathrm{aw}}$).

As discussed, this method assumed that when $T_{c,p}$ is sufficiently heated, the coolant will experience an adiabatic condition from the film cooling hole inlet to its outlet such that $T_{c,i,\mathrm{aw}} = T_{c,e,\mathrm{aw}}$. Though this adiabatic condition is theoretically attainable, the present work was unable to supply sufficiently high $T_{c,p}$. Similarly, assuming $T_{c,e}$ was equal to the directly measured value of $T_{c,i}$ does not account for the heat gained within the cooling hole. Thus, it was reasonable to assume that $T_{c,i} < T_{c,e} < T_{c,e,\mathrm{aw}}$. Since the true $T_{c,e}$ could not be measured directly, an approximation was used. Namely, $T_{c,e}$ was assumed to be the average of the $T_{c,i}$ at steady state after the coolant heater was engaged ($T_{c,i,f}$) and $T_{c,e,\mathrm{aw}}$ such that

$$T_{c,e} = 0.5(T_{c,i,f} + T_{c,e,\mathrm{aw}}) \tag{6.11}$$

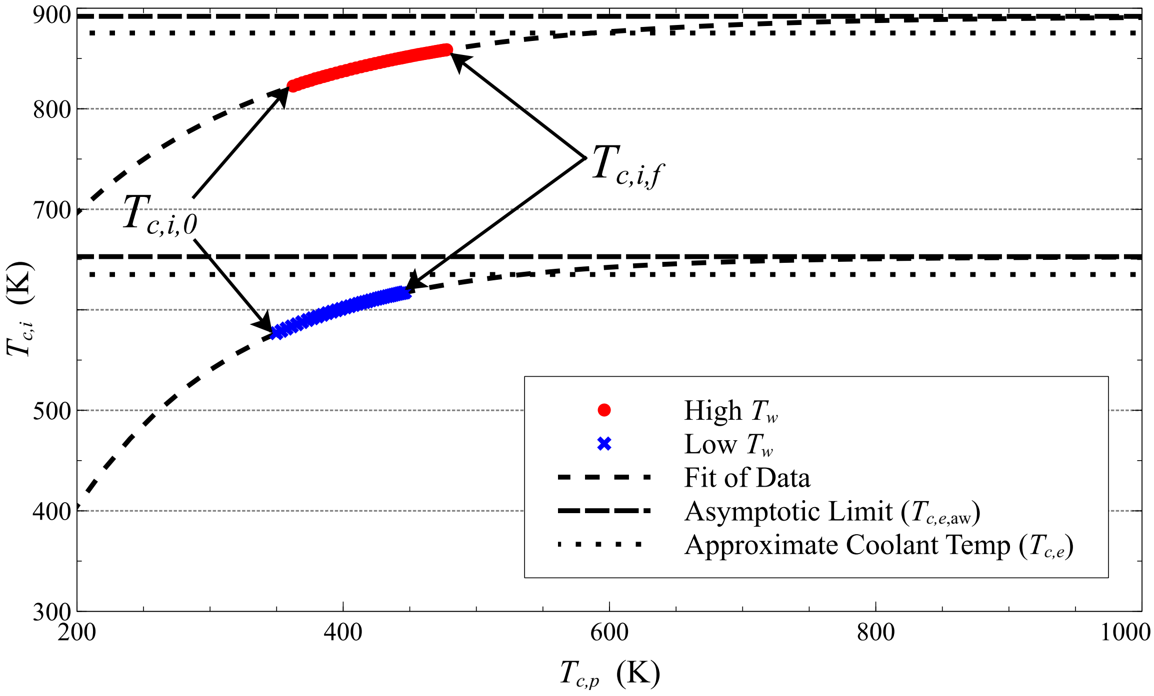

(a) 1-Row of Shaped Holes, $\Phi = 0.985$

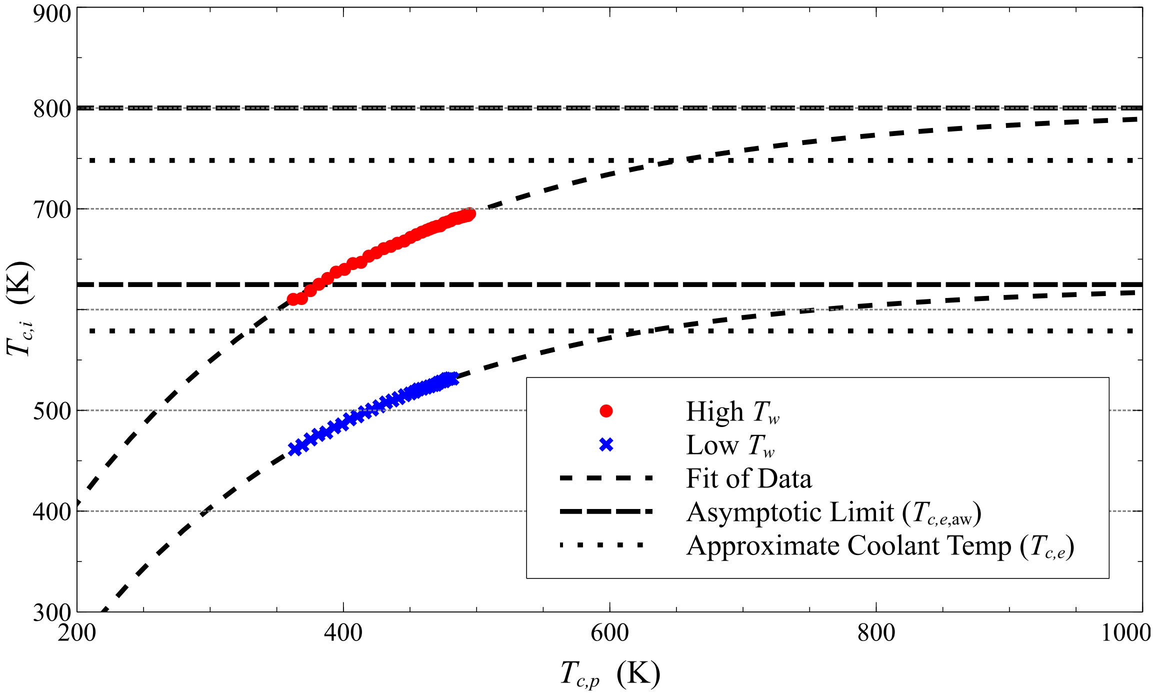

(b) 5-Rows of Trenches, $\Phi = 1.3$

Figure 6.29: Extrapolation of adiabatic coolant temperature ($T_{c,e,\mathbf{aw}}$) from quasi-transient $T_{c,i}$ response, $M = 1$

Last, since $T_{c,e}$ is bounded by $T_{c,i,f}$ and $T_{c,e,\mathrm{aw}}$, the maximum possible error in $T_{c,e}$ was calculated by

$$\delta T_{c,e} = T_{c,e} - T_{c,i,f} = T_{c,e,\mathrm{aw}} - T_{c,e} \tag{6.12}$$

Figure 6.29 compares the results of the extrapolation process applied to the single row of shaped holes configuration at $\Phi = 0.985$ and the five rows of trenches configuration at $\Phi = 1.3$. This figure indicates that the single row configuration has a much smaller difference between $T_{c,i,f}$ and $T_{c,e,\mathrm{aw}}$ compared to the five row configuration. This is due to the one row configuration having a fifth of the total mass flow resulting in more heating of the coolant such that it approaches the adiabatic condition. Thus, $\delta T_{c,e}$ is small for the one row configuration ($\sim 10\,\mathrm{K}$) while it is large for the five row configuration ($\sim 120\,\mathrm{K}$).

Given the approximations of $T_{c,e}$ at both the highest and lowest T_w conditions of each test configuration, the question arises of what $T_{c,e}$ to use for conditions between the maximum and minimum T_w. Two different methods were examined. First, a linear interpolation of $T_{c,e}$ between the highest and lowest T_w conditions was used. Second, an average of the $T_{c,e}$ values calculated at the highest and lowest T_w was used such that a constant $\overline{T_{c,e}}$ was assumed for all T_w. Since it was found in Section 6.1.2 that θ_w must be matched to scale NHFR, the experimental results will use θ_w to non-dimensionalize T_w and NHFR was plotted as a function of θ_w.

Each of these methods to quantify $T_{c,e}$ were used to plot NHFR as a function of θ_w in Fig. 6.30 such that their effects on the NHFR trends could be visualized. It is seen in Fig. 6.30(a) that using the linearly interpolated $T_{c,e}$ collapses the data to a very small range of θ_w. As a result, NHFR is seen to vary considerably with virtually no change in non-dimensional wall temperature (θ_w). This qualitative result is in stark disagreement with response of NHFR to variations in θ_w as calculated by CFD and seen in Fig. 6.22.

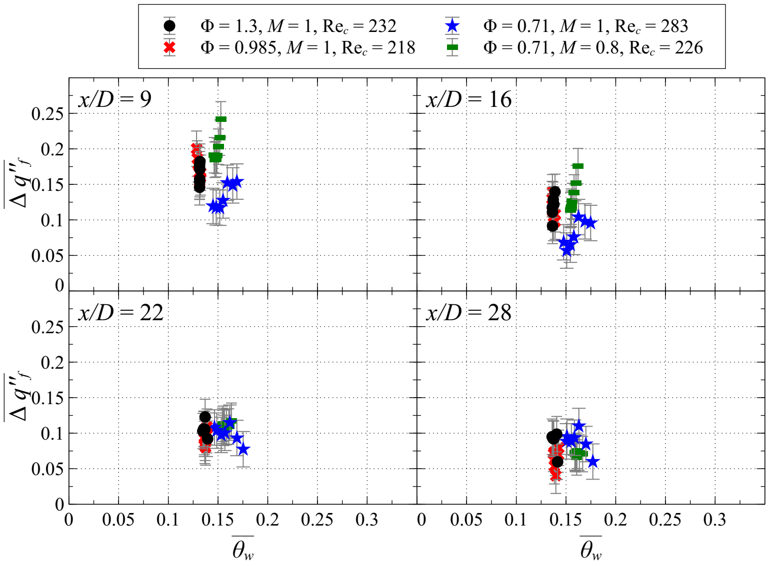

(a) Wall temperature dependent $T_{c,e}$

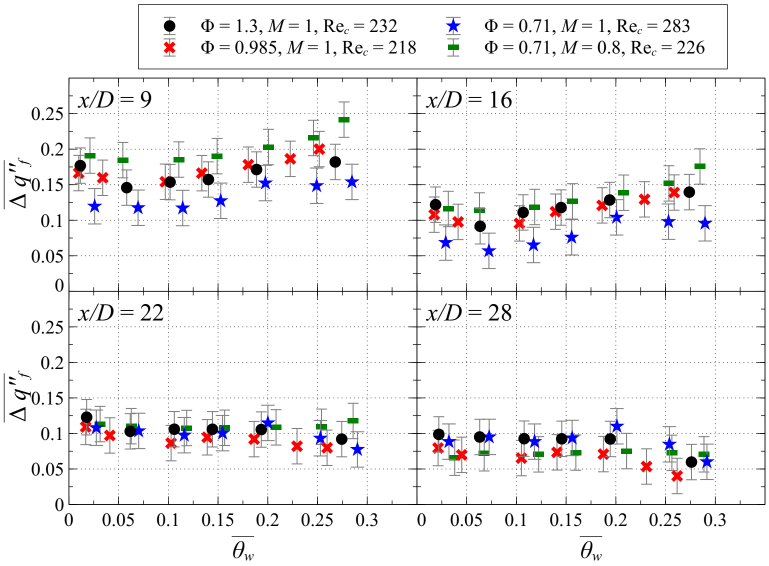

(b) Constant $T_{c,e}$

Figure 6.30: NHFR of the shaped hole geometry cases vs. θ_w calculated with temperature dependent and constant $T_{c,e}$

Alternatively, calculating θ_w using $\overline{T_{c,e}}$ is seen in Fig. 6.30(b) to produce results that are qualitatively consistent with the CFD results seen in Fig. 6.22. Specifically, NHFR is seen to increase with increasing θ_w for $x/D = 9$ and 16. For $x/D = 22$ and 28, NHFR is seen to remain somewhat constant with θ_w. This also reflects the qualitative trend of Fig. 6.22 that NHFR becomes less sensitive to changes in θ_w with increasing x/D. Thus, due to this superior qualitative agreement to the CFD results, θ_w was calculated using $\overline{T_{c,e}}$ for all the experimental results of the present work.

6.2.3 Radiation Correction of NHFR.

Previously, Section 5.3 presented a method to account for radiation in an environment with no film cooling. The method revealed that the radiative component comprised a significant portion of the total heat flux to the surface (q''_{cond}). Subsequently, the convective heat flux without film cooling (q''_0) was quantified by removing the radiative component of q''_{cond} via Eq. 5.9 where $q''_0 = q''_{\text{conv}}$.

The Net Heat Flux Reduction parameter (NHFR or $\Delta q''_f$) quantifies a film cooling scheme's ability to reduce heat flux to a surface. It does so by comparing the convective heat transfer with film cooling (q''_f) to q''_0 via Eq. 2.32. Thus, similar to the no cooling measurement, the radiative component must be removed from the q''_{cond} measurement with film cooling to isolate q''_f via Eq. 5.9 where $q''_f = q''_{\text{conv}}$.

The method presented in Section 5.3 quantified the radiative component of heat flux (q''_{rad}) by a linear regression of Eq. 5.10. The regression was used to solve for the two unknowns of the constant property convective heat transfer coefficient (h_{CP}) and the radiative component to the surface from the surroundings ($q''_{\text{rad},i}$). This linear regression method was enabled by direct measurement of the freestream temperature (T_∞) and assuming the surface is adiabatic when $T_w = T_{\text{aw}} = T_\infty$.

However, introduction of film cooling results in $T_{\text{aw}} \neq T_\infty$ such that the driving temperature is no longer known a priori. Thus, the linear regression model (Eq. 5.10) cannot be applied to a film cooled surface due to the additional unknown of T_{aw}. Furthermore, the linear regression model assumed that the temperature ratio exponent (n) could be quantified by Eq. 5.3 which was developed using the flat plate CFD results of Section 5.1.2. However, the CFD results of Section 6.1.4 indicated that the temperature ratio exponent n given by Eq. 5.3 was not valid for a film cooled surface. Moreover, it was observed the n required by a film cooled condition varied with x/D. Therefore, the lack of a well defined n for a film cooled cases deemed that this study could not quantify the radiative heat transfer component of a film cooled surface directly. An additional consequence was that, since the present facility could not achieve adiabatic conditions at combustion temperatures, T_{aw} could not be quantified.

Rather than direct quantification of the radiative component, an assumption was made. Specifically, diatomic molecules like O_2 and N_2 are transparent media which do not emit significant radiation. Thus, it was assumed that an addition of a thin layer of air or nitrogen above the surface played a negligible role in the radiative heat transfer component. Thus, it was assumed that $q''_{\mathrm{rad},i}$ quantified with no film cooling was equal to the $q''_{\mathrm{rad},i}$ after film cooling was applied. In addition, the non-film cooled and film cooled measurements were taken in parallel for each experimental test case given in Table 6.3. Thus, small deviations in conditions external to the experiment were assumed to have a negligible effect on $q''_{\mathrm{rad},i}$ between the non-film cooled and film cooled measurements.

The $h_{\mathrm{CP},0}$ and $q''_{\mathrm{rad},i}$ values measured for each test case in Table 6.3 via the method of Section 5.3 are given in Table 6.4. Though Table 6.3 lists these cases as having $M = 0.8$ or 1, these measurements were taken under a no-cooling condition with $M = 0$. Examining the $h_{\mathrm{CP},0}$ results of the $\Phi = 1.3$ test conditions reveals an

Table 6.4: Results of fitting Eq. 5.10 to the no-cooling measurements of each test condition listed in Table 6.3

#	$h_{\mathrm{CP},0}$	$q''_{\mathrm{rad},i} \cdot 10^{-4}$ (W/m^2)
1	190	6.09
2	214	4.83
3	192	6.34
4	237	4.45
5	211	5.38
6	219	3.71
7	195	5.58
8	210	4.07
9	210	4.89
10	201	5.16
11	194	5.49

average $h_{\mathrm{CP},0}$ amongst the cases of 204 W/m^2 K with a 95% confidence interval of ±21 W/m^2 K (±10.4%). This confidence interval compares well to the uncertainty calculated in Section A.6.7 of $\delta h_{\mathrm{CP},0} = \pm 22.4\,\mathrm{W/m^2\,K}$ (10.5% of $h_{\mathrm{CP},0}$).

A similar examination of the $q''_{\mathrm{rad},i}$ results of the $\Phi = 1.3$ test cases reveals an average $q''_{\mathrm{rad},i}$ amongst the cases of $4.98 \times 10^4\,\mathrm{W/m^2}$ with a 95% confidence interval of $\pm 0.790 \times 10^4\,\mathrm{W/m^2}$ (±31.7%). This is in considerable disagreement with the expected uncertainty calculated in Section A.6.7 of $\delta q''_{\mathrm{rad},i} = \pm 663\,\mathrm{W/m^2}$ (1.37% of $q''_{\mathrm{rad},i}$). This disagreement could be caused by two effects. First, the $\delta q''_{\mathrm{rad},i}$ calculated in Section A.6.7 seems exceedingly low. However, uncertainty quantification of a linear regression is difficult and no better uncertainty calculation was available. Second, since radiative heat transfer from the surroundings is proportional to T_s^4 and given Section 5.3 found a nominal temperature of $T_s = 1150\,\mathrm{K}$, a 31.7% variation in $q''_{\mathrm{rad},i}$ is the equivalent of a +80 K or −105 K change in T_s. Thus, the variability of T_∞ and the slightly different ambient temperatures in the facility between tests could also contribute to the variation in $q''_{\mathrm{rad},i}$ amongst the test cases.

The excellent agreement with $\delta h_{\mathrm{CP},0}$ is a good indicator that the convective heat transfer environment is relatively repeatable between test days and regardless of the upstream film cooling geometry. However, the disagreement with $\delta q''_{\mathrm{rad},i}$ indicates that the radiative component is not repeatable within the expected uncertainty between test days. Overall, this reiterates the difficulty in accurately quantifying or scaling radiative heat transfer as well as the importance of quantifying the radiative heat transfer in each high temperature experiment.

To visualize the effect of correcting the measurements for radiation, Fig. 6.31 compares the NHFR of the five rows of cylindrical holes configuration with and without accounting for radiation and in both a no-window configuration and the window configuration. The no-window configuration is show in Fig. 3.5(a) to have Hastelloy X [24] surfaces bounding the test channel cross-section. The window configuration is seen in Fig. 3.5(b) to have Hastelloy X [24] surfaces bounding much of the test channel cross-section with the exception of a quartz window on one side of the channel and a sapphire window above the test surface with a normal view of the film cooling plenum and instrumentation block. Since quartz, sapphire, and Hastelloy X [24] all have different radiative properties, these configurations were utilized to create two different radiative environments.

In addition to differences in material, the window configuration is also seen in Fig. A.10(b) to have a thicker block of Hastelloy X [24] bounding the upper surface of the test channel to support the sapphire window's mounding hardware. This is expected to increase the temperature of the upper surface and will be seen to increase the radiation to the test surface compared to the no-window configuration. In fact, Table 6.4 indicates a 20% increase in $\delta q''_{\mathrm{rad},i}$ between the no-window (Case 8) and window (Case 9) configurations.

Examining Fig. 6.31, reveals that both the no-window and window configurations produce NHFR results which agree within the experimental uncertainty. However, correcting the results for radiation resulted in slightly higher NHFR values than

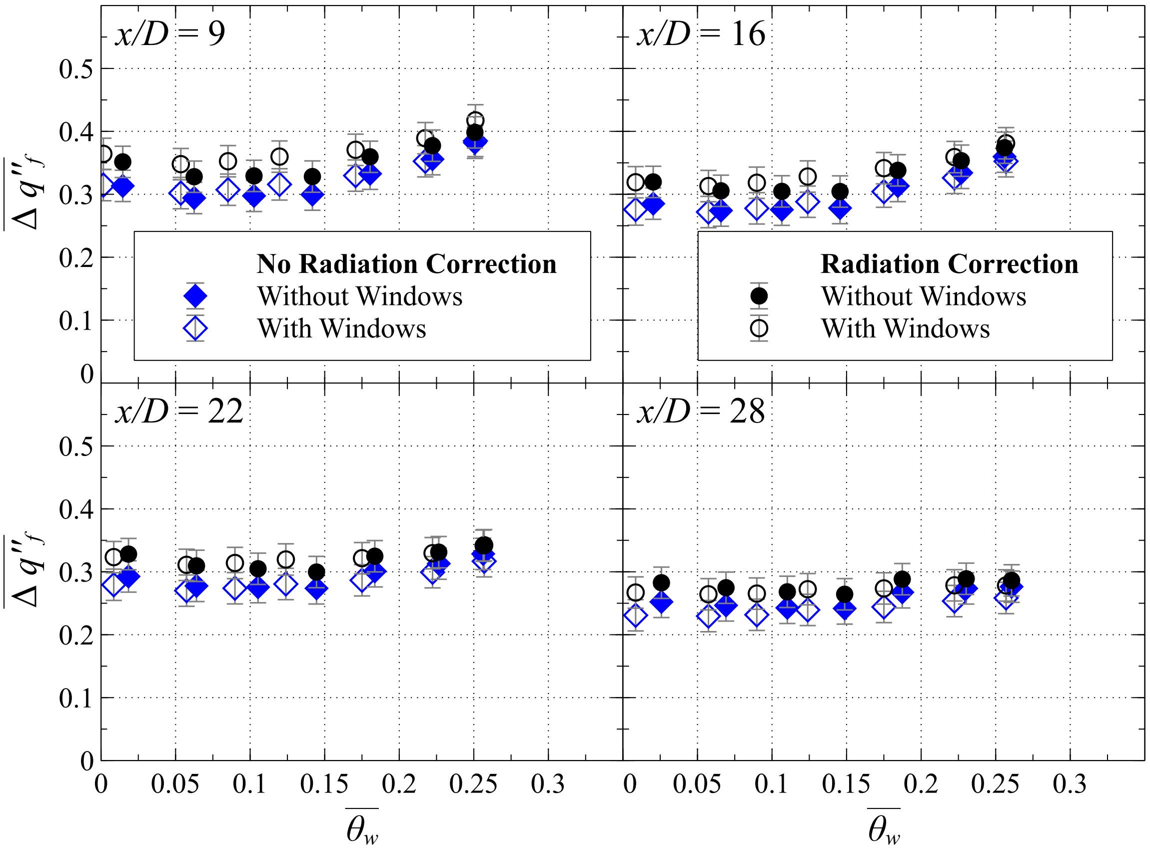

Figure 6.31: NHFR of the 5-row cylindrical geometries with and without a Radiation Correction; $M = 1$, $\Phi = 1.3$, N_2 Coolant

without a radiation correction. The small increase can be explained by examining the functional form of NHFR without correcting for radiation given by

$$\overline{\Delta q''_{f,\text{cond}}} = 1 - \frac{\overline{q''_{f,\text{cond}}}}{\overline{q''_{0,\text{cond}}}} = 1 - \frac{\overline{q''_f} - \overline{q''_\text{rad}}}{\overline{q''_0} - \overline{q''_\text{rad}}} \tag{6.13}$$

This equation illustrates that sufficiently large q''_f and q''_0 compared to q''_rad results in a negligible contribution of q''_rad to NHFR. However, as NHFR increases, q''_f will decrease relative to q''_0 and the q''_rad component will become an increasing factor in NHFR if not corrected. Thus, accurate quantification of q''_rad is paramount in highly effective cooling configurations to enable accurate quantification of NHFR.

The excellent agreement between the no-window and window configurations signal indicates that, regardless of the radiative condition incident on the test surface, the ability of the film cooling scheme to reduce convective heat flux to the wall (NHFR) remains the same at a given T_w. Thus, this result coupled with a method to scale NHFR facilitate the measurement of NHFR in a laboratory environment for application in a gas turbine engine environment and satisfy Objective 2 of the present research. The next section will be dedicated to validating the scalability of NHFR.

6.2.4 Validation of Net Heat Flux Reduction Scalability.

Section 6.1.2.2 gave computational evidence that net heat flux reduction (NHFR) can be scaled between temperatures by appropriate non-dimensional matching. Namely, scaling NHFR was contingent on matching density ratio (DR), blowing ratio (M), Prandtl number of the freestream (Pr_∞), Prandtl number of the coolant (Pr_c), Reynolds number of the coolant (Re_c), and the non-dimensional wall temperature (θ_w). Similar to the computational study, the experimental validation was completed using the single row of shaped holes geometry. The four single row of shaped hole test conditions in Table 6.3 (Cases 2-5) were designed to provide a spread of conditions to cover various non-dimensional matchings. A summary of the relevant scaling parameters is given in Table 6.5. The remainder of this section will compare and contrast the four conditions to validate the scaling method that was developed in Section 6.1.2.2.

The NHFR results of the four shaped hole cases are presented in Fig. 6.32. At $x/D = 9$, this figure indicates that the $\Phi = 0.71$ with $M = 1$ and $\Phi = 0.71$ with

Table 6.5: Summary of scaling parameters for 1-row shaped hole cases in Table 6.3

#	Φ	DR	M	I	$\mathrm{Re}_\infty \cdot 10^{-4}$	Re_c	Pr_∞	Pr_c
2	1.3	2.06	1	0.49	3.17	232	0.707	0.722
3	0.985	2.12	1	0.47	2.92	218	0.740	0.703
4	0.71	2.00	1	0.5	4.04	283	0.751	0.702
5	0.71	2.02	0.8	0.32	4.03	226	0.750	0.702

$M = 0.8$ conditions have the largest difference in NHFR at all θ_w examined. In addition, the latter case is seen to have a higher NHFR at $x/D = 9$ despite having a lower M.

Table 6.5 shows that these cases have momentum ratios of $I = 0.50$ and 0.32, respectively. Understanding that the former case has a higher M and I puts the results of the two $\Phi = 0.71$ cases in qualitative agreement with the literature. Namely, the $M = 0.8$ case was found to have a higher NHFR near the hole at $x/D = 9$ due to its lower I. This restates the conclusion of Baldauf et al. [5] that film cooling performance increased with decreasing I near the hole due to reduced separation of coolant from the surface.

Next, Fig. 6.33 presents the NHFR results as a function of x/D at an interpolated $\theta_w = 0.15$. This figure shows that the higher M case had a higher NHFR farther from the hole at $x/D = 28$. Again, this restates the conclusion of Baldauf et al. [5] that film cooling performance increases with increasing M far from the hole due to the increased quantity of coolant ejected from the hole. In comparison, Table 6.5 indicates that the $\Phi = 1.3$ and $\Phi = 0.985$ cases had $I = 0.47$ and 0.49, respectively. As a result, Fig. 6.33 shows that NHFR decreased with increasing I near the hole at $x/D = 9$.

Farther downstream at $x/D = 28$, the $\Phi = 0.985$ case was observed to have a lower NHFR than the $\Phi = 0.71$ with $M = 1$ case. Though Table 6.5 shows that these cases have identical M and nearly identical Pr_∞ and Pr_c, the $\Phi = 0.71$ case has a Re_∞ 38% larger than the $\Phi = 0.985$ case. This confirms the results of Liess [35] which showed that a decreased displacement thickness (i.e. increased Re_∞ at a constant length scale) increased cooling performance. He attributed this effect to higher momentum in the freestream boundary layer near the wall resulting in better jet attachment and lateral spreading.

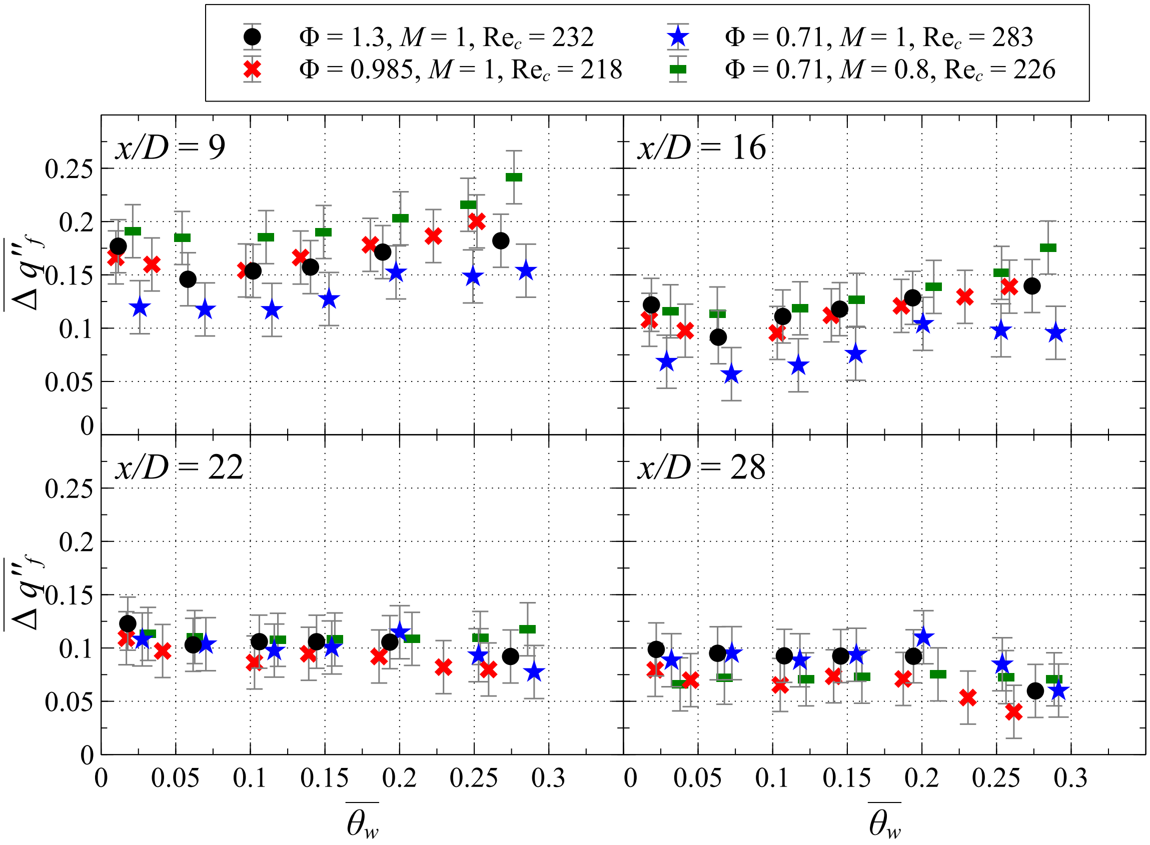

Figure 6.32: NHFR of the 1-row shaped hole geometry cases

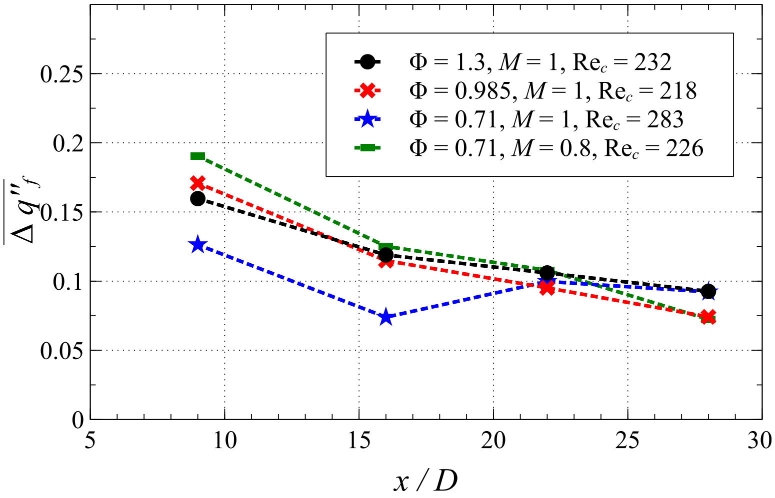

Figure 6.33: NHFR vs. x/D of the 1-row shaped hole geometry cases; $\theta_w = 0.15$

Facility constraints precluded testing of two experimental conditions which were perfectly matched non-dimensionally. However, the two most similar cases were the $\Phi = 1.3$ and $\Phi = 0.985$ cases. While these cases were non-dimensionally matched, their chemical compositions differed. Thus, clear differences existed between these two cases including the 115 K difference in T_∞. Despite these differences, Table 6.3 indicates that the $\Phi = 1.3$ and $\Phi = 0.985$ shaped hole cases have most of their non-dimensional parameters closely matched including DR, M, Re_∞, and Re_c. This resulted in these cases producing an agreement within 0.015 at $x/D = 9$, 16, and 22 at all $\theta_w$examined, as shown in Fig. 6.34.

At $x/D = 28$, the NHFR of the $\Phi = 0.985$ case is seen to drop up to 0.04 below the NHFR of the $\Phi = 1.3$ case. The source of this difference may be attributed to the slight difference in Pr_∞ between the two cases. Examining Table 6.2 reveals that the $\Phi = 0.985$ case has a Pr_∞ which is slightly elevated and a Pr_c which is slightly suppressed compared to the $\Phi = 1.3$ case.

Section 6.1.2.2 computationally compared the NHFR of a high temperature baseline to two non-dimensionally matched low temperature cases (Cases 7 and 8). The low temperature cases were seen in Table 6.2 to have $\mathrm{Pr}_c = 0.799$ compared to the high temperature baseline with $\mathrm{Pr}_c = 0.699$. Despite the large differences in Pr_c between the low and high temperature cases, they were found to agree well on NHFR. This suggests an insensitivity of NHFR to small changes in Pr_c.

It is theorized that, though Pr_c was elevated at the cooling hole exit, the film's Prandtl number would approach Pr_∞ as the film heats and mixes with the freestream. This mechanism would produce an insensitivity of NHFR on Pr_c far from the hole and a higher sensitivity near the hole. Revisiting Fig. 6.21 supports this hypothesis. Namely, both low temperature cases examined matched the high temperature baseline's NHFR least near the hole where the local Pr is most affected by Pr_c. Farther

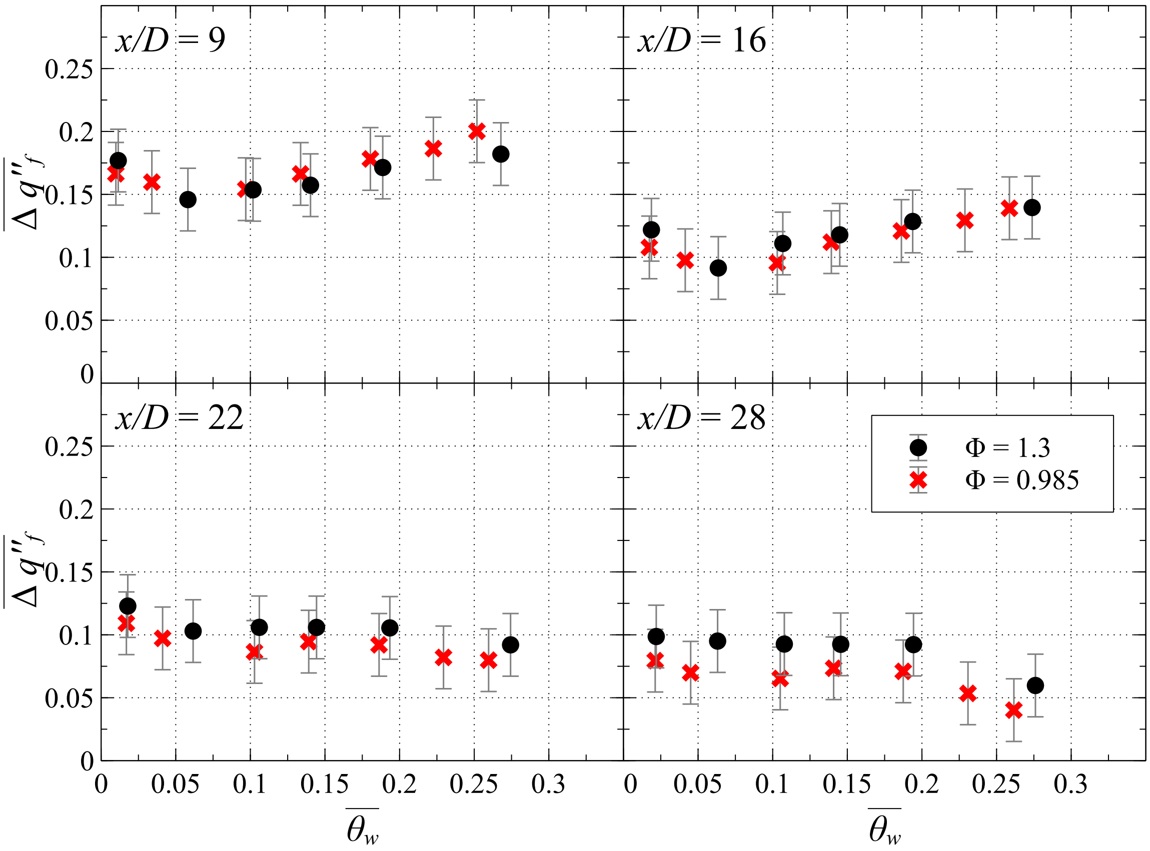

Figure 6.34: NHFR of the non-dimensionally matched 1-row shaped hole geometry cases; $M = 1$

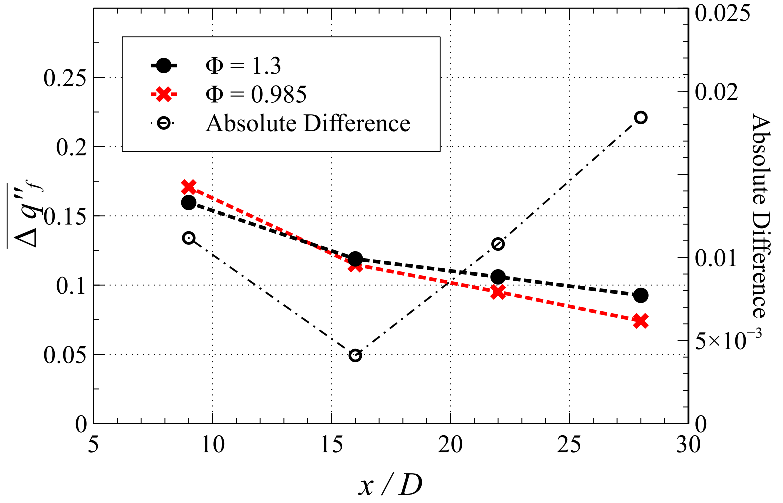

Figure 6.35: NHFR vs. x/D **of the non-dimensionally matched 1-row shaped hole geometry cases;** $M = 1$, $\theta_w = 0.15$

downstream, where the local Pr is least affected by Pr_c, the low temperature NHFR profiles were found to closely match the high temperture NHFR.

Alternatively, Pr_∞ is hypothesized to have a large effect on the film cooling layer at all x/D.

Unlike the coolant which heats up with x/D, T_∞ remains essentially constant with x/D. Thus, Pr_∞ is theorized to have a persistent effect on film cooling performance as a function of x/D. Table 6.2 shows the low and high temperature computational cases had $\mathrm{Pr}_\infty = 0.716$ and 0.699, respectively, for a difference of 0.017. Unlike Section 6.1.2.2, Table 6.5 displays that the $\Phi = 0.985$ case has a Pr_∞ which is 0.033 larger than the $\Phi = 1.3$ case. Thus, the effect of elevating Pr_∞ by the amount studied experimentally was not parameterized computationally. The elevated Pr_∞ of the $\Phi = 0.985$ case indicates that the freestream has an increased ability to thermally diffuse the coolant layer into the freestream. This increase is hypothesized to cause the more rapid decrease of the $\Phi = 0.985$ case's NHFR with x/D compared to the $\Phi = 1.3$ case as seen in Fig. 6.35

In summary, the results of this section restated knowledge which is common in the literature on the parameterized effects of M and I on film cooling performance. However, unlike the results in the literature, this section showed that these parameterizations which were developed in low temperature experiments remain valid in a high temperature environment where radiation is also a significant component of the overall heat transfer. Additionally, this section validated the computational conclusion of Section 6.1.2 that NHFR can be scaled by matching DR, M, Pr_∞, Pr_c, and Re_c. However, the validation was limited by the capabilities of the facility and could not cover a large variety of validation cases. Finally, the results of this section suggested that increased Pr_∞ causes a more rapid deterioration of the film cooling layer with downstream distance from the hole.

6.2.5 Comparison of Film cooling Geometries.

Film cooling experiments comparing film cooling geometries are often performed at near ambient temperatures. The relative performance of cylindrical hole, fan shaped hole, holes in a trench, and slot geometries were discussed in Section 2.3.3. Section 6.1.2 provided computational evidence that the NHFR film cooling performance parameter can be scaled to an engine condition by non-dimensional matching. Then, Section 6.2.4 provided a limited validation of the NHFR scaling methodology in support of Objective 2 of the present research. Thus, it follows that the relative performance of a given film cooling configuration compared to a different configuration should remain the same at high temperatures as at low temperatures.

The present experimental study is directed towards two research objectives. First, the experimental validation of scaling film cooling performance presented in the previous section, will be extended to better satisfy Objective 2. This will be accomplished by showing that the relative performance trends observed at low temperature are identical to those observed at high temperature. Specifically, the four geometries discussed in Section 2.3.3 (cylindrical, shaped, trench, and slot) will be examined.

The non-reacting NHFR results in this section will be used as a comparison for the reacting NHFR results in Chapter VII. Accordingly, the WSR was burned with $\Phi = 1.3$ to create a fuel rich freestream with $T_\infty \approx 1490\,\mathrm{K}$, as indicated in Table 6.3. To create a non-reacting film cooling layer, N_2 coolant was used with DR ≈ 2.1 and $M = 1$.

6.2.5.1 Single Row Configurations.

To study the fundamental effect of film cooling geometry, this section examines the Net Heat Flux Reduction (NHFR or $\Delta q''_f$) following a single row of film cooling. Four geometries were studied which take center stage in the literature: 1) cylindrical holes, 2) fan shaped holes, 3) cylindrical holes embedded in trenches, and 4) slots. Drawings with dimensions of each of these configurations are given in Figs. A.13-A.16, respectively. The relative benefits and drawbacks of these configurations were discussed in Section 2.3.3.

It should be noted that the first three configurations had identical coolant exit areas and number of holes such that a M amongst the cases also matched the total mass flow through all the holes. The slot configuration had a slot height equal to one diameter of the holes in the first three configurations. However, the width of the slot gave it an exit area that was five times larger. Thus, to ensure the slot configuration could be validly compared to the other three configurations, it was run at an equivalent mass flow rather than an equivalent M. Namely, while the first three geometries were tested with $M = 1$, the slot was tested with $M = 0.2$.

The experimental measurements of NHFR following each of these single row configurations are given in Fig. 6.36. In this figure, it is seen that the cylindrical configuration performs the worst of the four geometries. In fact, the cylindrical configuration is seen to produce essentially zero NHFR at the $x/D = 16$, 22, and 28 locations. This is in agreement with the computational results of Oguntade [47] who showed that cylindrical holes create intense counter rotating vortex pairs (CRVPs) which sweep hot core flow toward the wall and coolant away from the wall as seen in Fig. 2.6.

In contrast, the slot configuration was found to produce the best performance at all x/D. This is also in agreement with the literature and its superior performance is due to two effects. First, as discussed at the beginning of this section, the slot configuration has a much larger area than the other three configurations but is run at an equivalent mass flow. As shown by Hartnett et al. [23], this results in an extremely low momentum ratio I compared to the other geometries such that the coolant stays more attached to the test surface. Second, the slot configuration creates a 2-D flow

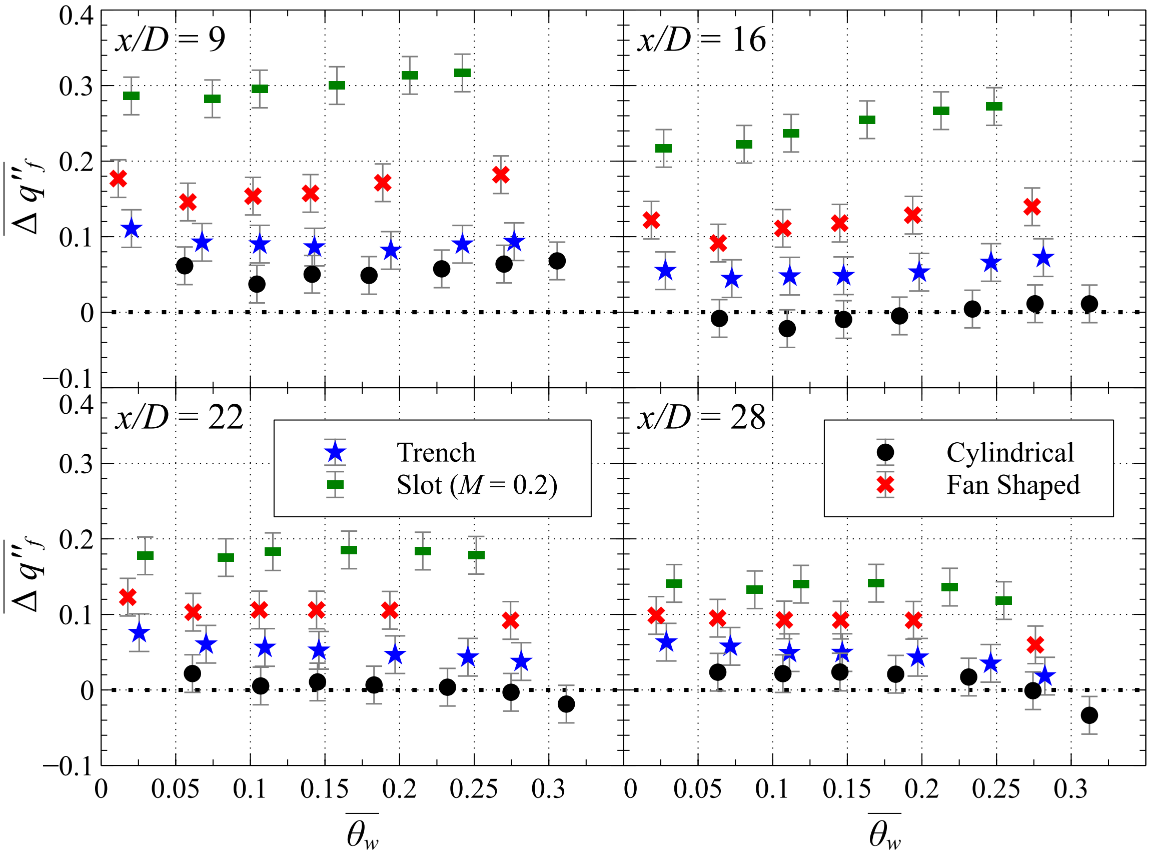

Figure 6.36: NHFR of the 1-row configurations; $M = 1$, $\Phi = 1.3$, **N_2 Coolant**

which prevents the formation of CRVPs as well as the subsequent degradation in performance CRVPs cause.

Though the slot configuration proved to have far superior cooling performance, it is not practical due to structural integrity issues. Both the trench and shaped hole geometries were proposed as improvements to the cylindrical hole geometry to diffuse the flow and approach the 2-D flow of a slot while avoiding the structural instability of a slot. Thus, it is not surprising that their cooling performance lies between that of the cylindrical and slot configurations. Specifically, the shaped hole geometry was found to have an NHFR which was approximately 0.15 lower at $x/D = 9$ and 0.02 lower at $x/D = 28$ compared to the slot geometry. Alternatively, the trench geometry was found to have an NHFR which was approximately 0.2 lower at $x/D = 9$ and 0.04

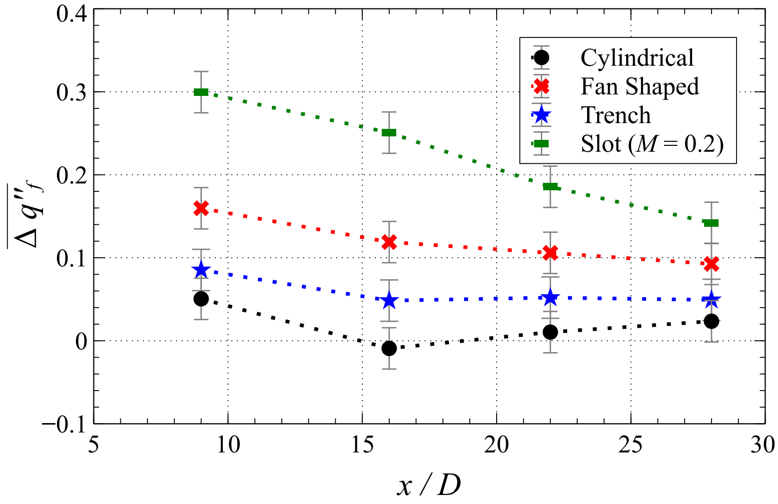

Figure 6.37: NHFR vs. x/D of the 1-row configurations; $M = 1$, $\Phi = 1.3$, N_2 Coolant, $\theta_w = 0.15$

lower at $x/D = 28$ compared to the slot geometry.

Comparing between the trench and shaped hole performance reveals that the shaped hole configuration has superior performance at all x/D examined over the trench configuration. This result is in agreement with the experimental results of Lu et al. [37]. However, despite the superior performance of shaped holes, Lu et al. [37] pointed out that shaped holes are significantly more expensive to produce which could potentially outweigh their benefit compared to the trench geometry.

To better visualize the decay of NHFR with downstream distance, Fig. 6.37 displays NHFR as a function of x/D at an interpolated $\theta_w = 0.15$. This figure shows that, though the slot had the highest NHFR at all x/D examined, it had the most rapid decay in performance with x/D. The shaped hole geometry was found to have a similar but less severe decline in NHFR with x/D. Alternatively, the trench configuration was found to decrease in NHFR between $x/D = 9$ and 16. Then, the trench's NHFR was observed to remain nearly constant from $x/D = 16$ to 28.

6.2.5.2 Five Row Configurations.

To study the effect of a build-up of coolant, this section examines five row configurations of three film cooling geometries: cylindrical holes, cylindrical holes embeded in a trench, and slots. These geometries are identical to those examined in Section 6.2.5.1 with the exception of the shape holes. Shaped holes were not examined due to the expense, difficulty, and time required to manufacture. Drawings with of the three configurations are presented in Figs. A.17-A.19, respectively.

The experimental measurements of NHFR following each of these five row configurations are given in Fig. 6.38. Similar to the single row results of the previous section, the cylindrical hole geometry was found to produce the worst results at $x/D = 9$, 16, and 22. However, the NHFR of the cylindrical geometry is seen in Fig. 6.39 begin at a low NHFR at $x/D = 9$ and remain fairly constant with x/D. Comparatively, the trench and slot geometries were observed to have higher NHFR at low x/D and decrease rapidly in NHFR with x/D.

Comparing the trench and slot geometry reveals a qualitative agreement with the literature. Namely, the slot produced a NHFR that was higher than the trench's NHFR at all x/D and θ_w considered by up to 0.15. Similar to the single row results, the 2-D and low I nature of the slot configuration results in its superior NHFR at all x/D. Furthermore, the theoretical absence of CRVPs following the slot geometry explains the less rapid decay of NHFR compared to the trench configuration. Quantitatively, Fig. 6.39 shows that the slot decreased in NHFR by 0.05 between $x/D = 9$ and 16. Alternatively, the the trench decreased by 0.1 over the same interval. Though the trench geometry is intended to approach the 2-D nature of the slot geometry, Lu et al. [37] showed computationally that CRVPs still exist at $x/D = 5$ and have an effect on the trench geometry's cooling performance.

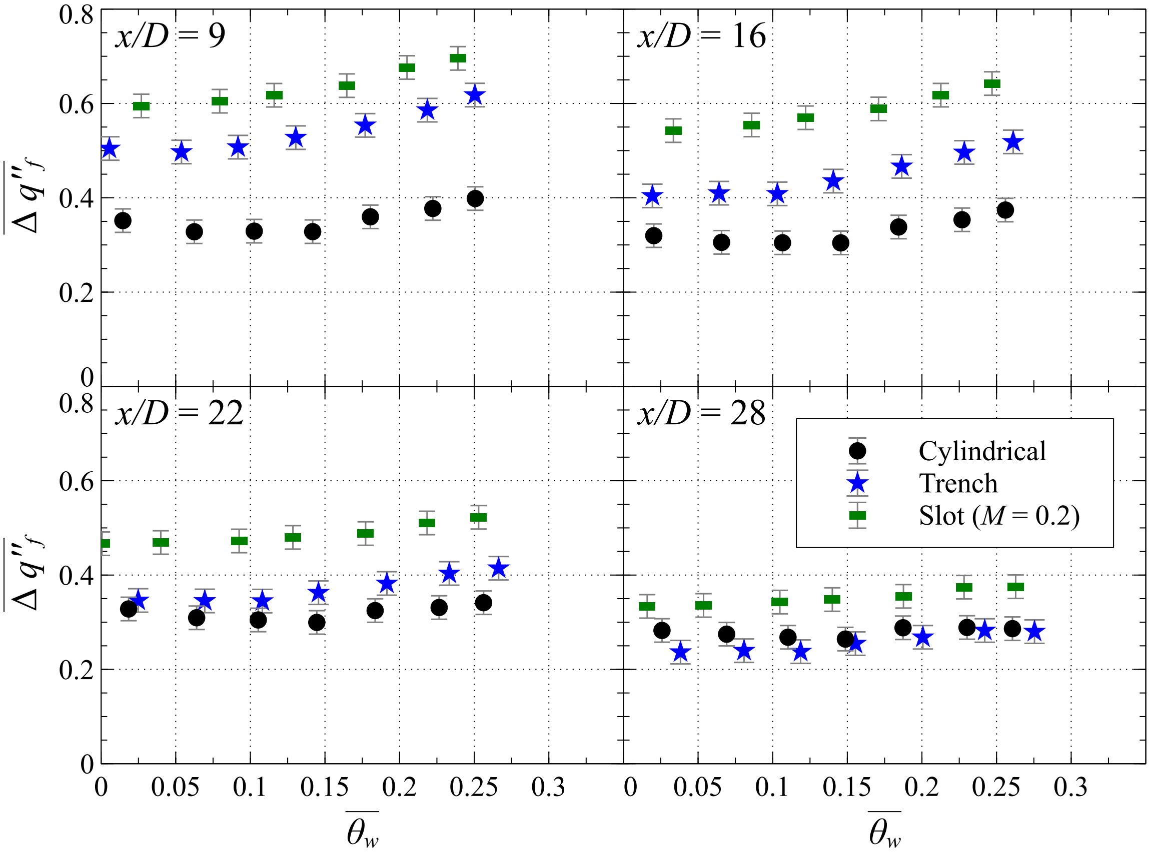

Figure 6.38: NHFR of the 5-row configurations; $M = 1$, $\Phi = 1.3$, N$_2$ Coolant

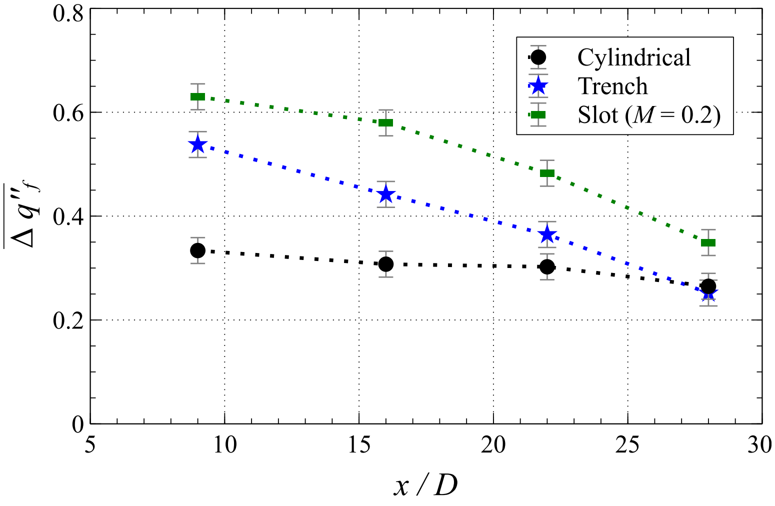

Figure 6.39: NHFR vs. x/D of the 5-row configurations; $M = 1$, $\Phi = 1.3$, N$_2$ Coolant, $\theta_w = 0.15$

6.2.6 Summary of Experimental Results.

The present section experimentally studied NHFR in a high temperature environment. Four film cooling geometries were examined: cylindrical holes, fan shaped holes, cylindrical holes embedded in trenches, and slots. These geometries were examined in a single row configuration to study their fundamental performance. The cylindrical, trench, and slot configurations were also examined in a five row configuration to study the effect of a build up of coolant.

The NHFR of the film cooling geometries were compared to show that the parameterizations of film cooling geometry developed at low temperature were the same at high temperatures. This study supplemented the computational and experimental studies of Sections 6.1 and 6.2.4, respectively, in satisfying Objective 2.

6.3 Chapter Summary

This chapter focused on addressing Objective 2 of the present research: Determine a methodology that enables scaling of non-reacting film cooling performance that is scalable from low temperature and pressure to engine conditions. The chapter began by developing a method to scale film cooling performance measured in a low temperature experiment to an engine temperature. The study concluded that both adiabatic effectiveness (η) and net heat flux reduction (NHFR) could be scaled by matching the density ratio (DR), blowing ratio (M), Prandtl number of the freestream (Pr_∞), Prandtl number of the coolant (Pr_c), and the coolant Reynolds number (Re_c). Next, this scaling method was validated in a high temperature experimental environment to satisfy Objective 2.

Previously, radiative heat transfer was shown to be significant in the present high temperature environment. Thus, a method to correct NHFR for radiative heat transfer was proposed. Finally, the effect of various film cooling geometries on NHFR was examined. The results of this study validated that the qualitative performance of each configuration developed in low temperature experiments and presented in the literature are consistent with their respective qualitative performance measured in the present high temperature environment.

VII. Cooling in a Fuel Rich Environment

The objective of film cooling is to reduce the heat flux (q'') to the cooled surface. Thus, film cooling performance can be non-dimensionally quantified by comparing the heat flux with film cooling (q''_f) to the heat flux without film cooling (q''_0). This comparison is captured by the Net Heat Flux Reduction (NHFR or $\Delta q''_f$) parameter given by Eq. 2.32.

Chapter VI examined non-reacting film cooling performance for several jet geometries in a high temperature environment. It was seen in Section 2.7.1 that film cooling layers can encounter energetic species due incomplete burning in the combustor. In addition, Section 2.7.1 discussed developing combustor concepts which will require film cooling a turbine vane in a fuel rich environment.

In both of these cases, the energetic species in the mainstream will encounter the oxidizer rich film coolant, burn near the wall, and create localized heating on the vane rather than the desired cooling. Given that the primary burning occurs in the combustor, this phenomenon is known as secondary reactions. However, the topic of film cooling in a fuel rich environment is a relatively new topic and little literature exists on the topic. Thus, the present chapter will focus on film cooling in a reacting environment.

Chapter VI studied film cooling in a non-reacting environment. To build upon these results, the present chapter will first examine the performance of film cooling in a fuel rich environment in the context of NHFR. Next, the chapter will examine various methods to quantify the effect of a reacting film cooling layer on cooling performance compared to the non-reacting cooling performance. Based on experimental evidence, an apt parameter to quantify the effect of reactions on film cooling will be proposed to satisfy Objective 3 of the present research: Determine a methodology to evaluate film cooling performance in a fuel rich, reacting environment. Last, the results presented in the present chapter will be used to develop an underlying methodology to successfully film cool a surface in a reacting environment to satisfy Objective 4: Determine the film cooling scheme characteristics which are effective at cooling a flat plate in a fuel rich, reacting environment.

7.1 Experimental Test Conditions

Section 6.2 experimentally examined NHFR following various film cooling jet geometries with a non-reacting film cooling layer. Namely, the cylindrical hole, fan shaped hole, trench, and slot geometries discussed in Section 2.3.3 were studied. To understand the fundamentals of these geometries, they were each tested in a single row configuration. Next, to study the effect of successive rows of film cooling all but the fan shaped hole geometry were tested in a five row configuration. The five row shaped hole configuration was not examined due to the excessive manufacturing cost and schedule. Detailed drawings of these geometries are included in Section A.4.2.

The results of the present chapter were obtained in parallel with the non-reacting film cooling results of Section 6.2. Thus, the present chapter's results will cover identical film cooling configurations but with a reacting film cooling layer. Consequently, the experimental test conditions of the present chapter are identical to those of Section 6.2 (see Table 6.3) with two exceptions.

First, it was shown by Anderson et al. [1] that secondary reactions are not present in a fuel lean environment. Thus, the fuel lean cases examined in Section 6.2 and outlined Table 6.3 were not examined in the results of the present chapter. Second, the test conditions with a fuel rich freestream studied in Section 6.2 and outlined in Table 6.3 used an inert coolant (N_2) to create a non-reacting film cooling layer. The results of the present chapter were obtained using air to study the effect of a reacting film cooling layer. However, some of the N_2 coolant data presented in Section 6.2 will be

Table 7.1: Reacting film cooling experimental conditions; $\Phi = 1.3$, Coolant = Air, $M = 1$; * = Temperature from similar cases, direct measurement not available; # corresponds to respective non-reacting case in Table 6.3

#	Geometry	Rows	$\overline{T_\infty}$ (K)	$\overline{T_{c,e}}$ (K)	Ma_∞	Ma_c	$\mathrm{Re}_\infty \cdot 10^{-4}$	Re_c	Pr_∞	Pr_c	DR
1	Cylindrical	1	1477	710	0.09	0.06	3.18	226	0.707	0.702	2.08
2	Shaped	1	1488	728	0.09	0.06	3.17	223	0.707	0.702	2.04
6	Trench	1	1472	713	0.09	0.06	3.19	226	0.707	0.702	2.06
7	Slot	1	1489	742	0.09	0.01	3.17	43.2	0.707	0.703	2.01
8	Cylindrical	5	1486	686*	0.09	0.06	317	2.31	0.707	0.701	2.17
10	Trench	5	1494	672	0.09	0.06	3.16	234	0.707	0.701	2.22
11	Slot	5	1498	686*	0.09	0.01	3.15	43.9	0.707	0.701	2.19

reused in the present chapter as a comparison case for the air coolant measurements. To differentiate between the reacting (air coolant) and non-reacting (N_2 coolant) film cooling layers, their results will be distinguished by r and f subscripts, respectively.

Analogous to the non-reacting test conditions (see Table 6.3), the experimental test conditions of the present chapter are given in Table 7.1. As discussed, many of the conditions are identical to the non-reacting conditions in Table 6.3 with the fuel lean freestream conditions removed and the coolant changed to air along with its associated fluid and flow properties. The coolant temperatures at the jet exit ($T_{c,e}$) given in Table 7.1 were approximated by the method presented in Section 6.2.2.2.

As discussed in Section 6.2.3 the heat flux measurements of the non-reacting film cooling conditions were corrected for radiation. However, the chemiluminescence of the reacting film cooling layers is expected to increase the radiative heat transfer to the film cooled surface. This adds considerable complexity to the total heat transfer between the reacting film cooling layer and the film cooled surface. Subsequently, the limited diagnostic capability of the experimental facility did not allow for independent quantification of the convective and radiative components of the net conductive heat transfer.

Correcting for radiation to and from the surroundings of the test surface was critical due to the inability to precisely match or scale radiative heat transfer. However, the radiative heat transfer from a reacting film cooling layer to the film cooled surface is unique to its flow conditions and should be relatively independent from the radiation to and from the surroundings. Thus, it was deemed appropriate that the radiative component of heat transfer from the reacting film cooling layer to the film cooled surface not be removed in order to include its effect in the total effect of secondary reactions.

The results of the present chapter employed an identical procedure to remove the radiative heat transfer to and from the surroundings from the heat flux measurements as that presented in Section 6.2.3. In addition to radiation, the procedure quantified the convective heat flux without film cooling (q''_0) as a function of the wall temperature (T_w). The results of this process are given in Table 6.4. Since the reacting and non-reacting film cooling data were gathered in parallel, the case numbers in Table 7.1 correspond to the non-reacting case numbers in Tables 6.3 and 6.4. The remainder of this chapter will utilize the raw measurements which were taken and corrected by the procedures above to study film cooling in a fuel rich environment.

7.2 Net Heat Flux Reduction

In traditional non-reacting film cooling, the coolant mixes with the freestream as it travels downstream from the injection sight. This mechanism results in an adiabatic wall temperature (T_{aw}) which generally increases with downstream distance. As a result, the heat flux to a surface from a non-reacting film cooling layer (q''_f) generally increases with downstream distance.

In reacting film cooling, however, the coolant is heated by both mixing with the hot freestream and by secondary reactions within the cooling layer. Thus, to denote this important distinction, the remainder of this work will refer to heat flux to a surface from a reacting film cooling layer as q''_r. Since Chapter VI proposed that NHFR is an appropriate parameter to evaluate non-reacting film cooling, NHFR will be the first parameter examined in the present study of reacting film cooling. However, to denote the NHFR of a reacting film cooling layer, it will be defined by

$$\Delta q_r'' = 1 - \frac{q_r''}{q_0''} \tag{7.1}$$

As with non-reacting NHFR ($\Delta q_f''$), both q_r'' and q_0'' in Eq. 7.1 are evaluated at an identical wall temperature. The procedure to correct for ambient radiation presented in Section 6.2.3 produces a model for q_0'' as a function of T_w. Thus, q_0'' was evaluated at the temperature of the q_r'' measurement for valid comparison of the two heat fluxes.

7.2.1 Single Row Configurations.

To display the ability of single row configurations to cool in a fuel rich environment, Fig. 7.1 compares the non-reacting NHFR ($\Delta q_f''$) presented in Section 6.2.5.1 and $\Delta q_r''$ for each of the single row configurations examined. In this figure it is seen that, rather than cooling the surface (positive $\Delta q_r''$), using air for coolant produces a negative $\Delta q_r''$ in most all cases.

The computational study of $\Delta q_f''$ in Section 6.1.2.2 indicated that decreasing θ_w decreased $\Delta q_f''$ monotonically from a vertical asymptote at $\theta_w = 1$ (i.e. as q_0'' goes to zero) toward zero. This trend was also observed in the experimental $\Delta q_f''$ results of Section 6.2.5, but only slightly due to the relatively small range of θ_w. However, unlike the non-reacting results, the reacting NHFR ($\Delta q_r''$) was found to decrease with increasing θ_w. This trend is hypothesized to be caused by quicker heating of the film cooling layer from the hotter wall with downstream distance.

The quicker heating of the film would drive two effects. First, it would cause quicker dissociation of the oxidizer resulting in quicker ignition of the secondary reactions. Second, once ignited, the Arrhenius equation given by Eq. 2.48 dictates that

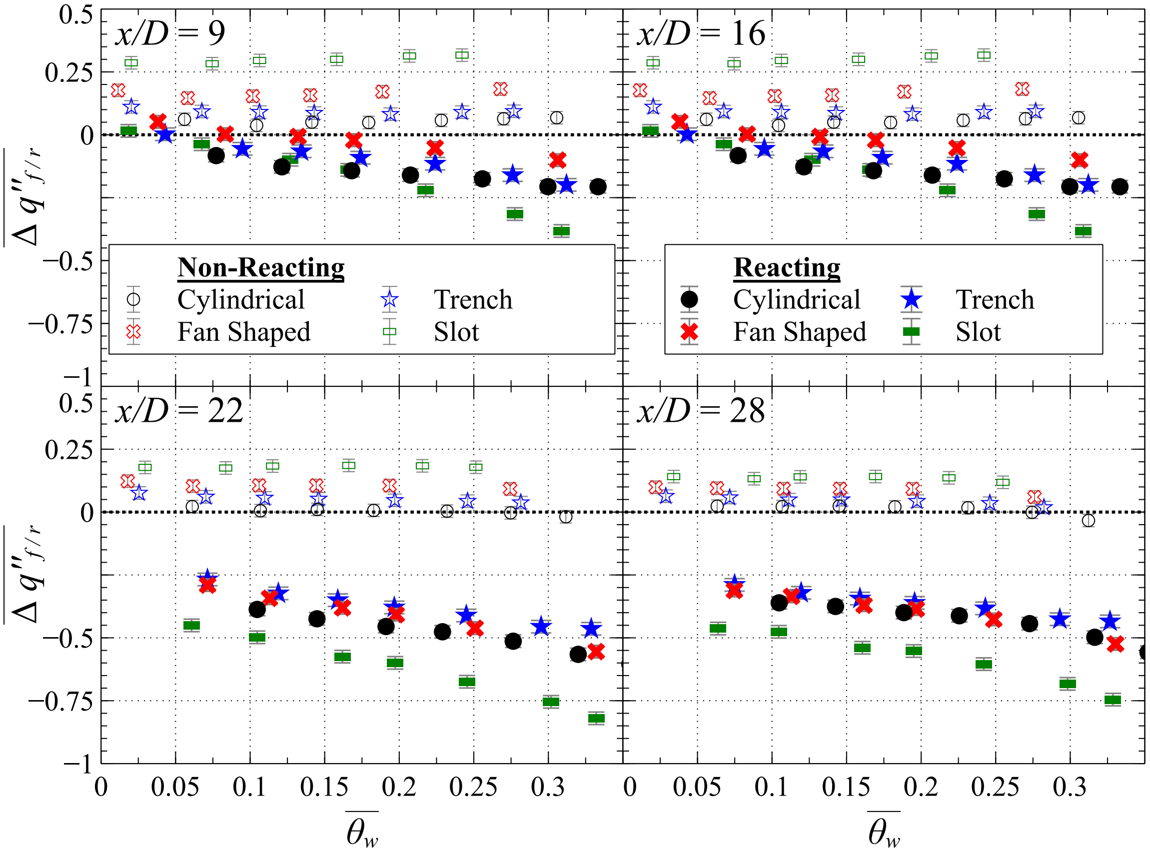

Figure 7.1: Spanwise averaged reacting net heat flux reduction ($\overline{\Delta q''_r}$) of single row configurations compared to non-reacting ($\overline{\Delta q''_f}$) from Fig. 6.36; $\Phi = 1.3$**,** $M = 1$

reaction rates increase exponentially with temperature. Thus, the higher film temperature would drive quicker reaction rates resulting in increased localized heating closer to the film cooling hole. Overall, these two effects are theorized to result in higher driving temperatures and heat fluxes near the hole with increasing θ_w. It is expected that a location sufficiently downstream from the hole would see q''_r decrease with θ_w due to reactions completing farther upstream with increased θ_w followed by diffusion of the localized heating into the freestream. However, the present experimental facility did not take measurements far downstream from the hole and, thus, could not validate this claim.

Alternatively, Fig. 7.2 shows that the NHFR results as a function of x/D at an

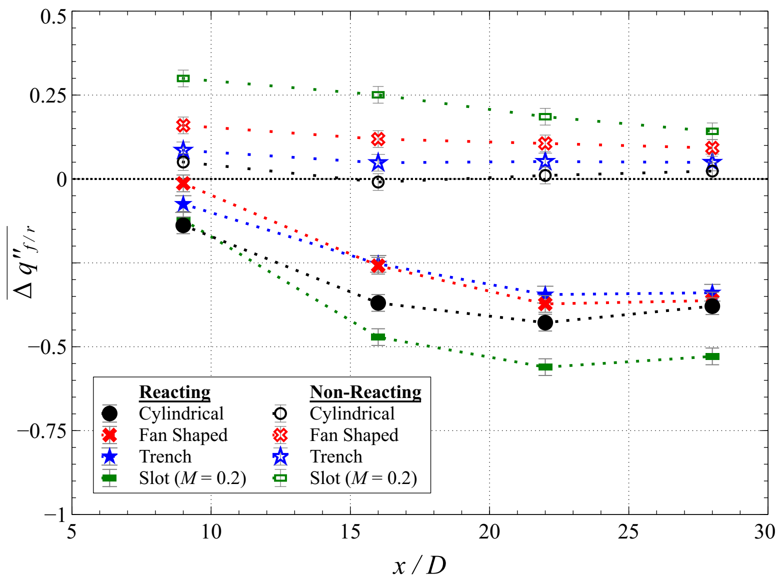

Figure 7.2: Spanwise averaged reacting net heat flux reduction ($\overline{\Delta q''_r}$) vs. x/D of single row configurations compared to non-reacting ($\overline{\Delta q''_f}$) from Fig. 6.37; $\Phi = 1.3$, $M = 1$, $\theta_w = 0.15$

interpolated $\theta_w = 0.15$. This figure indicates that $\Delta q''_r$ switches from decreasing to increasing between $x/D = 22$ and 28 for all four cases. It is hypothesized that at $x/D = 9$ and 16, reactions were heating the layer at a faster rate than the thermal energy could be diffused into the freestream. As a result, $\Delta q''_r$ decreased between $x/D = 9$ and 16. Alternatively, it was hypothesized that between $x/D = 22$ and 28, $\Delta q''_r$ increased because the local heating was being diffused into the freestream at a faster rate than it was being produced.

Previously, it was seen that the slot geometry produced the highest $\Delta q''_f$ of the four geometries. However, Fig. 7.1 indicates that the slot geometry produces the worst $\Delta q''_r$. Hartnett et al. [23] showed that the slot geometry creates a well attached jet. Thus, the present $\Delta q''_r$ results are in agreement with conclusion of Polanka et al. [51]. Namely, they found that single row configurations with good jet attachment resulted in the highest increase of heat flux to the surface compared to a non-reacting jet. As they discussed, good attachment kept the locally heated flow near the wall and maximized the temperature driving the heat flux to the surface.

However, Fig. 7.1 shows that the cylindrical configuration produces a similarly poor $\Delta q_r''$ as the slot configuration for $\theta_w < 0.2$ at $x/D = 9$ and 16. In addition, the $\Delta q_r''$ of the cylindrical configuration was worse than that of the shaped hole and trench configurations. This is also in agreement with the analogous experimental result of Polanka et al. [51]. Rather than comparing slots and co-flow cylindrical holes, their study examined shaped hole to normal cylindrical holes. In a parallel computational study, Lin et al. [36] showed that the shaped and normal cylindrical holes produced jets which were well attached and separated, respectively. Thus, the analogy between the present results and the results of Polanka et al. [51] was the comparison of a configuration with a well attached jet to a configuration with poor jet attachment characteristics.

Polanka et al. [51] first indicated that a shaped hole configuration reduced heat flux to the surface in a non-reacting case compared to normal cylindrical holes at $M = 1$. However, their measurements with reacting films indicated that the normal cylindrical holes and shaped holes produced similar heat fluxes at $M = 1$. Unlike the shaped hole geometry, their normal hole geometry formed a reacting jet which was separated from the wall such that the localized heating was further from the wall. However, the increased mixing due to Counter Rotating Vortex Pairs (CRVPs) resulted in an increased rate of heat release such that greater localized heating was realized. By this mechanism, the increased local heating and distance of the heating from the wall were seen to balance such that the normal holes produced a q_r'' similar to the shaped holes.

The results of Polanka et al. [51] can be translated to the context of the present data in Fig. 7.1 by recalling that $\Delta q_r''$ is q_r'' non-dimensionalized by q_0'' via Eq. 7.1. Given that the measurements of Polanka et al. [51] were taken at $x/D = 20$, the agreement between the $\Delta q_r''$ of the cylindrical and shaped holes at $x/D = 22$ qualitatively agrees well with their findings.

Since the present facility measured heat flux closer to the hole, the present data were able to extend the results of Polanka et al. [51]. First, near the hole at $x/D = 9$, the cylindrical hole geometry is seen to produce an $\Delta q''_r$ which is more negative than the shaped and trench hole geometries. In light of the understanding that cylindrical holes result in greater jet detachment than the shaped and trench geometries (see Section 2.3.3), this is in disagreement with the qualitative results of Polanka et al. [51] which were measured farther downstream. This seems to indicate that the increased mixing due CRVPs following the cylindrical holes results in quicker ignition and burning rates such that the localized heating is concentrated closer to the hole.

As discussed, the slot was observed to have a similarly negative $\Delta q''_r$ for $\theta_w < 0.2$ at $x/D = 9$ and 16. Like the cylindrical holes, the slot configuration can be viewed as increasing mixing by virtue of the jet geometry. Specifically, the jet spreads the coolant laterally before ejecting it into the mainstream. As a result, it encounters a larger cross-section of the fuel rich mainstream at the ejection site resulting in quicker ignition and burning. Thus, the similar mechanism of increased mixing expected to be present in the cylindrical hole and slot geometries explains their similar $\Delta q''_r$ for $\theta_w < 0.2$ at $x/D = 9$ and 16. Moreover, the slot has an exit area which is five times larger than the other configurations such that the jet exit velocity is approximately five times lower. As a result, the jet has more time to ignite and burn before reaching the $x/D = 9$ measurement location.

In the non-reacting experimental NHFR results of Section 6.2.5, it was seen that the trench configuration produced a lower $\Delta q''_f$ than the shaped hole configuration. Studying the $\Delta q''_f$ results in the context of the above hypotheses on the effect of mixing explains why the trench configuration produces a more negative $\Delta q''_r$ than the shaped hole configuration at $x/D = 9$ and 16 but a slightly less negative $\Delta q''_r$ at $x/D = 22$

and 28. Specifically, the lower non-reacting NHFR ($\Delta q''_f$) of the trench configuration indicates its coolant jet has increased mixing with the freestream. Thus, the higher mixing drove quicker ignition and faster burning near the hole resulting in increased localized heating near the hole compared to the shaped hole configuration.

Consequently, $\Delta q''_r$ of the trench configuration is worse than the shaped hole configuration at $x/D = 9$ and 16. However, the increased mixing of the trench configuration is hypothesized to more quickly diffuse the locally heated flow through the boundary layer compared to the shaped hole configuration. This combined with the localized heating of the shaped hole configuration occurring farther downstream of the trench configuration is hypothesized to have caused the shaped hole to have a more negative $\Delta q''_r$ at $x/D = 22$ and 28.

In summary, it was seen that the single row slot configuration, which produced the highest $\Delta q''_f$, produced the worst $\Delta q''_r$. This was due to the thinly spread, well attached coolant which had a high rate of burning very close to the wall. Though the excellent jet attachment of the slot jet was seen to significantly degrade its $\Delta q''_r$, the cylindrical geometry which produces the least jet attachment resulted a worse $\Delta q''_r$ than its more attached shaped hole and trench configuration companions. This was attributed to the increased mixing and burning rate of the cylindrical hole configuration due to CRVPs. Finally, the shaped hole and trench configurations produced similar $\Delta q''_r$ values with subtle differences due to different levels of mixing. The following section will build on results of this section by examining $\Delta q''_r$ following sequential rows of film cooling jets.

7.2.2 Five Row Configurations.

The previous section showed that ejecting air from a single row of film cooling holes in a fuel rich environment resulted in burning which occurred adjacent to the

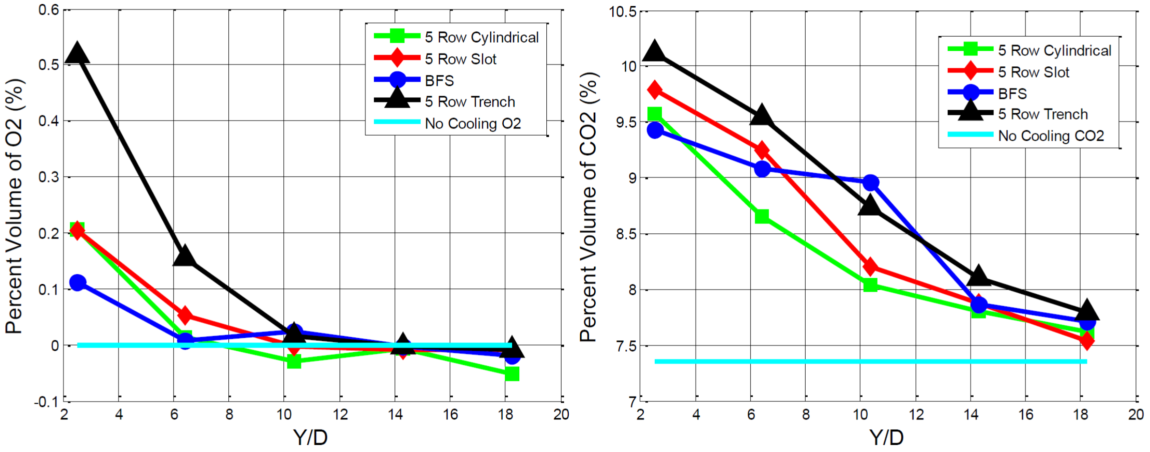

(a) O_2 Profile (b) CO_2 Profile

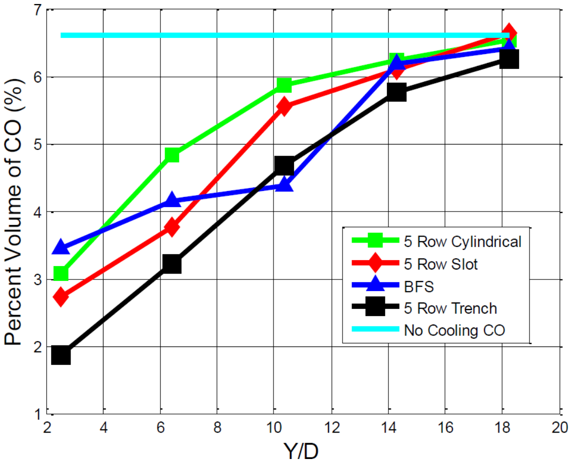

(c) CO Profile

Figure 7.3: Emissions profiles with distance from the wall (Y/D) at $x/D = 200$ of Shewhart [57]; $\Phi = 1.3$, $M = 2.0$, Backward Facing Step (BFS) geometry not studied in present work

film cooled wall resulting in local heating of the wall rather than cooling. However, it was hypothesized that, keeping the reacting layer close to the wall would result in a reduced concentration of fuel rich species near the wall. Corroborating this hypothesis, Shewhart [57] examined the O_2, CO_2, and CO emissions in the present facility as a function of distance off the wall (y/D) at $x/D = 200$. His results for the five row cylindrical, trench, and slot configurations with a $\Phi = 1.3$ freestream condition and a $M = 2.0$ cooling condition are displayed in Fig. 7.3.

Figure 7.3(a) shows that the $\Phi = 1.3$ condition left no O_2 in the flow for a no-cooling condition. However, he observed that cooling with the five row cylindrical, trench, and slot configurations examined in the present work had O_2 remaining at $y/D = 10$. Since the cooling holes were the only source of O_2 available in the flow, the presence of O_2 indicated unburned O_2 from the coolant holes near the wall. Moreover, he found that CO, a species which indicates a fuel rich flow, was depleted near the wall. Thus, it was surmised that sequential jets with geometries which maximize the jet attachment could result in coolant ejected from the downstream rows encountering a relatively fuel lean flow such that the secondary burning would be reduced. To test this hypothesis, this section examines $\Delta q_r''$ following five row configurations of all but the shaped hole configuration discussed in Section 7.2.1.

Figure 7.4 displays the measured $\Delta q_r''$ following each of these configurations. To be consistent with the single row results, the x/D reference locations were measured from the last row of film cooling injection. Consequently, all x/D locations in the five row configuration plots are an additional distance of $16D$ from the first row of injection. Unlike the single row results of the previous section, the $\Delta q_r''$ of the five row configurations were found to have the same order of performance as the $\Delta q_f''$ results of Section 6.2. Specifically, the slot configuration was observed to have the highest $\Delta q_r''$, followed by the trench configuration, followed by the cylindrical hole configuration with the lowest $\Delta q_r''$. Moreover, Fig. 7.5 shows the $\Delta q_r''$ and $\Delta q_f''$ results of the five row configurations have similar trends with x/D. Interestingly, Fig. 7.5 indicates that both the cylindrical and trench configurations have a nearly identical $\Delta q_f''$ and $\Delta q_r''$ to each other at $x/D = 28$.

Similar to the single row results of the previous section, the $\Delta q_r''$ of the cylindrical geometry was found to decrease with increasing θ_w. The trench and slot geometries were found to have an identical trend for $x/D = 22$ and 28. However, at $x/D = 9$

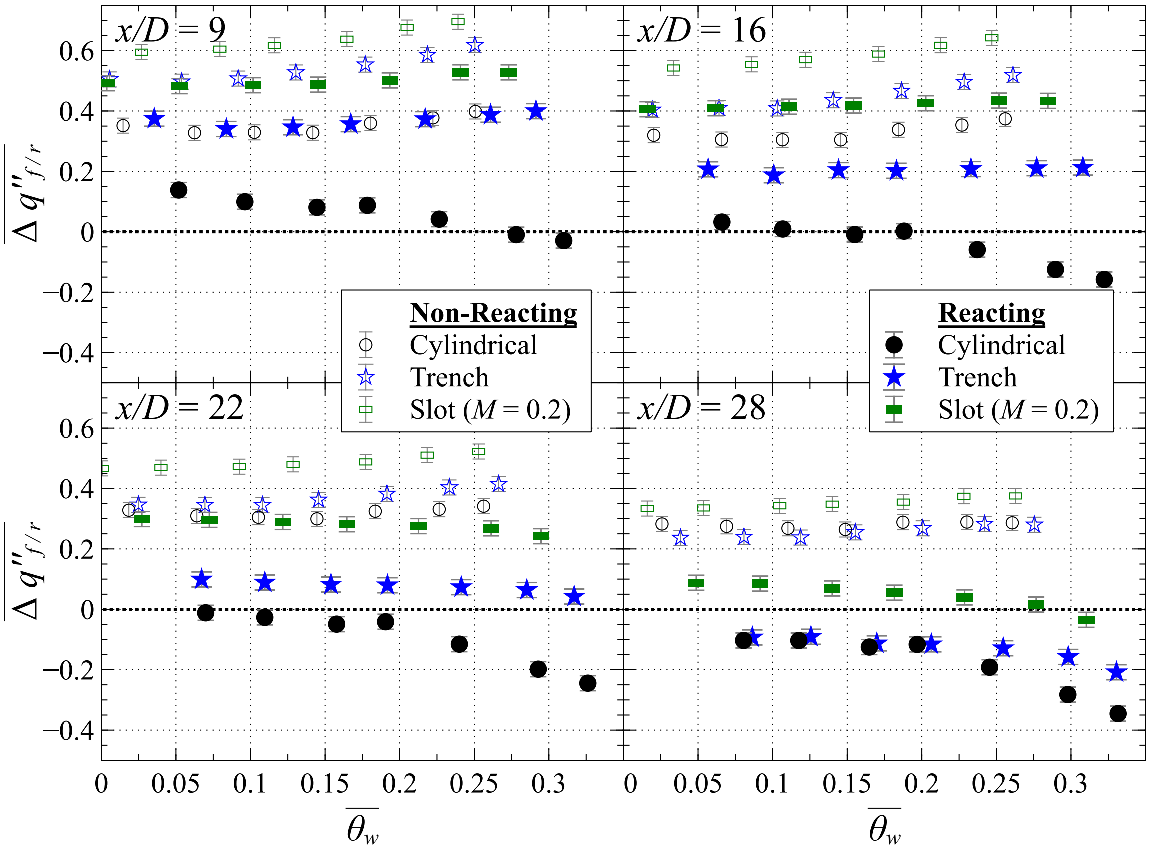

Figure 7.4: Spanwise averaged reacting net heat flux reduction ($\overline{\Delta q''_r}$) vs. x/D of five row configurations compared to non-reacting ($\overline{\Delta q''_f}$) from Fig. 6.38; $\Phi = 1.3$, $M = 1$

and 16, the trench and slot geometries were found to have increasing $\Delta q''_r$ with θ_w. This trend of increasing NHFR with θ_w is analogous to the non-reacting results. This is hypothesized that reactions have a small effect on the trench and slot at $x/D = 9$ and 16 such that they mimic the trends of the non-reacting $\Delta q''_f$.

Most notably, Fig. 7.5(b) indicates that the five row slot and trench configurations have positive $\Delta q''_r$ compared to the single row configurations. This signifies that the slot and trench configurations decreased the heat flux to the surface by up to 55% and 40%, respectively, at $x/D = 9$. However, by $x/D = 28$, the slot configuration has a nearly zero $\Delta q''_r$. Alternatively, at $x/D = 28$ the cylindrical and trench configurations were found to have similarly negative $\Delta q''_r$. These results suggest that the film cooling

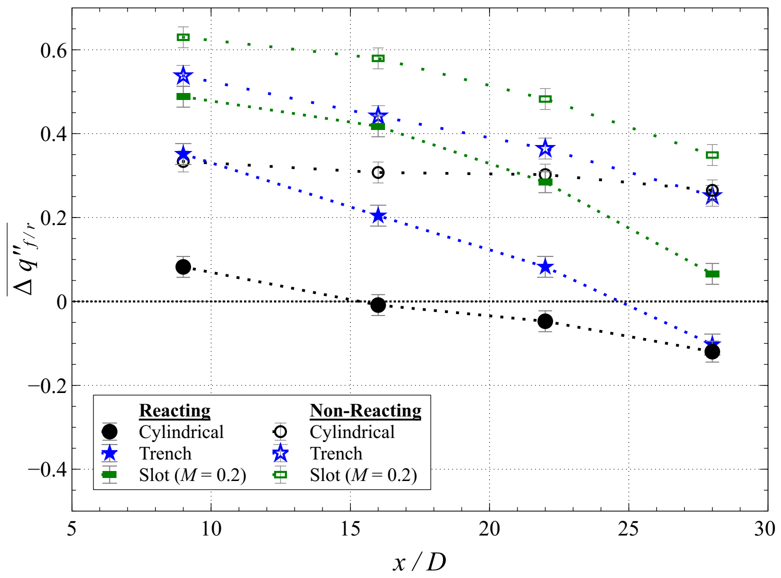

(a) Compared to non-reacting NHFR ($\overline{\Delta q''_f}$) of Fig. 6.39

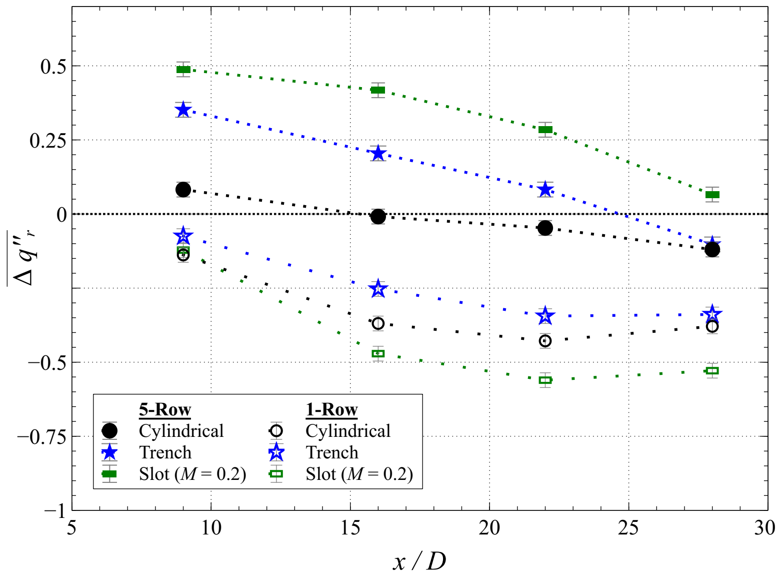

(b) Compared to single row configurations of Fig. 7.2

Figure 7.5: Spanwise averaged reacting net heat flux reduction ($\overline{\Delta q''_r}$) vs. x/D of five row configurations; $\Phi = 1.3$, $M = 1$, $\theta_w = 0.15$

layer must be supplemented by additional film cooling rows by around $x/D = 22$ or before to prevent a reversal from wall cooling to wall heating.

Examining the $\Delta q_r''$ of the cylindrical hole configuration in Fig. 7.5(b) yields an interesting result. The previous section hypothesized that the CRVPs created by the cylindrical hole configuration increased the rate of burning. However, the single row results were unable to capture the effect of an additional and critical effect of CRVPs: sweeping fuel rich freestream flow toward the surface. This effect results in each successive row of cooling holes encountering additional unburned, fuel rich flow which had been swept down from the freestream by the previous row's CRVPs. For this reason, the cylindrical hole configuration had a low but positive $\Delta q_r''$ at $x/D = 9$ which fades to an entirely negative $\Delta q_r''$ at $x/D = 22$ and 28.

In this context, the physical mechanisms which give the slot and trench performances seen in Fig. 7.5 can be deduced. First, Hartnett et al. [23] discussed that the slot configuration creates a 2-D jet which does not allow the formation of CRVPs. In addition, the slot has a momentum flux ratio (I) which is approximately five times lower than the cylindrical and trench configurations such that the jet is expected to be well attached to the surface. Thus, the same mechanism which makes the single row slot configuration the worst of the single row configurations examined is hypothesized to make it the best of the five row configurations. Namely, the absence of CRVPs in the slot jet prevents large scale turbulent mixing. Namely, it prevents CRVPs from sweeping of additional energetic species toward the wall and prevents CRVPs from lifting coolant off the wall. In addition, the low momentum and ideal lateral spreading of the jet keeps the coolant and, thus, the products of the secondary reactions very close to the wall.

By this mechanism, the first slot rows are presumed to lay down a sacrificial layer of coolant which consume the fuel near the wall while staying well attached to the wall. Subsequently, the downstream rows encounter the resulting fuel lean layer such that minimal further secondary reactions occur. Finally, after the last row of slot injection, a layer of cool unburned air is present near the wall. Meanwhile, the fuel rich freestream diffuses into the unburned layer. As a result, burning occurs on the outer interface of the coolant-freestream shear layer and diffuses toward the wall with downstream distance. This is expected to be the cause the more rapid decline of the five row slot's $\Delta q''_r$ with x/D compared to its $\Delta q''_f$ seen in Fig. 7.5. In fact, by $x/D = 28$, the five row slot's $\Delta q''_r$ was observed to decrease to near zero. This suggests that the slot geometry requires supplemental film cooling rows before $x/D = 28$ to maintain a non-reacting, cooling layer between the wall and the reacting coolant-freestream shear-layer.

The trench configuration is seen in Fig. 7.4 to share a similar trend with the slot configuration. Like the $\Delta q''_f$ results, the $\Delta q''_r$ of the trench configuration is seen to be consistently less than the slot configuration. Unlike the slot geometry, Lu et al. [37] computationally demonstrated that the trench geometry does not form a perfectly 2-D jet and suffers from some CRVP formation. However, the trench configuration it is presently theorized to follow the same cooling and burning mechanism as for the slot configuration.

In summary, five row configurations showed that $\Delta q''_r$ could be maximized by utilizing successive rows of jet geometries which maximize jet attachment and minimize CRVP formation. The former ensures that the succeeding rows benefit from the fuel consumption provided by the previous rows. The latter ensures that minimal additional fuel is swept toward the surface.

This section showed that heat flux to a surface in a fuel rich environment could be reduced by appropriate selection of a film cooling scheme. However, the studied parameter $\Delta q''_r$ only allows for a relative comparison between other geometries with reacting films. It alone does not have the ability to parameterize the effect of secondary reactions on a reacting film cooling layer compared to a non-reacting film cooling layer. The following section will address this by examining two parameters in particular and will give a recommendation on the appropriate parameter to quantify the effect of secondary reactions.

7.3 Quantifying Effect of Secondary Reactions

The previous section studied the ability of cylindrical holes, shaped holes, cylindrical holes embedded in trenches, and slots in both single and five sequential row configurations to film cool a surface in a fuel rich environment. The performance was quantified by the reacting net heat flux reduction parameter ($\Delta q_r''$) given in Eq. 7.1. It was seen that the single row configurations tended to increase heat flux (negative $\Delta q_r''$) to the surface while the five row configurations decreased the heat flux to the surface (positive $\Delta q_r''$) close to the hole. However, sufficiently far from from the hole it was seen that the five row configurations increased heat flux to the surface.

Though the study of the previous section provides valuable information on the cooling performance of each configuration, it does not quantify the individual contribution of secondary reactions to the overall heat transfer to the wall. A parameter which could isolate and quantify the contribution of secondary reactions would need to provide two insights. First, it would allow for identification of where the secondary burning begins and how the burning progresses with downstream distance. Second, it would quantify the reduction in cooling performance due to secondary reactions.

The following two sections will each propose a parameter to quantify the effect of secondary reactions. The proposed parameters will then be applied to the non-reacting experimental results of Section 6.2.5 and the reacting results of Section 7.2. The perspective of the experimental data provided by each parameter will then be compared to determine their abilities to meet the requirements discussed above. Last, a recommendation will be given on which parameter is most appropriate to satisfy Objective 3 of the present research.

7.3.1 Augmentation.

The first parameter examined was augmentation. As discussed in Section 2.7.3, this parameter was proposed by DeLallo [14] and compares the heat flux with and without reactions directly. For convenience, the equation for augmentation is repeated here

$$\sigma = \frac{q''_r}{q''_f} - 1 = \frac{1 - \Delta q''_r}{1 - \Delta q''_f} \tag{2.68}$$

Since the test facility did not allow for q''_f and q''_r to be measured at precisely the same T_w, the q''_f used in Eq. 2.68 was interpolated from the q''_f measurements at the T_w of the q''_r measurement. In the cases where q''_r was measured at a T_w higher than the T_w range of the q''_f measurements, σ was not calculated to avoid extrapolation of the q''_f data. The remainder of this section will apply the augmentation parameter to each of the single and five row film cooling configurations examined in Section 7.2.

7.3.1.1 Single Row Configurations.

The single row results of σ seen in Fig. 7.6 show that the slot geometry has a significantly higher σ than the other geometries. This clear difference is theorized to be caused by two effects. First, Fig. 6.36 showed that in a non-reacting environment the slot produced the lowest q''_f of all the single row configurations. Thus, the denominator of the slot's augmentation calculation (Eq. 2.68) was the smallest such that it aided in producing the large σ. Second, the excellent lateral spreading and attachment of the slot jet kept the secondary reactions close to the wall resulting in most negative $\Delta q''_r$ of all the single row geometries.

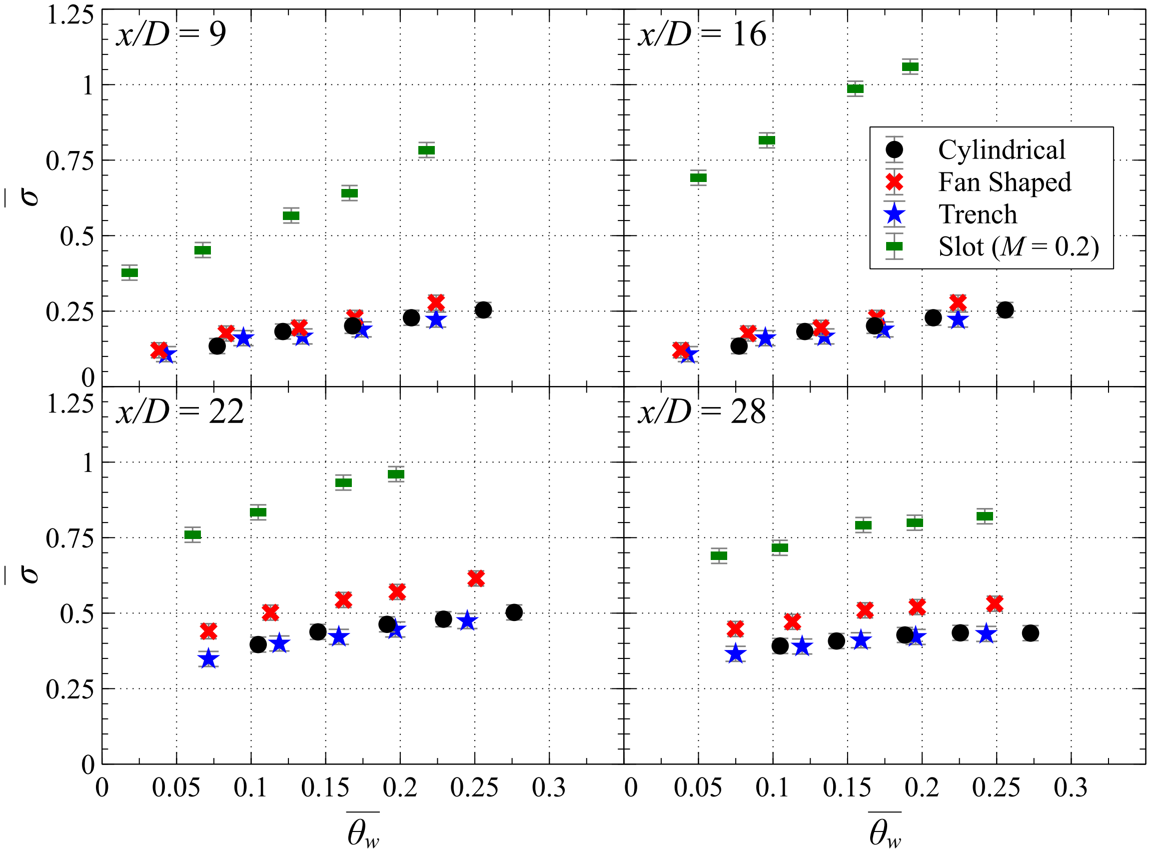

Figure 7.6: Spanwise averaged heat flux augmentation ($\overline{\sigma}$) vs. x/D of single row configurations; $\Phi = 1.3$, $M = 1$

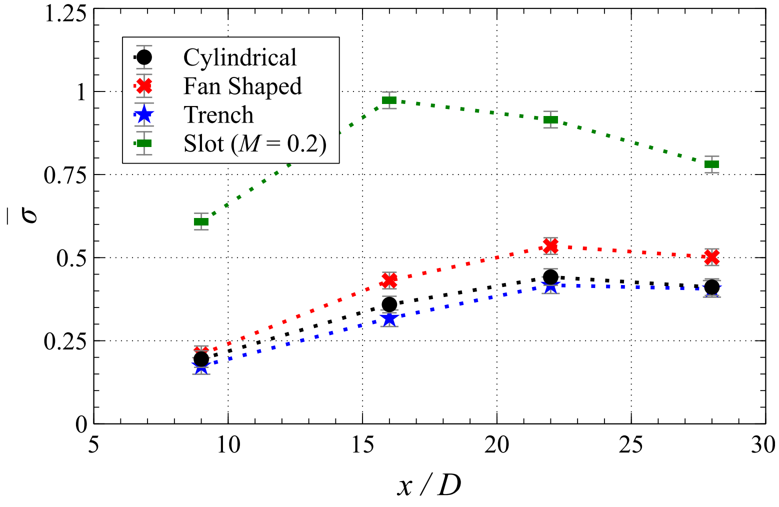

Figure 7.7: Spanwise averaged heat flux augmentation ($\overline{\sigma}$) vs. x/D of single row configurations; $\Phi = 1.3$, $M = 1$, $\theta_w = 0.15$

Interestingly, Fig. 7.6 shows that the cylindrical hole, shaped hole, and trench configurations produced similar σ at $x/D = 9$. The cylindrical hole and trench configurations continue to produce similar trends at $x/D = 16$, 22, and 28. However, the σ of the shaped hole configuration becomes elevated over the cylindrical hole and trench configurations at $x/D = 16$, 22, and 28. Reviewing Fig. 7.2 indicates that the shaped and trench configurations have nearly equal $\Delta q''_r$ at $x/D = 16$, 22, and 28. However, the shaped hole configuration has a slightly higher $\Delta q''_f$ resulting in its elevated σ.

In all cases, σ was found to increase from $x/D = 9$ until $x/D = 16$ or 22. Then, the σ of the four geometries was observed to decrease by $x/D = 28$. This indicates that, for the single row configurations, some of the most intense and hottest burning near the wall occurred around $x/D = 16$ for the slot configuration and $x/D = 22$ for the other three configurations. The observation that the slot geometry had a peak in augmentation at a smaller x/D than the other geometries corroborates the hypothesis of Section 7.2.1. Namely, the lower exit velocity resulted in ignition at a lower x/D and the lateral spreading of the slot caused faster burning. The next section will extend the discussion of augmentation from a single row configuration to multiple sequential rows of injection.

7.3.1.2 Five Row Configurations.

Examining the augmentation results of the five row configurations in Fig. 7.8 indicates that five rows of slots produced the lowest σ of the configurations examined at $x/D = 16$, 22 and 28. This is in contrast to the single row configurations which indicated that the slot had the highest σ as seen in Fig. 7.9. This can be explained by the secondary reaction mechanism of the five rows of slots configuration discussed in Section 7.2.2. Specifically, Hartnett et al. [23] discussed that the 2-D nature of the

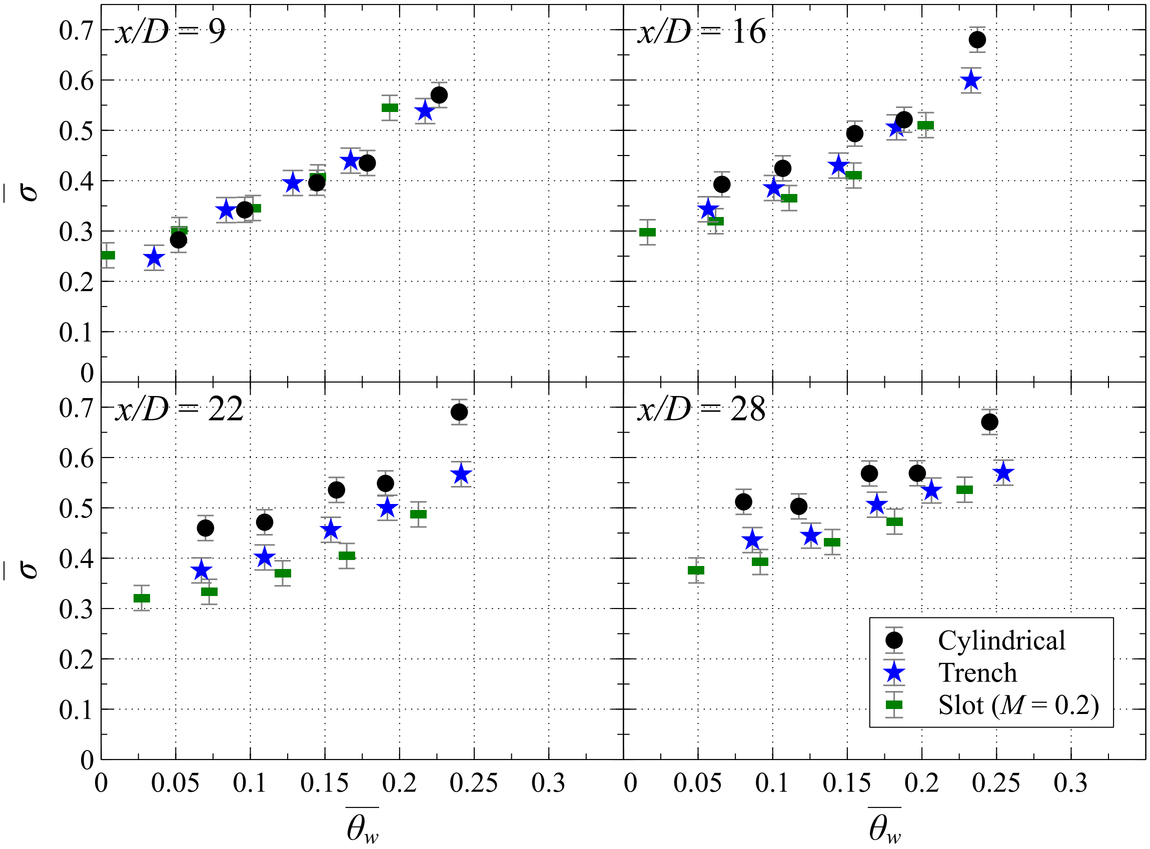

Figure 7.8: Spanwise averaged heat flux augmentation ($\overline{\sigma}$) vs. x/D of five row configurations; $\Phi = 1.3$, $M = 1$

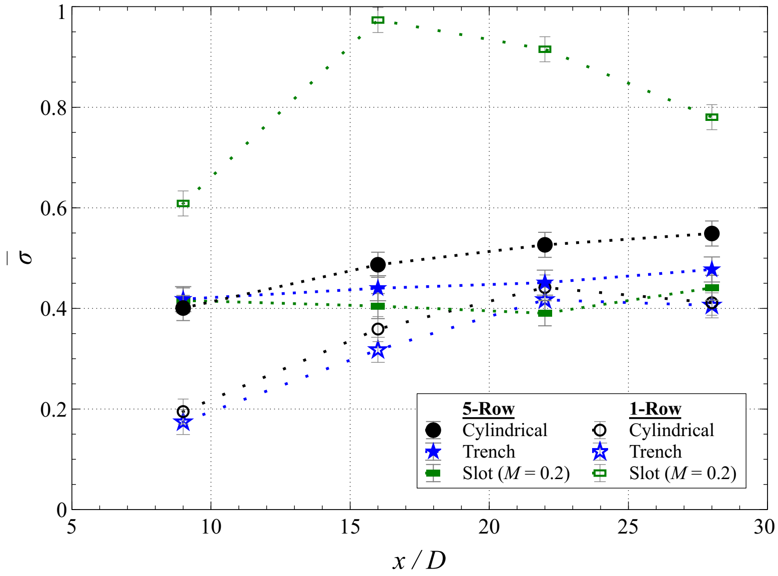

Figure 7.9: Spanwise averaged heat flux augmentation ($\overline{\sigma}$) vs. x/D of five compared to single row configurations; $\Phi = 1.3$, $M = 1$, $\theta_w = 0.15$

slot geometry's jet prevents the formation of counter rotating vortex pairs (CRVPs). In addition, they found that the low momentum of the slot geometry jet produces a well attached flow such that each successive row would be ejecting new coolant under the previous row's coolant. Consequently, the slot configuration's burning is theorized to occur by diffusion of the fuel rich freestream into the coolant.

In comparison, Oguntade et al. [48] and Lu et al. [37] showed that cylindrical and trench geometries, respectively, form CRVPs. These drive the more rapid process of large scale turbulent mixing of the coolant and freestream. Furthermore, the cylindrical hole geometry is expected to form more intense CRVPs, which explains the higher σ of the cylindrical hole configuration over the trench configuration at $x/D = 16$, 22, and 28.

Though the five row slot generally had the lowest σ, all three five row configurations were found to have nearly identical σ at $x/D = 9$. However, given each configuration was hypothesized in Section 7.2.2 to have different secondary reaction mechanisms, it does not seem likely that each of these geometries produce the same effect of secondary reactions on the wall. This disconnect between physical understanding and quantitative results is theorized to be due to non-dimensionalizing q''_r by q''_f in the σ parameter. In doing so, the σ parameter does not make any comparison to a case without film cooling. As a result, it is difficult to interpret σ and gain an understanding of the effect of reactions on a film cooling layer performance. This seemed to be a shortcoming of the augmentation parameter.

7.3.2 Degradation of Net Heat Flux Reduction.

The previous section examined secondary reactions in the context of the augmentation parameter which was proposed by DeLallo [14]. However, it was seen that the augmentation trends of the five row condition at $x/D = 9$ were not linked to the physical burning mechanisms. Thus, this section will evaluate a second parameter to see if it better captures the physics of secondary reactions.

It was seen in Chapter VI that film cooling performance is well parameterized by its ability to reduce heat flux to the surface. Therefore, it is proposed that the effect of secondary reactions on film cooling should be parameterized by how much it degrades net heat flux reduction as calculated by

$$\nabla q''_r = \frac{q''_r - q''_f}{q''_0} = \Delta q''_f - \Delta q''_r \tag{7.2}$$

Similar to σ, $\nabla q''_r$ defines $\nabla q''_r = 0$ as a condition where secondary reactions have no effect and $\nabla q''_r > 0$ quantifies by how much secondary reactions decrease NHFR. However, comparing Eq. 7.2 to the definition of augmentation (σ) in Eq. 2.68 reveals the subtle difference that $\nabla q''_r$ normalizes $q''_r - q''_f$ by q''_0 while σ normalizes by q''_f. Using this parameter, the next two sections will study the effect of secondary reactions following the single and five row configurations examined in Section 7.2.

7.3.2.1 Single Row Configurations.

The single row $\nabla q''_r$ results in Fig. 7.10 were found to have nearly identical qualitative trends as the σ results in Fig. 7.6. The qualitative difference between the two plots is that the σ parameter indicated that the peak effect of secondary reactions was at $x/D = 16$ while the $\nabla q''_r$ indicated that the peak occurred at $x/D = 22$. Interestingly, the $\nabla q''_r$ parameter indicated that all four geometries had a peak effect of secondary reactions at the same x/D. However, a higher resolution of x/D resolution would be required to better identify the peak $\nabla q''_r$.

Since both Figs. 7.10 and 7.6 display the same qualitative results, the reader is referenced to Section 7.3.1.1 for more discussion on the qualitative significance of Fig. 7.10. A discussion of which parameter produces quantitative results which are more

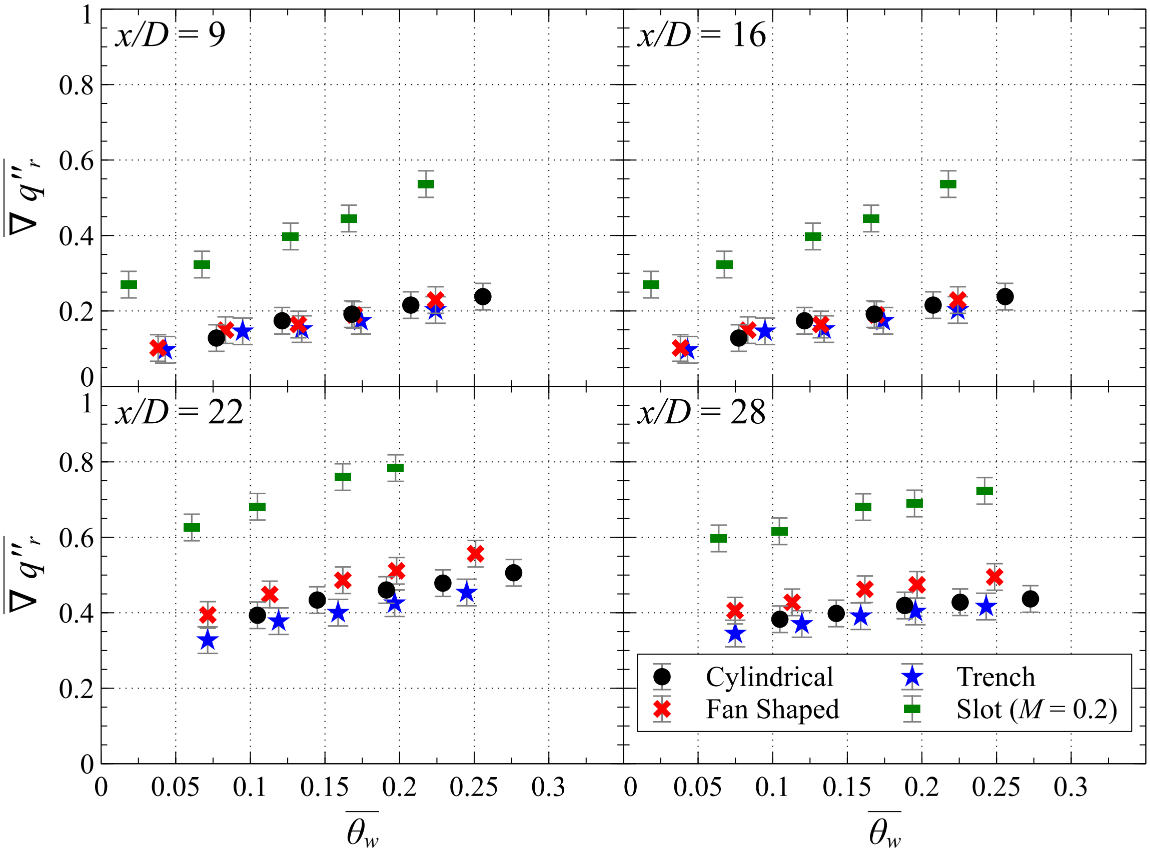

Figure 7.10: Spanwise averaged degradation of net heat flux reduction ($\overline{\nabla q''_r}$) of single row configurations; $\Phi = 1.3$, $M = 1$

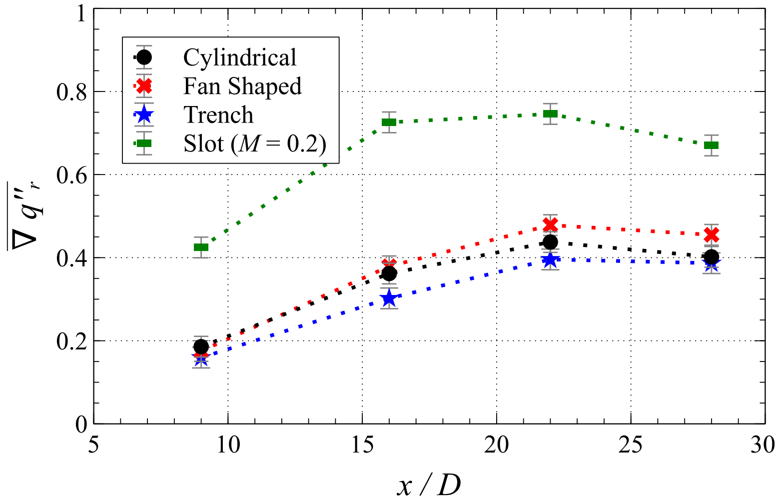

Figure 7.11: Spanwise averaged degradation of net heat flux reduction ($\overline{\nabla q''_r}$) vs. x/D of single row configurations; $\Phi = 1.3$, $M = 1$, $\theta_w = 0.15$

valuable will be presented in Section 7.3.3. The following section will extend the study of $\nabla q_r''$ by applying it to the five row configurations.

7.3.2.2 Five Row Configurations.

The previous section found that the σ and $\nabla q_r''$ results of the single row configurations produced similar qualitative conclusions. Likewise, the σ and $\nabla q_r''$ of the five row configurations can be compared by examining Figs. 7.8 and 7.12, respectively. Like the single row results, similar trends can be found in the the five row configurations between the σ and $\nabla q_r''$ results. However, there are important distinctions between the two plots.

Similar to the σ results in Fig. 7.8, the $\nabla q_r''$ results in 7.12 show that secondary reactions effect the slot configuration the least and the cylindrical configuration the most. However, at $x/D = 9$, the augmentation results indicate that each geometry has the same σ which leads to the conclusion that secondary reactions effect each geometry the same at this x/D. However, it was discussed in Section 7.3.1.2 that this conclusion does not compare well with the mixing and reaction mechanisms discussed in Section 7.2.2.

Alternatively, the $\nabla q_r''$ parameter indicates that secondary reactions effect the cylindrical hole configuration the most and the slot configuration the least at all x/D. Unlike the σ parameter, this aligns well with the mixing and reaction mechanisms discussed in Section 7.2.2. In addition, the $\nabla q_r''$ parameter seems to give a more quantitatively clear distinction amongst the configurations compared to the σ results which much more tightly grouped in the ordinate direction.

Interestingly, no peak is seen in the $\nabla q_r''$ data and $\nabla q_r''$ was found to increase with x/D. This agrees with the results of Shewhart [57] that oxygen remains near the surface such that heat release is still occurring past $x/D = 28$. Moreover, Fig. 7.14

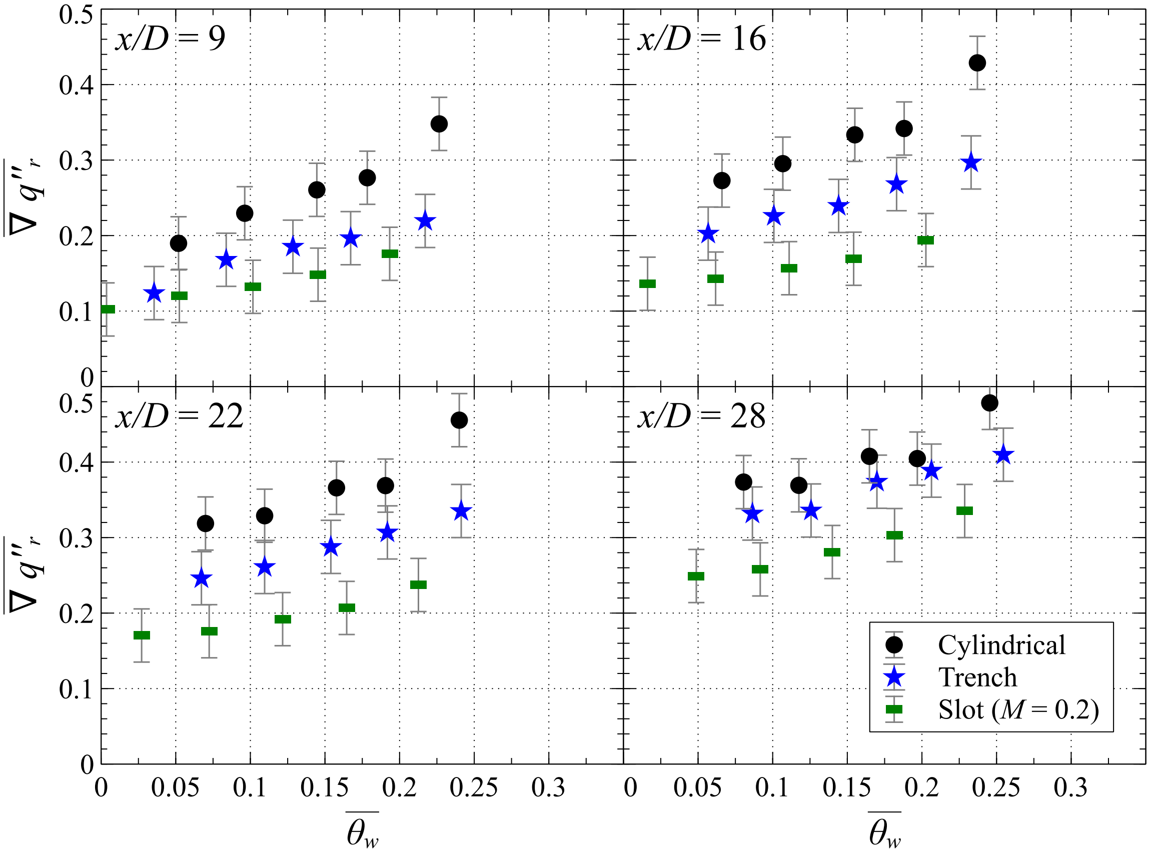

Figure 7.12: Spanwise averaged degradation of net heat flux reduction ($\overline{\nabla q''_r}$) of five row configurations; $\Phi = 1.3$, $M = 1$

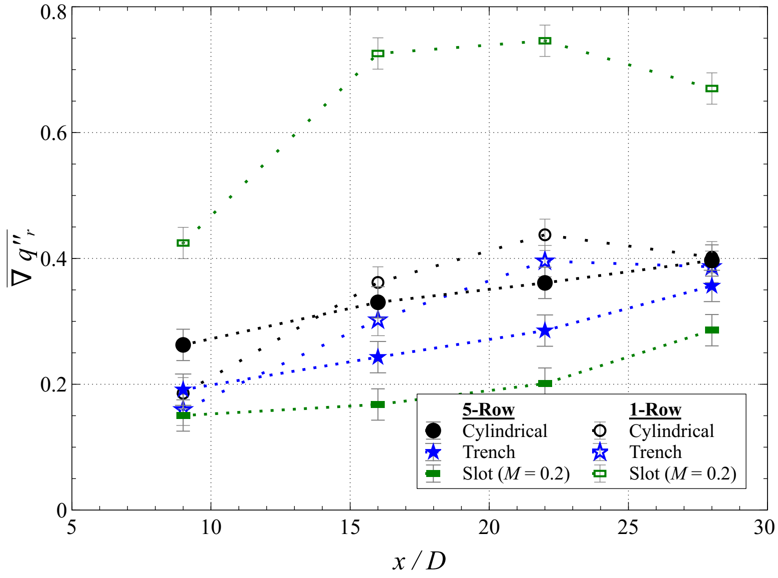

Figure 7.13: Spanwise averaged degradation of net heat flux reduction ($\overline{\nabla q''_r}$) vs. x/D of five compared to single row configurations; $\Phi = 1.3$, $M = 1$, $\theta_w = 0.15$

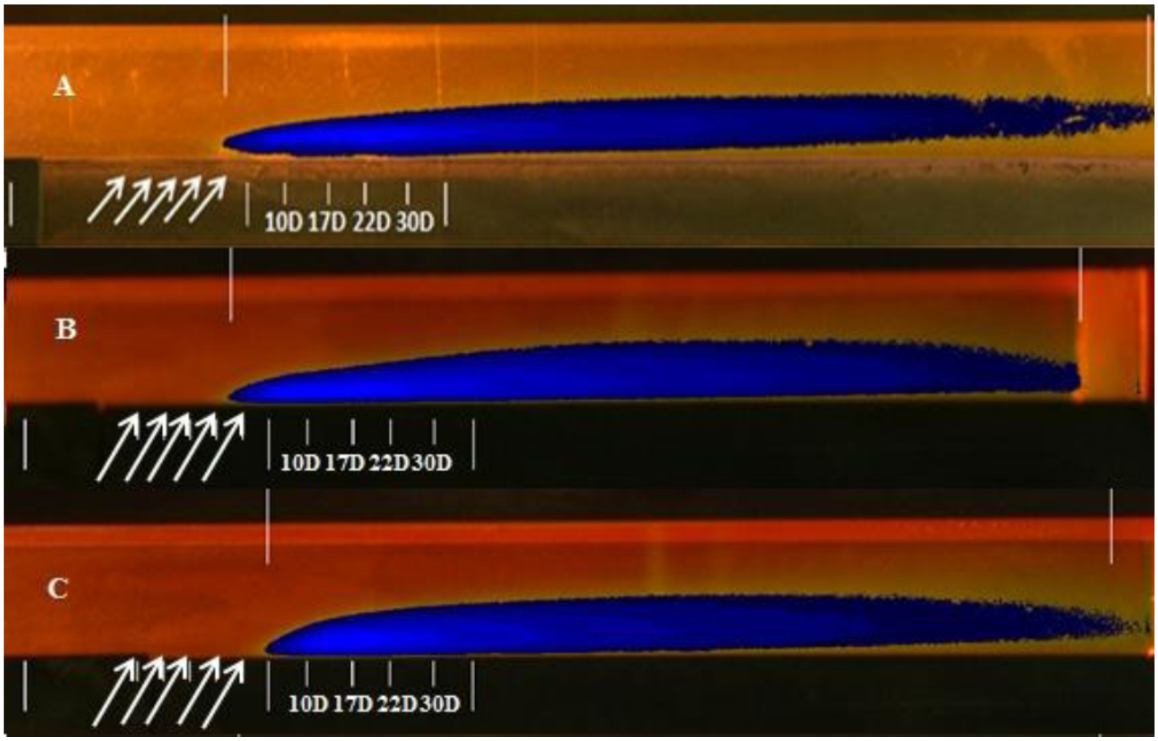

Figure 7.14: Side view of reacting five row film cooling layers from Shewhart [57]: A - Cylindrical, B - Slot, C - Trench; $M = 2.0$, $\Phi = 1.3$

shows side images of the reacting layers taken by Shewhart [57]. These images show that the flame extends far past the $x/D = 28$ measurement location. In comparison, the σ results of the five row trench and slot were found to remain essentially constant with x/D.

7.3.3 Comparison of Secondary Reaction Parameters.

Sections 7.3.1 and 7.3.2 examined the effect of secondary reactions in the context of the augmentation (σ) and degradation of net heat flux reduction ($\nabla q''_r$) parameters. Some comparison was made between the parameters in the previous sections, but the present section will take a more direct look at the distinctions between these two parameters. To simplify the comparison, Figs. 7.15(a) and 7.15(b) plot the σ and $\nabla q''_r$, respectively, of the single and five slot configurations at all x/D measurement locations.

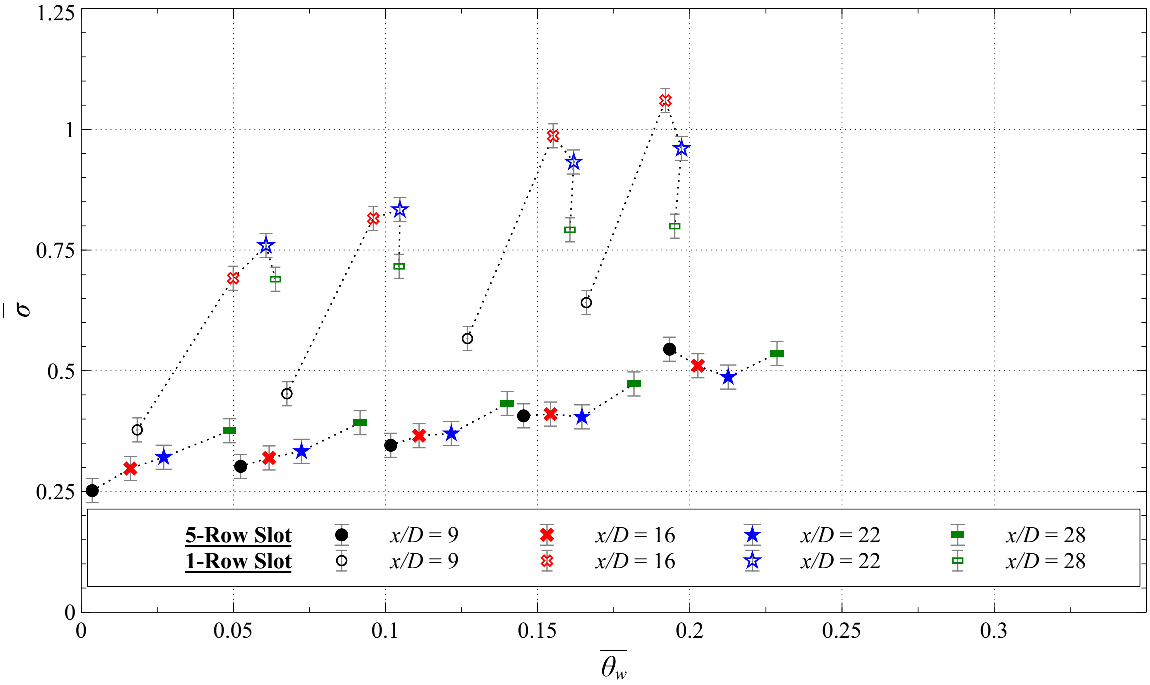

(a) Spanwise averaged heat flux augmentation ($\overline{\sigma}$)

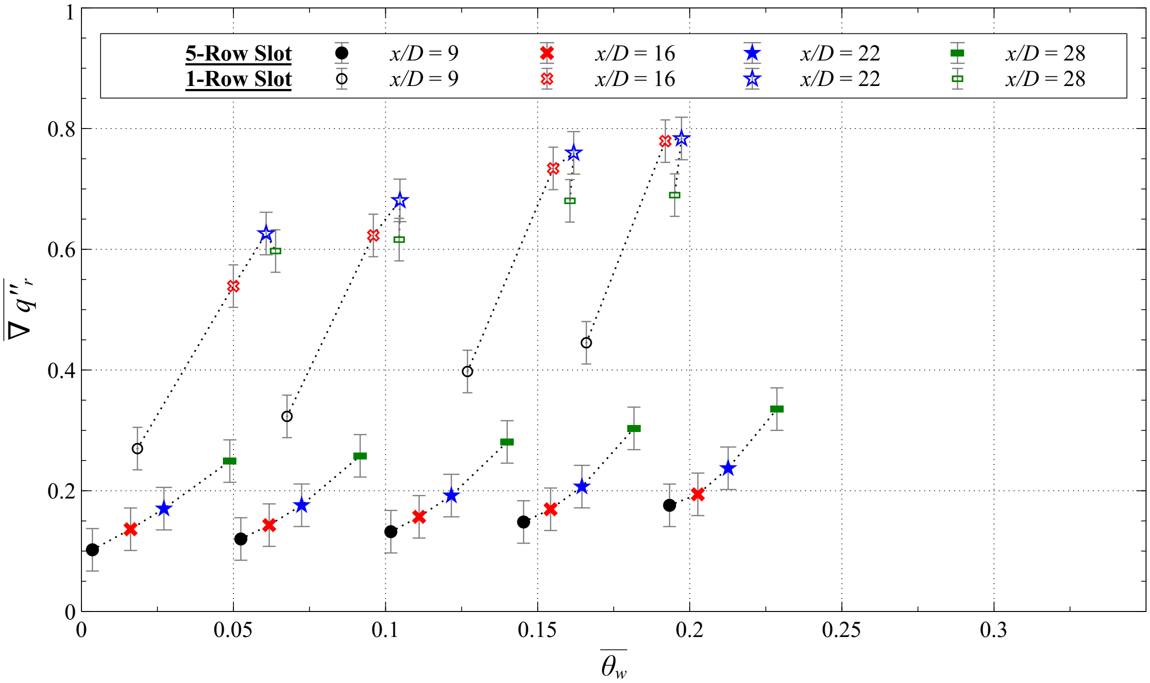

(b) Spanwise averaged degradation of net heat flux reduction ($\overline{\nabla q''_r}$)

Figure 7.15: Comparison of parameters to quantify the effect of secondary reactions on the single and five slot configurations; Data tied together by simultaneous measurements; $\Phi = 1.3$, $M = 0.2$

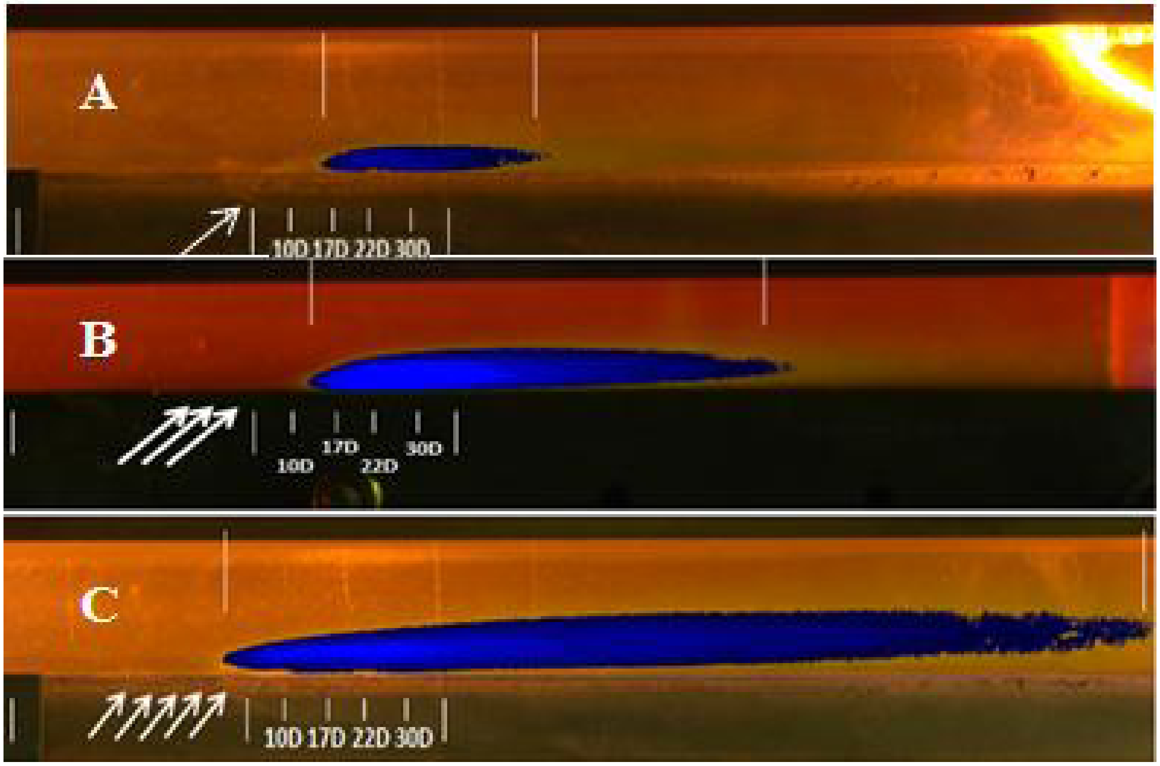

Figure 7.16: Side view of cylindrical hole reacting film cooling layers from Shewhart [57]: A - One row, B - Three row, C - Five row; $M = 2.0$, $\Phi = 1.175$

Though the x/D results which are banded together in Fig. 7.15 were measured simultaneously, the conjugate nature of the test surface resulted in different θ_w at each x/D. Thus, to discuss trends in the sets of x/D data with wall temperature, the following will compare the sets on the basis of a laterally and axially averaged θ_w of the data set defined as $\overline{\overline{\theta_w}}$.

Though the two parameters disagree on the quantification of the effect of secondary reactions, they produced identical qualitative conclusions for the single row slot configuration. Both indicated the σ and $\nabla q''_r$ parameters had a large increase between the $x/D = 9$ and 16 locations. Interestingly, Shewhart [57] identified that, for the single row cylindrical configuration, the flame begins between these two x/D as seen in Fig. 7.16.

In addition, for the present single row slot results, both parameters indicated a peak in the effect of secondary reactions between $x/D = 16$ and 22. For both parameters, the peak was found to move closer to the hole (toward lower x/D) with increasing $\overline{\overline{\theta_w}}$. This suggests that the increased wall temperature results in faster burning such that the peak effect of reactions occurs at a smaller x/D. These two observations give evidence of both the ignition of the burning between $x/D = 9$ and 16 as well as the tapering off of the fastest, most intense reactions around $x/D = 22$, respectively. It is possible that future research could utilize these observations coupled with knowledge of the characteristic time scale of the turbulence to calculate the Damköhler number of the secondary reactions.

Unlike the single row results, the σ and $\nabla q_r''$ parameters gave very different qualitative conclusions for the five row slot results. Most notably, the $\nabla q_r''$ parameter indicated that the effects of secondary reactions on the five row slot configuration increase with x/D at all $\overline{\overline{\theta_w}}$. In addition, the qualitative trend of how $\nabla q_r''$ varies with x/D seemed to remain constant regardless of $\overline{\overline{\theta_w}}$.

Alternatively, the σ parameter gave a similar indication for $\overline{\overline{\theta_w}}$ near zero. However, as $\overline{\overline{\theta_w}}$ increased, the σ parameter transitioned to indicating that secondary reactions had a larger effect on $x/D = 9$ and 28 than on the in between locations of 16 and 22. This result did not compare well with physical understanding of the slot configuration discussed in Section 7.2.2.

In summary, it was seen that the σ parameter indicated results that did not match well with the understanding of the underlying physics. In contrast, the $\nabla q_r''$ parameter gave results which agreed with the proposed physical mechanisms consistently across film cooling geometries, downstream distance (x/D), and non-dimensional wall temperature (θ_w). In addition, the physical significance of $\nabla q_r''$ is the amount NHFR was reduced by the presence of secondary reactions. Given the germane nature if its meaning along with its qualitatively reasonable and consistent results, it is proposed that $\nabla q''_r$ is an appropriate parameter to quantify the effect of secondary reactions on film cooling performance.

Though $\nabla q''_r$ captured the isolated effect of secondary reactions, it does not present the full details of its ability to cool a surface. Namely, it does not quantify a scheme's ability to reduce heat flux to the surface. Fortunately, this is quantified by the reacting net heat flux reduction parameter ($\Delta q''_r$). Thus, by examining film cooling in a reacting environment in the context of both $\Delta q''_r$ and $\nabla q''_r$ allows for quantification of the overall performance of a film cooling scheme along with the specific effect secondary reactions have on the scheme.

7.4 Summary

This chapter focused on film cooling in a fuel rich environment. It began by examining the reacting film cooling layers in terms of their ability to decrease the heat flux to the surface. Next, the ability of two different parameters to quantify the isolated effect of secondary reactions on a film cooling layer were examined.

In this study, it was determined that measuring the difference between the net heat flux reduction without and with secondary reactions provided the best quantification of the effect of secondary reactions. Given that this parameter addressed only the isolated effect of secondary reactions, it was determined that the complete picture of film cooling in a fuel rich environment was captured by a dual view of this parameter along with the scheme's ability to reduce heat flux to the surface. This conclusion was used to satisfy Objective 3 of this research.

Overall, this chapter revealed that configurations which had multiple rows of cooling geometries that kept coolant near the surface produced the best reduction in heat flux. Specifically, the five rows of slots and five rows of cylindrical holes embedded in trenches configurations were found to reduce the heat flux to the surface by up to

55% and 40%, respectively. In addition, secondary reactions were seen to have the least effect on such cooling schemes. Unfortunately, slot configurations significantly reduce the structural integrity of the turbine materials such that they are not viable in practical applications. However, the trench configuration has been proposed as a viable alternative. Thus, the viability of the trench configuration as well as its ability to significantly reduce heat flux to a surface in a fuel rich environment allow it to satisfy Objective 4 of this research.

VIII. Summary and Conclusions

The aviation gas turbine industry continuously strives to maximize turbine engine efficiency and thrust to weight ratio. To meet the former demand, increased pressure ratios and turbine inlet temperatures are desired. To meet the latter demand, increased thrust as well as smaller component weights and sizes are desired. However, as discussed in Chapter I, accomplishing these tasks provides many engineering challenges to cooling the combustor and turbine sections to maintain the integrity and durability of the engine.

One specific challenge that arises from increasing the turbine inlet temperature is an increased potential for heat transfer to the turbine surfaces. Thus, internal cooling and external film cooling are required to maintain turbine durability. However, since the coolant is bled from the compressor, increasing the pressure ratio also increases the temperature of the coolant. As a result, the coolant has less ability to remove heat or protect the surface from the hot core flow. Thus, future engines will have less margin for error in their cooling schemes and highly effective cooling designs coupled along with accurate heat transfer predictions will be essential. Despite the accuracy required, knowledge gaps exist in both understanding of high temperature flows and in modeling techniques of film cooling experiments, as identified in Sections 1.1 and 1.2, respectively.

Another challenge presented by future engine designs is film cooling in a fuel rich environment. As fuel-air ratios increase to meet the desire for an increased turbine inlet temperature and thrust, the probability that unburned fuel species will enter the turbine also increases. This is compounded by the desire to minimize combustor length. In doing so, the residence time in the combustor is minimized. The combination of increasing the fuel-air ratio and minimizing residence time increases the probability of unburned species exiting the combustor and entering the turbine.

Consequently, any unburned fuel in the turbine is likely to encounter the oxidizer rich film cooling schemes and combust creating a flame very close to the turbine surface. This effectively reverses the desired impact of film cooling from reducing heat flux to increasing heat flux to the turbine surface.

A method to further increase the thrust to weight ratio is the Ultra-Compact Combustor (UCC) discussed in Section 1.3. The UCC concept integrates a vane into the combustor which must be film cooled to prevent melting. Since the vane is within the combustor, the film cooling of the vane will be in a fuel rich environment such that reactions are expected occur within the film cooling layer. Though unintentional burning within the turbine and the UCC provide applications for film cooling in a fuel rich environment, reacting film cooling layers are not well understood.

8.1 Summary

The present research focused on addressing the knowledge gaps in high temperature flows, experimental modeling techniques of non-reacting film cooling, and film cooling in a fuel rich environment. Accordingly, Section 1.4 outlined four objectives for the present research which are restated here:

1. Develop a method to measure the convective and radiative heat transfer components in a high temperature environment with large freestream to wall temperature differences
2. Determine a methodology that enables scaling of non-reacting film cooling performance from near ambient conditions to engine conditions
3. Determine a methodology to evaluate film cooling performance in a fuel rich, reacting environment

4. Determine the film cooling scheme characteristics which are effective at cooling a flat plate in a fuel rich, reacting environment

Before addressing these objectives, Chapter II reviewed the literature relevant to the present research. The subsequent chapters were each directed toward satisfying these research objectives.

8.1.1 Experimental and Computational Methods.

To support each of the research objectives, experimental data were gathered in the facility detailed in Chapter III. The requirements for the facility were to create a high temperature flow which ranged from fuel lean to rich, support a study of various film cooling configurations, and support measurements of heat transfer to a test surface. To create the high temperature flow, a Well-Stirred Reactor (WSR) was used to burn a mixture of propane and air. The WSR enabled varying the fuel-air ratio from fuel lean to fuel rich conditions. The flow exiting the WSR was then routed through a flat plate test channel where heat transfer to the test surface with and without film cooling could be studied.

A modular insert was placed in the test channel flush with the test surface. This enabled the test surface to be film cooled with interchangeable cooling configurations. For the film cooled conditions with a fuel rich freestream, air and nitrogen were used as the coolant to study film cooling with and without reactions, respectively. Backside cooling channels were applied to the test surface. By providing these channels with various flow rates of water and nitrogen, the effect of surface temperature on the heat transfer measurements could be studied.

Though critical to the present research program, experiments at high temperatures present challenges such as significant radiative heat transfer and limited diagnostic techniques. Thus, Computational Fluid Dynamics (CFD) was employed to examine specific effects in the absence of the experimental difficulties. Then, the CFD observations were used as a tool to better analyze the experimental measurements. Specifically, computational domains modeling a 2-D zero-pressure-gradient flat plate and a fan-shaped hole on a flat plate were used to enhance the understanding of Objectives 1 and 2, respectively. The details of these computational domains as well as their grid convergence studies were presented in Chapter IV.

8.1.2 High Temperature Heat Transfer.

Chapter V focused on satisfying Objective 1. The topic of wall bounded flows with large property variations due to large freestream to wall temperature differences is not well studied in the literature. Thus, before studying coupled convective and radiative heat transfer, Section 5.1 computationally examined variable property flow over a zero-pressure-gradient flat plate in the absence of radiation.

First, the computational results were compared to the existing reference temperature and enthalpy methods of Eckert [15] (Eqs. 2.20 and 2.21, respectively) in Section 5.1.1. The computational shear stress and convective heat transfer data were found to agree with the methods of Eckert [15] for high freestream temperatures (1600 K and 1000 K) within 2%. In addition, the reference temperature method was found to be more accurate for the shear stress results while the reference enthalpy method was more accurate for the convective heat transfer results.

For a near ambient freestream (300 K) with much lower surface temperatures (as low as 100 K), the accuracy of his methods were found to decrease. Specifically, both the reference temperature and enthalpy methods decreased in accuracy to 4% at the lowest wall temperature examined. Despite the decreased agreement, his methods were six times more accurate compared to not accounting for variable property effects.

Next, the computational data were compared to the variable property temperature ratio method of Kays et al. [29] (Eqs. 2.24 and 2.25) in Section 5.1.2. Since the temperature ratio method requires an empirical exponent, several exponents were examined. No single exponent was optimal for the entire range of temperatures examined. Rather, an exponent which varied linearly with temperature was proposed and shown to accurately predicted the effect of variable properties on shear stress and convective heat transfer coefficient. Specifically for the freestream temperatures of 1600 K and 1000 K, the model was accurate to within 2% for wall to freestream temperature ratios of 0.2 and above. Alternatively, for a freestream temperature of 300 K the model was accurate to within 3% for temperature ratios of 0.3 and above.

Section 5.2 applied the methods of Eckert [15] and Kays et al. [29] to quantify the effect of variable properties on conventional constant property measurement techniques. As expected, variable properties were found to have a negligible effect on low temperature environments with small freestream to wall temperature differences. Alternatively, constant property methods were found to yield significant errors in environments with large temperature differences. Specifically, it was found that constant property methods could over-predict the convective heat transfer coefficient by up to 50% and under-predict the adiabatic wall temperature by up to 180 K. Subsequently, an inverse application of the temperature ratio method of Kays et al. [29] was proposed to predict adiabatic conditions from non-adiabatic measurements in a large temperature difference scenario. This method's predictions of adiabatic conditions were found have an accuracy of 0.9%.

To build upon the computational data, Section 5.3 presented experimental heat transfer measurements in a high temperature environment where both radiation and variable property convective heat transfer were expected to play a significant role. Specifically, the heat transfer coefficient was estimated to deviate up to 15% from its constant property value and radiation was estimated to contribute up to 25%

of the total heat transfer to the test surface. A method to measure the independent contributions of convective and radiative heat transfer to the total heat transfer conducted to the wall was proposed (Eq. 5.10) and validated to satisfy Objective 1. This method utilized the temperature ratio method of Kays et al. [29] to account for variable property convective heat transfer. Since radiation is difficult to quantify analytically, the primary benefit of this method was its ability to quantify radiation in an arbitrary environment by measurement without requiring analytical modeling of the surroundings.

Finally, though the temperature ratio method of Kays et al. [29] was found to be effective in both a computational and experimental setting, it required an empirical exponent which was not derived from underlying physics. Thus, to better understand the physics, Section 5.4 examined the effect of variable properties on the boundary layers of the computational data presented in Section 5.1. Using the knowledge gained in the boundary layer study, Section 5.5 developed a new method to account for variable property effects using a semi-empirical approach. Though the method was found to be effective, it was no more accurate than the method of Kays et al. [29]. However, the new method was significantly more complicated. Thus, the simpler method of Kays et al. [29] with the variable exponents proposed in the present work was deemed appropriate to account for variable properties in the present work.

Overall, Chapter V developed a method to satisfy Objective 1 of this research. The resulting methods to quantify convective and radiative heat transfer were used in the subsequent chapters. Specifically, the method remove the radiative component of the film cooled heat transfer measurements was used to evaluate the experimental data.

8.1.3 Non-Reacting Film Cooling.

Chapter VI primarily addressed Objective 2. First, Section 6.1 computationally examined scaling film cooling performance from near ambient conditions to engine conditions. This study compared film cooling in an environment with an engine temperature freestream of 1829 K to a condition with a near ambient freestream temperature. It was found that the adiabatic effectiveness of the engine temperature condition could be matched at near ambient conditions by non-dimensionally matching the density ratio, blowing ratio, Prandtl number of the freestream, Prandtl number of the coolant, and the freestream or coolant Reynolds number.

The variation of air's properties with temperature and fixed length scales prevented matching both the freestream and coolant Reynolds numbers simultaneously. Generally, the literature will report the freestream Reynolds number, but often the coolant Reynolds number is not reported or studied as an independent parameter. Despite this trend in the literature, matching the above non-dimensional parameters and the coolant Reynolds number was found to match the engine temperature's adiabatic effectiveness profile within 0.02 at all spatial locations. Comparatively, matching the freestream Reynolds number was found to be less accurate, but still matched the engine temperature's adiabatic effectiveness profile within 0.05. Thus, contrary to the trend in the literature to disregard the coolant Reynolds number, scaling adiabatic effectiveness was found to be more sensitive to matching the coolant Reynolds number than the freestream Reynolds number.

However, turbine engines are far from adiabatic such that adiabatic effectiveness alone does not give the full picture of film cooling performance. Since the intent of film cooling is to reduce heat flux to a turbine surface, it was concluded that Net Heat Flux Reduction (NHFR) was a better parameter to quantify film cooling performance. Similar to the above study of scaling adiabatic effectiveness, Section

6.1.2 examined the scalability of NHFR from a near ambient condition to and engine temperature. It was found that, by the same non-dimensional matching scheme used to match adiabatic effectiveness, the NHFR of a near ambient condition could be matched to an engine condition at an identical non-dimensional wall temperature. Again, matching the coolant Reynolds number was found to produce a NHFR profile which better matched the engine condition compared to matching the freestream Reynolds number. Specifically, they were found to be accurate to within 0.08 and 0.15, respectively.

Next, it was found in Section 6.1.4 that the temperature ratio method of Kays et al. [29] could not be employed to account for the effect of varying wall temperature on a film cooled convective heat transfer coefficient. Thus, unlike the no-cooling case, adiabatic conditions could not be determined from non-adiabatic measurements. In near ambient experiments, this is not an issue as adiabatic conditions can be measured directly. However, at combustion temperatures, measuring adiabatic conditions directly is impractical. Thus, without a method to quantify adiabatic effectiveness and the film cooled convective heat transfer coefficient, the present film cooling experiments quantified NHFR by direct measurement of heat flux with and without film cooling.

Section 6.2 experimentally verified the scalability of NHFR. To do so, the NHFR of the fan-shaped hole geometry was examined at three different freestream conditions with freestream temperatures between 1430 K to 1605 K. The freestream conditions of the three cases were selected to form various non-dimensional matching schemes between pairs of cases. This study showed that the non-dimensional matching of two cases with freestream temperatures of 1490 K and 1605 K by the scheme developed computationally produced matched spanwise averaged NHFR profiles. Specifically, the match was observed to be within 0.02 at 9, 16, 22, and 28 hole diameters downstream of the film cooling injection.

Many low temperatures studies exist in the literature which compare performance of film cooling geometries and parameterize the effect of non-dimensional characteristics on film cooling performance. The present work examined four geometries which are common in the literature: cylindrical holes, cylindrical holes embedded in a trench, fan-shaped holes, and slots. These configurations were examined in a single row configuration as well as a five sequential row configuration with the exception of a five row fan-shaped configuration. Using the low temperature literature on these geometries (summarized in Section 2.3.3), Section 6.2.5 showed that the film cooling parameterizations and qualitative performance relative to other configurations developed at low temperatures were identical at combustion temperatures. Thus, the results of these two experimental studies confirmed the computational scaling methodology and satisfied Objective 2. Though this was the primary objective of the non-reacting film cooling measurements, they were also used as a comparison for the reacting film cooling cases to support Objectives 3 and 4.

8.1.4 Reacting Film Cooling.

With a computational understanding of the parameters that characterize and scale non-reacting film cooling, Chapter VII addressed Objectives 3 and 4 using experimental data alone. First, Section 7.2 examined film cooling in a fuel rich environment in the context of NHFR. It was found that, for single row film cooling configurations, the application of film cooling resulted in a negative NHFR. This corresponds to an increase (rather than the desired decrease) in heat flux to the surface compared to a condition without film cooling.

The slot configuration was observed to produced the most negative NHFR with values as low as -0.85. According to the literature, the slot geometry creates a jet which is well attached to the wall and spread evenly in the lateral direction. With this understanding, the poor performance of the single row slot configuration agrees with other reacting film cooling literature. Namely, single row configurations with well attached jets create a flame which is equally well attached such that the wall is locally heated to a greater extent compared to a detached jet where the flame occurs farther from the wall. This is in contrast to non-reacting film cooling performance which is increased by increased jet attachment.

Despite the poor performance of the single row configurations, applying multiple sequential rows of film cooling was found to reduce heat flux to the surface by up to 50% compared to a case without film cooling. In addition, the multi-row cooling configurations with the highest NHFR were those that have been shown in the literature to keep coolant well attached to the surface. Given this result, it was theorized that using multiple rows of well attached jets allows the first rows of cooling to consume the energetic species while keeping the combustion products near the wall. As a result, the last rows of cooling jets would encounter the combustion products of the upstream rows such that a relatively inert film cooling layer would be ejected and kept near the wall. This layer would dilute the heat release from the upstream combustion and create a cool layer near the wall such that heat flux could be reduced.

Next, Section 7.3.3 examined two parameters to quantify the isolated effect of reactions on film cooling performance. It was concluded that the appropriate parameter was a difference between the non-reacting and reacting NHFR (Eq. 7.2). Since the purpose of film cooling is to reduce heat flux to the surface, this parameter gives a direct quantification of the reduction in film cooling performance. Using this parameter, it was again observed that configurations which kept coolant well attached to the wall were least affected by reactions in the layer. However, this difference did not fully characterize the cooling performance of the reacting layer. Thus, to satisfy Objective 3, it was recommended that reacting film cooling performance characterization be accomplished by two parameters. Namely, NHFR was recommended to quantify overall reacting film cooling performance. Alternatively, the difference between the non-reacting and reacting NHFR was recommended to quantify the isolated effect of reactions in the layer. Between these two parameters, it was unanimous that multi-row cooling configurations which maintain well attached cooling layers best protect the surface in a fuel rich environment. This conclusion satisfied Objective 4. Specifically, five rows of slots were found to have a NHFR of up to 50%, cylindrical holes in trenches had a NHFR of up to 40%, and cylindrical holes had a NHFR of up to 15%. In addition, this research indicated that, for the slot and trench configurations, the film cooling layer should be replenished between 22 and 28 hole diameters from the last row of injection to maintain a positive NHFR (i.e. to prevent local wall heating).

8.2 Conclusions

First, this work demonstrated computationally that large property variations within a gaseous turbulent boundary layer due to large freestream to wall temperature differences can result in a convective heat transfer coefficient which is 40% larger than the constant property value. The variable property reference methods of Eckert [15] were found to predict variable property effects on the convective heat transfer coefficient within 2% of the computational data at high freestream temperatures of 1600 K and 1000 K for wall to freestream temperature ratios between 0.0625 and 1. Next, the variable property temperature ratio method of Kays et al. [29] was found to not accurately model the computational data when using a constant empirical exponent. Rather, this research showed that an exponent which varies linearly with temperature ratio accurately captures the computational variable property data within 2% at high freestream temperatures of 1600 K and 1000 K for wall to freestream temperature ratios between 0.2 and 1. Subsequently, a method to quantify the contributions of radiative and variable property convective heat transfer to the total conductive heat transfer to a flat plate was proposed and experimentally validated.

The literature has shown that film cooling performance is affected by the coolant to freestream density ratio, mass flux (blowing) ratio, coolant and freestream Prandtl number, as well as the freestream Reynolds number. This research computationally demonstrated that the adiabatic effectiveness and net heat flux reduction of film cooling from a shaped hole on a flat plate could be scaled from a near ambient freestream temperature ($\sim 300\,\mathrm{K}$) to an engine freestream temperature (1829 K) by matching these same parameters. However, matching the coolant Reynolds number at the expense of the freestream Reynolds number was found to produce a superior match of the near ambient condition to the engine temperature condition. This is in contrast to the literature which focuses on the freestream Reynolds number and rarely studies the coolant Reynolds number. Next, this scaling methodology was validated experimentally for a single row of shaped holes at combustion temperatures (1430 K–1600 K) with a coolant to freestream density ratio of approximately 2. Then, the relative performance of the cylindrical hole, cylindrical holes embedded in a trench, shaped hole, and slot geometries identified at low temperatures were found to be identical at combustion temperatures.

Finally, film cooling in a fuel rich environment where reactions occur in the oxidizer rich film cooling layer was studied experimentally at combustion temperatures (1430 K–1600 K). Previous research on this topic quantified performance of a reacting layer by comparing the heat flux to the surface from a reacting film cooling layer to that of a non-reacting layer. However, this research identified deficiencies with this parameter and proposed that the net heat flux reduction parameter be used to quantify overall film cooling performance and that a difference of the reacting and non-reacting net heat flux reductions be used to quantify the isolated contribution of reactions within the layer to the overall film cooling performance. Analogous to previous research, the slot geometry, which has been shown in the low temperature literature to produce a well attached and laterally distributed jet, in a single row configuration was seen to result in the most negative net heat flux reduction compared to the cylindrical, trench, and fan-shaped geometries. Unlike previous research, which has focused on single row configurations or configurations with poor jet attachment characteristics, the present research found that five rows of slots produced a net heat flux reduction of up to 50%, while five rows of trenches had a net heat flux reduction of up to 40%. Low temperature literature identifies these configurations as having good jet attachment and lateral spreading characteristics. Thus, this work hypothesized that several rows of a film cooling geometry with good jet attachment and lateral spreading can significantly decrease heat flux to a surface in a fuel rich environment.

8.3 Research Applications

The continuous desire for increased pressure ratio and turbine inlet temperature drives the necessity to have accurate engine heat transfer predictions. The methods developed to satisfy Objective 1 of the present research will enable future experimenters to more accurately measure the convective and radiative heat transfer in high temperatures environments like a turbine. Moreover, heat transfer on end item turbine hardware is exceedingly difficult to measure. Thus, the method developed to scale film cooling performance from a near ambient experiment to an engine condition to satisfy Objective 2 allows film cooling experiments in a laboratory to predict heat transfer within a turbine.

To meet future thrust to weight ratio requirements, increased fuel to air ratios and shorter combustors are desired. However, both of these increase the probability that unburned fuel will enter the turbine. In addition, the UCC design places a film cooled vane in a fuel rich, combustion environment. Thus, satisfying Objective 3 provides experimenters of unintentional turbine burning and UCCs with the parameters necessary to quantify reacting film cooling performance. Likewise, satisfying Objective 4 provides a method to film cool in a fuel rich environment such that problems like unintentional turbine burning can be solved and applications like the UCC can be enabled.

Appendix A. Detailed Experimental Facility

The experimental program of the present work was accomplished at the Air Force Research Laboratory Combustion Branch's Lab 153 in Building 490 on Wright Patterson Air Force Base. This facility was used previously in many studies which laid the foundation of the present work. Chronologically, these were the studies of Evans [18], Anderson et al. [1], Polanka et al. [51], Bohan [9], DeLallo [14], Robertson [54], and Shewhart [57]. Similar to these studies, the present work selected this facility for its combustion capabilities, its ability to support high temperature heat transfer experiments, as well its ability to support a large number of simultaneous thermocouple measurements.

A diagram of the facility is seen in Fig. A.1. The facility housed a reactor which was capable of creating a high temperature flow ranging from fuel lean to fuel rich. A flat plate test rig was placed downstream of this reactor such that the high temperature reactor exhaust would flow over the flat plate and vent to atmospheric. The flat plate was fitted with backside cooling paths which, with varying coolant fluids and flow rates, was capable of varying the wall temperature. The flat plate was fitted with a film cooling plenum capable of accepting modular test coupons of selected film cooling schemes. Downstream of the cooling plenum was an instrumentation

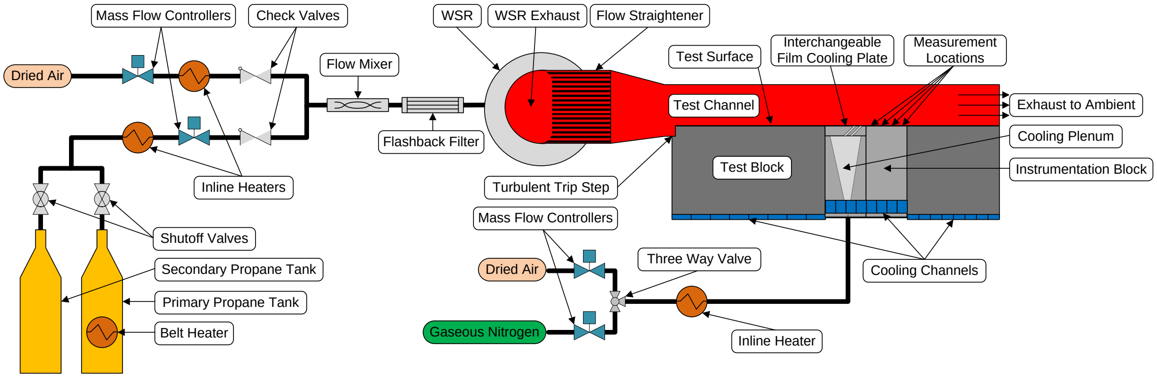

Figure A.1: Diagram of experimental facility

block capable of measuring the surface temperature and conductive heat flux. The remainder of this appendix will expand this general facility description into a detailed discussion of the relevant aspects of the facility.

A.1 Mass Flow Controllers

As seen in Fig. A.1, the facility used numerous mass flow controllers to provide air, nitrogen, and gaseous propane to the test rig. The present section will first provide an overview of the mass flow controllers' theory of operation. Last, the procedure for calibrating the mass flow controllers along with the accuracy of the calibrations will be presented.

A.1.1 Theory of Operation.

The controllers varied flow rate by a solenoid which throttled a valve restrict the flow appropriately. To measure the flow, the controllers pass the bulk flow through a restrictor to drive a large pressure drop. This pressure drop was used to drive a small amount of flow through a passage around the restrictor. The passage had a small diameter to length ratio such that the flow would be fully developed and laminar. Then, the temperature at the inlet and exit were measured and a known amount of heat was added to the flow to maintain a constant exit temperature. This amount of heat, the temperature difference and the specific heat of the fluid were then used to calculate the flow rate through the small tube. Finally, by knowing the flow rate through the small tube and the main flow were directly proportional, the total flow rate was calculated.

This method, though effective, came with drawbacks. Namely, a minimum pressure drop of 100 kPa was required across the controller. This reduced the pressure available for use downstream in the rig. Additionally, because the flow rate mea-

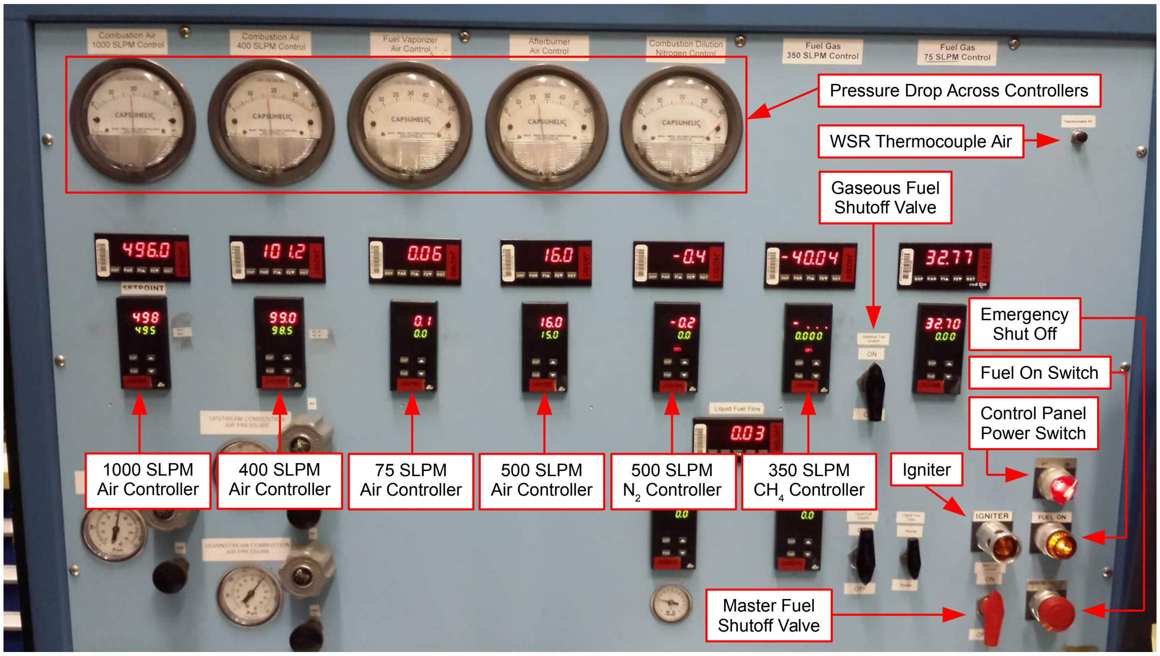

Figure A.2: Control panel used in experimental facility

surement relies on knowledge of the specific heat of the flow, maintaining a constant controller inlet temperature and pressure was critical to maintaining an accurate feedback measurement.

The flow controllers operated on a 4-20 mA command and feedback system system. In this system, the operator inputs the desired flow rate into the flow control interface seen in Fig. A.2 in units of standard liters per minute (SLPM). The unit of SLPM is defined as the equivalent volumetric flow rate at standard conditions of the desired mass flow rate. This is written in equation form as

$$\dot{V}_{\text{std}} = \frac{\dot{m}}{\rho_{\text{std}}} \tag{A.1}$$

where the subscript std denotes standard conditions of atmospheric pressure and a temperature of 294 K and $\dot{m}$ is the actual mass flow rate. The desired flow rate is then converted to a current signal such that 4 mA requests 0 flow, 20 mA requests maximum flow from the controller, and a linear interpolation for flow rates between minimum and maximum. The controller then adjusts to achieve the desired flow rate and responds with a feedback signal giving the measured flow rate on the same linear 4-20 mA (zero flow to maximum flow) scale.

A.1.2 Calibration.

To reduce the error in this command and feedback process, each mass flow controller was calibrated by commanding several flow rates followed by measuring the feedback current and the actual flow rate via a calibrated flow rate measurement. In this fashion, the feedback signal from the controller was calibrated to the actual flow rate through the controller. These linear calibrations are then input to the data acquisition system which measures the controller's feedback signal and calculates the flow rate from the calibration.

Three methods were used to calibrate the mass flow controllers: sonic nozzles, dry flow meter, and the Gilibrator system. For all of the air and nitrogen controllers shown in Fig. A.2, the sonic nozzle method was used. In this method, flow is passed through an orifice of known diameter. The orifice diameter must be selected such that, for a given flow rate, the flow is choked. Then, by measuring pressure and temperature upstream of the orifice and knowing the downstream pressure is atmospheric, the mass flow rates were be calculated using software accompanying the calibrated nozzles.

For the 1000, 400, and 500 SLPM air and the 500 SLPM nitrogen controllers seen in Fig. A.2, flow rates between 50 and 140 SLPM were measured using a 0.063" diameter nozzle (S/N 31014). Flow rates between 200 and 500 SLPM were measured using a 0.125" diameter nozzle (S/N 31015). Flow rates between 500 and 800 SLPM were measured using a 0.160" diameter nozzle (S/N 30163). Flow rates above 800 SLPM were not calibrated or used in the present work. For the 75 SLPM air controller, flow rates between 10 and 30 SLPM were measured using a 0.031" diameter nozzle

Table A.1: Uncertainty of the mass flow controller calibrations in the specified figures

Function	Figure	Controller	Gas	Uncertainty
Combustion	3.2	1000 SLPM	Air	±1.5%
Combustion	3.2	400 SLPM	Air	±3.0%
Film Cooling	3.2	75 SLPM	Air	±3.3%
Coolant Heater	3.2	500 SLPM	Air	±2.4%
Backside Cooling	3.2	500 SLPM	N_2	±2.2%
Combustion	3.2	350 SLPM	CH_4	±2.7%
Combustion	A.3	MKS 75 SLPM	C_3H_8	±2.4%
Film Cooling	A.3	Brooks 10 SLPM	Air	±4.2%
Film Cooling	A.3	Brooks 10 SLPM	N_2	±3.7%
Film Cooling	A.3	Brooks 5 SLPM	Air	±2.3%
Film Cooling	A.3	Brooks 5 SLPM	N_2	±2.6%

(S/N 31012). Flow rates between 40 and 75 SLPM were measured using a 0.044” diameter nozzle (S/N 31014). The accuracy of each of these calibrations is given in Table A.1.

Each of the sonic nozzle calibrations were subsequently validated by two dry flow meters with model numbers of DTM-200A and DTM-325 and serial numbers of 06F917011 and 06F917012, respectively. The dry flow meters measure the total volumetric flow over time up to 100,000 L where it resets to zero. Thus, the volumetric flow rate can be calculated by maintaining a constant flow rate for a known measured of time and noting the starting and ending readings. Then, the difference between these readings divided by the measured time gives volumetric flow rate. Finally, this volumetric flow rate was converted to standard liters by multiplying by the measured density to get a mass flow rate and dividing by the standard density as shown in Eq. A.1. Comparing the sonic nozzle calibration to the flow rate measured with the dry flow meter resulted in an agreement within 2% for all cases.

The dry flow meter method was also used to calibrate the 350 SLPM CH_4 controller. Though this controller was factory calibrated for methane (CH_4), it was used to control a flow of gaseous propane (C_3H_8). As discussed above, calibrations rely on

Figure A.3: User interface for the MKS propane controller (bottom) and low flow rate Brooks controllers (top)

knowledge of fluid properties to predict the flow rate. Thus, by changing the flowing gas, the maximum flow rate changes by a constant factor depending on the gas. Fortunately, the calibration process accounts for this conversion with no modification. Therefore, the propane calibration was accomplished by measuring the feedback signal from the controller in mA and measuring the flow rate via the dry flow meter. The accuracy of the resulting calibration is given in Table A.1.

During testing, the 350 SLPM CH_4 controller malfunctioned and was replaced. The controller which replaced it was an MKS (model number 647C-8-R-O-T) and was driven by the bottom control interface seen in Fig. A.3. It was calibrated in an identical fashion and it's calibration accuracy is given in Table A.1.

The final two controllers seen in Fig. A.1 were low flow rate Brooks (model number 0152BFC2B31A) controllers driven by the top interface seen in Fig. A.3. Unlike the previous controllers, these controllers did not report to the data acquisition system and calibrating a mA feed back to flow rate was not necessary. However, comparing the commanded flow rate to the achieved flow rate was accomplished to determine the accuracy of the controller.

The interface featured two channels which drove a 0-10 SLPM and 0-5 SLPM controller, respectively. The low flow rates were too small for the previous measurement techniques discussed above. Thus, the Gilibrator system (model number 850190, serial number 010180) which specializes in low flow rates was employed. This system consists of a hollow cylinder of known cross-sectional above a reservoir of soapy water. Then, by supplying a low flow rate at the base of the cylinder and the user dips a ring into the soapy water which forms a bubble spanning the cylinder's cross-section. The low flow rate then drives this bubble up the height of cylinder. Finally, the Gilibrator measures the time it takes for the bubble to travel from one height to another and calculates volumetric flow rate from the known diameter, height difference, and measured time. To cover the full range of flow rates, two hollow cylinder sizes were used to support flow rates of 0.02-6 SLPM (model number 800285, serial number 1007043-5) and 2-30 SLPM (model number 800285, serial number 1312002-H). Comparing the commanded flow rates and measured flow rates indicated the calibration accuracies given in Table A.1.

A.2 Well-Stirred Reactor

The experimental facility utilized a well-stirred reactor (WSR) to burn a propane and air mixture. The WSR was a 250 mL volume toroidal design similar to that presented by Zelina and Ballal [71] and discussed in Section 2.4.3. By varying the equivalence ratio (Φ, Eq. 2.45), the WSR would exhaust a high temperature flow which ranged from fuel lean (WSR $\Phi < 1.0$) to fuel rich (WSR $\Phi > 1.0$). This exhaust could then be routed through a modular test section to create an engine-like flow condition.

A.2.1 Well-Stirred Reactor Design.

The lower half of the toroidal WSR used in the present work can be seen in Fig. A.4. The WSR injects unburned fuel and air into a pressurized chamber outside the reactor chamber. Then, the fuel-air mixture flows from the pressurized chamber through small diameter holes in the jet ring and into the reactor chamber. Once in the reaction chamber, the fuel-air mixture is burned as it travels toward the core of the WSR as seen in Fig. A.4(b). Finally, Fig. A.5 shows the burnt gases entering the core of the WSR, being turned upwards and exhausted.

The jet ring seen in A.4 served three critical roles in the operation of the WSR. First, the small diameter of the jet ring's holes forced a large pressure drop across the jet ring such that approximately equal flow passed through each jet ring hole. Second, the jet ring holes were designed with a small enough diameter to prevent the flame front from traveling back through the jet ring. This prevented combustion from occurring within the pressurized chamber and further up-stream. Finally, the jet ring holes were angled to proved a tangential component to the injection velocity. This tangential component resulted in g-loading of the combusting gases to maximize the residence time of the unburned gases and increase the reactor stability as discussed in Section 2.4.3.

Unlike the WSR presented by Zelina and Ballal [71], the current WSR was not a purely ceramic, uncooled reactor. Rather, the WSR used in the present work was constructed of INCONEL$^{®}$ alloy 625 [61]. Since the combustion temperatures within the reactor far exceeded the melting temperature of the WSR, cooling channels were applied to the exterior of the reactor. The channels were supplied with water controlled by the needle valves shown in Fig. A.6. In addition to actively cooling the WSR, the interior of the reactor was lined with a Yttria stabilized Zirconia thermal barrier coating as seen in Fig. A.7 to reduce the heat load on the WSR.

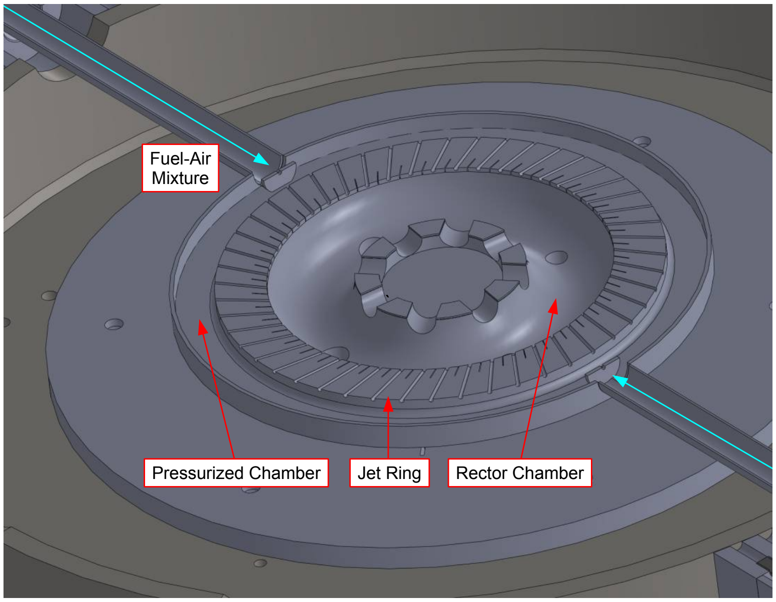

(a) Isometric view

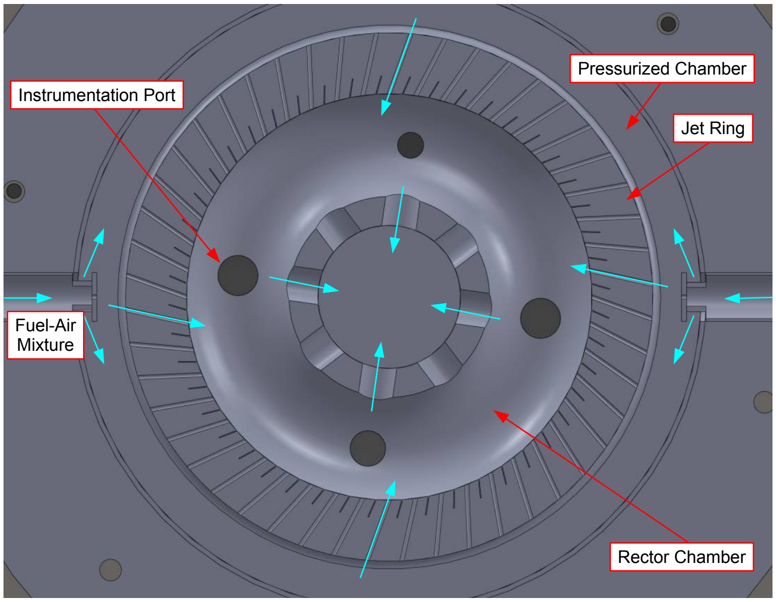

(b) Normal view

Figure A.4: Drawing of lower half of WSR and jet ring

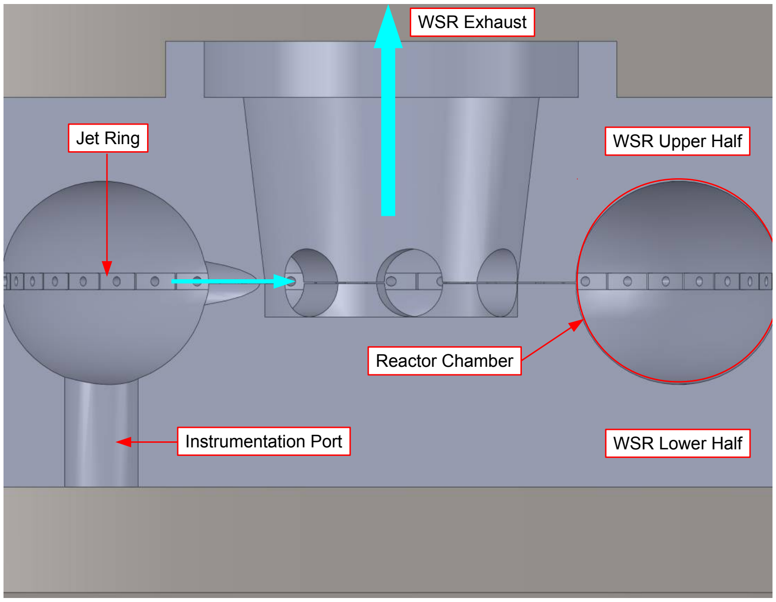

Figure A.5: Cut away view of the WSR from the side

Figure A.7 also shows the location of several OMEGA® K-Type thermocouples measuring the temperature of the jet ring. Though not shown, thermocouples were also mounted to the upper and lower halves of the WSR. Using these thermocouples, the water flow rate to the upper and lower halves was adjusted such that the measured material temperatures remained below 590 K. Nominally, this required a flow rate of 1.3 liters per minute to the lower half and 2.3 liters per minute to the upper half.

Four ports were machined in the lower half of the WSR. As seen in Fig. A.7(a), three of the ports were used to house an OMEGA® B-Type thermocouple to measure the combustion temperature, a static pressure tap, and a spark igniter while. The fourth port was unused. However, it allows for modularity of the rig to accommodate experiments with requirements such as flow seeding for Particle Image Velocimetry.

A.2.2 Well-Stirred Reactor Plumbing.

As shown in Fig. A.1, there were numerous plumbing features upstream of the WSR to provide the appropriate flows and provide an appropriate level of system

Figure A.6: Water needle valve flow controllers; Top bank (0-20 gallon per hour controllers): left and center - unused, right - rig wall cooling; Bottom bank (0-1 gallon per minute controllers): left - cooling for WSR bottom half, center - cooling for WSR top half, right - rig wall cooling

safety. Dried air was supplied to the WSR by the facility's compressors and was regulated by the 1000 and 400 SLPM mass flow controllers discussed in Section A.1.2. Propane fuel (C_3H_8) was supplied by 45 kg bottles housed in a locker outside the facility for safety. The fuel flow rate was controlled by the 75 SLPM MKS and 350 SLPM CH_4 controllers discussed in Section A.1.2.

As described in Section A.1.1, operation of the mass flow controllers required at least a 100 kPa pressure drop across the controller. Additionally, the controller's feedback loop was sensitive to the fluid's inlet temperature and pressure. Due to cooling of the propane bottle by expansion during operation and low external temperatures on some test days the bottle pressure and temperature were seen to vary greatly. Often cooling of the bottle caused the pressure to drop sufficiently such that the minimum

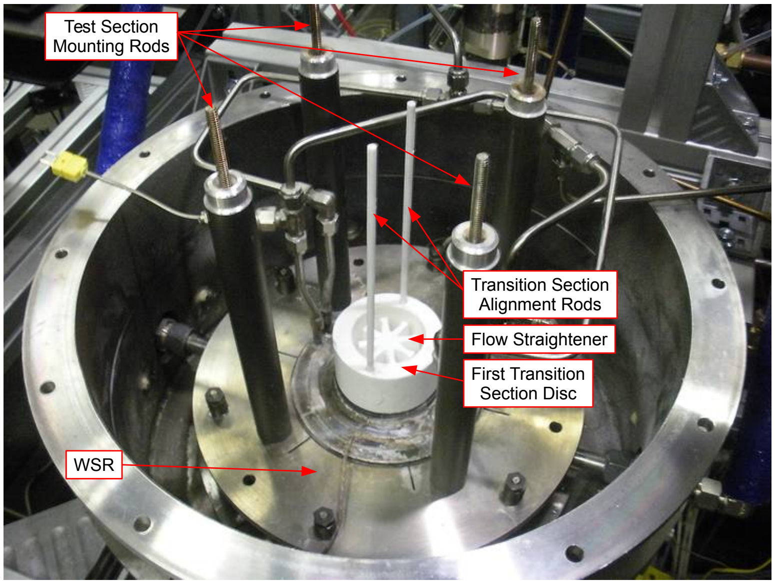

(a) Lower half

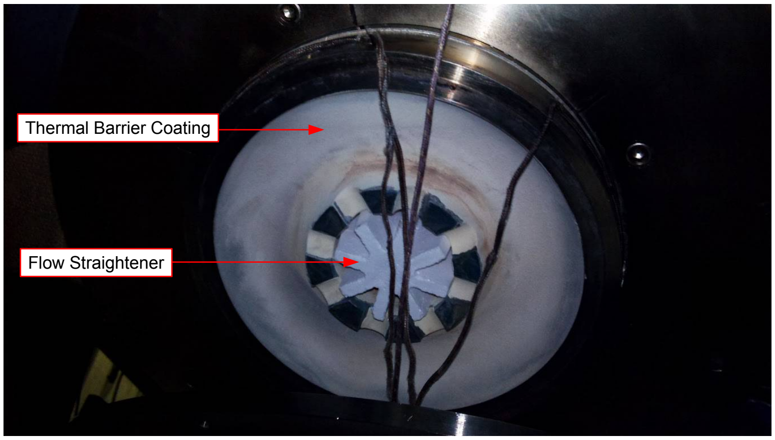

(b) Upper half with flow straightener

Figure A.7: Inconel® well stirred reactor used in the present research

drop across the controller of 100 kPa could not be maintained.

To counteract cooling of the bottle and maintain sufficient pressure in the propane system, belt heaters were applied to the exterior of the bottles as seen in Fig. A.1. However, once the gaseous propane exited the heated bottle, it traveled through a significant length external plumbing before entering the climate controlled interior of the facility. Though the external plumbing was insulated to minimize heat loss from the fuel flow, low external temperatures (as low as −25 °C), made the flow temperature entering the facility largely variable. Since the mass flow controller feedback measurement was highly sensitive to inlet temperature, the in-line heater seen in Fig. A.1 was applied to raise the temperature entering the controller to 22 °C± 1 °C.

Since the dried air was sourced and compressed within the climate controlled facility, the temperature and pressure of the air entering the controllers was sufficiently constant. Additionally, pressure regulators upstream and downstream of the controller were used to maintain a pressure drop of greater than 100 kPa across the controller. This pressure drop was monitored using the gauges seen in Fig. A.2. To increase the combustion temperature, the dried air was heated downstream of the controller before mixing with the fuel via the in-line heater seen in Fig. A.1.

After the fuel and air enter the same stream, they passed through a flow mixer as seen in Fig. A.1. This helped ensure the fuel-air mixture would be uniform entering the WSR. Finally, before entering the WSR, the flow passed through a flash back filter. This filter was made of a long metal honeycomb which forced the flow to pass through many long, small diameter passages. In the event of a flame front traveling upstream from the WSR, the flame front would be extinguished within these small passages to prevent a flame from propagating to the fuel and air sources.

As an additional safety feature, check valves were installed on the fuel and air supply lines as seen in Fig. A.1. These prevented the potentially dangerous condition of air leaking into the fuel line or conversely. During operation of the facility, the presence of the check valves required that the flow rates of fuel and air not be changed too rapidly. Changing the flow rate of air or fuel resulted in an increased pressure at the fuel-air junction. Thus, if the flow rate of air or fuel were changed too rapidly, the pressure at the fuel-air junction would rise before the fuel or air controller, respectively, could increase its pressure to maintain a constant flow rate resulting in temporary closure of the check valve. This would ultimately cause the undesirable result of a flame blowout in the WSR and a cessation of the experiment.

A.3 Test Channel

For the present work, a flat plate test channel was mounted to the exit of the WSR. This section will first discuss the ceramic channel which transitioned the flow from the WSR to the inlet of the test section. Last, it will describe the geometrical features of the test channel.

A.3.1 Transition Section.

As seen in Figs. A.7(b) and A.8, the flow exiting the WSR first entered a flow straightener. Since the WSR imparts a high degree of swirl on the flow, the straightener both removes the swirl and turns the flow axially up the test channel. To withstand the aero-loading and high temperature environment, the flow straightener was constructed of Alumina ceramic casted in a mold.

Next, the flow entered a transition section which modified the flow cross-sectional area from the circular WSR exit to the nearly rectangular entrance of the test section. Since the aero-loading of the transition section was small compared to the flow straightener, the transition was constructed of softer Zirconia Type FBD ceramic.

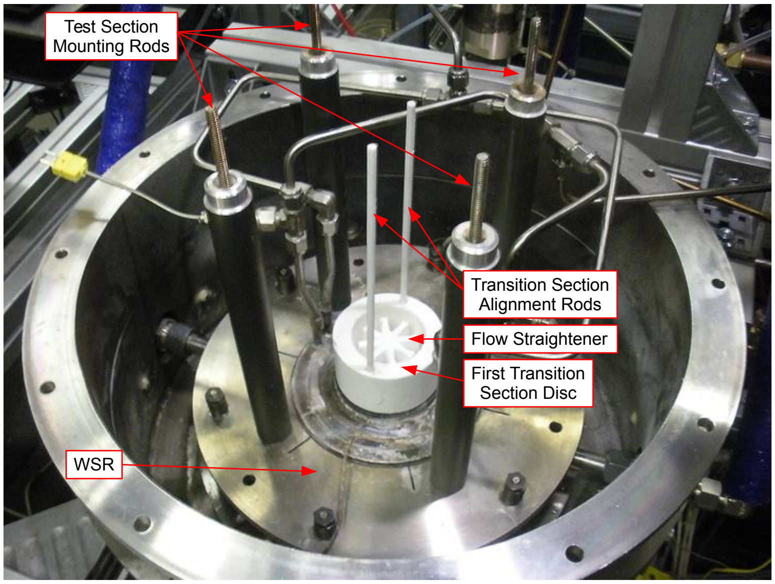

(a) Partially assembled

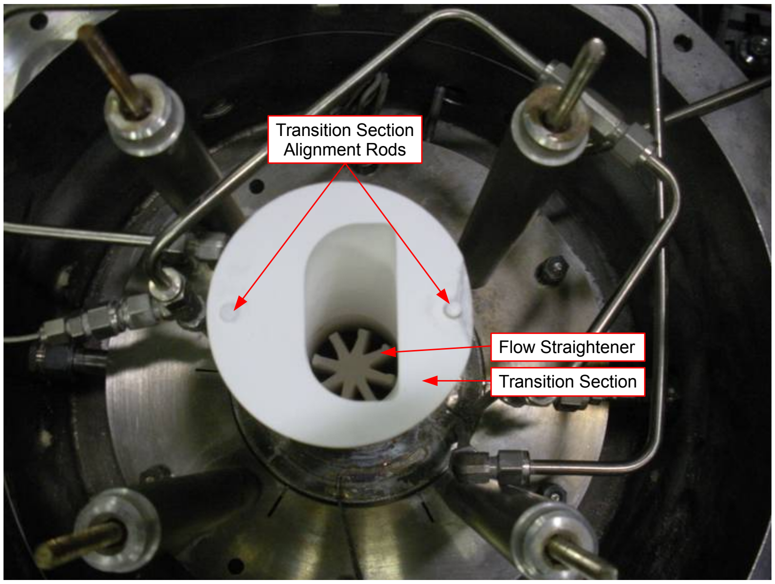

(b) Fully assembled

Figure A.8: Transition section adjusting flow cross-section from WSR exit to test section entrance

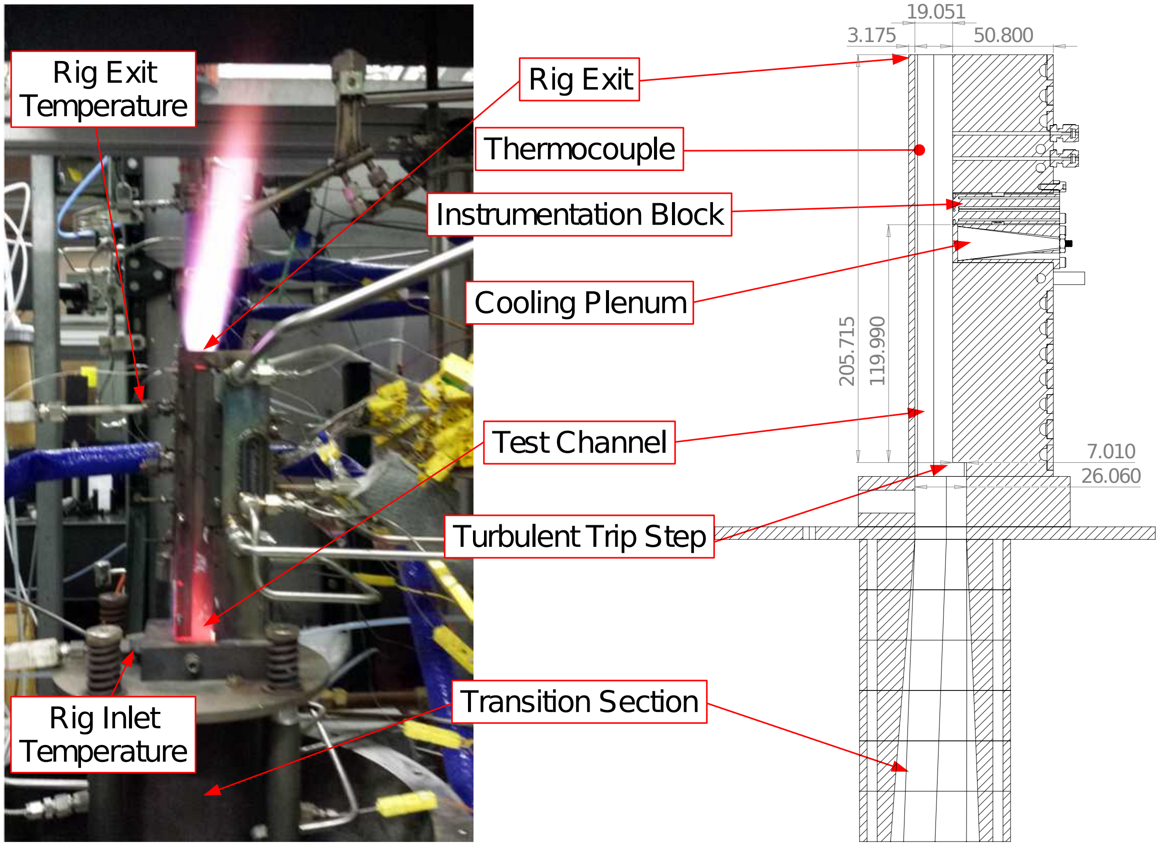

Figure A.9: Comparison of rig hardware (left) to cutaway drawing of transition section and test channel (right); flow from WSR (bottom) to rig exit (top); dimensions in mm

The ceramic initially came in several short, cylindrical discs. Then, the soft material allowed the interior of the disc to be machined out to form the appropriate transition geometry. Next, the discs were stacked and aligned by ceramic rods to form the full transition length as seen in Fig. A.8. Finally, a hollow cylinder of Zirconia Type ZYC was placed around the Zirconia Type FBD to help insulate the hot flow passing through the transition.

A.3.2 Test Section.

As seen in Fig. A.9, the flow exiting the transition section encounters a forward facing step before entering the test channel. This step was intended to trip the flow

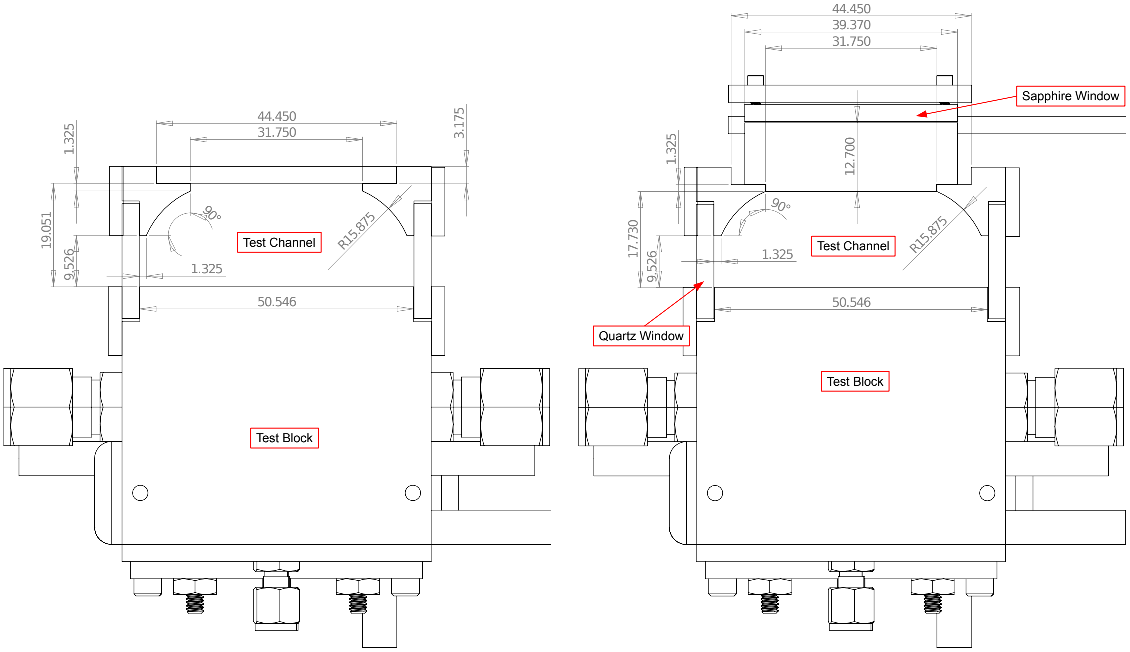

(a) Without windows (b) With windows

Figure A.10: Dimensions of test channel cross section in mm

and ensure a fully turbulent flow within the test channel. According to White [68], the criterion to trip a low Mach number flow into turbulence is to have a height of

$$\delta_{\text{trip}} \approx 850\nu_\infty/u_\infty \tag{A.2}$$

For nominal rig conditions of $T_\infty = 1500\,\text{K}$, $u_\infty = 60\,\text{m/s}$, and $\nu_\infty = 2.29\times10^{-6}\,\text{m}^2/\text{s}$, a minimum trip step height of $\delta_{\text{trip}} = 3.2\,\text{mm}$ was required. Thus, the 7 mm trip height used in the rig was deemed sufficient to trip the flow into turbulence.

To measure the core flow temperature within the test channel, two OMEGA® B-Type thermocouples were used to measure the inlet and exit temperatures. The inlet temperature measurement was taken in the flow exiting the transition section just before it encounters the turbulent trip step as seen in Fig. A.9. The exit core flow temperature measurement was located 40 mm downstream of last row of the instrumentation block thermocouples and in the center of the channel cross-section.

Since the exit temperature was closest to the measurement location, its temperature measurement was used as T_∞ in the present research.

After passing over the forward facing step, the flow entered the test channel. Two channel configurations were used in the present work with two slightly different cross sections. The first configuration (Fig. A.10(a)) used Hastelloy X [24] for all surfaces bounding the channel. The configuration had a hydraulic diameter of $D_h = 27.2\,\mathrm{mm}$ and cross sectional area of $A = 871\,\mathrm{mm}^2$.

The second configuration (Fig. A.10(b)) had two windows installed. A quartz window was installed on the left wall seen in Fig. A.10(b) to allow visual spectrum images of the secondary burning flames in the plane normal to the wall and parallel with the flow. The top wall in Fig. A.10(b) is thicker in the second configuration and has a small notch extending into the flow that is not present in the first configuration. This notch accounts for the second configuration's slightly smaller dimensions of $D_h = 26.4\,\mathrm{mm}$ and $A = 828\,\mathrm{mm}^2$. The thicker wall in the second configuration had a small cavity in which a 38 mm diameter sapphire window was installed which allowed for infrared imaging of the test surface.

Much of the present work focused on heat transfer over a wide range of wall temperatures. As seen in Fig. A.11, cooling channels were applied to the backside of the test surface to prevent the material from melting and provide a method for varying the wall temperature. By providing the channels with various flow rates of water or nitrogen, the heat flux through the test block and surface temperature were varied.

However, excessive cooling drove significant heat extraction from the hot core flow resulting in a core temperature which decreased with downstream distance. To minimize the streamwise temperature gradient, the lower cooling channel was isolated from the side and upper cooling channels in Fig. A.11. The lower channel was provided

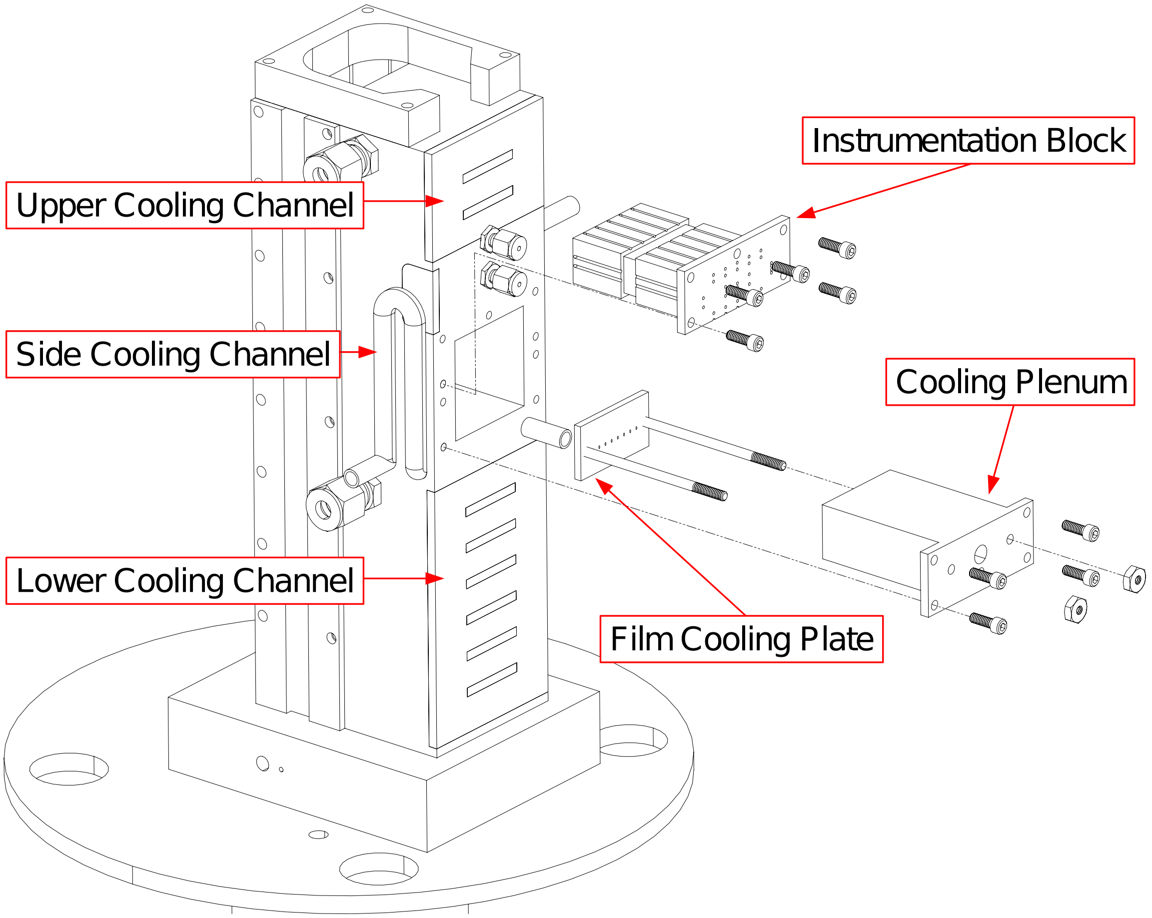

Figure A.11: Drawing of rig cooling channels and test insert assembly with hardware

with a small flow rate of nitrogen (5 SLPM) to prevent the material from melting while extracting a minimal amount of heat from the core flow. The upper and side cooling channels were run in series with various flow rates of water or nitrogen depending on the desired test condition.

Figure A.11 shows that two modular blocks were inserted between the upper and lower cooling paths. The first insert was the cooling plenum which supplied air or nitrogen to a modular film cooling plate. The second insert was the instrumentation block which measured the wall temperature and heat flux downstream of the film cooling injection site. The following sections will discuss these inserts in detail.

A.4 Film Cooling Configuration

Many film cooling configurations were tested in the present work. Rather than producing a film cooling plenum for each hole geometry, a single film cooling plenum was developed to accept modular film cooling geometry plates. An exploded view of the film cooling assembly is seen in Fig. A.11. This section will discuss the features of the common film cooling plenum design and the film cooling configuration plates.

A.4.1 Modular Film Cooling Plenum.

The film cooling plenum was supplied with air or nitrogen depending on the test case. As seen in Fig. A.12, flow entered the plenum from a circular supply line and expanded to a $445\,\text{mm}^2$ cross-sectional area at the film cooling configuration plate interface. Also seen in Fig. A.12 is a hole in the plenum wall used to insert a K-Type thermocouple to measure the coolant temperature just before it ejects from the film cooling holes.

As shown in Fig. A.1, a heater was used to increase the coolant temperature entering the rig. Due to the low flow rates of coolant, using a heater directly on the flow was impractical. Attempting to do so resulted in major over and undershoots in coolant temperature due to the large response time of the coolant flow. Thus, to heat the flow, a separate 100-200 SLPM flow of air was heated by a Hotwatt PFO-12 1200 W, 120 V heater. Then, to use this heated process air to heat the coolant air, a concentric tube heat exchanger was constructed. Finally, by flowing the coolant air through the inner concentric tube and the process air through the outer concentric tube in the opposite direction, the coolant air was heated and the over and undershooting in coolant temperature was abated.

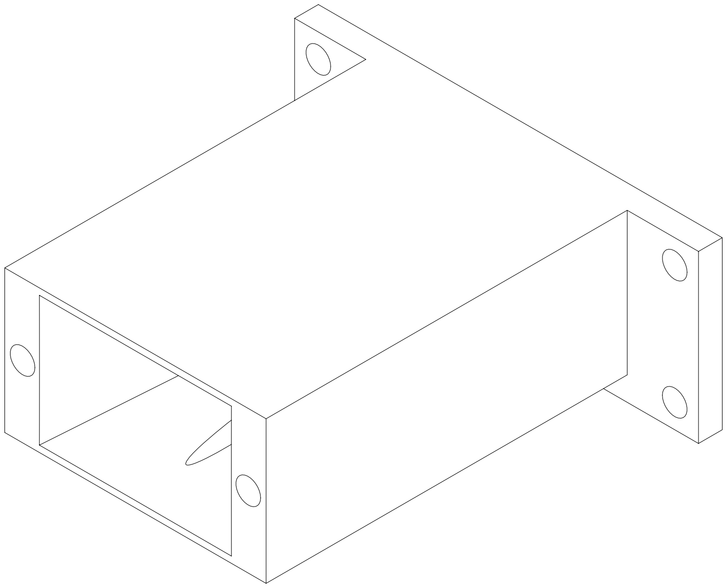

(a) Isometric view

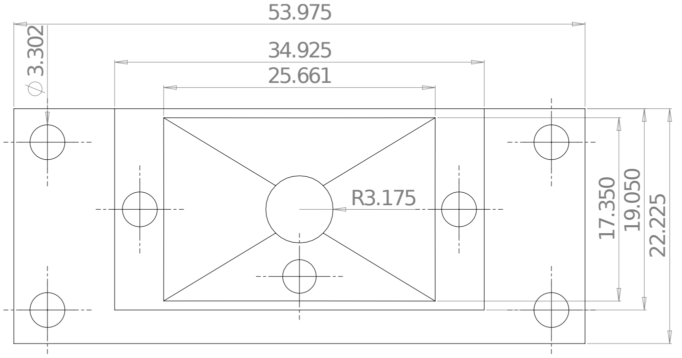

(b) Top view

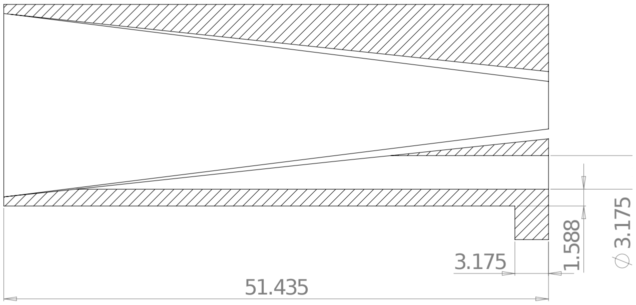

(c) Cutaway side view; coolant flow from right to left

Figure A.12: Drawing of modular cooling plenum; freestream flow from bottom to top; dimensions in mm

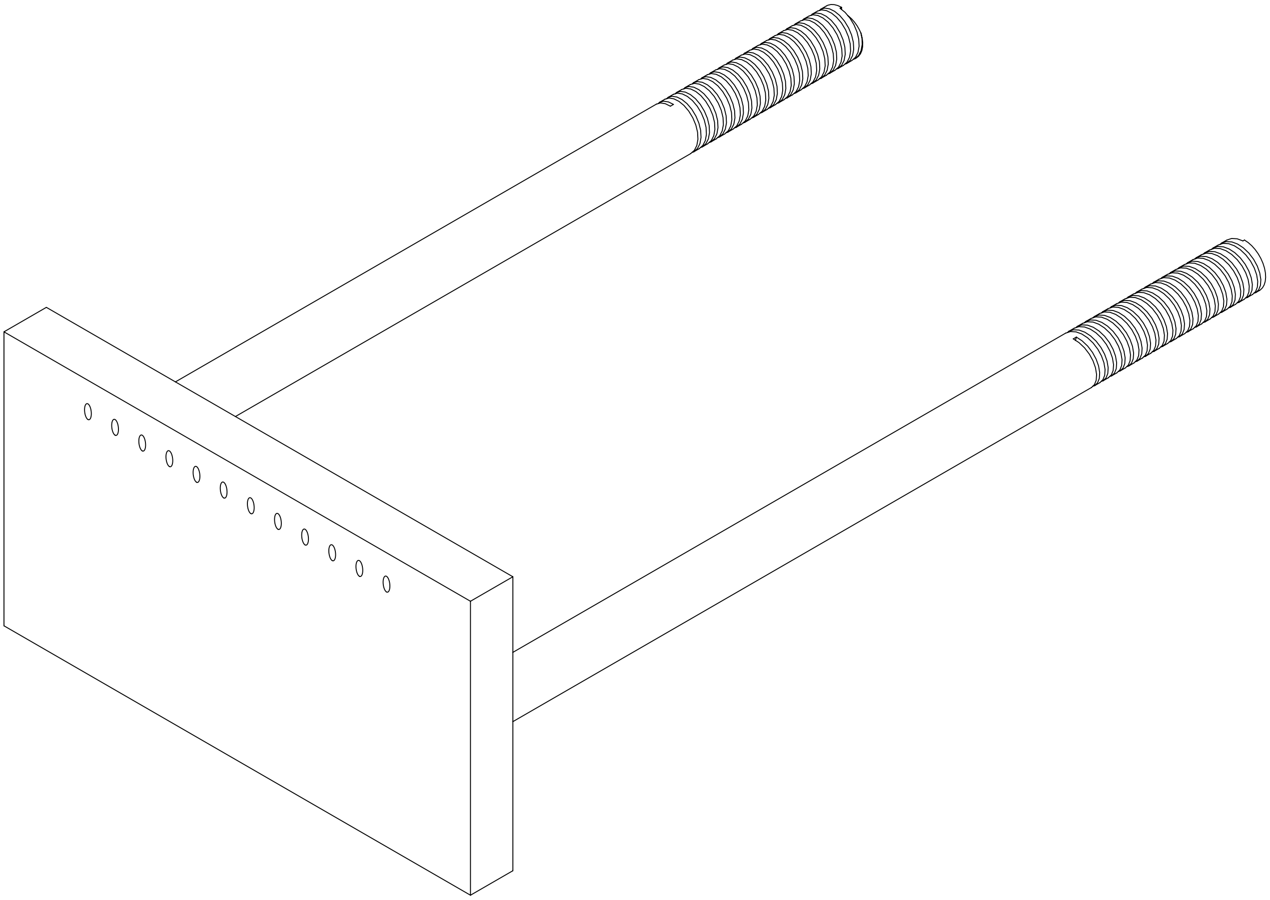

(a) Isometric view

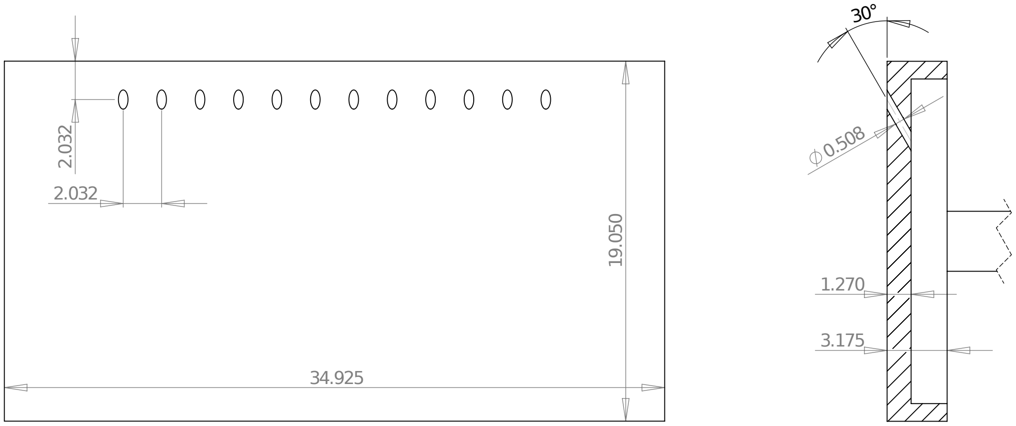

(b) Front view

(c) Cutaway side view

Figure A.13: Drawing of one row of cylindrical hole test coupon; freestream flow from bottom to top; dimensions in mm

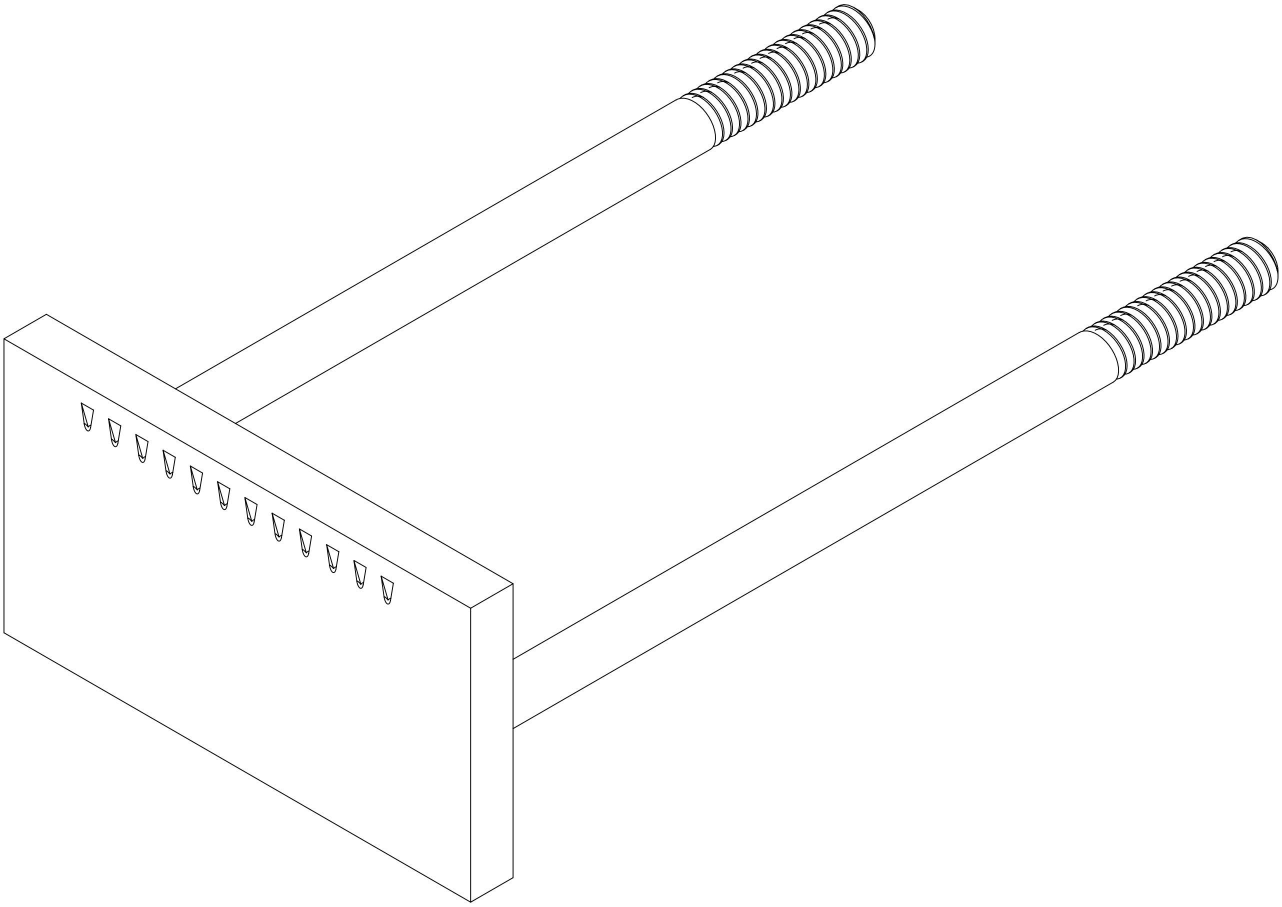

(a) Isometric view

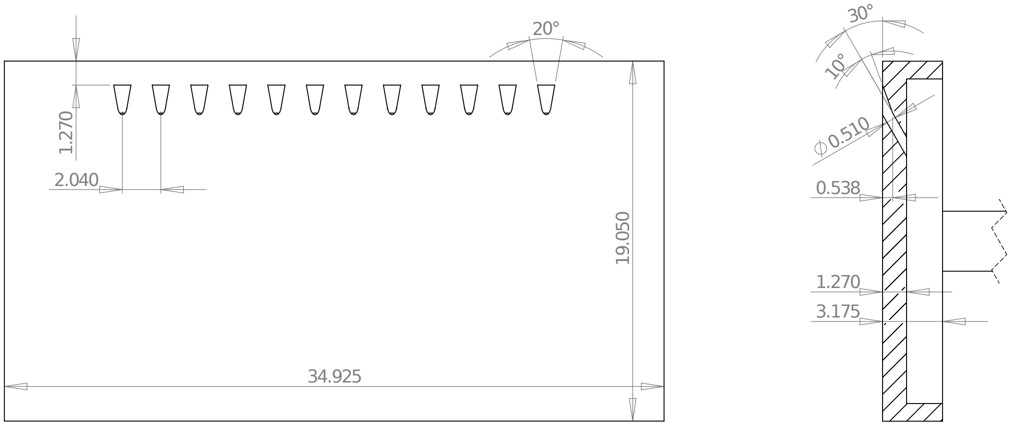

(b) Front view

(c) Cutaway side view

Figure A.14: Drawing of one row of shaped hole test coupon; freestream flow from bottom to top; dimensions in mm

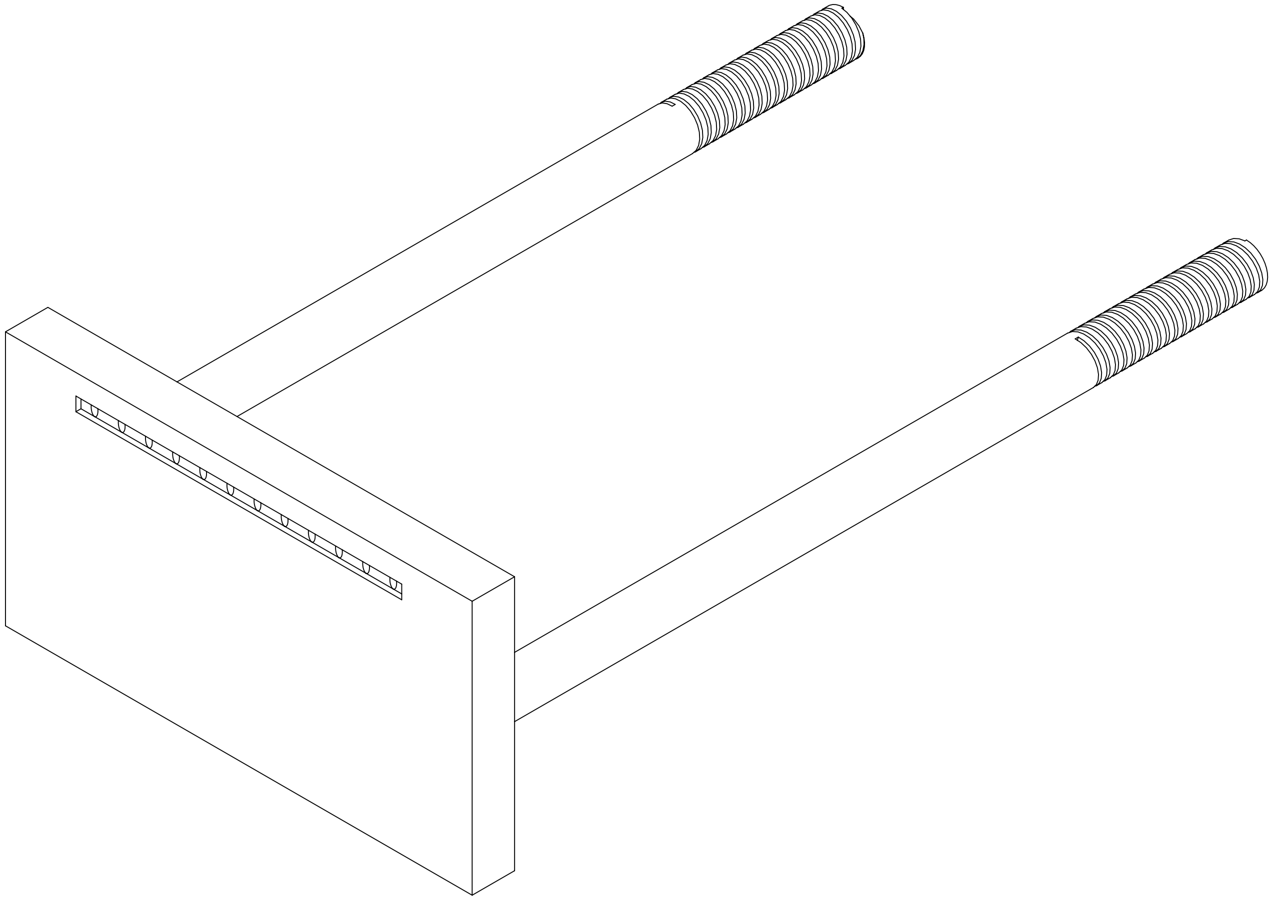

(a) Isometric view

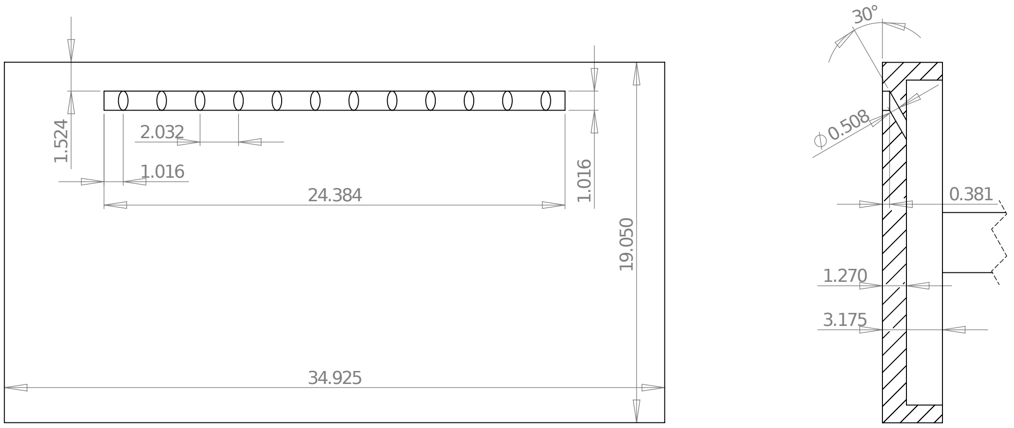

(b) Front view

(c) Cutaway side view

Figure A.15: Drawing of one trench row test coupon; freestream flow from bottom to top; dimensions in mm

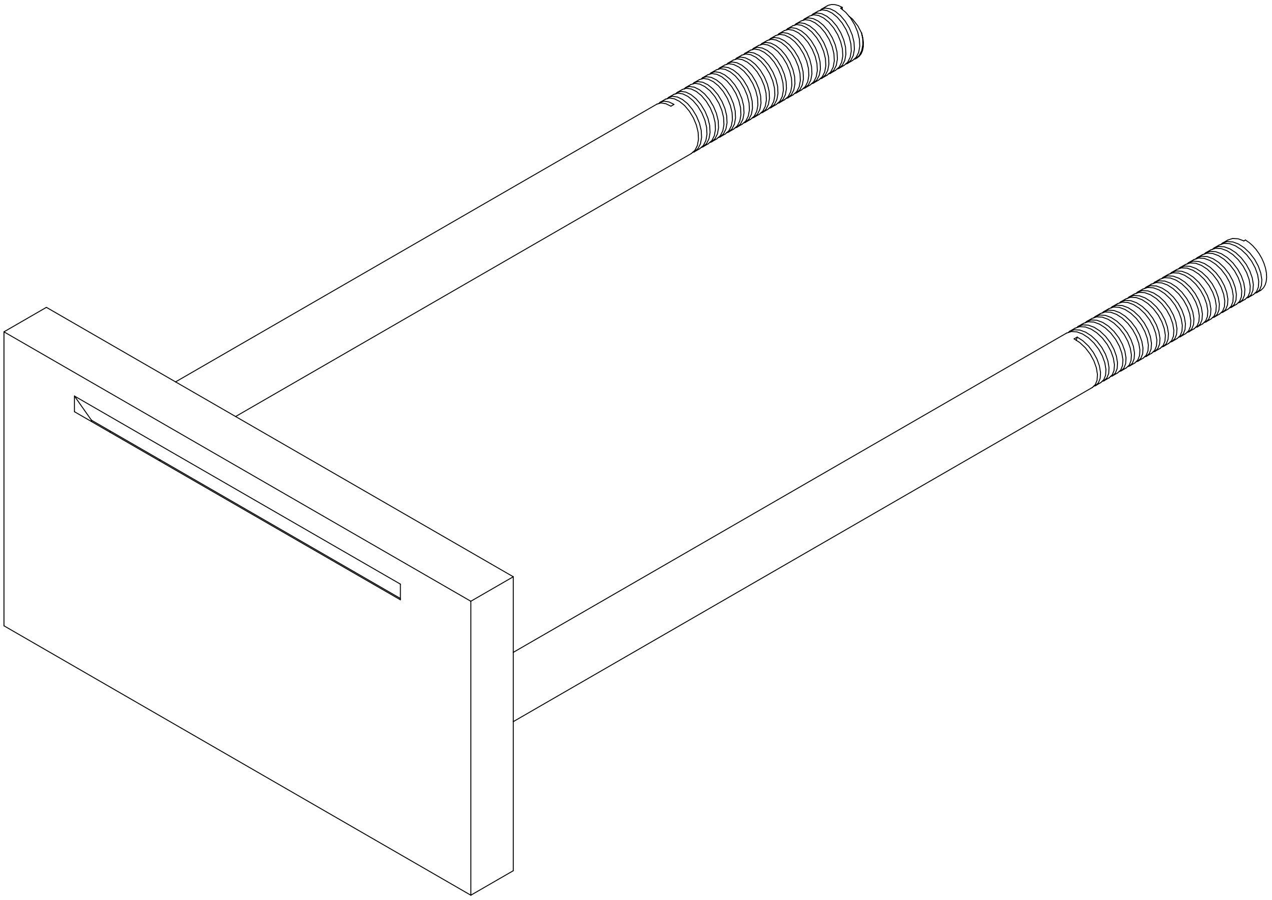

(a) Isometric view

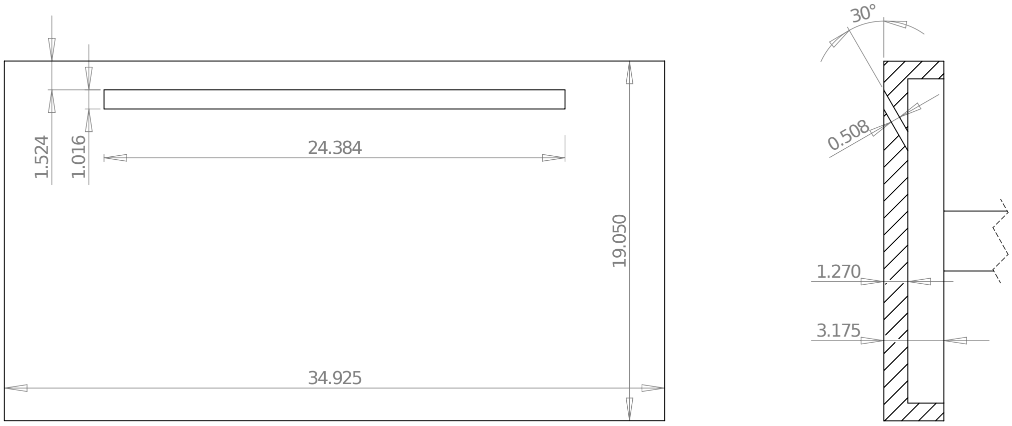

(b) Front view

(c) Cutaway side view

Figure A.16: Drawing of one slot row test coupon; freestream flow from bottom to top; dimensions in mm

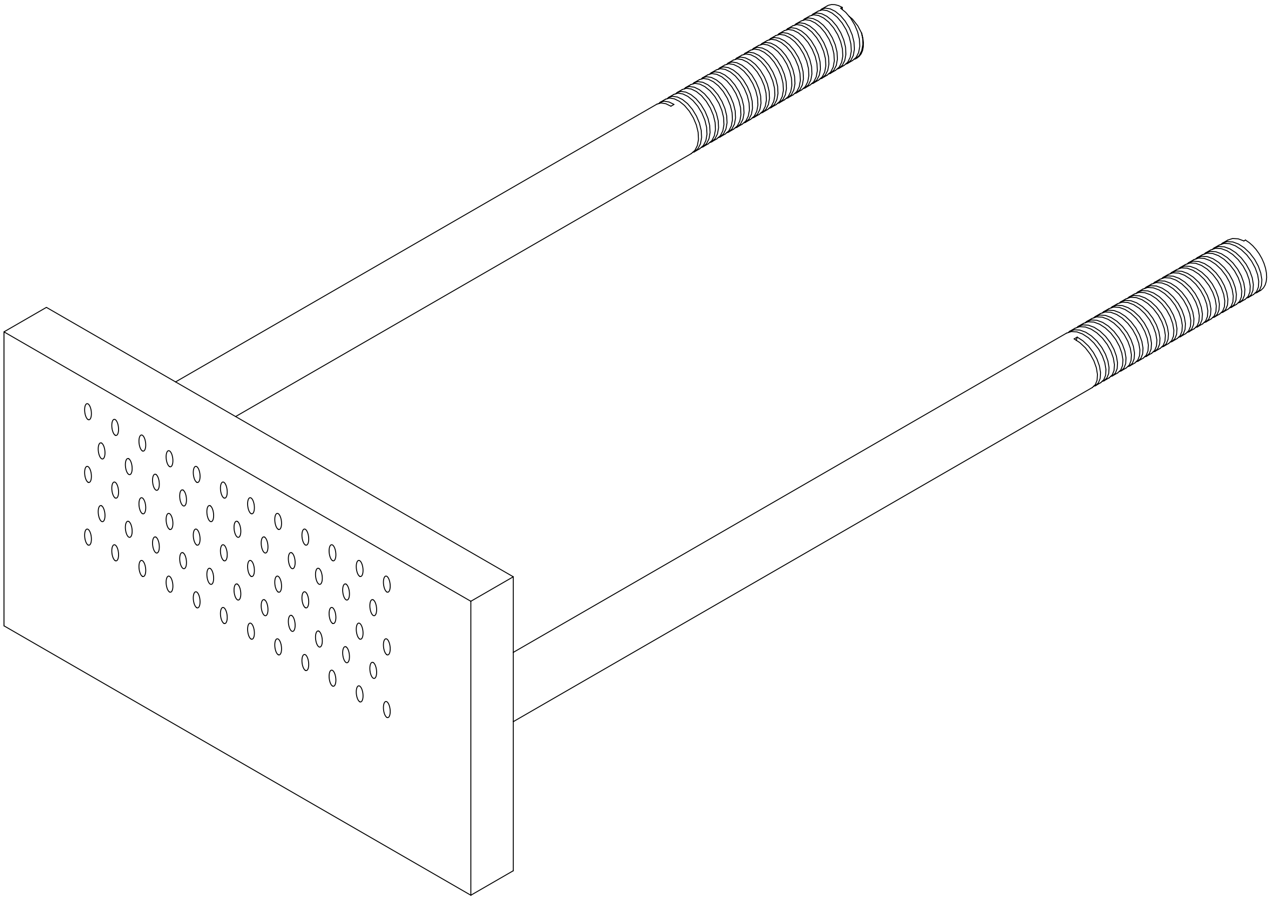

(a) Isometric view

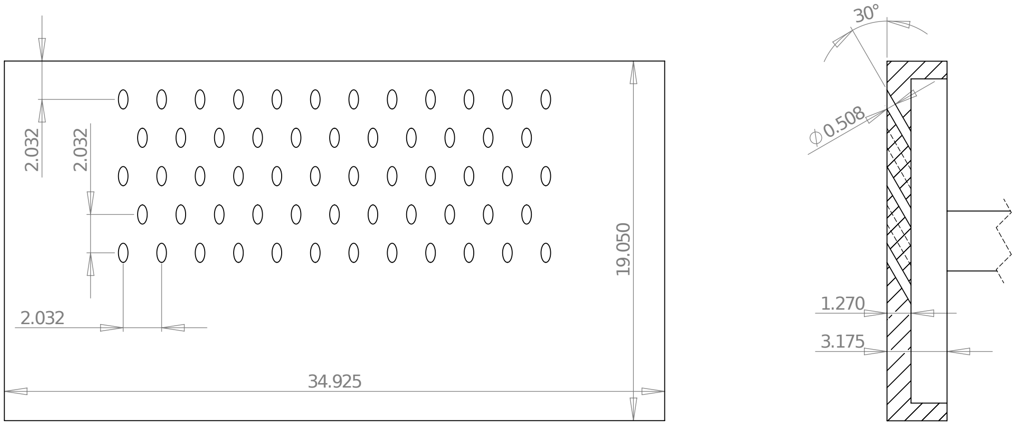

(b) Front view

(c) Cutaway side view

Figure A.17: Drawing of five row of cylindrical hole test coupon; freestream flow from bottom to top; dimensions in mm

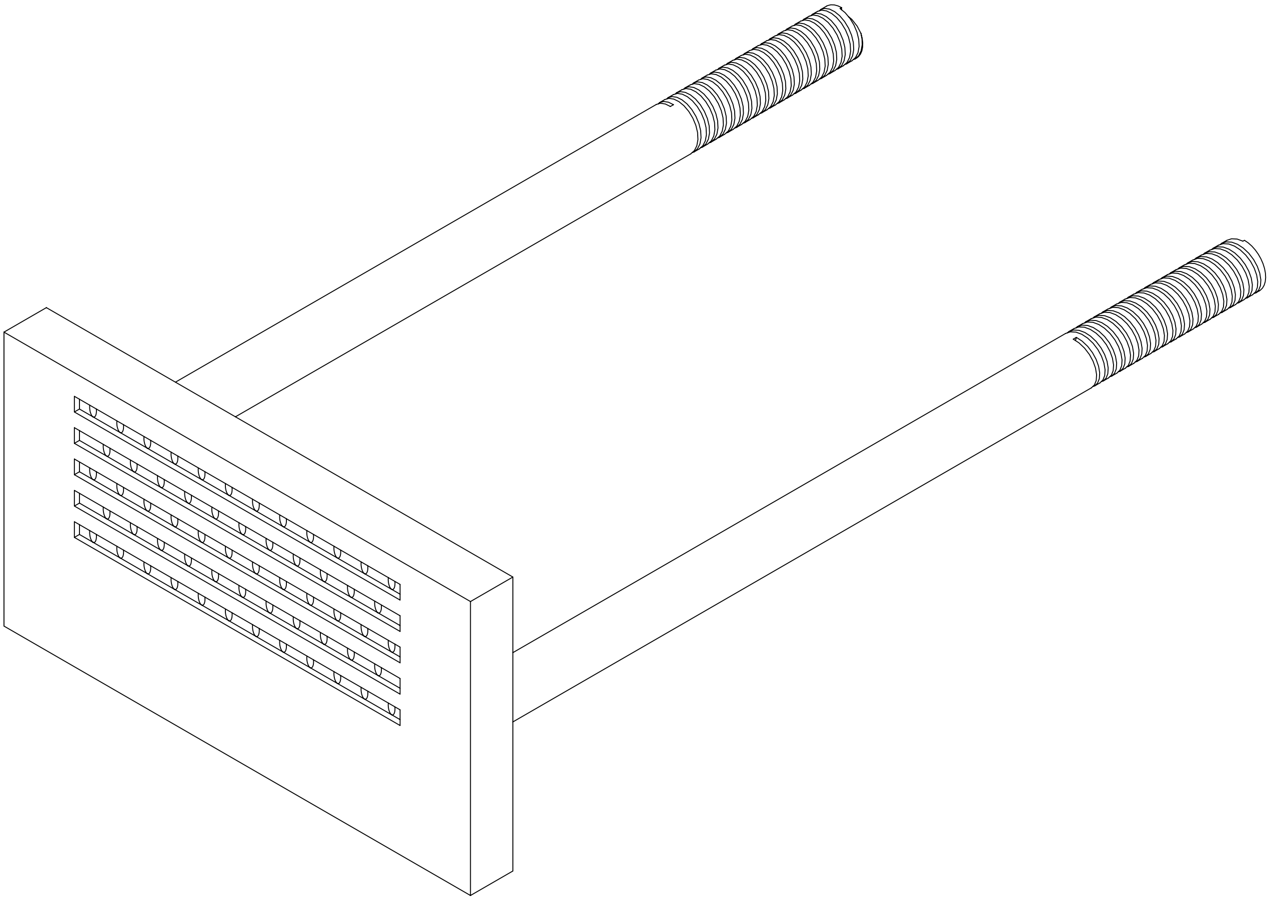

(a) Isometric view

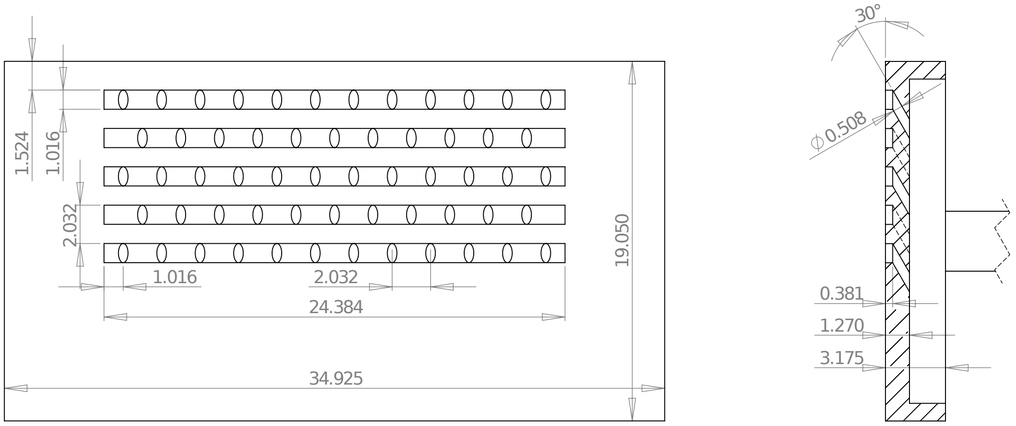

(b) Front view

(c) Cutaway side view

Figure A.18: Drawing of five trench row test coupon; freestream flow from bottom to top; dimensions in mm

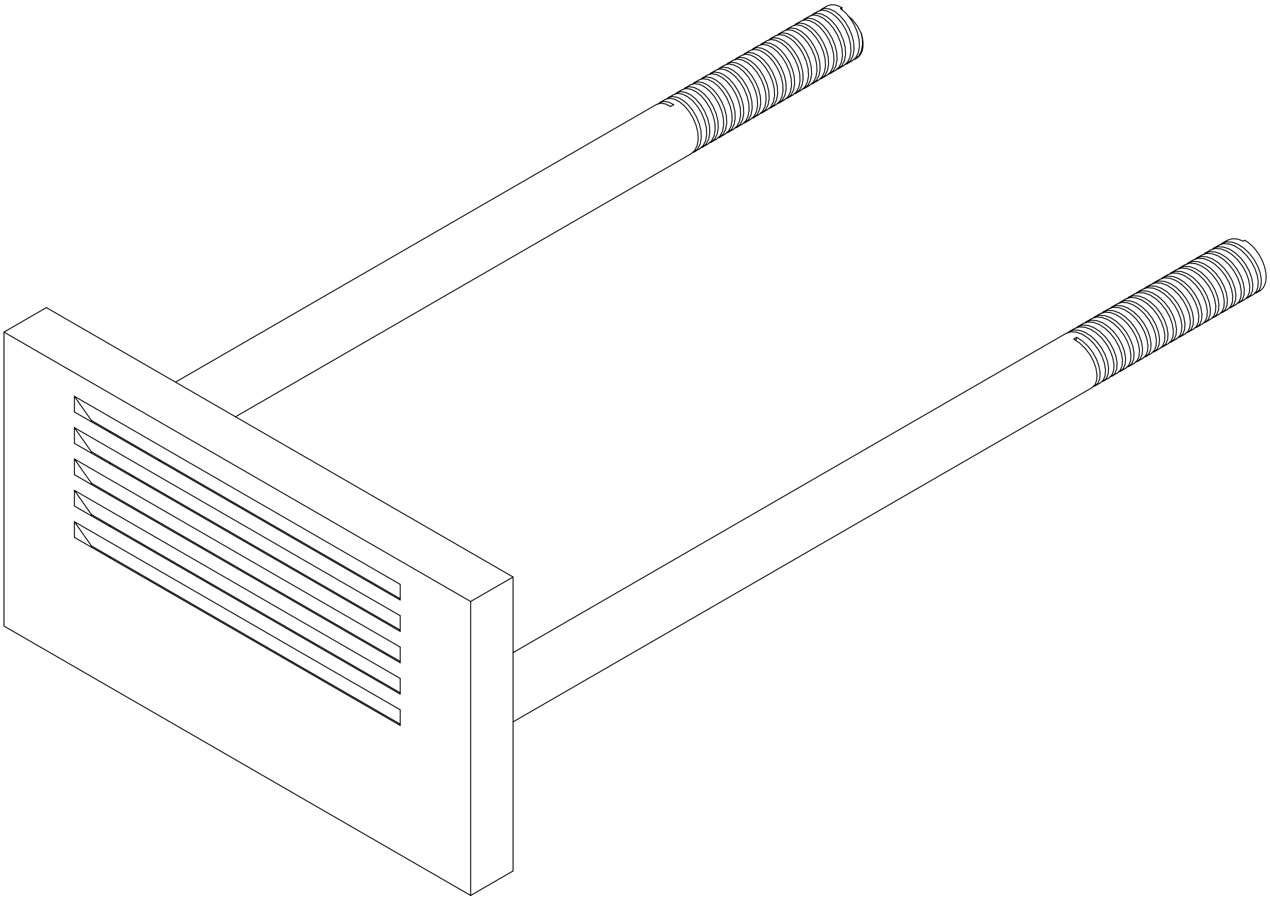

(a) Isometric view

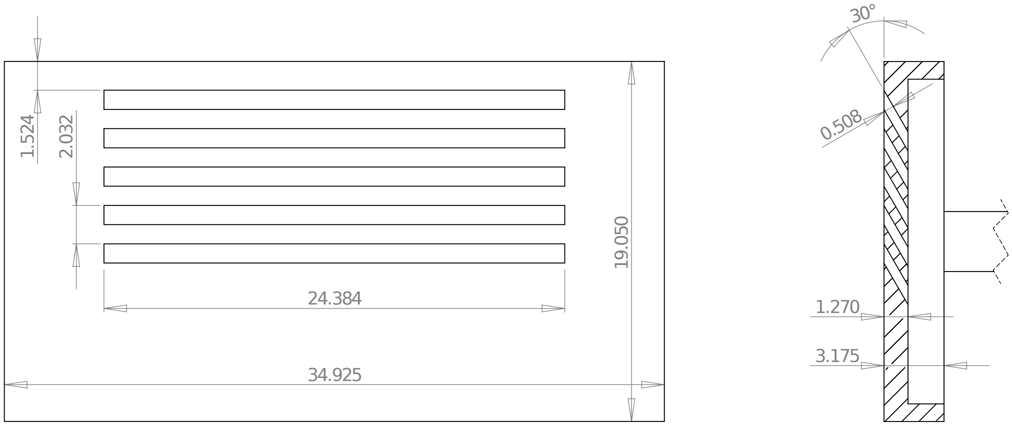

(b) Front view

(c) Cutaway side view

Figure A.19: Drawing of five slot row test coupon; freestream flow from bottom to top; dimensions in mm

A.4.2 Film Cooling Plate Geometries.

The film cooling plenum allowed for arbitrary film cooling schemes to be tested within the bounds of the cooling plate-plenum interface. For the present work, seven film cooling geometries were tested. The first four were single row configurations of co-flow cylindrical holes (Fig. A.13), shaped holes (Fig. A.14), cylindrical holes within a trench (Fig. A.15), and a slot (Fig. A.16). The final three were five row configurations of co-flow cylindrical holes (Fig. A.17), cylindrical holes within trenches (Fig. A.18), and slots (Fig. A.19). Due to manufacturing costs, a five row configuration of shaped holes could not be included in the current work. The relative benefits and drawbacks of each of these configurations are discussed in Section 2.3.3.

A.5 Instrumentation Block

The instrumentation block seen in Fig. A.20 was inserted downstream of the film cooling plenum as shown in Fig. A.11. Its role was to measure the wall temperature (T_w) and conductive heat flux (q''_{cond}) to the wall downstream the film cooling scheme. These measurements were made at four distances downstream of the last row of film cooling holes and at three or five spanwise locations per row. The details of the measurement locations are given in Table A.2 with the distance downstream of the last row of film cooling holes (x) and distance from centerline (z) normalized by the film cooling hole diameter $D = 0.51\,\text{mm}$.

The design of the instrumentation block was intended to measure T_w and q''_{cond} at each streamwise and spanwise location by embedding two OMEGA$^{\circledR}$ K-Type thermocouples at known depths. The nominal depths of the thermocouples are given in Fig. A.20(c) and the depths of each hole was measure independently after manufacturing to ensure accuracy. Then, by assuming the heat flux is 1-D in the wall normal direction, the temperature measurements at known depths could be used to quantify

Table A.2: Instrumentation block gauge locations with x measured from the exit of the final row of holes and z measured from centerline of the cooling row

Row	Col	x/D	z/D
1	1	9	-18
	2		-10
	3		0
	4		8
	5		18
2	2	15	-10
	3	17	0
	4	15	8
3	2	20	-10
	3	23	0
	4	20	8
4	1	28	-18
	2		-10
	3		0
	4		8
	5		18

T_w and q''_{cond}. Since the measurement technique hinges on 1-D heat flux, the following section will validate this assumption. Once one dimensionality is established, Section A.5.2 will present the methodology for calculating T_w and q''_{cond} from the embedded temperature measurements.

A.5.1 1-D Heat Transfer Analysis.

Two methods were used to validate the 1-D heat flux assumption required by the measurement technique. The first modeled the rig using a Finite Element Analysis to evaluate the heat flux components in the region of the instrumentation block. The second used the three dimensionality of the measurements taken during testing to reconstruct the heat flux in the the streamwise, spanwise, and wall-normal directions to determine dominance and one dimensionality.

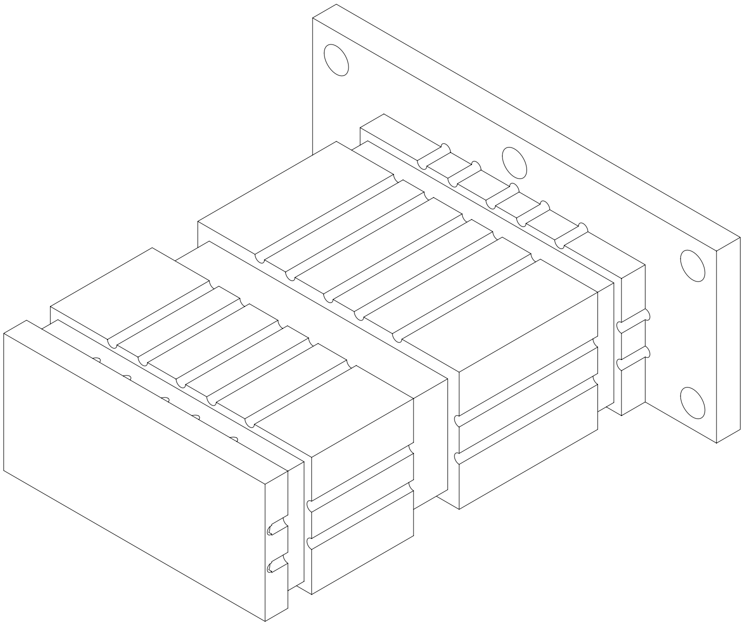

(a) Isometric view

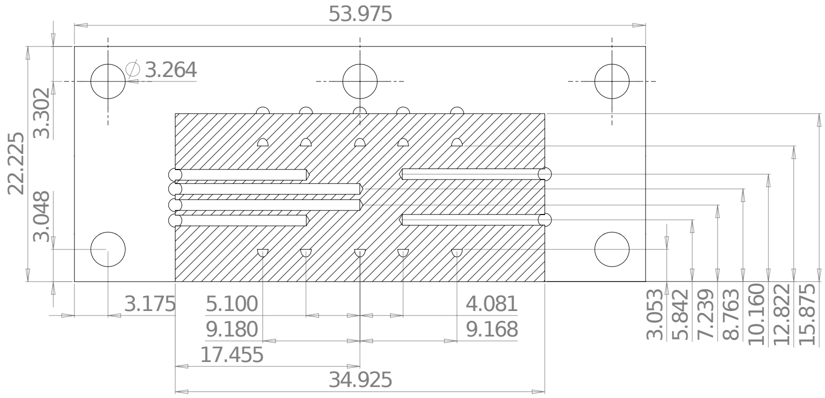

(b) Top view

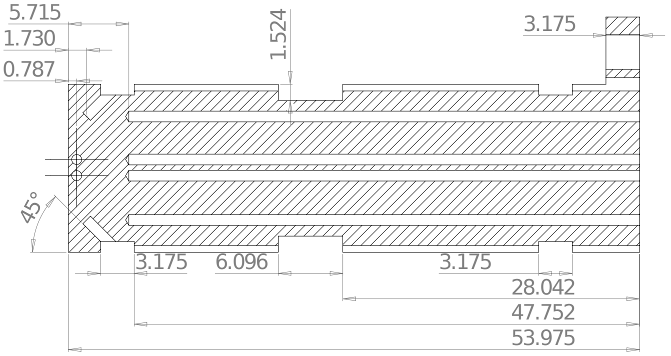

(c) Side view

Figure A.20: Drawing of instrumentation block; freestream flow from bottom to top; dimensions in mm

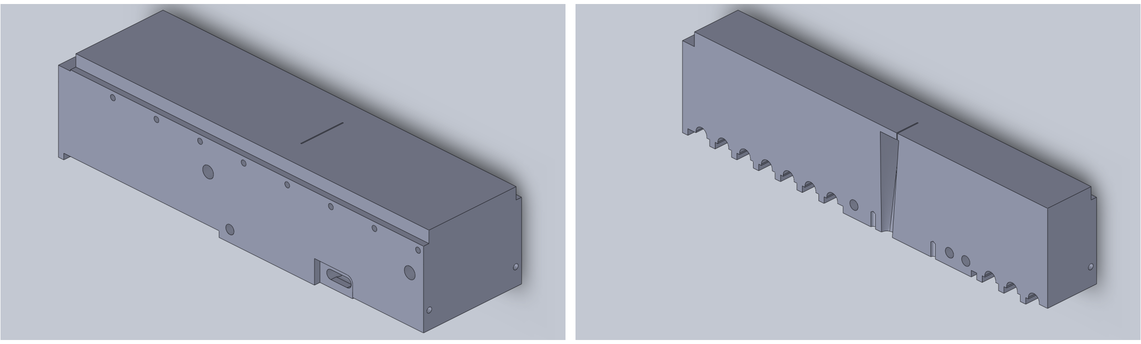

(a) Isometric view (b) Isometric view cut along centerline

Figure A.21: Drawing of test block geometry used in the Finite Element Analysis of 1-D Heat Flux Assumption

A.5.1.1 Finite Element Analysis.

The Finite Element Analysis utilized the the commercially available Abaqus [13] software using the rig geometry generated by Computer Automated Design (CAD) during the design process. First the CAD model was reduced from the full rig assembly seen in Figs. A.9, A.10, and A.11 to only include the main test block seen in Fig. A.21(a). This allowed for easy modeling in Abaqus [13] without having to define complex part interaction boundary conditions.

Since the cooling plenum and instrumentation blocks were removed to create this reduced order model, the volume they occupied was filled with material as seen in Fig. A.11. This was applied to simulate the test block, cooling plenum, and instrumentation block as a single part rather than as an assembly. Then, the plenum geometry was cut out of the solid part and a single normal slot was cut into the surface to simulate a simple film cooling geometry. The resulting plenum and cooling hole geometry are seen in Fig. A.21(b).

Next, the CAD model was imported into Abaqus [13] for a steady state heat transfer simulation. The geometry was meshed using the native Abaqus [13] mesh tool. The tool completed the mesh using quadratic 10 node tetrahedral heat transfer elements (DC3D10) to give a second order spatially accurate solution. To verify grid

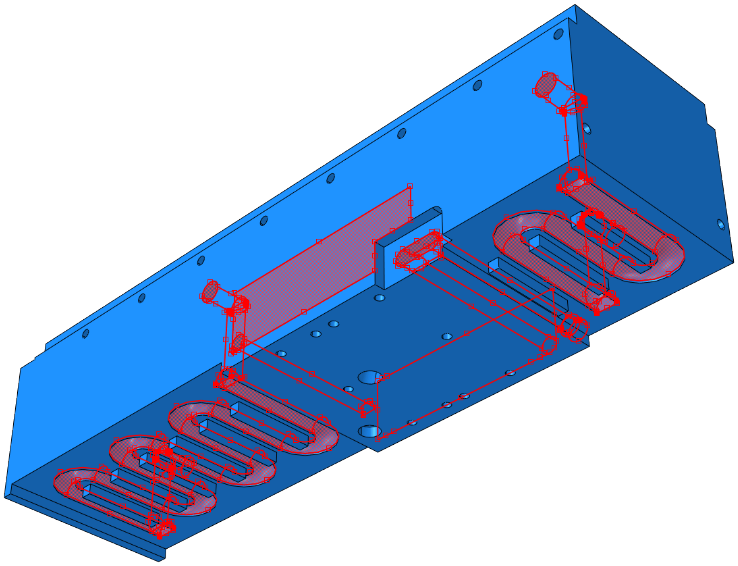

Figure A.22: Areas where block coolant temperature boundary conditions were applied in the Finite Element Analysis of 1-D Heat Flux Assumption

convergence, a course and fine grid with 113,126 and 528,354 elements, respectively, were used for each analysis case.

Since the test block was constructed from Hastelloy X [24], the temperature dependence of the material thermal conductivity with temperature was modeled using linear interpolations of conductivity data tabulated by Haynes International [24]. The boundary conditions consisted of cooling lines at the base and sides of the block seen Fig. A.11, convective heat transfer of the hot gas on the upper surface and convective cooling of the air through the plenum. All other surfaces were modeled as adiabatic.

The cooling lines were modeled by specifying a constant temperature wherever the coolant contacts the block. The areas affected by the coolant boundary condition are highlighted in Fig. A.22. This boundary condition assumes that the temperature profile of the fluid within a cooling line is relatively constant. Further, it assumes that the change in fluid temperature between the entrance and exit of the cooling line is negligible. This assumption was compared to the measurements of coolant temperatures collected during the experiments of the present work to determine its validity.

The experiments used two fluids to cool the test block: water and nitrogen. In the case of using water as a coolant, the temperature of the water was seen to increase less than 4 K within the cooling channels. Thus, the thermal gradients were sufficiently low using water as the coolant to assume an isothermal wall condition. A nominal wall temperature of 300 K was applied wherever water was used as a coolant.

In the case of using nitrogen as a coolant, the coolant was seen to increase from room temperature by up to a maximum value of 700 K within the cooling channels. Thus, unlike the water coolant case, modeling the walls with an isothermal condition would capture the temperature gradients within the cooling channels. However, precise modeling of the gradients would require a level of effort exceeding the demand of the present order-of-magnitude assessment. Therefore, the reduction in modeling fidelity was accepted and the nitrogen coolant cases were modeled as isothermal boundary conditions. To capture the maximum nitrogen coolant temperature within the channels, the isothermal temperature was selected to be 800 K, 100 K higher than the maximum nitrogen temperature.

To reflect the experimental conditions, three cooling cases were examined as outlined in Table A.3. The first case represents minimal wall cooling with a low flow rate of nitrogen to achieve a high wall temperature on the hot side of the block. The second represents maximum cooling with a large flow rate of water to achieve as cold a wall temperature as possible on the hot side of the block.

During experimentation, it was determined that cooling the lower channel with water resulted in large heat extraction from the hot core flow before reaching the measurement location. This effectively drove a freestream temperature which was dependent on the cooling condition in the lower channel. To mitigate this effect, a

Table A.3: Film Coolant Temperatures used in FEA Simulation experimental rig

	Block Coolant Fluid			Film Coolant Temperatures (K)		
Case	Lower	Side	Upper	Plenum Inlet	Slot Inlet	Slot Exit
1	Nitrogen	Nitrogen	Nitrogen	460	830	835
2	Water	Water	Water	450	610	630
3	Nitrogen	Water	Water	450	610	630

constant low flow rate of nitrogen (5 SLPM) was used to cool the lower channel to prevent the material from melting while maintaining a relatively constant freestream temperature within the test channel. The third and final case in Table A.3 was intended to model this experimental condition. The analysis of this case determined the effect of the thermal gradient caused by this uneven cooling and the conclusions are discussed later in this section.

Convective boundary conditions were applied to the film cooling plenum, film cooling jet exit, and the hot core flow interface surfaces. The cooling plenum geometry blends a circular cross-section at the entrance to a rectangular cross-section at the plenum exit. So, to model the convective heat transfer on the plenum geometry, convective coefficients were derived by assuming fully developed laminar flow through the circular entrance geometry and the exit rectangular geometry. The result was averaged to estimate a convective coefficient which approximates over the whole channel. There are several effects such as flow separation and turbulence which were not captured by this technique. However, this technique was deemed sufficient for the present order-of-magnitude analysis.

To take advantage of analytical solutions of laminar internal heat transfer, either an isothermal or constant heat flux boundary condition must be assumed. A large temperature gradient is expected to exist on the plenum walls which invalidates an isothermal assumption. Thus, to simplify the analysis, a constant heat flux was assumed throughout the channel. With this assumption, the Nussult number

Table A.4: Boundary conditions used in FEA simulation of experimental rig for each case listed in Table A.3

			Case		
BC Area	BC Type	Settings	1	2	3
Cooling Plenum	Convective	h (W/m^2 K)	16.3	16.0	16.0
		T_c (K)	645	530	530
Coolant Slot	Convective	h (W/m^2 K)	474	382	382
		T_c (K)	835	630	630
Hot Core Flow	Convective	h (W/m^2 K)	246	264	264
		T_∞ (K)	1410	1410	1410
Lower Cooling Channel	Temperature	T_w (K)	800	300	800
Side Cooling Channel	Temperature	T_w (K)	800	300	300
Upper Cooling Channel	Temperature	T_w (K)	800	300	300

for laminar flow through the circular entrance geometry was $\mathrm{Nu}_D = 4.364$ [29]. The rectangular exit geometry had an aspect ratio of 1.48. Kays et al. [29] derived Nusselt numbers of $\mathrm{Nu}_{D_h} = 3.73$ and $\mathrm{Nu}_{D_h} = 4.12$ for aspect ratios of 1.43 and 2.0, respectively. By linearly interpolating these derived values at an aspect ratio of 1.48, the Nussult number of the rectangular exit was calculated to be $\mathrm{Nu}_{D_h} = 3.76$. The diameter of the entrance geometry and hydraulic diameter of the exit geometry were $D = 6.25\,\mathrm{mm}$ and $D_h = 15.2\,\mathrm{mm}$, respectively.

From the experiments of the present work, the coolant temperature at three locations between the plenum inlet and film cooling jet outlet were nominally measured to be the values found in Table A.3. Using these temperatures as well as the Nusselt numbers and hydraulic diameters discussed above, the convective heat transfer coefficient at the entrance and exit of the plenum were calculated. Then, to simplify the analysis, the convective heat transfer coefficients were averaged to approximate an appropriate value for the plenum walls. The convective heat transfer coefficients resulting from this process are listed in Table A.4 along with the average coolant temperatures.

Also within the plenum was the plenum side of the film cooling plate. Here the plenum air stagnates on the surface before entering the film cooling slot and being ejected into the core flow. Though the convective heat transfer is fundamentally different on this stagnation surface, a more detailed model for this surface would require more assumptions or CFD modeling. Thus, to reduce the modeling effort for the current order-of-magnitude analysis, the stagnation surface was assumed to share the same convective heat transfer coefficient as the neighboring plenum walls found in Table A.4.

To approximate the heat transfer to the coolant in the film cooling holes, the ejection site was modeled as a single normal slot with a height and width equal to the slot used in the present work (see Fig. A.16). With an analysis similar to that of the cooling plenum, the coolant ejection channel was modeled as fully developed laminar flow through an infinite channel with $\mathrm{Nu}_{D_h} = 8.235$ and $D_h = 1.2\,\mathrm{mm}$. Using the coolant temperature found in Table A.3, the heat transfer coefficient was calculated and is listed in Table A.4.

Finally, the hot core flow was modeled as a convection boundary condition on the contacted surface. From experimental measurements, the heat transfer coefficients and freestream temperatures were set as listed in Table A.4. Again, to simplify the modeling fidelity, the convective condition was applied uniformly to the hot side surface without regard to variations along the plate due to boundary layer development.

Each case was solved by direct inversion of the finite element matrix for both the coarse and fine meshes. Then, to show mesh convergence, profiles of hot side surface temperature were plotted as seen in Figs. A.23, A.24, and A.25 for cases listed in Table A.4, respectively. Comparing temperature profiles of the coarse and fine meshes for each case, respectively, reveals a negligible difference. Thus, the mesh was taken to be sufficiently converged. However, since the fine mesh solutions are readily available, they will be used exclusively for the remaining analysis.

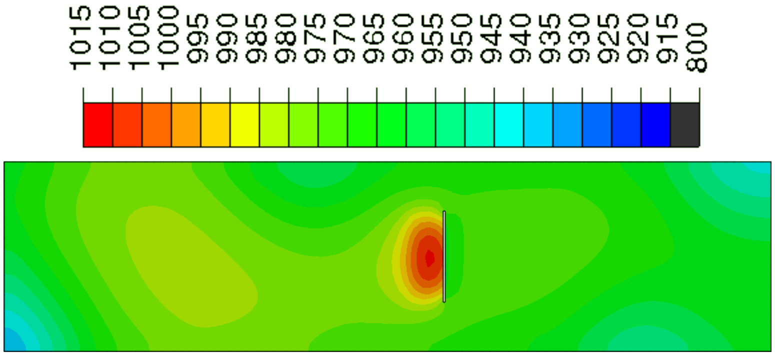

(a) Coarse mesh

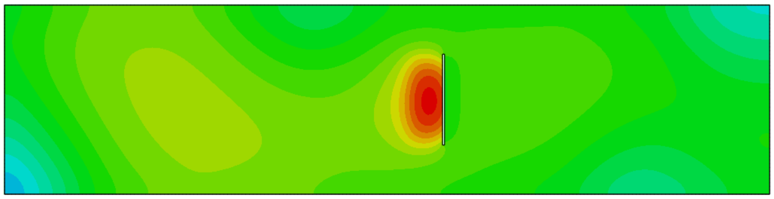

(b) Fine mesh

Figure A.23: Test block hot side surface temperature (K) profiles for Case 1 using a coarse and fine mesh; core flow from left to right

Each of these images have three distinguishing features. First, each has a slot cut out slightly right of the center of the image. This slot represented a single row of slot film cooling configuration to better model the experimental geometry. Second, a hot spot is seen to the left of each of these slots. This hot spot is above the cooling plenum seen in Fig. A.21(b) and occurs due to the decreased ability of the film coolant to cool the surface compared to the backside cooling. A similar hot spot above the cooling plenum was also observed in the infrared images of Shewhart [57]. Finally, a temperature gradient from bottom to top of the images is seen to the right of the slot. This was caused by the 3-D nature of the cooling channels and was also observed in the infrared images of Shewhart [57].

The present work was primarily concerned with measuring surface wall temperature (T_w) and heat flux to the wall from external sources (q''_{cond}). In the present rig, heat flux to the test surface was the sum of the external convective and radiative com-

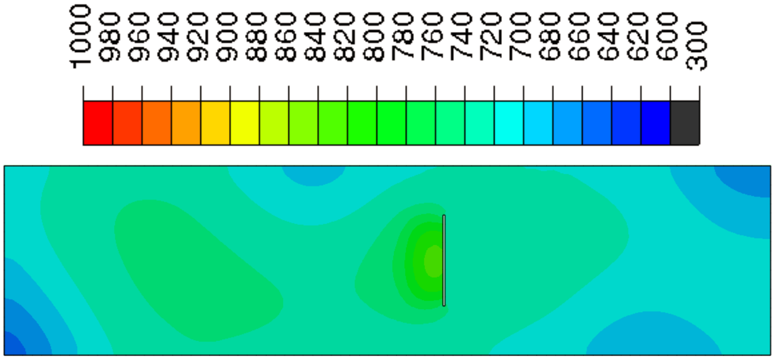

(a) Coarse mesh

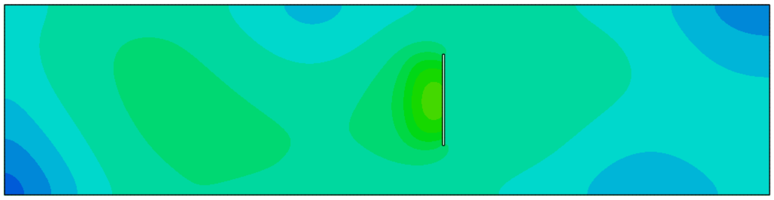

(b) Fine mesh

Figure A.24: Test block hot side surface temperature (K) profiles for Case 2 using a coarse and fine mesh; core flow from left to right

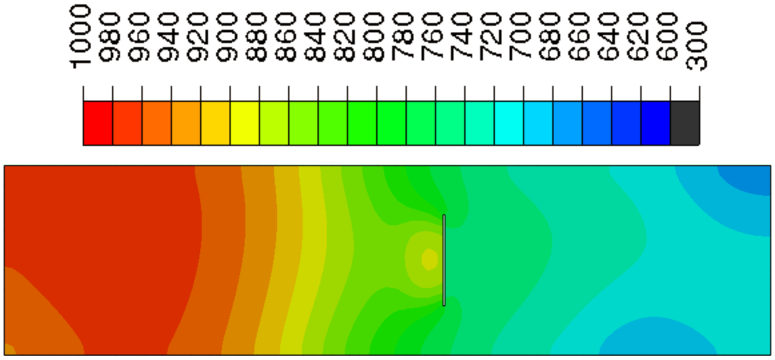

(a) Coarse mesh

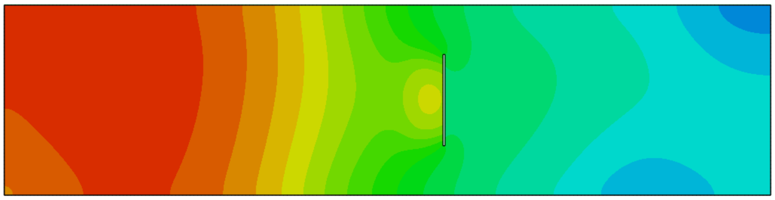

(b) Fine mesh

Figure A.25: Test block hot side surface temperature (K) profiles for Case 3 using a coarse and fine mesh; core flow from left to right

ponents. Thus, by a vector decomposition, it is seen that these heat flux components enter in the wall normal direction at any given x and z such that

$$q''_{\text{cond}}(x,z) = q''_{\text{conv}}(x,z) - q''_{\text{rad}}(x,z) = q''_y(x,y,z) = -k_b \left.\frac{\mathrm{d}T}{\mathrm{d}y}\right|_{(x,0,z)} \tag{A.3}$$

where the streamwise (x) and spanwise (z) distances are measured from an arbitrary origin and, for the present analysis, y is measured from the test block's hot side test surface. For perfectly 1-D heat transfer in the y-direction, q''_y(x,y,z) is constant for all y, $q''_x = q''_z = 0$ and, for constant material conductivity (k_b), Eq. A.3 can be written as

$$q''_{\text{cond}}(x,z) = q''_y(x,y,z) = -k_b \left.\frac{T_2 - T_1}{y_2 - y_1}\right|_{(x,z)} \tag{A.4}$$

where T_1 and T_2 are measured at known depths y_1 and y_2. Additionally, T_w can be extrapolated from the measurements by

$$T_w = -\frac{T_2 - T_1}{y_2 - y_1}(y_1) + T_1 \tag{A.5}$$

Since the material of the instrumentation block was constructed of Hastelloy X, k_b was evaluated by a 3rd order interpolation of the tabular data provided by Haynes International [24] as shown in Fig. A.26.

The geometry and boundary conditions presented in Table A.4 will produce heat transfer which is not perfectly 1-D. Therefore, from the directional heat flux components, the magnitude of the heat flux at a point is calculated by

$$q''(x,y,z) = \sqrt{q''_x(x,y,z)^2 + q''_y(x,y,z)^2 + q''_z(x,y,z)^2} \tag{A.6}$$

As discussed above, the instrumentation block used two thermocouples embedded in the wall at two know depths (y) at the same x and z to measure T_w and q''_{cond}.

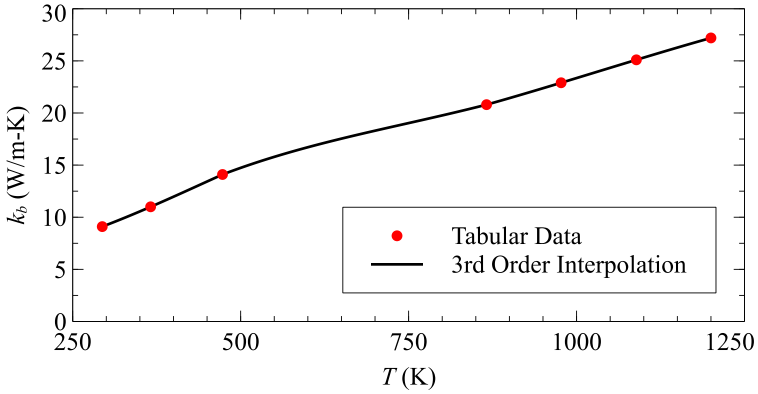

Figure A.26: Interpolation of instrumentation block conductivity data reported by Haynes International [24]

Thus, the methodology to measure T_w and q''_{cond} relies on a 1-D heat flux assumption. To validate the measurement methodology, the degree to which the heat flux can be approximated as 1-D was assessed at select instrumentation locations. Next, the measurement methodology was applied to the FEA temperature profiles at the same select instrumentation locations to assess how accurately T_w and q''_{cond} were measured.

To assess one dimensionality at the instrumentation locations, the heat flux through the block in the y-direction (q''_y) was compared to the total conductive heat flux through the block (q''). Five instrumentation locations were selected for analysis as shown in Fig. A.27. These locations represent the four corners and a point near the center of the measurement area as see in Fig. A.20(b). Since Fig. A.20 shows that the deepest embedded thermocouple is located 5.7 mm below the surface, this examination focused on $0 > y > -6\,\text{mm}$, just slightly deeper than the deepest thermocouple.

The results in Fig. A.27 indicate that, for all cases and thermocouple locations, the magnitude of q''_y was greater than 98.9% of the magnitude of q''. Given this q''_y/q'', Eq. A.6 can be solved to show that the magnitude of the wall parallel component ($\sqrt{q''_x(x,y,z)^2 + q''_z(x,y,z)^2}/q'' = 0.148$). Though 14.8% seems to be a significant portion of q'', the squaring of the directional components of heat flux causes q'' to be nearly equal to q''_y. Thus, the heat flux is verified as being nearly one dimensional in

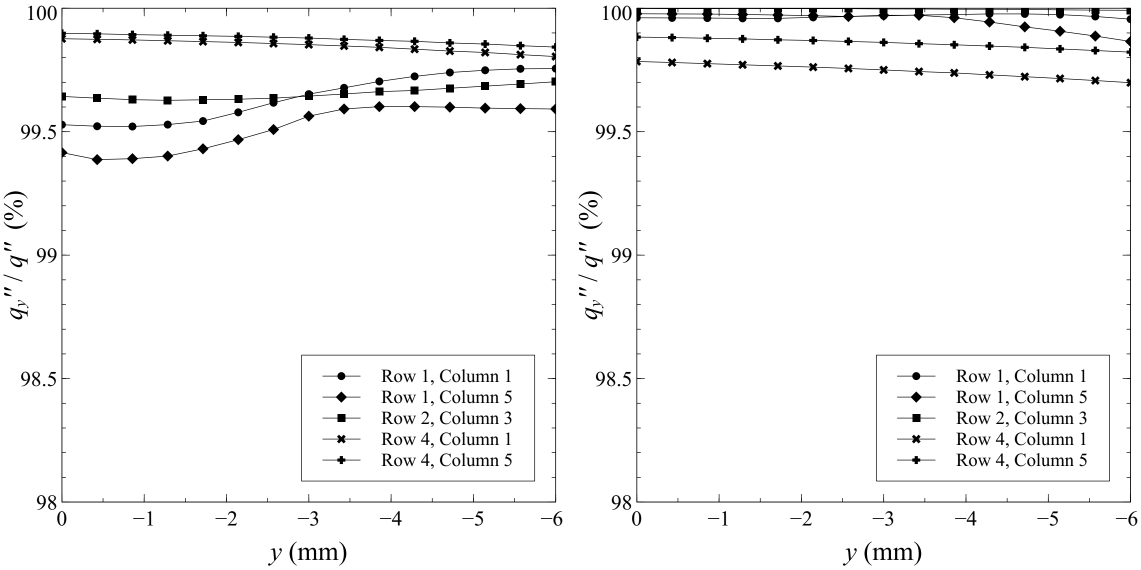

(a) Case 1 (b) Case 2

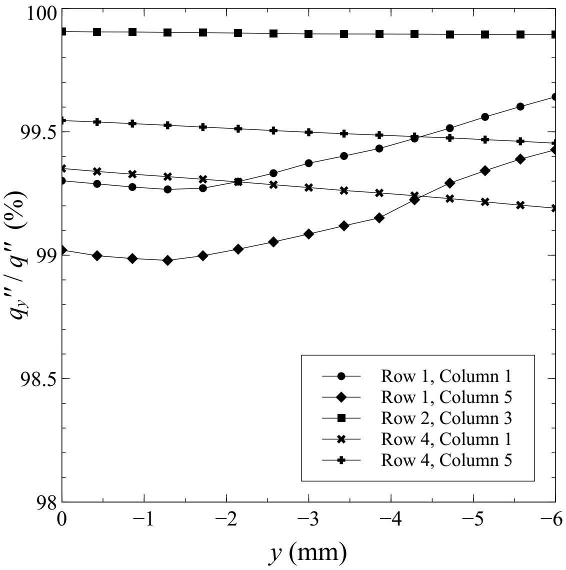

(c) Case 3

Figure A.27: Comparison of the wall normal component of heat flux (q_y'') to the magnitude of total heat flux (q'') at depths below the test surface (y) at select instrumentation locations listed in Table A.2 for each case in Table A.4

Table A.5: Difference (bias) between actual and measured surface heat flux (q''_{cond}) and temperature (T_w) at select instrumentation locations listed in Table A.2 for FEA solutions of each case listed in Table A.3; actual value taken directly from data at surface locations; measured values calculated using Eqs. A.4 and A.5, respectively

			Case		
Row	Column	Bias	1	2	3
1	1	q''_{cond}(%)	-5.1	2.2	1.9
		T_w (K)	0.20	-0.48	-0.45
	5	q''_{cond}(%)	-5.0	2.2	2.0
		T_w (K)	0.18	-0.51	-0.49
2	3	q''_{cond}(%)	-4.9	-0.56	-0.72
		T_w (K)	0.12	-0.04	-0.03
4	1	q''_{cond}(%)	-3.8	-0.38	-1.1
		T_w (K)	0.15	-0.15	-0.05
	5	q''_{cond}(%)	-3.8	-0.26	-1.1
		T_w (K)	0.15	-0.16	-0.05

the y-direction.

Finally, to validate the measurement methodology, Eqs. A.4 and A.5 were applied to the FEA temperature data at the instrumentation locations and cases examined in Fig. A.27 to calculate q''_{cond} and T_w. Though the heat flux is not perfectly 1-D, the near one dimensionality shown above enabled measuring T_1 and T_2 at known y_1 and y_2, respectively, to provide a good approximation of q''_{cond} and T_w at a given x and z. Also built into Eq. A.4 is the assumption of constant k_b. Section A.5.2 will validate this assumption and the remaining analysis will assume constant k_b evaluated at the average of T_1 and T_2 without proof.

First, T_1 and T_2 were extracted from the FEA solutions at instrumentation locations listed in Fig. A.27 at thermocouple depths seen in Fig. A.20. Using T_1 and T_2, q''_{cond} and T_w were then approximated by Eqs. A.4 and A.5, respectively. Finally, Table A.5 quantified the bias of the approximated q''_{cond} and T_w from the actual q''_{cond} and T_w extracted directly from the surface.

The results in Table A.5 indicate that the first row of instrumentation is expected to see the biases in heat flux. This is attributable to the proximity of the first row to the cooling plenum. Comparing the nitrogen cooled Case 1 to the water cooled Cases 2 and 3 shows that a larger bias is realized in the nitrogen cooled case. Since the nitrogen case has a higher T_w, less heat flux is drawn from the hot core flow. This increases the relative effect of the cooling plenum and introduces increased three dimensionality to the heat transfer.

Overall, the measurement uncertainty which will be derived in Section A.6 reveals that the biases in Table A.5 are on the order of the measurement uncertainty. Thus, the FEA results indicate that the measurement methodology can be employed to give sufficiently accurate estimations of q''_{cond} and T_w. The following section will examine experimental data to substantiate the conclusion of one dimensionality drawn from the above FEA results.

A.5.1.2 Analysis of Measurements.

As discussed in the previous section, the instrumentation block quantified the surface heat flux (q''_{cond}) by using two thermocouples embedded near the surface at known depths and with a known material conductivity (k_b) via Eq. A.4. The thermocouples were embedded in the instrumentation block at 16 streamwise and spanwise location as shown in Fig. A.20. Thus, for each embedded thermocouple, there was a second thermocouple located at a known distance in each of the streamwise (x), wall normal (y), and spanwise (z) directions. This section takes advantage of the inherent three dimensionality of the instrumentation block measurements to substantiate the 1-D heat flux assumption.

For each experiment in the present work, the heat flux components (q''_x, q''_y, q''_z) were approximated at the upper thermocouple location for each measurement location in Fig. A.20. The components were calculated using a more general form of Eq. A.4

given by

$$q_i''(x, y, z) = -k_b \frac{T_2 - T_1}{\Delta x_i} \tag{A.7}$$

In this form, q_i'' is the heat flux in direction i and Δx_i is the distance between thermocouple measurements in direction i.

Last, q_y''/q'' was quantified at each upper thermocouple location for each measurement taken in the present work. This revealed that the minimum q_y''/q'' over the entire test campaign was 98% while the majority of the individual days of testing achieved a q_y''/q'' over 99.5%. This result coupled with the FEA findings in Section A.5.1.1 give strong evidence that the heat flux is sufficiently 1-D to validly employ the embedded thermocouple measurement technique. With this established, the next section will describe the measurement methodology in more detail.

A.5.2 Measurement Methodology.

The measurements of T_w and q''_{cond} were attained by embedding two K-Type thermocouples at known depths in a material of known thermal conductivity (k_b). The nominal depths of the thermocouples are given in Fig. A.20(c). After manufacturing the instrumentation block, the depths of each hole was measured independently to ensure accuracy. The measured depths compared to the nominal depths were then used as an input to the calculation of measurement uncertainty that will be presented in Section A.6.4.

To calculate the surface temperature and heat flux from the embedded temperature measurements, the temperature as a function of depth must be derived from the governing conductive heat transfer equation. Using the 1-D heat transfer assumption which was validated in Section A.5.1, the governing equation simplifies to [44]

$$\frac{\mathrm{d}}{\mathrm{d}y}\left[k_b(T)\frac{\mathrm{d}T}{\mathrm{d}y}\right] = 0 \tag{A.8}$$

subject to the measured temperature boundary conditions

$$\begin{aligned} T(y_1) &= T_1 \\ T(y_2) &= T_2 \end{aligned} \tag{A.9}$$

at embedded depths y_1 and y_2.

The temperature dependent thermal conductivity ($k_b(T)$) in Eq. A.8 was modeled by a 3rd order interpolation of the tabular data provided by Haynes International [24] as seen in Fig. A.26. The temperature dependence of k_b introduces a non-linearity in Eq. A.9. The differential equation can be linearized and solved by first introducing Kirchhoff's transformation given by

$$\hat{T} = \frac{1}{k_{b,\mathrm{ref}}} \int_{T_{\mathrm{ref}}}^{T} k_b(T) dT \tag{A.10}$$

where T_{ref} is an arbitrary temperature such that $k_{\mathrm{b,ref}} = k_b(T_{\mathrm{ref}})$. Then, by the chain rule,

$$\frac{\mathrm{d}T}{\mathrm{d}y} = \frac{\mathrm{d}T}{\mathrm{d}\hat{T}} \frac{\mathrm{d}\hat{T}}{\mathrm{d}y} = \frac{k_{b,\mathrm{ref}}}{k_b(T)} \frac{\mathrm{d}\hat{T}}{\mathrm{d}y} \tag{A.11}$$

Combining Eqs. A.8 and A.8 transforms the non-linear governing equation to a linear differential equation

$$\frac{\mathrm{d}^2\hat{T}}{\mathrm{d}y^2} = 0 \tag{A.12}$$

subject to the $\hat{T}$ boundary conditions that result from combining Eqs. A.9 and A.10. With $\hat{T}(y)$ known from solving of Eq. A.12, $T(y)$ can then be determined by solving Eq. A.10. Finally, with $T(y)$ known, T_w and q''_{cond} can be calculated by $T_w = T(0)$ and Eq. A.3, respectively.

The above calculation procedure, while mathematically ideal, is computationally expensive. Fortunately, because the change in temperature is relatively small between the surface and deepest thermocouple, k_b can be assumed to be constant in Eq. A.8.

Under this method, k_b is evaluated at the average of the T_1 and T_2 measurements to minimize the error in k_b between the two temperatures. Thus, Eq. A.8 simplifies to

$$\frac{\mathrm{d}^2 T}{\mathrm{d}y^2} = 0 \tag{A.13}$$

Then, by applying the boundary conditions of Eq. A.9 to Eq. A.13, q''_{cond} and T_w can be calculated by Eqs. A.4 and A.5, respectively.

During the testing campaign, all measured temperature drops between T_1 and T_2 were less than 80 K. Therefore, 80 K can be examined as the extreme case where the variation of k_b between T_1 and T_2 is maximized. Next, the variable and constant conductivity methods were compared by assuming a T_1, setting $T_2 = T_1 - 80\,\mathrm{K}$, and calculating q''_{cond} and T_w via the respective methods. To ensure relevant values for T_1 were selected for the analysis, the comparison was performed at several T_1 between 600 K and 1100 K. This range completely covers the range of T_w measured during the experimental campaign with at least 50 K extra range on both extremes.

The results of the above comparison revealed that, for all T_1, the variable and constant conductivity methods agreed on q''_{cond} and T_w to within 0.05%. Here, the T_w agreement was calculated by the difference in the calculated values compared to $T_\infty - T_w$ with a nominal test condition of $T_\infty = 1400\,\mathrm{K}$. Thus, the nearly identical q''_{cond} and T_w results indicated that the less computationally expensive constant conductivity would be sufficient for the present work.

A.6 Uncertainty Analysis

This section will derive the uncertainty of the experimental measurements presented in the present work. The uncertainty will be calculated by the method of Moffat [43]. The section will begin with the most fundamental measurement uncertainties such that the more complicated, multi-faceted uncertainties can be calculated later in the section.

A.6.1 Non-combustion Temperatures.

The experimental facility used OMEGA® K-Type thermocouples for all temperature measurements except the hot core flow. The OMEGA® K-Type thermocouples are quoted to have an uncertainty of $\delta T = \pm 0.75\% T$ of the temperature measurement in °C.

A.6.2 Core Flow Temperature.

All hot core flow temperatures (including T_∞) were measured by OMEGA® B-Type thermocouples which are quoted to have an uncertainty of $\delta T_\infty = \pm 0.5\% T_\infty$ of the temperature measurement in °C.

A.6.3 Thermocouple Depths.

The instrumentation block embedded two K-Type thermocouples at known depths to measure the conductive heat flux (q''_{cond}) and surface temperature (T_w). The nominal thermocouple depths are given in Fig. A.20(c). After manufacturing, the thermocouple depths were measured for accuracy. The mean and standard deviation of the measured thermocouple depths were then calculated. Next, the uncertainty in the thermocouple depth was calculated by a 95% confidence interval to be $\delta y = \pm 0.32\,\text{mm}$. The uncertainty in $\Delta y = (y_2 - y_1)$ is given by [43]

$$\delta(\Delta y) = \left[\left(\frac{\partial(\Delta y)}{\partial y_1} \delta y \right)^2 + \left(\frac{\partial(\Delta y)}{\partial y_2} \delta y \right)^2 \right]^{1/2} = \sqrt{2}\delta y \qquad \text{(A.14)}$$

Finally, inserting the value of δy calculated above gives $\delta(\Delta y) = \pm 0.45\,\text{mm}$

A.6.4 Conductive Heat Transfer: Uncorrected.

Sections A.5.1 and A.5.2 showed that, at the instrumentation locations, the heat flux could be treated as 1-D and that the temperature dependent material thermal conductivity (k_b) could be sufficiently approximated by a constant k_b assumption. As a result, Eq. A.4 could be used to approximate q''_{cond}.

To apply the method of Moffat [43] and quantify the uncertainty in Eq. A.4, k_b as a function of temperature is required. To simplify the form of k_b, the function used a linear interpolation rather than the third order polynomial that was used in the data reduction such that

$$k_b(T) = a\left(\frac{T1 + T_2}{2}\right) + b \tag{A.15}$$

where a and b are the fit coefficients for appropriate temperature range.

Now, applying the method of Moffat [43] to Eq. A.4 gives the uncertainty as

$$\delta q''_{\text{cond}} = \left[\left(\frac{\partial q''_{\text{cond}}}{\partial T_1}\delta T\right)^2 + \left(\frac{\partial q''_{\text{cond}}}{\partial T_2}\delta T\right)^2 + \left(\frac{\partial q''_{\text{cond}}}{\partial(\Delta y)}\delta(\Delta y)\right)^2\right]^{1/2} \tag{A.16}$$

where

$$\frac{\partial q''_{\text{cond}}}{\partial T_1} = -\frac{aT_1 + b}{\Delta y} \tag{A.17}$$

$$\frac{\partial q''_{\text{cond}}}{\partial T_2} = \frac{aT_2 + b}{\Delta y} \tag{A.18}$$

$$\frac{\partial q''_{\text{cond}}}{\partial(\Delta y)} = -\frac{(T_2 - T_1)(0.5a(T_1 + T_2) + b)}{\Delta y^2} \tag{A.19}$$

Next, these equations were applied to highest and lowest T_w measurements from the shaped hole film cooling geometry with no film cooling flow ($M = 0$) to bound the uncertainty. Since the above equations show uncertainty is inversely proportional to Δy, this analysis was performed on the Row 4, Column 3 instrumentation location which had the minimum Δy of 4.8 mm.

The low T_w, high q''_{cond} case had $T_1 = 725\,\text{K}$ and $T_2 = 682\,\text{K}$ with $a = 0.0170\text{W/m}\,\text{K}^2$, $b = 6.04\text{W/m}\,\text{K}$, and a measured $q''_{\text{cond}} = \pm 1.62 \times 10^5\,\text{W/m}^2$. Inserting these values into Eq. A.16 gave $\delta q''_{\text{cond}} = \pm 0.229 \times 10^5\,\text{W/m}^2$ or 14.2% of the q''_{cond} measurement. For this uncertainty, the root sum squared of the temperature uncertainty components contributed a 10.8% uncertainty. Similarly, the uncertainty in Δy contributed 9.39%. Thus, for the low temperature case, the uncertainty was attributed near equally to δT and $\delta(\Delta y)$, respectively.

The high T_w, low q''_{cond} case had $T_1 = 926\,\text{K}$ and $T_2 = 901\,\text{K}$ with $a = 0.0189\text{W/m}\,\text{K}^2$, $b = 4.42\text{W/m}\,\text{K}$, and a measured $q''_{\text{cond}} = \pm 1.41 \times 10^5\,\text{W/m}^2$. Inserting these values into Eq. A.16 gave $\delta q''_{\text{cond}} = \pm 0.325 \times 10^5\,\text{W/m}^2$ or 29.2% of the q''_{cond} measurement. For this uncertainty, the root sum squared of the temperature uncertainty components contributed a 27.6% uncertainty. Similarly, the uncertainty in Δy contributed 9.59%. Thus, for the high temperature case, the uncertainty attribution was heavily weighted to δT with a much smaller relative contribution from $\delta(\Delta y)$. This uncertainty is exceedingly high, so the next section will present a correction procedure to reduce the uncertainty.

A.6.5 Conductive Heat Transfer: Corrected.

The instrumentation block design came with two drawbacks. First, the uncertainty derived in the previous section was exceedingly large for the high temperature case. Both the uncertainty in the temperature measurements and the thermocouple depths were found to contribute significantly to the overall uncertainty in the low temperature case while the temperature uncertainty dominated in the high temperature case. Second, the thermocouples were not securely fastened in place. Thus, during operations such as changing test configurations, the thermocouple could change to an unknown depth if the thermocouple leads were inadvertently perturbed.

To help alleviate these two sources of measurement uncertainty, a correction procedure was implemented. The procedure examines the repeatability measurement which was taken at the beginning of each test day. Then, from the embedded temperature measurements, T_w and q''_{cond} were calculated via Eqs. A.4 and A.5, respectively, using the y_1 and y_2 measured after manufacturing the instrumentation block.

Next, the Central Limit Theorem [4] was applied to reduce the measurement uncertainty. This was accomplished by assuming the T_w and q''_{cond} profiles were constant at all locations on the instrumentation block surface. These assumptions were validated by two concepts. First, the surface temperature profiles calculated using FEA (Figs. A.23 and A.25) show a nearly isothermal surface in the area immediately downstream of the cooling hole within $\pm 10\,\mathrm{K}$. Second, Eq. A.3 asserts that the uniformity of q''_{cond} would be contingent on uniform q''_{conv} and q''_{rad}. Given a nearly isothermal surface, the radiation leaving the surface would also be nearly uniform. Further, the relatively small size of the instrumentation surface directs that the radiation incident on the wall should also be constant such that q''_{rad} should be nearly uniform. Examining Eq. 2.2 reveals that q''_{conv} will also be constant if T_∞ and h are constant over the instrumentation surface. The small streamwise length of the instrumentation surface suggests that T_∞ will be nearly invariant. Similarly, the proportionality of h to $x^{-0.2}$ [29] for a turbulent flat plate indicates that h will vary less than 2.5% over the instrumentation surface. Thus, q''_{cond} was accepted to be uniform on the test surface.

With uniform T_w and q''_{cond} established for the cases without film cooling, the T_w and q''_{cond} calculated using the y_1 and y_2 measured after manufacturing the instrumentation block could be averaged to approximate the true T_w and q''_{cond} on the surface. Since it was possible for a thermocouple to drift significantly from its measured depth, the Central Limit Theorem [4] was used to identify measurement locations with q''_{cond} greater than $2\sigma/\sqrt{n}$ from the average q''_{cond} as outliers. In this test criteria, σ was the standard deviation and n is the number of measurement locations.

With the outliers identified, the T_w and q''_{cond} calculated at locations which were not outliers using the y_1 and y_2 measured after manufacturing the instrumentation block were averaged to approximate the true values of $\overline{T_w}$ and $\overline{q''_{\text{cond}}}$ on the instrumentation surface. Next, the averaged q''_{cond} and the embedded thermocouple measurements at each location were used to solve Eq. A.4 for $\Delta y_{\text{corr}} = y_{2,\text{corr}} - y_{1,\text{corr}}$ such that

$$\Delta y_{\text{corr}} = -k_b \frac{T_2 - T_1}{\overline{q''_{\text{cond}}}} \tag{A.20}$$

Similarly, Eq. A.5 was used to solve for $y_{1,\text{corr}}$ such that

$$y_{1,\text{corr}} = \Delta y_{\text{corr}} \frac{\overline{T_w} - T_1}{T_2 - T_1} \tag{A.21}$$

Since Eq. A.21 could produce a non-physical result of $y_{1,\text{corr}} < 0$, cases where this occurred were forced to be $y_{1,\text{corr}} = 0$ instead.

The above correction procedure focused on removing measurement bias, a systematic, non-random deviation of samples from the true average. Unlike random error, a bias cannot be reduced by increasing the number of samples. Specifically, the correction procedure addressed two biases. First, it reduced the bias in thermocouple depths resulting from thermocouples moving slightly from their intended depth. Second, assuming the bias of the K-Type thermocouple population follows a normal distribution, it reduced the bias in the individual thermocouple temperature measurements. Though the correction procedure did not directly correct the T_1 and T_2 measurements, it inserted a temperature bias correction into the Δy_{corr} and $y_{1,\text{corr}}$ calculations. Thus, the only remaining uncertainty was assumed to be the random error of the thermocouple depths and temperature measurements.

Since each experimental measurement was taken after the temperatures had reached steady state to within a 0.6 K tolerance, the correction procedure reduced the temperature uncertainty to $\delta T_{\text{corr}} = 0.6\,\text{K}$. Next, the uncertainty in Δy_{corr} and $y_{1,\text{corr}}$ were quantified. The uncertainty for Δy_{corr} is given as [43]

$$\delta(\Delta y_{\text{corr}}) = \left[\left(\frac{\partial(\Delta y_{\text{corr}})}{\partial T_1}\delta T\right)^2 + \left(\frac{\partial(\Delta y_{\text{corr}})}{\partial T_2}\delta T_{\text{corr}}\right)^2 + \left(\frac{\partial(\Delta y_{\text{corr}})}{\partial \overline{q''_{\text{cond}}}}\delta\overline{q''_{\text{cond}}}\right)^2\right]^{1/2} \tag{A.22}$$

where

$$\frac{\partial(\Delta y_{\text{corr}})}{\partial T_1} = -\frac{aT_1 + b}{\overline{q''_{\text{cond}}}} \tag{A.23}$$

$$\frac{\partial(\Delta y_{\text{corr}})}{\partial T_2} = \frac{aT_2 + b}{\overline{q''_{\text{cond}}}} \tag{A.24}$$

$$\frac{\partial(\Delta y_{\text{corr}})}{\partial \overline{q''_{\text{cond}}}} = -\frac{(T_2 - T_1)(0.5a(T_1 + T_2) + b)}{\overline{q''_{\text{cond}}}} \tag{A.25}$$

As in the previous section, the low T_w, high q''_{cond} case had $T_1 = 725\,\text{K}$ and $T_2 = 682\,\text{K}$ with $a = 0.0170\text{W/m}\,\text{K}^2$ and $b = 6.04\text{W/m}\,\text{K}$. By implementing the correction procedure discussed above, the average heat flux was $\overline{q''_{\text{cond}}} = 2.08 \times 10^5\,\text{W/m}^2$ with $\delta\overline{q''_{\text{cond}}} = \pm 0.271 \times 10^5\,\text{W/m}^2$. Inserting these values into Eq. A.22 gives an uncertainty of $\delta(\Delta y_{\text{corr}}) = \pm 0.49\,\text{mm}$ or 13% of Δy_{corr}.

Similarly, the high T_w, low q''_{cond} case had $T_1 = 926\,\text{K}$ and $T_2 = 901\,\text{K}$ with $a = 0.0189\,\text{W/m}\,\text{K}^2$ and $b = 4.42\,\text{W/m}\,\text{K}$. By implementing the correction procedure discussed above, the average heat flux used in was $\overline{q''_{\text{cond}}} = 1.41 \times 10^5\,\text{W/m}^2$ with $\delta\overline{q''_{\text{cond}}} = \pm 0.159 \times 10^5\,\text{W/m}^2$. Inserting these values into Eq. A.22 gives an uncertainty of $\delta(\Delta y_{\text{corr}}) = \pm 0.45\,\text{mm}$ or 12% of Δy_{corr}.

The correction procedure outlined, though effective in grounding the q''_{cond} measurements to a common calibration, did nothing to reduce uncertainty in Δy_{corr} due to the large uncertainties in q''_{cond}. Therefore, to reduce the uncertainty in Δy_{corr}, a multiple measurement correction was used. During the course of any experiment,

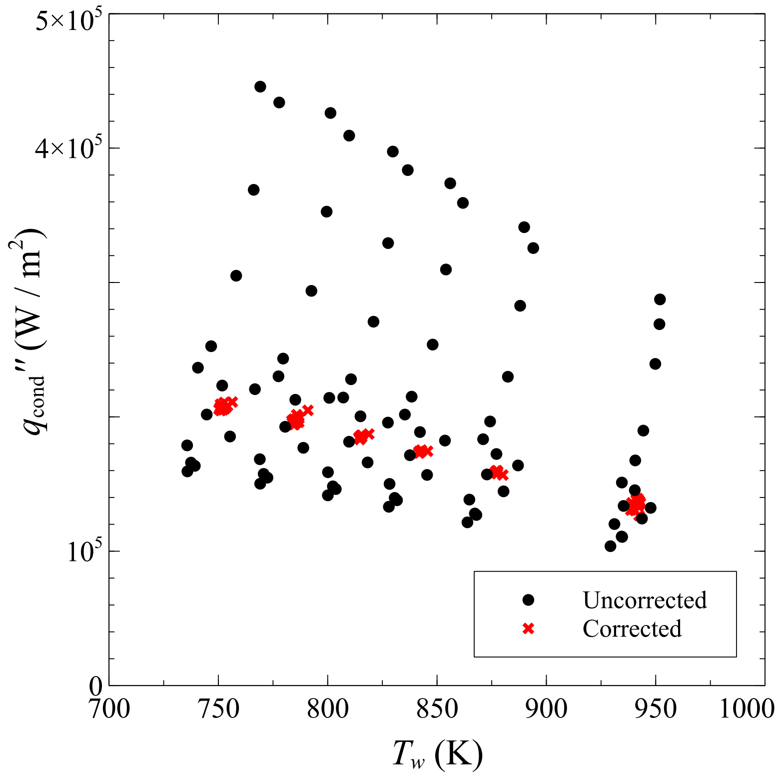

Figure A.28: Comparison of q''_{cond} measurements at many T_w before and after thermocouple depth correction

measurements with no film cooling mass flow were taken at many wall temperatures. Thus, at each of these measurement conditions (k), the assumption of constant T_w and q''_{cond} could be used to calculate a $y_{1,\text{corr},k}$ and $\Delta y_{\text{corr},k}$. Then, the average of the $y_{1,\text{corr},k}$ and $\Delta y_{\text{corr},k}$ were used in Eqs. A.4 and A.5 to calculate q''_{cond} and T_w, respectively.

This process was applied to the all the measurements from the shaped hole film cooling geometry with no film cooling flow ($M = 0$) to determine the uncertainty. This was accomplished by examining the distribution of the $y_{1,\text{corr},k}$ and $\Delta y_{\text{corr},k}$ at the Row 4, Column 3 instrumentation location. Then, $\delta y_{1,\text{corr}}$ and $\delta(\Delta y_{\text{corr}})$ were quantified via the Central Limit Theorem [4] to be ±0.079 mm and ±0.062 mm, respectively.

With these values, the uncertainty of $\delta q''_{\text{cond}}$ reduced to $\pm 0.0508 \times 10^5$ W/m^2 (2.48% of q''_{cond}) and $\pm 0.0514 \times 10^5$ W/m^2 (3.70% of q''_{cond}) for the low and high T_w cases discussed above, respectively. Comparing these uncertainties to the uncorrected uncertainties reveals that the correction procedure drastically reduced the uncertainty. Figure A.28 shows the clear benefit of correcting the measurements to remove biases by comparing the uncorrected to the corrected T_w versus q''_{cond} data.

A.6.6 Surface Temperature.

The corrected thermocouple depths found using the process in the previous section were also used to approximate T_w by Eq. A.5. The uncertainty of this approximation is expressed as [43]

$$\delta T_w = \left[\left(\frac{\partial T_w}{\partial T_1} \delta T \right)^2 + \left(\frac{\partial T_w}{\partial T_2} \delta T \right)^2 + \left(\frac{\partial T_w}{\partial (\Delta y_{\mathrm{corr}})} \delta (\Delta y_{\mathrm{corr}}) \right)^2 + \left(\frac{\partial T_w}{\partial y_{1,\mathrm{corr}}} \delta y_{1,\mathrm{corr}} \right)^2 \right]^{1/2} \tag{A.26}$$

where

$$\frac{\partial T_w}{\partial T_1} = 1 + \frac{y_{1,\mathrm{corr}}}{\Delta y_{\mathrm{corr}}} \tag{A.27}$$

$$\frac{\partial T_w}{\partial T_2} = - \frac{y_{1,\mathrm{corr}}}{\Delta y_{\mathrm{corr}}} \tag{A.28}$$

$$\frac{\partial T_w}{\partial (\Delta y_{\mathrm{corr}})} = (T_2 - T_1) \frac{y_{1,\mathrm{corr}}}{(\Delta y_{\mathrm{corr}})^2} \tag{A.29}$$

$$\frac{\partial T_w}{\partial y_{1,\mathrm{corr}}} = \frac{(T_2 - T_1)}{(\Delta y_{\mathrm{corr}})} \tag{A.30}$$

For the the low T_w, high q''_{cond} case discussed above ($T_1 = 725\,\mathrm{K}$, $T_2 = 682\,\mathrm{K}$, $\Delta y_{\mathrm{corr}} = 3.8\,\mathrm{mm}$, and $y_{1,\mathrm{corr}} = 2.4\,\mathrm{mm}$), δT_w was calculated to be 1.4 K. For the the high T_w, low q''_{cond} case discussed above ($T_1 = 926\,\mathrm{K}$, $T_2 = 901\,\mathrm{K}$, $\Delta y_{\mathrm{corr}} = 3.8\,\mathrm{mm}$, and $y_{1,\mathrm{corr}} = 2.4\,\mathrm{mm}$), δT_w was calculated to be $\pm 0.6\,\mathrm{K}$.

A.6.7 Convective and Radiative Heat Transfer.

The conductive heat flux at the test surface was the sum of the convective and radiative components as modeled by Eq. 5.10. A linear regression of this equation was applied to the corrected q''_{cond} measurements at many corrected T_w to calculate the slope (h_{CP}) and intercept $q''_{\mathrm{rad},i}$. Though Eq. 5.10 is clearly non-linear, it can be linearized with respect to h_{CP} and $q''_{\mathrm{rad},i}$ by assuming

$$X = -\frac{1}{\epsilon_w}\left(\frac{T_w}{T_\infty}\right)^n (T_\infty - T_w) \tag{A.31}$$

$$Y = -\left(\frac{q''_{\mathrm{cond}}}{\epsilon_w} + \sigma_0 T_w^4\right) \tag{A.32}$$

such that

$$Y = h_{\mathrm{CP}} \cdot X + q''_{\mathrm{rad},i} \tag{A.33}$$

According to Bain and Engelhardt [4], the uncertainty of h_{CP} and $q''_{\mathrm{rad},i}$ can be calculated by a Maximum Likelihood Estimate such that

$$\delta h_{\mathrm{CP}} = 2\left[\frac{(\delta q''_{\mathrm{cond}}/2)^2}{\sum (x_k - \overline{x})^2}\right]^{1/2} \tag{A.34}$$

$$\delta q''_{\mathrm{rad},i} = 2\left[\frac{(\delta q''_{\mathrm{cond}}/2)^2 \sum x_k^2}{N \sum (x_k - \overline{x})^2}\right]^{1/2} \tag{A.35}$$

where x_k is the kth measurement of x as defined by Eq. A.31, $\overline{x}$ is the average of x_k, and N is the number of x_k measurements. Equations A.34 and A.35 required that $\delta q''_{\mathrm{cond}}$ be constant. So the average of the low and high temperature cases above was used such that $\delta q''_{\mathrm{cond}} = 0.0511 \times 10^5\,\mathrm{W/m^2}$. Applying Eqs. A.34 and A.35 to the shaped hole, $M = 0$ data discussed earlier reveals $\delta h_{\mathrm{CP}} = \pm 22.4\,\mathrm{W/m^2\,K}$ (10.5% of h_{CP}) and $\delta q''_{\mathrm{rad},i} = \pm 663\,\mathrm{W/m^2}$ (1.37% of $q''_{\mathrm{rad},i}$).

From the above analysis, the uncertainty in the total radiative heat flux is given by [43]

$$\delta q''_{\text{rad}} = \left[\left(4\epsilon_w \sigma_0 T_w^3 (\delta T_w) \right)^2 + (\delta q''_{\text{rad},i})^2 \right]^{1/2} \tag{A.36}$$

The a low and high wall temperature cases had $T_w = 752\,\text{K}$ and $T_w = 942\,\text{K}$, respectively, with $\epsilon_w = 0.85$. Inserting these values into Eq. A.36 gave uncertainties of $\delta q''_{\text{rad}} = \pm 703\,\text{W/m}^2$ (2.02% of q''_{rad}) and $\delta q''_{\text{rad}} = \pm 664\,\text{W/m}^2$ (8.07% of q''_{rad}) at the low and high wall temperatures, respectively.

The convective heat flux was determined from the measurements by removing the radiative component from the measured conductive heat flux (solving Eq. 5.9 for q''_{conv}). Thus, the uncertainty in q''_{conv} was quantified by [43]

$$\delta q''_{\text{conv}} = \sqrt{(\delta q''_{\text{cond}})^2 + (\delta q''_{\text{rad}})^2} \tag{A.37}$$

Inserting the appropriate values for the low and high temperature cases discussed previously gave convective heat flux uncertainties of $\delta q''_{\text{conv}} = \pm 0.0513 \times 10^5\,\text{W/m}^2$ (2.98% of q''_{conv}) and $\pm 0.0518 \times 10^5\,\text{W/m}^2$ (3.98% of q''_{conv}), respectively.

The current work also presented the convective heat transfer coefficient (h) calculated from the q''_{conv} measurement. Thus, the uncertainty in h was given by [43]

$$\delta h = \left[\left(\frac{\partial h}{\partial q''_{\text{conv}}} \delta q''_{\text{conv}} \right)^2 + \left(\frac{\partial h}{\partial T_\infty} \delta T_\infty \right)^2 + \left(\frac{\partial h}{\partial T_w} \delta T_w \right)^2 \right]^{1/2} \tag{A.38}$$

where

$$\frac{\partial h}{\partial q''_{\text{conv}}} = \frac{1}{(T_\infty - T_w)} \tag{A.39}$$

$$\frac{\partial h}{\partial T_\infty} = -\frac{q''_{\text{conv}}}{(T_\infty - T_w)^2} \tag{A.40}$$

$$\frac{\partial h}{\partial T_w} = \frac{q''_{\text{conv}}}{(T_\infty - T_w)^2} \tag{A.41}$$

Inserting the appropriate values for the low temperature case discussed above with

$T_\infty = 1488\,\mathrm{K}$ gave an uncertainty of $\delta h = \pm 7.06\,\mathrm{W/m^2\,K}$ (2.84% of h). Similarly, the high temperature case discussed above gave an uncertainty of $\delta h = \pm 9.72\,\mathrm{W/m^2\,K}$ (4.05% of h).

The temperature ratio method of Kays et al. [29] given by Eq. 2.25 was used to account for the variable property flow present in the experiments. Thus, it was important to quantify the uncertainty in the method's two non-dimensional terms: the temperature ratio (T_w/T_∞) and the convective heat transfer ratio (h/h_{CP}). Since these both take the same form, the T_w/T_∞ uncertainty will be derived in detail and the h/h_{CP} uncertainty will be calculated by analogy.

The uncertainty in T_w/T_∞ is given as [43]

$$\delta(T_w/T_\infty) = \left[\left(\frac{\partial(T_w/T_\infty)}{\partial T_w}\delta T_w\right)^2 + \left(\frac{\partial(T_w/T_\infty)}{\partial T_\infty}\delta T_\infty\right)^2\right]^{1/2} \tag{A.42}$$

where

$$\frac{\partial(T_w/T_\infty)}{\partial T_w} = \frac{1}{T_\infty} \tag{A.43}$$

$$\frac{\partial(T_w/T_\infty)}{\partial T_\infty} = -\frac{T_w}{T_\infty^2} \tag{A.44}$$

From these equations, it was found that $\delta(T_w/T_\infty) = 0.0020$ (0.42% of (T_w/T_∞)) and $\delta(T_w/T_\infty) = 0.0026$ (0.41% of T_w/T_∞) for the low and high temperature cases discussed above, respectively. By analogy, the uncertainty in h/h_{CP} was calculated by replacing T_w with h and T_∞ with h_{CP} in Eq. A.42. In this way, it was found that $\delta(h/h_{\mathrm{CP}}) = 0.126$ (11.2% of h/h_{CP}) and $\delta(h/h_{\mathrm{CP}}) = 0.126$ (10.8% of h/h_{CP}) for the low and high temperature cases, respectively.

A.6.8 Film Cooling Performance.

Some of the above measurements were non-dimensionalized into four parameters to describe the film cooling layer's performance. Namely, they were the non-dimensional wall temperature θ_w (Eq. 2.34), net heat flux reduction $\Delta q''_f$ (Eq. 2.33), heat flux augmentation σ (Eq. 2.68), and degradation of heat flux $\nabla q''_r$ (Eq. 7.2). The uncertainty in each of these quantities will be derived below.

The uncertainty of θ_w can be written as [43]

$$\delta\theta_w = \frac{1}{\sqrt{N}}\left[\left(\frac{\partial\theta_w}{\partial T_w}\delta T_w\right)^2 + \left(\frac{\partial\theta_w}{\partial T_{c,e}}\delta T_{c,e}\right)^2 + \left(\frac{\partial\theta_w}{\partial T_\infty}\delta T_\infty\right)^2\right]^{1/2} \tag{A.45}$$

where

$$\frac{\partial\theta_w}{\partial T_w} = \frac{1}{T_\infty - T_2} \tag{A.46}$$

$$\frac{\partial\theta_w}{\partial T_{c,e}} = -\frac{T_\infty - T_w}{(T_\infty - T_{c,e})^2} \tag{A.47}$$

$$\frac{\partial\theta_w}{\partial T_\infty} = -\frac{T_w - T_{c,e}}{(T_\infty - T_{c,e})^2} \tag{A.48}$$

where N was the number of thermocouples in the row. The main source of uncertainty in these equations is the uncertainty of $T_{c,e}$. Thus, to bound the uncertainty, the single row of shaped holes was examined at low and high wall temperature conditions.

Since the coolant temperature at the exit of the film cooling jet ($T_{c,e}$) was not measured directly, Section 6.2.2.2 proposed a method to approximate $T_{c,e}$. This method involved measuring the temperature of the coolant before it entered the film cooling and predicting upper and lower bounds for $T_{c,e}$. Last, $T_{c,e}$ was selected at the average of the bounds to minimize the potential error. Since no better estimation of $T_{c,e}$ was available, the maximum potential error was used for the uncertainty, $\delta T_{c,e}$.

Though the coolant temperature was lower for the five row geometries than the single row geometries, all cases produce similar $\delta T_{c,e}$. Since Eq. A.45 dictates that

$\delta T_{c,e}$ increases with $T_{c,e}$, the single row shaped hole conditions examined above were used to calculate a worst case uncertainty. With $\delta T_{c,e} = \pm 125\,\mathrm{K}$, $T_{c,e} = 720\,\mathrm{K}$, and $N = 5$, the uncertainty in θ_w was calculated to be $\delta\theta_w = \pm 0.072$ and $\delta\theta_w = \pm 0.053$ for the low and high T_w conditions, respectively.

Next, the uncertainty in $\overline{\Delta q''_f}$ (Eq. 6.9) was quantified by [43]

$$\delta\left(\overline{\Delta q''_f}\right) = \frac{\delta q''_{\mathrm{conv}}}{\sqrt{N}}\left[\left(\frac{\partial\left(\overline{\Delta q''_f}\right)}{\partial\overline{q''_{\mathrm{conv},f}}}\right)^2 + \left(\frac{\partial\left(\overline{\Delta q''_f}\right)}{\partial\overline{q''_{\mathrm{conv},0}}}\right)^2\right]^{1/2} \tag{A.49}$$

where N is the number of thermocouples the given row and

$$\frac{\partial\left(\overline{\Delta q''_f}\right)}{\partial\overline{q''_{\mathrm{conv},f}}} = -\frac{1}{\overline{q''_{\mathrm{conv},0}}} \tag{A.50}$$

$$\frac{\partial\left(\overline{\Delta q''_f}\right)}{\partial\overline{q''_{\mathrm{conv},0}}} = -\frac{\overline{q''_{\mathrm{conv},f}}}{\left(\overline{q''_{\mathrm{conv},0}}\right)^2} \tag{A.51}$$

The uncertainty was calculated for the first row of thermocouples which had $N = 5$ working instrumentation locations. For the single row of shaped holes at low temperature, the measured heat fluxes were $\overline{q''_{\mathrm{conv},f}} = 1.56 \times 10^5\,\mathrm{W/m^2}$ and $\overline{q''_{\mathrm{conv},0}} = 1.89 \times 10^5\,\mathrm{W/m^2}$ giving an uncertainty of $\delta\left(\overline{\Delta q''_f}\right) = \pm 0.0176$. At high temperature, the measured heat fluxes were $\overline{q''_{\mathrm{conv},f}} = 1.10 \times 10^5\,\mathrm{W/m^2}$ and $\overline{q''_{\mathrm{conv},0}} = 1.35 \times 10^5\,\mathrm{W/m^2}$ giving an uncertainty of $\delta\left(\overline{\Delta q''_f}\right) = \pm 0.0249$.

Section 7.2 introduces a distinction between the non-reacting NHFR ($\Delta q''_f$) and the reacting NHFR ($\Delta q''_r$). The definition of $\Delta q''_r$ given by Eq. 7.1 shows that $\Delta q''_f$ and $\Delta q''_r$ take analogous forms. As such, the individual terms share identical uncertainties. Thus, there is no difference in the uncertainty of $\Delta q''_r$ such that $\delta\left(\overline{\Delta q''_f}\right) \approx \delta\overline{\Delta q''_r}$. The same can be said of augmentation (σ, Eq. 2.68) such that $\delta\left(\overline{\Delta q''_f}\right) \approx \delta\overline{\sigma}$.

Finally, degradation of NHFR ($\nabla q''_r$) is defined in Eq. 7.2 to be the difference of the non-reacting and reacting NHFR. Thus, the uncertainty was derived to be

$$\delta\left(\overline{\nabla q_r''}\right) = \left[\left(\frac{\partial\left(\overline{\Delta q_f''}\right)}{\partial\overline{\Delta q_f''}}\right)^2 + \left(\frac{\partial\left(\overline{\nabla q_r''}\right)}{\partial\overline{\Delta q_r''}}\right)^2\right]^{1/2} = \sqrt{2}\delta\left(\overline{\Delta q_f''}\right) \tag{A.52}$$

By inserting the $\delta\left(\overline{\nabla q_r''}\right)$ calculated above, it was found that $\delta\left(\overline{\nabla q_r''}\right) = \pm 0.0249$ and $\delta\left(\overline{\nabla q_r''}\right) = \pm 0.0352$ at the low and high T_w cases, respectively.

A.7 Emissions

The present research relied heavily on the emissions from the WSR to create the appropriate fuel rich core flow. Emissions measurements were taken to ensure the appropriate chemical composition existed within the test channel. The gas sample was extracted by a Mokon (HC4118-RC) oil cooled emissions probe mounted at the rig exit as seen in Fig. A.29(a). This oil temperature was regulated to 422 K to cool and quench the gas sample while being hot enough to prevent the H_2O combustion product from condensing in the sample line. The sample then traveled through a line from the probe to the sample pump. Like the probe, line temperature was regulated to 422 K by a heater to prevent condensation within the line. Next, the sample was cooled and passed through a condenser to remove most of the water from the sample. Last, the sample passed in series through the Horriba gas analyzers seen in Fig. A.29(b) to measure the volumetric percentage of CO (model number VIA-510), CO_2 (model number VIA-510), and O_2 (model number MPA-510) in the gas sample. To ensure accuracy of the measurements, the analyzers were calibrated daily by zeroing with pure N_2 and spanning with flows of 3.9% CO, 9.01% CO_2, and 18.1% O_2, respectively.

Many factors could affect the emissions at the rig inlet. For example, leaks in the fuel-air plumbing or inaccurate calibration of the fuel-air controllers would cause the

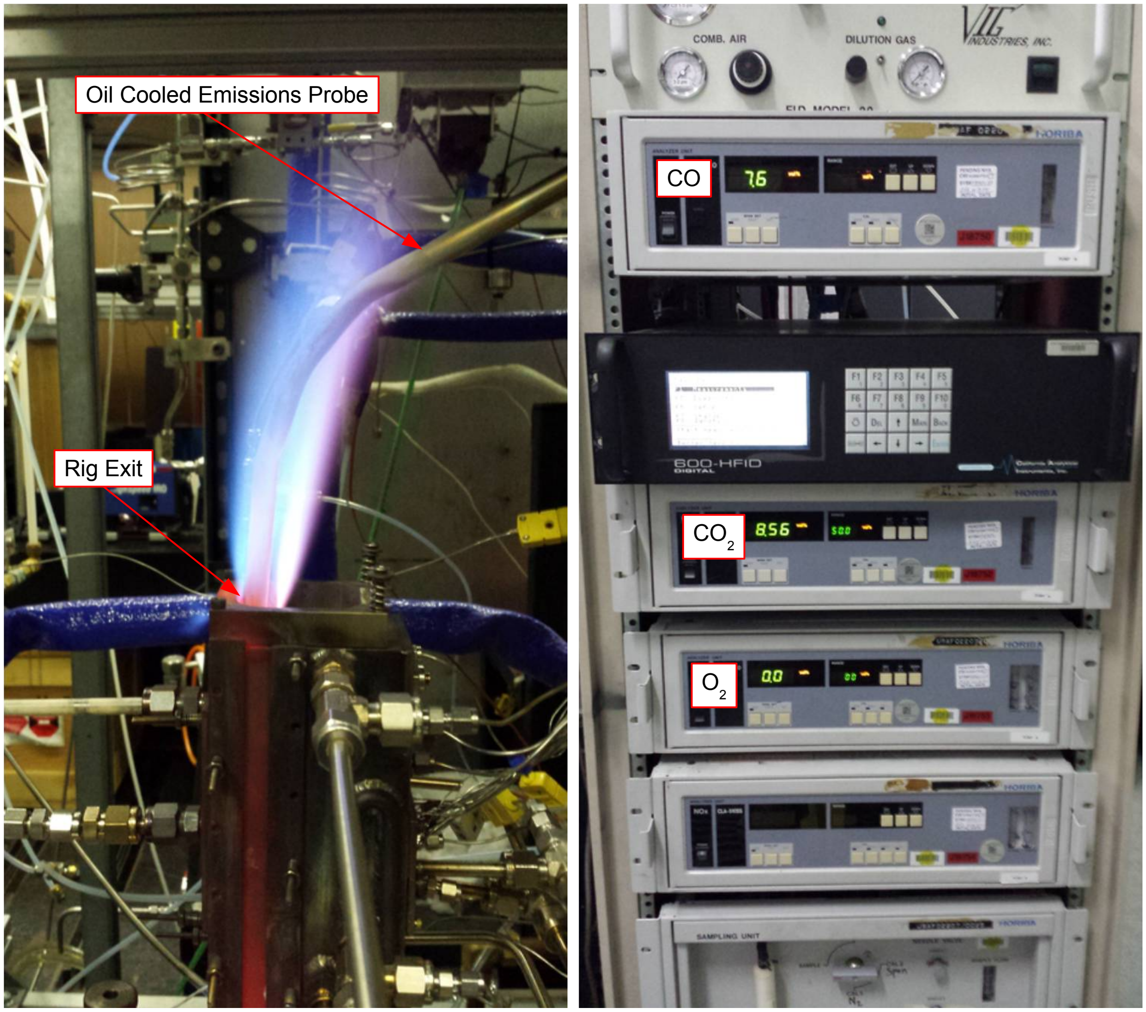

(a) Oil Cooled Emissions Probe (b) Emissions Gas Analyzers

Figure A.29: Emissions measurement system for CO, CO_2, and O_2

combustion to occur at an undesired equivalence ratio (Φ). As a result, the WSR's emissions would have an undesired emission distribution. Thus, to verify that the emissions measurements were as desired, the measured emissions were compared to the expected emissions from chemical equilibrium theory.

The expected emissions were calculated using the Chemical Equilibrium with Applications (CEA) [41] code. The nominal core flow temperature and pressure along with the Φ of the propane-air mixture were given as inputs to CEA [41]. The code then found the equilibrium composition of the combustion products. This was accomplished by balancing the atoms present in the combustion reactants with the possible combustion products to minimize Gibbs free energy at the given core flow conditions.

The volumetric percentages of CO, CO_2, and O_2 resulting from the CEA [41] code could not be directly compared to percentages measured experimentally. This was due to water being present in the CEA [41] while most water was removed in the experimental measurement in the condenser. Thus, the volumetric percentages of CO, CO_2, and O_2 calculated by CEA [41] were corrected to reflect the water removal.

First, the volumetric percentage of H_2O in the sample after condensing was calculated. The condenser operated at a nominal temperature of 278 K and pressure of 1 atm. At this temperature, the partial pressure of saturated water is 841 Pa. Thus, the volumetric percentage of water after condensing was $\chi_{\mathrm{H_2O,dried}} = 0.830\%$. Finally, the volumetric percentages of CO, CO_2, and O_2 were corrected by

$$\chi_{k,\mathrm{corr}} = \frac{\chi_k}{1 - \chi_{\mathrm{H_2O}} + \chi_{\mathrm{H_2O,dried}}} \tag{A.53}$$

where χ_k is the volumetric fraction of molecule k. After correction, the measured and calculated volumetric percentages agreed within an absolute difference of 0.2% for all three gases.

A.8 Data Acquisition

The LabView [46] program seen in Fig. A.31 was employed to record and display data in real-time. Figure A.30 shows the National Instruments Data Acquisition system that was used to read the thermocouple temperatures and report the data to the LabView [46] program. The majority of the LabView [46] code was reused from the work of DeLallo [14]. However, DeLallo [14] only measured heat flux at four locations. Thus, since the present work required many more thermocouples, the LabView [46]

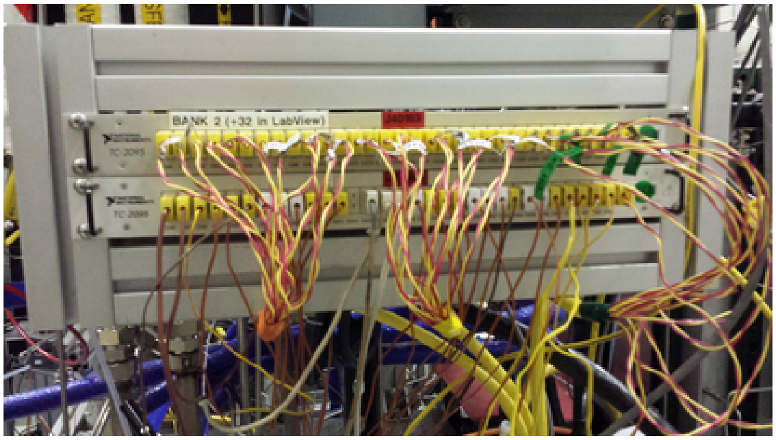

Figure A.30: Thermocouple Data Acquisition

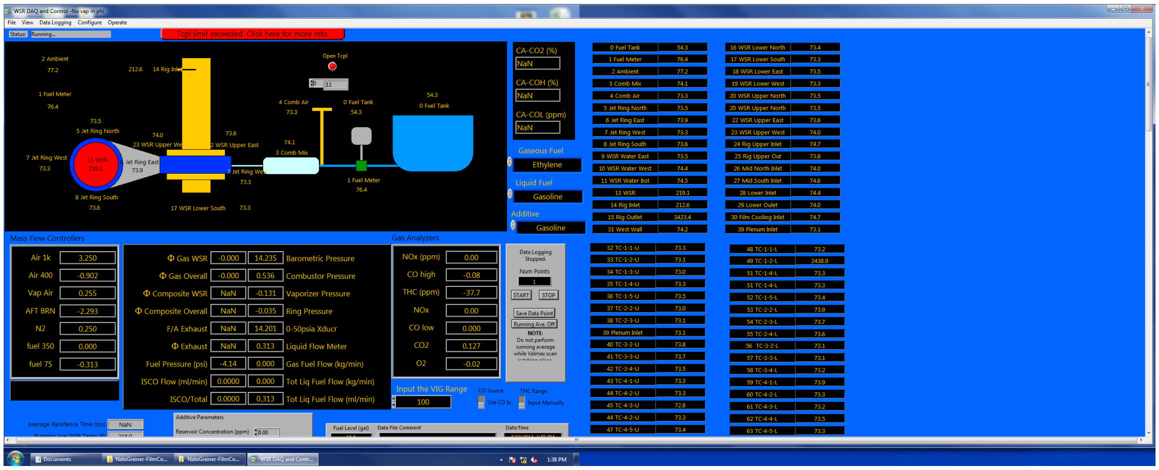

Status: Running...

Tcpl limit exceeded. Click here for more info.

CA-CO2 (%) NaN

CA-COH (%) NaN

CA-COL (ppm) NaN

Gaseous Fuel: Ethylene

Liquid Fuel: Gasoline

Additive: Gasoline

Air 1k	3.250
Air 400	-0.902
Vap Air	0.255
AFT BRN	-2.293
N2	0.250
fuel 350	0.000
fuel 75	-0.313

Φ Gas WSR	-0.000	14.235	Barometric Pressure
Φ Gas Overall	-0.000	0.536	Combustor Pressure
Φ Composite WSR	NaN	-0.131	Vaporizer Pressure
Φ Composite Overall	NaN	-0.035	Ring Pressure
F/A Exhaust	NaN	14.201	0-50psia Xducr
Φ Exhaust	NaN	0.313	Liquid Flow Meter
Fuel Pressure (psi)	-4.14	0.000	Gas Fuel Flow (kg/min)
ISCO Flow (ml/min)	0.0000	0.000	Tot Liq Fuel Flow (kg/min)
ISCO/Total	0.0000	0.313	Tot Liq Fuel Flow (ml/min)

NOx (ppm)	0.00
CO high	-0.08
THC (ppm)	-37.7
NOx	0.00
CO low	0.000
CO2	0.127
O2	-0.02

Data Logging Stopped.

Num Points 1

NOTE: Do not perform running average while Velmex scan

Input the VIG Range 100

CO Source: Use CO lo

THC Range: Input Manually

Average Residence Time (ms) NaN

Additive Parameters

Reservoir Concentration (ppm) 0.00

Fuel Level (gal)

Data File Comment

Date/Time

0 Fuel Tank	54.3	16 WSR Lower North	73.4
1 Fuel Meter	76.4	17 WSR Lower South	73.3
2 Ambient	77.2	18 WSR Lower East	73.5
3 Comb Mix	74.1	19 WSR Lower West	73.3
4 Comb Air	73.3	20 WSR Upper North	73.5
5 Jet Ring North	73.5	20 WSR Upper North	73.5
6 Jet Ring East	73.9	22 WSR Upper East	73.6
7 Jet Ring West	73.3	23 WSR Upper West	74.0
8 Jet Ring South	73.6	24 Rig Upper Inlet	74.7
9 WSR Water East	73.5	25 Rig Upper Out	73.8
10 WSR Water West	74.4	26 Mid North Inlet	74.0
11 WSR Water Bot	74.5	27 Mid South Inlet	74.6
13 WSR	219.1	28 Lower Inlet	74.4
14 Rig Inlet	212.6	29 Lower Oulet	74.0
15 Rig Outlet	3423.4	30 Film Cooling Inlet	74.7
31 West Wall	74.2	39 Plenum Inlet	73.1

32 TC-1-1-U	73.3	48 TC-1-1-L	73.2
33 TC-1-2-U	73.1	49 TC-1-2-L	2438.9
34 TC-1-3-U	73.0	51 TC-1-4-L	73.3
35 TC-1-4-U	73.3	51 TC-1-4-L	73.3
36 TC-1-5-U	73.5	52 TC-1-5-L	73.4
37 TC-2-2-U	73.0	53 TC-2-2-L	73.9
38 TC-2-3-U	73.1	54 TC-2-3-L	73.7
39 Plenum Inlet	73.1	55 TC-2-4-L	73.6
40 TC-3-2-U	73.8	56 TC-3-2-L	73.1
41 TC-3-3-U	73.7	57 TC-3-3-L	73.1
42 TC-3-4-U	73.5	58 TC-3-4-L	73.2
43 TC-4-1-U	73.3	59 TC-4-1-L	73.9
44 TC-4-2-U	73.3	60 TC-4-2-L	73.3
45 TC-4-3-U	72.8	61 TC-4-3-L	73.2
44 TC-4-2-U	73.3	62 TC-4-4-L	73.5
47 TC-4-5-U	73.4	63 TC-4-5-L	73.3

Figure A.31: Screenshot of LabView [46] Data Display

code was expanded to accomodate the increased number of thermocouples.

A.9 Procedure for Operating the Facility

This section provides the step-by-step procedure used for facility preparation, lighting the WSR, achieving the desired test condition, and shutting down the facility.

A.9.1 Facility Preparation.

1. Turn on vent hood

2. Turn on air heater switch
3. Pre-heat reactor by flowing 400 SLPM of air heated to 500 °F through reactor
    (a) Wait until the jet ring temps to exceed 250-300 °F
    (b) Should take about 40-60 minutes
    (c) Calibrate and set up emissions
    (d) Open span gas bottles
    (e) Zero emissions with N_2
    (f) Span CO to 3.9% (bottle 3)
    (g) Span CO_2 to 9.01% (bottle 9)
    (h) Span O_2 to 18.1% (bottle 18)
    (i) Turn on sample pump and line heater
    (j) Shut span gas bottles

A.9.2 Lighting the WSR.

1. Increase water to the Mokon system until green band is fully exposed
2. Turn on Mokon system and set the oil temperature to 300 °F
3. Turn on rig backside cooling
4. Plug in propane bottle and line heaters (if required)
5. Turn on 0.1 GPM of water to bottom and top of reactor
6. Keep air at 400 SLPM & keep the combustion air heater at 500 °F
7. To light, hold igniter while brining propane up to 11.76 SLPM ($\Phi = 0.7$, set pt of 12.00 on MKS)

8. After lit, increase WSR water to 0.35 GPM and 0.6 GPM for bottom and top, respectively
9. Hold conditions steady and allow rig to heat up until the rig inlet temperature is $> 2000\,^{\circ}\mathrm{F}$

A.9.3 Achieving Desired Test Condition.

1. Increase propane to 13.87 SLPM ($\Phi = 1.1$)
    (a) Reactor tends to be more stable at rich conditions than lean
    (b) Ramping up the flow rate at $\Phi = 1.1$ tends to prevent blowouts due to small deviations from $\Phi = 1.1$
2. Increase air and fuel by commanding alternating increases:
    (a) Increase fuel to achieve $\Phi = 1.2$
    (b) Increase air to achieve $\Phi = 1.08$
    (c) Repeat until desired air and fuel flow rates are reached
    (d) CAUTION: DO NOT HOLD KEYS IN. Only increase by taping buttons. Holding keys in can cause a severe over/undershoot on Φ.
    (e) CAUTION: Ramping up air too quickly will cause fuel check valve to close, will cut off the fuel supply and cause a blowout
3. Lower air heater set point such that utilization is $< 100\%$ to avoid an open loop control system
4. Begin testing with repeatability point
5. Run test
6. End with repeatability point

A.9.4 Shutting Down the Facility.

1. Decrease fuel flow to zero
2. Shut off air heater above control panel and air heater switch
3. Decrease Mokon temp set point to 60 °F
4. Shut valve on propane bottle and unplug belt heaters (if used), leave bottle ball valve open
5. Once rig inlet temperatures are below 300 °F:
    (a) Turn on 30 PSI of hood dilution air
    (b) Open fuel bleed ball valve leading to the vent hood
    (c) Turn on bleed pressure regulator to 15 PSI
    (d) Bleed until the regulator pressure drops to 0 PSI
    (e) Close the regulator and bleed ball valve
    (f) Open bleed ball valve at the bottle to release remaining pressure
    (g) Close the ball valve at the propane tank
    (h) Shut propane ball valve just inside the back door and shut off line heater (if used)
6. Empty water vessel on emissions sample drier
7. Shut off emissions pump and heaters
8. Ensure emissions span gas bottles are closed
9. Shut off Mokon system once temperature is < 140 °F (press stop and turn switch on right side) and shut off water to Mokon

10. Once jet ring temperatures drop below 150 °F, shut off water to the reactor
11. Once rig is sufficiently cool, leave 5-20 SLPM of N_2 flowing through the cooling paths (does not apply if using Mokon)
12. Turn emissions sample to N_2 and adjust flow rate to within the bands
13. Shut off vent hood
14. Stop VI, extract data from computer, shut off computer
15. Double check everything was completed, leave lab and shut off lights (switch outside the door)
16. Ensure doors are locked and closed

Appendix B. Air Property Models

To accurately model the temperature variation of air properties in the CFD simulations of the present work, continuous functions of temperature for each property were developed to closely match tabular property data found in Kays et al. [29]. To model the density of air the Ideal Gas Law was used such that

$$\rho(T) = \frac{p}{R_{\mathrm{air}} T} \tag{B.1}$$

where $p = 1\,\mathrm{atm}$ and $R_{\mathrm{air}} = 287.04\,\mathrm{J/(kg \cdot K)}$. A plot of the tabular ρ data, Eq. B.1, and the accuracy of Eq. B.1 compared to the tabular ρ data are shown in Fig. B.1.

Sutherland's law is often used to model dynamic viscosity. The law is defined by White [68] as

$$\mu(T) = \mu_0 \left(\frac{T}{T_0}\right)^{3/2} \frac{T_0 + S}{T + S} \tag{B.2}$$

where $\mu_0 = 1.72 \times 10^{-5}\,\mathrm{Pa \cdot s}$, $T_0 = 273.11\,\mathrm{K}$, and $S = 110.56\,\mathrm{K}$. However, compared to tabular data [29], Sutherland's law was found to diverge for temperatures below 200 K and above 1000 K. The divergence above 1000 K is attributed to the inability of Sutherland's law to capture the effect of air molecules dissociating at high temperatures on dynamic viscosity. Thus, to more accurately model dynamic viscosity, a high order polynomial was fit to tabular data [29] such that

$$\mu(T) = [1\; T\; T^2\; T^3\; T^4\; T^5\; T^6\; T^7] \cdot \begin{bmatrix} -4.54026 \cdot 10^{-7} \\ 8.36824 \cdot 10^{-8} \\ -8.84704 \cdot 10^{-11} \\ 7.97666 \cdot 10^{-14} \\ -4.62274 \cdot 10^{-17} \\ 1.66553 \cdot 10^{-20} \\ -3.4155 \cdot 10^{-24} \\ 3.05854 \cdot 10^{-28} \end{bmatrix}, \; \epsilon\; 100 \leq T \leq 2500 \qquad \text{(B.3)}$$

where T has units of K and μ has units of Pa·s. A plot of the tabular μ data, Eq. B.3, and the accuracy of Eq. B.3 compared to the tabular μ data are shown in Fig. B.2.

The remaining properties of air (c_p and k) were modeled by high order polynomials. For specific heat, the tabular data were modeled by two polynomials covering different temperature ranges such that

$$c_p(T) = [1\; T\; T^2\; T^3\; T^4\; T^5\; T^6\; T^7] \cdot \begin{bmatrix} 1161.4822 \\ -2.368819 \\ 0.014855111 \\ -5.0349092 \cdot 10^{-5} \\ 9.9285693 \cdot 10^{-8} \\ -1.1110966 \cdot 10^{-10} \\ 6.5401962 \cdot 10^{-14} \\ -1.5735877 \cdot 10^{-17} \end{bmatrix}, \; \epsilon\; 100 \leq T < 1000 \quad \text{(B.4)}$$

$$c_p(T) = [1 \; T \; T^2 \; T^3 \; T^4 \; T^5 \; T^6 \; T^7] \cdot \begin{bmatrix} -7.0698 \cdot 10^{3} \\ 3.370 \cdot 10^{1} \\ -5.8128 \cdot 10^{-2} \\ 5.4216 \cdot 10^{-5} \\ -2.9367 \cdot 10^{-8} \\ 9.2375 \cdot 10^{-12} \\ -1.5656 \cdot 10^{-15} \\ 1.1123 \cdot 10^{-19} \end{bmatrix}, \; \epsilon \; 1000 \leq T \leq 3000 \quad \text{(B.5)}$$

where T has units of K and c_p has units of J/(kg · K). A plot of the tabular c_p data, Eqs. B.4 and B.5, and the accuracy of Eqs. B.4 and B.5 compared to the tabular c_p data are shown in Fig. B.3.

For thermal conductivity, the tabular data were modeled by a single equation given by

$$k(T) = [1 \; T \; T^2 \; T^3 \; T^4 \; T^5 \; T^6 \; T^7] \cdot \begin{bmatrix} -0.00129058 \\ 0.000113044 \\ -9.06608 \cdot 10^{-8} \\ 6.61287 \cdot 10^{-11} \\ -2.0265 \cdot 10^{-14} \\ -5.78161 \cdot 10^{-19} \\ 1.36595 \cdot 10^{-21} \\ -9.55415 \cdot 10^{-26} \end{bmatrix}, \; \epsilon \; 100 \leq T \leq 2500 \quad \text{(B.6)}$$

where T has units of K and k has units of W/(m · K). A plot of the tabular k data, Eq. B.6, and the accuracy of Eq. B.6 compared to the tabular k data are shown in Fig. B.4. Tabular data of Pr, a continuous function for Pr calculated from its definition via Eqs. B.2, B.4, B.5, and B.6 along with the accuracy of the calculated

Pr to the tabular data are show in Fig. B.5.

The final parameter modeled was the speed of sound after the tabular data measured by Lemmon et al. [33] at atmospheric pressure. The data were modeled by a high order polynomial such that

$$a(T) = [1\; T\; T^2\; T^3\; T^4\; T^5\; T^6\; T^7] \cdot \begin{bmatrix} 84.1328 \\ 1.34079 \\ -0.00226706 \\ 3.13522 \cdot 10^{-6} \\ -2.7659 \cdot 10^{-9} \\ 1.46304 \cdot 10^{-12} \\ -4.20827 \cdot 10^{-16} \\ 5.04262 \cdot 10^{-20} \end{bmatrix}, \; \epsilon\; 100 \leq T \leq 2000 \qquad \text{(B.7)}$$

where T has units of K and a has units of m/s. A plot of the tabular a data, Eq. B.7, and the accuracy of Eq. B.7 compared to the tabular a data are shown in Fig. B.6.

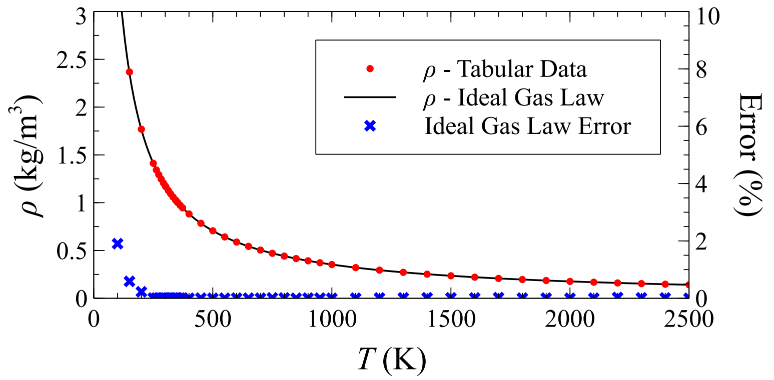

Figure B.1: Accuracy of the Ideal Gas Law (Eq. B.1) to model tabular data of density (ρ) [29] for air at various temperatures

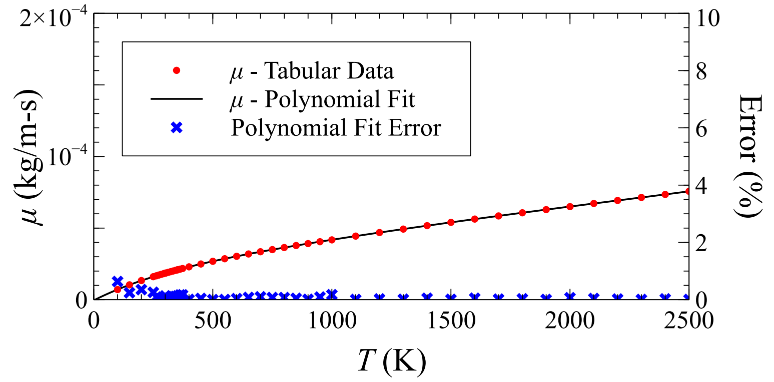

Figure B.2: Accuracy of Eq. B.3 to model tabular data of dynamic viscosity (μ) [29] for air at various temperatures

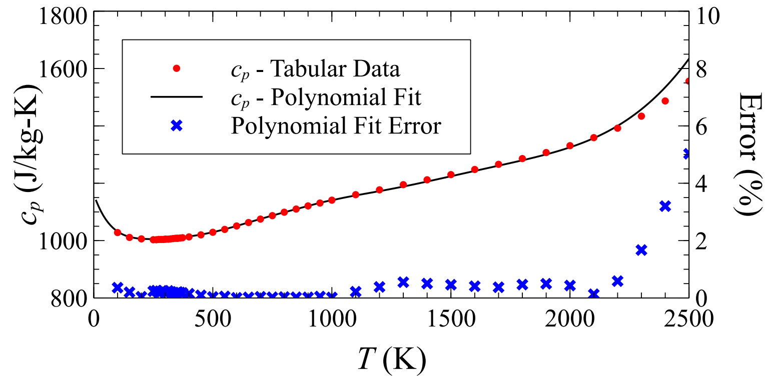

Figure B.3: Accuracy of Eqs. B.4 and B.5 to model tabular data of specific heat (c_p) [29] for air at various temperatures

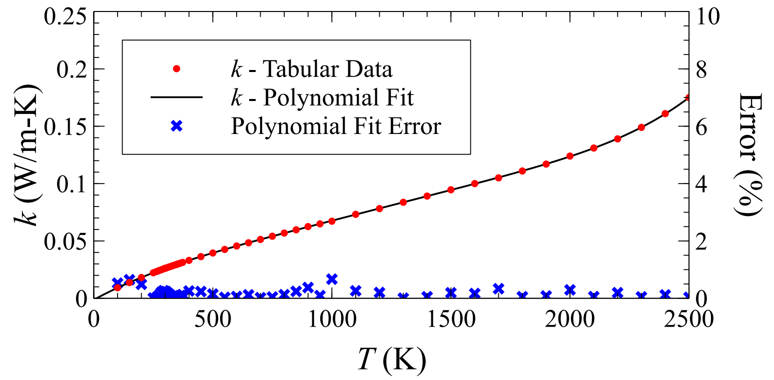

Figure B.4: Accuracy of Eq. B.6 to model tabular data of thermal conductivity (k) [29] for air at various temperatures

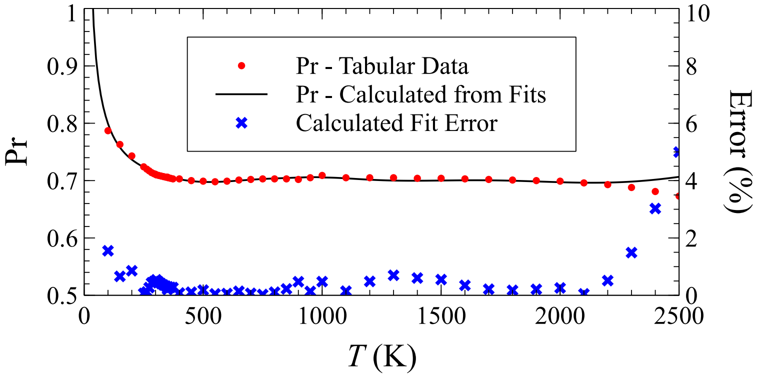

Figure B.5: Accuracy of Eqs. B.2, B.4, B.5, and B.6 to model tabular data of Prandtl number (Pr) [29] for air at various temperatures

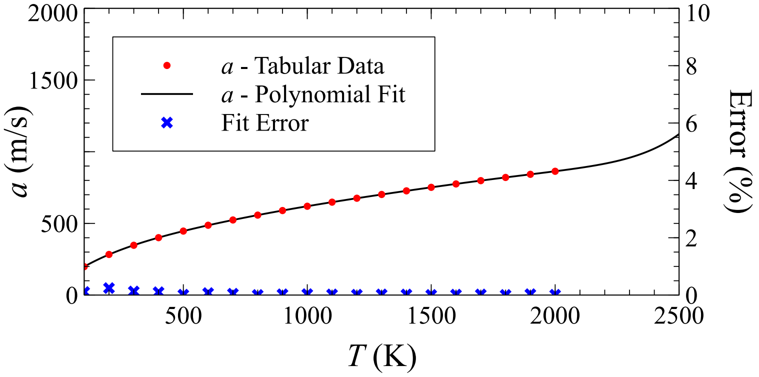

Figure B.6: Accuracy of Eq. B.7 to model tabular data of the speed of sound (a) [33] for air at various temperatures

Bibliography

[1] Anderson, W. S., M. D. Polanka, J. Zelina, D. S. Evans, S. D. Stouffer, and G. R. Justinger. "Effects of a Reacting Cross-Stream on Turbine Film Cooling". *J. Eng. Gas Turbines Power*, 132(5), 2010.

[2] Andrews, G. E. "Full Coverage Effusion Cooling with a Narrow Duct Backside Coolant Supply". *Proceedings of ASME Turbo Expo*, GT2012-68629. 2012.

[3] ANSYS, Inc, Canonsburg, PA. *ANYSYS FLUENT 14.5 User's Guide*, 2012.

[4] Bain, L. and M. Engelhardt. *Introduction to Probability and Mathematical Statistics.* Classic Series. Duxbury, 1992.

[5] Baldauf, S., M. Scheurlen, A. Schulz, and S. Wittig. "Correlation of Film-Cooling Effectiveness from Thermographic Measurements at Enginelike Conditions". *J. Turbomach.*, 124(4):686–698, 2002.

[6] Ballal, D. R. and J. Zelina. "Progress in Aeroengine Technology (1939–2003)". *J. Aircraft*, 41(1):43–50, 2004.

[7] Blazek, J. *Computational Fluid Dynamics: Principles and Applications.* Elsevier, 2005.

[8] Bogard, D. G. and K. A. Thole. "Gas Turbine Film Cooling". *J. Propul. Power*, 22(2):249–270, 2006.

[9] Bohan, B. T. *Analysis of Flow Migration in an Ultra-Compact Combustor.* MS Thesis, Air Force Institute of Technology, Wright-Patterson AFB, OH, March 2011.

[10] Bunker, R. S. "Film Cooling Effectiveness Due to Discrete Holes Within a Transverse Surface Slot". *Proceedings of ASME Turbo Expo*, GT-2002-30178. 2002.

[11] Çengel, Y. A. and M. A. Boles. *Thermodynamics: An Engineering Approach.* McGraw-Hill Series in Mechanical Engineering. McGraw-Hill Higher Education, 2006.

[12] Colban, W. F. *A Detailed Study of Fan-Shaped Film-Cooling for a Nozzle Guide Vane for an Industrial Gas Turbine.* PhD Thesis, Virginia Polytechnic Institute and State University, 2005.

[13] Dassault Systems, Providence, RI. *Abaqus 6.10 Analysis User's Manual*, 2010.

[14] DeLallo, M. R. *Impact of Trench and Ramp Film Cooling Designs to Reduce Heat Release Effects in a Reacting Flow.* MS Thesis, Air Force Institute of Technology, Wright-Patterson AFB, OH, March 2012.

[15] Eckert, E. R. G. "Engineering Relations for Friction and Heat Transfer to Surfaces in High Velocity Flow". *J. Aero. Sci.*, 22(8):585–587, 1955.

[16] Ekkad, S. V., S. Ou, and R. B. Rivir. "A Transient Infrared Thermography Method for Simultaneous Film Cooling Effectiveness and Heat Transfer Coefficient Measurements from a Single Test". *J. Turbomach.*, 126(4):597–603, 2004.

[17] Esgar, J. "Turbine Cooling-Its Limitations and Its Future". *High Temperature Turbines*, AGARD-CP-73-71. 1971.

[18] Evans, D. S. *The Impact of Heat Release in Turbine Film Cooling.* MS Thesis, Air Force Institute of Technology, Wright-Patterson AFB, OH, January 2008.

[19] Gritsch, M., A. Schulz, and S. Wittig. "Adiabatic Wall Effectiveness Measurements of Film-Cooling Holes with Expanded Exits". *J. Turbomach.*, 120(3):549–556, 1998.

[20] Han, J.-C., S. Dutta, and S. Ekkad. *Gas Turbine Heat Transfer and Cooling Technology.* Taylor & Francis Group, 2000.

[21] Harrington, M. K., M. A. McWaters, D. G. Bogard, C. A. Lemmon, and K. A. Thole. "Full-Coverage Film Cooling with Short Normal Injection Holes". *J. Turbomach.*, 123(4):798–805, 2001.

[22] Harrison, K. L., R. S. Bunker, J. R. Dorrington, J. E. Dees, and D. G. Bogard. "Turbine Airfoil Net Heat Flux Reduction With Cylindrical Holes Embedded in a Transverse Trench". *J. Turbomach.*, 131(1), 2008.

[23] Hartnett, J. P., R. C. Birkebak, and E. R. G. Eckert. "Velocity Distributions, Temperature Distributions, Effectiveness and Heat Transfer for Air Injected Through a Tangential Slot into a Turbulent Boundary Layer". *J. Heat Transfer*, 293–306, 1961.

[24] Haynes International, Kokomo, IN. *Hastelloy® X Material Data Sheet H-3009B*, 1997.

[25] Horlock, J. H. and B. Lakshminarayana. "Secondary Flows: Theory, Experiment, and Application in Turbomachinery Aerodynamics". *Annual Review of Fluid Mechanics*, 5:247–280, 1973.

[26] Howell, J. R., R. Siegel, and M. P. Mengüç. *Thermal Radiation Heat Transfer.* CRC press New York, NY, 2011.

[27] Johnson, D. D. *Cooling Requirements for the Ultra-Compact Combustor.* MS Thesis, Air Force Institute of Technology, Wright-Patterson AFB, OH, March 2012.

[28] Kakade, V. U., S. J. Thorpe, and M. Gerendás. "Effusion-Cooling Performance at Gas Turbine Combustor Representative Flow Conditions". *Proceedings of ASME Turbo Expo*, GT2012-68115. 2012.

[29] Kays, W. M., M. E. Crawford, and B. Weigand. *Convective Heat and Mass Transfer*. McGraw-Hill Series in Mechanical Engineering. McGraw-Hill Higher Education, 2005.

[30] Kirk, D. R., G. R. Guenette, S. P. Lukachko, and I. A. Waitz. "Turbine Durability Impacts of High Fuel-Air Ratio Combustors Part 2: Near Wall Reaction Effects on Film-Cooled Heat Transfer". *Proceedings of ASME Turbo Expo*, GT-2002-30182. 2002.

[31] Launder, B. E. and D. B. Spalding. "The Numerical Computation of Turbulent Flows". *Comput. Methods in Appl. Mech. and Eng.*, 3:269–289, 1974.

[32] LeBay, K. D. *Characterization of Cetrifugally-Loaded Flame Migration for Ultra-Compact Combustors*. PhD Thesis, Air Force Institute of Technology, Wright-Patterson AFB, OH, October 2011.

[33] Lemmon, E. W., R. T. Jacobsen, S. G. Penoncello, and D. G. Friend. "Thermodynamic Properties of Air and Mixtures of Nitrogen, Argon, and Oxygen from 60 to 2000 K at Pressures to 2000 MPa". *J. Phys. Chem. Ref. Data*, 29(3):331–385, 2000.

[34] Lewis, G. D. "Centrifugal-Force Effects on Combustion". *International Symposium on Combustion*, volume 14, 413–419. Elsevier, 1973.

[35] Liess, C. "Experimental Investigation of Film Cooling with Ejection from a Row of Holes for the Application to Gas Turbine Blades". *J. Eng. Power*, 97(1):21–27, 1975.

[36] Lin, C.-X., R. J. Holder, B. Sekar, J. Zelina, M. D. Polanka, H. J. Thornburg, and A. M. Briones. "Heat Release in Turbine Cooling II: Numerical Details of Secondary Combustion Surrounding Shaped Holes". *J. Propul. Power*, 27(2):269–281, 2011.

[37] Lu, Y., A. Dhungel, S. V. Ekkad, and R. S. Bunker. "Effect of Trench Width and Depth on Film Cooling from Cylindrical Holes Embedded in Trenches". *J. Turbomach*, 129(1):1–13, 2009.

[38] Lukachko, S. P., D. R. Kirk, and I. A. Waitz. "Turbine Durability Impacts of High Fuel-Air Ratio Combustors Part 1: Potential for Intra-Turbine Oxidation of Partially Reacted Fuel". *Proceedings of ASME Turbo Expo*, GT-2002-30077. 2002.

[39] Marosky, A., V. Seidel, S. Bless, T. Sattelmayer, and F. Magni. "Impact of Cooling Air Injection on the Primary Combustion Zone of a Swirl Burner". *Proceedings of ASME Turbo Expo*, GT2012-68898. 2012.

[40] Mattingly, J. D., W. H. Heiser, and D. T. Pratt. *Aircraft Engine Design.* AIAA, 2002.

[41] McBride, B. J. and S. Gordon. *Computer Program for Calculation of Complex Chemical Equilibrium Compositions and Applications.* National Aeronautics and Space Administration, Cleveland, OH, 1996.

[42] Milanes, D. W., D. R. Kirk, K. J. Fidkowski, and I. A. Waitz. "Gas Turbine Engine Durability Impacts of High Fuel-Air Ratio Combustors: Near Wall Reaction Effects of Film-Cooled Backward Facing Step Heat Transfer". *Proceedings of ASME Turbo Expo*, GT-2004-53259. 2004.

[43] Moffat, R. J. "Describing the Uncertainties in Experimental Results". *Exp. Therm. Fluid Sci.*, 1(1):3–17, 1988.

[44] Myers, G. E. *Analytical Methods in Conduction Heat Transfer.* AMCHT Publications, Madison, WI, 1998.

[45] National Institute of Standards and Technology, Gaithersburg, MD. *RADCAL: A Narrow-Band Model for Radiation Calculations in a Combustion Environment*, 1993.

[46] National Instruments, Austin, TX. *Getting Started with LabView*, 2010.

[47] Oguntade, H. I., G. E. Andrews, A. D. Burns, D. B. Ingham, and M. Pourkashanian. "Conjugate Heat Transfer Predictions of Effusion Cooling: The Influence of Injection Hole Size on Cooling Performance". *Proceedings of ASME Turbo Expo*, GT2012-68516. 2012.

[48] Oguntade, H. I., G. E. Andrews, A. D. Burns, D. B. Ingham, and M. Pourkashanian. "Conjugate Heat Transfer Predictions of Effusion Cooling: The Influence of the Coolant Jet-flow Direction on Cooling Effectiveness". *Proceedings of ASME Turbo Expo*, GT2012-68517. 2012.

[49] Parks, A. K. *Desensitizing Flame Structure and Exhaust Emissions to Flow Parameters in an Ultra-Compact Combustor.* MS Thesis, Air Force Institute of Technology, Wright-Patterson AFB, OH, March 2012.

[50] Pointwise, Inc., Fort Worth, TX. *Pointwise User Manual*, 2013.

[51] Polanka, M. D., J. Zelina, W. S. Anderson, B. Sekar, D. S. Evans, C.-X. Lin, and S. D. Stouffer. "Heat Release in Turbine Cooling I: Experimental and Computational Comparison of Three Geometries". *J. Propul. Power*, 27(2):257–268, 2011.

[52] Pope, S. B. *Turbulent Flows.* Cambridge University Press, 2000.

[53] Popp, O., D. E. Smith, J. V. Bubb, H. C. I. Grabowski, T. Diller, J. A. Schetz, and N. W. F. "Steady and Unsteady Heat Transfer in A Transonic Film Cooled Turbine Cascade". *ASME 99-GT-259*, 1999.

[54] Robertson, J. J. *Film Cooling in Fuel Rich Environments.* MS Thesis, Air Force Institute of Technology, Wright-Patterson AFB, OH, March 2013.

[55] Rumsey, C. L. and P. R. Spalart. "Turbulence Model Behavior in Low Reynolds Number Regions of Aerodynamic Flowfields". *AIAA J.*, 47(4):982–993, 2009.

[56] Rutledge, J. L. and M. D. Polanka. "Computational Fluid Dynamics Evaluations of Unconventional Film Cooling Scaling Parameters on a Simulated Turbine Blade Leading Edge". *J. of Turbomach.*, 136(10), 2014.

[57] Shewhart, A. T. *Minimization of the Effects of Secondary Reactions on Turbine Film Cooling in a Fuel Rich Environment.* MS Thesis, Air Force Institute of Technology, Wright-Patterson AFB, OH, June 2014.

[58] Simpson, R. L. and Kays, W. M. and Moffat, R. J. *The Turbulent Boundary Layer on a Porous Plate: An Experimental Study of the Fluid Dynamics with Injection and Suction.* Technical Report HMT-2, Thermosciences Division, Department of Mechanical Engineering, Stanford University, 1967.

[59] Sirignano, W. A., J. P. Delplanque, and F. Liu. "Selected Challenges in Jet and Rocket Engine Combustion Research". *33rd AIAA/ASME/SAE/ASEE Joint Propulsion Conference.* 1997.

[60] Smith, D. E., J. V. Bubb, O. Popp, H. C. I. Grabowski, T. Diller, J. A. Schetz, and N. W. F. "An Investigation of Heat Transfer in a Film Cooled Transonic Turbine Cascade, Part I: Steady Heat Transfer". *ASME 2000-GT-202*, 2000.

[61] Special Metals Corporation, Huntington, WV. *INCONEL® 625 Material Data Sheet*, 2013.

[62] Stouffer, S., R. Pawlik, G. Justinger, J. Heyne, J. Zelina, and D. Ballal. "Combustion Performance and Emissions Characteristics for a Well-Stirred Reactor for Low Volatility Hydrocarbon Fuels". *AIAA*, 2007-5663, 2007.

[63] Thole, K. A., A. Sinha, D. G. Bogard, and M. E. Crawford. "Mean Temperature Measurements of Jets with a Crossflow for Gas Turbine Film Cooling Application". *Rotating Machinery Transport Phenomena*, 69–85, 1992.

[64] Turns, S. R. *An Introduction to Combustion: Concepts and Applications.* McGraw-Hill Series in Mechanical Engineering. McGraw-Hill Education, 2000.

[65] Vedula, R. J. and D. E. Metzger. "A Method for the Simultaneous Determination of Local Effectiveness and Heat Transfer Distributions in Three-Temperature Convection Situations". *36th ASME, International Gas Turbine and Aeroengine Congress and Exposition*. 1991.

[66] Wade, W. R. *Measurements of Total Hemispherical Emissivity of Several Stably Oxidized Metals and Some Refractory Oxide Coatings*. Technical report, National Aeronautics and Space Administration; Langley Research Center, Langley Field, Va., 1959.

[67] Waye, S. K. and D. G. Bogard. "High-resolution Film Cooling Effectiveness Measurements of Axial Holes Embedded in a Transverse Trench with Various Trench Configurations". *J. Turbomach*, 129(2):294–302, 2007.

[68] White, F. M. *Viscous Fluid Flow*. McGraw-Hill Series in Mechanical Engineering. McGraw-Hill Higher Education, 2006.

[69] Wilcox, D. C. "Reassessment of the Scale-Determining Equation for Advanced Turbulence Models". *AIAA*, 26(11):1299–1310, 1988.

[70] Wurm, B., A. Schulz, and H.-J. Bauer. "Impact of Swirl Flow on the Cooling Performance of and Effusion Cooled Combustor Liner". *Proceedings of ASME Turbo Expo*, GT2012-68972. 2012.

[71] Zelina, J. and D. R. Ballal. "Combustor Stability and Emissions Research Using a Well-Stirred Reactor". *J. Eng. Gas Turbines Power*, 119:70–75, 1997.

[72] Zelina, J., G. J. Sturgess, and D. T. Shouse. "The Behavior of an Ultra-Compact Combustor (UCC) Based on Centrifugally-Enhanced Turbulent Burning Rates". *AIAA*, 2004-3541, 2004.

Vita

Nathan J. Greiner was raised in Lakeville, Minnesota where he graduated from Lakeville High School in June of 2004. He then studied at the University of Saint Thomas in Saint Paul, Minnesota. In May of 2008, he earned a Bachelor of Science in Mechanical Engineering with Cum Laude honors. After graduating, he was commissioned in the United States Air Force. He was then assigned to Hill Air Force Base, Utah where he served as the lead engineer on the Paveway III guided munitions program. While at Hill Air Force Base, he earned a Master of Science in Mechanical Engineering at the University of Utah in August of 2010. In September of 2011, he entered the Graduate School of Engineering and Management at the Air Force Institute of Technology where he studied Aeronautical Engineering. Upon graduation he will be assigned to the Air Force Research Laboratory's Combustion Branch at Wright-Patterson Air Force Base, Ohio.

REPORT DOCUMENTATION PAGE

Form Approved
OMB No. 0704–0188

1. REPORT DATE *(DD–MM–YYYY)* 18–09–2014	**2. REPORT TYPE** Doctoral Dissertation	**3. DATES COVERED** *(From — To)* Sep 2011 — Sep 2014

4. TITLE AND SUBTITLE

Convective Heat Transfer with and without Film Cooling in High Temperature, Fuel Rich and Lean Environments

5a. CONTRACT NUMBER

5b. GRANT NUMBER

5c. PROGRAM ELEMENT NUMBER

6. AUTHOR(S)

Nathan J. Greiner, Capt, USAF

5d. PROJECT NUMBER

5e. TASK NUMBER

5f. WORK UNIT NUMBER

7. PERFORMING ORGANIZATION NAME(S) AND ADDRESS(ES)

Air Force Institute of Technology
Graduate School of Engineering and Management (AFIT/EN)
2950 Hobson Way
WPAFB OH 45433-7765

8. PERFORMING ORGANIZATION REPORT NUMBER

AFIT-ENY-DS-14-S-28

9. SPONSORING / MONITORING AGENCY NAME(S) AND ADDRESS(ES)

Dale Shouse (dale.shouse@us.af.mil)
AFRL/RQTC
1790 LOOP RD N
WPAFB, OH 45433-7251

10. SPONSOR/MONITOR'S ACRONYM(S)

AFRL/RQTC

11. SPONSOR/MONITOR'S REPORT NUMBER(S)

12. DISTRIBUTION / AVAILABILITY STATEMENT

DISTRIBUTION STATEMENT A. APPROVED FOR PUBLIC RELEASE; DISTRIBUTION UNLIMITED.

13. SUPPLEMENTARY NOTES

14. ABSTRACT

Modern turbine engines require high turbine inlet temperatures and pressures to maximize thermal efficiency. Increasing the turbine inlet temperature drives higher heat loads on the turbine surfaces. In addition, increasing pressure ratio increases the turbine coolant temperature such that the ability to remove heat decreases. As a result, highly effective external film cooling is required to reduce the heat transfer to turbine surfaces. Testing of film cooling on engine hardware at engine temperatures and pressures can be exceedingly difficult and expensive. Thus, modern studies of film cooling are often performed at near ambient conditions. However, these studies are missing an important aspect in their characterization of film cooling effectiveness. Namely, they do not model effect of thermal property variations that occur within the boundary and film cooling layers at real engine conditions. Also, turbine surfaces can experience significant radiative heat transfer that is not trivial to estimate analytically.

15. SUBJECT TERMS

Variable Properties, Radiative Heat Transfer, Film Cooling, Reacting Film Cooling

16. SECURITY CLASSIFICATION OF:			**17. LIMITATION OF ABSTRACT**	**18. NUMBER OF PAGES**	**19a. NAME OF RESPONSIBLE PERSON**
a. REPORT	**b. ABSTRACT**	**c. THIS PAGE**			Dr. Marc D. Polanka
U	U	U	U	432	**19b. TELEPHONE NUMBER** *(include area code)* (937) 255-3636, x4714; marc.polanka@afit.edu

Standard Form 298 (Rev. 8–98)
Prescribed by ANSI Std. Z39.18